# Novel Mechanical Failure Assessment and Shape Control Methods for Smart Laminated Composite Structures

**by**

**Scott Gohery**


Thesis submitted in fulfillment of the requirement for the degree of

**Doctor of Philosophy (Mechanical Engineering)**

College of Engineering and Science, Victoria University, Australia

August 2017

# ABSTRACT

Laminated composite structures are now commonly adopted in mechanical applications requiring high stiffness-to-weight and strength-to-weight ratios. One of the main disadvantages of using laminated composite members is the difficulty of inspecting their critical-to-failure regions when undergoing critical loads. Piezoelectric materials as sensors and actuators have transformed conventional laminated composite structures into smart-intelligent ones. For instance, piezoelectric sensors can be used to assess the critical mechanical deformation while piezoelectric actuators can be used to induce the stiffness in laminated composite structures. Comprehensive analytical and numerical solutions for the mechanical failure and shape control analysis of smart laminated composite structures under complex loads still remain unavailable.

This thesis presents a systematic development of novel analytical and numerical models for the mechanical failure and shape control of laminated composite structures integrated with piezoelectric sensors and actuators. An experimental setup is also devised to assess the effectiveness of PZT sensors for structural monitoring and mechanical failure prediction of laminated composite structures, and to verify the proposed analytical and numerical models. Effects of various parameters, such as laminated composite structures type and geometry, material properties, complex thermo-electro-mechanical loads, stacking sequence configurations, sensors/actuators size, inclination angles and placements, intensity of electrical voltages, and residual thermal stresses are investigated in detail.

The results of this study provide an improved insight into the fundamental behaviour of smart laminated composite structures and are valuable to mechanical and structural designers. The proposed analytical methods can accurately predict critical mechanical loads, do not require pre-defection function to be predetermined, and can be used for both embedded and bounded piezoelectric actuators for shape control task. The residual thermal stresses effect on shape control task is also considered. In addition, these models can easily be adapted for complex boundary and loading conditions. The proposed numerical models are shown to be efficient, simple, and accurate tools for designing safe smart composite laminated structures.

# DECLARATION

"I, Scott , declare that the PhD thesis entitled 'Novel Mechanical Failure Assessment and Shape Control Methods for Smart Laminated Composite Structures' is no more than 100,000 words in length including quotes and exclusive of tables, figures, appendices, bibliography, references and footnotes. This thesis contains no material that has been submitted previously, in whole or in part, for the award of any other academic degree or diploma. Except where otherwise indicated, this thesis is my own work".

Signature: 

Date: 07/Aug/2017

## ACKNOWLEDGMENTS

The author would like to thank his principal supervisor Associate Professor Dr. Zora Vrcelj for her close supervision, productive discussions and invaluable suggestions throughout the period of this research project.

The research presented in this thesis was conducted in the College of Engineering and Science at Victoria University (2013-2017). The author was supported by the Victoria University International Postgraduate Research Scholarship (VUIPRS), offered by the College of Engineering and Science. This financial support is gratefully acknowledged.

The author would also like to thank all staffs in the College of Engineering and Science and Postgraduate Research Office, his friends and colleagues for their kind assistance and support. I am grateful to staffs of the Victoria University library for their strong support of my enthusiasm to find research articles and reports.

Last, but certainly not the least, I would like to thank my spouse Libby Loh Moi Sin, my father and mother for their support and understanding during my PhD study

## LIST OF PUBLICATIONS

Based on this research work, the candidate has written the following papers, which have been published or resubmitted for publication in various international journals.

### Journal Articles

1) **S. Gohery**, S. Sharifi, Z. Vrcelj, and M. Y. Yahya, "First-ply failure prediction of an unsymmetrical laminated ellipsoidal woven GFRP composite shell with incorporated surface-bounded sensors and internally pressurized," *Compos. Part B Eng*., vol. 77, pp. 502–518, 2015.

2) S. Sharifi, **S. Gohery**, M. Sharifiteshnizi, and Z. Vrcelj, "Numerical and experimental study on mechanical strength of internally pressurized laminated woven composite shells incorporated with surface-bounded sensors," *Compos. Part B Eng*., vol. 94, pp. 224–237, 2016.

3) **S. Gohery**, S. Sharifi, and Z. Vrcelj, "New explicit solution for static shape control of smart laminated cantilever piezo-composite-hybrid plates/beams under thermo-electro-mechanical loads using piezoelectric actuators," *Compos. Struct*., vol. 145, pp. 89–112, 2016.

4) **S. Gohery**, S. Sharifi, and Z. Vrcelj, "A novel explicit solution for twisting control of smart laminated cantilever composite plates/beams using inclined piezoelectric actuators," *Compos. Struct*., vol. 161, pp. 477–504, 2016.

5) **S. Gohery**, S. Sharifi, and Z. Vrcelj, "Quadratic finite element analysis of smart laminated Piezo composite plates induced by MFC actuators," *Smart Mater. Struct*., 2017 (Revised and Resubmitted).

VICTORIA UNIVERSITY
MELBOURNE AUSTRALIA

**PART A:**

**DETAILS OF INCLUDED PAPERS: THESIS BY PUBLICATION**

Please list details of each Paper included in the thesis submission. Copies of published Papers and submitted and/or final draft Paper manuscripts should also be included in the thesis submission

| Item/ Chapter No. | Paper Title | Publication Status (e.g. published, accepted for publication, to be revised and resubmitted, currently under review, unsubmitted but proposed to be submitted) | Publication Title and Details (e.g. date published, impact factor etc.) |
|---|---|---|---|
| 3 | First-ply failure prediction of an unsymmetrical laminated ellipsoidal woven GFRP composite shell with incorporated surface-bounded sensors and internally pressurized | Published | Composites Part B: Engineering (2015), 502-518<br>Journal Ranking: Q1<br>Impact Factor: 3.850 |
| 3 | Numerical and experimental study on mechanical strength of internally pressurized laminated woven composite shells incorporated with surface-bounded sensors | Published | Composites Part B: Engineering (2016) 224-237<br>Journal Ranking: Q1<br>Impact Factor: 3.850 |
| 4 | New explicit solution for static shape control of smart laminated cantilever piezo-composite-hybrid plates/beams under thermo-electro-mechanical loads using piezoelectric actuators | Published | Composite Structures: Engineering (2016), 81-112<br>Journal Ranking: Q1<br>Impact Factor: 3.853 |
| 4 | A novel explicit solution for twisting control of smart laminated cantilever composite plates/beams using inclined piezoelectric actuators | Published | Composite Structures: Engineering (2016), 477-504<br>Journal Ranking: Q1<br>Impact Factor: 3.853 |
| 5 | Quadratic finite element analysis of smart laminated composite plates induced by MFC actuators | Revised and Resubmitted | Smart Materials and Structures<br>Journal Ranking: Q1<br>Impact Factor: 2.769 |
| | | | |

**Declaration by** [candidate name] Scott Gohery **Signature:** [redacted] **Date:** 30/03/2017

## CONTENTS

**Page No.**

# Chapter 1

# INTRODUCTION

## 1.1. COMPOSITE LAMINATES

A composite is a structure which consists of two or more combined constituents, combined at the macroscopic level. These levels are generally categorized as reinforcing phase and matrix phase and the combined constituents are not soluble in each other. The reinforcing phase may include fibres, particles, or flakes. The matrix phase may include polymers, metals, and ceramics. Fibre-reinforced composites consist of high-strength fibres embedded in a matrix with different material properties. In this form, both fibres and matrix are not soluble in each other but retain their chemical and physical material properties [1,2]. However, the combined form of these phases can form a combination of properties, unachievable with either of the constituents acting alone. Basically, fibres are designated to carry out loads and matrix is aimed at keeping and arranging the fibres in a desired orientation and location. Other roles of the matrix in a fibre-reinforced

composite material can be described as transferring load between fibres, and protecting fibres from environmental damages, such as humidity. Therefore, even though the fibres have the main role in keeping fibres intact, matrix plays an important function in a fibre-reinforced composite material [1,2]. Fig.1.1 illustrates the various types of composite materials.

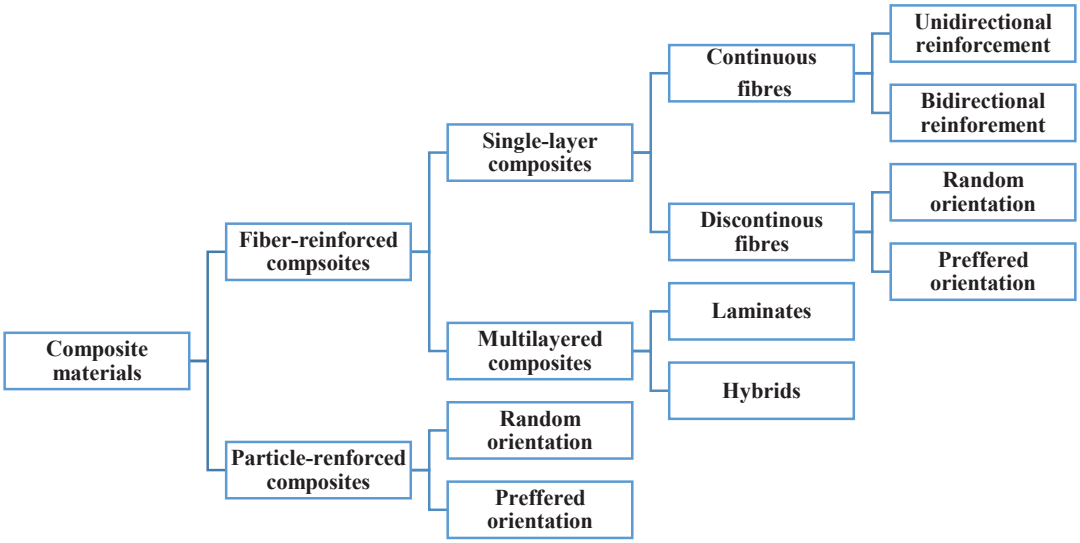


**Fig.1.1** Types of composite materials [1,2]

Various types of fibres are used in industry such as glass, carbon, Kelver-49. However, others types of fibres such as boron, aluminium oxide, and silicon carbide are occasionally used. The greatest portion of commercial application accounts for glass and carbon fibres reinforced in polymer matrix which are known as graphite fibre reinforced polymer (GFRP) and carbon fibre reinforced polymer (CFRP) composites, respectively. This class of composite materials is generally made of thin layers of fibres and matrix, consolidated into a preferred thickness. In composite manufacturing

process, all fibres are incorporated into a matrix. The matrix can be made of a variety of materials such as metal, polymer, or ceramic [1,2].

A laminate layup consists of multiple fibre-reinforced composite layers. Each layer has different thickness and fibre angle orientation, as depicted in Fig.1.2. The angle between fibre directions and global coordinate of each layer is called the winding angle. Each layer can be selected to have different materials properties. In addition, different material properties are achieved for various orientations at each layer. However, the highest material elasticity module accounts for the fibre angle orientation denoted longitudinal (*L*). The orientation perpendicular to the fibre direction is called transverse (*T*). *L* and *T* coordinates are so-called local material orientation. Composites local material orientation plays an important function for optimum design. For instance, different layers stacking sequence configuration as well as each layer winding angle can be controlled in order to generate a wide range of mechanical and physical properties of a composite laminate [1-3].

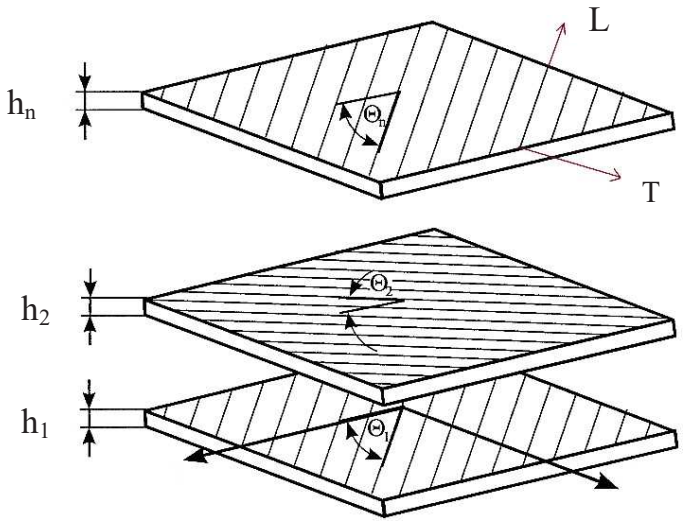


**Fig.1.2** Schematic of composite laminate and local material orientations *LT*.

The function of fibres is to produce high strength and stiffness at the lowest possible weight while the function of matrix is to maintain the shape of the structure, hold the fibres together, transfer stresses from fibre to fibre, protect fibres and carry interlaminate shear [1-3]. Industrial and commercial applications of fibre-reinforced composite materials are numerous, particularly GFRP and CFRP composites. The most common applications include: marine, civil, mechanical, and aerospace engineering, oil and gas platforms, pressure vessels manufacturing, military air force, sport science, and automobile industry [2].

The most common application has been reported to be in the aerospace engineering discipline, since this industry is looking for light-weight materials to reduce fuel consumptions per passenger [4]. As an example, nearly fifty percent of the total materials used in the structure of Boeing-787 accounts for CFRP and GFRP composites, as illustrated in Fig.1.3 [5].

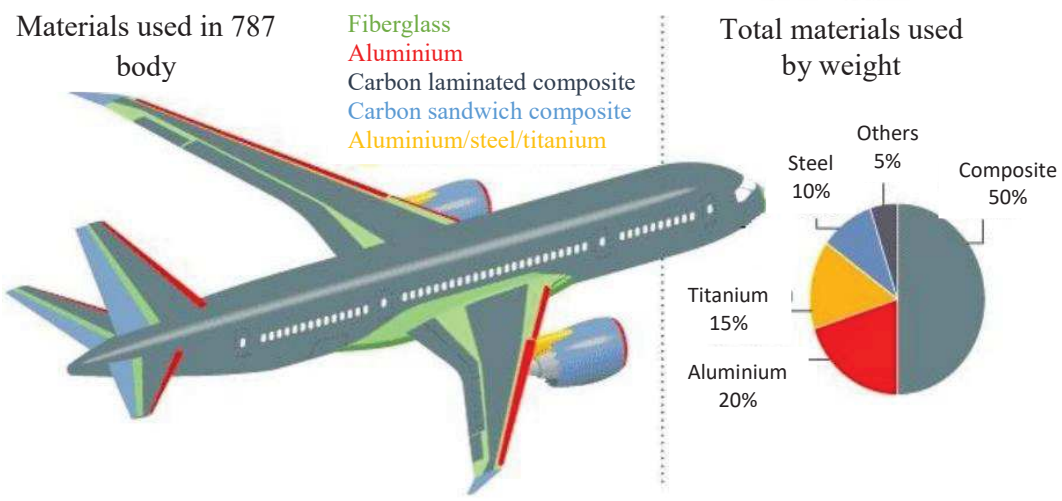


**Fig.1.3** Use of CFRP and GFRP composites in the structure of Boeing 787 Dream liner [5].

## 1.2. PIEZOELECTRIC MATERIALS

Piezoelectric materials have recently been increasingly used in advanced structures for transforming them into “smart” or “adaptive” structures. The examples of smart materials can be piezoelectric materials, shape memory alloys (SMAs), electrostrictive materials, and electroheological fluids [3].

The ancient Greeks were first to discover this class of materials, realizing their electrical features, particularly development of piezoelectric static charges when rubbed. The word “piezoelectricity” was named by Jacques and Pierre Curie more than century ago. The relationship between material structures and piezoelectricity was rigorously investigated by Voigt in 1894. According to his theory, applying an electric voltage across a piezoelectric material causes a geometric change to occur, known as piezoelectric effect [3].

Among smart materials, the use of piezoelectric materials, as either sensors or actuators, has been significant. Piezoelectric sensors are used to measure the physical quantities intensity such as measuring the amount of stress and strain in structures. Piezoelectric actuators, in contrast, are used to deliberately cause strain in a structure by applying voltage. Both piezoelectric sensors and actuators are reincorporated into the structure in the form of either embedded or bounded [3]. For example, Rochelle salt, tourmaline, quartz, and barium titanate exhibit a piezoelectric effect. A piezoelectric transducer was first proposed by Langevin in early 1918 during World War II for application in sensors. PZT was discovered by researchers at Massachusetts Institute of Technology

(MIT) prior to World War II. In 1969, the polyvinylidene fluoride (PVDF) was determined to be highly piezoelectric by Kawai [3]. The schematic of piezoelectric response in piezoelectric materials is illustrated in Fig.1.4. According to Fig.1.4, it can be observed that the difference in average location of the positive and negative charges results in piezoelectric response.

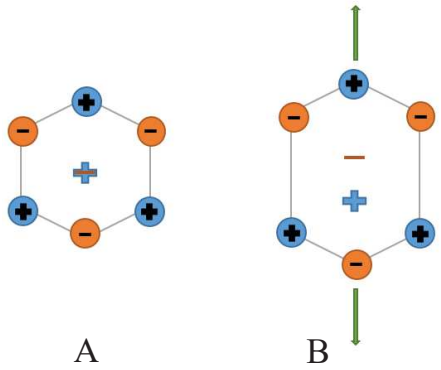


**Fig.1.4** A crystal material in A) undeformed state and B) deformed state.

In piezoelectric materials, displacements and force changes range can be precisely measured. One of the advantages of using piezoelectric materials is that if manufactured in rugged solid-state, they can operate under most harsh environmental conditions like dirt, oil, and most chemical atmospheres. They have an accurate performance over a wide temperature range and resist damage from severe shock and/or vibration. Piezoelectricity exists in some naturally occurring crystals such as quartz and rochelle salt [6]. However, the bulk of the piezoelectric materials used for commercial sensing applications come from synthetic polycrystalline ferroelectric ceramics, such as PZT, which is used in the current research. Compared to single crystals, ceramics generally have the advantage of high strength and easy manufacturing, particularly when made into complex shapes and large area pieces [6]. Piezoelectric materials have great applications in resonators, crystal and ceramic filters, delay lines, watches, SAW filters,

underwater acoustic devices, ultrasonic transducers, underwater speakers and microphones, diagnostic acoustic devices, and fish-finders. Moreover, high-voltage generation for ignition and piezoelectric transformers exemplifies one of the applications of piezoelectric materials [7,8].

In recent years, piezoelectric actuators have played an important function in precision instrumentation, manufacturing, and industrial engineering. Piezoelectric device applications include: pressure and vibration measurement, stress and strain gages, acceleration measurement, position sensors, and impact detectors. In all cases, most of these materials can convert mechanical strain into electrical charge when used as sensors, and do the opposite when used as actuators. Using piezoelectric materials as either sensors or actuators represents direct and converse piezoelectric effect, respectively [8,9]. In summary, technical applications of piezoelectricity can topically be categorized as shown in Fig.1.5.

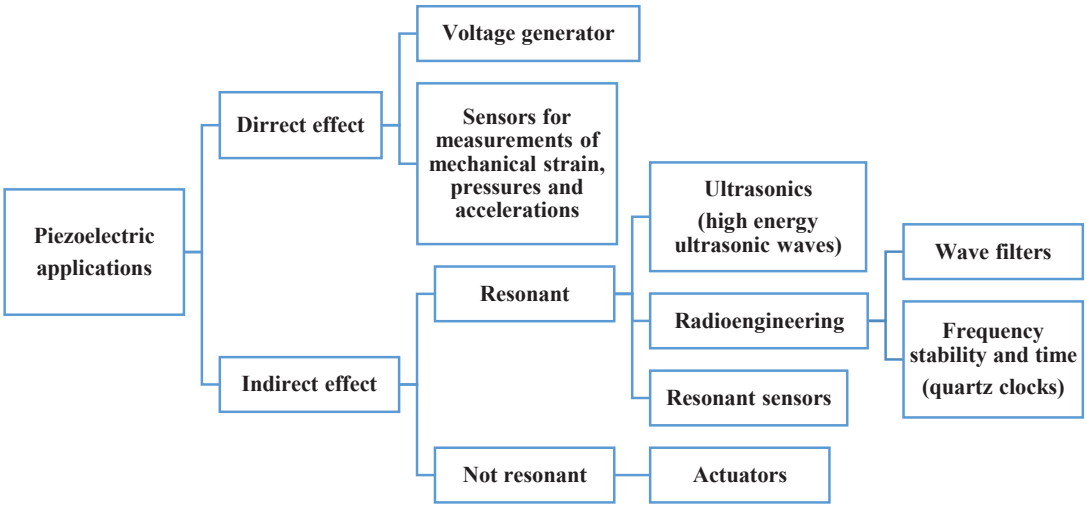


**Fig.1.5** Technical applications of piezoelectricity [7]

## 1.3. SMART LAMINATED COMPOSITE STRUCTURES

A typical smart composite laminate is comprised of fibre-reinforced composite lamination (host structure) with a variety of embedded sensors and actuators to monitor the performance of the structure. The advantage of incorporating these special types of materials into the structure is that the sensing and actuating mechanism becomes part of the structure by sensing and actuating strains directly. Material damage could occur due to environmental conditions or mechanical loads and replacing the entire component is not cost-effective in many cases. Extensive research was undertaken on the methods of repairing the composite structures through robust and reliable structural bounded procedures in order to restore the damaged composite components [10]. There are also a few studies on damage, repair and failure control of advanced composite structures using piezoelectric materials [11]. The main applications of smart laminated composite structures are categorized in Fig.1.6.

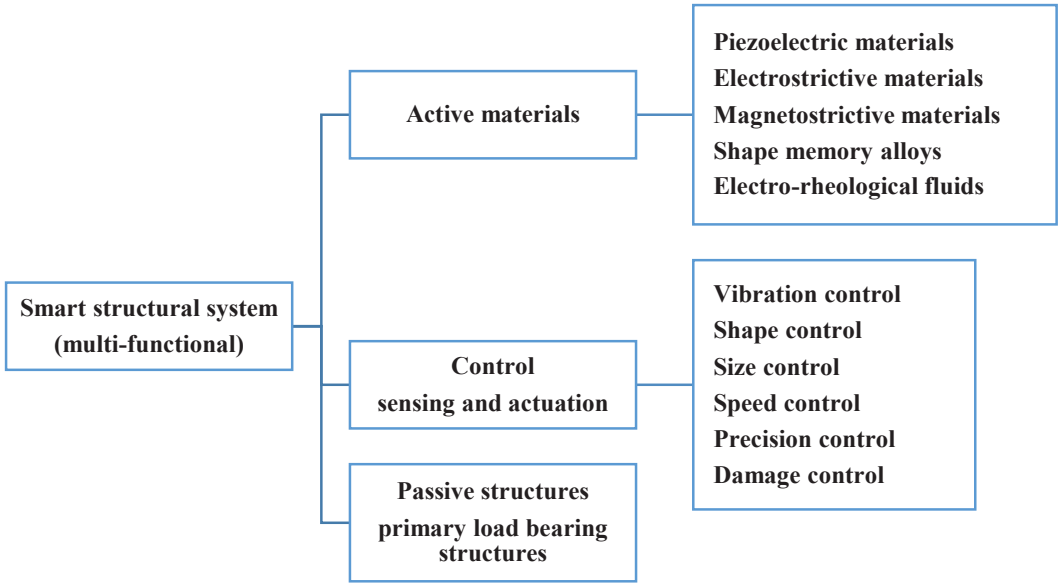


**Fig.1.6** Components of a smart composite structural system [12]

The phrase smart structural system refers to a wide variety of active material and passive structural systems. For instance, a sufficiently general system is a composite (beam, plate, shell, or any other fundamental form) with embedded or surface mounted piezoelectric or electrostrictive patches, or even layers of active materials in a laminated system [8,13].

## 1.4. RESEARCH SIGNIFICANCE

Over recent decades, piezoelectric sensors and actuators have been extensively used for monitoring the stress/strains or controlling the shape deformation, and vibration, in the adaptive structure [14]. However, it is noticeable that the exact solutions are not possible for anisotropic problems with general boundary conditions and arbitrary loadings. The exact solutions for simple cases are important to verify the numerical solutions for more general problems. As to date, there are very limited analytical, experimental and numerical studies which use sensors and actuators to predict the critical mechanical deformation, failure and shape control of laminate composite hybrid structures [15]. There are numerous internal and external factors which influence the structural shape deformation of laminated composite hybrid structures [16]. Some of these factors can be categorized as follows:

- laminated composite hybrid (host) structure stacking sequence configuration;
- effect of bending-twisting coupling due to host structures unsymmetrical layup;
- material properties and geometry of host structure;
- performance of sensors/actuators due to residual thermal stresses;

- boundary conditions prescribed to host structure; and
- sensors/actuators type, size, inclination angle, material axis, and placement.

Furthermore, the shape and failure control analysis of this class of composite structures are limited to experimental studies and numerical analysis, though approximate solutions have been adapted as part of analytical investigations [16]. According to the studies available in the literature, smart laminated composite structures were only subjected to the simple loading conditions [15] while in reality the combination of arbitrary loads like thermo-electro-mechanical loads, are applied. Residual thermal stresses can significantly affect the shape and failure of smart laminated composite structures and, yet to date there is no evidence of any analytical solution for assessing piezoelectric actuators shape control performance in a thermal environment. The variation of thermo-elastic properties with temperature should be carefully modelled, especially when transverse behaviour of piezoelectric actuators are deemed critical [17]. Therefore, the current setback is addressed in this study by developing analytical models and performing comprehensive parametric studies.

## 1.5. AIMS OF THE RESEARCH WORK

The main aim of this research work is to obtain novel explicit and numerical solutions to predict the critical mechanical deformation and shape control of laminated composite hybrid structures. The composite hybrid structures adopted in this research include beams, plates and shells. Various boundary conditions and complex loads are also considered. The aims are listed as follows:

- Develop an analytical solution using the linear shell theory to predict the critical mechanical deformations and possible failure in laminated composite shells incorporated with surface-bounded PZT sensors.

- Develop a series of three-dimensional (3D) Finite Element (FE) models using ABAQUS [18] to predict the critical mechanical deformations and possible failure in laminated composite shells using surface-bounded PZT sensors.

- Devise an experimental setup in which surface bounded PZT sensors are used to measure the critical mechanical deformations of laminated composite shells.

- Develop an exact solution using the linear plate and piezoelectricity theory for the bending control of laminated composite hybrid plates/beams in thermal environment.

- Develop an exact solution using the linear plate and piezoelectricity theory for the twisting control of laminated composite hybrid plates/beams.

- Develop a series of quadratic two-dimensional (2D) linear FE formulations and a 3D FE model analysis using ABAQUS for bending-twisting control of laminated composite plates/beams induced by MFC actuators.

- Compare the results and propose the design recommendations.

## 1.6. LAYOUT OF THE THESIS

This study is composed of six chapters. An introduction to laminated fibre-reinforced composite structures, piezoelectric materials, and smart structures is provided in chapter one. An extensive literature review on general classifications and main categories of composite laminates, piezoelectric materials, and smart laminated composite structures is then performed in chapter 2. In this chapter, the use of sensor strain gauges on health monitoring of laminated composite structures based on experimental, numerical and analytical approaches is reviewed. Subsequently, a comprehensive literature is devoted to the mechanical shape control of laminated composite hybrid structures integrated with piezoelectric actuators. The limitations of the available studies and the need for further research are discussed.

In Chapter 3, the mechanical shape deformation and possible failure of the internally pressurized laminated woven GFRP composite shells integrated with surface-bounded PZT strain gauge sensors are investigated. Various types of shells (hemispherical, ellipsoidal, and torispherical) are selected as analysis models. The exact analytical solution and 3D non-linear FE simulation are adopted to obtain the critical mechanical and failure strain/displacements. In analytical study, the linear interpolation technique is employed to interpolate the critical points conveniently. The shells boundary is fixed at its end. Tsai-Wu failure criterion [19] is adopted as the composite failure design factor. The analytical and numerical results, including critical internal pressure and strains in the global directions, are validated with the experimental results for some arbitrarily selected points on the shells surface along meridian axis. Manufacturing of laminated

ellipsoidal composite shells is performed by using the Vacuum Infusion Process (VIP), a method commonly adopted for the fabrication of laminated composite shells. Surface-bounded sensors are installed on the shells surface to measure the strain values after the internal pressure is applied. Subsequently, the effect of various parameters including thickness, aspect ratio, and stacking sequence on the shape deformation and failure of the laminated woven GFRP composite shells are investigated and the critical mechanical factors to avoid failure are determined. The language of technical computing (MATLAB) is used for the analytical investigation component and ABAQUS is adopted for the numerical simulations.

In Chapter 4, two novel explicit analytical solutions are proposed for obtaining static bending and twisting deformation and optimal shape control of laminated cantilever piezo composite hybrid plates and beams using the non-angled and inclined piezoelectric actuators. The linear piezoelectricity and plate theories are adapted for theanalysis. A novel double integral multivariable Fourier transformation method combined with discretised higher order partial differential unit step function equations are employed. The effect of various parameters including arbitrary loads such as non-uniform thermal stresses, electrical and mechanical loads, layup thickness, piezoelectric actuators size and placement, stacking sequence, and geometrical dimension is investigated. The results are then compared with some published benchmark results and a series of simple, accurate and robust 3D nonlinear FE analysis models developed by using ABAQUS and MATLAB.

In Chapter 5, a quadratic 2D FE formulation using first order shear deformation theory (FOSDT) is developed to predict the linear strain-displacement static deformation in the laminated piezo composite plates induced by MFC actuators. Cantilever and simply-supported laminated piezo composite plates are the focus of this study. FOSDT is adapted from the Reissner-Mindlin plate theory [20]. An eight-node quadratic shell element with five degrees of freedom is introduced for the FE formulation. Two types of MFC actuators are investigated: 1) MFC-$d_{31}$ and 2) MFC-$d_{33}$, which differ in their actuation forces. Subsequently, the electro-mechanically coupled quadratic FE model is compared with the results derived by the 3D FE simulation software package ABAQUS. MATLAB is also adopted to derive the solution of the quadratic FE equations. Furthermore, due to the lack of comprehensive and in-depth research on MFC materials, the effect of various parameters such as boundary conditions, laminate stacking sequence configuration, unsymmetrical layup, electrical voltage intensity, MFC type, and piezoelectric fibre orientation on shape deformation of laminated composite structures induced by MFC actuators is investigated herein.

Important conclusions drawn from the current study are presented in Chapter 6. Novel contributions in this research work are summarized. Recommendations for further research in this field are also summarised in this chapter.

# Chapter 2

# LITERATURE REVIEW

## 2.1. INTRODUCTION

The structural health monitoring and shape control of laminated composite hybrid structures have recently become popular research topics. Numerous research and development work has been undertaken in this field in the last couple of years. This chapter covers the extensive literature in the area of structural health monitoring and shape control of laminated composite hybrid structures through analytical, numerical, and experimental approaches [21,22].

The incorporation of sensors and actuators with laminated composite structures creates a smart-intelligent material system with broad engineering applications. For instance, sensors can be used to predict the critical strain/displacements in a mechanical system under external loads and also to predict the critical mechanical factors in order to

prevent mechanical failure [19]. However, a sensor can act as an actuator by applying the direct electrical voltage to it and ultimately inducing the elastic stiffness of a mechanical system [23].

The literature review given in the following section focusses on general characteristics and main classifications of fibre-reinforced composite laminates and piezoelectric materials. Subsequently, numerous old and recent approaches in experimental, numerical and analytical analysis of smart laminated piezo composite hybrid structures incorporated with sensors and actuators are considered.

## 2.2. GENERAL CHARACTERISTICS OF FIBER-REINFORCED COMPOSITE LAMINATES

Fibre-reinforced composite laminates deliver a combination of modulus and strength, particularly composite laminates with polymer-based matrix such as GFRP and CFRP. The advantages of using composite laminates overweight those found in traditional metallic materials since low density in composite materials can result in superior modulus-weight and strength-weight ratios. In addition, fatigue strength and fatigue damage tolerance of numerous laminated fibre-reinforced composites are considerably high. The use of polymer-based matrix in this type of composite materials makes them even more ideal for adaptation in aerospace, automotive, and marine industries. The advantages and disadvantages of laminated fibre-reinforced composite materials are categorized as below [2,3]:

*Advantages:*

- The specific strength and stiffness properties are much higher than those of commonly used metals which make them highly desirable for design of advanced light-weight structures.
- Fibre-reinforced composite laminates can be assembled from unidirectional layers whose angular directions correspond to those of the principle load paths.
- Integral construction methods are possible with few parts of near final shape and therefore few joints.

*Disadvantages:*

- Cost of raw material and fabrication is high.
- Low transverse properties.
- Matrix is weak, has low toughness, and can be easily attacked by environment.
- Difficult to reuse and recycle.
- Difficult to analyse.
- Progress is hampered by overly conservative user attitude.

## 2.3. MECHANICS OF FIBRE-REINFORCED COMPOSITE LAMINATES

Stress, strain, and failure of structures subjected to thermal, electrical, and mechanical loads are studied in the field of mechanics of materials. There are common studies on

mechanics of isotropic materials such as steel and aluminium. This class of material is considered homogeneous since its material properties is content in all directions.

On the other hand, composite materials have more complex structures due to different material properties at different orientations. Therefore, analytical evaluation of material principles of fibre-reinforced composite laminates is quite complex. The mechanics of fibre-reinforced composite materials can be categorized as follows [1-3]:

1. *The micro mechanics level*: The interaction of constituent materials on a microscopic scale is examined. Thus, the equations describing the thermal and elastic behaviour of a lamina are based on micromechanics principles

2. *The macro mechanics level*: The response of fibre-reinforced composite materials subjected to various loadings such as electrical, thermal, and mechanical loads, is examined on the macroscopic scale. Based on this analysis, the fibre reinforced lamina is considered as non-homogeneous with orthotropic elasticity characterization used for stress, strain, and failure calculations.

Considering the interactions between fibres and matrix in a fibre-reinforced composite lamina subjected to compression and tensile loadings, some basic assumptions for simplification of theoretical analysis are required as follows [12]:

- Fibres distribution throughout the matrix is uniform.
- There is a perfect bounding between fibres and matrix.

- Fibres dislocations and disarrangements through the matrix are avoided.
- The matrix is perfectly fabricated with no voids and impurity.
- The loads applied are either perpendicular or parallel to the fibres orientation.
- The lamina is not initially pre-stressed.
- The matrix and fibres behave linearly within elastic domain.

Fig.2.1 indicates the stress-strain curve of a fibre-reinforced composite lamina when subjected to longitudinal tensile loading. The state of fibres, matrix, and composite lamina are illustrated within elastic domain. Based on the basic assumption described above, the elasticity module of fibres, matrix, and composite lamina is linear within elastic zone.

## 2.4. FIBER-RENFORCED COMPOSITE LAMINATE FAILURE PREDICTION

The comparison of stresses (or strains) due to applied loads with the allowable strength (or strain capacity) of a structure must be considered for structural engineering design. Various factors may affect the structural failure of materials such as electrical, mechanical and thermal stress/strains resulting in fracture and raptures in the host structures [24].

Some appropriate failure criteria may be used based on the type of loads applied on the structure. The loading system can be either biaxial or multi-axial. There are various failure criteria used to assess the failure strength of the isotropic materials exhibiting yielding subjected to various loads.

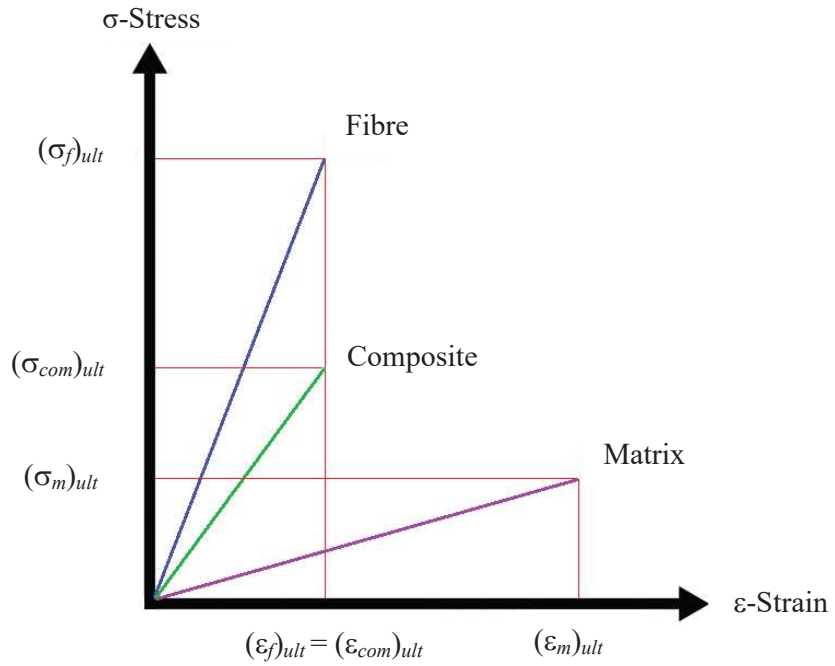


**Fig.2.1** Stress-strain curve for a composite laminate under uniaxial tensile load along fibres [2]

For instance, mild steel and aluminium alloy are considered failed when their stress (or strain) values reach the yielding point due to external loads. Maximum shear stress theory and the distortional energy theory (Von Mises yield criterion) are commonly used for isotropic materials design against yielding [2].

However, it must be taken into consideration that composite materials are not isotropic and exhibit different properties in different directions. Therefore, some failure theories were developed for orthotropic (non-isotropic) materials where the conventional failure theories used for isotropic materials are not [1].

For the failure analysis of laminated fibre-reinforced composite materials, the plane stress condition of a general orthotropic lamina containing unidirectional fibres is

considered (see Fig.1.2). Four so-called elastic constants are required to define a fibre-reinforced lamina elastic characteristics. A lamina elastic constants include longitudinal elastic module ($E_{11}$), transverse elastic module ($E_{22}$), in-plane Poisson's ratio ($\upsilon_{12}$), and in-plane shear module ($G_{12}$).

However, for failure prediction, five strength values are also required to be added and these values are named longitudinal tensile strength, transverse tensile strength, longitudinal compressive strength, transverse compressive strength, and in-plane shear strength, respectively [2,19].

Experimental procedures are required to measure fibre-reinforced lamina's strength properties. The direction of shear stress is independent from its strength in the principle material directions while there is a relationship between longitudinal and transverse strengths and the direction of applied loads named tensile or compressive. Numerous phenomenological theories have been introduced for the prediction of unidirectional lamina under plane-stress conditions. These theories are categorized as [2]:

- Maximum stress theory
- Maximum strain theory
- The Azzi-Tsai-Hill failure theory
- Tsai-Wu theory

The maximum stress theory is considered the simplest one of all four. The maximum strain theory and the Azzi-Tsai-Hill are more commonly used despite the Tsai-Wu

theory being more generalized since the direction of applied loads in longitudinal and transverse orientations is taken into consideration in the proposed formula. To use these theories, applied stress (or strains) in the global material orientations are first transformed into principal (local) material orientations and subsequently these values are substituted into the proposed failure theories. Eventually, the condition of each failure theory should be satisfied to avoid failure in the fibre-reinforced lamina.

## 2.5. GENERAL CHARACTRISCTIS OF PIEZOELECTRIC MATERIALS

A piezoelectric material can either elongate or shrink in different orientations depending on polling direction and material orientation. Conversely, if a piezoelectric material is stressed due to mechanical loadings such as tensile, compression, and shear load, an electrical voltage will be released known as a direct piezoelectric effect. Thus, piezoelectric materials can be used as actuators or sensor for a structure and could serve as both at different times [6].

Fig.2.2 shows both, the converse and direct piezoelectric effects. A piezoelectric element dimensions change when stressed electrically by applying the electrical voltage through its crystals. In contrast, when subjected to mechanical loading, it releases an electrical charge. However, a voltage associated with the electrical charge appears if the electrodes are not short-circuited [3,12]. Piezoelectricity can be studied using quartz crystals. A plate cut at right angle to the X- coordinate axis and called X-cut is considered. It is assumed that the plate thickness is negligible since it is significantly smaller than those in other directions. This plate is subjected to pressure parallel with the thickness. The polarization $P_1$ is parallel to the thickness and proportional to the

stress $T_{11} = F/A$ since the propositional force (size) $F$ is used. Therefore, the piezoelectric polarization charge on electrodes covering the major forces $A$ is proportional to the force resulting in straining the plate [9]. If tension is applied to a quartz plate, the signs of pressure and electric polarization both reverse. When an electric filed $E$ is applied along the plate thickness, a deformation in the quartz plate is noticed. The sign of strain $S_{11}$ varies when the field polarity is reversed. The direct piezoelectric effect is described as shown in Eq.2.1. Conversely, a strain $S_{11}$ is produced when an external electrical filed $E_1$ is applied. It is described as the converse piezoelectric effect as shown in Eq.2.2 [7].

$$P_1 = d_{111} T_{11} \tag{2.1}$$

$$S_{11} = d_{111} E_1 \tag{2.2}$$

where, $P_1$ is the polarization vector component, $T_{11}$ is the stress tensor component, $d_{111}$ is the piezoelectric coefficient, and $E_1$ is an external electrical field. Material properties in piezoelectric materials can be modelled by the constitutive equations in the stress charge form as stated in Eqs.2.3 and 2.4, respectively [25].

$$\sigma = \overline{C}\varepsilon - eE \tag{2.3}$$

$$D = e^T \varepsilon + kE \tag{2.4}$$

where $\overline{C}$ is the elastic material matrix, $e$ and $e^T$ are the piezoelectric material matrix and its transpose, respectively, $k$ is the permittivity matrix, $e$ is the strain and $E$ is the electrical field [25].

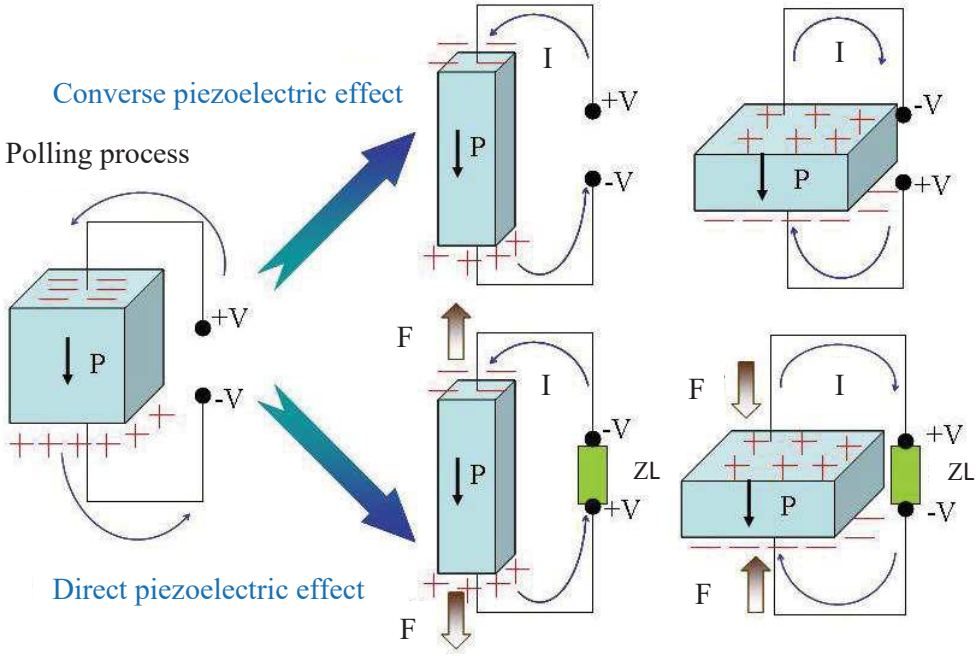


**Fig.2.2** Schematic of piezoelectric effects after poling process [26]

The actuation and sensing science has developed rapidly since the introduction of smart structures technologies. The ability to conform to the curved surface, anisotropic actuation and sensing, and the ability to cover the large area have allowed active fibre composites (AFCs) and MFCs to be perfectly bounded to or integrated into composite laminations (host structures). The development of AFCs and MFCs has extended the applications of piezo-composites in comparison with the piezoelectric system. AFCs and MFCs have recently been adopted for engineering applications such as vibration control, energy harvesting, structural health monitoring and morphing, and shape control [27-37]:

Various engineering fields such as aerospace, civil, acoustic, semiconductor production, information, and sports engineering have benefited from the use of piezoelectric

damping system for controlling the structural vibration. Active and passive damping systems have been developed by engineers. Among various types of piezoelectric materials, MFCs proved to be ideal for a variety of vibrational and noise control in composite structures [27,28,38].

### 2.5.1. Piezoelectric Fibre Composites (PFCs)

Smart materials and structures filed is one of the emerging and rapidly developing fields over the past few decades. Among this generation of materials, piezoelectric materials have received the most interest. Monolithic piezoceramic wafer is one of the commonly used typical piezoelectric materials for actuation and sensing in numerous engineering applications in which the electrical filed is applied through surface electrodes. However, there were some problems with this type of piezoelectric materials such as abrupt breakage during handling and bonding producers since they are naturally brittle. In addition, it is difficult to use them for structural shape controls due to their stiff mechanical properties. Additional mass is another major problem which prevented them from being used in light-weight and flexible structures. Thus, a new class of piezoelectric materials is required for wider applications such as controlling the large deflections for the purpose of shape-changing applications, particularly in objects with irregularity and curved shaped surfaces [9].

PFCs were finally developed by researchers motivated to solve the aforementioned problems. They have orthotropic material properties due to unidirectionally aligned piezoelectric fibres with circular cross-section. The fibres are impregnated into a resin

matrix system to boost PFCs properties when sharing the mechanical load. PFCs have novel structures consisting of fibres made of piezoceramics embedded in polymer matrix. PFCs was later upgraded to interdigitated electrode piezoelectric fibre composites (IDEPFCs) which is also referred to as AFCs in order to increase the strain output, directional actuation, flexibility, and durability [39,40,41].

### 2.5.2. General Characteristics of AFCs

Among PFCs, active fibre composites (AFCs) and MFCs as shown in Fig.2.3 are more popular due to their higher and flexible industrial applications [9,20]. AFCs were first developed by the laboratory of active materials and structures at MIT University, USA. To provide in-plane actuation, monolayer of aligned, continuous unidirectional piezoceramic fibres was embedded in polymer matrix. Much of the actuation capability of the bulk ceramic accounts for piezoceramic fibres with higher strength than monolithic form since flaws have decreased volume fraction. The polymer matrix plays an important function in providing efficient path for load sharing among fibres, transferring the stress around broken fibres when the damage occurs since the piezoelectric fibres have brittle nature with low mechanical strains [20].

Thus, polymer matrix can contribute to increase the mechanical strength of AFCs by adjusting the fibres and preventing crack propagating in a fibre. Thus, AFCs represent improved reliability and flexible structural properties, particularly at macroscopic and catastrophic damages compared with conventional piezoelectric wafers. Moreover, the polymer matrix gives flexible properties to AFCs, allowing it to be easily embedded or

bounded to the curved structures. Embedded piezoelectric fibres are sandwiched between laminas of the film made of the polyimide with a conductive electrode pattern printed in the inner surface. The use of the interdigitated electrode (IDE) results in AFCs to be superior than other conventional piezoelectric materials, leading to anisotropic actuation. AFCs have great applications in numerous fields such as morphing, vibration control, and structural health monitoring [20]. Despite the great application of AFCs in many engineering fields, there are still some disadvantages of using this class of PFCs. Some negative factors influencing AFCs performance have been determined. For instance, the difficulty handling piezoelectric fibres when assembled is considered as one of the main disadvantages of AFC technology.

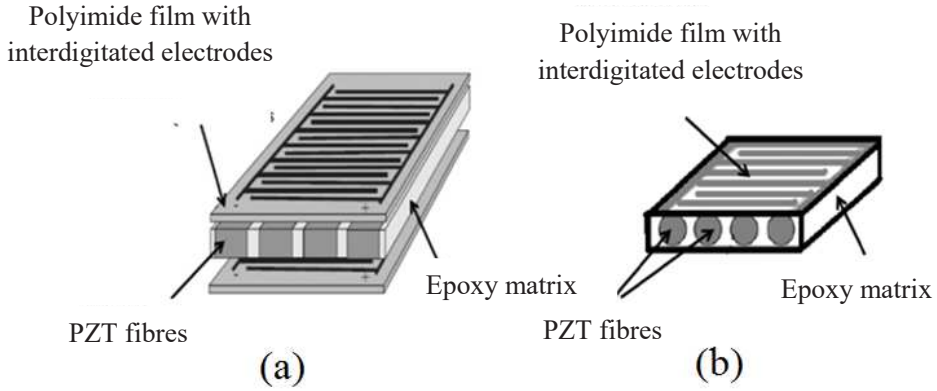


**Fig.2.3** The schematics of PFCTs: (a) MFC [42] and (b) AFC [20]

AFCs fibres have circular-shaped characteristics with diameters of 100-250$\mu m$. The process of aligning the fine fibres to form the piezoelectric monolayers is generally carried out manually, which often negatively affects the assembly process. For example, fibres may be aligned poorly with possible broken patterns. Manual assembly process also leads to the higher manufacturing costs as well as performing complex procedures.

One of the main problems faced during the manufacturing of AFCs is the difficulty to remove the air bubbles completely during assembly of fibres and matrix even after the vacuum process is performed. This phenomena can lead to electrical failure of AFCs [9].

Furthermore, AFCs structure itself is a disadvantage since it negatively affects AFCs performance. Firstly, the driving electrical field requires high electrical voltage. The driving electrical field is primarily determined by the spacing between the IDE fingers. This results in AFC to be impractical in numerous realistic engineering applications. Secondly, there is a low permittivity matrix due to the small contact area between IDE finger and the circular cross-sectional fibre. The matrix between fibres and the electrode fingers results in both higher driving voltage and accumulation of the most of driving electrical field. This factor leads to insufficient and weakened transfer of the electrical field into the piezoelectric fibres in AFCs [9,43,44]. The schematic of an AFC structure including its cross-section is illustrated in Fig.2.4.

Therefore, the NASA developed MFC actuators whose piezoelectric fibres have rectangular cross sectional shape. All fibres are surrounded by polymer matrix. The other components of MFCs are protective and electrode layers bounded to piezoelectric fibres. MFC materials are composed of seven active layers, two electrodes, two kapton and two acrylic layers [20]. AFCs are also more responsive than conventional electrodes. Developed by the NASA-Langley Research Centre, MFC actuators and sensors present superior quality among AFCs and have higher performance and response. They also have easier manufacturing process in comparison with AFCs [45].

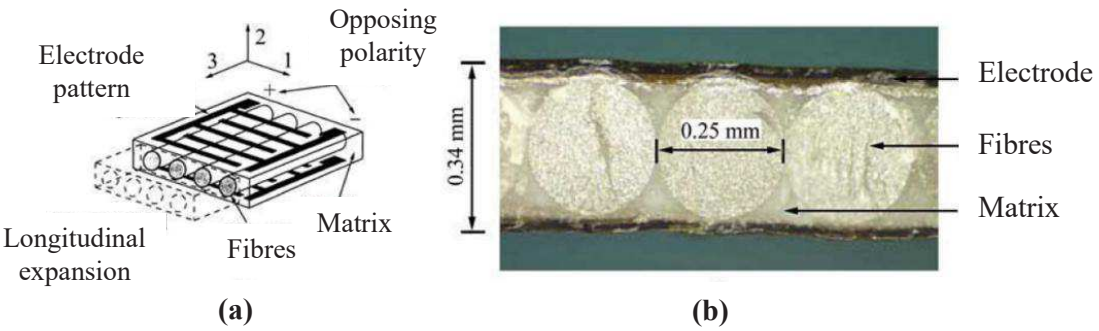


**Fig.2.4** Schematic structure (a) [9,43] and cross section (b) of an AFC [9,44]

### 2.5.3. General Characteristics of MFCs

MFCs were first developed at the NASA Langley research Centre [16]. AFCs and MFCs have the same primary constituents. They both consist of IDE, piezoelectric fibres, and polymer matrix. However, MFCs represent the most advantageous features of AFCs such as high energy density, durability, conformability, and directional actuation. The main difference is noticed in the shape of cross-sectional fibres as rectangular cross-sectional fibres account for MFCs and circular cross-sectional fibres, in contrast, account for AFCs. Furthermore, fibres are embedded in a thermosetting matrix in MFC [46]. The schematic of MFC structure including its cross-sectional view is illustrated in Fig.2.5.

In manufacturing of MFC, the piezoelectric wafers are fist machined to fabricate the piezo-fibre sheets using a so-called method of dicing. This is a reputable and precise manufacturing process of MFC devices. The piezo-fibre sheets can be easily handled compared with individual fibres, leading the piezoelectric fibres to be accurately aligned during assembly process. Precise group handling of fibres results in lower production cost of MFC device. The rectangular shape of fibres leads to the maximum and direct

contact with electrode fingers and conclusively most efficient transfer of electrical fields into the fibres. Furthermore, the volume fraction of MFCs is more than AFCs since there is a restriction in AFCs fibre geometry. This factor can lead to improved stiffness and strength of MFCs compared with AFCs [47].

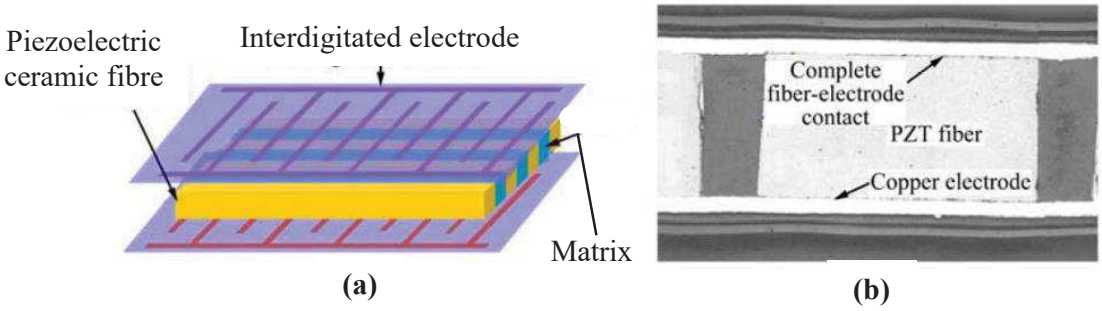


**Fig.2.5** Schematic structure of a) a MFC material [9,46] and b) a MFC cross section [9,46]

## 2.6. STRUCTURAL HEALTH MONITORING AND FAILURE PREDICTION OF LAMINATED COMPOSITE STRUCTURES

Piezoelectric materials can often be incorporated with laminated composite hybrid structures and act as strain gauge sensors to detect the strain/displacements of host structures. It is called a direct effect of piezoelectric materials. Using sensors to detect damage and failure in composite structures requires understanding of the sensing characteristics of piezoelectric materials.

Monitoring the stress/strain in composite structures, acting as strain gauge sensors lies within the field of structural health monitoring of composite materials. The sensors can also be used to detect the critical stress/strain values throughout composite structures,

particularly concentration stresses between host structure and piezoelectric ply depending on the area the piezoelectric sensors are installed on.

The condition-based maintenance, useful life, and safety prolong of the structures are categorized in the field of structural health monitoring, which is one of the emerging fields with great potential in industries. From the structural health monitoring prospective, the sensor/actuators are incorporated into the host structures (orthotropic, hybrid or isotropic structures) to detect the structural damage.

Assessment of structural stability, damage and failure strength of composite material is a crucial task to prevent a catastrophe. Numerous researches have been conducted in the recent years to evaluate and assess the structural stability, damage and elastic failure of smart composite structures analytically, numerically, and experimentally. A monitoring system is composed of a number of either bounded or embedded sensors to monitor the environment and the structural response to loads [48].

These sensors are used to obtain the critical mechanical strains/displacements occurring in host structures due to static or dynamic loads. A typical architecture of the monitoring systems is based on remote sensors wired directly to a centralized data acquisition system. However, the expensive nature of this architecture, due to high installation and maintenance costs associated with system wires is causing replacement of wire-based systems with new low-cost wireless sensing units by spreading knowledge over the entire monitoring network. Therefore, a larger effort is currently required to build effective data processing algorithms considering such a new

architecture. Another important task is related to the implementation of strategies to manage data and combine information coming from a variety of sensors and, thus, related to different physical variables [48]. Piezoelectric transducers are based on the piezoelectric effect. Considering the piezoelectric theory, some known crystals produce a charge under mechanical stress which is known as the direct piezoelectric effect. On the other hand, if a force is applied to such a kind of crystal, the electric charge to be measured is a function of the force and the kind of crystal that is used, which is known as the indirect piezoelectric effect. The piezoelectric strain gauge sensors represent a high drift. This phenomenon results from the transformation of force into charge [48].

A drift-free piezoelectric measurement chain would result in infinitely high insulation resistances which do not exist. Thus, those sensors are limited to measurements that are not zero related or to measurement of very high forces. Those forces lead to high charges and the change in signal caused by drift becomes small relative to those signals [49]. Critical infrastructure engineering structures such as highways, buildings, bridges, aircraft, ships, and pipelines, form the lifeline of economic and industrial hubs. These are highly likely during their lifetime to be subjected to severe loading conditions due to extreme events such as earthquakes, hurricanes, and other natural disasters. Failure may occur by just simply applying critical loads which exceed the elastic stiffness of a structural system. The loading system can range from internal/external pressure, residual thermal loads, critical cycling loads, and many more.

To prevent catastrophic failures and subsequent loss of life, it is essential to continuously monitor the state of the structure and identify any initiation of damage in

real time by using structural health monitoring techniques as strain sensing. SHM provides an autonomous way of tracking changes in the system in real time using a combination of instrumentation systems and analytical methods. Instrumentation systems consist primarily of transducers to measure physical quantities, such as strain, displacement, and acceleration, which can give insight into the behaviour of structures. Among the quantities of interest for SHM, strain is a local and direct measure of the state of the structure and is thus widely used as a reliable indicator of the damage induced in the structure. Hence, strain sensors are used extensively in SHM applications [50].

Konka et al [51] studied the failure characteristics of smart composite structures embedded inside the composite laminate's material interfaces to detect the critical stress/strain concentration levels led by significant differences in material interfaces. The analysis was carried out through series of experimental tests. The aim of this research was to: 1) detecting all loading condition acting on the structures, 2) damage prediction in the host structure due to applied dynamic loadings while in-service, and 3) monitoring pre-existing damages inside the host structure to prevent brittle failure or eventual catastrophic. Furthermore, two types of PFCTs' sensing characteristics in detecting damages were used: 1) MFC; and 2) PFC. The host structure were glass fibre reinforced epoxy composite laminate samples. It was noticed that selected sensors could detect the changes in the applied mechanical stress/strains effectively. In addition, a linear relationship was observed between the applied input mechanical stress and electrical voltage generated by sensors. In another study concerting on structural health monitoring of composite structures, Selva et al [52] used electro-mechanical impedance

(EMI) technique using piezoelectric sensors to detect the damages and assess the structural failure of the host structure. Piezoelectric transducers were used as high-frequency model sensors.

Damage-monitoring of smart composite structures with use of piezoelectric films was investigated by Yin et al [53]. The feasibility of adoptive piezoelectric films as the strain gauge sensors to detect the damage failure in the composite structure was studied. The purpose of using piezoelectric film as a sensor in their study was to assess the mechanical strength of the host structure (three types of composite laminates) against failure. The finite element modelling was used as a numerical approach in this study. Their results showed that piezoelectric films can be utilized as sensors to detect damages through the composite laminates due to an abrupt voltage output variation around the crack tip inside the host structure. In addition, the influence of damage on damage-monitoring sensors was specifically analysed.

In another study concerning the structural health monitoring of smart structures, an experimental setup was developed by Valdes and Soutis [54] to detect the effect of delamination on the modal frequencies of the composite beam. To study the effect of delamination on the modal frequencies of the composite beam specimens and to examine the performance of piezoelectric materials as sensor/actuator devices, a piezoelectric strain gauge sensor was incorporated at the top surface of the composite beam. The main contribution of their study was the development of an active damage-assessment system (array of sensors) capable of detecting damage in composites using piezoelectric devices incorporated in structures. Such a system would ideally be able to

continuously monitor the integrity of structural members avoiding expensive maintenance evaluation programs. A sensor driven piezoceramic film with a linear rapid frequency sweep was employed to respond to predict the delamination growth due to the vibration. Modal frequencies were obtained by applying concepts of a novel method known as resonant ultrasound spectroscopy. Changes of the modal frequencies after delamination initiation, compared to those of a non-delaminated specimen, gave a good indication of the degree of damage, demonstrating the feasibility of using measured changes in the vibration characteristics to detect damage.

Song et al [55] designed a new type of piezoelectric strain gauge sensor for strain/displacements deformation measurement of civil engineering structures using 3D printing technology. The sensor consisted of piezoelectric ceramic chip as the functional phase and a new composite material as the packing phase. Through using the frequency scanning and amplitude scanning tests, the sensors frequency independence, linearity, sensitivity, response rate, and service performance were examined and subsequently the electro-mechanical coupling performance of this type of strain gauge sensors were tested. The experimental results indicated that the fabricated sensors have quite good mechanical and workability properties within the vibration frequency of civil engineering structures. However, their approach was limited to experimental analysis. In addition, the mechanical properties and geometries of the host structures and their influence on the performance of the piezoelectric strain gauge sensors were neglected.

In some cases, embedded PZT sensors can be used for structural health monitoring. The reason behind this is to consider the fragility and fugitiveness of surface-bounded PZT

sensors for damage monitoring of host structures under impact loads. Ai et al [56] used the embedded and bounded PZT sensor patches to measure the critical mechanical strain/displacements in a concrete beam subjected to an impact load. The sensitivity parameters between the embedded and bounded PZT strain gauge sensors were then discussed. The analytical solution was the step stone of their research in which a 2D electromechanical impedance model based on effective impedance was proposed. The validity of embedded PZT sensor in quantification of structural damage studied using slope-based root mean square deviation (RMSD) index, a new baseline-changeable RMSD index was also proposed to evaluate the impact effect for the two types of active embedded PZT sensors. Subsequently, the proposed analytical model was varied using experimental results.

In the experimental setup, the PZT strain gauge sensors were either embedded inside or bounded to the concrete beam which was damaged by knocking off concrete covers. The results from both approaches demonstrated that the embedded PZT sensor can effectively filter out the impact effect in structural damage indication and quantification, which benefits the accurate evaluation of structural damage. However, the critical mechanical factors to prevent structural deformation and ultimately possible failure were not taken into consideration.

Laminated composite structures may be damaged during the manufacturing process. Some fibres may be wrongly impregnated into the epoxy or break out, leading to material discontinuity in composite layup. Composite fibres can come in different shapes and geometries. Fibre discontinuity in piezoelectric fibre composite sensors can

drastically affect their measurement performance. Furthermore, the effect of broken fibres embedded inside the fibre composite piezoelectric materials affects the elastic strength as well as electrical potential distribution through the piezoelectric layer after polarization [57].

Martinez et al [57] investigated the effect of fibre breakage on failure strength and damage behaviour of AFC piezoelectric laminates numerically. Finite element method (FEM) was the framework of their study. A FEM model was developed for simulating the performance of AFCs with piezoelectric fibres. The focus was on the effect of discontinuous fibres embedded into AFCs with interdigitated electrode pattern. Furthermore, the FE simulation models in which the gap regions in the fibre were depolarized were developed. The result proved that the existing gap between fibres in AFCs lead to the loss of contribution by 10 % from the whole fibre segment between the two electrodes into the actuation due to electrical filed concentration in the fibres' gap regions. In addition, results showed that any decrease in the effective stiffness due to damaged fibres lead to the degradation of AFCs actuation performance and the loss of the piezoelectricity effect in broken fibre segments.

Martinez et al [58] studied the effect of damaged fibres on the performance of hollow active fibre composites (HAFCs) using numerical simulation. The FE simulation models were developed to assess the structural stability of HAFCs subjected to electrical loading. The FE simulations were performed for HAFCs with healthy and damaged fibres. The effect of broken fibres on both sensing and actuation was studied. Finally, the results were validated by experimental analysis. The results obtained from

their research showed that the performance of HAFCs is affected by the gap in the fibres. Furthermore, the direct relationship between the location of damaged fibres and its proximity to the electrical potential source and the performance of HAFCs was observed.

Piezoelectric strain gauge sensor can be made using different types of materials such as PZT and piezo-film (PVDF) sensors which have been extensively used for strain measurements in composite structures. As discussed before, in piezoelectric strain gauge sensors, strain is measured in terms of the charge generated by the element due to the direct piezoelectric effect. Thus, based on the direct piezoelectric effect, each type of piezoelectric strain gauge sensor can have different sensitivity and performance when subjected to a thermal environment. Thermal stresses can induce the piezoelectric sensors elastic stiffness as well as electrical performance. Sirohi and Chopra [59] conducted a research on the behaviour of two types of piezoelectric elements as strain sensors. The surface-bounded sensors were integrated with a beam. The sensors were calibrated over a frequency range of 5 to 500 [*Hz*]. Correction factors were introduced to take into consideration the transverse strain and shear lag effects due to the bond layer. The analytical investigation was the main approach to the problem while experimental analysis was carried out for the analytical design verification. The results from both approaches demonstrated the effectiveness of the temperature on the output of PZT strain. Furthermore, design of signal conditioning electronics for the signals collection from the piezoelectric sensors was addressed. The performance of piezoelectric sensors in terms of sensitivity and signal to noise ratio was also demonstrated. Since impact damage caused by impact load is hidden and cannot be

detected by visual inspection; the use of piezoelectric strain gauge sensor can be beneficial in detecting the critical mechanical strains and monitoring impact damage initiation and possible propagation in laminated composite structures. For that purpose, Kim et al [60] demonstrated the effectiveness of polyvinylidene fluoride (PVDF) and PZT sensors and illustrated their potential benefit in structural health monitoring of laminated composite structures through experimental analysis. According to their study, several tests for monitoring the stress wave signals including acoustic emission due to failure modes, such as matrix cracking, delamination, and fibre breakage were taken into account. A series of impact tests at various impact energies by changing the impact mass and height was performed on the instrumented drop weight impact tester. The wavelet transform (WT) and short time Fourier transform (STFT) were used to decompose the piezoelectric sensor signals in the study. Test results demonstrated that the particular waveform of sensor signals implying the damage initiation and propagation were detected above the damage initiation impact energy. It was noticed that both PZT and PVDF sensors can be used to detect the impact damage.

It is evident from the literature that there are a very few novel analytical, numerical, and experimental research studies on sensors exploited in predicting the critical mechanical deformation, failure of laminate composite hybrid structures. Furthermore, most of the studies in the literature deal with the monitoring the structural deformation and obtaining the mechanical strains/displacements without considering the critical areas and points at which the mechanical failure may occur. The lack of research on determining the effectiveness and performance of sensors in obtaining some critical design specifications and parameters is notable. Some of these mechanical factors can

be classified as composite hybrid laminates stacking sequence configuration, laminate thickness and symmetry, prescribed boundary conditions, type of applied loading condition, location of sensors, and type of host structure. Novel analytical, numerical, and experimental investigations of critical points and factors in laminated composite hybrid structures with complex geometry such as hemispherical, ellipsoidal, and torispherical shells is crucial for designers since these factors are required in optimizing the mechanical characteristics of laminated composite hybrid structures.

## 2.7. INDUCING/CONTROLING LAMINATED COMPOSITE STRUCTURES SHAPE USING PIEZOELECTRIC ACTUATORS

Piezoelectric actuators can release mechanical strains if induced by electrical load which is known as the indirect piezoelectric effect. Thus, these can be appropriately integrated with laminated composite hybrid structures for inducing the host structure shape [61]. The induction in the composite hybrid laminates can be different depending on the intensity of electrical voltage applied to the piezoelectric actuators. Therefore, the ultimate shape of host structure can be controlled desirably. Some of the unique advantages of using piezoelectric actuators in structures and turning them into the intelligent mechanical system were discussed thoroughly in the previous chapter. Smart materials have been used extensively to control the shape of various types of engineering structures [62]. Several different types of piezoelectric materials such as PZT, MFCs, and AFCs could be used for this purpose. The structural shape deformation and distortion may be transient (dynamic), or it may be slowly varying in time (quasi-

/static). Shape control represents a branch of structural engineering that is closely related to control engineering [63].

In the following section, the shape deformation and control analysis of laminated composite hybrid structures using various types of piezoelectric actuators are broadly investigated. There are numerous experimental, numerical, and analytical approaches in the literature adopted for structural shape deformation and control. Some of the theories proposed to demonstrate the piezoelectric phenomenon in effecting distributed control and sensing of bending, torsion, shearing, shrinking, and stretching of a flexible plate are discussed next.

Lee [64] proposed a piezoelectric laminate theory capable of modelling the electromechanical (actuating) and mechanoelectrical (sensing) behaviour of a piezo composite laminate. An analytical approach was exploited for the formulation of distributed piezoelectric sensors and actuators. Furthermore, the reciprocal relationship of the piezoelectric sensors and actuators was also taken into account. Generalized functions were introduced to disclose the physical concept of the piezoelectric sensors and actuators. It was demonstrated that the reciprocal relationship is a generic feature of all piezoelectric laminates.

Koconis et al [13] developed an analytical model to calculate the shape changes of fibre-reinforced composite beams, plates, and shells induced by embedded piezoelectric actuators. The effect of applied electrical voltage intensity in the shape deformation analysis was the main goal of their research. A mathematical model was proposed using

two-dimensional, linear, shallow shell theory, considering the effect of transverse shear deformation. The Ritz method was used to solve the governing electro-mechanically coupled equations. A computationally efficient computer code with a user-friendly interface was written which is suitable for performing the numerical calculations. The results were then validated with the existing analytical and experimental results and an excellent agreement was confirmed.

In another similar study, Koconis et al [65] developed an analytical model to investigate the shape changes of laminated fibre-reinforced structures such as beams, plates, and shells and subsequently to obtain the required voltage for a specific desired shape. A mathematical model based on 2D linear, shallow shell theory was adapted for that purpose, considering the effect of transverse shear deformation. The proposed model showed the importance of transverse shear deformation in thick composite structures such as FGMs. To achieve the desired shape, a series of numerical calculations were performed to compute a minimization of an error function based on the difference between the deformed shape caused by the application of voltages and the desired shape. The results were then compared with experimental ones and a good agreement between the results was observed.

A host structure can be subjected to various loading conditions such as thermo-electro-mechanical loads which can result in the induction of host structure stiffness matrix. The cylindrical bending of the smart laminated composite plates against their elastic strength was studied through the proposed analytical solutions by Kant and Shiyekar [66]. The framework of their analytical investigation was based on a higher order shear

and normal deformation theory. The through-thickness displacements and the exact nature of the electrical potential were taken into account. The host structure was subjected to the arbitrary and complex loading conditions (electrical, mechanical, and electro-mechanical loads). The electrical potential function was evaluated by solving a second order ordinary differential equation. The host structure used in their analysis comprised of the unidirectional fibre-reinforced composite laminate with the incorporated actuators and sensors. Comparison of results with exact solution was presented. Results for non-piezoelectric plates were also compared with elasticity and other solutions of cylindrical bending.

Her and Lin [67] used a pair of surface-bounded piezoelectric actuators to induce the elastic stiffness of the laminate cross-ply composite plates using an analytical solution based on the classical laminated plate theory. The piezoelectric patches were polarized through thickness. Applying the electrical voltage to the piezoelectric patches created deflection in the host structure. The piezoelectric actuators had the opposite polling directions. The induced elastic strength of the host structure due to pure electrical loadings was assessed. Subsequently, the analytical results were verified by using a series of robust electro-mechanically coupled FE simulations. ANSYS FE simulation package was adopted for this purpose. Comparison of the results showed a good agreement. According to the results from refs [66,67], it was observed that the host structure elastic stiffness is noticeably induced as a result of the external electrical voltage applied to the actuators. The permissible boundary condition was selected to be simply-supported in both studies.

Vel and Batra [68] investigated the cylindrical bending deformation of linear piezoelectric laminated plates analytically using Eshelby-Stroh formulation. The laminate consisted of homogeneous elastic and/or piezoelectric layers with arbitrary thickness and width. The analytical approach was based on three-dimensional equations of equilibrium in terms of infinite series. The formulation admits different boundary conditions at the edges and is applicable to thick and thin laminated plates. Results were presented for the laminated elastic plates with a distributed piezoelectric actuator on the upper surface and a sensor on the lower surface and subjected to the different sets of boundary conditions at the edges. Results were also provided for a piezoelectric bimorph and an elastic plate with segmented piezoelectric actuators bonded to its upper and lower surfaces. According to the results, the effect of various parameters such as different boundary conditions, stacking sequence, bounded or embedded piezoelectric actuators, and applied electrical voltage on elastic strength induction of the smart laminated composite plates as well as stress/strain distribution levels throughout laminate was significant.

Elastic failure of laminated composite hybrid structures can be induced by applying the appropriate voltage to the piezoelectric actuators. Therefore, the elastic stiffness matrix in plates, shells, beams made of fibre-reinforced composite hybrid laminates and undergoing stress/strain levels, can be strengthened by integrating piezoelectric actuators to the host structure and then applying the optimized electrical voltage to the actuators. Delamination deformation and failure is common in fibre-reinforced composite laminates due to buckling loads. There is possibility of boosting the elastic stiffness of composite laminates against buckling failure. For instance, the delamination

effect on the failure strength of smart functionally graded laminated piezoelectric (FGLP) composites was studied analytically by Yang et al [69]. They analysed the nonlinear elastic failure of smart FGLM composite shells subjected to thermo-electro-mechanical loadings. The nonlinear buckling and expansion behaviour near the surface of FGLP composite shell was considered. The effect of various parameters such as thermo-electrical loading, stacking sequence, and pattern of delamination on critical axial loading of locally delaminated buckling were described and discussed. In the subsequent analysis, the directions of buckling failure growth for the delaminated sub-shells were described through analytical calculation of the expanding forces along the length and short axis of the delaminated sub-shells.

Wang et al [70] studied the behaviour of interface cracks between a piezoelectric ply and elastic substrate considering shear effect analytically. The analytical solution was the frame work of his study using Timoshenko beam theory. Interface stresses, mode I and II energy release rate of the straight crack subjected to electro-mechanical loading were studied. Effect of various parameters such as applied electrical loading, material mismatch and geometry of the interface crack in a typical smart composite structure with piezoelectric layers was considered. The effect of shear on an interface deformation due to material discontinuity between the piezoelectric actuators and the host structure has a potential application in the field of safety assessment of piezoelectric composite structures. However, the present study does not consider the crack surface contact, but the exact crack surface contact condition should be considered in the follow up work to better reflect the real situation.

In order to control the structural shape of elastic shell continua, spatially distributed model piezoelectric actuators was proposed and some generic distributed feedback algorithms with spatial feedback functions were then formulated by Tzou et al [71]. The analytical formulation resulted in the distributed structural control of elastic shells. The reason behind choosing the distributed actuators to be spatially shaped is to prevent spillovers from the modal couplings of feedback forces. To prove the utilities of the generic theory, distributed orthogonal convolving modal actuators designed for a circular ring shell were proposed and their control effectiveness evaluated. To increase the control effect, the structural stiffness must decrease or, on the other hand, the structural flexibility must increase. Furthermore, increasing the control moment arm of the actuator layer was not noticeable in the overall control effect for lower natural modes.

Agrawal and Tong [72] outlined an analytical procedure using elastic plate theory to model the deflection of an isotropic plate induced by embedded piezoelectric actuators. The mathematical formulation relating the electro-mechanical couples were then computed using finite difference method. Moreover, an algorithm was proposed to obtain the optimal actuator voltages to match the plate deflection to a desired one. To develop and algorithm, a quadratic cost function of nodal deflection errors subjected to limits on the actuator voltages was minimized. This algorithm was later resolved using the Kuhn-Tucker optimality conditions. One of the advantages of this research was its ability to consider unlimited number of piezoelectric actuators for the shape control purpose. No results verification was implemented for the proposed analytical solution.

Han and Lee [73] formulated an FE model to analyse the closed loop performance of composite plates incorporated with piezoelectric actuators and subjected to dynamic loadings. The main purpose of their study was to obtain parameters such as: natural frequency, damping ratio, and modal actuation forces. The effect of each parameter on vibrational control was studied, thereafter. The refined strain distributions and boundary condition modelling was described using the likewise displacement theory. Comparison of the results with some published benchmarks showed a good agreement. It was concluded that the developed model can describe more realistically smart composite plates with distributed piezoelectric actuators.

There are some works on coupled buckling and post-buckling analysis of active laminated piezoelectric composite plates. Buckling results from in-plane compressive loading accompanied by structural imperfections or out-of-plane loads can lead to large deflection, structural instability, and finally structural failure. Thus, understanding of buckling failure is vital in engineering design. Substantial experimental and theoretical analysis were carried out to design and control the bucking and post-bucking of fibre-reinforced composite structures. In addition, critical mode of failure is expected in smart structures with distributed piezoelectric materials since the external electrical voltage applied to the actuator leads ton additional in-plane loads in conjunction with in-plane mechanical loads. The buckling analysis of a cantilever piezoelectric composite plate subjected to the electrical and mechanical loads was investigated by Varelis et al [74]. A smart cantilever plate was integrated with the bounded PVDF piezoelectric layers. It was noticed that electrical and mechanical loads contribute to induction of buckling failure in a smart cantilever plate.

Milazzo [14] developed a family of two dimensional (2D) refined equivalent single layer models for vibration analysis of multilayered and functionally graded smart magneto-electro-elastic plates based on variable kinematics and quasi-static behaviour for the electromagnetic fields. Numerical analysis using FEM was adopted to solve the governing equations. First, the electromagnetic state of the plate was determined by solving the strong form of the electromagnetic governing equations coupled with the corresponding interface continuity conditions and external boundary conditions. Subsequently, the electromagnetic state was condensed into the plate kinematics, whose governing equations can be written using the generalized principle of virtual displacements. The single layer FE model presented in his work was then validated against available benchmark 3D solutions.

There are numerous studies on the AFCs and MFCs actuation performance to analyse their power to induce and control the shape of various engineering structures. MFCs developed by NASA have been increasingly used in engineering structures due to their high actuation power, compatibility, and flexibility. Since AFC and MFC piezoelectric actuators are incorporated into fibre-reinforced laminate, understating their performance is most important [45]. Characteristics and properties of this class of piezoelectric materials were discussed comprehensively before. In the following paragraphs, some of the published materials concerning the AFCs and MFCs performance and actuation parameters for shape induction and control of engineering structures, particularly laminated composite hybrid structures, are reviewed.

There have been numerous analytical, numerical, and experimental studies on AFCs and MFCs actuators in the recent years. Chen et al [75] studied the electrical field distribution effects on AFC and MFCs performance controlled by geometrical parameters. Their study demonstrated that electrical filed lines are homogeneous along fibres and perpendicular to the IDE plane beneath the electrodes. Furthermore, linear performance of AFCs and MFCs was studied numerically and analytically in order to investigate the influence of configuration parameters on the actuation behaviour of AFCs and MFCs by Rossetti et al [76] and Warkentin [77]. Their work demonstrated that smaller ratio between the electrode finger spacing and the fibre diameter could result in better actuations at lower electrical voltage. However, the steep curvature of the electric filed near the electrode areas makes the actuation less efficient. On the contrary, larger ratio between electrode finger spacing and fibre diameter leads to the more efficient actuation despite the higher electrical voltage is required to achieve actuation at the same electrical field level. Therefore, optimizing the abovementioned parameters can significantly affect the actuation power of AFCs and MFCs for structural shape induction and control.

Nonlinear characteristics and their effect on actuation performance of AFCs and MFCs were investigated by several researchers. Cesnik et al [78] worked on nonlinear performance of AFC/MFCs and concluded that nonlinear behaviour of this type of piezoelectric materials is also significants since they are capable of inducing high free-strains and are topically incorporated into structures to control large strains. Williams et al [17] developed a nonlinear model to obtain thermo-mechanical coefficients properties of MFCs using FEM and classical lamination theory. The thermos-mechanical

properties of MFC actuators were modelled as a temperature function. The required temperature-dependent properties of each constituent material were obtained. The orthotropic layer properties were acquired using various micromechanics models. The analytical results were then compared with FEM. The most accurate model was chosen by a comparison with ANSYS FE models. By using a classical lamination approach, equations of four independent stiffness parameters and two coefficients of thermal expansion of the entire MFC actuator were derived. There was a good agreement between the analytical results and those derived by ANSYS FE model of the unit cell of MFC actuators.

Williams et al [79] measured the linear elastic constants of an orthotropic MFCs within elastic zone. They characterized the nonlinear constitutive behaviour of MFCs under short-circuit conditions with use of tensile test procedures. Ramberg-Osgood quadratic least square methods were adopted to fit the experimental results during the nonlinear analysis. In their further experiments, nonlinear tensile and shear stress-strain behaviour and Poisson's effect were characterized. The results could then be readily incorporated into the piezoelectric constitutive equation and ultimately into structural actuation models that accurately considered nonlinear mechanical behaviour. MFC actuators can control bending-twisting deformations of mechanical structures such as plates, beams, and shells due to their high actuation power and compatibility to host structure. Therefore, the application of MFCs in shape control aeronautic structures is being growing rapidly. For instance, Chen et al [80] studied the effect of a hydraulic rudder actuator on controlling the first bending mode of a full-scale F/A-18 vertical fin. The design approach was based on numerical simulation and experimental analysis. For that

purpose, the distributed MFC actuators were bounded on both sides of the vertical fin surface to control first torsional mode.

The schematic of Buffet load alleviation system on F/A-18 is illustrated in Fig.2.6a. To control the premature fatigue failure of the structure as well as mission availability, Chen et al [80] also developed a novel hybrid actuation system for actively alleviating the buffet response. The schematic of the actuation system is illustrated in Fig.2.6b. The results demonstrated the ability of MFC actuators to reduce dynamic strain and acceleration at aft fin root to 41% and 43%, respectively. More consistent performance under increased buffeting load levels due to MFC actuators high frequency response was also observed. The schematic of the MFC actuators integration with the F/A-18 tail wing for bending-twisting as the phase-1 buffet load alleviation system is shown in Fig.2.7.

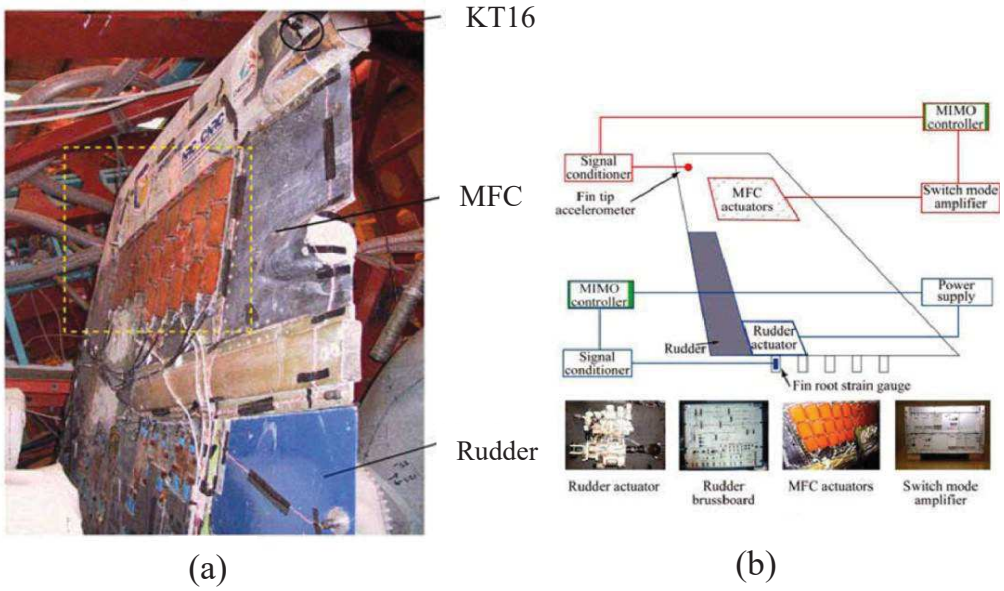


**Fig.2.6** a) Buffet load alleviation system on F/A-18 [80] and b) Configuration of hybrid actuation system [80]

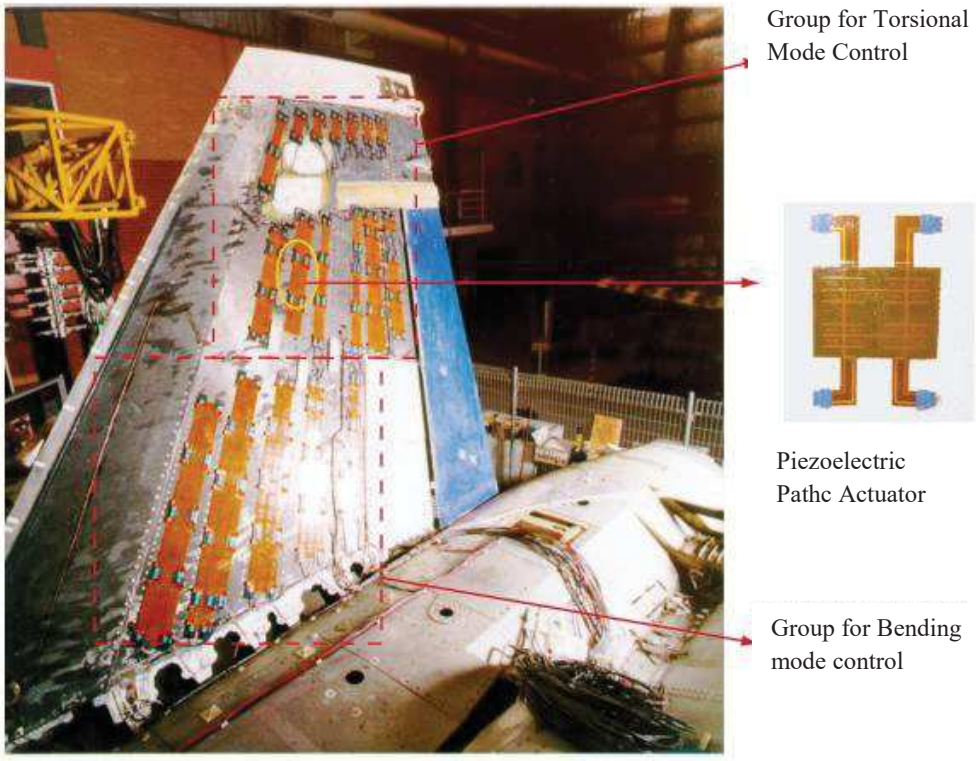


**Fig.2.7** Experimental test setup illustrating the MFC actuators integration with the F/A-18 tail wing for bending-twisting as the phase-1 buffet load alleviation system [80]

MFC actuators can also be used in morphing airplanes. Morphing is a kind of structure whose shape or state can vary in response to the environment or to change the operation characteristics. Current aircraft designs already employ winglets aimed at increasing the cruise flight efficiency by induced drag reduction. Smart intelligent structures propose a state of the art technology that incorporates a wing tip active trailing edge, which could be a means of reducing winglet and wing loads at key flight conditions. For instance, the morphing aircraft can be achieved through changes in its wing geometry. In addition, replacing the mechanically driven control surfaces and helicopter blade control can be achieved using reliable actuators [81].

The application of piezoelectric actuators in shape induction and control of cantilever structures is increasing. Laminated cantilever composite plates have been widely used in various engineering applications such as airplane wings, corrugated plates, reinforced concrete slaps, decks of contemporary steel bridges, boom arms of industrial cranes, and flight control surfaces. One of the great advantages of piezoelectric materials is to be able to respond to changing environment and control structural deformation which has led to the new generation of aerospace structures like morphine airplanes [8].

Kim and Han [82] studied the mimic of birds flapping motion by using experimental investigation. They designed and fabricated a smart graphite reinforced epoxy (GFRP) composite laminate incorporated with MFC actuator to monitor the deformation of the wing surface generated by MFC actuator. To mimic the birds flying mechanism, they investigated birds' aerodynamic characteristic. An experimental setup was developed for measuring the flapping devices aerodynamic forces. A series of dynamic tests were performed for that purpose. The experimental setup consisted of the smart wing with the multiples bounded MFC actuators. The smart wing shape could be changed by applying various electrical voltages to the MFC actuators. Therefore, the appropriate electrical voltage was applied to the surface-bounded MFC actuators to boost the wing's aerodynamic performance. Subsequently, the smart wing was placed in the subsonic wind tunnel to assess its dynamic characteristics. According to the experimental results, by inducing the flapping frequency using MFC actuators, unsteady flow effects were increased with low velocity in high flapping frequency regions. Furthermore, the wing surface shape changes generated by the MFC actuators were enough to control the lift

and thrust. It was concluded that there was a twenty percent increase in lift achieved by changing the wing camber at the different stage of flapping motion.

Paradies and Ciresa [83] implemented MFC actuators into an active composite wing used in an unmanned aerial vehicle (UAV) with a thin profile and integrated roll control with piezoelectric elements. The smart composite wing was modelled numerically based on a fully coupled structural fluid dynamics model. An experimental analysis was then implemented for computational results verification. The static and preliminary dynamic tests were carried out on the prototype wing to validate the design model. Dynamic tests were also performed on a sandwich wing of the same size with conventional aileron control for comparison. Even though the roll moment generated by the active wing was lower, it proved sufficient for the intended roll control of the UAV. There was a total displacement of 3 mm achieved at the tip of a wing with span of 500 [*mm*] and seven integrated MFC elements working at 1.5 [*KV*] as shown in Fig.2.8. It was sufficient for the roll control of airplane despite the small amount of roll moment in the active wing. More research regarding how to generate novel morphing and deployable structures can be found in Ref [84].

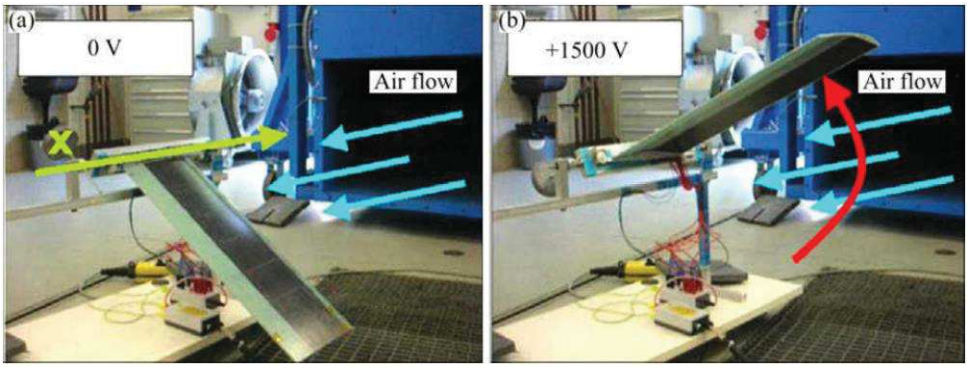


**Fig.2.8** Active wings with deactivated and activated MFC in air flow [9,83]

There are some circumstances under which shape deformation due to piezoelectric actuators can result in changes in the host structures stiffness matrix in a negative manner. For example, Woo and Goo [85] worked on the effect of electrical cyclic loading on fatigue failure and cracking of a bending piezoelectric hybrid composite actuator with the aid of an acoustic emission (AE) technique. The experimental analysis was the framework of their study. Electrical fatigue tests were performed for up to $10^7$ cycles on the fabricated experimental samples. The external electrical voltage ranging from -150 [$V$] up to +150 [$V$] was applied to the structure. The source location and distribution of AE behaviour over the fatigue range were analysed to ensure the fatigue damage initiation and its pathway. It was concluded that electrical cycle loading can result in fatigue failure in a smart composite structure but did not result in final failure of the bending piezoelectric composite actuator. It was also observed that factors as the onset time of the fatigue damage varied significantly depending on an existing GFRP ply as a protecting bottom layer.

To study the effect of bounded piezoelectric actuator patches on vibration control of cross-ply composite laminates, Her and Lin [86] developed an analytical model based on linear piezoelectricity and elasticity theories to assess the effect of time harmonic voltages on shape deformation of laminated composite plates. The analytical solution was then compared with the numerical simulation results for results verification. ANSYS FE package was used to model the smart piezo composite plates under dynamic loads. The results showed a good agreement. However, the study was only limited to simply supported plates and no further research on complex boundary conditions and loading system was conducted.

The literature review presented in this section demonstrates various analytical, numerical and experimental studies of shape induction and control of various mechanical structures using isotropic and orthotropic piezoelectric actuators. Based on the published studies, the lack of novel analytical and numerical analysis for shape deformation and control of various complex engineering structures was evident. In many shape control problems, the lack of novel exact and numerical solutions to consider many mechanical factors is observed. Some of the factors to be taken into an account are host structures layup stacking sequence configuration, shape control performance of piezoelectric actuators in thermal environments, complex loads and boundaries, piezoelectric actuators piezoelectric fibre angle variations, and piezoelectric actuators inclination angle and placements.

## 2.8. CONCLUDING REMARKS

This chapter presented an extensive literature review on general characteristics of fibre-reinforced composite laminates and piezoelectric materials. A detailed account of earlier and recent studies on shape deformation assessment and failure prediction in laminated composite structures using piezoelectric strain gauge sensors was then presented. Finally, the numerous studies on the use of piezoelectric actuators to control the shape of laminated composite structures were reviewed.

Based on the benchmark studies available in the literature, it was observed that there are a very few novel analytical and numerical studies on sensors and actuators suitable for predicting the critical mechanical deformation, failure and shape control of laminate

composite hybrid structures. The available studies lacked the consideration of some crucial mechanical factors which can significantly influence the shape monitoring, failure prediction, shape deformation and control of laminated composite hybrid structures integrated with sensors and actuators. Furthermore, the shape and failure control analysis of this class of composite structures are mostly limited to numerical and experimental studies, though approximation solution has also been adopted as part of the analytical investigations. Based on the literature, many smart laminated composite structures were subjected to only simple loading conditions while in real-life engineering problems, the combination of arbitrary loads such as thermo-electro-mechanical loads are applied.

Therefore, some novel analytical and numerical solutions are required to account for these factors. Experimental analysis of smart structures is expensive and requires excessive amount of time and calibration to obtain a satisfactory result. Thus, relying on analytical and numerical evaluation of this class of materials can be cost-effective and save a lot of time. In the following chapters, several novel analytical and numerical methods are proposed for structural shape deformation measurement and shape control of laminated composite hybrid structures using sensors and actuators respectively. The proposed methods are validated through numerical simulation, experimental analysis and by comparing the results with the published benchmark results available in the literature.

# Chapter 3

# MECHANICAL DEFORMATION AND FAILURE ASSESSMENT OF LAMINATED COMPOSITE STRUCTURES USING PZT STRAIN GAUGE SENSORS

## 1.1. INTRODUCTION

In this chapter, a novel analytical solution and numerical simulation are proposed to assess the mechanical shape deformation and possible failure of the internally pressurized laminated woven GFRP composite shells using surface-bounded PZT strain gauge sensors. PZT sensors are classified as piezoceramic materials made of lead zirconate titanate which can be used as strain gauges for measuring the mechanical strains created in structures. The mechanical loads applied to the host structures result in PZT sensors releasing electrical voltage, which is used to measure the mechanical strains. Various types of shells with complex geometries such as hemispherical,

ellipsoidal, and torispherical are selected for model analysis. The sensors are aimed at obtaining the critical mechanical strain/displacements and possible failure in the critical regions. Tsai-Wu failure criterion was adapted for that purpose. In the analytical study, the linear interpolation technique is adopted to interpolate the critical points conveniently. The shells boundary is fixed at its end. A series of 3D FE model analysis are used for the numerical simulation of critical mechanical strains/displacements and predicting the critical shell regions.

Both the analytical and numerical results are validated by using the experimental test results developed in this study. In the experimental investigation, some arbitrary points on the shell surface are selected and their strain values are measured using surface-bounded PZT strain gauge sensors. Manufacturing of laminated composite shells is performed by using the Vacuum Infusion Process (VIP), a method commonly adopted for the fabrication of laminated composite shell structures. The effect of various parameters including thickness, aspect ratio, and stacking sequence on the shape deformation and failure of the laminated woven GFRP composite shells are investigated and the critical mechanical factors to avoid deformation and possible failure are determined. The analytical and numerical studies adopted in this research investigation can be easily extended to other types of laminated composite structures such as plates and beams.

This chapter includes the following papers:

1) S. Gohery, S. Sharifi, Z. Vrcelj, and M. Y. Yahya, “First-ply failure prediction of an unsymmetrical laminated ellipsoidal woven GFRP composite shell with incorporated surface-bounded sensors and internally pressurized,” *Compos. Part B Eng.*, vol. 77, pp. 502–518, 2015.

2) S. Sharifi, S. Gohery, M. Sharifiteshnizi, and Z. Vrcelj, “Numerical and experimental study on mechanical strength of internally pressurized laminated woven composite shells incorporated with surface-bounded sensors,” *Compos. Part B Eng.*, vol. 94, pp. 224–237, 2016.

VICTORIA UNIVERSITY
MELBOURNE AUSTRALIA

**PART B:**

**DECLARATION OF CO-AUTHORSHIP AND CO-CONTRIBUTION: PAPERS INCORPORATED IN THESIS BY PUBLICATION**

This declaration is to be completed for each conjointly authored publication and placed at the beginning of the thesis chapter in which the publication appears.

**Declaration by** [candidate name]: Scott Gohery **Signature:** **Date:** 4/01/2017

**Paper Title:**
First-ply failure prediction of an unsymmetrical laminated ellipsoidal woven GFRP composite shell with incorporated surface-bounded sensors and internally pressurized

In the case of the above publication, the following authors contributed to the work as follows:

| Name | Contribution % | Nature of Contribution |
|---|---|---|
| Scott Gohery | 60 | Initial concept, Literature review, Analytical and experimental investigation, Writing of the manuscript |
| Shokrollah Sharifi | 20 | Experimental test rig fabrication, Specimens calibration and date measurement |
| Zora Vrcelj | 15 | Provided critical revision of the manuscript, Initial and final approval of the manuscript |
| Mohd Yazid Yahya | 5 | Provided finincial assistance for the experimental consumabales |
| | | |
| | | |

Page - 1 - of 2

VICTORIA UNIVERSITY
MELBOURNE AUSTRALIA

**DECLARATION BY CO-AUTHORS**

The undersigned certify that:

1. They meet criteria for authorship in that they have participated in the conception, execution or interpretation of at least that part of the publication in their field of expertise;
2. They take public responsibility for their part of the publication, except for the responsible author who accepts overall responsibility for the publication;
3. There are no other authors of the publication according to these criteria;
4. Potential conflicts of interest have been disclosed to a) granting bodies, b) the editor or publisher of journals or other publications, and c) the head of the responsible academic unit; and
5. The original data is stored at the following location(s):

| Location(s): |
| --- |
| 1) College of Engineering and Science, Victoria University, Melbourne, VIC 8001, Australia<br>2) Centre for Composites, Universiti Teknologi Malaysia, Skudai, 81310 Johor, Malaysia |

and will be held for at least five years from the date indicated below:

| | | Date |
| --- | --- | --- |
| Signature 1 | [redacted] | 20/12/2016 |
| Signature 2 | | 20/12/2016 |
| Signature 3 | | 20/12/2016 |
| Signature 4 | | 20/12/2016 |

Page - 2 - of 2

VICTORIA UNIVERSITY
MELBOURNE AUSTRALIA

**PART B:**

**DECLARATION OF CO-AUTHORSHIP AND CO-CONTRIBUTION: PAPERS INCORPORATED IN THESIS BY PUBLICATION**

This declaration is to be completed for each conjointly authored publication and placed at the beginning of the thesis chapter in which the publication appears.

Declaration by [candidate name]: Scott Gohery

Signature [redacted]

Date: 4/01/2017

Paper Title:
Numerical and experimental study on mechanical strength of internally pressurized laminated woven composite shells incorporated with surface-bounded sensors

In the case of the above publication, the following authors contributed to the work as follows:

| Name | Contribution % | Nature of Contribution |
|---|---|---|
| Shokrollah Sharifi | 25 | Initial concept, Experimental test rig fabrication, Specimens calibration and date measurement |
| Scott Gohery | 65 | Literature review, Numerical and experimental investigation, Writing of the manuscript |
| Masoumeh Sharifiteshnizi | 5 | Literature review,Provided critical revision of the manuscript |
| Zora Vrcelj | 5 | Provided critical revision of the manuscript, Initial and final approval of the manuscript |
| | | |
| | | |

Page - 1 - of 2

VICTORIA UNIVERSITY
MELBOURNE AUSTRALIA

**DECLARATION BY CO-AUTHORS**

The undersigned certify that:

1. They meet criteria for authorship in that they have participated in the conception, execution or interpretation of at least that part of the publication in their field of expertise;
2. They take public responsibility for their part of the publication, except for the responsible author who accepts overall responsibility for the publication;
3. There are no other authors of the publication according to these criteria;
4. Potential conflicts of interest have been disclosed to a) granting bodies, b) the editor or publisher of journals or other publications, and c) the head of the responsible academic unit; and
5. The original data is stored at the following location(s):

| Location(s): |
| --- |
| College of Engineering and Science, Victoria University, Melbourne, VIC 8001, Australia |

and will be held for at least five years from the date indicated below:

| | | Date |
| --- | --- | --- |
| Signature 1 | [redacted] | 20/12/2016 |
| Signature 2 | | 20/12/2016 |
| Signature 3 | | 20/12/2016 |
| Signature 4 | | 20/12/2016 |

Page - 2 - of 2

Composites Part B 77 (2015) 502–518

Contents lists available at ScienceDirect

Composites Part B

journal homepage: www.elsevier.com/locate/compositesb

# First-ply failure prediction of an unsymmetrical laminated ellipsoidal woven GFRP composite shell with incorporated surface-bounded sensors and internally pressurized

Scott Gohery [a,*], Shokrollah Sharifi [a], Zora Vrcelj [a], Mohd Y. Yahya [b]

[a] College of Engineering and Science, Victoria University, Melbourne, VIC 8001, Australia
[b] Centre for Composites, Universiti Teknologi Malaysia, Skudai, 81310 Johor, Malaysia

ARTICLE INFO

*Article history:*
Received 23 May 2014
Received in revised form
12 February 2015
Accepted 17 March 2015
Available online 26 March 2015

*Keywords:*
C. Analytical modeling
D. Mechanical testing
C. Laminate mechanics
B. Strength
Unsymmetrical laminated ellipsoidal woven GFRP shell

ABSTRACT

First-ply failure of an unsymmetrical laminated ellipsoidal woven Glass Fiber Reinforced Polymer (GFRP) composite shell internally pressurized was investigated analytically using the linear interpolation technique. The shell's boundary was fixed at its end. Tsai-Wu failure criterion was used as the composite failure design factor. The analytical results, including critical internal pressure and strains in global directions, were validated with the experimental results for some arbitrarily selected points on the shell surface along meridian axis. Manufacturing of laminated ellipsoidal composite shells was performed by using the Vacuum Infusion Process (VIP), a novel method commonly adopted for the fabrication of laminated composite shells. Surface-bounded sensors were installed on the shells' surface to measure the strain values after the internal pressure was applied. According to the analytical investigation findings, the failure factor was critical at the innermost ply. In addition, for each ply, the shell's edge was observed to be the region with the highest failure factor. The experimental findings confirmed that the failure occurred in the regions close to the shell's edge, as predicated by the analytical approach. The results from both approaches were in a close agreement. Subsequently, the effect of various parameters including thickness, aspect ratio, and stacking sequence on the first-ply failure of laminated ellipsoidal woven GFRP composite shell were investigated and the critical mechanical factors to avoid failure were determined.



## 1. Introduction

Pressure vessel is a form of closed container used to hold gas and liquid at a pressure which substantially differs from the circumfused pressure. Ambient pressure can also be significant in some cases such as under water pipe lines or a pressure vessel subjected to internal and external pressure. Different materials, including composite materials, can be employed in manufacturing of pressure vessels. Recently, more emphasis has been placed on composite pressure vessels since they are lighter than steel and can be much stronger than isotropic materials. They are vastly exploited in commercial and airspace applications in recent years [1–5]. Applications include breathing device, such as self-contained breathing apparatuses used by fire-fighters and emergency personnel, scuba tanks for divers, oxygen cylinders for medical and aviation cylinders for emergency slide inflation, opening doors or lowering of landing gear, mountaineering expedition equipment, paintball gas cylinders and etc. The great portion of applications has been related to the manufacturing and engineering designs. Most commercially produced composites use polymer matrix materials often called resin solutions. Significant advances in construction and design of ellipsoidal shells have taken place over recent years [4,5]. In addition, static, vibrational, and buckling of axisymmetric ellipsoidal shells has been reported. This type of shell has a great application in internally pressurized vessels and cylindrical tanks' heads and bottoms [6].

Failure analysis of composite structures is commonly based on some different failure modes such as maximum stress criterion, maximum strain criterion, Hoffman failure criterion, Tsai-Wu failure criterion and Tsai-Hill failure criterion. All methods are used for theoretical failure analysis of composite structures [7–11]. Tsai-Wu has been adopted widely for failure analysis of composite structures [12–15]. Extensive research has been conducted on failure strength of laminated composite panels and laminated

* Corresponding author. Tel.: +61 423656484.
*E-mail addresses:* scott.gohery@unimelb.edu.au (S. Gohery), sharifi.te@gmail.com (S. Sharifi).

http://dx.doi.org/10.1016/j.compositesb.2015.03.058
1359-8368/

**Notation**

| | |
|---|---|
| $\varphi$ | meridian direction |
| $\theta$ | circumferential direction |
| $r$ | radial direction |
| $N_\varphi$, $N_\theta$, $N_{\theta\varphi}$ | in-plane normal and shear force resultants, respectively (per unit length) |
| $r_\varphi$ | radius of curvature of meridian |
| $r_\theta$ | radius of curvature of parallel |
| $t$ | ply thickness |
| $r$ | radius of a parallel circle |
| $P^o_{r\varphi}$, $P^o_{r\theta}$, $P^o_r$ | outer surface stresses in the direction of meridian, circumference and radius, respectively |
| $P^i_{r\varphi}$, $P^i_{r\theta}$, $P^i_r$ | inner surface stresses in the direction of meridian, circumference and radius, respectively |
| $a$, $b$ | semi-major and semi-minor radius of ellipse, respectively |
| $H$ | composite laminate's total thickness |
| $h$ | distance from mid-plane to the $k^{th}$ ply |
| $\beta$ | fibre angle orientation |
| $k$ | number of layers |
| $K$ | curvature matrix |
| $N$ | vector of stress resultants |
| $\sigma^{(K)}$ | vector of stresses for the$k^{th}$ ply |
| $\overline{Q}$ | transformed material stiffness |
| $Z$ | distance from the mid-plane in the thickness direction |
| $T$ | transformation matrix |
| $M_\varphi$, $M_\theta$, $M_{\varphi\theta}$ | in-plane bending and twisting moment resultants (per unit length) |
| $A$, $B$, $D$ | extensional, coupling, and bending stiffness matrices, respectively |
| $F_{1t}$, $F_{2t}$ | tensile strength in a composite laminate along longitudinal and transverse directions, respectively |
| $F_{1C}$, $F_{2C}$ | compressive strength in a composite laminate along longitudinal and transverse directions, respectively |
| $F_6$ | in-plane shear strength |
| $P_f$, $P_{Cr}$ | failure and critical pressures, respectively |
| $E_L$, $E_T$ | Young's modulus in a composite laminate's local material orientation |
| $\varepsilon_\varphi$, $\varepsilon_\theta$, $\gamma_{\theta\varphi}$ | in-plane strains |

hemispherical and cylindrical composite shells pressurized internally and/or externally. These analyses include but are not limited to static, dynamic, and impact response of cylindrical and hemispherical composite shells and panels [16–20]. However, in all those reported studies, the research was carried out on unidirectional fibre-reinforced composites rather than woven fibres.

Woven fabric composites have been adopted in numerous engineering applications during the past two decades [21,22]. This class of fibre-reinforced material can have as many engineering applications as laminated unidirectional fibre composites due to its high in-plane specific strength and high in-plane specific stiffness. Woven fabric composite has a unique property of having thought-thickness arrangement of fibres to boost interlaminate strength and toughness, and compressive strength called textile reinforcement. Thus, due to this unique property of woven composite structures, it can have a great potential in aerospace engineering design [23]. However, less research contribution has been made toward the failure behaviour of woven reinforced polymer composites since many difficulties in failure analysis of woven composites have been reported [23]. A great portion of failure analyses of woven composites accounts for mechanical properties, failure mechanism of woven-glass fabric-epoxy composites and failure strength of woven glass fibre-epoxy composites pinned joints [23–25]. The literature review has revealed that no research has been conducted on laminated ellipsoidal shells made of woven composites. The only available minor study is on the plastic collapse and controlling failure pressures of thin ellipsoidal shells subjected to internal pressure [26].

The characteristics of various laminated composite shells subjected to internal pressure have been studies through different approaches. The effect of winding angle and thickness with other winding parameters such as the tape width and thickness were studied using multi-scale shell lay-up simulation. The results were compared with the experimental radiographic images. The results showed that a good correlation between simulation and experimental data is possible [27]. Optimal design of high-pressure composite storage tanks subjected to internal pressure was studied to boost their structural strength. Finite element (FE) method with Reddy's progressive damage law and Genetic Algorithm (GA) optimization were compared with results obtained from Continuum Damage Mechanics (CDM) theory and a Three Dimensional Finite Element (3DFE) technique incorporating a modified GA and advantages and limitation of each method were discussed thoroughly [28]. Also, laminate stacking sequence, winding tension, winding-tension gradient, winding time, and the interaction between winding-tension gradient and winding time, geometric factor, winding angle and pre-crack angle proved to significantly affect failure strength of composite shells subjected to internal pressure based on experimental and theoretical investigations [29–31].

In this study, the emphasis is placed on the first-ply failure characteristics of laminated ellipsoidal composite shell made of woven/epoxy subjected to internal pressure with use of linear interpolation technique. This technique is used to interpolate the critical and failure pressure, leading to the first-ply failure. The results acquired from the analytical investigation are validated with the finding of the experimental approach. The experimental data to determine the critical internal pressure to avoid failure is obtained from strain gauge sensors. Subsequently, the further discussion is made toward analytical solution to assess the effect of various parameters on first-ply failure of a laminated ellipsoidal woven-epoxy composite shell subjected to internal pressure. Tsai-Wu failure criterion for orthotropic materials was adopted in the theoretical analysis. A number of assumptions were adopted in the analysis.

This study can help the designers and manufacturers to choose an adequate fibre angle orientation, and also how to reinforce the elliptical shape of composite shells under internal pressure. Several research investigations have been conducted on the effect of internal pressure on the laminated composite structures, but the behaviour of woven fibre composite with unsymmetrical stacking sequence under internal pressure has not yet been studied. Furthermore, the investigation of critical points and factors in composite pressure vessels with complex geometry such as ellipse is crucial for designers since these factors are required in optimizing the mechanical characteristics of composite pressure vessels. Therefore, this research focuses on the failure of the elliptical composite shells under internal pressure.

## 2. Problem statement

In this study, the ellipsoidal shell is incorporated with surface-bounded sensors in order to measure the strain values, occurring on the shell surface after pressurized. The schematic of spherical

coordinate axis, presenting the meridian direction $\varphi$, parallel (circumferential) direction $\theta$, and radial direction $r$, as well as location of the surface-bounded sensors on the shell surface, are illustrated in Fig. 1. According to Fig. 1, eight surface-bounded sensors are installed on the shell surface with four sensors placed parallel and four sensors placed perpendicular to the circumferential direction for the purpose of measuring the circumferential and meridian strains, respectively.

The principle equilibrium equations for a pressure vessel, whose cross-section is ellipse with major and minor axis 2a and 2b respectively, are represented in Eqs. (1)–(3) [32]. These equations are expressed in terms of usual shell stress resultants. Shell's stress resultants acted on a shell element are shown in Fig. 2. Here, coordinates oriented along the tangent to the meridian, the tangent to the parallel and normal to the surface are labelled as $X$, $Y$, and $Z$, respectively. In addition, the angle between the shell axis of revolution and the normal to surface is labelled as $\varphi$.

$$\frac{\partial(N_\varphi r)}{\partial\varphi}+\frac{\partial(N_{\varphi\theta})}{\partial\theta}r_\varphi - N_\theta r_\varphi\cos\varphi+\Delta P_{r\varphi} r r_\varphi = 0 \tag{1}$$

$$\frac{\partial(N_{\varphi\theta} r)}{\partial\varphi}+\frac{\partial(N_\theta)}{\partial\theta}r_\varphi + N_{\varphi\theta} r_\varphi\cos\varphi+\Delta P_{r\theta} r r_\varphi = 0 \tag{2}$$

$$\frac{N_\varphi}{r_\varphi}+\frac{N_\theta}{r_\theta}+\Delta P_r = 0 \tag{3}$$

where;

$$r_\varphi = \frac{a^2b^2}{\left(a^2\sin^2\varphi + b^2\cos^2\varphi\right)^{1.5}}$$

$$r_\theta = \frac{a^2}{\left(a^2\sin^2\varphi + b^2\cos^2\varphi\right)^{0.5}}$$

$$\Delta P_{r\varphi} = P^o_{r\varphi} - P^i_{r\varphi}$$

$$\Delta P_{r\theta} = P^o_{r\theta} - P^i_{r\theta}$$

$$\Delta P_r = P^o_r - P^i_r$$

$$r = r_\theta \sin\varphi$$

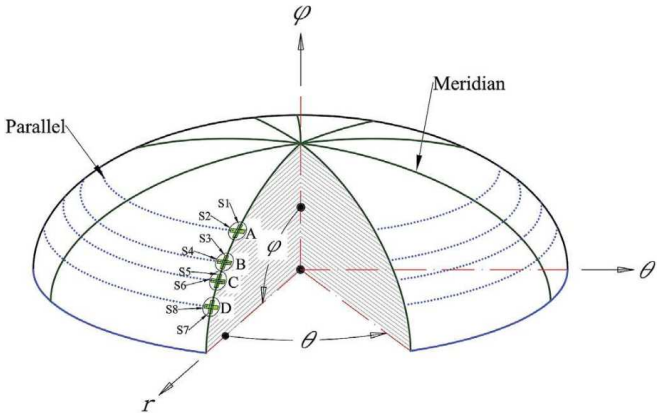


**Fig. 1.** Schematic of spherical coordinate axis and location of the surface-bounded sensors in an ellipsoidal composite shell.

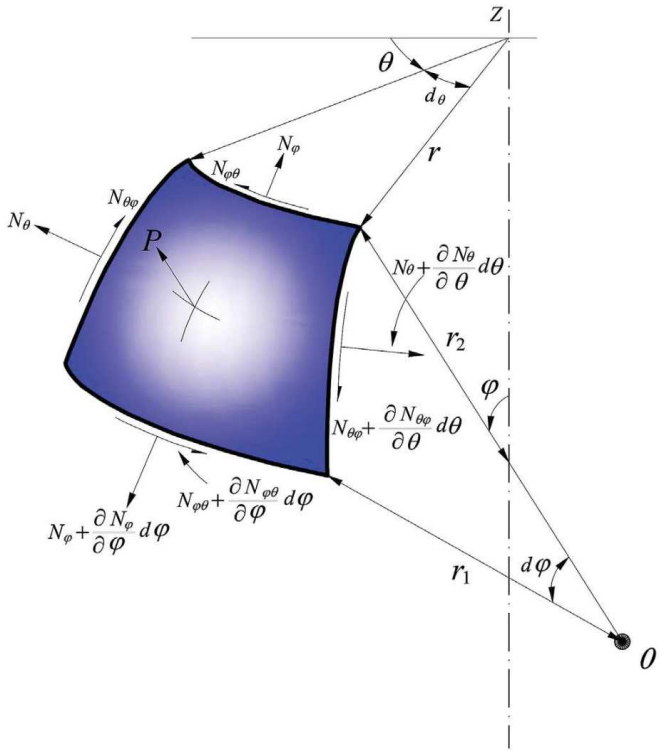


**Fig. 2.** Direct and shear stress resultants in a shell element subjected to internal pressure.

As shown in Fig. 1, $r_\varphi$ and $r_\theta$ are defined as radius of the ellipsoidal shell's curvature, $r$ is the radius of a parallel circle$P^o_{r\varphi}$,$P^o_{r\theta}$,$P^o_r$ and $P^i_{r\varphi}$,$P^i_{r\theta}$,$P^i_r$ are the outer and inner surface stresses in the direction of meridian, circumference and radius, respectively. $r_\varphi$ and $r_\theta$ being substituted into Eq. (3) results in a relationship between Shell's stress resultants as shown in Eq. (4).

$$N_\theta = -\left[N_\varphi\frac{\left(a^2\sin^2\varphi + b^2\cos^2\varphi\right)}{b^2} + \Delta P_r\frac{a^2}{\left(a^2\sin^2\varphi + b^2\cos^2\varphi\right)^{0.5}}\right] \tag{4}$$

Eq. (4) is then substituted into Eq. (1) to obtain the following differential equation for $N_\varphi$, as shown in Eq. (5).

$$\begin{aligned}&\frac{\partial N_\varphi}{\partial\varphi}+N_\varphi\left[\frac{b^2\cot\varphi}{a^2\sin^2\varphi+b^2\cos^2\varphi}+\cot\varphi\right]\\&+\frac{\partial N_{\varphi\theta}}{\partial\theta}\left[\frac{b^2}{\sin\varphi\left(a^2\sin^2\varphi+b^2\cos^2\varphi\right)}\right]\\&+\Delta P_r\left[\frac{a^2b^2\cot\varphi}{\left(a^2\sin^2\varphi+b^2\cos^2\varphi\right)^{1.5}}\right]\\&+\Delta P_{r\varphi}\left[\frac{a^2b^2}{\left(a^2\sin^2\varphi+b^2\cos^2\varphi\right)^{1.5}}\right]\\&=0\end{aligned} \tag{5}$$

The integration factor method is used to solve the first order differential equation for $N_\varphi$, resulting in Eq. (6).

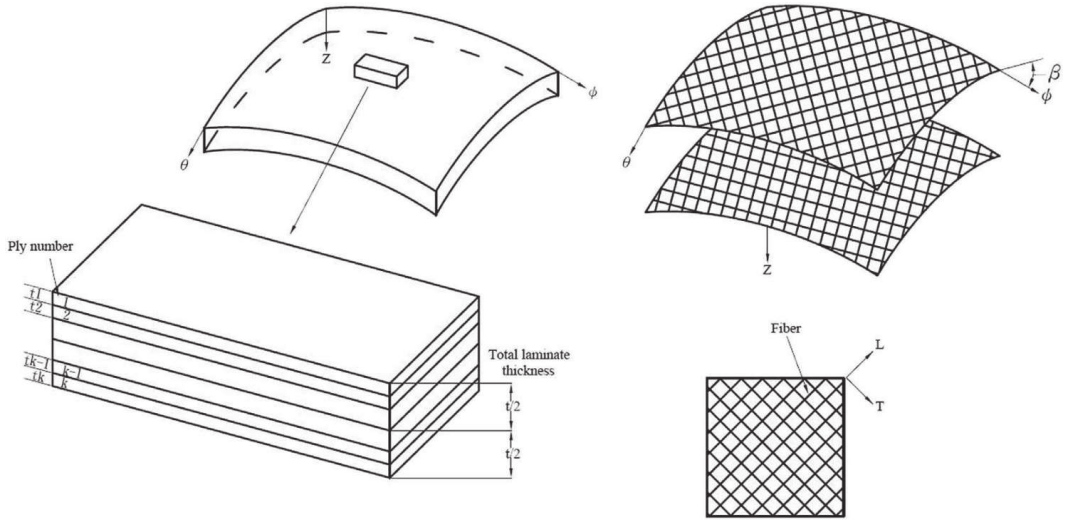


**Fig. 3.** Schematic of a Lamination Geometry with fibres' winding angle.

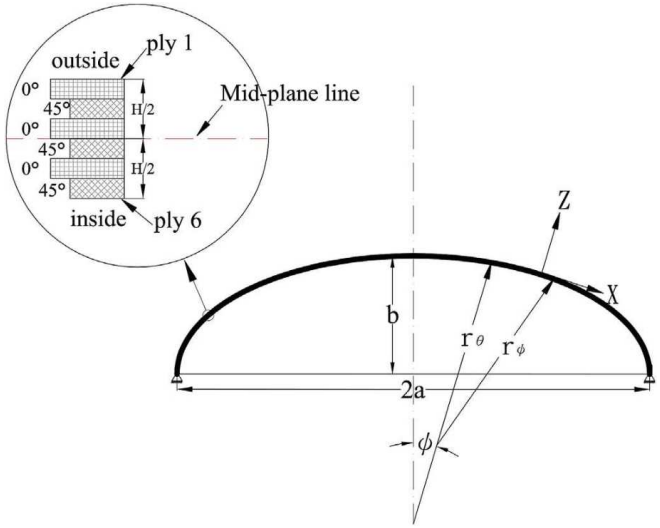


**Fig. 4.** Schematic of laminated ellipsoidal shell with cross-sectional view.

$$N_\varphi = \left[\frac{(a^2\sin^2\varphi + b^2\cos^2\varphi)^{0.5}}{\sin^2\varphi}\right] \times \left[C - \int \frac{S\sin^2\varphi}{(a^2\sin^2\varphi + b^2\cos^2\varphi)^{0.5}}d\varphi\right] \quad (6)$$

where;

$$S = \frac{\partial N_{\varphi\theta}}{\partial\theta}\left[\frac{b^2}{\sin\varphi(a^2\sin^2\varphi + b^2\cos^2\varphi)}\right] + \Delta P_r\left[\frac{a^2b^2\cot\varphi}{(a^2\sin^2\varphi + b^2\cos^2\varphi)^{1.5}}\right] + \Delta P_{r\varphi}\left[\frac{a^2b^2}{(a^2\sin^2\varphi + b^2\cos^2\varphi)^{1.5}}\right]$$

In this study, some assumptions have been adopted to simplify the stress resultants equations. It is assumed that the shell is subjected to the constant internal pressure $P_r^i = P$. Thus, it can be concluded that $N_{\varphi\theta} = \Delta P_{r\varphi} = \Delta P_{r\theta} = P_r^o = 0$ , since internal pressure results in shell being symmetrically loaded. It is further assumed that there is no external pressure applied on the shell. The constant of integration $C$ presented in Eq. (6) is also assumed to be equal to zero to prevent unbounded result at $\varphi = 0$. Finally, based on the assumptions made, the meridian and radial stress resultants can be obtained using Eqs. (7) and (8).

$$N_\varphi = \frac{P}{2}\left[\frac{a^2}{(a^2\sin^2\varphi + b^2\cos^2\varphi)^{0.5}}\right] \quad (7)$$

$$N_\theta = \left[\frac{Pa^2}{2(a^2\sin^2\varphi + b^2\cos^2\varphi)^{0.5}}\right]\left[2 - \frac{a^2\sin^2\varphi + b^2\cos^2\varphi}{b^2}\right] \quad (8)$$

In this study, the shell's total thickness is defined as $H$. It is assumed that each ply's thickness defined as $h$ is constant. Fibre angle orientation (winding angle of fibre with respect to $\varphi$ direction) is $\beta$ as shown in Fig. 3, and the distance from mid-plane (plane between plies numbers 3 and 4 as shown in Fig. 4) to the $k$th ply is $h$. $t$ is ply thickness as stated in Eq. (9). Here, the stress resultants in the geometric coordinate axes are stated in Eq. (10).

$$t = \frac{H}{k} \quad (9)$$

$$[N] = [A][\varepsilon] + [B][K] \quad (10)$$

where $k$ is number of layers; $K$ is the curvature matrix in the laminate; $H$ is the total thickness; $N$ is the vector of stress resultants [$N/m$], [$A$] and [$B$] stand for the extensional and flexural stiffness matrixes, respectively; and $\varepsilon$ is the strains vector. The relationship between stresses and strains for the $k$th orthotropic layer is represented in Eq. (11).

$$\sigma^{(k)} = \overline{Q}^{(k)}\varepsilon + zK^{(k)} \quad (11)$$

$\sigma^{(K)}$ stands for the vector of stresses for the $k$th ply; $\overline{Q}$ is known as transformed material stiffness content (refer to Appendix A) and z

**Table 1**
Characteristics of laminated woven GFRP shell incorporated with surface-bounded sensors.

| Shell's geometry | Shell's elastic properties | Sensor characteristics |
|---|---|---|
| $\beta^o = [0/45/0/45/0/45]$ | $E_L = E_T = 20.8[GPa]$ | Type. FCA-3-11 |
| $a = 200$ [mm] | $G_{LT} = 3.92$ [GPa] | Lot No. A601522 |
| $b = 100$ [mm] | $\upsilon_{LT} = 0.173$ | Batch No. II28K |
| $t = 0.35$ [mm] | $F_{1t} = F_{1C} = 473$ [MPa] | Gauge Length. 3 [mm] |
| | $F_{2t} = F_{2C} = 473$ [MPa] | Gauge Resistance. 120 ± 0.5 [Ω] |
| | $F_6 = 85$ [MPa] | Gauge Factor. 1 = 2.12, 2 = 2.12, ±1 [%] |
| | | Transverse Sensitivity. 0.2 [%] |

stands for distance from the mid-plane in the thickness direction. Local stress resultants can be obtained using Eq. (12).

$$[\sigma]_k^{Local} = [T][\sigma]_k^{Global} \tag{12}$$

In Eq. (12) $T$ is the transformation matrix (refer to Appendix A) which varies as fibre angle orientation changes. Global load resultants $N_\varphi$ and $N_\theta$, applied per unit length [N/m] in the meridian and radial directions respectively in a shell element internally pressurized (refer to Fig. 1), can be obtained using Eq. (9) and Eq. (10), respectively. The shear stress value shown is equal to zero due to symmetric loading. Bending and twisting moments $M_\varphi$, $M_\theta$ and $N_{\varphi\theta}$ are assumed to be zero. The relationship between in-plane stress resultants is defined in Eqs.(13)–(15) [32]. These equations relate the normal load resultants with the stress values at $k$th ply in the shell.

$$N_\varphi = \int_0^H \sigma_\varphi \left(1 + \frac{z}{r_\theta}\right) dz \tag{13}$$

$$N_\theta = \int_0^H \sigma_\theta \left(1 + \frac{z}{r_\varphi}\right) dz \tag{14}$$

$$N_{\varphi\theta} = \int_0^H \tau_{\varphi\theta} \left(1 + \frac{z}{r_\varphi}\right) dz \tag{15}$$

After defining the shell principle equations, they are combined with laminated composite materials theory. The coordinate axis of

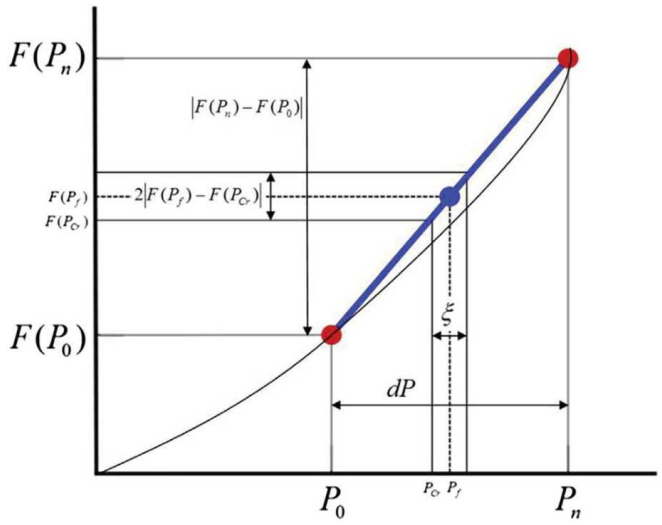


**Fig. 5.** Schematic of linear interpolation technique used to predict the shell's first-play failure at $k$th ply.

local material orientations along fibre and perpendicular to fibres are defined as longitudinal and transfer axis, respectively, shown as $L$ and $T$ orientations in Fig. 3. Reduced stiffness matrix and transformation matrix are both dependent on the material properties of composite materials (refer to appendix A). The compliance matrices, A, B and D of the composite shell internally pressurized are shown in Eq. (16), Eq. (17), Eq. (18) and Eq. (19), respectively. The constitutive form of the compliance matrices, A, B and D consists of 12 elements for $i,j = 1,2, \ldots,6$. However, in this study the simple form of the stiffness matrix is considered, neglecting shear deformation and transverse normal stress, letting $i,j = 3,4,5 = 0$ [33]. Values of global load resultants [N/m] for $N_\varphi$ and $N_\theta$ in ellipsoidal shell subjected to static internal pressure can be obtained using Eq. (9), Eq. (10) and Eq. (11), respectively. Schematic of ellipsoidal shell semi-minor and semi-major axis with its cross-sectional view is illustrated in Fig. 4.

$$\begin{bmatrix} N_\varphi \\ N_\theta \\ N_{\varphi\theta} \\ M_\varphi \\ M_\theta \\ M_{\varphi\theta} \end{bmatrix} = \begin{bmatrix} A_{11} & A_{12} & A_{16} & B_{11} & B_{12} & B_{16} \\ A_{12} & A_{22} & A_{26} & B_{12} & B_{22} & B_{26} \\ A_{16} & A_{26} & A_{66} & B_{16} & B_{26} & B_{66} \\ B_{11} & B_{12} & B_{16} & D_{11} & D_{12} & D_{16} \\ B_{12} & B_{22} & B_{26} & D_{12} & D_{22} & D_{26} \\ B_{16} & B_{26} & B_{66} & D_{16} & D_{26} & D_{66} \end{bmatrix} \cdot \begin{bmatrix} \varepsilon_\varphi \\ \varepsilon_\theta \\ \varepsilon_{\varphi\theta} \\ K_\varphi \\ K_\theta \\ K_{\varphi\theta} \end{bmatrix} \tag{16}$$

$$A_{ij} = \sum_{K\equiv 1}^{n} \left[\overline{Q}_{ij}\right]_K (h_K - h_{k-1}),\ i = 1,2,6;\ j = 1,2,6 \tag{17}$$

$$B_{ij} = \frac{1}{2}\sum_{K\equiv 1}^{n} \left[\overline{Q}_{ij}\right]_K \left(h_K^2 - h_{K-1}^2\right),\ i = 1,2,6;\ j = 1,2,6 \tag{18}$$

$$D_{ij} = \frac{1}{3}\sum_{K\equiv 1}^{n} \left[\overline{Q}_{ij}\right]_K \left(h_K^3 - h_{K-1}^3\right),\ i = 1,2,6;\ j = 1,2,6 \tag{19}$$

where, the initial conditions are;

$$N_{\varphi\theta} = M_\varphi = M_\theta = M_{\varphi\theta} = 0$$

$$N_\varphi = \frac{P}{2}\left[\frac{a^2}{\left(a^2 \sin^2\varphi + b^2\cos^2\varphi\right)^{0.5}}\right]$$

$$N_\theta = \left[\frac{Pa^2}{2\left(a^2\sin^2\varphi + b^2\cos^2\varphi\right)^{0.5}}\right]\left[2 - \frac{a^2\sin^2\varphi + b^2\cos^2\varphi}{b^2}\right]$$

To assess the strength of a shell structure, a failure criterion is needed. In this study, Tsai-Wu failure is adopted in the study of the laminated ellipsoidal shell internally pressurized. Tsai–Wu failure criterion stipulates that for non-failure the constraint given in Eq. (20) below should be satisfied.

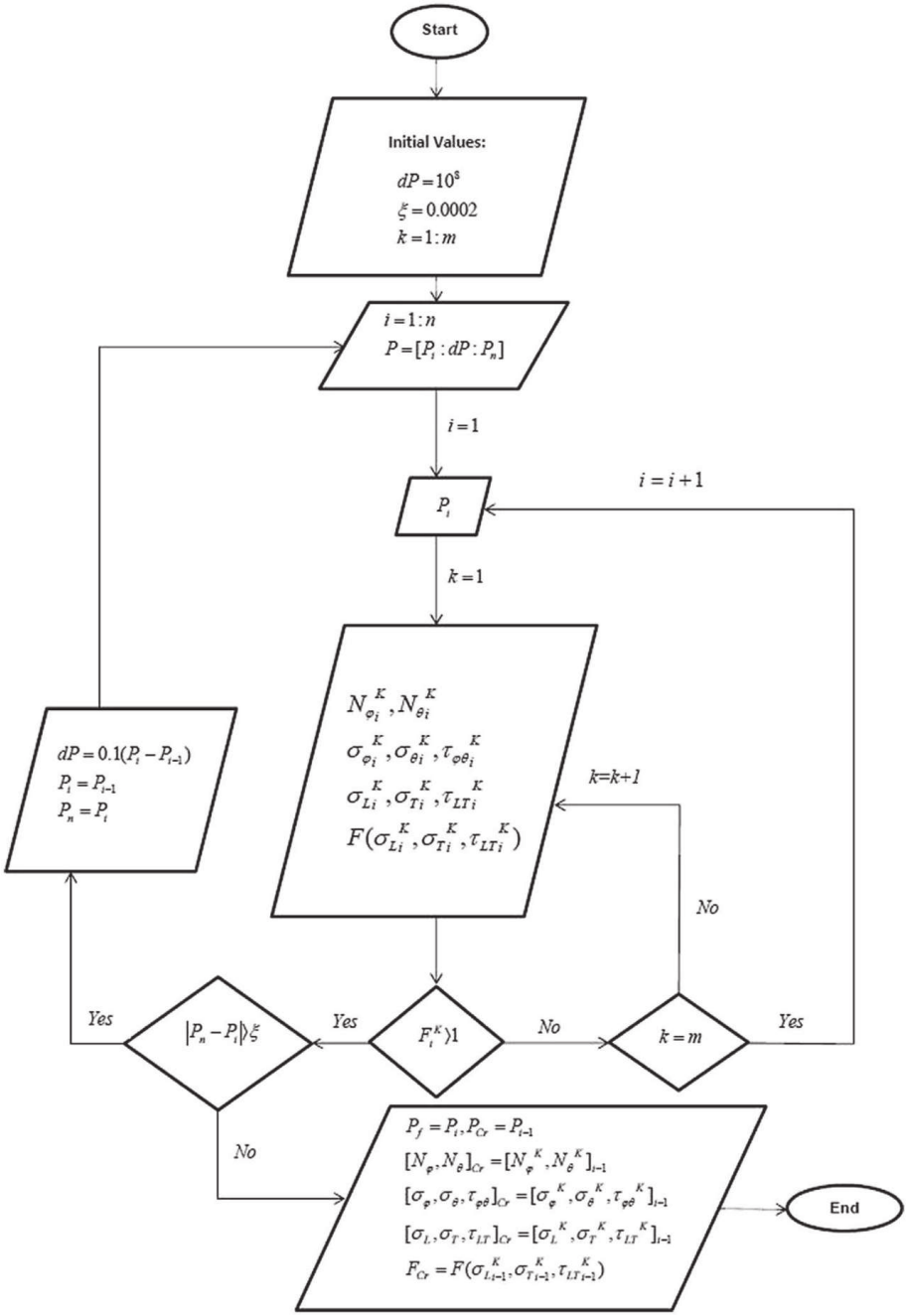


**Fig. 6.** The algorithm used for the theoretical analysis to interpolate the shell's first-ply failure at *k*th ply.

$$F_{11}\left(\sigma_L^{(K)}\right)^2 + F_{22}\left(\sigma_T^{(K)}\right)^2 + F_{66}\left(\tau_{TL}^{(K)}\right)^2 + 2F_{12}\sigma_L^{(K)}\sigma_T^{(K)} + F_1\sigma_L^{(K)} + F_2\sigma_T^{(K)} \le 1$$

$$F(\sigma_L, \sigma_T, \sigma_{LT})_K \le 1 \tag{20}$$

where,

$$F_{11} = (F_{1t}\times F_{1C})^{-1}, F_{22} = (F_{2t}\times F_{2C})^{-1}, F_{66} = (F_6)^{-2},$$
$$F_1 = (F_{1t})^{-1} - (F_{1C})^{-1}, F_2 = (F_{2t})^{-1} - (F_{2C})^{-1},$$
$$F_{12} = -0.5(F_{1t}\times F_{1C}\times F_{2t}\times F_{2C})^{-0.5}$$

$F_{1t}$, $F_{2t}$, $F_{1c}$ and $F_{2c}$ are the tensile and compressive strength of the composite material along longitudinal and transverse directions respectively, and $F_6$ is the in-plane shear strength. Material properties and geometry of woven GFRP composite are shown in Table 1.

Finally, the linear interpolation technique is used to interpolate (with high accuracy) the failure and critical pressure values $P_f$ and $P_{Cr}$, respectively over the initial pressure interval at which the first-ply failure occurs. This numerical technique is adopted because the theoretical prediction of the failure pressure in the selected pressure interval at which the first-ply failure occurs is impossible. It must be taken into account that load stress resultants vary at each meridian angle. This problem becomes more crucial when the number of layers increases. The schematic of linear interpolation technique and its application in the current study is shown in Fig. 5.


**Fig. 7.** Elliptical shell pattern made of polyurethane foam. (a) Covered by putty; (b) Polished.

In addition, the analytical procedures performed are summarized in the form of an algorithm as shown in Fig. 6.

According to Fig. 6, the initial input values are selected in the interpolation algorithm. These values include *dp*, $\xi$ and *k* which stand for the initial range of internal pressure interval in which the failure pressure lies within, the range of interpolation accuracy, and number of plies in the composite laminate, respectively. Subsequently, the initial values undergo the series of systematic loops

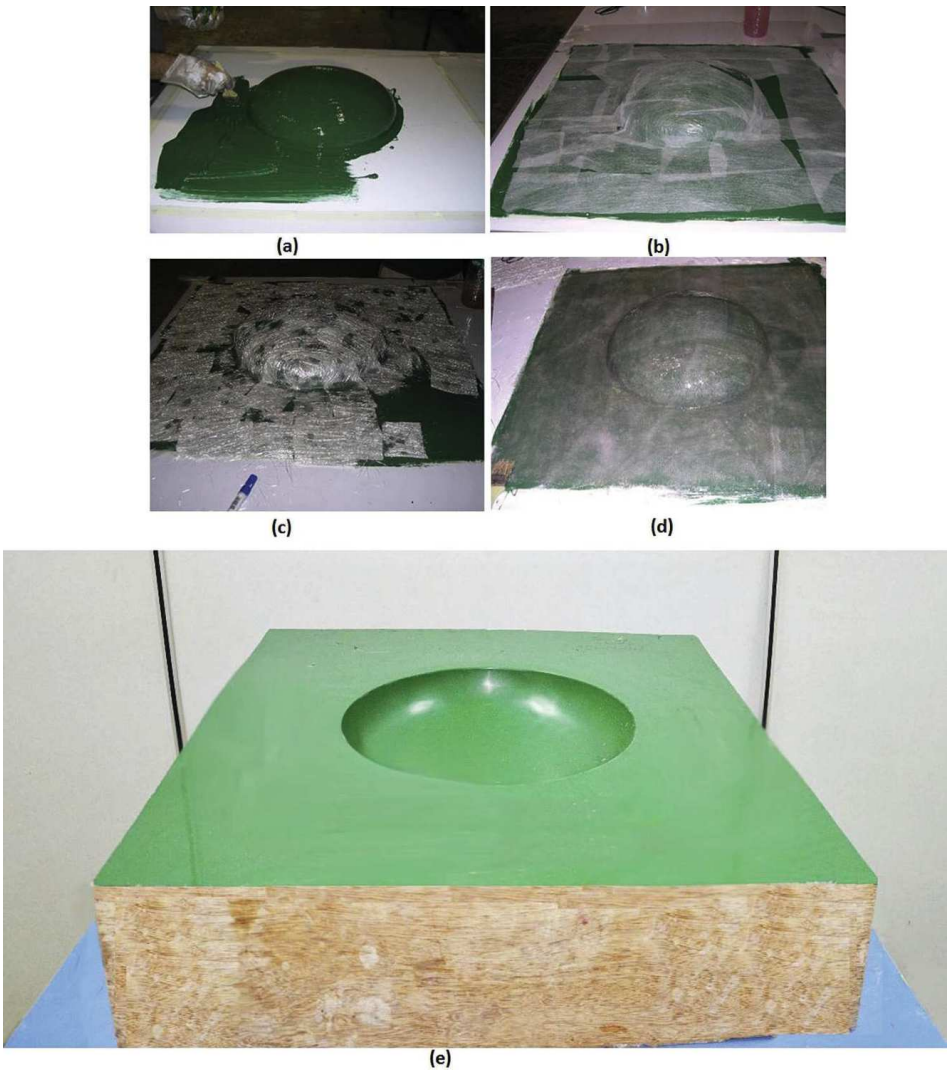


**Fig. 8.** Mould manufacturing process, (a) Applying gelcoat; (b) Laying up tissues; (c) CSM laying up; (d) Curing; (e) Final composite mould.

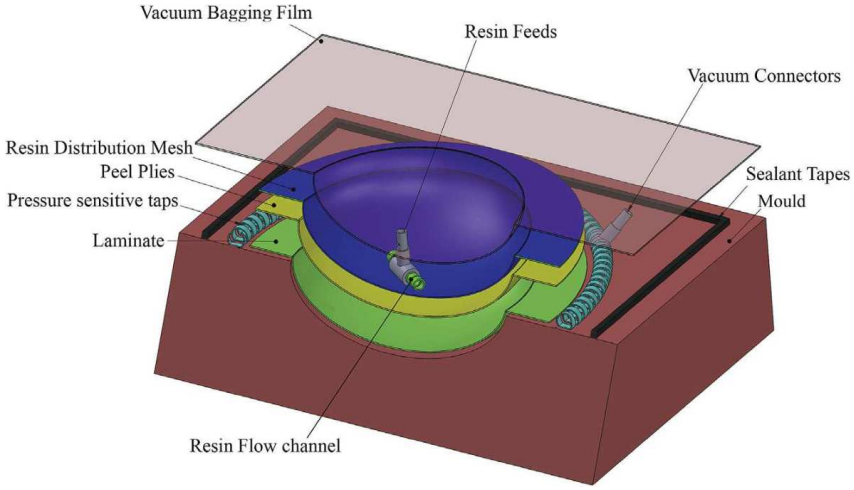


**Fig. 9.** Schematic of the test rig including Sequences of Layers and material used in infusion process.

until the desired failure/critical internal pressure and the output parameters such as failure/critical external load resultants applied to the shell elements, failure/critical stress/strains at the particular layer, and critical failure factor to avoid failure according to Tsai-Wu failure criterion, are accurately interpolated. Upon successfully obtaining all failure/critical output parameters, the loops are terminated and the interpolation algorithm ends.

## 3. Experimental procedures

### 3.1. Preparation of the laminated ellipsoidal shell model

In the experimental work the VIP method was used to fabricate the shells. The VIP is a method in which vacuum pressure is applied to drive resin into dry fibre reinforcement material. Dry fibres are placed in the mould before vacuum is applied. Once a complete vacuum is achieved, resin is sucked into the dry fibres through resin feed tubing. A vacuum pump is utilized for evacuating the air and consolidating the dry materials and finally creating a "vacuum cavity". Resin is then injected into the cavity via resin feeder lines. The pressure difference between the cavity and atmospheric pressure causes the resin to flow through the porous materials until the part is completely saturated. The vacuum is continued until the part is consolidated. In this research, epoxy resin (type: 1006) and fibre glass (type 290gsm plain weave Woven Rovings (WR)) were used to produce composite shells using VIP technique. Epoxy resin is the matrix. Direction of the fibres was based on WR $[0/45]_3$ procedures during the manufacturing process. The mould and plug as well as design and fabrication of the test rig and experimental tests will be explained here.

The schematic of the laminated ellipsoidal composite shell and its cross-section as shown in Fig. 3 was discussed in section.2. The geometry was determined at pre-processing section.

### 3.2. Mould preparation

Male (plug) and female moulds are two fundamental types of moulds; however they produce significantly different parts. Mould which is also called female mould is the reverse of the reverse of the object's shape. Making the mould is the first step in the procedure of manufacturing a composite shell through vacuum infusion method. In this work, hand lay-up method was used for preparing the mould. Manufacturing process of glass fibre mould started by producing a plug, which is an exact representation of the object to be made.

#### 3.2.1. Constructing the plug

Successful mould construction requires proper preparation of the plug, including the exact shape and dimension of the final part, used to create the female mould. In this research, elliptical shell pattern is prepared by shaping closed cell polyurethane foam based on geometries. Computer Numerical Control (CNC) milling machine was used to form shell patterns. The plug needs to have a finish surfaces as good as the desired part to be produced. Some of imperfections in the plug surface will be transferred to the mould, and then to future parts made from the mould. The preferable surface for the plug is a polished smooth finish without any scratches or porosity. In order to achieve an acceptable mould surface and a long mould life, the plug was covered with means of plaster putty and, subsequently polished uniformly in order to have a smooth surface-finish. It is far more effective to remove defects from the plug surface than attempting to remove defects from the mould surface. Fig. 7a and b shows the elliptical shell pattern made of polyurethane foam.

#### 3.2.2. Constructing the female mould

After forming the plug, female mould is manufactured using plug mould. For manufacturing the female mould in the first step, a mould release agent is applied to the plug. If the mould does not release properly from the plug, the mould and the plug could be either damaged or destroyed. Due to this, the release wax was applied several times on the surface of the plug. Once this step was completed, the gelcoat was applied on the surface. Gelcoat is used to make the mould surface strong and scratch resistant. It also contributes to a high-quality surface-finish in shells. After the surface coat was applied, it was left for 3–4 h to become approximately cured and then the procedure was followed by putting a layer of tissues on the gel coat. Subsequently, Chopped Strand Mat (CSM) fibres with resin were hand layup on the plug surface. Applying CSM and resin continued several times to achieve desired number of layers and to also ensure the coated mould has become string enough. Eventually, the mould was left for 24–48 h to cure completely.

It must be distinguished that the first layer of reinforcement is the most critical layer in the mould to lay down without trapping air bubbles. For the other layers also, the air must be released from laminate at least every other layer. The other important thing to

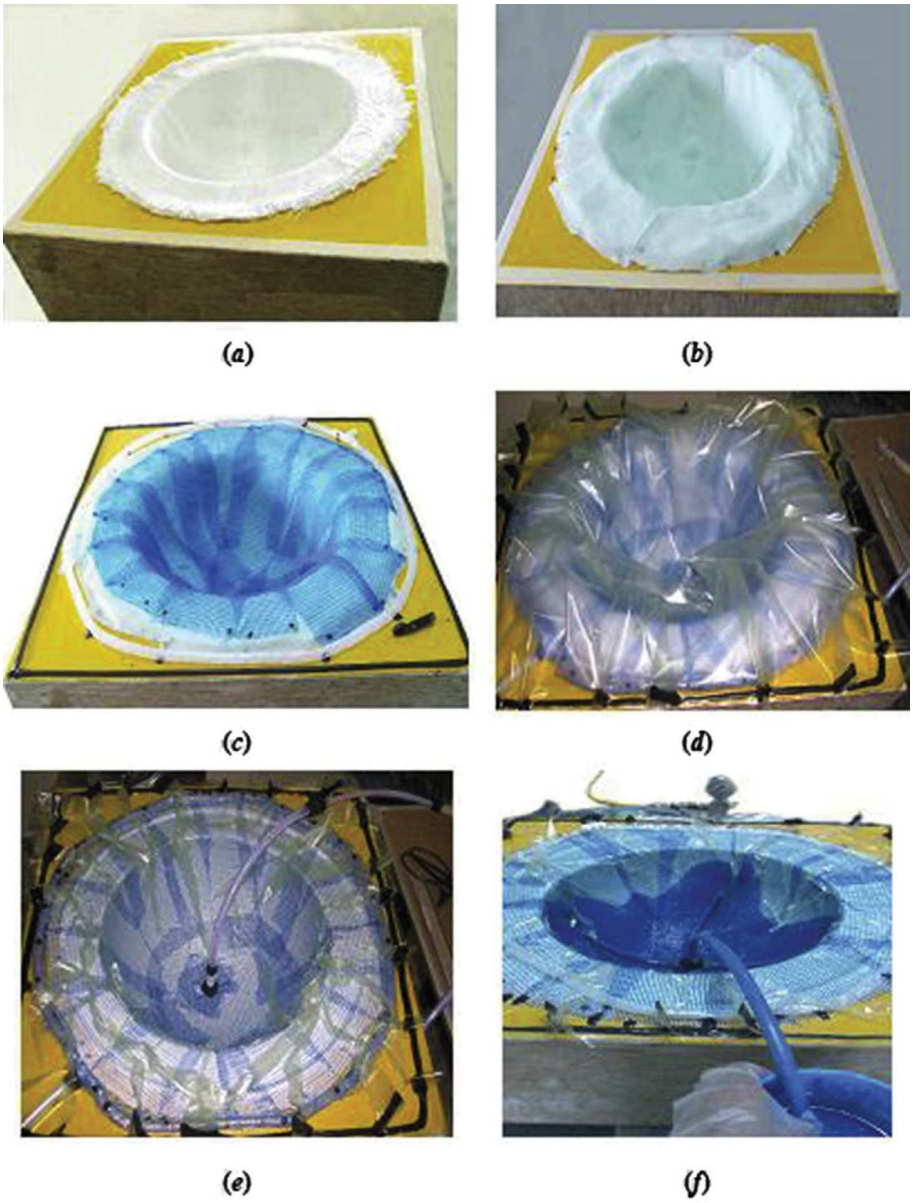


**Fig. 10.** The sequences of producing composite shell, (*a*) Woven fibre glass placed on the mould; (*b*) Peel ply; (*c*) Resin flow mesh; (*d*) Vacuum bagging film; (*e*) Vacuum pressure applied; (*f*) Resin infusion.

**Fig. 11.** Schematic of the test ring, pressure gauge hydraulic oil pump and connecting hose.

take into consideration in making female mould is that in case of using chopped strand mat, it must be torn (not cut) into manageable chunks so the frayed edges blend well with one another without trapping air like sharp scissor cut edges do. When the mould is sufficiently cured, it can be separated from the plug. In order to separate the female mould off the plug, the wedge is released and air shut gun can is used. The produced female mould is used in VIP or manufacturing shells. Fig. 8a–e illustrate the sequence of mould manufacturing.

### 3.3. Laminated ellipsoidal shell fabrication

Manufacturing of laminated ellipsoidal composite shells was performed using VIP. The advantages of using VIP are that the parts fabricated using VIP method are stronger, lighter, and more economical. In addition, quality control issues are much easier. Inspections can be easily carried out before the resin is introduced

**Fig. 12.** Schematic of shell's boundary condition and gauge sensors instalment on the second sample.

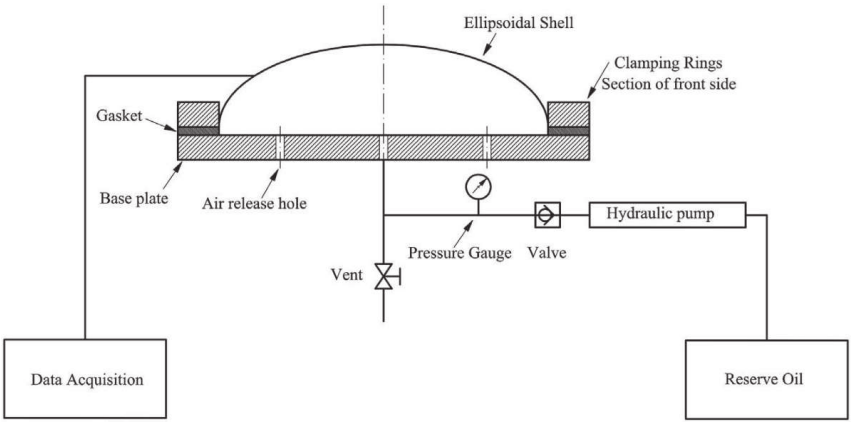


**Fig. 13.** Schematic of the testing setup of the composite shell under internal pressure.

**Table 2**
Critical internal pressure and strains at $k = 1$ based on analytical and experimental approaches.

| | | $P_{Cr}$ [MPa] | | | | $e^1$ [%] | | | |
|---|---|---|---|---|---|---|---|---|---|
| Ana. | | 1.6449 | | | | 8.80 | | | |
| Exp. | | 1.5 | | | | | | | |
| | | $\varphi = 45^o$ | $e$ [%] | $\varphi = 67^o$ | $e$ [%] | $\varphi = 74^o$ | $e$ [%] | $\varphi = 80^o$ | $e$ [%] |
| Ana. | $\varepsilon_\varphi$ | 0.0037 | 26 | 0.0054 | 14.81 | 0.0058 | 15.51 | 0.0061 | 1.63 |
| Exp. | | 0.0050 | | 0.0046 | | 0.0049 | | 0.0060 | |
| Ana. | $\varepsilon_\theta$ | −0.0025 | 26.47 | −0.0068 | 16.17 | −0.0082 | 7.31 | −0.0089 | 13.48 |
| Exp. | | −0.0034 | | −0.0057 | | −0.0076 | | −0.0077 | |

$e^1 = \left|\frac{x_1 - x_2}{x_1}\right| \times 100.$

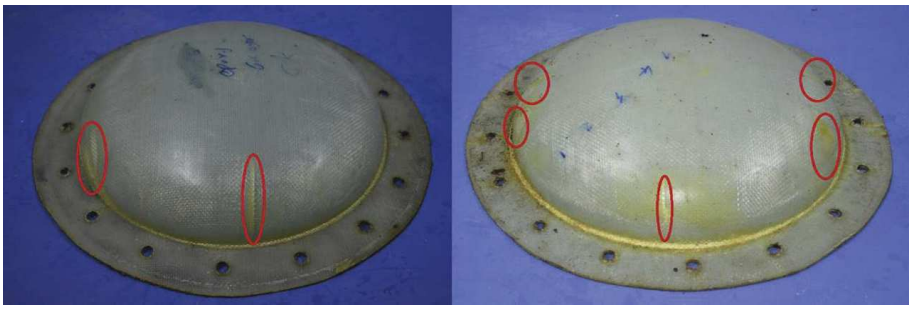

**Fig. 14.** Observation of failure in the shell's outermost ply ($k = 1$) at pressure of $P_f = 1.7$ [MPa] at $\varphi = [70–90]$.

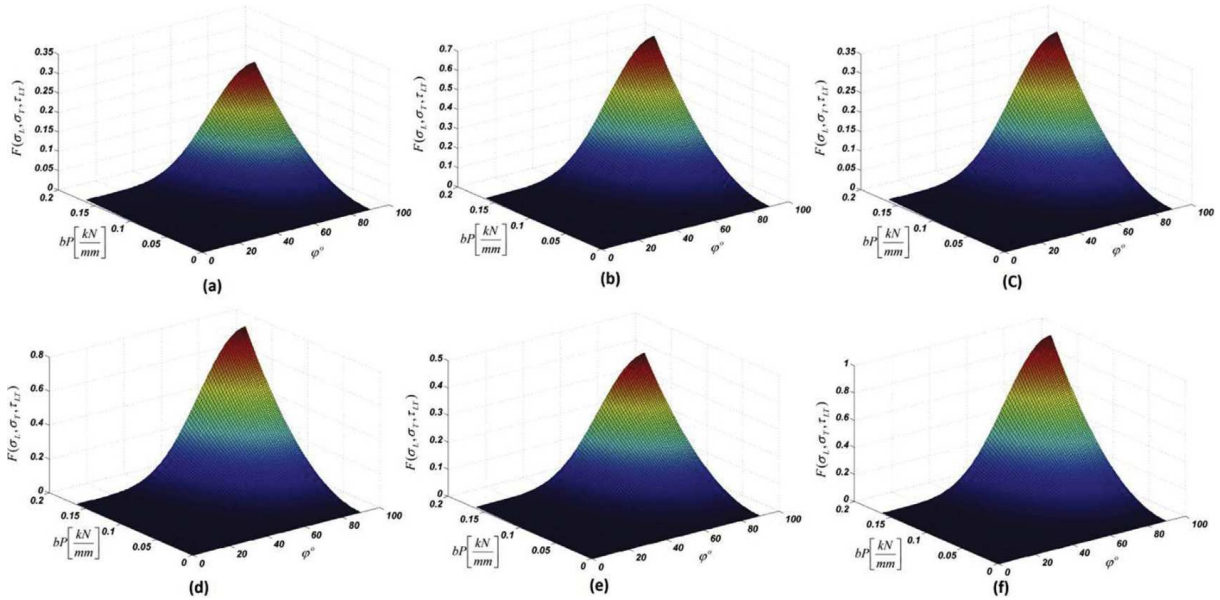


**Fig. 15.** Failure factor distribution against meridian and *b. P* factor in the laminated ellipsoidal GFRP shell with *(a/b)* = 2 at a) $k = 1$, b) $k = 2$, c) $k = 3$, d) $k = 4$, e) $k = 5$, and f) $k = 6$, respectively.

into the part, and with the use of clear gel coat, the part is very easily examined for flaws after the infusion process. The vacuum evenly applies pressure, conforming to both simple and complex shapes. Application of vacuum provides control of part thickness by compressing the laminate during cure. Furthermore, the process is environmentally friendly. This also means that the working environment is greatly improved. Today, VIP is drawing significant interest due to its low capital investment and easily manageable learning curve [34,35].

In this study, materials are first laid up dry into the mould and the vacuum is applied before resin is introduced. Once a complete vacuum is achieved, resin is literally sucked into the laminate via carefully placed resin-feed tubing. A vacuum pump is used to evacuate the air and apply atmospheric pressure to consolidate the dry materials and create a "vacuum cavity". Subsequently, resin is introduced into the cavity via strategically placed resin feeder lines. The pressure differential between the cavity and the outside atmospheric pressure pushes the resin through the porous materials until the part is completely saturated. The vacuum is maintained until the part is consolidated. The surface-bounded sensors characteristics used in the experimental analysis are shown in Table 1. Meanwhile, some bubbles were detected in the resin mixture during the fabrication process. Voids caused by bubbles were released from the resin before performing VIP to boost the quality of the shell. The following procedures were performed during the shell's fabrication using VIP method:

- Controlling the environmental temperature at 22 °*C*.
- Mould preparation and surface impregnation using wax.
- Selecting stanching sequence for woven glass fibres, as shown in Fig. 4.
- Laying peal ply and resin flow mesh on the mould surface based on the stacking sequence.
- Placing resin flow channel circumferentially on the shell and using vacuum bagging film and sealant tape to cover and seal the channel, respectively.
- Making resin through blending epoxy and hardener with ratio of 10:6 by weight.

The materials and tools required for infusion process to manufacture a part as well as the materials location on the mould during the infusion process are illustrated in Fig. 9.

The following sequences were carried out to fabricate the ellipsoidal shell via the infusion method. As the initial step, the surface of the mould was polished by releasing wax. Woven glass fibres were placed on the mould with layup sequence of WR [0/45] 3 (Fig. 10a), peel ply and resin flow mesh were then placed on the surface of the mould in the same order (Fig. 10b and c). After that, the resin flow channels were placed circumferentially on the mould and all were covered with a vacuum bagging film and sealed with a sealant tape (Fig. 10d). In the next step, the fibres were held under 1 bar vacuum pressure for 8–12 h in order to release the air bubbles and the moisture (Fig. 10e). The resin was then produced by blending epoxy and hardener in the exact ratio of 10:6 by weight. During the mixing of the epoxy and hardener, some bubbles appeared in the resin that led to some voids in the composite shell. Thus, to solve this problem the resin was held under a 1 bar vacuum pressure for 5 min before starting the infusion process. At that point, the infusion process was started by flow of the resin through the resin feeder and then the fibres were impregnated by resin. In this project, the time taken for saturating the whole fibres with resin was around 30 min (Fig. 10f). The saturated fibres with resin were held under a 1 bar vacuum pressure for approximately 12 h to achieve adequate harness. After that, the shell could be separated from the mould by means of wedges and air shut gun.

### 3.4. Test rig setup

A special test rig was designed and fabricated for the purpose of this test. The composite shells were pressurized by pumping hydraulic oil continuously from an oil container. To release the air during injecting oil in the shell, four holes were made in the base plate. The schematic of the test rig, as well as the method of applying the internal pressure, is shown in Fig. 11. Rate of pressurization such that the rate of strain was adequately low and therefore the effect of loading rate on the behaviour of the composite shell during test was trivial. The oil pressure in the shell that

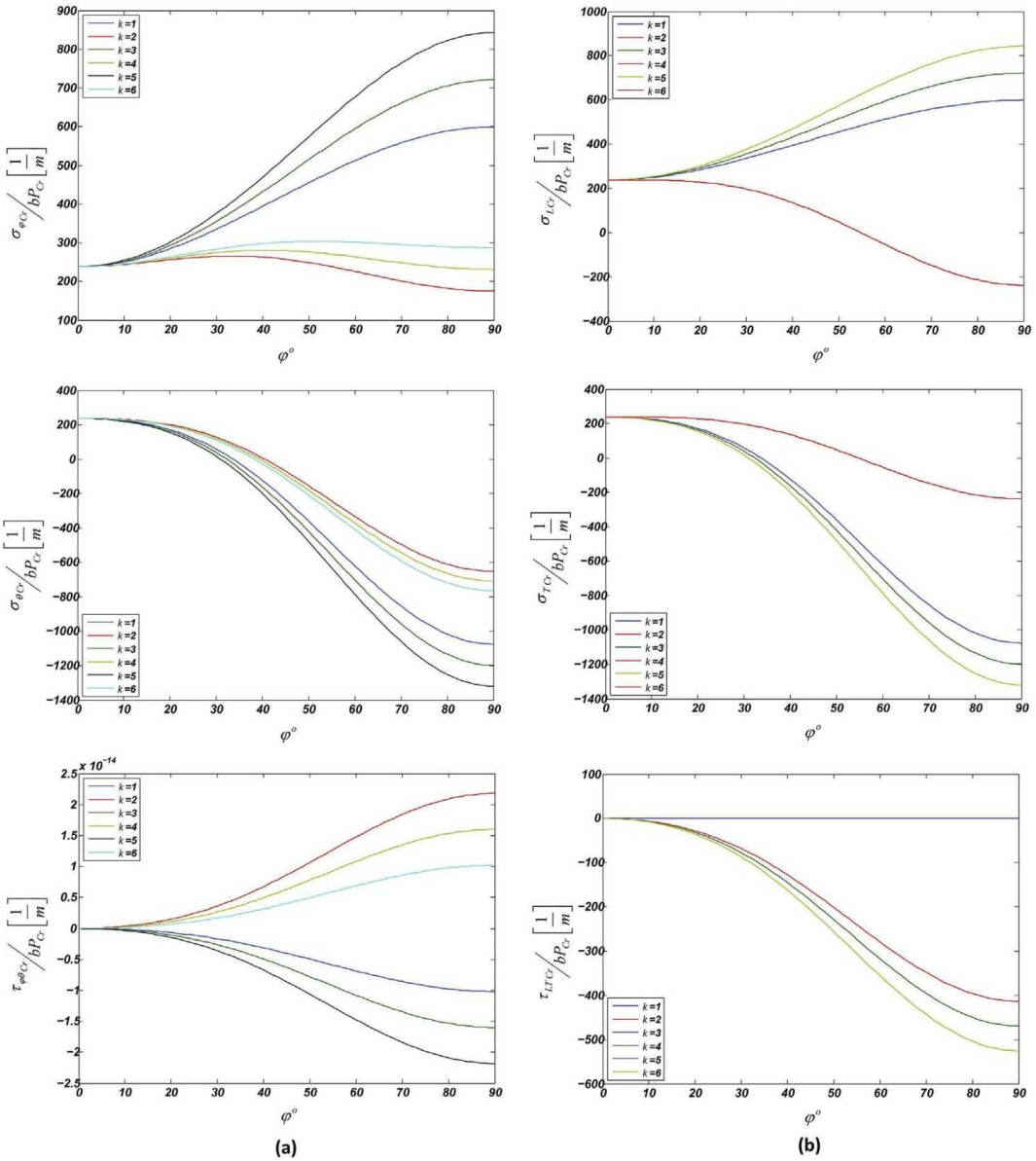


**Fig. 16.** Critical stress distribution Vs meridian angle in a) global and b) local material orientations, $(a/b) = 2$.

was measured by the installed pressure gauges, increased from 0 to 15 bars gradually. The gauge sensors were used to measure the strain values at some selected points along meridian directions. All gauge sensors were met in a data acquisition unit to record the history of strains as the pressure was increased in the shell. The schematic of fixing the shell's boundary conditions and installing the gauges sensors on the shell's surface is shown in Fig. 12. The sensors were then connected to a data acquisition unit to record the history of strains as pressure in the shell was increasing. The schematic of the testing setup of the composite shell under internal pressure is shown in Fig. 13.

## 4. Results and discussions

First-play failure of laminated ellipsoidal woven GRP shell internally pressurized, and with geometrical characteristics as shown in Figs. 1 and 4, was investigated analytically and experimentally. The Tsai-Wu failure criterion was used during the theoretical analysis to inspect the critical ply. Firstly, the critical and failure pressures were interpolated using the linear interpolation technique for some arbitrary points along the meridian direction. Subsequently, the analytical results were validated by the findings derived by the experimental analysis for the corresponding points along the meridian orientation in the actual model. The experimental analysis limitations are listed below:

- The first-ply failure occurred at the innermost ply ($k = 6$) according to Eq. (20), and the algorithm used during the theoretical analysis to interpolate the shell's first-ply failure as shown in Fig. 6. However, it was practically impossible to install sensors on such ply. The sensors could only be installed on the shell's surface ($k = 1$). Thus, the critical strains at $k = 1$, as a result of critical internal pressure, were compared with the corresponding values obtained from the experimental analysis.
- Since the concentrated stresses at boundary conditions were not considered in the analytical investigation, in the experimental analysis the shell is considered failed when the failure occurs at the regions regardless of the boundary conditions.

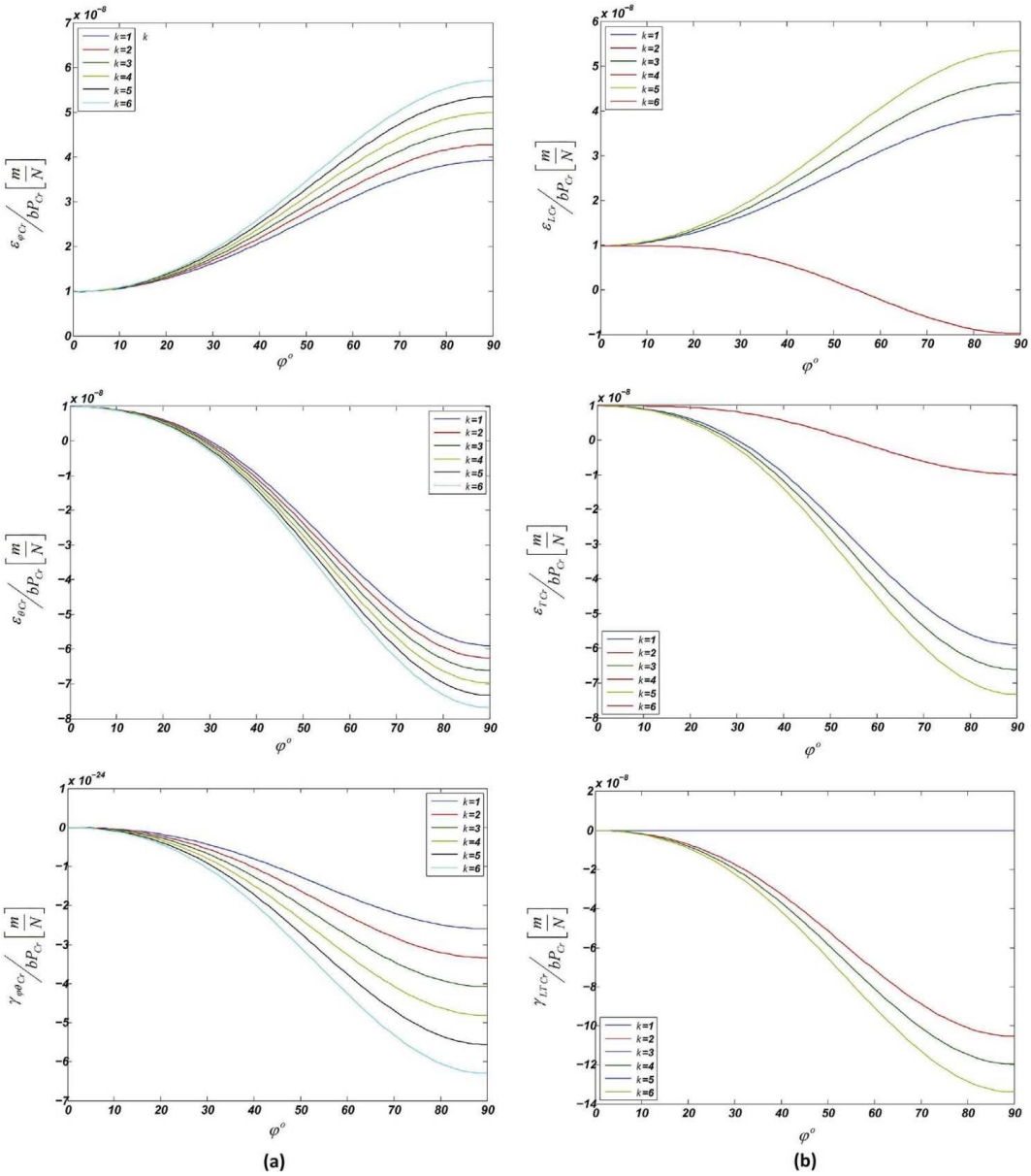


**Fig. 17.** Critical strain distribution Vs meridian angle in a) global and b) local material orientations, $(a/b) = 2$.

- The pressure recorded from pressure gauge represents the failure pressure at $k = 1$ rather than $k = 6$. The critical pressure to avoid first-ply failure must be less than the value recorded from pressure gauge. Thus, the shell's critical pressure at which the first-ply failure occurs is selected based on the critical pressure at $k = 1$.

In this study, two samples were fabricated during the experimental analysis. One sample was used for the purpose of obtaining the failure pressure. Subsequently, the gauge sensors were installed on the second sample in order to measure the strain values at critical pressure. The failure occurred at ply $k = 1$ and a pressure of 17 bar. Thus, the estimated critical pressure to avoid failure at the outmost ply was 16 *bar*. Conversely, a pressure of 15 *bar* was selected as a critical pressure to avoid failure at innermost ply. Table 2 shows the comparison between analytical and experimental results for the laminated ellipsoidal woven GFRP composite shell internally pressurized. According to Eq. (20) and the linear interpolation algorithm shown in Fig. 6, the failure occurs at higher meridian angles, which is around the shell's edges since for any ply, the failure factor increases as $\varphi \rightarrow 90^{\circ}$. According to the experimental analysis, the failure area was observed to be close to the shell's edges, where it was fixed to its boundaries regardless of concentrated stresses at that area. According to the experimental test of the first sample, a small amount of hydraulic oil drops was observed at the pressure of nearly 17 *bar*. Furthermore, the shell's surface colour at the area along the meridian axis and close to the boundary varied significantly, indicating the shell's instability in that region. The analytical investigation, which shows the failure factor distribution along the meridian direction for $k^{th}$ ply as shown in Fig. 14, also indicates the same trend of failure. Thus, it can be concluded that as the meridian angle increases ($\varphi \rightarrow 90^{\circ}$) the failure factor rises. Therefore, the first-ply failure occurs in the regions close to the shell's edge. In addition, the innermost ply sustains higher stresses for all meridian angles compared with the outermost ply, since the failure factor is close to 1 at the innermost layer.

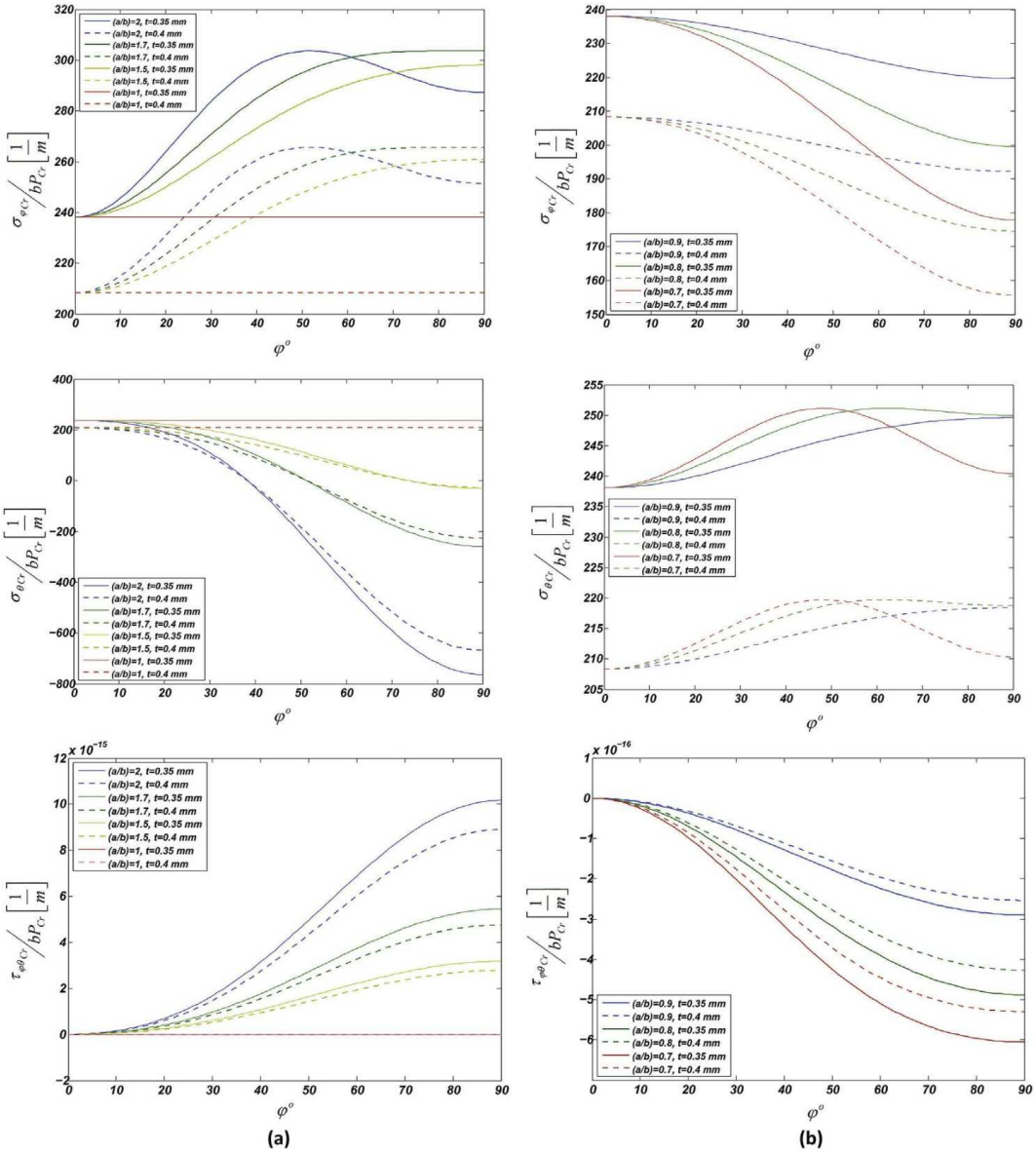


**Fig. 18.** Effect of thickness on the failure strength of laminated ellipsoidal woven GFRP composite shell internally pressurized in a) $a/b \geq 1$ and b) $a/b < 1$.

The schematic of failure facture distribution for all plies is illustrated in Fig. 15.

In order to correct the amount of error between analytical and experimental results, an offset factor $R$ can be defined as shown in Eq. (21). . In the current study the offset factor is $R = 1.0966$.

$$R = \frac{P_{Cr}^{Ana}}{P_{Cr}^{Exp}} \tag{21}$$

### 4.1. Further extension to the analytical study

Effect of various parameters such as lay-up thickness, aspect ratio, and stacking sequence on failure strength of the laminated ellipsoidal woven GFRP composite shells were then investigated in this study. The critical stress and strains in the global and local orientation respectively, as well as critical internal pressure to avoid failure, were plotted against meridian direction.

Figs. 16 and 17 show the critical stress/strain distribution for an ellipsoidal shell with semi-major over semi-minor axis ratio for an unsymmetrical laminated ellipsoidal GFRP composite shell with stacking sequence of 0/45/0/45/0/45. The results were computed using MATLAB software.

Fig. 16 shows the distribution of critical stresses versus meridian axis in global and local material orientations for each ply. Nonlinear distribution of critical stresses is observed in both global and local material orientations. All plies present the highest critical stresses in both material orientations as $\varphi \rightarrow 90^{\circ}$. If the critical internal pressure was kept constant, for a particular meridian angle, the maximum critical meridian, circumferential, longitudinal, and transverse stresses are detected to be at $k = 5$. However, the shear stress varies significantly with regard to material orientations. The shear stress in global material orientation is negligible as it is small, while the innermost ply presents the maximum critical shear stress in local material orientation. In addition, the shear stress in global material orientation appears to vary symmetrically for even and odd plies being stretched and compressed, respectively.

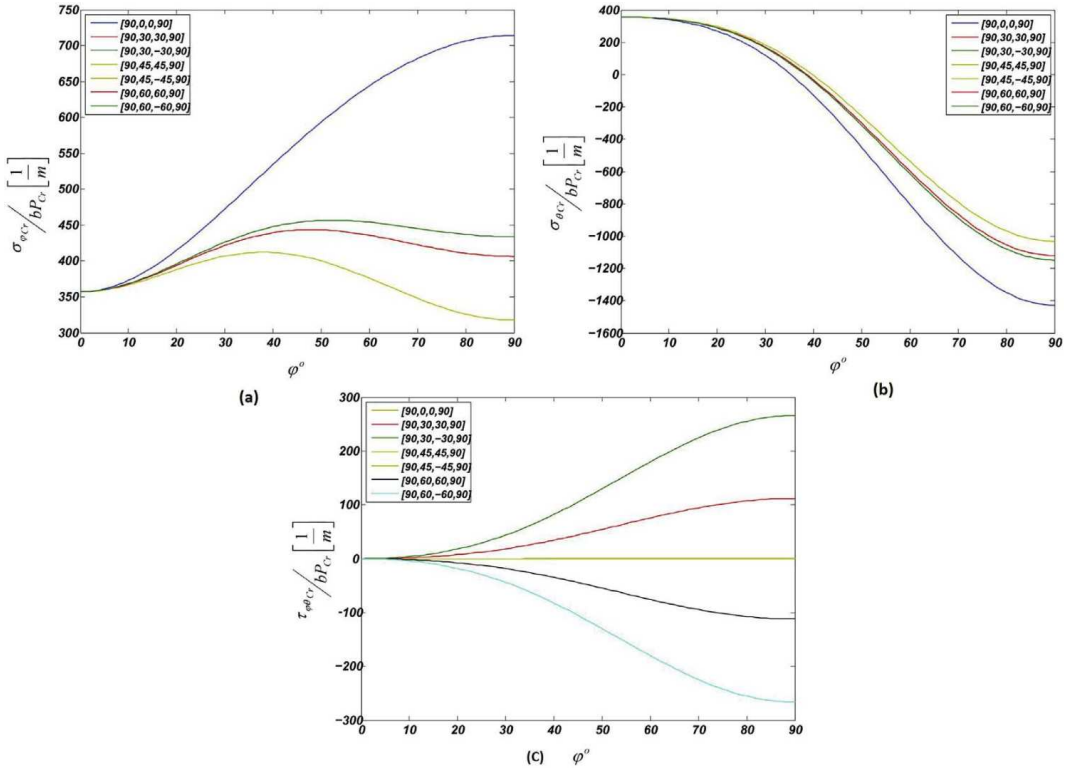


**Fig. 19.** Effect of stacking sequence on the failure strength of laminated ellipsoidal woven GFRP composite, $a/b = 2$.

Fig. 17 shows the distribution of critical strain distribution versus meridian axis in global and local material orientations for each ply. Nonlinear distribution of critical stresses is also observed in both global and local material orientations. According to Fig. 17, the maximum critical strain distribution occurs at innermost ply along meridian, circumferential and shear directions and $k = 5$ at longitudinal, transverse, and local shear directions. There is a consistency in critical strain distribution in global material orientation, as $k \rightarrow 6$ the critical strain distribution increases. However, no such consistency is observed in local material orientation as ply number changes. Similar to Fig. 16, Fig. 17 also illustrates that all plies present the highest critical strain in both material orientations as $\varphi \rightarrow 90^{\circ}$.

Fig. 18 illustrates the effect of both thickness and semi-major over semi-minor axis ratio on the first-ply failure strength of a laminated ellipsoidal woven GFRP composite shell internally pressurized and with stacking sequence of 0/45/0/45/0/45. Nonlinear critical stress distribution along meridian axis in global material orientation accounts for a composite shell with ellipsoidal geometry. However, for $a/b = 1$, which is a geometry for hemispherical shell, the stress and critical pressure remain constant in global material orientations along the meridian axis, proving that the failure factor distribution does not vary throughout the hemispherical shell. However, any slight change in $a/b$ ratio resulted in critical internal pressure fluctuating considerably. Furthermore, a slight change in the shell lay-up thickness can also affect the failure strength of the shell. Higher failure strength accounted for shells with thicker lay-up.

Effect of stacking sequence on failure strength of laminated ellipsoidal woven GFRP composite shell with semi-major over semi-minor axis ratio of two is illustrated in Fig. 19. Various stacking sequences were selected for this purpose and the critical stress distribution in global material orientation versus meridian axis for each particular case was plotted. The comparison of the results shows the significant changes in first-play failure as the stacking sequence changes. For instance, the cross play laminate with the stacking sequence of 90,0,0,90 represents the highest critical stresses in meridian and circumferential directions with no shear stress distribution through laminate. However, non-cross-ply laminates represent lower critical stress distribution in meridian and circumferential direction but higher critical shear stress distribution in comparison with cross-ply laminates. Furthermore, all laminates present the nonlinear trend in critical stress distribution in global material orientation. Similarly, all laminates present the highest critical stress distribution in global material orientation as $\varphi \rightarrow 90^{\circ}$ regardless of stacking sequence.

## 5. Conclusion

The failure characteristics of laminated ellipsoidal woven GFRP composite shell were studied analytically and experimentally. The failure criterion of Tsai-Wu was adopted in this study and the linear interpolation technique was adopted to interpolate the critical internal pressure. The analytical results were verified for some arbitrarily selected meridian angles on the shell surface with the results derived by the experimental approach. The results obtained by the two approaches showed a good agreement. Following the verification of the analytical results, the effect of various parameters on failure strength of laminated ellipsoidal woven GFRP composite shell was investigated. Based on the analytical and experimental findings derived in this study, the following conclusions are made:

1. A laminated ellipsoidal woven GFRP composite shell is more vulnerable to failure at regions close to higher meridian angels ($\varphi \rightarrow 90^{\circ}$) when subjected to internal pressure regardless of the boundary conditions.
2. The failure occurs at the shell's innermost ply while the outermost ply is the last layer at which the failure occurs.

3. In order to correct the amount of error between analytical and experimental results, an offset factor $R$ can be defined as shown in Eq. 21. Since the critical failure pressure obtained from experimental study is lower than that of analytical results, an offset factor can minimize the analytical results error. Thus, the results obtained from analytical solution become closer to the results obtained from the actual modelling.
4. Effect of various parameters such as layup thickness, semi-major axis over semi-minor axis ratio, and stacking sequence on failure strength of a laminated ellipsoidal woven GFRP composite shell is significant. The higher critical stress distribution accounts for laminates with lower thickness regardless of their stacking sequence. For $a/b \geq 1$, higher ratio resulted in increase in the critical stress distribution in global material orientation while no consistency was observed if $a/b < 1$. Thus, the ellipsoidal composite shells with $a/b < 1$ could not be a good choice for a design against the first-ply failure. Furthermore, the ellipsoidal composite shell with non-cross-ply stacking sequence presented the higher critical shear stress distribution and lower critical meridian and circumferential stress distributions in comparison with cross-ply laminates when subjected to internal pressure.

## Acknowledgements

The work reported in this paper was supported by the International Postgraduate Research Scholarship made available to the first author by the College of Engineering and Science at Victoria University, Melbourne. This financial support is gratefully acknowledged.

## Appendix. (A)

The elements of the reduced stiffness matrix $[\overline{Q}]$ of a laminate shown in Eq. (8), Eq (9) and Eq. (10) are described as

$$\overline{Q}_{11} = Q_{11}c^4 + 2(Q_{12} + 2Q_{66})c^2s^2 + Q_{22}s^4 \tag{A.1}$$

$$\overline{Q}_{12} = (Q_{11} + Q_{22} - 4Q_{66})c^2s^2 + Q_{12}\left(c^4 + s^4\right) \tag{A.2}$$

$$\overline{Q}_{22} = Q_{11}s^4 + 2(Q_{12} + 2Q_{66})c^2s^2 + Q_{22}c^4 \tag{A.3}$$

$$\overline{Q}_{66} = (Q_{11} + Q_{22} - 2Q_{12})c^2s^2 + Q_{66}\left(c^2 - s^2\right)^2 \tag{A.4}$$

$$\overline{Q}_{16} = -Q_{22}cs^3 + Q_{11}c^3s - (Q_{12} + 2Q_{66})\left(c^2 - s^2\right)cs \tag{A.5}$$

$$\overline{Q}_{26} = -Q_{22}c^3s + Q_{11}cs^3 - (Q_{12} + 2Q_{66})\left(c^2 - s^2\right)cs \tag{A.6}$$

The standard transformation matrix is

$$[T] = \begin{bmatrix} c^2 & s^2 & 2cs \\ s^2 & c^2 & -2cs \\ -cs & cs & (c^2 - s^2) \end{bmatrix} \tag{A.7}$$

where $c$ is $cos(\beta)$ and $s$ is $sin(\beta)$.

The lamina stiffness matrix $[Q]$ elements can be represented as below:

$$Q_{11} = \frac{E_1}{(1 - \nu_{12})\nu_{21}} \tag{A.8}$$

$$Q_{22} = \frac{E_2}{(1 - \nu_{12})\nu_{21}} \tag{A.9}$$

$$Q_{12} = \frac{\nu_{12}E_2}{(1 - \nu_{12})\nu_{21}} \tag{A.10}$$

$$Q_{16} = Q_{26} = 0 \tag{A.11}$$

$$Q_{66} = G_{12} \tag{A.12}$$

## References

[1] Kulkarni SV, Zweben CH. Composites in pressure vessels and piping. American Society of Mechanical Engineers; 1977.
[2] Tauchert TR. Optimum design of a reinforced cylindrical pressure vessel. J Compos Mater 1981;15(5):390–402.
[3] Fukunaga H, Uemura M. Optimum design of helically wound composite pressure vessels. J Compos Struct 1983;1(1):31–49.
[4] Zu L, Koussios S, Beukers A. Design of filament–wound shells based on continuum theory and non-geodesic roving trajectories. Compos Part A – Appl Sci Manuf 2010;41(9):1312–20.
[5] Zu L, Koussios S, Beukers A. Design of filament-wound isotensoid pressure vessels with unequal polar openings. Compos Struct 2010;92(9):2307–13.
[6] Krivoshapko SN. Research on general and axisymmetric ellipsoidal shells used as domes, pressure vessels, and tanks. Appl Mech Rev 2007;60(6):336–55.
[7] Fukunaga H, Chou TW. Simplified design techniques for laminated cylindrical pressure vessels under stiffness and strength constrains. J Compos Mater 1988;22:1156–69.
[8] Adali S, Summers EB, Verijenko VE. Optimization of laminated cylindrical presser vessels under strength criterion. Compos Struct 1993;25(1–4):305–12.
[9] Ayob AB, Moffat DG, Mistry J. Interaction of pressure, in-plane moment and torque loadings on piping elbows. Int J Press Vessels Pip 2003;80(12):861–9.
[10] Chang RR. Experimental and theoretical analysis of first-ply failure of laminated composite pressure vessel. Compos Struct 2000;49(2):237–43.
[11] Ross CTF, Huat BH, Chei TB, Chong MC, Mackney MDA. Buckling of GRP hemi-ellipsoidal shell shells under external hydrostatic pressure. Ocean Eng 2003;30(5):691–705.
[12] Tsai SW, Wu EM. A general theory of strength for anisotropic materials. J Compos Mater 1971;5(1):58–80.
[13] Peters M, Hackl K. Numerical aspects of the extended finite element method. Proc PAMM 2005;5:355–6.
[14] Kam TY, Liu YW, Lee FT. First-ply failure strength of laminated composite pressure vessels. Compos Struct 1997;38(1–4):65–70.
[15] Liang CC, Chen HW, Wang CH. Optimum design of dome contour for filament-wound composite pressure vessels based on a shape factor. Compos Struct 2002;58:469–82.
[16] Saghafi H, Minak G, Zucchelli A. Effect of preload on the impact response of curved composite panels. Compos Part B 2014;60:74–81.
[17] Qu Y, Chen Y, Long X, Hua H, Meng G. A modified variational approach for vibration analysis of ring-stiffened conical–cylindrical shell combinations. Eur J Mech A – Solids 2013;37:200–15.
[18] Morinière FD, Alderliesten RC, Benedictus R. Modelling of impact damage and dynamics in fibre-metal laminates – a review. Int J Impact Eng 2014;67:27–38.
[19] Chou HY, Bunsell AR, Mair G, Thionnet A. Effect of the loading rate on ultimate strength of composites. Application: pressure vessel slow burst test. Compos Struct 2013;104:144–53.
[20] Feng D, Aymerich F. Damage prediction in composite sandwich panels subjected to low-velocity impact. Compos Part A 2013;52:12–22.
[21] Taggart DG, Schwan FJ. Evaluation of woven fabric composites for automotive applications. J Mater Shap Technol 1987;5:41–51.
[22] Advani SG, Gillespie JW. In: Proceedings of the 9th international conference on textile composites. Centre for Advanced Composites. University of Delaware; 2008. p. 13–5.
[23] Içten BM, Okutan B, Karakuzu R. Failure strength of woven glass fiber-epoxy composites pinned joints. J Compos Mater 2003;37:1337–49.
[24] Yang B, Kozey V, Adanur S, Kumar S. Bending, compression and shear behaviour of woven glass fiber-epoxy composites. Compos Part B 2000;31(8):715–21.
[25] Bystrom J, Jekabsons N, Varna J. An evaluation of different models for prediction of elastic properties of woven composites. Compos Part B – Eng 2000;31(1):7–20.
[26] Galletly GD, Aylward RW. Plastic collapse and the controlling failure pressures of thin 2:1 ellipsoidal shells subjected to internal pressure. J Press Vessel Technol 1979;101(1):64–72.

[27] Leh D, Saffré P, Francescato P, Arrieux R. Multi-sequence dome lay-up simulations for hydrogen hyper-bar composite pressure vessels. Compos Part A 2013;52:106–17.
[28] Francescato P, Gillet A, Leh D, Saffré P. Comparison of optimal design methods for type 3 high-pressure storage tanks. Compos Struct 2012;94(6):2087–96.
[29] Cohen D, Mantell SC, Zhao L. The effect of fiber volume fraction on filament wound composite pressure vessel strength. Compos Part B – Eng 2001;32(5):413–29.
[30] Jia X, Chen G, Yu Y, Li G, Zhu J, Luo X, et al. Effect of geometric factor, winding angle and pre-crack angle on quasi-static crushing behavior of filament wound CFRP cylinder. Compos Part B – Eng 2013;45(1):1336–43.
[31] Rafiee R. Experimental and theoretical investigations on the failure of filament wound GRP pipes. Compos Part B – Eng 2013;45(1):257–67.
[32] Logan DL, Hourani M. Membrane theory for layered ellipsoidal shells. J Press vessel Technol 1983;105(4):356–62.
[33] Vinson JR. Plate and panel structures of isotropic, composite and piezoelectric materials, including sandwich construction. Solid mechanics and its applications. 2005. p. 120.
[34] Campbell FC. Manufacturing processes for advanced composites. Liquid molding. Elsevier Advanced Technology; 2004.
[35] Strong AB. Fundamentals of composites manufacturing. 2nd ed. Materials, Methods and Applications. Society of manufacturing Engineers; 2008.

Composites Part B 94 (2016) 224–237

Contents lists available at ScienceDirect

Composites Part B

journal homepage: www.elsevier.com/locate/compositesb

# Numerical and experimental study on mechanical strength of internally pressurized laminated woven composite shells incorporated with surface-bounded sensors

S. Sharifi*, Scott Gohery, M. Sharifiteshnizi, Z. Vrcelj

*College of Engineering and Science, Victoria University, Melbourne, VIC 8001, Australia*

ARTICLE INFO

*Article history:*
Received 16 August 2015
Received in revised form
3 November 2015
Accepted 11 March 2016
Available online 19 March 2016

*Keywords:*
C. Finite element analysis (FEA)
A. Polymer-matrix composites (PMCs)
B. Strength
A. Laminate
Internally pressurized laminated woven composite shells

ABSTRACT

In this study, strain deformation of three types of internally pressurized laminated composite shells (hemispherical, ellipsoidal, and torispherical) with two types of woven roving (WR) stacking sequence (WR $[0]_6$ and WR $[0/45]_3$) was studied numerically and experimentally. The regions at which the critical strain occurs were determined by using finite element analysis (FEA). Careful experimental study was carried out for results validation. Vacuum infusion process (VIP) was employed for the composite shell fabrication. The surface-bounded sensors were used to measure strain values occurring at the outermost ply. In general, a good agreement between strain variation rates derived by the two approaches was observed. However, some discrepancy was observed for strain magnitude, particularly the ones close to the boundary. The possible reasons behind this were then discussed. Furthermore, the effect of staking sequence and geometrical shape on the mechanical strength of laminated woven composite shells was investigated and critical mechanical factors were accounted for. Laminated composite shells with WR $[0/45]_3$ were found to be the preferred choice over WR $[0]_6$. Laminated hemispherical shells were also found to be the preferred choice against mechanical failure while laminated tosipherical shells were found to be the least choice.



## 1. Introduction

Fibre reinforced composites have received considerable attention in numerous and diverse applications due to low weight, good corrosion and chemical resistance, and high specific stiffness compared to conventional metallic counterparts [1–3]. Woven is one type of fibre-reinforced composite which has recently attracted engineers and industry applications since it offers a number of attractive properties such as high capacity to conform to complicated contours, suitability for manufacturing components with complex shape, and greater flexibility in processing options compared to metals and unidirectional composites [4–7].

One of the main applications of composite materials is in pressure vessels design and fabrication. Pressure vessels have been increasingly used in industrial compressed air receivers, distillation towers, oil refineries, aerospace, automotive, hot water storage tanks, portable oxygen storage, fuel tanks, and compressed natural gas (CNG) tank. A common feature of such products is that they must safely undergo a certain working pressure which makes these structures vulnerable and exposed to failure, fatigue and fracture [8,9]. Consequently, several studies have been reported on optimal structural analysis of composite pressure vessels subjected to arbitrarily loading conditions such as external load [10–15], internal pressure [16–19], combined axial and impact load [20–22], pure impact load [23–27], combined aerodynamic torque and axial thrust [28], and thermo-mechanical loads [29].

Internally pressurized laminated composite pressure vessels have been studied extensively by several researchers. Uemura and Fukunaga [30] presented an analytical method to predict probabilistic burst strength of carbon fibre filament wound cylinders subjected to internal pressure. Tarakcioglu et al. [31] studied fatigue behaviour of fibre glass reinforced plastic composite pipes under alternating internal pressure. Limam et al. [32] conducted experimental and numerical analyses to investigate collapse and inelastic wrinkling of tubes subjected to combined bending and internal pressure. Shen et al. [33] studied post buckling in composite cylindrical shells under internal pressure. Blachut [34] studied strain

* Corresponding author.
*E-mail addresses:* sharifi.te@gmail.com (S. Sharifi), scott.gohery@unimelb.edu.au, (S. Gohery).

http://dx.doi.org/10.1016/j.compositesb.2016.03.020
1359-8368/

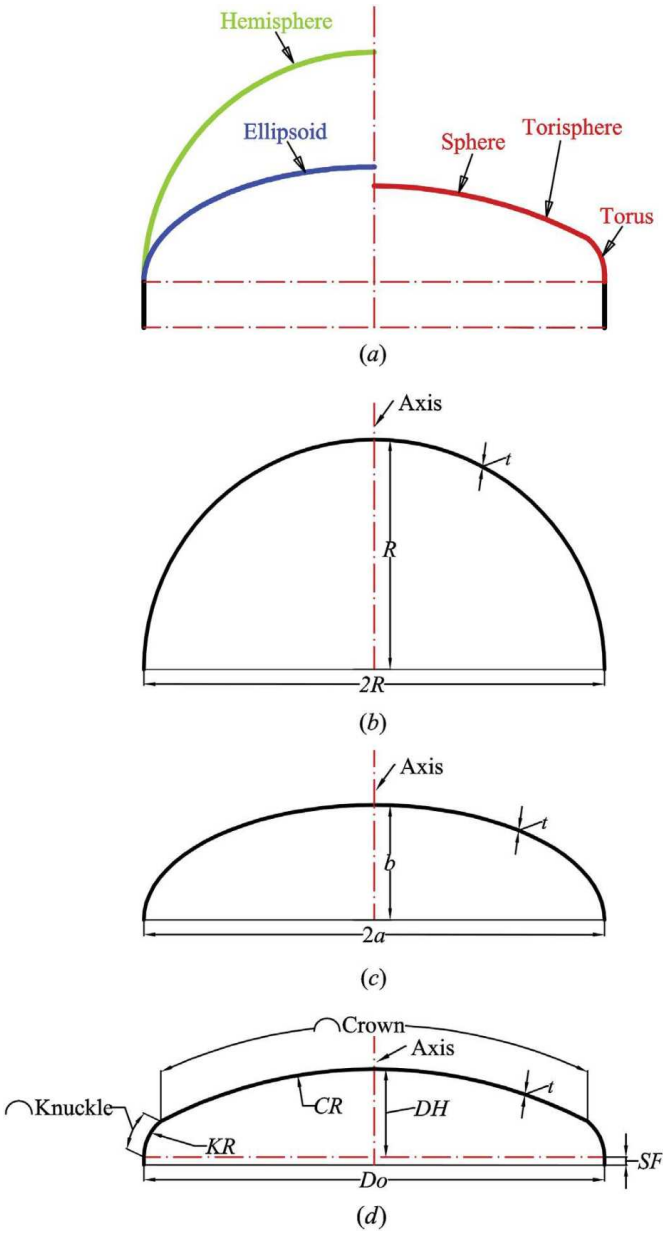


**Fig. 1.** (a) Schematic of hemispherical, ellipsoidal and torispherical shells; geometrical profiles: (b) hemispherical, (c) elliptical, and (d) torispherical.

and stress distribution of steel torispherical shells subjected to internal pressure experimentally and numerically. Sorić and Zahlten [35] presented some numerical results for elasto-plastic analysis of internally pressurized torispherical shells under internal pressure.

A pressure vessel consists of two main parts including drum (cylindrical region) and dome (cap region). Parameters such as constituent materials, head shape, shell radius, layer thickness, fibre angle, stacking sequence, and volumetric fibre fraction are crucial in designing composite pressure vessels. Since head part undergoes high stress levels, it is generally the most significant part in designing pressure vessels. End-closure, or shell, is the major and most complex part of the design of any pressure vessel [36–38]. According to the study conducted by Vafaeesefat and Khani [39], domes are the most important part in pressure vessels design. Circular cylindrical pressure vessels are mostly closed with curved heads including hemispherical, torispherical, and elliptical shapes.

**Table 1**
Shell geometry.

| Type of dome | Description | Dimension [*mm*] |
|---|---|---|
| Hemispherical | R | 200 |
| | *t* | 2.1 |
| Elliptical | *a* | 200 |
| | *b* | 100 |
| | *t* | 2.1 |
| Torispherical | *Do* | 400 |
| | *CR* | 400 |
| | *KR = 0.1 Do* | 40 |
| | DH = 0.1935–0.455 *t* | 76.4 |
| | *Thi = SF + DH* | 83.7 |
| | *t* | 2.1 |

Pressure vessel manufacturing requires careful selection of dome shape as it influences the capacity of vessel volume and its resistance to arbitrary loads like burst pressure, internal and external pressure, and impact load. Extensive research has been conducted on various shell dome shapes under different loading conditions. Blachut and Galletly [40] conducted a research on elastic buckling of torispheres due to local shape imperfections. Ross [41] studied elastic buckling and vibration of thin-walled hemi-elliptical shells subjected to uniform external pressure. In another study, effect of geometry and material on stresses occurring in various internally pressurized laminated composite shells was studied by Won et al. [42]. Hwang et al. [43] predicted probabilistic deformation and strength for filament wound pressure vessels. Dong and Blachut [11] used woven carbon fibre reinforced for externally pressurized shells to examine the sensitivity of buckling, first and last ply failure for a range of torispherical shells.

Additionally, Błachut [10] studied buckling of multi-layered hemispherical and torispherical metal shells under external pressure based on numerical and experimental approaches. Crisp [44] analysed elastic stress distributions in torispherical dome heads utilizing a computer program. Aggarwal and Nayak [45] conducted investigations based on elasto-plastic analysis using FEM to design cylindrical steel pressure vessels with different end closures (hemispherical, torispherical, semi-ellipsoidal, and toriconical shapes). Yeom and Robinson [46] studied behaviour of pressure vessels with torispherical and ellipsoidal heads loaded by internal pressure. Magnucki and Lewinski [47] studied head shape of vessel under internal pressure. Magnucki et al. [48] conducted a numerical and analytical study on minimizing stress concentration in cylindrical pressure vessels with ellipsoidal heads. Vafaeesefat and Khani [39] studied winding angle and head shapes of composite pressure vessels. Carbonari et al. [49] adapted shape optimization for designing pressure vessels. Şenalp [50] investigated the effect of perturbation forces on buckling in thin-walled torispherical pressure vessels subjected to internal pressure. Various design methods against buckling failure of torispherical heads under internal pressure was studied by Muscat and Camilleri [16]. Hu et al. [51] conducted some careful experimental tests on structural design of filament wound toroidal pressure vessels.

However, none of these studies has directly investigated the influence of stacking sequence and geometrical shape on strain behaviour of woven fibre composite shells. Furthermore, comparison between strain behaviour of laminated hemispherical, elliptical, and torispherical shell shapes under same amount of internal pressure has not been studied yet. To gain an insight into the possible effect of lay-up angle on strain behaviour of laminated composite shells, a study on strain distribution occurring in internally pressurized laminated woven composite shells with two proposed stacking sequences is undertaken herein. To this end, the numerical and experimental analyses were conducted to

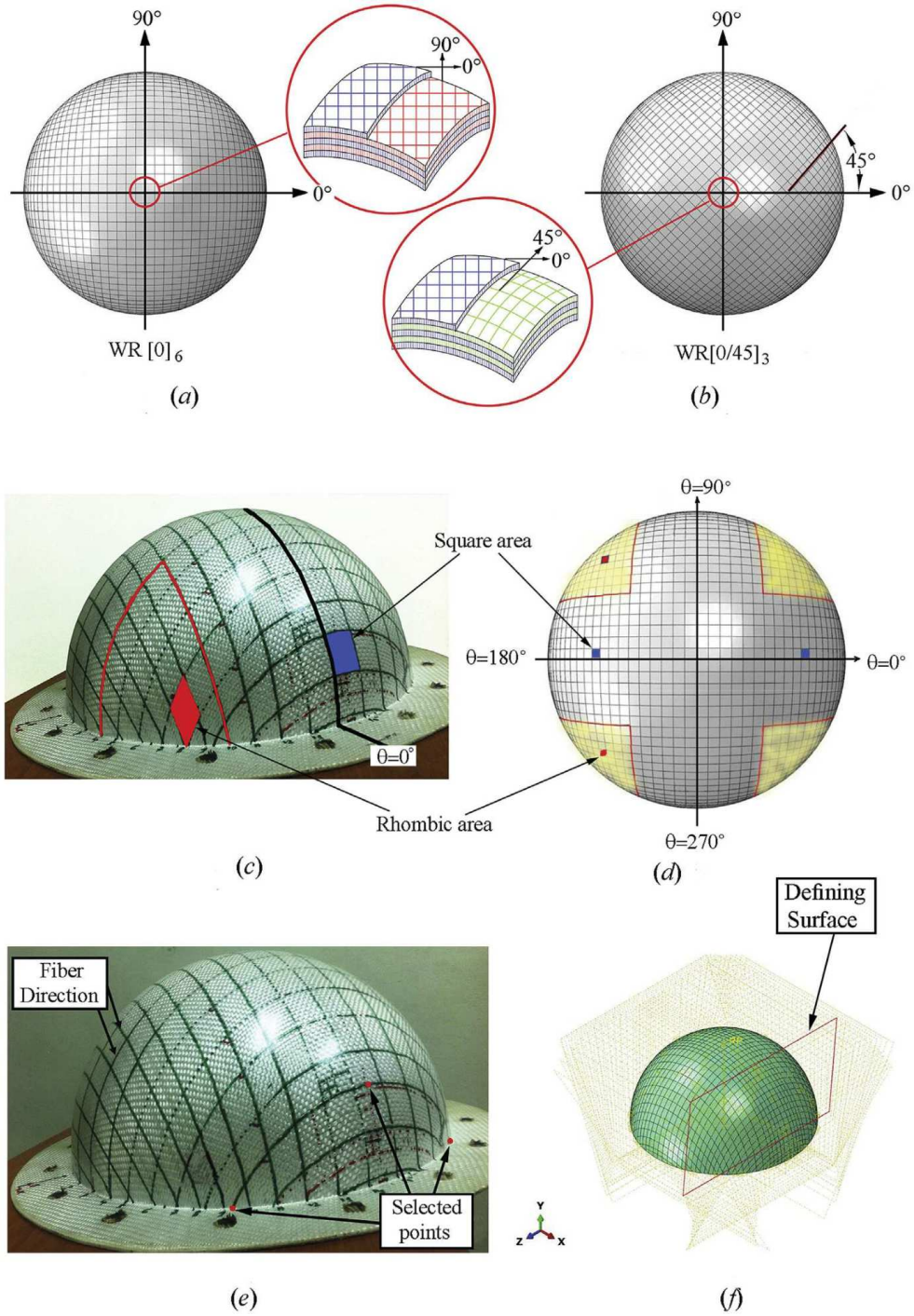


**Fig. 2.** Stacking sequence configurations: (a) WR $[0]_6$, and (*b*) WR $[0/45]_3$; square and rhombic areas in fibres configuration for a layer of laminated woven composite shell: (c) side view and (d) top view; Shell partition: (e) selecting the point on the shell along fibres and (f) defining a surface based on the critical points.

investigate strain behaviours of two various stacking sequences (WR $[0]_6$ and WR $[0/45]_3$) in three different types of shells. Similarly, three geometrical shapes of composite shells were analysed to determine the desirable shape with highest strength against delamination and deformation.

## 2. Methodology

### *2.1. Numerical method: FE simulation*

To select shells with optimal stacking sequence three shapes of the laminated composite shells (hemisphere, ellipsoid, and torisphere) were studied numerically using ABAQUS/CAE 6.13

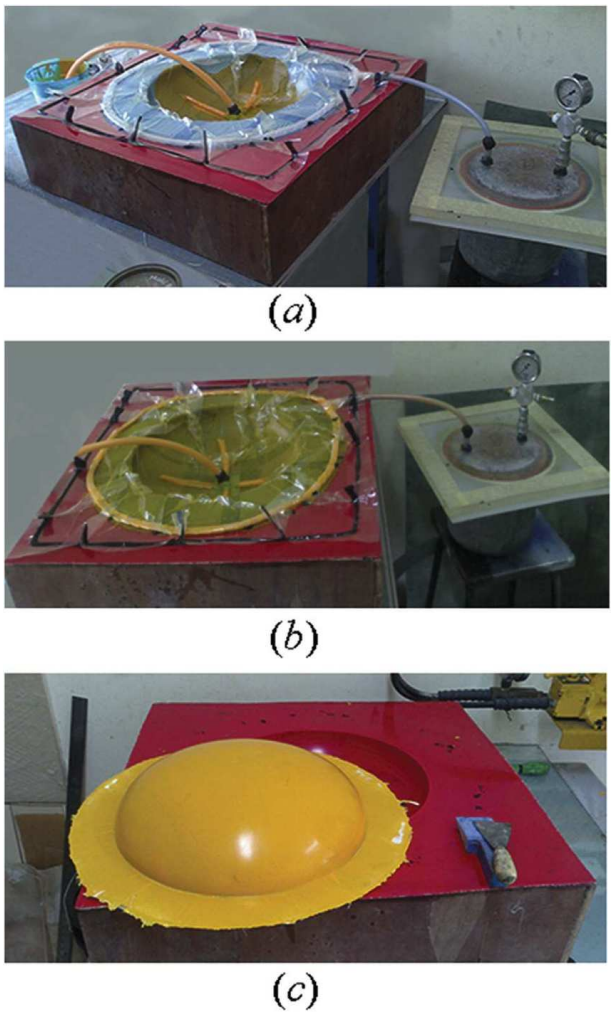


**Fig. 3.** Vacuum infusion: (a) flow of resin through resin feeder and fibres saturation, (b) applying 1 [*bar*] vacuum pressure on saturated fibres, and (c) prepared shell.

software. The profiles, geometry, and dimensions of the shells studied in this research are shown in Fig. 1a and d, and Table 1, respectively. Shells were modelled by adopting six layers of woven fibre glass reinforced epoxy composite laminate with particular patterns as illustrated in Fig. 2a and b. They were then fixed at their boundary with no degree of rotation and displacement. According to Fig. 2a and b, the concept of WR $[0]_6$ stipulates that for manufacturing the laminated woven composite shell specimens, every six sheets of woven fibres should be set on each other following the same direction as shown in Fig. 2a. However, when considering WR $[0/45]_3$, the second sheet should be located on the first sheet with winding angle of 45°. The process is repeated sequentially until the last layer is properly incorporated into the laminates (see Fig. 2b.)

Fig. 2c and d shows the woven fibres configuration in the laminated woven composite shells in which some areas of woven remain in initial geometry (square shape) while the rests are deformed into the rhombic shape. The side and top views of the laminated woven fibre composite shell is also shown in Fig. 2c and d, respectively. In case of dividing the shells into four equal quadrants, two different types of shapes for woven fibres would appear in each quadrant. It is noticed that around the region $\theta = 0°$, the woven fibres are almost square in shape. By moving along circumferential direction from the area close to $\theta = 0°$ to $\theta = 45°$, and $\theta = 45°$ to $\theta = 90°$, the shape of woven fibres changes gradually from square to rhombic, and rhombic to square, respectively. In other words, woven fibres in the regions near $\theta = 0°$, $\theta = 90°$, $\theta = 180°$, and $\theta = 270°$ are square-like shape while the areas close to $\theta = 45°$, $\theta = 135°$, $\theta = 225°$ and $\theta = 315°$ represent the rhombic-like shape. The effect of woven fibres transformation from square to rhombic was taken into account during the shells fabrication.

Due to different stacking sequences and geometrical shapes in the laminated woven composite shells, different strain distributions under the same loading condition are expected. In FEA of the shells, quadrilateral linear S4R (shell, four node, reduced integration) elements in ABAQUS were selected for simulation of fabrics. In order to accomplish this, the "partition cell using datum plane" method was chosen. In this method, a surface must be defined for forming each partition. The partitions were created in the conjunction area of the surface and the model. Fig. 2e and f illustrate the selected points and defined surface on the shells, respectively. Various surfaces were defined for partitioning whole shell model following the mentioned method. In the next step, the laminated woven composite shells were partitioned in the direction of the shell fibres. The boundary conditions and static internal pressure were then applied afterwards. It must be taken into account that from ABAQUS package, the letter E means strain.

### 2.2. Experimental analysis

#### 2.2.1. Manufacturing process

In this step, the experimental setup and analysis of the hemispherical, elliptical, and torispherical shells with WR $[0/45]_3$ are discussed and the results are then compared with the ones obtained from numerical approach. In this study, VIP method is adopted for the laminated woven composite shell fabrication and epoxy resin (type 1006) made by blending epoxy and hardener in the exact ratio of 10:6 and fibre glass (type 290 gsm plain weave woven roving) are used. VIP method involves preparing plug, female mould, and vacuum infusion. The primary factor for constructing a suitable mould for VIP process is the adequate preparation of the plug used to create the female mould. In this study, shell patterns (plug) were prepared by shaping closed cell polyurethane foam based on geometries, as shown in Fig. 1a and d and Table 1, respectively. Computer numerical control (CNC) milling machine was employed to make shell patterns (plugs). After forming the plugs, female mould was manufactured via hand lay-up method. Following this, VIP was applied to fabricate the laminated woven composite shells. To this end, the infusion process started by flow of the resin through the resin feeder and subsequently, the fibres were impregnated by resin as shown in Fig. 3a. The estimated time taken for saturating the whole fibres with resin was around 30 min. After fibres were completely saturated, they were kept under the vacuum pressure of 1 [*bar*] for approximately 12 h to achieve adequate hardness (see Fig. 3b). The comparison between Fig. 3a and b are that Fig. 3a shows resin flow through the woven fibres at initial step when the resin has not yet flowed throughout woven fibres in the laminated woven composite shells. However, Fig. 3b shows the whole woven fibres being completely impregnated into the resin epoxy. The final form of the laminated woven composite shell made of woven fibres when using VIP method is illustrated in Fig. 3c. The detailed discussion of VIP manufacturing method for laminated woven fibre composite shells was presented by Gohari et al. [52]. The volume fraction of the laminated composite shells fabricated by using this method was 54.5%.

#### 2.2.2. Experimental set-up and testing procedures

In order to measure the internal pressure induced strains, sensors type FCA-3-11 with resistance of 120 Ω were installed on

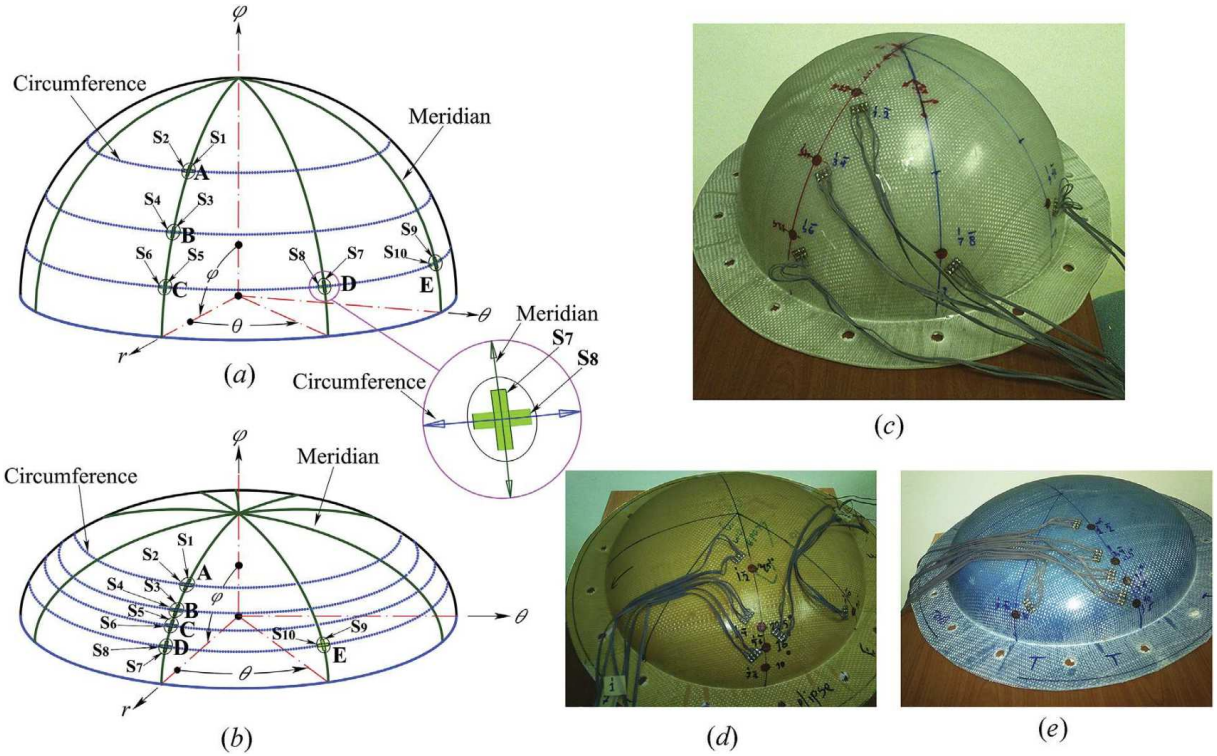


**Fig. 4.** Sensors locations on the shell outermost ply: (a) hemisphere, (b) elliptical, and torisphere shell; sensors locations: (c) hemisphere, (d) elliptical, and (e) torisphere shell. (Note: S stands for strain).

**Table 2**
Coordinates of strain-gauges locations on outer surface of hemispherical, elliptical, and torispherical shell.

| | Strain gauge | Hemispherical | | Elliptical | | Torispherical | | Direction |
|---|---|---|---|---|---|---|---|---|
| | | $\theta^\circ$ | $\varphi^\circ$ | $\theta^\circ$ | $\varphi^\circ$ | $\theta^\circ$ | $\varphi^\circ$ | |
| A | S1 | 0 | 22.5 | 0 | 45 | 0 | 45 | Meridian |
| | S2 | 0 | 22.5 | 0 | 45 | 0 | 45 | Circumference |
| B | S3 | 0 | 45 | 0 | 60 | 0 | 65 | Meridian |
| | S4 | 0 | 45 | 0 | 60 | 0 | 65 | Circumference |
| C | S5 | 0 | 70 | 0 | 70 | 0 | 70 | Meridian |
| | S6 | 0 | 70 | 0 | 70 | 0 | 70 | Circumference |
| D | S7 | 45 | 70 | 0 | 80 | 0 | 80 | Meridian |
| | S8 | 45 | 70 | 0 | 80 | 0 | 80 | Circumference |
| E | S9 | 90 | 70 | 45 | 80 | 45 | 80 | Meridian |
| | S10 | 90 | 70 | 45 | 80 | 45 | 80 | Circumference |

surface of the laminated composite shells. The circumferential and meridian coordinates and sensors location in the woven composite shells are illustrated in the Fig.4a and b. The locations of sensors on the laminated woven composite shells' outermost ply are shown in Fig. 4c and e. In this study, the strains along meridian and circumference axis are named meridional and circumferential strains, respectively. The exact location of sensors in the laminated hemispherical, ellipsoidal, and torispherical shells are tabulated in Table 2. A special test rig was designed and fabricated in order to fix the shell sections to the boundaries. After enforcing the boundary conditions, the laminated woven composite shells were pressurized through pumping hydraulic oil continuously from an oil container. The oil pressure was raised from 0 to 5 [*bar*] gradually and then measured with an installed pressure gauge. The sensors were then connected to the data acquisition unit to record the history of strains. The schematic of the experimental test rig, applied boundary conditions and actual test components are illustrated in Fig. 5a and c, respectively.

## 3. Results and discussions

Strain distribution in the internally pressurized laminated woven composite shells were obtained and the critical points were determined. The numerical results for the laminated hemispherical, ellipsoidal, and torispherical woven composite shells are illustrated in Figs. 6, 8 and 10, respectively. Comparison between the pressure-strain diagrams of WR $[0]_6$ and WR $[0/45]_3$ lay-ups for different geometrical shapes (See Figs. 6, 8 and 10) were analysed and compared to identify the appropriate geometrical shape and stacking sequence. The results demonstrated that the laminated composite shells with WR $[0/45]_3$ are an optimal choice over WR $[0]_6$ due to higher uniform strain distribution regardless of geometrical shape, while no consistency was observed in WR $[0]_6$. Therefore, the specimens with WR $[0/45]_3$ were selected for the experimental tests. In the next step, comparison of numerical and experimental results in the laminated hemispherical, ellipsoidal, and torispherical woven

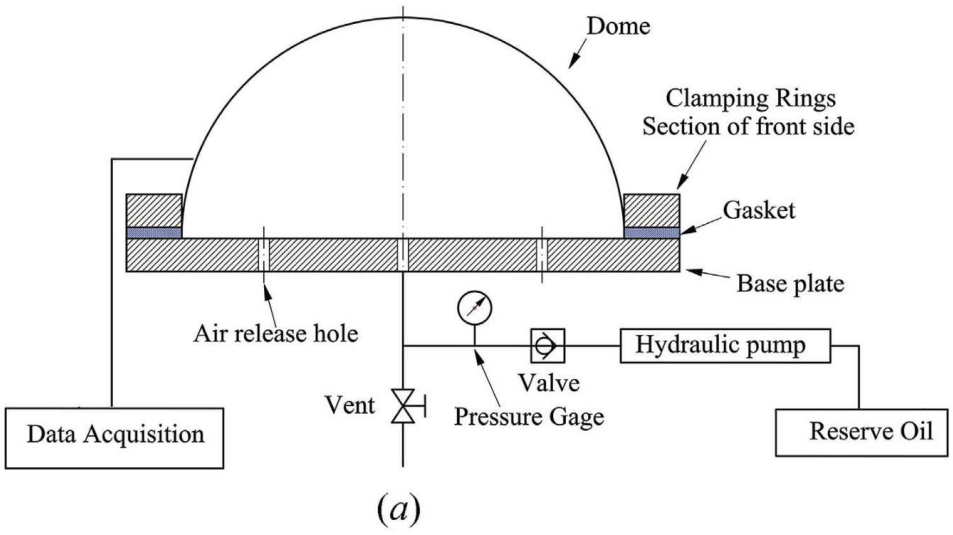


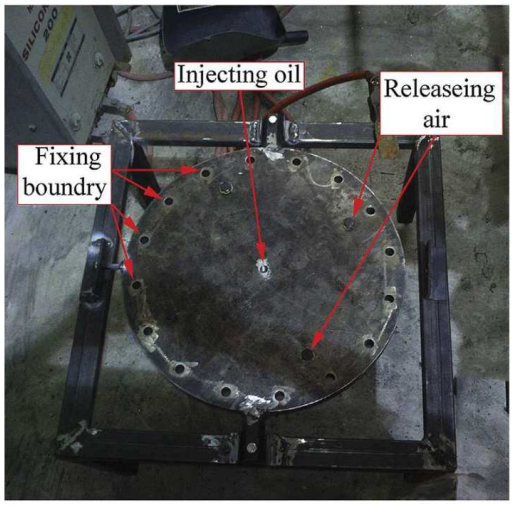


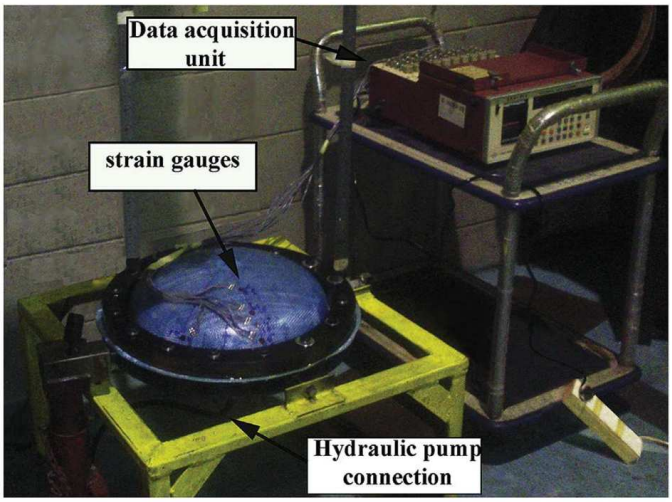


**Fig. 5.** (a) Schematic of circuit design in the experimental analysis; (b) schematic of the boundary conditions and the basement at which the laminated composite shells are fixed to; (c) actual model of experimental set up and test rig.

composite shells are discussed, respectively. It must be noted that the letter "*E*" in FE simulation contour plots refers to strain values.

### *3.1. Numerical and experimental results for the laminated hemispherical woven composite shell*

In order to numerically investigate the effect of stacking sequence on strain distribution in the laminated hemispherical woven shell, two stacking sequences of WR $[0]_6$ and WR $[0/45]_3$ are considered. To understand strain distribution direction as shown in Fig. 4a and e, the directions along which the sensors are bounded horizontally and vertically are called circumferential and meridional, respectively. The mid-plane meridional and circumferential strain distribution FE contour plots are illustrated in Fig. 6a and d, respectively. Fig. 6a and d represent the analysis for WR $[0]_6$ and WR $[0/45]_3$, respectively. According to Fig. 6, more stable uniform strain distribution was observed in WR $[0/45]_3$ than in WR $[0]_6$, for both meridional and circumferential strains. This is due to the fact that in WR $[0]_6$ the rhombic and square areas in different layers face the rhombic and square areas of adjacent layers, respectively. However, in WR $[0/45]_3$, the rhombic regions meet the normal woven configuration (square area) from one layer to another. Consequently, weak areas (rhombic area) could be strengthened by strong areas (square area) and favourite lay-up configuration can be achieved. Thus, the laminated hemispherical woven composite shells with the stacking sequence of WR $[0/45]_3$ should be the optimal choice.

To obtain the meridional and circumferential strains distribution occurring on the laminated hemispherical woven shell, three different paths from $\varphi = 0^\circ$ to $\varphi = 90^\circ$ are selected on the shells' surface at $\theta = 0^\circ$, $\theta = 45^\circ$ and $\theta = 90^\circ$ and five critical points (*A, B, C, D* and *E*) from the view point of strain are set on the paths (see Figs. 4a and 7a). The strains occurring at these points are used as the benchmark for numerical and experimental investigation. According to Fig. 7b and c, the meridian and circumferential strains have equal values in angels up to $\varphi = 40^\circ$. However, after passing this point, strain values deviate in WR $[0]_6$ while the ones along both circumferential and meridional axis remain constant in WR $[0/45]_3$.

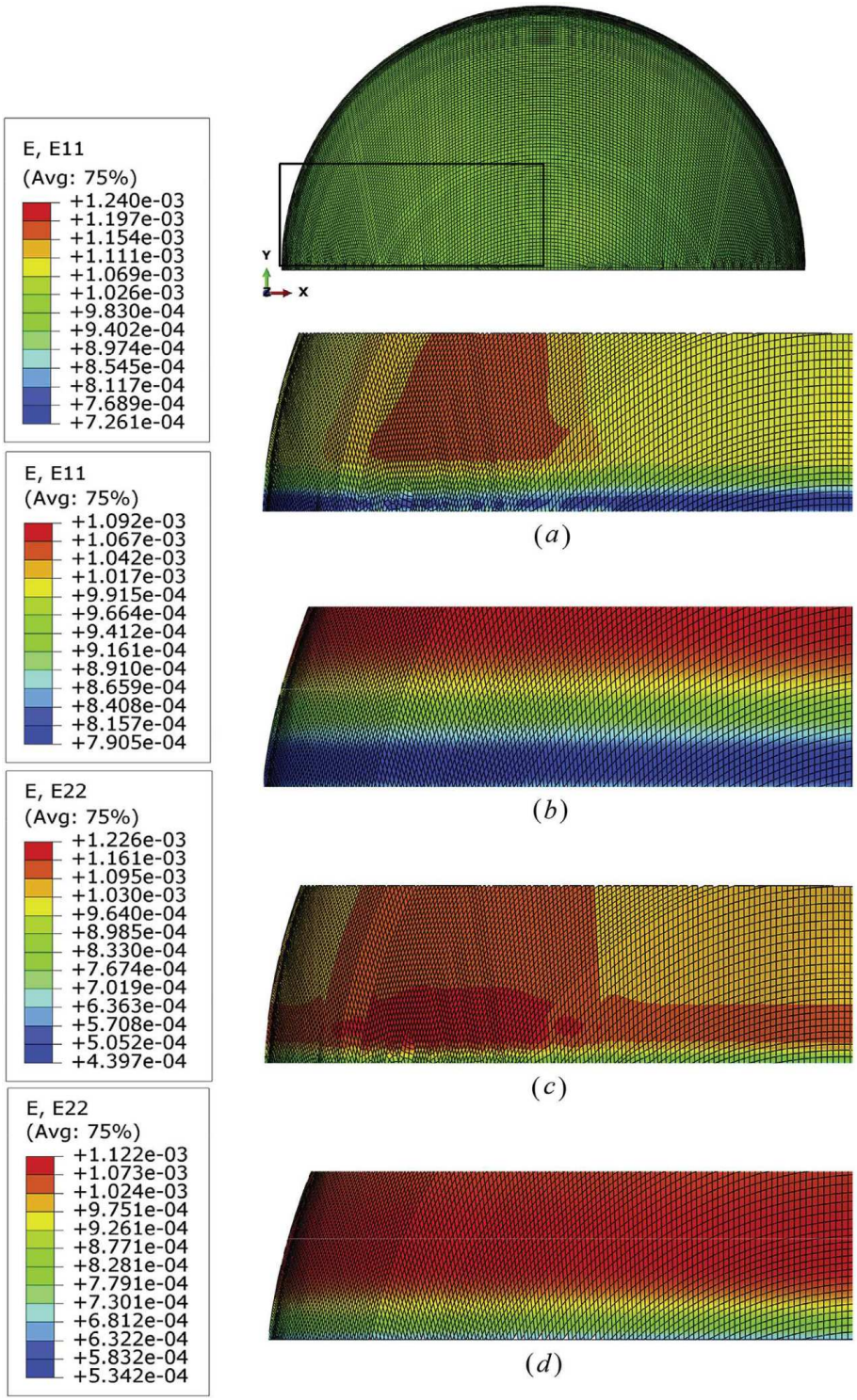


**Fig. 6.** Strain variation in the laminated hemispherical shell under internal pressure, meridional strains: (a) WR $[0]_6$ and (b) WR $[0/45]_3$; circumferential strains: (c) WR $[0]_6$ and (d) WR $[0/45]_3$ (Note: $E_{11}$-meridian strain and $E_{22}$-circumferential strain).

The numerical results in WR $[0]_6$ and WR $[0/45]_3$ at the critical points *C*, *D* and *E*, which are located along circumferential axis, indicate that in WR $[0]_6$ strain-pressure at point *D* is higher compared with WR $[0/45]_3$. Furthermore, strain values in WR $[0/45]_3$ at three points *C*, *D* and *E* are almost the same, while there is a discrepancy at these points in WR $[0]_6$. The numerical results also showed that strain values at point *D* are 6.5% higher than those at points *C* and *E* in WR $[0]_6$. This behaviour can be observed along the circumferential and meridian direction at each selected point. The comparison between strains at points *C*, *D* and *E* in both stacking sequences shows that the fibre angel affects the pressure-induced strains of the laminated hemispherical composite shell.

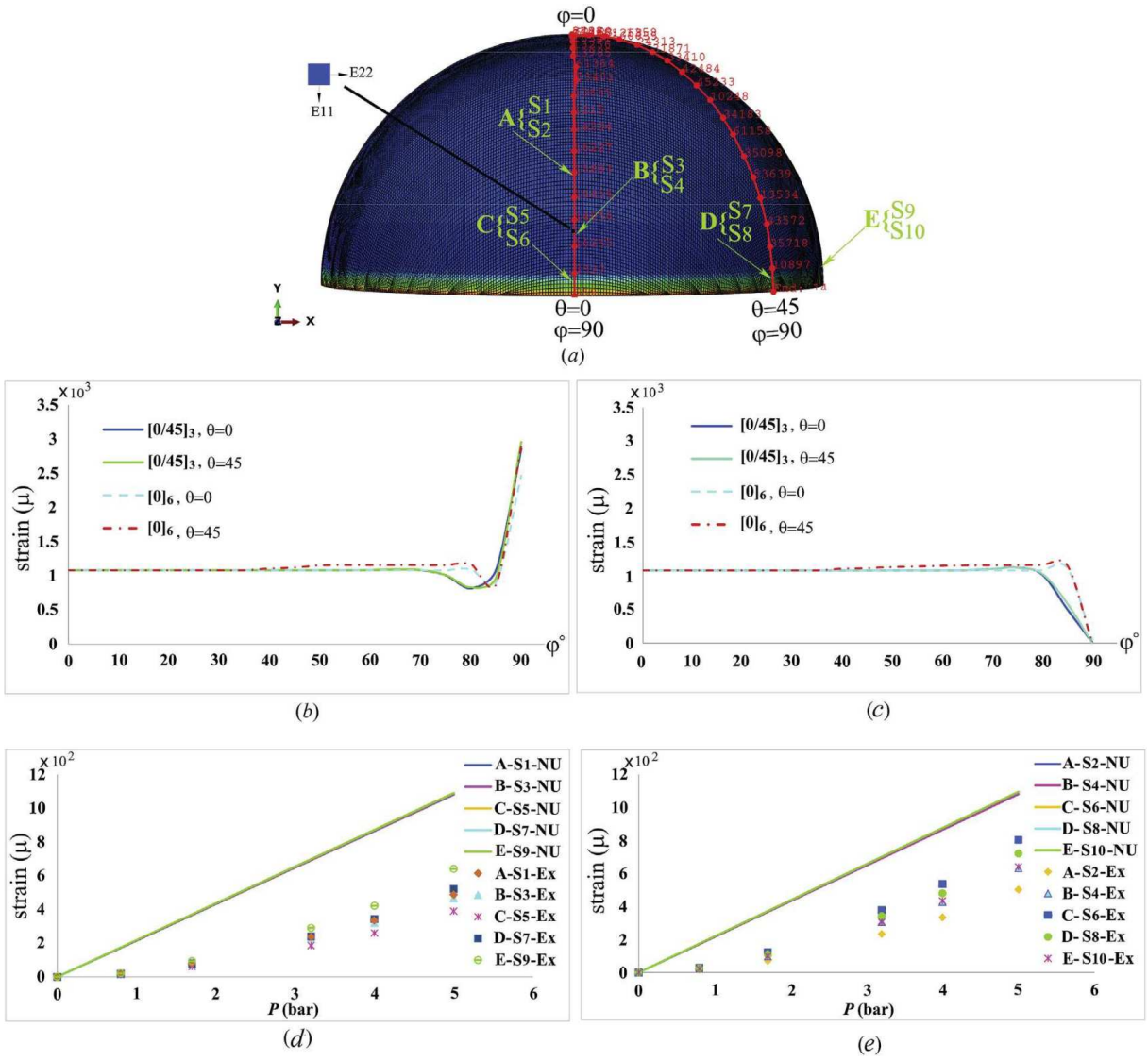


**Fig. 7.** (a) Selected path on the laminated hemispherical woven composite shell; strain distribution in the laminated hemispherical woven composite shell under 5 [*bar*] internal pressure: (b) meridian direction, and (c) circumferential direction; numerical and experimental results in the laminated hemispherical shell with WR $[0/45]_3$: (d) Meridian direction, and (e) Circumferential direction (Note: NU-Numerical, Ex-Experimental).

In the next step, the numerical results obtained for the laminated hemispherical shell were compared with the results of experimental test. WR $[0/45]_3$, as an optimal stacking sequence, was selected for the fabrication using VIP method. The shell boundary was constrained before applying the internal pressure via oil injecting. The schematic of the point selection and installation of the surface-bounded sensors on the laminated composite shells are illustrated in Fig. 4c. The points' description is explained in Table 2. In the experimental analysis, strain values selected at the critical points (*A, B, C, D* and *E*) were measured using the surface-bounded sensors and then compared with the numerical results. According to Fig. 7d and e, five sensors were surface-bounded on the laminated hemispherical shell along the meridian direction and five others along the circumferential direction, respectively. The numerical and experimental results comparison at points *A* to *E* showed that the meridional and circumferential strains were constant and had the positive signs. It was demonstrated that WR $[0/45]_3$ undergoes the constant uniform deformation when internally pressurized.

Comparison of results obtained from experimental and numerical approaches showed a good agreement in the strain rate deformation as strain variation followed the same pattern. However, considering the magnitude of strains, no consistency was observed for the points close to the boundary conditions. The higher error margin between the results could be due to the stress concentration factor, oil liquid expansion coefficient, and residual stress creation during the fabrication process and/or environmental conditions. These factors were neglected in numerical analysis which may affect strain values in the actual test. In addition, the experimental and numerical results shown in Fig. 7d and e demonstrated that any increase in the amount of internal pressure results in higher strains.

### *3.2. Numerical and experimental results for the laminated ellipsoidal woven composite shell*

In this section, the same procedure discussed in the Section 3.1 is performed for the laminated ellipsoidal woven composite shell.

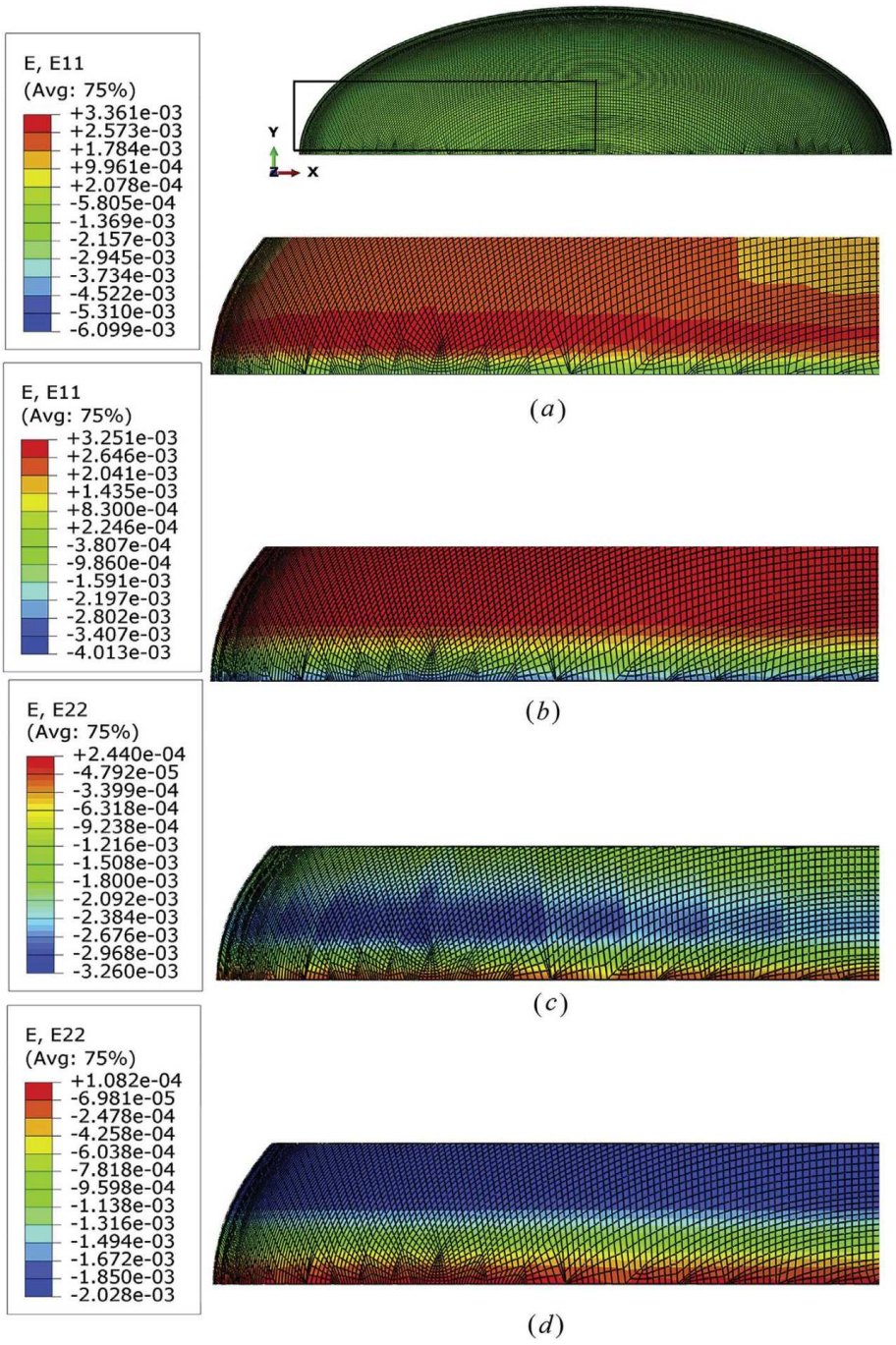


**Fig. 8.** Strain variation in the laminated ellipsoidal shell under internal pressure, meridional Strains: (a) WR $[0]_6$ and (b) WR $[0/45]_3$; circumferential strains: (c) WR $[0]_6$ and (d) WR $[0/45]_3$ (Note: $E_{11}$-meridian strain and $E_{22}$-circumferential strain).

The numerical analysis is carried out first to select the optimal stacking sequence. Subsequently, the experimental tests are conducted on the optimal specimens.

The FE contour plots of the mid-plane meridional and circumferential strains occurring in the laminated ellipsoidal woven composite shell are illustrated in Fig. 8a and d, respectively. According to Fig. 8a and d, more uniform strain distribution was observed in WR $[0/45]_3$ while there was no consistency in WR $[0]_6$.

The paths crossing the laminated ellipsoidal woven composite shell surface along the meridian axis are illustrated in Fig.9a. The paths are located at $\theta = 0^\circ$ and $\theta = 45$, respectively. In the next step, the critical points (*A, B, C, D* and *E*) are set on the paths (see Figs. 4b and 9a). The strains occurring at these points are used as the benchmark for numerical and experimental investigation. The meridional and circumferential strains distribution along the paths are illustrated in Fig. 9b and c, respectively. According to the numerical results, circumferential and meridian strains were constant in WR $[0/45]_3$. However, no consistency was observed in WR $[0]_6$ as the circumferential and meridian strains remained slightly constant up to $\varphi = 30^\circ$ and then, both fluctuated afterward, resulting in non-uniform strain distribution. In details, circumferential and meridional strains in WR $[0]_6$ at the point *E* are nearly30% and

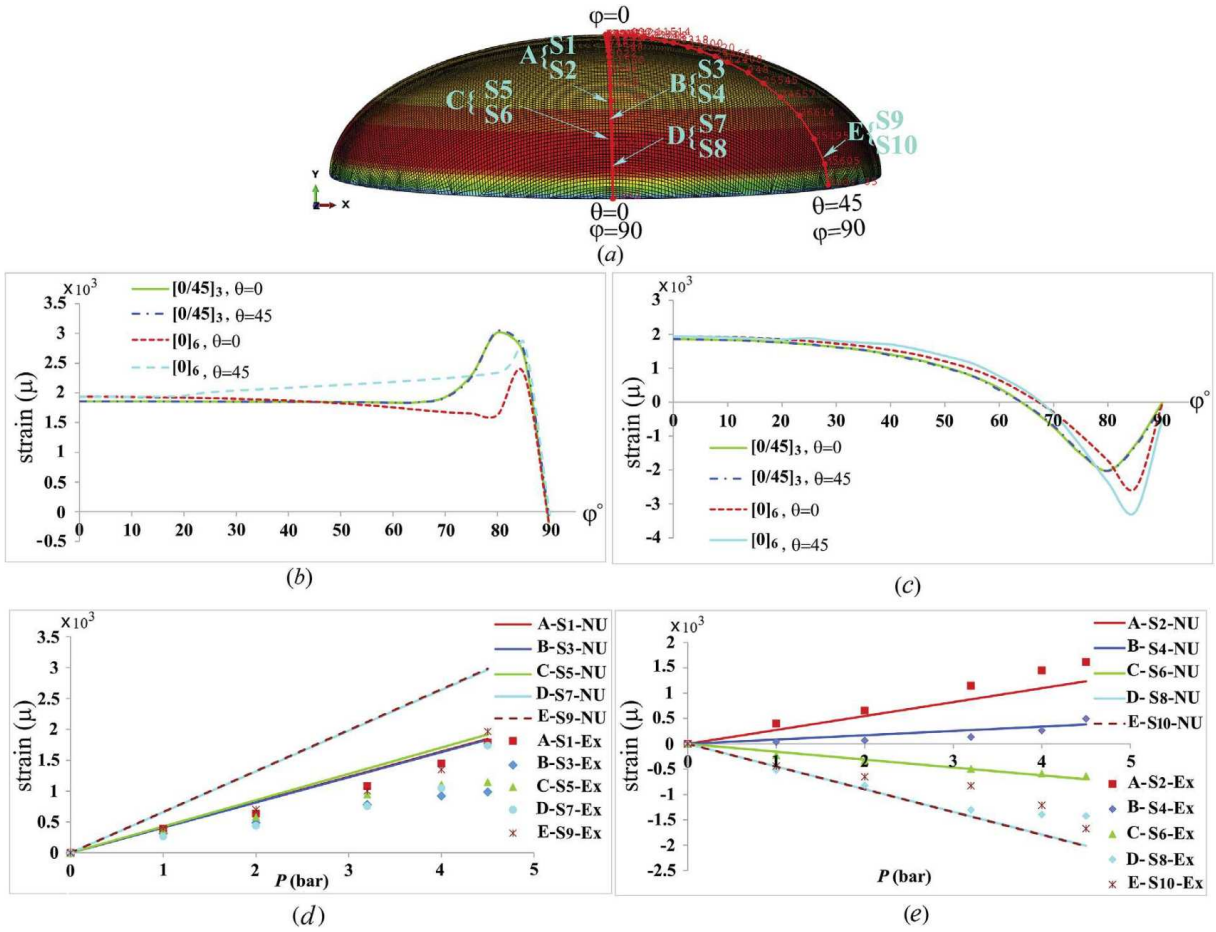


**Fig. 9.** (a) Selected path on the laminated elliptical composite shell; Strain distribution of elliptical composite shell under 5 [*bar*] internal pressure: (b) Meridian direction, and (c) circumferential direction; Numerical and experimental results in the laminated elliptical composite shell with WR $[0/45]_3$: (d) meridian direction, and (e) circumferential direction (Note: NU-Numerical, Ex-Experimental).

27% more than point *D*, respectively. In other words, strain values in the selected circumferential circle ($0<\theta<45$) remained constant in WR $[0/45]_3$ unlike in WR $[0]_6$ which no consistency was seen. Furthermore, It was noticed that the sign in circumferential strains varied from negative to positive at $\varphi = 65^\circ$ along meridian axis in WR $[0/45]_3$ and WR $[0]_6$ (see Fig. 9c).

In the next step, the same experimental procedures as explained in the Section 3.1 is performed in the laminated ellipsoidal composite shell. The numerical results were compared with the results of experimental analysis. WR $[0/45]_3$ as an optimal stacking sequence was selected for the fabrication by using VIP method afterwards. The shells were first configured during the manufacturing process and then fixed to the boundaries (see Fig. 5b). In the next step, the critical points (*A, B, C, D,* and *E*) are set on the two paths in the laminated ellipsoidal shell. After the experimental setup was prepared and the internal pressure was applied, the laminated ellipsoidal woven composite shell was deformed due to creation of the pressure-induced strains. Subsequently, the meridional and circumferential strains at the critical points were measured using the surface-bounded sensors (see Fig. 4d).

The meridional and circumferential strains comparison between the numerical and experimental results under various internal pressures is shown in Fig. 9d and e. It is noticed that slight changes in the amount of internal pressure result in strain values fluctuating significantly regardless of strains type and location. In addition, the circumferential strains at points *C*, *D* and *E* have negative trends, which is due to the fact that these points are located in the shell's region with inward displacements while other points (*A* and *B*) have outward displacement. As in the previous section, comparison of the results obtained by the two approaches showed a strong agreement in strain rate deformation, as strain changes followed the same pattern. However, considering the magnitude of strains, no consistency was observed between the results particularly for the points close to the boundary conditions.

### 3.3. Numerical and experimental results for the laminated torispherical woven composite shell

In this section, numerical and experimental analyses of the laminated torispherical woven composite shell is discussed. The first step is to find the optimal stacking sequence since the experimental specimens are selected for fabrication based on the numerical results. The FE contour plots of the mid-plane meridional and circumferential strains are illustrated in Fig. 10a and d, respectively. Fig. 10a and d represents the shells with WR $[0]_6$ and WR $[0/45]_3$, respectively. Again, the two paths along the meridian axis are chosen (Fig. 11a). The paths are located at $\theta = 0^\circ$ and $\theta = 45$, respectively. The points (*A, B, C, D,* and *E*) are set on the two paths (see Figs. 4b and 11a).

The meridional and circumferential strains distribution occurring along the selected paths are illustrated in Fig. 11b and c. WR [0/

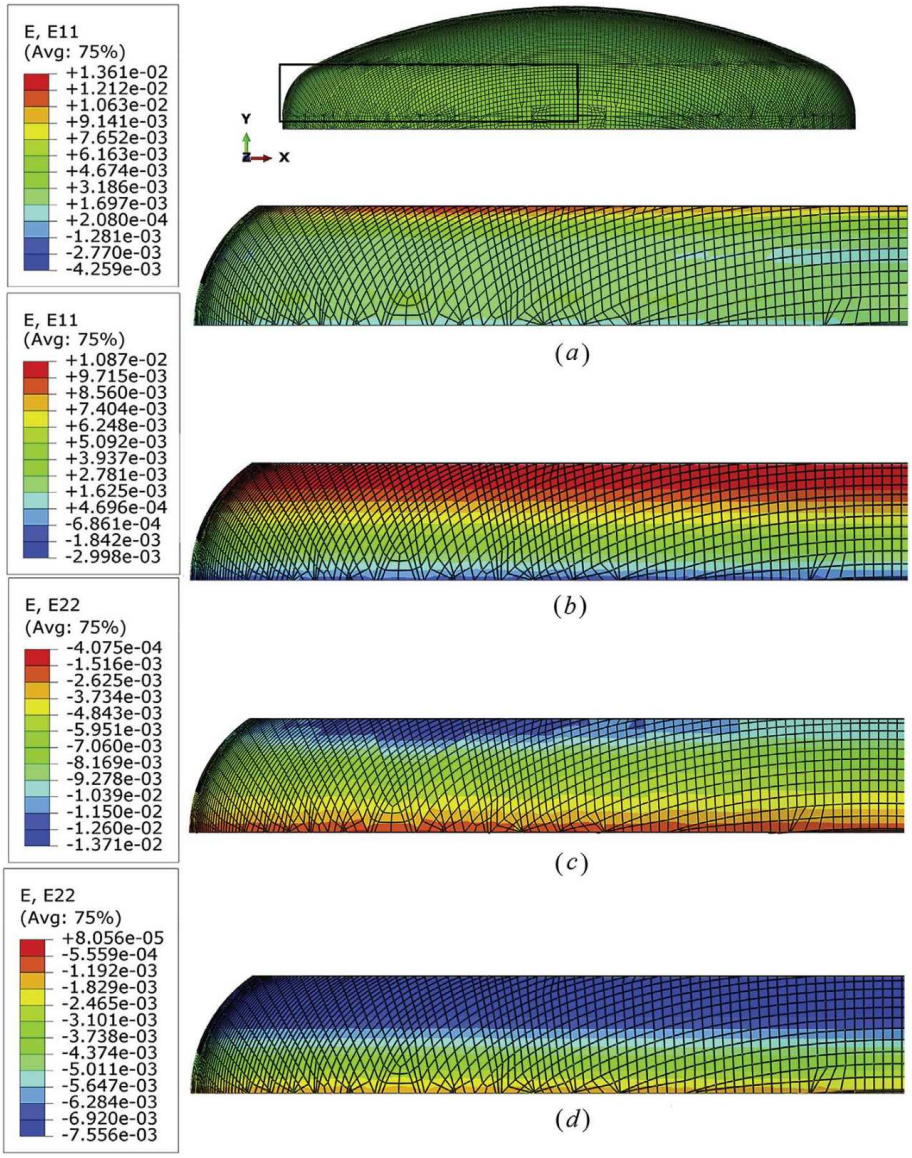


**Fig. 10.** Strain variation in the laminated torispherical shell under internal pressure, meridional strains: (a) WR $[0]_6$ and (b) WR $[0/45]_3$; circumferential strains: (c) WR $[0]_6$ and (d) WR $[0/45]_3$ (Note: $E_{11}$-meridian strain and $E_{22}$-circumferential strain).

$45]_3$ showed a more uniform strain distribution over WR $[0]_6$, as also seen in previous sections. Furthermore, the strains occurring in WR $[0/45]_3$ at points *D* and *E* are comparably equal as long as they are located at the same circumferential path. However, there is a moderate discrepancy between strains at points *D* and *E* in WR $[0]_6$ since the amounts of circumferential and meridian strains at point *E* were measured to be nearly 24.3% and 33% higher than at point *D*, respectively. No circumferential and meridional strain changes were seen at points A and B in WR $[0/45]_3$ and WR $[0]_6$. It can also be observed that in the crown area, the amount of meridional and circumferential strains remains constant in WR $[0/45]_3$ and WR $[0]_6$. However, no consistency was observed in WR $[0]_6$ in the regions near the junction between knuckle and crown. There is also a sharp increase in the amounts of strains deformation near the knuckle region regardless of the shell's stacking sequence. However, the strains occurring at $\theta = 0^\circ$ and $\theta = 45^\circ$ in WR $[0/45]_3$ remained constant. According to Fig. 11b and c, the sign of circumferential strains is negative near the knuckle region at points *C*, *D* and *E* due to inward displacement when internally pressurized and positive near crown region due to onward displacement at all critical points.

Experimental analyses on the laminated torispherical woven composite shell adopted the same procedures as described before. The sensors were installed at the points (*A*, *B*, *C*, *D* and *E*) as shown in Fig. 4e. The meridian and circumferential strains were measured experimentally and then compared with the numerical results (see Fig. 11d and e) at the selected points. Good agreements between the numerical and experimental results were seen in circumferential and meridional strains. According to the numerical results, there was a significant discrepancy between strain values at points *D* and *E* in WR $[0]_6$ unlike WR $[0/45]_3$. According to the both approaches, the effect of internal pressure on strain distribution is significant. For instance, if the internal pressure is raised, the strain distribution varies considerably as seen in previous sections. It must be taken into account that the points close to the boundary are affected by some factors in actual modelling.

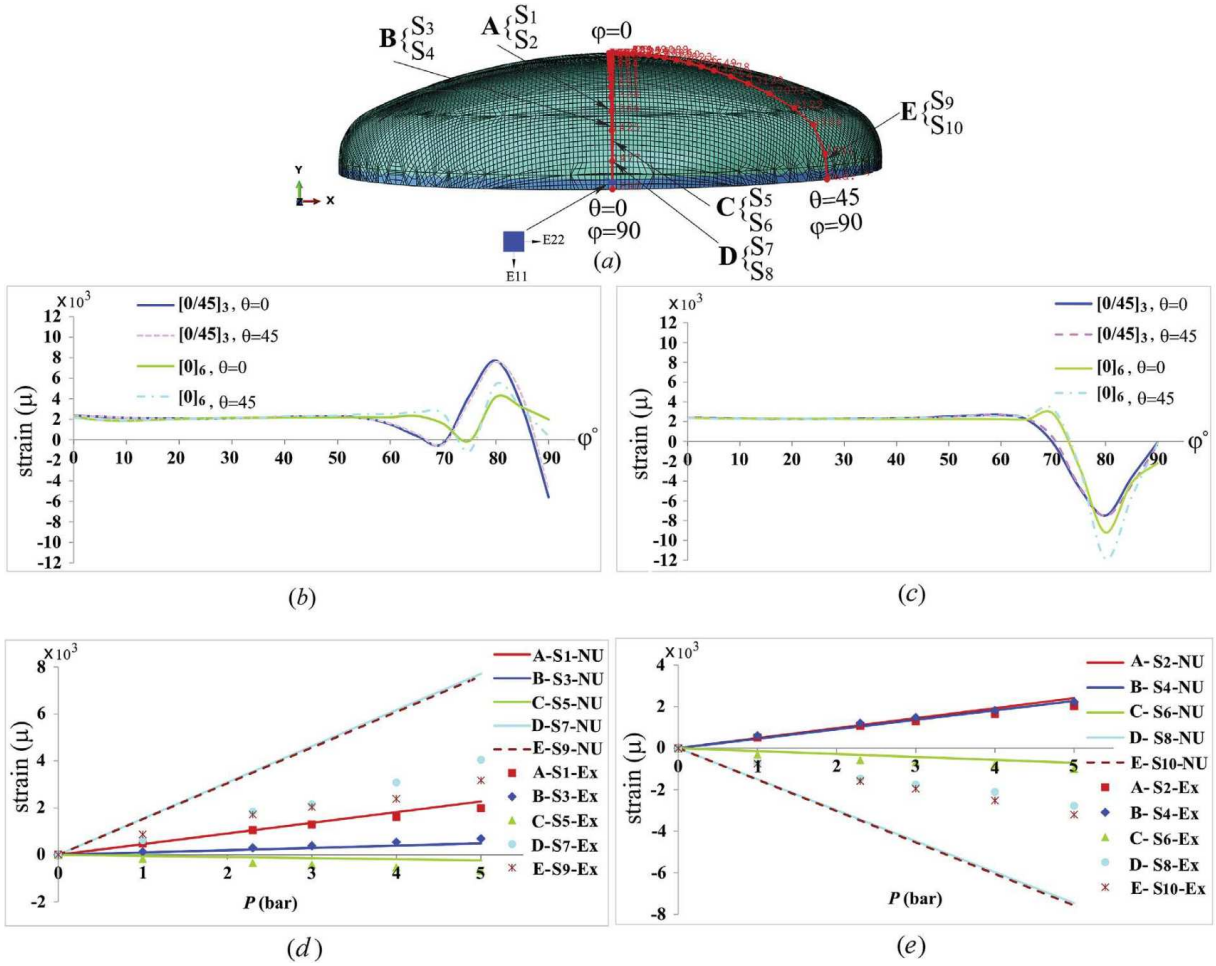


**Fig. 11.** (a) Selected path on the laminated torispherical composite shell; Strain distribution in the laminated torispherical shell under 5 [*bar*] internal pressure: (b) meridian direction, and (c) circumferential direction; numerical and experimental results in the laminated torispherical shells with WR $[0/45]_3$: (d) meridian direction, and (e) circumferential direction (Note: NU-Numerical, Ex-Experimental).

### *3.4. Pressure-strains at critical points in the laminated hemispherical, elliptical, and torispherical woven composite shells*

In this step, the meridional and circumferential strain distribution diagrams of the critical points (*A*, *B*, *C*, *D* and *E*) on the paths in the laminated hemispherical, elliptical and torispherical woven composite shells are compared and plotted in Fig. 12a and b, respectively. The amount of internal pressure was kept constant at $P_o = 5$ [*bar*]. Under the same amount of internal pressure and regardless of the stacking sequence, both meridional and circumferential strains were minimum in the laminated hemispherical woven composite shell while the torispherical one presented the maximum strain deformation. In addition, more structural stability was observed when selecting WR $[0/45]_3$ due to the uniform strain distribution throughout the woven composite shells. Considering geometrical properties, hemispherical shell is the preferred choice compared to ellipsoidal and torispherical shells according to Fig. 12a and b.

## 4. Conclusion

In this research, the mechanical strength of the internally pressurized laminated hemispherical, ellipsoidal and torispherical composite shells with two different stacking sequences, WR $[0]_6$ and WR $[0/45]_3$, was studied numerically and experimentally. The laminated composite shells were made of woven fibres reinforced glass/epoxy. The effect of geometrical shape and stacking sequence on the strain distribution throughout the samples was significant which led to the following remarks:

1. Considering the uniform strain distribution, WR $[0/45]_3$ was observed to be the optimal choice compared to WR $[0]_6$. This is due to the adequate coverage of the week areas in woven fabric in WR $[0/45]_3$. However, no consistency was observed in WR $[0]_6$. Nevertheless, both numerical and experimental results demonstrated that slight changes in the amount of internal pressure induce the pressure-strain deformation significantly, regardless of the geometrical shape and stacking sequence employed.
2. The numerical and experimental results showed that the internally pressurized shell with hemispherical geometry could be the best choice if the space limitation is of no concern, as the hemispherical shell takes up more space than other types. Furthermore, most instability in the strain distribution when the laminated composite shell is subjected to internal pressure was measured in the torispherical shell, which makes it the least choice.
3. The entire reign of the laminated hemispherical shell when internally pressured had positive strain distribution trends, which results in more uniform strain distribution. However, it is

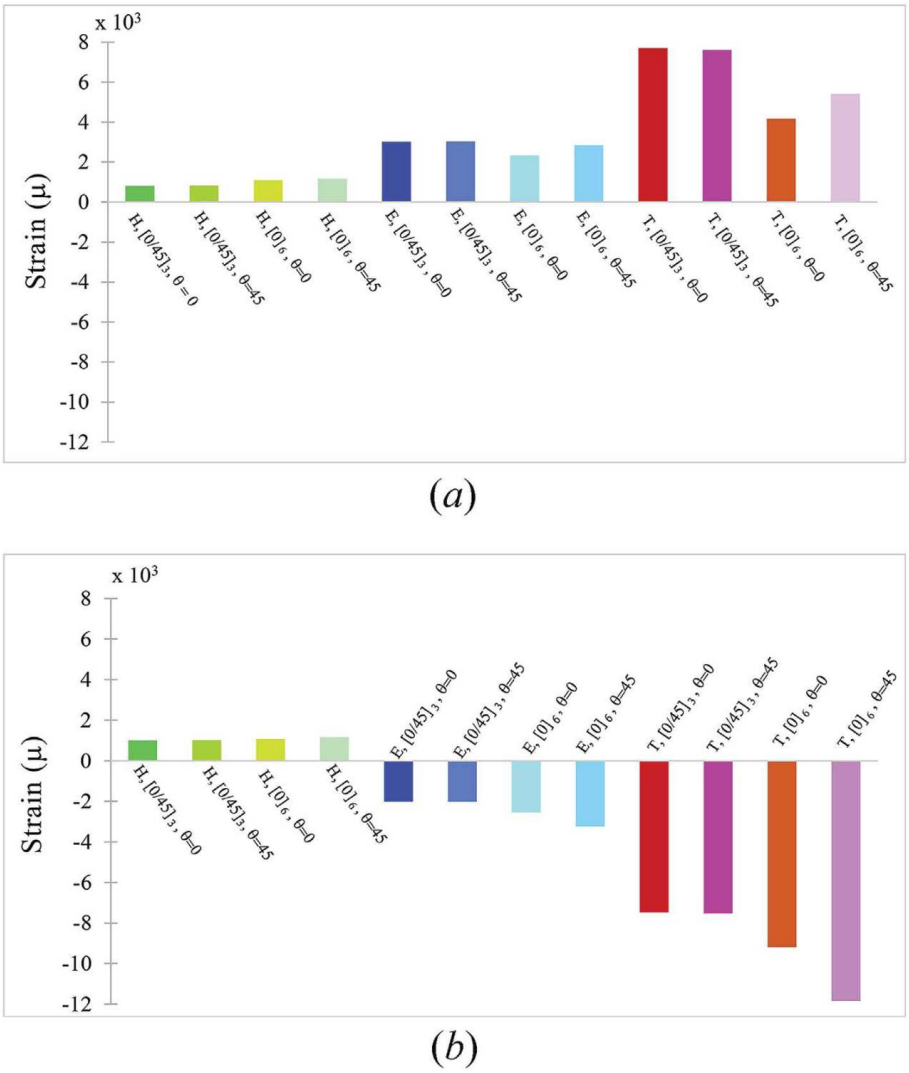


**Fig. 12.** (a) Maridional strain values in the critical points of a pressurized laminated hemispherical (H), elliptical (E) and torispherical (T) shell; (b) circumferential Strain values in the critical points of a pressurized laminated hemispherical (H), elliptical (E) and torispherical (T) shell.

not the case for the elliptical and torispherical shells which both have positive and negative strain distribution trends. In addition, the laminated elliptical and torispherical shells were found to have an outward deformation with negative strains near the knuckle region. Therefore, according to the deformation analysis of the laminated elliptical and torispherical shells, a turning point, which is estimated to be around the junction area between the knuckle and crown region, must be strengthened.

4. Comparison of the numerical and experimental results showed a good agreement in the rate of strain variation as the strain fluctuation followed the same pattern. In addition, well agreement in the strain signs (compression or tensile) at particular critical points (*A*, *B*, *C*, *D*, and *E*) was seen. However, considering the magnitude of strains, no consistency was observed between the results in the critical points, particularly the ones close to the boundary. The higher error margin between the results could be due to the stress concentration factor, oil liquid expansion coefficient, residual stress creation during the fabrication process and/or environmental conditions. These factors were neglected in the numerical analysis but may have some effects on the strain values in the actual experimental tests.

## Acknowledgment

The help and support of the College of Engineering and Science at Victoria University, Melbourne, Center For Composite (CFC) at University Technology Malaysia (UTM), and Dr. M.Y. Yahya the director of CFC to conduct this research are gratefully acknowledged.

## References

[1] Perillo G, Grytten F, Sørbø S, Delhaye V. Numerical/experimental impact events on filament wound composite pressure vessel. *Compos Part B Eng* 2015;**69**:406–17.
[2] Pisano AA, Fuschi P. Mechanically fastened joints in composite laminates: evaluation of load bearing capacity. *Compos Part B Eng* 2011;**42**:949–61.
[3] Walker M, Smith R. A methodology to design fibre reinforced laminated composite structures for maximum strength. *Compos Part B Eng* 2003;**34**:209–14.
[4] Khan MA, Mabrouki T, Vidal-Salle E, Boisse P. Numerical and experimental analyses of woven composite reinforcement forming using a hypoelastic behaviour. Application to the double dome benchmark. *J Mater Process Technol* 2010;**210**:378–88.
[5] Xie J, Yao L, Xu F, Li Y, Shan Z, Hui D, et al. Fabrication and characterization of three-dimensional PMR polyimide composites reinforced with woven basalt fabric. *Compos Part B* 2014;**66**:268–75.

[6] Gao T, Zhao Y, Zhou G, Han Y, Zheng Y, Shan Z, et al. Fabrication and characterization of three dimensional woven carbon fiber. *Compos Part B* 2015;**77**:122–8.
[7] Tsai C, Chiang C. Pneumatic strains in woven glass/epoxy composite laminate induced by fluctuating air pressure. *Compos Sci Technol* 2002;**62**:451–6.
[8] Takeda T, Narita F, Shindo Y, Sanada K. Cryogenic through-thickness tensile characterization of plain woven glass/epoxy composite laminates using cross specimens: experimental test and finite element analysis. *Compos Part B* 2015;**78**:42–9.
[9] Liu PF, Xing LJ, Zheng JY. Failure analysis of carbon fiber/epoxy composite cylindrical laminates using explicit finite element method. *Compos Part B Eng* 2014;**56**:54–61.
[10] Błachut J. Buckling of multilayered metal domes. *Thin-Walled Struct* 2009;**47**:1429–38.
[11] Dong L, Blachut J. Use of woven CFRP for externally pressurized domes. *Compos Struct* 1997;**38**:553–63.
[12] Bisagni C. Numerical analysis and experimental correlation of composite shell buckling and post-buckling. *Compos Part B Eng* 2000;**31**:655–67.
[13] Cui Z, Bhattacharyya D, Moltschaniwskyj G. Experimental and numerical study of buckling response of composite shells compressed transversely between rigid platens. *Compos Part B Eng* 2005;**36**:478–86.
[14] Ross C, Hock B, Boon T, Chong M, Mackney M. The buckling of GRP hemi-ellipsoidal dome shells under external hydrostatic pressure. *Ocean Eng* 2003;**30**:691–705.
[15] Hernandez-Moreno H, Douchin B, Collombet F, Choqueuse D, Davies P. Influence of winding pattern on the mechanical behavior of filament wound composite cylinders under external pressure. *Compos Sci Technol* 2008;**68**:1015–24.
[16] Muscat M, Camilleri D. Comparison between different design approaches to prevent buckling of torispherical heads under internal pressure. *Int J Press Vessel Pip* 2013;**108**–**109**:61–6.
[17] Bouhafs M, Sereir Z, Chateauneuf A. Probabilistic analysis of the mechanical response of thick composite pipes under internal pressure. *Int J Press Vessel Pip* 2012;**95**:7–15.
[18] Bai J, Seeleuthner P, Bompard P. Mechanical behaviour of ± 55° filament-wound glass-fibre/epoxy-resin tubes: I. Microstructural analyses, mechanical behaviour and damage mechanisms of composite tubes under pure tensile loading, pure internal pressure, and combined loading. *Compos Sci Technol* 1997;**57**:141–53.
[19] Tutuncu N, Ozturk M. Exact solutions for stresses in functionally graded pressure vessels. *Compos Part B* 2001;**32**:683–6.
[20] Bakaiyan H, Hosseini H, Ameri E. Analysis of multi-layered filament-wound composite pipes under combined internal pressure and thermomechanical loading with thermal variations. *Compos Struct* 2009;**88**:532–41.
[21] Teshnizi SHS, Koloor SSR, Sharifishourabi G, Ayob A Bin, Yahya MY. Effect of ply thickness on displacements and stresses in laminated GFRP cylinder subjected to radial load. *Adv Mater Res* 2012;**488**–**489**:367–71.
[22] Teshnizi SHS, Koloor SSR, Sharifishourabi G, Ayob A Bin, Yahya MY. Mechanical behavior of GFRP laminated composite pipe subjected to uniform radial patch load. *Adv Mater Res* 2012;**488**–**489**:542–6.
[23] Russo P, Acierno D, Simeoli G, Iannace S, Sorrentino L. Flexural and impact response of woven glass fiber fabric/polypropylene composites 2013;**54**:415–21.
[24] Matadi Boumbimba R, Froustey C, Viot P, Gerard P. Low velocity impact response and damage of laminate composite glass fibre/epoxy based tri-block copolymer. *Compos Part B Eng* 2015;**76**:332–42.
[25] Zhao Han, Gerard G. An experimental failure strength matrix composite investigation of compressive of fibre reinforced polymer- plates under impact loading. *Compos Sci Technol* 1997;**57**:287–92.
[26] Alif Nidal, Carlsson Leif A, Boogh L. The effect of weave pattern and crack propagation direction on mode I delamination resistance of woven glass and carbon composites. *Compos Part B Eng* 1998;**29**:603–11.
[27] Caputo F, De Luca A, Sepe R. Numerical study of the structural behaviour of impacted composite laminates subjected to compression load. *Compos Part B Eng* 2015;**79**:456–65.
[28] Liang CC, Chen HW. Optimum design of fiber-reinforced composite cylindrical skirts for solid rocket cases subjected to buckling and overstressing constraints. *Compos Part B Eng* 2003;**34**:273–84.
[29] Kursa M, Kowalczyk-Gajewska K, Petryk H. Multi-objective optimization of thermo-mechanical properties of metal-ceramic composites. *Compos Part B Eng* 2014;**60**:586–96.
[30] Uemura M, Fukunaga H. Probabilistic burst strength of filament-wound cylinders under internal pressure. *J Compos Mater* 1981;**15**:462–80.
[31] Tarakcioglu N, Samanci A, Arikan H, Akdemir A. The fatigue behavior of (±55°) filament wound GRP pipes with a surface crack under internal pressure. *Compos Struct* 2007;**80**:207–11.
[32] Limam A, Lee L-H, Corona E, Kyriakides S. Inelastic wrinkling and collapse of tubes under combined bending and internal pressure. *Int J Mech Sci* 2010;**52**:637–47.
[33] Shen H-S, Yang J, Kitipornchai S. Postbuckling of internal pressure loaded FGM cylindrical shells surrounded by an elastic medium. *Eur J Mech A/Solids* 2010;**29**:448–60.
[34] Blachut J. Plastic loads for internally pressurised torispheres. *Int J Press Vessel Pip* 1995;**64**:91–100.
[35] Sorić J, Zahlten W. Elastic-plastic analysis of internally pressurized torispherical shells. *Thin-Walled Struct* 1995;**22**:217–39.
[36] Francescato P, Gillet A, Leh D, Saffré P. Comparison of optimal design methods for type 3 high-pressure storage tanks. *Compos Struct* 2012;**94**:2087–96.
[37] Hojjati M, Ardebili VS, Hoa SV. Design of domes for polymeric composite pressure vessels. *Compos Eng* 1995;**5**:51–9.
[38] Cohen D, Mantell SC, Zhao L. The effect of fiber volume fraction on filament wound composite pressure vessel strength. *Compos Part B Eng* 2001;**32**:413–29.
[39] Vafaeesefat A, Khani A. Head shape and winding angle optimization of composite pressure vessels based on a multi-level strategy. *Appl Compos Mater* 2008;**14**:379–91.
[40] Blachut J, Galletly G. Influence of local imperfections on the collapse strength of domed end closures. *J Mech Eng Sci* 1993;**207**:197–207.
[41] Ross CTF. Vibration and elastic instability of thin-walled domes under uniform external pressure. *Thin-Walled Struct* 1996;**26**:159–77.
[42] Cho Won-Man, Lee Bang-Eop, Koo Song-Hoe, Lee Young-Shin. Effects of geometric and material nonlinearity on the stresses of various pressure vessel dome shapes. *Compos Struct* 1995;**55**:1063–75.
[43] Hwang TK, Hong CS, Kim CG. Probabilistic deformation and strength prediction for a filament wound pressure vessel. *Compos Part B Eng* 2003;**34**:481–97.
[44] CRISP RJ. A computer survey of the behaviour of torispherical drum heads under internal pressure loading Part I: the elastic analysis. *Eng Des* 1970;**11**:457–76.
[45] Aggarwal SK, Nayak GC. Elasto-plastic analysis as a basis for design of cylindrical pressure vessels with different end closures. *Int J Press Vessel Pip* 1982;**10**:271–96.
[46] Yeom DJ, Robinson M. Numerical analysis of the elastic-plastic behaviour of pressure vessels with ellipsoidal and torispherical heads. *Int J Press Vessel Pip* 1996;**65**:147–56.
[47] Magnucki K, Lewinski J. Fully stressed head of a pressure vessel. *Thin-Walled Struct* 2000;**38**:167–78.
[48] Magnucki K, Szyc W, Lewinski J. Minimization of stress concentration factor in cylindrical pressure vessels with ellipsoidal heads. *Int J Press Vessel Pip* 2002;**79**:841–6.
[49] Carbonari RC, Muñoz-Rojas PA, Andrade EQ, Paulino GH, Nishimoto K, Silva ECN. Design of pressure vessels using shape optimization: an integrated approach. *Int J Press Vessel Pip* 2011;**88**:198–212.
[50] Şenalp AZ. Investigation of the effects of perturbation forces to buckling in internally pressurized torispherical pressure vessel heads. *Adv Eng Softw* 2012;**45**:232–8.
[51] Hu H, Li S, Wang J, Zu L. Structural design and experimental investigation on filament wound toroidal pressure vessels. *Compos Struct* 2015;**121**:114–20.
[52] Gohery S, Sharifi S, Vrcelj Z, Yahya MY. First-ply failure prediction of an unsymmetrical laminated ellipsoidal woven GFRP composite shell with incorporated surface-bounded sensors and internally pressurized. *Compos Part B* 2015;**77**:502–18.

## 3.5. CONCLUDING REMARKS

This chapter presented novel analytical and numerical methods to investigate the effectiveness of PZT strain gauge sensors for obtaining the critical mechanical strains and possible failure in various types of internally pressurized laminated composite shells with complex geometries. The laminated composite shells with ellipsoidal geometry were studied using the analytical method while more comprehensive studies on the laminated ellipsoidal, hemispherical, and torisoherical composite shells were conducted through numerical simulations.

The analytical and numerical results were then verified by using the experimental test results known as VIP. The analytical results were derived by adopting the linear interpolation technique to accurately interpolate the critical regions at which failure may occur. Tsai-Wu failure criterion was adapted as a failure design factor. The numerical analysis was based on the 3D FE simulation using ABAQUS. MATLAB was adapted for the analytical investigation. During the experimental analysis, the surface-bounded PZT strain gauge sensors were installed on the outmost layer of the laminated composite shells to measure the strain values after internal pressure was applied. The data obtained by PZT sensors were then compared with the analytical and numerical results. Based on the findings in this chapter, the following conclusions are made:

- Observation of a good agreement between the experimental, analytical and numerical results demonstrated the effectiveness of PZT strain gauge sensors in predicting the strain values in laminated composite structures under mechanical

loads. Furthermore, the use of analytical and numerical methods to predict the mechanical deformation as presented in the current research eliminates the need for the experimental analysis which is often time-consuming and expensive.

- The effect of various parameters such as layup thickness, shells axis ratio, stacking sequence configuration, laminate thickness, layup symmetry, and mechanical loads intensity on the mechanical deformation and failure strength of laminate composite shells is significant.

- Maximum mechanical strains occur in the innermost layers and the areas close to the boundary conditions, where it is usually difficult to install PZT sensors for structural monitoring.

- Relying on the analytical solutions and FE simulations as proposed in this study is beneficial since measurement of mechanical strains in the regions close to boundary conditions is complicated and difficult. Moreover, the experimental analysis for structural health monitoring of laminated composite structures is costly and requires extensive tests and specimen calibrations to acquire accurate results.

- To correct the trade-off between the analytical and experimental results, an offset factor R must be defined. Since the critical failure pressure obtained from the experimental study is lower, an offset factor can minimize the analytical results error. Thus, the results obtained analytically become closer to the results obtained from the actual modelling.

# Chapter 4

# SHAPE CONTROL OF LAMINATED COMPOSITE HYBRID STRUCTURES USING PIEZOELECTRIC ACTUATORS: A NOVEL ANALYTICAL SOLUTION

## 1.1. INTRODUCTION

In this chapter, an analytical solution is proposed to obtain the static bending-twisting deformation and optimal shape control of laminated piezo composite hybrid plates and beams by using the non-angled and inclined piezoelectric actuators. The linear piezoelectricity and plates theories are adapted for the analysis. Although the analytical solution proposed in this research is adapted for cantilever plates and beams, it can also be modified and extended to cover various boundary conditions and geometrical shapes. The major part of the investigation in this chapter relies on a double integral multivariable Fourier transformation method and discretised higher order partial

differential unit step function equations. This chapter is divided into two sections. First, pure bending control of the laminated composite hybrid plates and beams using the piezoelectric actuators is investigated. Second, the proposed analytical solution is extended to cover more complex shape control tasks such as twisting deformation control. The inclined piezoelectric actuators are then used to control the twisting deformation created in the laminated composite plates and beams.

One of the advantages of the proposed analytical method is its ability to consider the effect of residual thermal stresses during the shape control performance. The effect of various parameters including arbitrary loads such as non-uniform thermal stresses, electrical and mechanical loads, layup thickness, piezoelectric actuators size and placement, stacking sequence, and geometrical dimension are investigated. To verify the reliability of the proposed analytical solution, the results are compared with some published benchmark results and a series of simple, accurate and robust 3D analysis models by using ABAQUS.

This chapter includes the following papers:

1) S. Gohery, S. Sharifi, and Z. Vrcelj, "New explicit solution for static shape control of smart laminated cantilever piezo-composite-hybrid plates/beams under thermo-electro-mechanical loads using piezoelectric actuators," *Compos. Struct.*, vol. 145, pp. 89–112, 2016.

2) S. Gohery, S. Sharifi, and Z. Vrcelj, "A novel explicit solution for twisting control of smart laminated cantilever composite plates/beams using inclined piezoelectric actuators," *Compos. Struct.*, vol. 161, pp. 477–504, 2016.

VICTORIA UNIVERSITY
MELBOURNE AUSTRALIA

**PART B:**

**DECLARATION OF CO-AUTHORSHIP AND CO-CONTRIBUTION: PAPERS INCORPORATED IN THESIS BY PUBLICATION**

This declaration is to be completed for each conjointly authored publication and placed at the beginning of the thesis chapter in which the publication appears.

Declaration by [candidate name]: Scott Gohery

Signature: [redacted]

Date: 5/01/2017

Paper Title:
New explicit solution for static shape control of smart laminated cantilever piezo-composite-hybrid plates/beams under thermo-electro-mechanical loads using piezoelectric actuators

In the case of the above publication, the following authors contributed to the work as follows:

| Name | Contribution % | Nature of Contribution |
|---|---|---|
| Scott Gohery | 75 | Initial concept, Literature review, Analytical investigation, Computer programming, Writing of the manuscript |
| Shokrollah Sharifi | 20 | Provided critical revision of the manuscript, Sketching Figs using AutoCad and SolidWorks softwares |
| Zora Vrcelj | 5 | Provided critical revision of the manuscript, Initial and final approval of the manuscript |
| | | |
| | | |
| | | |

Page - 1 - of 2

VICTORIA UNIVERSITY
MELBOURNE AUSTRALIA

**DECLARATION BY CO-AUTHORS**

The undersigned certify that:

1. They meet criteria for authorship in that they have participated in the conception, execution or interpretation of at least that part of the publication in their field of expertise;
2. They take public responsibility for their part of the publication, except for the responsible author who accepts overall responsibility for the publication;
3. There are no other authors of the publication according to these criteria;
4. Potential conflicts of interest have been disclosed to a) granting bodies, b) the editor or publisher of journals or other publications, and c) the head of the responsible academic unit; and
5. The original data is stored at the following location(s):

| Location(s): |
| --- |
| College of Engineering and Science, Victoria University, Melbourne, VIC 8001, Australia |

and will be held for at least five years from the date indicated below:

| | | Date |
| --- | --- | --- |
| Signature 1 | [redacted] | 20/12/2016 |
| Signature 2 | | 20/12/2016 |
| Signature 3 | | 20/12/2016 |
| Signature 4 | | |

Page - 2 - of 2

VICTORIA UNIVERSITY
MELBOURNE AUSTRALIA

**PART B:**

**DECLARATION OF CO-AUTHORSHIP AND CO-CONTRIBUTION: PAPERS INCORPORATED IN THESIS BY PUBLICATION**

This declaration is to be completed for each conjointly authored publication and placed at the beginning of the thesis chapter in which the publication appears.

Declaration by [candidate name]: Scott Gohery

Signature: [redacted]

Date: 5/01/2017

Paper Title:
A novel explicit solution for twisting control of smart laminated cantilever composite plates/ beams using inclined piezoelectric actuators

In the case of the above publication, the following authors contributed to the work as follows:

| Name | Contribution % | Nature of Contribution |
|---|---|---|
| Scott Gohery | 75 | Initial concept, Literature review, Analytical investigation, Computer programming, Writing of the manuscript |
| Shokrollah Sharifi | 20 | Provided critical revision of the manuscript, Sketching Figs using AutoCad and SolidWorks softwares |
| Zora Vrcelj | 5 | Provided critical revision of the manuscript, Initial and final approval of the manuscript |
| | | |
| | | |
| | | |

Page - 1 - of 2

VICTORIA UNIVERSITY
MELBOURNE AUSTRALIA

**DECLARATION BY CO-AUTHORS**

The undersigned certify that:

1. They meet criteria for authorship in that they have participated in the conception, execution or interpretation of at least that part of the publication in their field of expertise;
2. They take public responsibility for their part of the publication, except for the responsible author who accepts overall responsibility for the publication;
3. There are no other authors of the publication according to these criteria;
4. Potential conflicts of interest have been disclosed to a) granting bodies, b) the editor or publisher of journals or other publications, and c) the head of the responsible academic unit; and
5. The original data is stored at the following location(s):

| Location(s): |
| --- |
| College of Engineering and Science, Victoria University, Melbourne, VIC 8001, Australia |

and will be held for at least five years from the date indicated below:

| | | Date |
| --- | --- | --- |
| Signature 1 | [redacted] | 20/12/2016 |
| Signature 2 | | 20/12/2016 |
| Signature 3 | | 20/12/2016 |
| Signature 4 | | |

Page - 2 - of 2

Composite Structures 145 (2016) 89–112

Contents lists available at ScienceDirect

Composite Structures

journal homepage: www.elsevier.com/locate/compstruct

# New explicit solution for static shape control of smart laminated cantilever piezo-composite-hybrid plates/beams under thermo-electro-mechanical loads using piezoelectric actuators

Scott Gohery *, S. Sharifi, Zora Vrcelj

*College of Engineering and Science, Victoria University, Melbourne, VIC 8001, Australia*

ARTICLE INFO

*Article history:*
Available online 26 February 2016

*Keywords:*
Explicit analytical solution
Static shape control
Smart cantilever piezo composite hybrid laminates
Thermo-electro-mechanical loads
Piezoelectric actuators

ABSTRACT

In this paper, a new explicit exact analytical solution is proposed for obtaining static deformation and optimal shape control of smart laminated cantilever piezo composite hybrid plates and beams under thermo-electro-mechanical loads using piezoelectric actuators. The linear piezoelectricity and plates theories were adapted for the analysis. A novel double integral multivariable Fourier transformation method combined with discretised higher order partial differential unit step function equations were employed. The effect of various parameters including arbitrary loads such as non-uniform thermal stresses, electrical and mechanical loads, layup thickness, piezoelectric actuators size and placement, stacking sequence, and geometrical dimension were considered. The results were then compared with some published benchmark results and good agreement was observed. Unlike the earlier studies, the proposed method does not require the characteristic and trial deflection function to be predetermined. Both, the embedded and bounded actuators are considered. Until now, the shape control task of reducing mid-plane deformation at free end in smart laminated cantilever plates and beams was unsolvable and approximations were typically employed in numerical analysis Yu et al. (2009). This problem becomes more complicated for wider and longer plates but the method proposed herein successfully resolves this issue.



## 1. Introduction

Piezoelectric materials have recently drawn much attention due to their low power consumption, high material linearity, and quick response when induced by external forces [1–3]. Numerous smart engineering structures incorporated with smart devices such as piezoelectric sensors and actuators have proved to be superior to their conventional counterparts for being capable of acoustical noise reduction, damage identification, structural health monitoring, vibration suppression, static torsional control of helicopter blades, deflection control of missile fines, airfoil shape changes, and many more [4–9]. One of the great advantages of piezoelectric materials is to be able to respond to changing environment and control structural deformation which has led to the new generation of aerospace structures like morphine airplanes [10]. Among piezoelectric materials, bounded piezoceramic actuators have been commonly used for shape control of online monitoring systems. They can also be embedded in laminated composite structures to induce structural stiffness system to the advantage [2,11–13]. Laminated composite structures are being used considerably in aerospace, automotive, civil, mechanical and structural engineering applications due to their high stiffness and strength to weight ratio [14]. Piezoelectric materials can be integrated with laminated composite structures to provide smart-intelligent composite system. Laminated cantilever composite plates have been widely used in various engineering applications such as airplane wings, corrugated plates, reinforced concrete slaps, decks of contemporary steel bridges, boom arms of industrial cranes, and flight control surfaces [15–17].

Numerous numerical and experimental studies have been carried out to analyse smart piezo composite laminates subjected to arbitrary loads. Milazzo [18] developed a family of two dimensional (2D) refined equivalent single layer models for vibration analysis of multilayered and functionally graded smart magneto-electro-elastic plates. The single layer FE model presented in his work was then validated against available benchmark three dimensional (3D) solutions. In another study, Milazzo [18] developed a FE model for large deflection analysis of multi-layered smart plates. Sartorato et al. [5] worked on a FE formulation for smart composite shells. This smart shell FE formulation was the

* Corresponding author. Tel.: +61 423656484.
*E-mail addresses:* scott.gohery@unimelb.edu.au (S. Gohery), sharifi.te@gmail.com (S. Sharifi), Zora.Vrcelj@vu.edu.au (Z. Vrcelj).

http://dx.doi.org/10.1016/j.compstruct.2016.02.047
0263-8223/

benchmark for his work on dynamic analysis of laminated curved isotropic and orthotropic structures integrated with piezoelectric layers. The presented FE model was then compared and verified against experimental research and FE formulations in the literature. Zhang et al. [19] developed a linear electro-mechanically coupled FE model for thin-walled smart composite laminates bounded with macro-fibre composite (MFC) actuators. The proposed method was then compared with numerical simulation and experimental results. In another similar study, Zhang and Schmidt [9] formulated a FE model based on large rotation shell theory for static and dynamic analysis of thin-walled smart piezoelectric composite laminates. Plattenburg et al. [20] studied vibration excitation of a thin plate with free boundary conditions with multiple bounded piezoelectric actuator patches analytically, numerically, and experimentally. In another study by Lin and Nien [21], static and dynamic shape deformations of laminated plates integrated with piezoelectric actuators and subjected to unknown loads were studied numerically and experimentally. The study demonstrated the effectiveness of piezoelectric actuators on the shape and deflection control of composite laminates. Other experimental and numerical studies concerning the deflection and shape control of smart laminated cantilever and simply-supported composite plates and beams as well as unattached laminates can be found in Refs [22–25].

There are a number of explicit exact analytical solutions available in the literature for analysis of smart cantilever composite laminates incorporated with piezoelectric actuators. Huang and Sun [26] worked on effect of surface bounded piezoelectric actuators on the load transfer and wave propagation of an anisotropic elastic medium. The effect of optimal piezoelectric actuators placements on the static and dynamic control of simply supported laminated composite structures was studied analytically by using the principle of virtual work [27]. Multiscale analysis of the plates is one of the semi-analytical studies based on the asymptotic expansion homogenization method used to couple the micro-scale and macro-scale field variables [8]. In another study, the effect of surface load and residual thermal stresses on the buckling of an isotropic cantilever plate was studied [16]. In another study focusing on the theoretical analysis of plates static deflection, Sader and White [15] emphasized the minimization of an isotropic plate's potential energy by implementing calculus of variation to obtain the governing equation of deflection function under external transverse load. However, the exact solution was approximated and it was assumed that the variation along the plate width was negligible.

It can be observed from literature that most studies on the smart piezocomposite laminates were based on experimental and numerical approaches. Furthermore, theories adapted for the analysis of smart structures displacement fields result in significant computational time required due to a large number of degrees of freedom [28]. There are a number of explicit analytical solutions available in this area. However, most studies were conducted on unattached laminates, and clamped and simply supported plates and beams, without taking into account the effect of various parameters such as thickness, residual thermal stresses, and complex boundary conditions. Smart cantilever composite plates and beams are important structural elements while their exact analytical evaluation has been one of the most difficult problems in the theory of elasticity. Multiscale and approximation solutions, typically adapted for analytical evaluation of smart composite laminates, are complex and require characteristic function.

In the present paper, a new explicit exact analytical solution for the shape deformation control of smart laminated cantilever piezo composite hybrid plates and beams is obtained. The approach is based on a novel double integral multivariable transformation method combined with discretised higher order partial differential unit step function equations. The shape of smart piezo composite hybrid laminates is induced using multiple piezoelectric actuators either bounded or embedded to the host structure (composite hybrid laminate). The advantages of the proposed explicit analytical solution presented in this research paper are that it eliminates the need for characteristic and trial deflection functions to be predetermined. Furthermore, unlike in previous research studies were bounded sensors and actuators were typically the framework of study, both embedded and bounded actuators' effect can now be considered using the proposed explicit method. In addition, it is also adapted for variety of complex loading systems including but not limited to thermo-electro-mechanical loads, residual thermal stresses, uniform lateral pressure, mechanical patch loading, and point loads. Furthermore, the shape control task of reducing the mid-plane deformation at free end in smart laminated cantilever plates and beams was unsolvable by using the Hamilton and virtual work principle, and the FE method [1]. The problem becomes even more complicated for wider and longer plates, and the proposed method has clearly demonstrated its ability to overcome this issue. The results were compared and verified against those available in the literature and a good agreement was achieved. MATLAB was adopted to obtain the structural shape deformation values. Calculation of required optimal voltages to suppress the deflection of smart cantilever piezo composite hybrid laminates was based on classical trial and error techniques.

## 2. Mathematical modeling

Consider a piezo composite hybrid laminate with a total layup thickness of $H$ and composed of $N$ orthotropic layers as shown in Fig. 1. Various piezoelectric layers are presumably incorporated into the laminate. Considering the material linearity for small displacements, the Kirchhoff hypothesis leads to the general form of displacement fields as shown in Eq. (1) [29]. Considering the composite hybrid laminates and piezoelectric layers/patches, some initial assumptions for mathematical modeling are made as follows [29,30]:

- Fibers distribution throughout the matrix is uniform.
- There is a perfect bonding between fibers and matrix, avoiding fibers dislocations and disarrangements through the matrix. No slip also occurs between the lamina interfaces.
- The matrix is perfectly fabricated with no voids and impurity.
- The lamina is initially pre-stressed (thermal stresses may exist). Thus, there are residual stresses in presence of matrix and fibers.
- The matrix and fibers behave linearly within elastic domain.

For the smart part of the laminates, the linear piezoelectricity theory is adapted with assumptions made as follows [30]:

- The strain-electric filed varies linearly.
- The piezoelectric confidents are constant within the linear zone. Thus, they cannot be electrically turned with a bias field.
- The electric field is assumed to be constant across each lamina.
- The piezoelectric actuators are polarized through thickness. Therefore, the electrical discharge through thickness $E_z$ is considered in this study ($E_x = E_y = 0$).

$$\begin{aligned} u(x,y,z) &= u_0(x,y) - z\frac{\partial w_0}{\partial x} \\ v(x,y,z) &= v_0(x,y) - z\frac{\partial w_0}{\partial y} \\ w(x,y,z) &= w_0(x,y) \end{aligned} \tag{1}$$

$u_0$, $v_0$, and $w_0$ are the mid-plane displacements along $x$, $y$, and $z$ directions, respectively on the $xy$-plane. $z$ is the vertical distance from the mid-plane to the $k$th layer which is located between $z = h_k$ and $z = h_{k+1}$ through laminate thickness, as shown in Fig. 1.

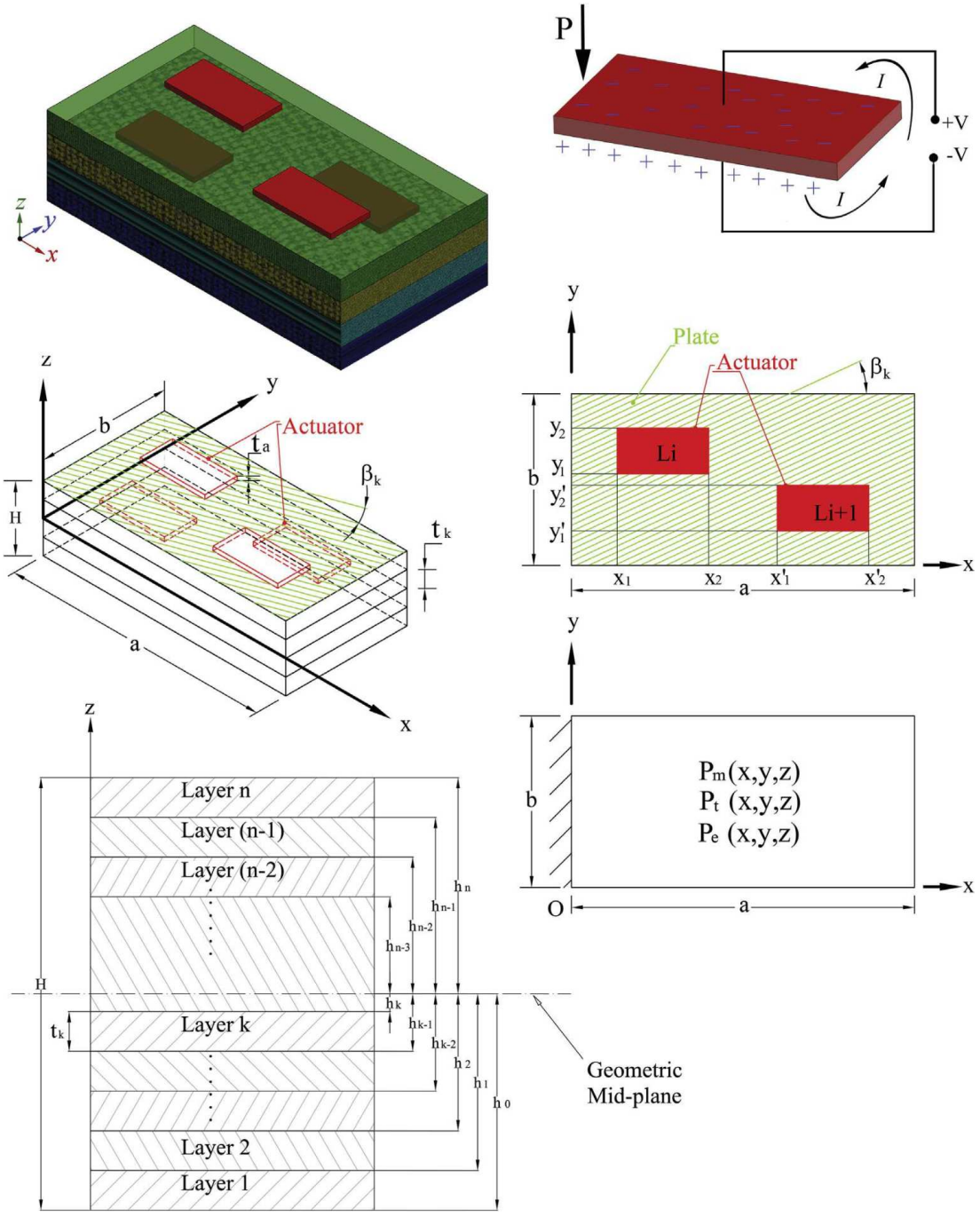


**Fig. 1.** Schematics of smart laminated cantilever piezo composite hybrid plate induced by thermo-electro-mechanical loads.

After obtaining the mid-plane displacements, the displacements of any arbitrary point, *x*, *y*, and *z* in 3D space can be determined. The linear strain–displacement relation is stated in Eq. (2). It is assumed that all strain components change linearly in entire laminate independent from changes in material properties through layup thickness.

$$\left[\varepsilon_{xx} \quad \varepsilon_{yy} \quad \gamma_{xy}\right]^T = \left[\frac{\partial u}{\partial x} \frac{\partial v}{\partial y} \frac{\partial u}{\partial y} + \frac{\partial v}{\partial x}\right]^T = \left[\varepsilon^0_{xx} \quad \varepsilon^0_{yy} \quad \tau^0_{xy}\right]^T + z\left[\varepsilon^f_{xx} \quad \varepsilon^f_{yy} \quad \tau^f_{xy}\right]^T \tag{2}$$

where,

$$\left[\varepsilon^0_{xx} \quad \varepsilon^0_{yy} \quad \gamma^0_{xy}\right]^T = \left[\frac{\partial u_0}{\partial x} \frac{\partial v_0}{\partial y} \frac{\partial u_0}{\partial y} + \frac{\partial v_0}{\partial x}\right]^T$$

$$\left[\varepsilon^f_{xx} \quad \varepsilon^f_{yy} \quad \gamma^f_{xy}\right]^T = \left[-\frac{\partial^2 w_0}{\partial x^2} - \frac{\partial^2 w_0}{\partial y^2} - 2\frac{\partial^2 w_0}{\partial x \partial y}\right]^T$$

$\varepsilon^0_{xx}$, $\varepsilon^0_{yy}$, and $\gamma^0_{xy}$ are the laminate's mid-plane strains, $\varepsilon^0_{ff}$, $\varepsilon^f_{yy}$, and $\gamma^f_{xy}$ are the flexural (bending) strains and $w_o$ is the transverse deflection of a composite laminate's mid-plane. The bending strains are topically caused by laminate's stacking sequence asymmetric or external thermo-electro-mechanical bending and twisting loads. Since the flexural shape control of the lateral displacements due to thermo-electro-mechanical loads acting on smart symmetrical laminates is considered in this study, thus the effect of laminate's mid-plane strains can be neglected and the effect of flexural strains are taken into account. The in-plane

stress–strain relationship for a $k$th smart orthotropic piezo composite hybrid laminate is shown in Eq. (3a) [30]. The derivation of 2D piezoelectric electromechanical equations from 3D equations of theory of elasticity and three charged equilibrium equations of piezoelectric medium are discussed in Appendix A.

$$\begin{bmatrix}\sigma_{xx}\\ \sigma_{yy}\\ \tau_{xy}\end{bmatrix}^k = \begin{bmatrix}\bar{Q}_{11} & \bar{Q}_{12} & \bar{Q}_{16}\\ \bar{Q}_{12} & \bar{Q}_{22} & \bar{Q}_{26}\\ \bar{Q}_{16} & \bar{Q}_{26} & \bar{Q}_{66}\end{bmatrix}^k \left( \begin{Bmatrix}\varepsilon_{xx}\\ \varepsilon_{yy}\\ \gamma_{xy}\end{Bmatrix}^k - \begin{Bmatrix}\bar{\alpha}_1\\ \bar{\alpha}_2\\ \bar{\alpha}_6\end{Bmatrix}^k \Delta T(x,y,z) \right) - \begin{bmatrix}\bar{e}_{31}\\ \bar{e}_{32}\\ \bar{e}_{36}\end{bmatrix}^k E_3^k(x,y,z) \tag{3a}$$

$\overline{Q}_{ij}^k$, $\bar{e}_{ij}^k$, $\bar{\alpha}_1$, and $\bar{\alpha}_2$ are the transformed reduced stiffness matrix, the piezoelectric moduli, and the coefficients of material expansion in the $k$th orthotropic layer, respectively. $\sigma_{ij}^k$, $\varepsilon_{ij}^k$, and $E_{ij}^k$ are the in-plane stress, strain, and electrical field components of the $k$th orthotropic layer, respectively. $\Delta T$ is temperature gradient function which is the difference between reference (room) temperature $T_1 = 20$ [°C] and final temperature $T_2$. The elements of transformed reduced stiffness matrix are described in Eq. (3b), respectively [14,30].

$$\begin{aligned}
\bar{Q}_{11} &= Q_{11}c^4 + 2(Q_{12} + 2Q_{66})c^2s^2 + Q_{22}s\\
\bar{Q}_{12} &= (Q_{11} + Q_{22} - 4Q_{66})c^2s^2 + Q_{12}(c^4 + s^4)\\
\bar{Q}_{22} &= Q_{11}s^4 + 2(Q_{12} + 2Q_{66})c^2s^2 + Q_{22}c^4\\
\bar{Q}_{16} &= -Q_{22}cs^3 + Q_{11}c^3s - (Q_{12} + 2Q_{66})(c^2 - s^2)cs\\
\bar{Q}_{26} &= -Q_{22}c^3s + Q_{11}cs^3 - (Q_{12} + 2Q_{66})(c^2 - s^2)cs\\
\bar{Q}_{66} &= (Q_{11} + Q_{22} - 2Q_{12})c^2s^2 + Q_{66}(c^2 - s^2)^2\\
Q_{11} &= \tfrac{E_1}{1-v_{12}v_{21}},\ Q_{22} = \tfrac{E_2}{1-v_{12}v_{21}},\ Q_{12} = \tfrac{v_{12}E_2}{1-v_{12}v_{21}},\ Q_{66} = G_{12}
\end{aligned} \tag{3b}$$

$c$ is $\cos(\beta)$ and $s$ is $\sin(\beta)$. $\beta$ is the winding angle made between fibres and $x$ axis. $E_1$, $E_2$, $v_{12}$, and $G_{12}$ are in-plane local elasticity modules of an orthotropic layer in the material coordinate system. The transformed thermal coefficients and piezoelectric moduli of expansion are described in Eq. (4), respectively [30].

$$\begin{aligned}
&\bar{\alpha}_1 = \alpha_1c^2 + \alpha_2s^2\ \bar{\alpha}_2 = \alpha_1s^2 + \alpha_2c^2\ \bar{\alpha}_6 = 2(\alpha_1 - \alpha_2)sc\\
&\bar{e}_{31} = \overline{Q}_{11}\overline{d}_{31} + \overline{Q}_{12}\overline{d}_{32} = \overline{Q}_{11}(d_{31}c^2 + d_{32}s^2) + \overline{Q}_{12}(d_{31}s^2 + d_{32}c^2)\\
&\bar{e}_{32} = \overline{Q}_{12}\overline{d}_{31} + \overline{Q}_{22}\overline{d}_{32} = \overline{Q}_{12}(d_{31}c^2 + d_{32}s^2) + \overline{Q}_{22}(d_{31}s^2 + d_{32}c^2)\\
&\bar{e}_{36} = \overline{Q}_{66}\overline{d}_{36} = 2\overline{Q}_{66}(d_{31} - d_{32})sc
\end{aligned} \tag{4}$$

$d_{ij}^k$, $\alpha_1$, and $\alpha_2$ are the piezoelectric dielectric constants and coefficients of material expansion in the $k$th orthotropic layer, respectively. The relationship between stress resultants and flexural moments for the mid-plane in a composite laminate is described as stated in Eq. (5) [4]. First, Eq. (2) is substituted into Eq. (3a). Subsequently, Eq. (6) is derived by substituting Eq. (3a) into Eq. (5).

$$[M_{xx}\quad M_{yy}\quad M_{xy}]^T = \int_{-H/2}^{H/2} z(\sigma_{xx}, \sigma_{yy}, \tau_{xy})dz - \left[M_{xx}^T + M_{xx}^P \quad M_{yy}^T + M_{yy}^P \quad M_{xy}^T + M_{xy}^P\right]^T \tag{5}$$

$$\begin{bmatrix}M_{xx}\\ M_{yy}\\ M_{xy}\end{bmatrix} = \begin{bmatrix}B_{11} & B_{12} & B_{16}\\ B_{12} & B_{22} & B_{26}\\ B_{16} & B_{26} & B_{66}\end{bmatrix}\begin{bmatrix}\frac{\partial u_0}{\partial x}\\ \frac{\partial v_0}{\partial y}\\ \frac{\partial u_0}{\partial y} + \frac{\partial v_0}{\partial x}\end{bmatrix} + \begin{bmatrix}D_{11} & D_{12} & D_{16}\\ D_{12} & D_{22} & D_{26}\\ D_{16} & D_{26} & D_{66}\end{bmatrix} \times \begin{bmatrix}-\frac{\partial^2 w_0}{\partial x^2}\\ -\frac{\partial^2 w_0}{\partial y^2}\\ -2\frac{\partial^2 w_0}{\partial x \partial y}\end{bmatrix} - \begin{bmatrix}M_{xx}\\ M_{yy}\\ M_{xy}\end{bmatrix}^T - \begin{bmatrix}M_{xx}\\ M_{yy}\\ M_{xy}\end{bmatrix}^P \tag{6}$$

$[M_{xx}]^T$,$[M_{yy}]^T$,$[M_{xy}]^T$,$[M_{xx}]^P$,$[M_{yy}]^P$, and $[M_{xy}]^P$ are bending and twisting moments induced by thermal and electrical loads, respectively. It is assumed that the temperature and electric positional fields vary linearly through laminate thickness. Therefore, the linear interpolation functions can be used to simplify the temperature and electrical gradients, as shown in Eqs. (7a–b), respectively.

$$\Delta T(x,y,z) = T_1^k(x,y,z)\omega_1^k(z) + T_2^k(x,y,z)\omega_2^k(z) \tag{7a}$$

$$E_z(x,y,z) = E_1^k(x,y,z)\omega_1^k(z) + E_2^k(x,y,z)\omega_2^k(z) \tag{7b}$$

$\omega_i^k$, $i = \{1,2\}$ shown in Eq. (8) represents the linear interpolation function of the $k$th orthotropic layer in a smart piezo composite hybrid laminate.

$$\omega_1^k = \frac{h_{k+1} - h}{t_k} = \frac{h_{k+1} - h}{P_n t_a + N t_p},\quad \omega_2^k = \frac{h - h_k}{t_k} = \frac{h - h_k}{P_n t_a + N t_p},\quad h_k \leqslant h \leqslant h_{k+1} \tag{8}$$

$P_n$, $t_a$, and $t_p$ in Eq. (8) are the number of piezoelectric actuators, and actuator thickness, and host structure (composite hybrid laminate) thickness, respectively. Governing partial differential equation relating the transverse bending and twisting moments to mid-plane displacements and thermo-electro-mechanical loads in a smart laminated piezo composite hybrid plate is stated in Eq. (9) [2]. In this study, thin symmetrical cross-ply laminates are considered. Thus, the effects of bending–stretching coupling matrix ($[B_{ij}] = 0$), bending–twisting elements of flexural stiffness matrix ($D_{16} = D_{26} = 0$), and thermo-electrical twisting moment resultants ($[M_{xy}]^T = [M_{xy}]^P = 0$) in Eq. (6) are neglected. The linear interpolation of thermo-electrical functions in Eqs. (7a–b) are also substituted into thermo-electrical bending moment resultants ($[M_{xx}]^T$, $[M_{yy}]^T$, $[M_{xx}]^P$, $[M_{yy}]^P$) in Eq. (6). Thus, by applying the initial conditions to Eq. (6), it can be simplified to Eq. (10). Finally, Eq. (11) is derived by substituting Eq. (10) into Eq. (9).

$$\frac{\partial^2\left(M_{xx} - M_{xx}^T - M_{xx}^P\right)}{\partial x^2} + 2\frac{\partial^2\left(M_{xy} - M_{xy}^T - M_{xy}^P\right)}{\partial x \partial y} + \frac{\partial^2\left(M_{yy} - M_{yy}^T - M_{yy}^P\right)}{\partial y^2} = P_m(x,y) \tag{9}$$

$$\begin{bmatrix}M_{xx}\\ M_{yy}\\ M_{xy}\end{bmatrix} = \begin{bmatrix}D_{11} & D_{12} & 0\\ D_{12} & D_{22} & 0\\ 0 & 0 & D_{66}\end{bmatrix}\begin{bmatrix}-\frac{\partial^2 w_0}{\partial x^2}\\ -\frac{\partial^2 w_0}{\partial y^2}\\ -2\frac{\partial^2 w_0}{\partial x \partial y}\end{bmatrix} - \begin{bmatrix}M_{xx}^T\\ M_{yy}^T\\ 0\end{bmatrix} - \begin{bmatrix}M_{xx}^P\\ M_{yy}^P\\ 0\end{bmatrix} \tag{10}$$

$$D_{11}\frac{\partial^4 w_0}{\partial x^4} + 2(D_{12} + 2D_{66})\frac{\partial^4 w_0}{\partial x^2 \partial y^2} + D_{22}\frac{\partial^4 w_0}{\partial y^4} = P_m(x,y) + \frac{\partial^2 M_{xx}^T}{\partial x^2} + \frac{\partial^2 M_{xx}^P}{\partial x^2} + \frac{\partial^2 M_{yy}^T}{\partial y^2} + \frac{\partial^2 M_{yy}^P}{\partial y^2} \tag{11}$$

where,

$$P_t(x,y) = \frac{\partial^2 M_{xx}^T}{\partial x^2} + \frac{\partial^2 M_{yy}^T}{\partial y^2}$$

$$P_e(x,y) = \frac{\partial^2 M_{xx}^P}{\partial x^2} + \frac{\partial^2 M_{yy}^P}{\partial y^2}$$

$$\left[M_i^T\right] = \sum_{k=1}^{N}\int_{h_k}^{h_{k+1}} \left[\bar{Q}_{ij}\right]^k \{\bar{\alpha}_j\}^k \Delta T z\, dz = \frac{1}{6}\sum_{k=1}^{N}\sum_{j=1,2,6} [\bar{Q}_{ij}]^k [\bar{\alpha}_j]^k \{T_1^k(h_k + 3z_k) + T_2^k(2h_k + 3z_k)\}h_k$$

$$\left[M_i^P\right] = \sum_{k=1}^{N}\int_{h_k}^{h_{k+1}} [\bar{Q}_{ij}]^k [\bar{d}_{3j}]^k E_z^k z\,dz = \frac{1}{6}\sum_{k=1}^{N}\sum_{j=1,2,6} [\bar{Q}_{ij}]^k [\bar{d}_{3j}]^k \left\{E_1^k(h_k+3z_k) + E_2^k(2h_k+3z_k)\right\} h_k$$

$$D_{ij} = \frac{1}{3}\sum_{K=1}^{N}\sum_{j=1,2,6} [\overline{Q}_{ij}]_k (h_K^3 - h_{K-1}^3)$$

$i = j = \{1,2,6\}$, $D_{11}$ and $D_{22}$ are flexural stiffness about $x$ and $y$ axis, respectively, $D_{12}$ and $D_{66}$ stand for effective torsional rigidity. $P_m(x,y)$, $P_t(x,y)$, and $P_e(x,y)$ are mechanical, thermal, and electrical loads applied to the smart piezo composite hybrid laminate, respectively. The schematic of coordinate system and geometry of the smart laminated cantilever piezo composite hybrid plate with incorporated piezoelectric actuators, actuators size, placement, and polarization, layers winding angle, and applied thermo-electro-mechanical load functions is illustrated in Fig. 1. Activated piezoelectric actuators are capable of inducing bending moments which can be expressed in terms of 2D unit step functions [2]. In this study, mechanical load function, thermal and electrical moments are expressed in the form of multivariable unit step functions according to Eqs. (12a–c), respectively.

$$[M_i]^T = \frac{1}{6}\sum_{L=1}^{Tn}\sum_{k=1}^{N}\sum_{j=1,2,6} [\bar{Q}_{ij}]^k [\bar{\alpha}_j]^k \left\{T_1^k(h_k+3z_k) + T_2^k(2h_k+3z_k)\right\} \times h_k[U_k^L(x-x_{1T}) - U_k^L(x-x_{2T})]\left[U_k^L(y-y_{1T}) - U_k^L(y-y_{2T})\right] \quad (12a)$$

$$[M_i]^P = \frac{1}{6}\sum_{L=1}^{Pn}\sum_{k=1}^{N}\sum_{j=1,2,6} [\bar{Q}_{ij}]^k [\bar{d}_{3j}]^k \{E_1^k(h_k+3z_k) + E_2^k(2h_k+3z_k)\} \times h_k\left[U_k^L(x-x_{1P}) - U_k^L(x-x_{2P})\right]\left[U_k^L(y-y_{1P}) - U_k^L(y-y_{2P})\right] \quad (12b)$$

$$P_m = \sum_{L=1}^{Mn} P_m(x,y)\left[U_k^L(x-x_{1M}) - U_k^L(x-x_{2M})\right]\left[U_k^L(y-y_{1M}) - U_k^L(y-y_{2M})\right] \quad (12c)$$

$i = j = \{1,2,6\}$ and $U_k^L(x,y)$ presents the unit step function expressed for effective areas at which the thermo-electro-mechanical bending moments are applied at the $L$th location and in the $k$th ply. $M_n$, $P_n$, and $T_n$ are the number of effective areas at which the mechanical, electrical, and thermal loads are applied, respectively (see Fig. 1). The general load resultants applied to a plate element are expressed in Eqs. (13a–g).

$$M_{xx} = -\left[D_{11}\frac{\partial^2 w_0}{\partial x^2} + D_{12}\frac{\partial^2 w_0}{\partial y^2}\right] \quad (13a)$$

$$M_{yy} = -\left[D_{22}\frac{\partial^2 w_0}{\partial y^2} + D_{12}\frac{\partial^2 w_0}{\partial x^2}\right] \quad (13b)$$

$$M_{xy} = -2D_{66}\frac{\partial^2 w_0}{\partial x \partial y} \quad (13c)$$

$$Q_{xx} = -\frac{\partial}{\partial x}\left[D_{11}\frac{\partial^2 w_0}{\partial x^2} + 2(D_{12}+D_{66})\frac{\partial^2 w_0}{\partial y^2}\right] \quad (13d)$$

$$Q_{yy} = -\frac{\partial}{\partial y}\left[D_{22}\frac{\partial^2 w_0}{\partial y^2} + 2(D_{12}+D_{66})\frac{\partial^2 w_0}{\partial x^2}\right] \quad (13e)$$

$$V_{xx} = -\frac{\partial}{\partial x}\left[D_{11}\frac{\partial^2 w_0}{\partial x^2} + 2(D_{12}+D_{66})\frac{\partial^2 w_0}{\partial y^2}\right] - 2D_{66}\frac{\partial}{\partial y}\left[\frac{\partial^2 w_0}{\partial x \partial y}\right] \quad (13f)$$

$$V_{yy} = -\frac{\partial}{\partial y}\left[D_{22}\frac{\partial^2 w_0}{\partial y^2} + 2(D_{12}+D_{66})\frac{\partial^2 w_0}{\partial x^2}\right] - 2D_{66}\frac{\partial}{\partial x}\left[\frac{\partial^2 w_0}{\partial x \partial y}\right] \quad (13g)$$

$M_{xx}$, $M_{yy}$, $M_{xy}$, $Q_{xx}$, $Q_{yy}$, $V_{xx}$, and $V_{yy}$ are bending moment resultants, torsional moment resultants, shear force resultants, and the total shear force resultants per unit length, respectively [4]. The boundary conditions should be prescribed to a cantilever plate as stated in Eqs. (14a–j).

$$w_0(0,y) = 0 \quad (14a)$$

$$\frac{\partial w_0}{\partial x}(0,y) \quad (14b)$$

$$M_{xx}(a,y) = 0 \quad (14c)$$

$$M_{yy}(x,0) = 0 \quad (14d)$$

$$M_{yy}(x,b) = 0 \quad (14e)$$

$$V_{xx}(a,y) = 0 \quad (14f)$$

$$V_{yy}(x,0) = 0 \quad (14g)$$

$$V_{yy}(x,b) = 0 \quad (14h)$$

$$M_{xy}(a,0) = 0 \quad (14i)$$

$$M_{xy}(a,b) = 0 \quad (14j)$$

The double finite integral transformation of the mid-plane vertical displacement of function $w_o(x,y)$ is shown in Eq. (15).

$$w_{mn} = \int_0^a\int_0^a w_0(x,y)\sin\left(\frac{\alpha_m}{2}x\right)\cos(\beta_n y)dxdy \quad (m = 1,3,5,\ldots)\ (n = 0,1,2,\ldots) \quad (15)$$

Eq. (15) is then inversed to represent the exact mid-plane vertical displacement of function $w_o(x,y)$ as stated in Eq. (16).

$$w_0(x,y) = \frac{4}{ab}\sum_{m=1,3,5,\ldots}^{\infty}\sum_{n=0,1,2,\ldots}^{\infty} w_{mn}\lambda_n \sin\left(\frac{\alpha_m}{2}x\right)\cos(\beta_n y) \quad (16)$$

where,

$$\alpha_m = \frac{m\pi}{a}, \quad \beta_n = \frac{n\pi}{b} \text{ and } \lambda_n = \begin{cases} 0.5 \rightarrow (n=0) \\ 1 \rightarrow (n = 1,2,3,\ldots) \end{cases}$$

The double integral transformation of higher-order partial derivatives of the multivariable function $w_o(x,y)$ taken over Eq. (11) results in Eqs. (17a–g):

$$\int_0^a\int_0^b\left[D_{11}\frac{\partial^4 w_0}{\partial x^4} + 2(D_{12}+2D_{66})\frac{\partial^4 w_0}{\partial x^2\partial y^2} + D_{22}\frac{\partial^4 w_0}{\partial y^4}\right]\sin\left(\frac{\alpha_m}{2}x\right) \times \cos(\beta_n y)dxdy = \int_0^a\int_0^b\left[P_m(x,y) + \frac{\partial^2 M_{xx}^T}{\partial x^2} + \frac{\partial^2 M_{yy}^T}{\partial y^2} + \frac{\partial^2 M_{xx}^P}{\partial x^2} + \frac{\partial^2 M_{yy}^P}{\partial y^2}\right]\sin\left(\frac{\alpha_m}{2}x\right)\cos(\beta_n y)dxdy \quad (17a)$$

$$I_1 = \int_0^a \int_0^b \frac{\partial^4 w_0}{\partial x^4} \sin\left(\frac{\alpha_m}{2}x\right) \cos(\beta_n y) dxdy \tag{17b}$$

$$I_2 = \int_0^a \int_0^b \frac{\partial^4 w_0}{\partial y^4} \sin\left(\frac{\alpha_m}{2}x\right) \cos(\beta_n y) dxdy \tag{17c}$$

$$I_3 = \int_0^a \int_0^b \frac{\partial^4 w_0}{\partial x^2 \partial y^2} \sin\left(\frac{\alpha_m}{2}x\right) \cos(\beta_n y) dxdy \tag{17d}$$

$$I_4 = \int_0^a \int_0^b P_m(x,y) \sin\left(\frac{\alpha_m}{2}x\right) \cos(\beta_n y) dxdy \tag{17e}$$

$$I_5 = \int_0^a \int_0^b \left(\frac{\partial^2 M_{xx}^T}{\partial x^2} + \frac{\partial^2 M_{yy}^T}{\partial y^2}\right) \sin\left(\frac{\alpha_m}{2}x\right) \cos(\beta_n y) dxdy \tag{17f}$$

$$I_6 = \int_0^a \int_0^b \left(\frac{\partial^2 M_{xx}^P}{\partial x^2} + \frac{\partial^2 M_{yy}^P}{\partial y^2}\right) \sin\left(\frac{\alpha_m}{2}x\right) \cos(\beta_n y) dxdy \tag{17g}$$

Considering the integral by parts principle and applying the boundary conditions in Eqs. (14a,b,i,j) to $I_1$, $I_2$, and $I_3$, the double integral transformations of higher-order partial derivatives of the function $w_o(x,y)$ over Eqs. (17b–e) result in Eqs. (18a–d), respectively.

$$\begin{aligned} I_1 &= \int_0^a \int_0^b \frac{\partial^4 w_0}{\partial x^4} \sin\left(\frac{\alpha_m}{2}x\right) \cos(\beta_n y) dxdy \\ &= \int_0^b \left[ (-1)^{\frac{m-1}{2}} \left( \frac{\partial^3 w_0}{\partial x^3}\middle| x=a \right) + \frac{\alpha_m}{2} \left( \frac{\partial^2 w_0}{\partial x^2}\middle| x=0 \right) \right. \\ &\quad - (-1)^{\frac{m-1}{2}} \frac{\alpha_m^2}{4} \left( \frac{\partial w_0}{\partial x}\middle| x=a \right) - \left. \frac{\alpha_m^3}{8} (w_0 | x=0) \right] \cos(\beta_n y) dy \\ &\quad + \frac{\alpha_m^4}{16} w_{mn} = \int_0^b \left[ (-1)^{\frac{m-1}{2}} \left( \frac{\partial^3 w_0}{\partial x^3}\middle| x=a \right) + \frac{\alpha_m}{2} \left( \frac{\partial^2 w_0}{\partial x^2}\middle| x=0 \right) \right. \\ &\quad - \left. (-1)^{\frac{m-1}{2}} \frac{\alpha_m^2}{4} \left( \frac{\partial w_0}{\partial x}\middle| x=a \right) \right] \cos(\beta_n y) dy + \frac{\alpha_m^4}{16} w_{mn} \end{aligned} \tag{18a}$$

$$\begin{aligned} I_2 &= \int_0^a \int_0^b \frac{\partial^4 w_0}{\partial y^4} \sin\left(\frac{\alpha_m}{2}x\right) \cos(\beta_n y) dxdy \\ &= \int_0^a \left[ (-1)^n \left( \frac{\partial^3 w_0}{\partial y^3}\middle| y=b \right) - \left( \frac{\partial^3 w_0}{\partial y^3}\middle| y=0 \right) \right. \\ &\quad \left. - (-1)^n \beta_n^2 \left( \frac{\partial w_0}{\partial y}\middle| y=b \right) + \beta_n^2 \left( \frac{\partial w_0}{\partial y}\middle| y=0 \right) \right] \sin\left(\frac{\alpha_m}{2}x\right) dx + \beta_n^4 w_{mn} \end{aligned} \tag{18b}$$

$$\begin{aligned} I_3 &= \int_0^a \int_0^b \frac{\partial^4 w_0}{\partial x^2 \partial y^2} \sin\left(\frac{\alpha_m}{2}x\right) \cos(\beta_n y) dxdy \\ &= (-1)^n (-1)^{\frac{m-1}{2}} \left( \frac{\partial^2 w_0}{\partial x \partial y}\middle| \begin{matrix} x=a \\ y=b \end{matrix} \right) - (-1)^{\frac{m-1}{2}} \left( \frac{\partial^2 w_0}{\partial x \partial y}\middle| \begin{matrix} x=a \\ y=0 \end{matrix} \right) \\ &\quad + (-1)^n \frac{\alpha_m}{2} \left( \frac{\partial w_0}{\partial y}\middle| \begin{matrix} x=0 \\ y=b \end{matrix} \right) - \frac{\alpha_m}{2} \left( \frac{\partial w_0}{\partial y}\middle| \begin{matrix} x=0 \\ y=0 \end{matrix} \right) + \frac{\alpha_m^2 \beta_n^2}{4} w_{mn} \\ &\quad - \frac{\alpha_m^2}{4} \int_0^a \left[ (-1)^n \left( \frac{\partial w_0}{\partial y}\middle| y=b \right) - \left( \frac{\partial w_0}{\partial y}\middle| y=0 \right) \right] \sin\left(\frac{\alpha_m}{2}x\right) dx \\ &\quad - \beta_n^2 \int_0^b \left[ (-1)^{\frac{m-1}{2}} \left( \frac{\partial w_0}{\partial x}\middle| x=a \right) + \frac{\alpha_m}{2} (w_0 | x=0) \right] \cos(\beta_n y) dy \\ &= -\frac{\alpha_m^2}{4} \int_0^a \left[ (-1)^n \left( \frac{\partial w_0}{\partial y}\middle| y=b \right) - \left( \frac{\partial w_0}{\partial y}\middle| y=0 \right) \right] \sin\left(\frac{\alpha_m}{2}x\right) dx \\ &\quad - (-1)^{\frac{m-1}{2}} \beta_n^2 \int_0^b \left[ \left( \frac{\partial w_0}{\partial x}\middle| x=a \right) \right] \cos(\beta_n y) dy + \frac{\alpha_m^2 \beta_n^2}{4} w_{mn} \end{aligned} \tag{18c}$$

Let $P_m(x,y) = P_0$ be defined as uniform distributed pressure or patch loading magnitude, hence:

$$\begin{aligned} I_4 &= \int_0^a \int_0^b \sum_{L=1}^{Mn} P_0 \left[ U_k^L(x - x_{1M}) - U_k^L(x - x_{2M}) \right] \\ &\quad \times \left[ U_k^L(y - y_{1T}) - U_k^L(y - y_{2M}) \right] \sin\left(\frac{\alpha_m}{2}x\right) \cos(\beta_n y) dxdy \end{aligned}$$

$$I_4 = \begin{cases} n = 0, \quad m = 1,3,5,\ldots \\ \rightarrow \sum_{L=1}^{Mn} \left( \frac{-2P_0}{\alpha_m} \right) (y_{1M} - y_{2M})_L \left( \cos\left(\frac{\alpha_m}{2}x_{1M}\right) - \cos\left(\frac{\alpha_m}{2}x_{2M}\right) \right)_L \\ n = 1,2,3,\ldots, \quad m = 1,3,5,\ldots \\ \rightarrow \sum_{L=1}^{Mn} \left( \frac{-2P_0}{\alpha_m \beta_n} \right) \left( \cos\left(\frac{\alpha_m}{2}x_{1M}\right) - \cos\left(\frac{\alpha_m}{2}x_{2M}\right) \right)_L (\sin(\beta_n y_{1M}) - \sin(\beta_n y_{2M}))_L \end{cases} \tag{18d}$$

The second derivatives of partial differential 2D unit step function equations of thermo-electrical bending moments (Eqs. (17f,g)) acting on a smart laminated cantilever piezo composite hybrid plate with respect to $x$ and $y$ are expanded as shown in Eqs. (19a–d), respectively.

$$I_5 = I_5^A + I_5^B \rightarrow I_5 = \begin{cases} I_5^A = \int_0^a \int_0^b \left( \frac{\partial^2 M_{xx}^T}{\partial x^2} \right) \sin\left(\frac{\alpha_m}{2}x\right) \cos(\beta_n y) dxdy \\ I_5^B = \int_0^a \int_0^b \left( \frac{\partial^2 M_{yy}^T}{\partial y^2} \right) \sin\left(\frac{\alpha_m}{2}x\right) \cos(\beta_n y) dxdy \end{cases}$$

$$\begin{aligned} \frac{\partial^2 M_{xx}^T}{\partial x^2} &= \frac{1}{6} \sum_{L=1}^{Tn} \sum_{k=1}^{N} \sum_{j=1,2,6} [\bar{Q}_{1j}]^k [\bar{\alpha}_j]^k \{T_1^k(h_k + 3z_k) + T_2^k(2h_k + 3z_k)\} h_k \frac{\partial^2}{\partial x^2} \\ &\quad \times \left( [U_k^L(x - x_{1T}) - U_k^L(x - x_{2T})][U_k^L(y - y_{1T}) - U_k^L(y - y_{2T})] \right) \\ &= \frac{1}{6} \sum_{L=1}^{Tn} \sum_{k=1}^{N} \sum_{j=1,2,6} [\bar{Q}_{1j}]^k [\bar{\alpha}_j]^k \{T_1^k(h_k + 3z_k) + T_2^k(2h_k + 3z_k)\} h_k \\ &\quad \times \left[ U_k^L(y - y_{1T}) - U_k^L(y - y_{2T}) \right] [\delta_k'^L(x - x_{1T}) - \delta_k'^L(x - x_{2T})] \end{aligned} \tag{19a}$$

$$\begin{aligned} \frac{\partial^2 M_{yy}^T}{\partial x^2} &= \frac{1}{6} \sum_{L=1}^{Tn} \sum_{k=1}^{N} \sum_{j=1,2,6} [\bar{Q}_{2j}]^k [\bar{\alpha}_j]^k \{T_1^k(h_k + 3z_k) + T_2^k(2h_k + 3z_k)\} h_k \frac{\partial^2}{\partial y^2} \\ &\quad \times \left( [U_k^L(x - x_{1T}) - U_k^L(x - x_{2T})][U_k^L(y - y_{1T}) - U_k^L(y - y_{2T})] \right) \\ &= \frac{1}{6} \sum_{L=1}^{Tn} \sum_{k=1}^{N} \sum_{j=1,2,6} [\bar{Q}_{2j}]^k [\bar{\alpha}_j]^k \{T_1^k(h_k + 3z_k) + T_2^k(2h_k + 3z_k)\} h_k \\ &\quad \times \left[ U_k^L(x - x_{1T}) - U_k^L(x - x_{2T}) \right] [\delta_k'^L(y - y_{1T}) - \delta_k'^L(y - y_{2T})] \end{aligned} \tag{19b}$$

$$\begin{aligned} I_5^A &= \frac{1}{6} \int_0^a \int_0^b \sum_{L=1}^{Tn} \sum_{k=1}^{N} \sum_{j=1,2,6} [\bar{Q}_{1j}]^k [\bar{\alpha}_j]^k \{T_1^k(h_k + 3z_k) + T_2^k(2h_k + 3z_k)\} \\ &\quad \times h_k [U_k^L(y - y_{1T}) - U_k^L(y - y_{2T})][\delta_k'^L(x - x_{1T}) - \delta_k'^L(x - x_{2T})] \\ &\quad \times \sin\left(\frac{\alpha_m}{2}x\right) \cos(\beta_n y) dxdy = \frac{1}{6} \sum_{L=1}^{Tn} \sum_{k=1}^{N} \sum_{j=1,2,6} \frac{\alpha_m}{2\beta_n} [\bar{Q}_{1j}]^k [\bar{\alpha}_j]^k \\ &\quad \times \left\{ T_1^k(h_k + 3z_k) + T_2^k(2h_k + 3z_k) \right\} \left( \cos\left(\frac{\alpha_m}{2}x_{1T}\right) - \cos\left(\frac{\alpha_m}{2}x_{2T}\right) \right)_L \\ &\quad \times (\sin(\beta_n y_{1T}) - \sin(\beta_n y_{2T}))_L \end{aligned} \tag{19c}$$

$$I_5^B=\frac{1}{6}\int_0^a\int_0^b\sum_{L=1}^{Tn}\sum_{k=1}^{N}\sum_{j=1,2,6}[\bar{Q}_{2j}]^k[\bar{\alpha}_j]^k\{T_1^k(h_k+3z_k)+T_2^k(2h_k+3z_k)\}h_k$$
$$\times\left[U_k^L(x-x_{1T})-U_k^L(x-x_{2T})\right]\left[\delta_k'^L(y-y_{1T})-\delta_k'^L(y-y_{2T})\right]$$
$$\times\sin\left(\frac{\alpha_m}{2}x\right)\cos(\beta_n y)dxdy=\frac{1}{6}\sum_{L=1}^{Tn}\sum_{k=1}^{N}\sum_{j=1,2,6}\frac{2\beta_n}{\alpha_m}[\bar{Q}_{2j}]^k[\bar{\alpha}_j]^k$$
$$\times\left\{T_1^k(h_k+3z_k)+T_2^k(2h_k+3z_k)\right\}\left(\cos\left(\frac{\alpha_m}{2}x_{1T}\right)-\cos\left(\frac{\alpha_m}{2}x_{2T}\right)\right)_L$$
$$\times(\sin(\beta_n y_{1T})-\sin(\beta_n y_{2T}))_L \quad (19d)$$

Hence, the effect of thermal bending moments acting on a smart laminated cantilever piezo composite hybrid can be stated in Eq. (20).

$$I_5=\begin{cases} n=0,\quad m=1,3,5,\ldots\rightarrow \\ \sum_{L=1}^{Tn}\left[\frac{\alpha_m[M_x^T]^\Theta}{2}\right](\cos(\frac{\alpha_m}{2}x_{1T})-\cos(\frac{\alpha_m}{2}x_{2T}))_L(y_{1T}-y_{2T})_L \\ n=1,2,3,\ldots,\quad m=1,3,5,\ldots\rightarrow \\ \sum_{L=1}^{Tn}\left[\frac{[M_x^T]^\Theta\alpha_m^2+4[M_y^T]^\Theta\beta_n^2}{2\alpha_m\beta_n}\right](\cos(\frac{\alpha_m}{2}x_{1T}) \\ -\cos(\frac{\alpha_m}{2}x_{2T}))_L(\sin(\beta_n y_{1T})-\sin(\beta_n y_{2T}))_L \end{cases} \quad (20)$$

where,

$$[M_x^T]^\Theta=\frac{1}{6}\sum_{k=1}^{N}\sum_{j=1,2,6}[\bar{Q}_{1j}]^k[\bar{\alpha}_j]^k\{T_1^k(h_k+3z_k)+T_2^k(2h_k+3z_k)\}h_k$$

$$[M_y^T]^\Theta=\frac{1}{6}\sum_{k=1}^{N}\sum_{j=1,2,6}[\bar{Q}_{2j}]^k[\bar{\alpha}_j]^k\{T_1^k(h_k+3z_k)+T_2^k(2h_k+3z_k)\}h_k$$

Same procedures for $I_5$ are performed over equation $I_6$ to obtain the electrical induced bending moments in the smart cantilever piezo composite hybrid plate as shown in Eq. (21). It is assumed that the electrical intensity field ($E_z$) varies linearly through actuator thickness.

$$I_6=I_6^A+I_6^B\rightarrow I_6=\begin{cases} I_6^A=\int_0^a\int_0^b\left(\frac{\partial^2M_{xx}^P}{\partial x^2}\right)\sin(\frac{\alpha_m}{2}x)\cos(\beta_n y)dxdy \\ I_6^B=\int_0^a\int_0^b\left(\frac{\partial^2M_{yy}^P}{\partial y^2}\right)\sin(\frac{\alpha_m}{2}x)\cos(\beta_n y)dxdy \end{cases}$$

$$I_6=\begin{cases} n=0,\quad m=1,3,5,\ldots\rightarrow \\ \sum_{L=1}^{Pn}\left[\frac{\alpha_m[M_x^P]^\Theta}{2}\right](\cos(\frac{\alpha_m}{2}x_{1P})-\cos(\frac{\alpha_m}{2}x_{2P}))_L(y_{1P}-y_{2P})_L \\ n=1,2,3,\ldots,\quad m=1,3,5,\ldots\rightarrow \\ \sum_{L=1}^{Pn}\left[\frac{[M_x^P]^\Theta\alpha_m^2+4[M_y^P]^\Theta\beta_n^2}{2\alpha_m\beta_n}\right](\cos(\frac{\alpha_m}{2}x_{1P}) \\ -\cos(\frac{\alpha_m}{2}x_{2P}))_L(\sin(\beta_n y_{1P})-\sin(\beta_n y_{2P}))_L \end{cases} \quad (21)$$

where,

$$E_z^k=\frac{V_a^k}{t_a^k}$$

$$[M_x^P]^\Theta=\frac{1}{6}\sum_{k=1}^{N}\sum_{j=1,2,6}[\bar{Q}_{1j}]^k[\bar{d}_{3j}]^k\left\{\left(\frac{V_a}{t_a}\right)^k(3h_k+6z_k)\right\}h_k$$

$$[M_y^P]^\Theta=\frac{1}{6}\sum_{k=1}^{N}\sum_{j=1,2,6}[\bar{Q}_{2j}]^k[\bar{d}_{3j}]^k\left\{\left(\frac{V_a}{t_a}\right)^k(3h_k+6z_k)\right\}h_k$$

The values $x_{1M}$, $x_{2M}$, $x_{1T}$, $x_{2T}$, $x_{1P}$, $x_{2P}$, $y_{1M}$, $y_{2M}$, $y_{1T}$, $y_{2T}$, $y_{1P}$, and $y_{2P}$ are the placements of effective mechanical, thermal, and electrical loads along $x$ and $y$ axis, respectively. $V_a^k$ stands for the applied electrical voltage through the $k$th layer's thickness and $t_a^k$ presents the thickness of the piezoelectric actuators in the $k$th layer. $E_x = E_y = 0$ is based on the fact that for the shell/plate type piezoelectric materials, only the transverse electric field component $E_z$ is dominant when the electrical voltage $V_a$ is only applied to the actuators through thickness [31,32].

In the next step, parameters $I_1, I_2, \ldots, I_6$ are substituted into Eq. (17a), resulting in Eq. (22). Simplifying and rearranging both sides of Eqs. (22) leads to Eq. (23).

$$D_{11}\int_0^b\left[(-1)^{\frac{m-1}{2}}\left(\frac{\partial^3w_0}{\partial x^3}\middle|x=a\right)+\frac{\alpha_m}{2}\left(\frac{\partial^2w_0}{\partial x^2}\middle|x=0\right)\right.$$
$$\left.-(-1)^{\frac{m-1}{2}}\frac{\alpha_m^2}{4}\left(\frac{\partial w_0}{\partial x}\middle|x=a\right)\right]\cos(\beta_n y)dy$$
$$+D_{11}\frac{\alpha_m^4}{16}w_{mn}D_{22}\int_0^a\left[(-1)^n\left(\frac{\partial^3w_0}{\partial y^3}\middle|y=b\right)-\left(\frac{\partial^3w_0}{\partial y^3}\middle|y=0\right)\right.$$
$$\left.-(-1)^n\beta_n^2\left(\frac{\partial w_0}{\partial y}\middle|y=b\right)+\beta_n^2\left(\frac{\partial w_0}{\partial y}\middle|y=0\right)\right]\sin\left(\frac{\alpha_m}{2}x\right)dx$$
$$+D_{22}\beta_n^4w_{mn}+(D_{12}+2D_{66})\frac{\alpha_m^2\beta_n^2}{2}w_{mn}$$
$$-(D_{12}+2D_{66})\frac{\alpha_m^2}{2}\int_0^a\left[(-1)^n\left(\frac{\partial w_0}{\partial y}\middle|y=b\right)-\left(\frac{\partial w_0}{\partial y}\middle|y=0\right)\right]$$
$$\times\sin\left(\frac{\alpha_m}{2}x\right)dx-2(D_{12}+2D_{66})(-1)^{\frac{m-1}{2}}\beta_n^2\int_0^b\left[\left(\frac{\partial w_0}{\partial x}\middle|x=a\right)\right]$$
$$\times\cos(\beta_n y)dy=\sum_{L=1}^{Mn}C_{mn}^1\left(\frac{-2P_0}{\alpha_m\beta_n}\right)\left(\cos\left(\frac{\alpha_m}{2}x_{1M}\right)-\cos\left(\frac{\alpha_m}{2}x_{2M}\right)\right)_L$$
$$\times(\sin(\beta_n y_{1M})-\sin(\beta_n y_{2M}))_L+\sum_{L=1}^{Pn}C_{mn}^2\left[\frac{[M_x^P]^\Theta\alpha_m^2+4[M_y^P]^\Theta\beta_n^2}{2\alpha_m\beta_n}\right]$$
$$\times\left(\cos\left(\frac{\alpha_m}{2}x_{1P}\right)-\cos\left(\frac{\alpha_m}{2}x_{2P}\right)\right)_L(\sin(\beta_n y_{1P})-\sin(\beta_n y_{2P}))_L$$
$$+\sum_{L=1}^{Tn}C_{mn}^3\left[\frac{[M_x^T]^\Theta\alpha_m^2+4[M_y^T]^\Theta\beta_n^2}{2\alpha_m\beta_n}\right]\left(\cos\left(\frac{\alpha_m}{2}x_{1T}\right)-\cos\left(\frac{\alpha_m}{2}x_{2T}\right)\right)_L$$
$$\times(\sin(\beta_n y_{1T})-\sin(\beta_n y_{2T}))_L \quad (22)$$

$$D_{11}(-1)^{\frac{m-1}{2}}\int_0^b\left(\frac{\partial^3w_0}{\partial x^3}\middle|x=a\right)\cos(\beta_n y)dy$$
$$+D_{22}(-1)^n\int_0^a\left(\frac{\partial^3w_0}{\partial y^3}\middle|y=b\right)\sin\left(\frac{\alpha_m}{2}x\right)dx$$
$$-(-1)^n\left(D_{22}\beta_n^2+\frac{(D_{12}+2D_{66})\alpha_m^2}{2}\right)\int_0^a\left(\frac{\partial w_0}{\partial y}\middle|y=b\right)\sin\left(\frac{\alpha_m}{2}x\right)dx$$
$$-D_{22}\int_0^a\left(\frac{\partial^3w_0}{\partial y^3}\middle|y=0\right)\sin\left(\frac{\alpha_m}{2}x\right)dx+\left(D_{22}\beta_n^2+\frac{(D_{12}+2D_{66})\alpha_m^2}{2}\right)$$
$$\times\int_0^a\left(\frac{\partial w_0}{\partial y}\middle|y=0\right)\sin\left(\frac{\alpha_m}{2}x\right)dx-(-1)^{\frac{m-1}{2}}$$
$$\times\left(\frac{D_{11}\alpha_m^2}{4}+2(D_{12}+2D_{66})\beta_n^2\right)\int_0^b\left(\frac{\partial w_0}{\partial x}\middle|x=a\right)\cos(\beta_n y)dy$$

$$+\left(\frac{D_{11}\alpha_m}{2}\right)\int_0^b\left(\frac{\partial^2 w_0}{\partial x^2}\middle|x=0\right)\cos(\beta_n y)dy$$
$$+\left(\frac{D_{11}\alpha_m^4}{16}+\frac{(D_{12}+2D_{66})\alpha_m^2\beta_n^2}{2}+D_{22}\beta_n^4\right)w_{mn}$$
$$=\sum_{L=1}^{Mn}C_{mn}^1\left(\frac{-2P_0}{\alpha_m\beta_n}\right)\left(\cos\left(\frac{\alpha_m}{2}x_{1M}\right)-\cos\left(\frac{\alpha_m}{2}x_{2M}\right)\right)_L(\sin(\beta_n y_{1M})$$
$$-\sin(\beta_n y_{2M}))_L+\sum_{L=1}^{Pn}C_{mn}^2\left[\frac{[M_x^{P_1}]^{\Theta}\alpha_m^2+4[M_y^{P_1}]^{\Theta}\beta_n^2}{2\alpha_m\beta_n}\right]\left(\cos\left(\frac{\alpha_m}{2}x_{1P}\right)\right.$$
$$\left.-\cos\left(\frac{\alpha_m}{2}x_{2P}\right)\right)_L(\sin(\beta_n y_{1P})-\sin(\beta_n y_{2P}))_L$$
$$+\sum_{L=1}^{Tn}C_{mn}^3\left[\frac{[M_x^{T_1}]^{\Theta}\alpha_m^2+4[M_y^{T_1}]^{\Theta}\beta_n^2}{2\alpha_m\beta_n}\right]\left(\cos\left(\frac{\alpha_m}{2}x_{1T}\right)-\cos\left(\frac{\alpha_m}{2}x_{2T}\right)\right)_L$$
$$\times(\sin(\beta_n y_{1T})-\sin(\beta_n y_{2T}))_L \tag{23}$$

where,

$$C_{mn}^1=\begin{cases}n=0,\quad m=1,3,5,\ldots\rightarrow 1\\ n=1,2,3,\ldots,\quad m=1,3,5,\ldots\rightarrow\beta_n\left[\dfrac{y_{1M}-y_{2M}}{\sin(\beta_n y_{1M})-\sin(\beta_n y_{2M})}\right]_L\end{cases}$$

$$C_{mn}^2=\begin{cases}n=0,\quad m=1,3,5,\ldots\rightarrow\dfrac{[M_x^{P}]^{\Theta}\alpha_m^2\beta_n}{[M_x^{P}]^{\Theta}\alpha_m^2+4[M_y^{P}]^{\Theta}\beta_n^2}\left[\dfrac{y_{1P}-y_{2P}}{\sin(\beta_n y_{1P})-\sin(\beta_n y_{2P})}\right]_L\\ n=1,2,3,\ldots,\quad m=1,3,5,\ldots\rightarrow 1\end{cases}$$

$$C_{mn}^2=\begin{cases}n=0,\quad m=1,3,5,\ldots\rightarrow\dfrac{[M_x^{T}]^{\Theta}\alpha_m^2\beta_n}{[M_x^{T}]^{\Theta}\alpha_m^2+4[M_y^{T}]^{\Theta}\beta_n^2}\left[\dfrac{y_{1T}-y_{2T}}{\sin(\beta_n y_{1T})-\sin(\beta_n y_{2T})}\right]_L\\ n=1,2,3,\ldots,\quad m=1,3,5,\ldots\rightarrow 1\end{cases}$$

$C_{mn}{}^1$, $C_{mn}{}^2$, and $C_{mn}{}^3$ are effective mechanical, electrical and thermal coefficients in a smart laminated cantilever piezo composite hybrid plate, respectively. The boundary conditions in Eqs. (14f–h) are expanded as shown in Eqs. (24a–c) and then substituted into Eq. (23). Rearranging Eq. (23) results in Eq. (25). For simplicity purposes, unknown variables$\Delta_m$, $\Omega_m$, $\Pi_n$, and $\Psi_n$ are defined as shown in Eqs. (26a–d), respectively.

$$D_{11}\int_0^b\left(\frac{\partial^3 w_0}{\partial x^3}\middle|x=a\right)\cos(\beta_n y)dy$$
$$=(3D_{12}+2D_{66})\beta_n^2\int_0^b\left(\frac{\partial w_0}{\partial x}\middle|x=a\right)\cos(\beta_n y)dy \tag{24a}$$

$$D_{22}\int_0^a\left(\frac{\partial^3 w_0}{\partial y^3}\middle|y=0\right)\sin\left(\frac{\alpha_m}{2}x\right)dx$$
$$=\frac{1}{4}(3D_{12}+2D_{66})\alpha_m^2\int_0^a\left(\frac{\partial w_0}{\partial y}\middle|y=0\right)\sin\left(\frac{\alpha_m}{2}x\right)dx \tag{24b}$$

$$D_{22}\int_0^a\left(\frac{\partial^3 w_0}{\partial y^3}\middle|y=b\right)\sin\left(\frac{\alpha_m}{2}x\right)dx$$
$$=\frac{1}{4}(3D_{12}+2D_{66})\alpha_m^2\int_0^a\left(\frac{\partial w_0}{\partial y}\middle|y=b\right)\sin\left(\frac{\alpha_m}{2}x\right)dx \tag{24c}$$

$$-(-1)^n\left[D_{22}\beta_n^2+D_{12}\frac{\alpha_m^2}{4}\right]\int_0^a\left(\frac{\partial w_0}{\partial y}\middle|y=b\right)\sin\left(\frac{\alpha_m}{2}x\right)dx$$
$$+\left[D_{22}\beta_n^2+D_{12}\frac{\alpha_m^2}{4}\right]\int_0^a\left(\frac{\partial w_0}{\partial y}\middle|y=0\right)\sin\left(\frac{\alpha_m}{2}x\right)dx$$
$$-(-1)^{\frac{m-1}{2}}\left[D_{12}\beta_n^2+D_{11}\frac{\alpha_m^2}{4}\right]\int_0^b\left(\frac{\partial w_0}{\partial x}\middle|x=a\right)\cos(\beta_n y)dy$$
$$+D_{11}\frac{\alpha_m}{2}\int_0^b\left(\frac{\partial^2 w_0}{\partial x^2}\middle|x=0\right)\cos(\beta_n y)dy$$
$$+\left[\frac{D_{11}\alpha_m^4}{16}+\frac{(D_{12}+2D_{66})\alpha_m^2\beta_n^2}{2}+D_{22}\beta_n^4\right]w_{mn}$$
$$=\sum_{L=1}^{Mn}C_{mn}^1\left(\frac{-2P_0}{\alpha_m\beta_n}\right)\left(\cos\left(\frac{\alpha_m}{2}x_{1M}\right)-\cos\left(\frac{\alpha_m}{2}x_{2M}\right)\right)_L(\sin(\beta_n y_{1M})$$
$$-\sin(\beta_n y_{2M}))_L+\sum_{L=1}^{Pn}C_{mn}^2\left[\frac{[M_x^{P_1}]^{\Theta}\alpha_m^2+4[M_y^{P_1}]^{\Theta}\beta_n^2}{2\alpha_m\beta_n}\right]\left(\cos\left(\frac{\alpha_m}{2}x_{1P}\right)\right.$$
$$\left.-\cos\left(\frac{\alpha_m}{2}x_{2P}\right)\right)_L(\sin(\beta_n y_{1P})-\sin(\beta_n y_{2P}))_L$$
$$+\sum_{L=1}^{Tn}C_{mn}^3\left[\frac{[M_x^{T_1}]^{\Theta}\alpha_m^2+4[M_y^{T_1}]^{\Theta}\beta_n^2}{2\alpha_m\beta_n}\right]\left(\cos\left(\frac{\alpha_m}{2}x_{1T}\right)-\cos\left(\frac{\alpha_m}{2}x_{2T}\right)\right)_L$$
$$\times(\sin(\beta_n y_{1T})-\sin(\beta_n y_{2T}))_L \tag{25}$$

$$\Delta_m=\int_0^a\left(\frac{\partial w_0}{\partial y}\middle|y=b\right)\sin\left(\frac{\alpha_m}{2}x\right)dx \tag{26a}$$

$$\Omega_m=\int_0^a\left(\frac{\partial w_0}{\partial y}\middle|y=0\right)\sin\left(\frac{\alpha_m}{2}x\right)dx \tag{26b}$$

$$\Pi_n=\int_0^b\left(\frac{\partial w_0}{\partial x}\middle|x=a\right)\cos(\beta_n y)dy \tag{26c}$$

$$\Psi_n=\int_0^b\left(\frac{\partial^2 w_0}{\partial x^2}\middle|x=0\right)\cos(\beta_n y)dy \tag{26d}$$

Substituting Eqs. (26a–d) into Eq. (25) and then rearranging Eq. (25) yields Eq. (27) which satisfies the boundary conditions in Eq. (11). Finally, the remaining boundary conditions in Eq. (11i,c,d,e) are substituted into Eq. (16) and then simplified as shown in Eqs. (28a–d). Eq. (27) represents the double finite integral transformation of the mid-plane vertical displacement of function $w_o(x, y)$ in a smart laminated cantilever piezo composite hybrid plate incorporated with arbitrarily positioned piezoelectric actuators and under thermo-electro-mechanical loads which can be expressed in terms of function $w_{mn}$. The first and second partial derivatives of the double Fourier series $w_o(x,y)$, presented in Appendix B, were used to expand the boundary conditions in Eqs. (14f–h).

$$w_{mn}=\left[\frac{D_{11}\alpha_m^4}{16}+\frac{(D_{12}+2D_{66})\alpha_m^2\beta_n^2}{2}+D_{22}\beta_n^4\right]^{-1}$$
$$\times\left\{\sum_{L=1}^{Mn}C_{mn}^1\left(\frac{-2P_0}{\alpha_m\beta_n}\right)\left(\cos\left(\frac{\alpha_m}{2}x_{1M}\right)-\cos\left(\frac{\alpha_m}{2}x_{2M}\right)\right)_L\right.$$
$$\times(\sin(\beta_n y_{1M})-\sin(\beta_n y_{2M}))_L+\sum_{L=1}^{Pn}C_{mn}^2\left[\frac{[M_x^{P_1}]^{\Theta}\alpha_m^2+4[M_y^{P_1}]^{\Theta}\beta_n^2}{2\alpha_m\beta_n}\right]$$
$$\times\left(\cos\left(\frac{\alpha_m}{2}x_{1P}\right)-\cos\left(\frac{\alpha_m}{2}x_{2P}\right)\right)_L(\sin(\beta_n y_{1P})-\sin(\beta_n y_{2P}))_L$$
$$+\sum_{L=1}^{Tn}C_{mn}^3\left[\frac{[M_x^{T_1}]^{\Theta}\alpha_m^2+4[M_y^{T_1}]^{\Theta}\beta_n^2}{2\alpha_m\beta_n}\right]\left(\cos\left(\frac{\alpha_m}{2}x_{1T}\right)\right.$$
$$\left.-\cos\left(\frac{\alpha_m}{2}x_{2T}\right)\right)_L(\sin(\beta_n y_{1T})-\sin(\beta_n y_{2T}))_L$$
$$+(-1)^n\left[D_{22}\beta_n^2+D_{12}\frac{\alpha_m^2}{4}\right]\Delta_m-\left[D_{22}\beta_n^2+D_{12}\frac{\alpha_m^2}{4}\right]\Omega_m$$
$$\left.+(-1)^{\frac{m-1}{2}}[D_{12}\beta_n^2+D_{11}\frac{\alpha_m^2}{4}]\Pi_n-\left[\frac{D_{11}\alpha_m}{2}\right]\Psi_n\right\} \tag{27}$$

$$\sum_{m=1,3,5,\ldots}^{\infty}\sum_{n=0,1,2,\ldots}^{\infty}\alpha_m w_{mn}\cos(\beta_n y)=0 \tag{28a}$$

$$\sum_{m=1,3,5,\ldots}^{\infty}\sum_{n=0,1,2,\ldots}^{\infty}(-1)^{\frac{m-1}{2}}\left[D_{12}(-1)^n\Delta_m-D_{12}\Omega_m+D_{11}(-1)^{\frac{m-1}{2}}\Pi_n-\left[D_{12}\beta_n^2+\frac{D_{11}\alpha_m^2}{4}\right]w_{mn}\right]\cos(\beta_n y)=0 \tag{28b}$$

$$\sum_{m=1,3,5,\ldots}^{\infty}\sum_{n=0,1,2,\ldots}^{\infty}\lambda_n\left[D_{22}(-1)^n\Delta_m-D_{22}\Omega_m+D_{12}(-1)^{\frac{m-1}{2}}\Pi_n-\left[D_{22}\beta_n^2+\frac{D_{12}\alpha_m^2}{4}\right]w_{mn}\right]\sin\left(\frac{\alpha_m}{2}x\right)=0 \tag{28c}$$

$$\sum_{m=1,3,5,\ldots}^{\infty}\sum_{n=0,1,2,\ldots}^{\infty}\lambda_n\left[D_{22}\Delta_m-D_{22}(-1)^n\Omega_m+D_{12}(-1)^n(-1)^{\frac{m-1}{2}}\Pi_n-(-1)^n\left[D_{22}\beta_n^2+\frac{D_{12}\alpha_m^2}{4}\right]w_{mn}\right]\sin\left(\frac{\alpha_m}{2}x\right)=0 \tag{28d}$$

The double finite integral transformation $CI_n$ and $SI_m$ are performed over Eqs. (28a–b) and Eqs. (28c–d), respectively. The $CI_n$ and $SI_m$ are stated in Eqs. (29a–b), respectively. Taking integration over the specified domains results in Eqs. (30a–d), respectively.

$$CI_n=\int_0^b\cos(\beta_n y)dy \tag{29a}$$

$$SI_m=\int_0^a\sin\left(\frac{\alpha_m}{2}x\right)dx \tag{29b}$$

$$\sum_{m=1,3,5,\ldots}^{\infty}\sum_{n=0,1,2,\ldots}^{\infty}\alpha_m w_{mn}=0 \tag{30a}$$

$$\sum_{m=1,3,5,\ldots}^{\infty}\sum_{n=0,1,2,\ldots}^{\infty}(-1)^{\frac{m-1}{2}}\left[D_{12}(-1)^n\Delta_m-D_{12}\Omega_m+D_{11}(-1)^{\frac{m-1}{2}}\Pi_n-\left[D_{12}\beta_n^2+\frac{D_{11}\alpha_m^2}{4}\right]w_{mn}\right]=0 \tag{30b}$$

$$\sum_{m=1,3,5,\ldots}^{\infty}\sum_{n=0,1,2,\ldots}^{\infty}\lambda_n\left[D_{22}(-1)^n\Delta_m-D_{22}\Omega_m-D_{12}(-1)^{\frac{m-1}{2}}\Pi_n-\left[D_{22}\beta_n^2+\frac{D_{12}\alpha_m^2}{4}\right]w_{mn}\right]=0 \tag{30c}$$

$$\sum_{m=1,3,5,\ldots}^{\infty}\sum_{n=0,1,2,\ldots}^{\infty}\lambda_n\left[D_{22}\Delta_m-D_{22}(-1)^n\Omega_m+D_{12}(-1)^n(-1)^{\frac{m-1}{2}}\Pi_n-(-1)^n\left[D_{22}\beta_n^2+\frac{D_{12}\alpha_m^2}{4}\right]w_{mn}\right]=0 \tag{30d}$$

Finally, Eq. (27) is substituted into Eqs. (30a–d) to obtain the four finite systems of linear simultaneous multivariable equations as stated in Eqs. (31a–d), respectively. The sufficient finite terms of $m$ and $n$ in each set of multivariable equations are considered in order to accurately compute the constant values of unknown variables $\Delta_m$, $\Omega_m$, $\Pi_n$, and $\Psi_n$.

$$\sum_{m=1,3,5,\ldots}^{\infty}\sum_{n=0,1,2,\ldots}^{\infty}S_{mn}^1\Delta_m+\sum_{m=1,3,5,\ldots}^{\infty}\sum_{n=0,1,2,\ldots}^{\infty}S_{mn}^2\Omega_m+\sum_{m=1,3,5,\ldots}^{\infty}\sum_{n=0,1,2,\ldots}^{\infty}S_{mn}^3\Pi_n+\sum_{m=1,3,5,\ldots}^{\infty}\sum_{n=0,1,2,\ldots}^{\infty}S_{mn}^4\Psi_n=\sum_{m=1,3,5,\ldots}^{\infty}\sum_{n=0,1,2,\ldots}^{\infty}S_{mn}^5 \tag{31a}$$

$$\sum_{m=1,3,5,\ldots}^{\infty}\sum_{n=0,1,2,\ldots}^{\infty}S_{mn}^6\Delta_m+\sum_{m=1,3,5,\ldots}^{\infty}\sum_{n=0,1,2,\ldots}^{\infty}S_{mn}^7\Omega_m+\sum_{m=1,3,5,\ldots}^{\infty}\sum_{n=0,1,2,\ldots}^{\infty}S_{mn}^8\Pi_n+\sum_{m=1,3,5,\ldots}^{\infty}\sum_{n=0,1,2,\ldots}^{\infty}S_{mn}^9\Psi_n=\sum_{m=1,3,5,\ldots}^{\infty}\sum_{n=0,1,2,\ldots}^{\infty}S_{mn}^{10} \tag{31b}$$

$$\sum_{m=1,3,5,\ldots}^{\infty}\sum_{n=0,1,2,\ldots}^{\infty}S_{mn}^{11}\Delta_m+\sum_{m=1,3,5,\ldots}^{\infty}\sum_{n=0,1,2,\ldots}^{\infty}S_{mn}^{12}\Omega_m+\sum_{m=1,3,5,\ldots}^{\infty}\sum_{n=0,1,2,\ldots}^{\infty}S_{mn}^{13}\Pi_n+\sum_{m=1,3,5,\ldots}^{\infty}\sum_{n=0,1,2,\ldots}^{\infty}S_{mn}^{14}\Psi_n=\sum_{m=1,3,5,\ldots}^{\infty}\sum_{n=0,1,2,\ldots}^{\infty}S_{mn}^{15} \tag{31c}$$

$$\sum_{m=1,3,5,\ldots}^{\infty}\sum_{n=0,1,2,\ldots}^{\infty}S_{mn}^{16}\Delta_m+\sum_{m=1,3,5,\ldots}^{\infty}\sum_{n=0,1,2,\ldots}^{\infty}S_{mn}^{17}\Omega_m+\sum_{m=1,3,5,\ldots}^{\infty}\sum_{n=0,1,2,\ldots}^{\infty}S_{mn}^{18}\Pi_n+\sum_{m=1,3,5,\ldots}^{\infty}\sum_{n=0,1,2,\ldots}^{\infty}S_{mn}^{19}\Psi_n=\sum_{m=1,3,5,\ldots}^{\infty}\sum_{n=0,1,2,\ldots}^{\infty}S_{mn}^{20} \tag{31d}$$

where,

$$S_{mn}^1=(-1)^n\left(\frac{\alpha_m\left(\frac{(D_{12})\alpha_m^2}{4}+D_{22}\beta_n^2\right)}{\frac{D_{11}\alpha_m^4}{16}+\frac{(D_{12}+2D_{66})\alpha_m^2\beta_n^2}{2}+D_{22}\beta_n^4}\right)$$

$$S_{mn}^2=-\left(\frac{\alpha_m\left(\frac{(D_{12})\alpha_m^2}{4}+D_{22}\beta_n^2\right)}{\frac{D_{11}\alpha_m^4}{16}+\frac{(D_{12}+2D_{66})\alpha_m^2\beta_n^2}{2}+D_{22}\beta_n^4}\right)$$

$$S_{mn}^3=(-1)^{\frac{m-1}{2}}\left(\frac{\alpha_m\left(\frac{D_{11}\alpha_m^2}{4}+D_{12}\beta_n^2\right)}{\frac{D_{11}\alpha_m^4}{16}+\frac{(D_{12}+2D_{66})\alpha_m^2\beta_n^2}{2}+D_{22}\beta_n^4}\right)$$

$$S_{mn}^4=-\frac{D_{11}}{2}\left(\frac{\alpha_m^2}{\frac{D_{11}\alpha_m^4}{16}+\frac{(D_{12}+2D_{66})\alpha_m^2\beta_n^2}{2}+D_{22}\beta_n^4}\right)$$

**Table 1**
Material properties.

| Material properties | Aluminum [34] | PZT G1195 N [1,2,31] | T300/976 GFRP [1] | AS/3501 GFRP [33] | KYNAR [35] | Prepreg CFRP [36] |
|---|---|---|---|---|---|---|
| $E_1$ [GPa] | 75.22 | 63 | 150 | 144.8 | 2 | 135 |
| $E_2$ [GPa] | 75.22 | 63 | 9 | 9.65 | 2 | 8.8 |
| $\nu_{12}$ | 0.33 | 0.3 | 0.3 | 0.3 | 0.29 | 0.33 |
| $G_{12}$ [GPa] | 28.28 | 24.2 | 7.1 | 7.1 | 0.77 | 4.47 |
| $\alpha_1[10^{-6}/^\circ C]$ | 23 | 0.00012 | – | – | – | 0.19 |
| $\alpha_2[10^{-6}/^\circ C]$ | 23 | 0.00012 | – | – | – | 40.3 |
| $d_{31}$ [$10^{-10}$ m/V] | 0.0 | 1.9 | 0.0 | 0.0 | 0.23 | 0.0 |
| $d_{32}$ [$10^{-10}$ m/V] | 0.0 | 1.9 | 0.0 | 0.0 | 0.046 | 0.0 |

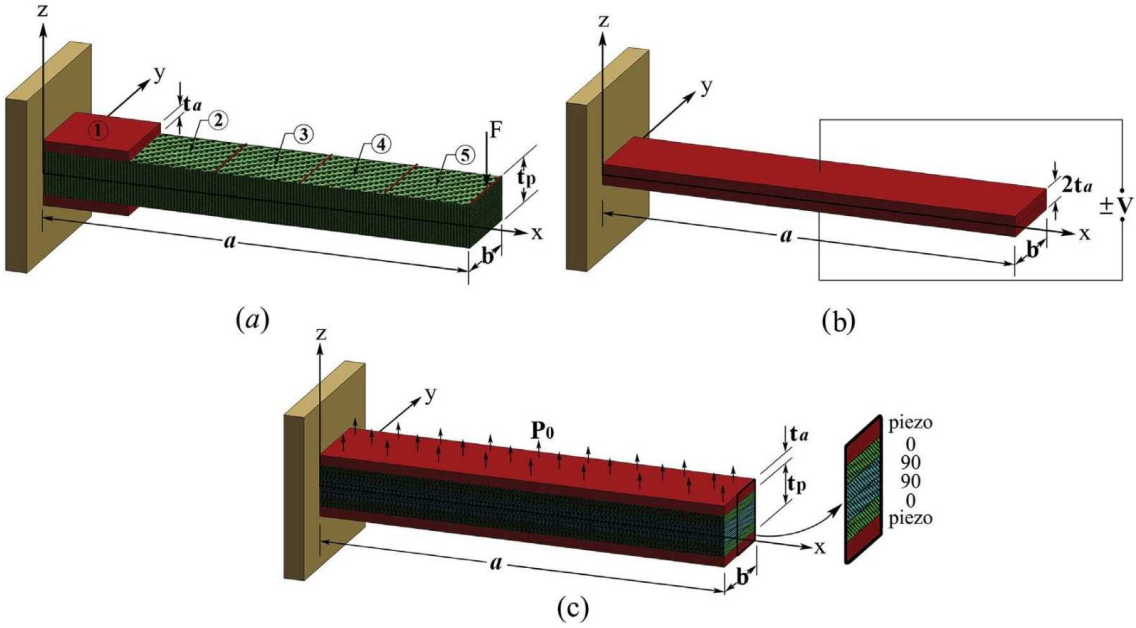


**Fig. 2.** Schematic of (a) smart laminated piezo composite beam incorporated with bounded actuator patches, (b) 2th-layer KYNAR bimorph beam, (c) smart laminated piezo composite beam incorporated with bounded actuator layers.

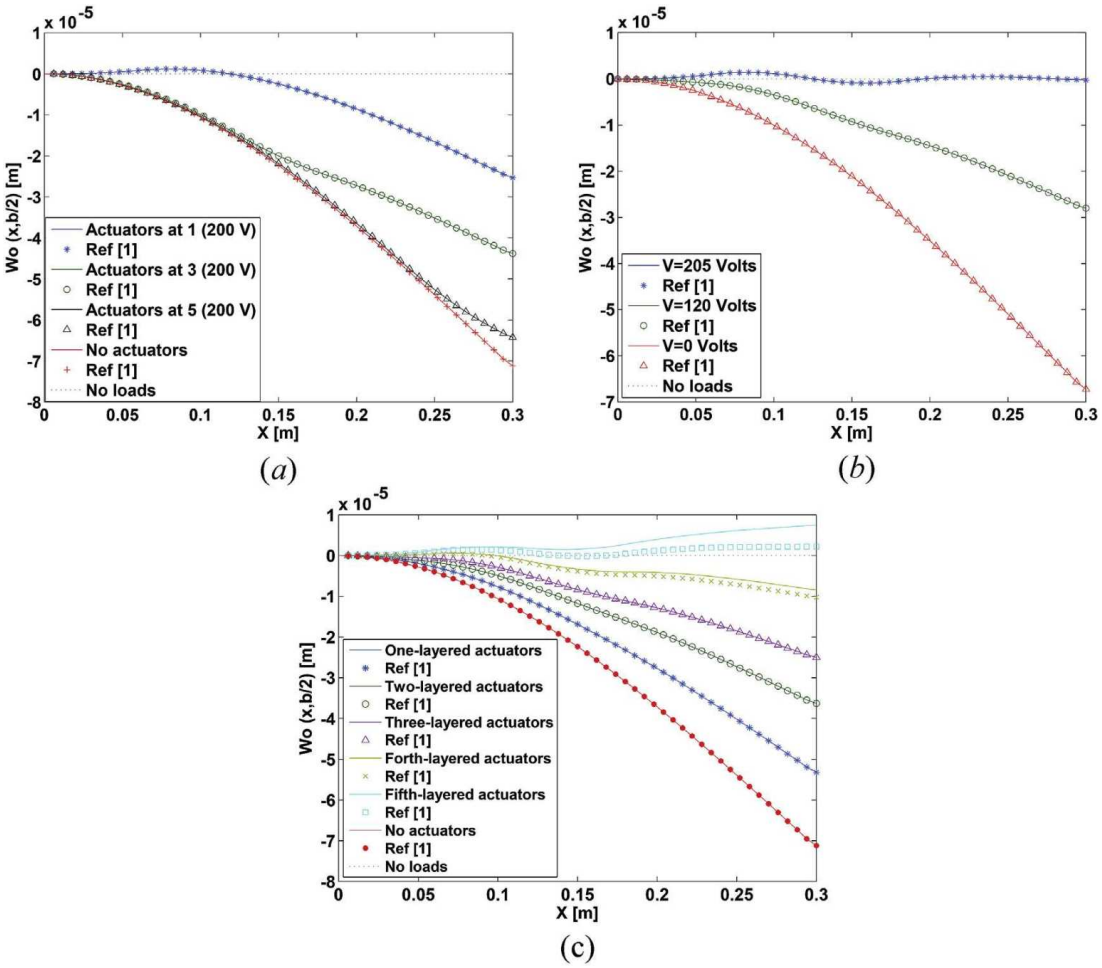


**Fig. 3.** $W_o(x,b/2)$ 2D graphs of shape control task of smart laminated cantilever piezo composite beam (see Fig. 2a) (a) separate actuator patches centred at ①, ③, or ⑤, (b) combined actuator patches centred at ① and ③, (c) combined multi-layered actuator patches centred at ① and ③.

$$S^5_{mn}=\left(\frac{-\alpha_m}{\frac{D_{11}\alpha_m^4}{16}+\frac{(D_{12}+2D_{66})\alpha_m^2\beta_n^2}{2}+D_{22}\beta_n^4}\right)\times\left\{\sum_{L=1}^{Mn}C^1_{mn}\left(\frac{-2P_0}{\alpha_m\beta_n}\right)\left(\cos\left(\frac{\alpha_m}{2}x_{1M}\right)-\cos\left(\frac{\alpha_m}{2}x_{2M}\right)\right)_L\times(\sin(\beta_n y_{1M})-\sin(\beta_n y_{2M}))_L+\sum_{L=1}^{Pn}C^2_{mn}\left[\frac{[M_x^{P_1}]^\Theta\alpha_m^2+4[M_y^{P_1}]^\Theta\beta_n^2}{2\alpha_m\beta_n}\right]\times\left(\cos\left(\frac{\alpha_m}{2}x_{1P}\right)-\cos\left(\frac{\alpha_m}{2}x_{2P}\right)\right)_L(\sin(\beta_n y_{1P})-\sin(\beta_n y_{2P}))_L+\sum_{L=1}^{Tn}C^3_{mn}\left[\frac{[M_x^{T}]^\Theta\alpha_m^2+4[M_y^{T}]^\Theta\beta_n^2}{2\alpha_m\beta_n}\right]\left(\cos\left(\frac{\alpha_m}{2}x_{1T}\right)-\cos\left(\frac{\alpha_m}{2}x_{2T}\right)\right)_L\times(\sin(\beta_n y_{1T})-\sin(\beta_n y_{2T}))_L\right\}$$

$$S^6_{mn}=(-1)^n(-1)^{\frac{m-1}{2}}\left[D_{12}-\frac{\left(D_{22}\beta_n^2+\frac{D_{12}\alpha_m^2}{4}\right)\left(\frac{D_{11}\alpha_m^2}{4}+D_{12}\beta_n^2\right)}{\frac{D_{11}\alpha_m^4}{16}+\frac{(D_{12}+2D_{66})\alpha_m^2\beta_n^2}{2}+D_{22}\beta_n^4}\right]$$

$$S^7_{mn}=-(-1)^{\frac{m-1}{2}}\left[D_{12}-\frac{\left(D_{22}\beta_n^2+\frac{D_{12}\alpha_m^2}{4}\right)\left(\frac{D_{11}\alpha_m^2}{4}+D_{12}\beta_n^2\right)}{\frac{D_{11}\alpha_m^4}{16}+\frac{(D_{12}+2D_{66})\alpha_m^2\beta_n^2}{2}+D_{22}\beta_n^4}\right]$$

$$S^8_{mn}=(-1)^{m-1}\left(D_{11}-\frac{\left(\frac{D_{11}\alpha_m^2}{4}+D_{12}\beta_n^2\right)^2}{\frac{D_{11}\alpha_m^4}{16}+\frac{(D_{12}+2D_{66})\alpha_m^2\beta_n^2}{2}+D_{22}\beta_n^4}\right)$$

$$S^9_{mn}=\frac{D_{11}}{2}(-1)^{\frac{m-1}{2}}\left(\frac{\alpha_m\left(\frac{D_{11}\alpha_m^2}{4}+D_{12}\beta_n^2\right)}{\frac{D_{11}\alpha_m^4}{16}+\frac{(D_{12}+2D_{66})\alpha_m^2\beta_n^2}{2}+D_{22}\beta_n^4}\right)$$

$$S^{10}_{mn}=(-1)^{\frac{m-1}{2}}\left[\frac{D_{11}\alpha_m^4}{16}+\frac{(D_{12}+2D_{66})\alpha_m^2\beta_n^2}{2}+D_{22}\beta_n^4\right]^{-1}\times\left(\frac{D_{11}\alpha_m^2}{4}+D_{12}\beta_n^2\right)\left\{\sum_{L=1}^{Mn}C^1_{mn}\left(\frac{-2P_0}{\alpha_m\beta_n}\right)\left(\cos\left(\frac{\alpha_m}{2}x_{1M}\right)-\cos\left(\frac{\alpha_m}{2}x_{2M}\right)\right)_L(\sin(\beta_n y_{1M})-\sin(\beta_n y_{2M}))_L+\sum_{L=1}^{Pn}C^2_{mn}\left[\frac{[M_x^{P_1}]^\Theta\alpha_m^2+4[M_y^{P_1}]^\Theta\beta_n^2}{2\alpha_m\beta_n}\right]\left(\cos\left(\frac{\alpha_m}{2}x_{1P}\right)-\cos\left(\frac{\alpha_m}{2}x_{2P}\right)\right)_L(\sin(\beta_n y_{1P})-\sin(\beta_n y_{2P}))_L+\sum_{L=1}^{Tn}C^3_{mn}\left[\frac{[M_x^{T}]^\Theta\alpha_m^2+4[M_y^{T}]^\Theta\beta_n^2}{2\alpha_m\beta_n}\right]\left(\cos\left(\frac{\alpha_m}{2}x_{1T}\right)-\cos\left(\frac{\alpha_m}{2}x_{2T}\right)\right)_L(\sin(\beta_n y_{1T})-\sin(\beta_n y_{2T}))_L\right\}$$

$$S^{11}_{mn}=\lambda_n(-1)^n\left[D_{22}-\frac{\left(\frac{D_{12}\alpha_m^2}{4}+D_{22}\beta_n^2\right)^2}{\frac{D_{11}\alpha_m^4}{16}+\frac{(D_{12}+2D_{66})\alpha_m^2\beta_n^2}{2}+D_{22}\beta_n^4}\right]$$

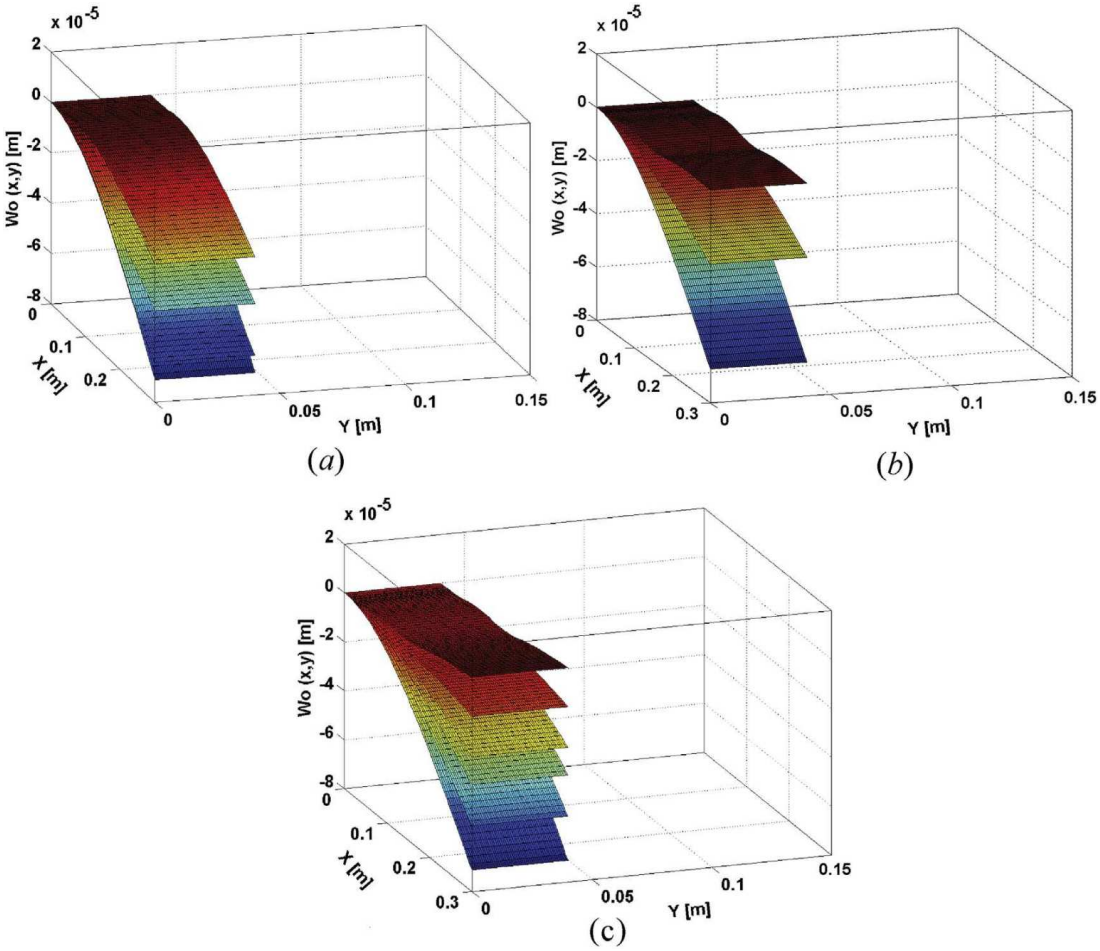


**Fig. 4.** $W_o(x,y)$ 3D graphs of shape control task in smart laminated cantilever piezo composite beam (see Fig. 2a) (a) separate actuator patches centred at ①, ③, or ⑤, (b) combined actuator patches centred at the ① and ③, (c) combined multi-layered actuator patches centred at ① and ③.

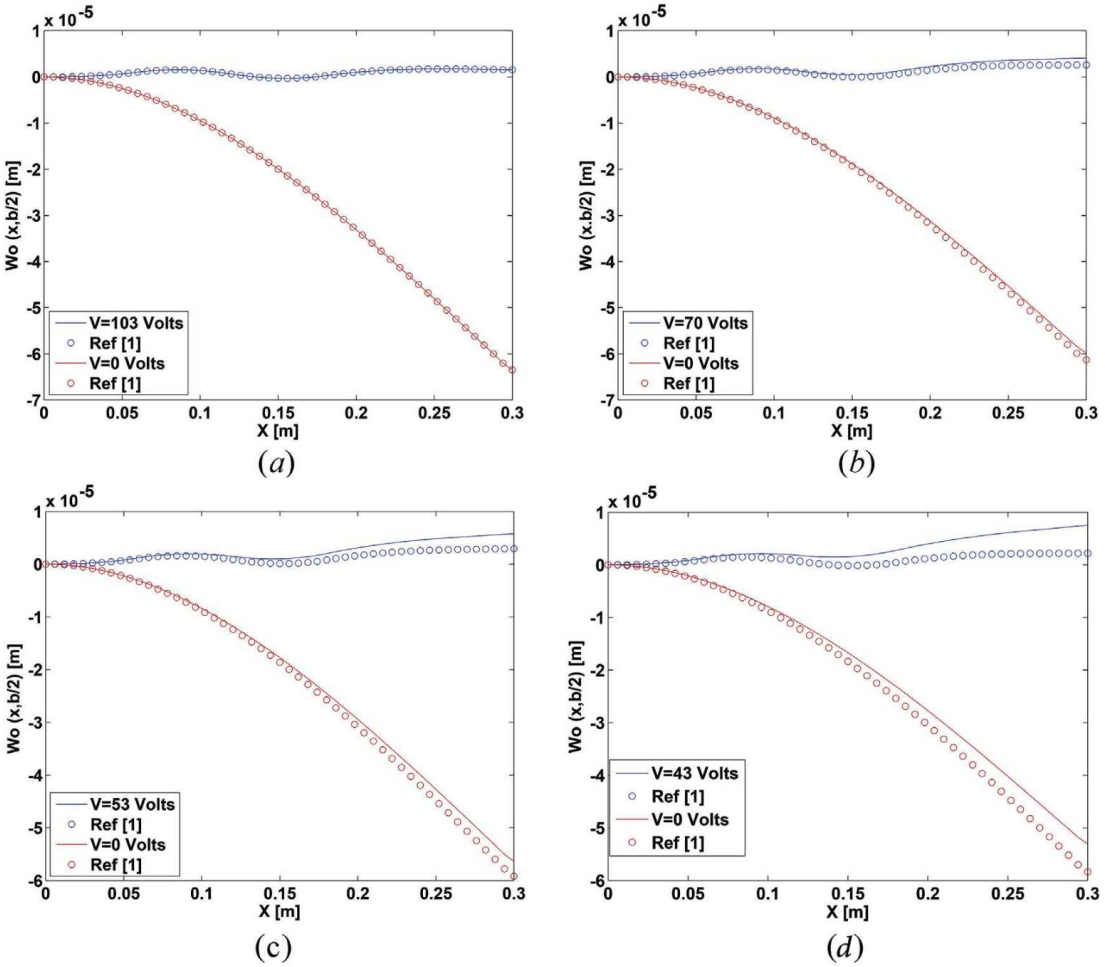


**Fig. 5.** $W_o(x,b/2)$ 2D graphs of optimal shape control task in smart laminated cantilever piezo composite beam using combined multi-layered actuator patches centred at ① and ③ in Fig. 2a with the stacking sequence (a) $[(\text{piezo})_2/0/[(\text{piezo})_2]$, (b) $[(\text{piezo})_3/0/[(\text{piezo})_3]$, (c) $[(\text{piezo})_4/0/[(\text{piezo})_4]$, (d) $[(\text{piezo})_5/0/[(\text{piezo})_5]$.

$$S_{mn}^{12} = -\lambda_n \left[ D_{22} - \frac{\left(\frac{D_{12}\alpha_m^2}{4} + D_{22}\beta_n^2\right)^2}{\frac{D_{11}\alpha_m^4}{16} + \frac{(D_{12}+2D_{66})\alpha_m^2\beta_n^2}{2} + D_{22}\beta_n^4} \right]$$

$$S_{mn}^{13} = \lambda_n (-1)^{\frac{m-1}{2}} \left[ D_{12} - \frac{\left(\frac{D_{12}\alpha_m^2}{4} + D_{22}\beta_n^2\right)\left(\frac{D_{11}\alpha_m^2}{4} + D_{12}\beta_n^2\right)}{\frac{D_{11}\alpha_m^4}{16} + \frac{(D_{12}+2D_{66})\alpha_m^2\beta_n^2}{2} + D_{22}\beta_n^4} \right]$$

$$S_{mn}^{14} = \frac{D_{11}}{2}\lambda_n \left[ \frac{\alpha_m\left(\frac{D_{12}\alpha_m^2}{4} + D_{22}\beta_n^2\right)}{\frac{D_{11}\alpha_m^4}{16} + \frac{(D_{12}+2D_{66})\alpha_m^2\beta_n^2}{2} + D_{22}\beta_n^4} \right]$$

$$S_{mn}^{15} = \lambda_n \left[ \frac{D_{11}\alpha_m^4}{16} + \frac{(D_{12}+2D_{66})\alpha_m^2\beta_n^2}{2} + D_{22}\beta_n^4 \right]^{-1} \left( \frac{D_{12}\alpha_m^2}{4} + D_{22}\beta_n^2 \right) \times \left\{ \sum_{L=1}^{Mn} C_{mn}^1 \left( \frac{-2P_0}{\alpha_m\beta_n} \right) \left( \cos\left(\frac{\alpha_m}{2}x_{1M}\right) - \cos\left(\frac{\alpha_m}{2}x_{2M}\right) \right)_L \times (\sin(\beta_n y_{1M}) - \sin(\beta_n y_{2M}))_L + \sum_{L=1}^{Pn} C_{mn}^2 \left[ \frac{[M_x^p]^\Theta \alpha_m^2 + 4[M_y^p]^\Theta \beta_n^2}{2\alpha_m\beta_n} \right] \times \left( \cos\left(\frac{\alpha_m}{2}x_{1P}\right) - \cos\left(\frac{\alpha_m}{2}x_{2P}\right) \right)_L (\sin(\beta_n y_{1P}) - \sin(\beta_n y_{2P}))_L + \sum_{L=1}^{Tn} C_{mn}^3 \left[ \frac{[M_x^T]^\Theta \alpha_m^2 + 4[M_y^T]^\Theta \beta_n^2}{2\alpha_m\beta_n} \right] \left( \cos\left(\frac{\alpha_m}{2}x_{1T}\right) - \cos\left(\frac{\alpha_m}{2}x_{2T}\right) \right)_L (\sin(\beta_n y_{1T}) - \sin(\beta_n y_{2T}))_L \right\}$$

$$S_{mn}^{16} = \lambda_n \left[ D_{22} - \frac{\left(\frac{D_{12}\alpha_m^2}{4} + D_{22}\beta_n^2\right)^2}{\frac{D_{11}\alpha_m^4}{16} + \frac{(D_{12}+2D_{66})\alpha_m^2\beta_n^2}{2} + D_{22}\beta_n^4} \right]$$

$$S_{mn}^{17} = -\lambda_n (-1)^n \left[ D_{22} - \frac{\left(\frac{D_{12}\alpha_m^2}{4} + D_{22}\beta_n^2\right)^2}{\frac{D_{11}\alpha_m^4}{16} + \frac{(D_{12}+2D_{66})\alpha_m^2\beta_n^2}{2} + D_{22}\beta_n^4} \right]$$

$$S_{mn}^{18} = \lambda_n (-1)^n (-1)^{\frac{m-1}{2}} \left[ D_{12} - \frac{\left(\frac{D_{12}\alpha_m^2}{4} + D_{22}\beta_n^2\right)\left(\frac{D_{11}\alpha_m^2}{4} + D_{12}\beta_n^2\right)}{\frac{D_{11}\alpha_m^4}{16} + \frac{(D_{12}+2D_{66})\alpha_m^2\beta_n^2}{2} + D_{22}\beta_n^4} \right]$$

$$S_{mn}^{19} = \lambda_n \frac{D_{11}}{2}(-1)^n \left[ \frac{\alpha_m\left(\frac{D_{12}\alpha_m^2}{4} + D_{22}\beta_n^2\right)}{\frac{D_{11}\alpha_m^4}{16} + \frac{(D_{12}+2D_{66})\alpha_m^2\beta_n^2}{2} + D_{22}\beta_n^4} \right]$$

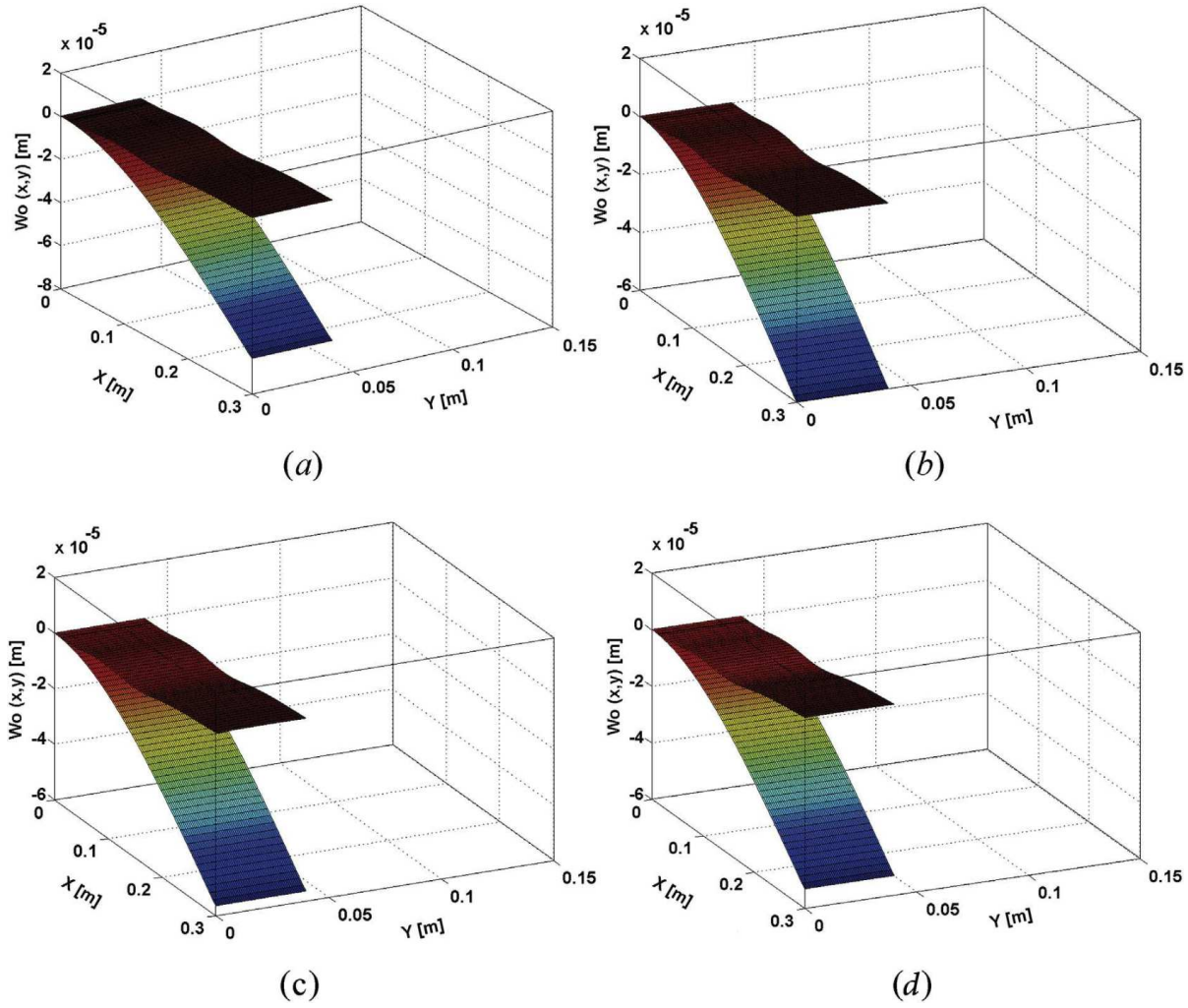


**Fig. 6.** $W_o(x,y)$ 3D graphs of optimal shape control task in smart laminated cantilever piezo composite beam using combined multi-layered actuator patches centred at ① and ③ in Fig. 2a with the stacking sequence (a) $[(\text{piezo})_2/0/[(\text{piezo})_2]$, (b) $[(\text{piezo})_3/0/[(\text{piezo})_3]$, (c) $[(\text{piezo})_4/0/[(\text{piezo})_4]$, (d) $[(\text{piezo})_5/0/[(\text{piezo})_5]$.

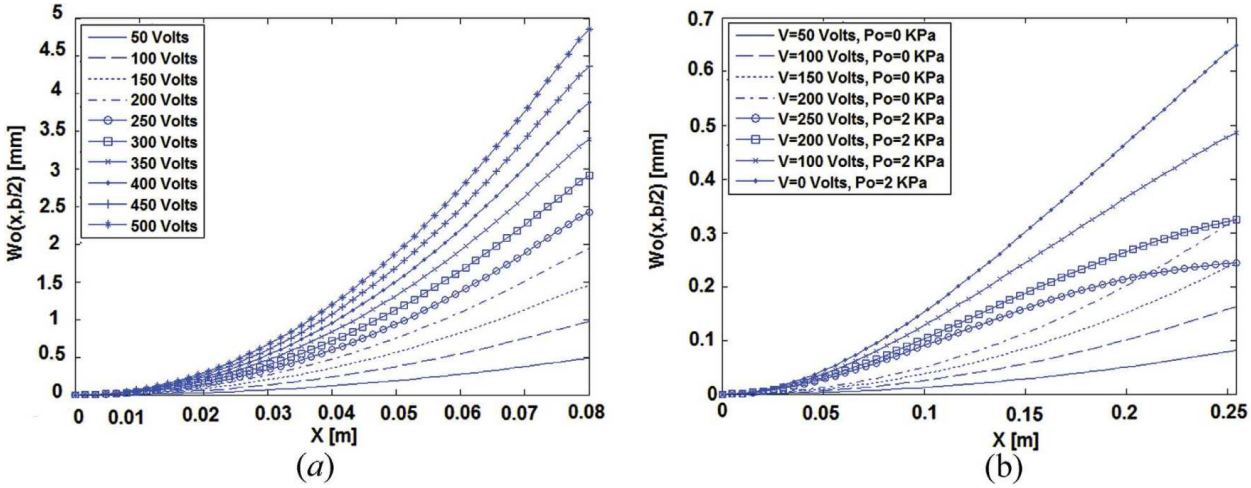


**Fig. 7.** (a) Effect of electrical voltage on shape deformation of 2th-layered bimorph beam, (b) shape control of smart laminated cantilever piezo composite beam under uniform pressure $P_o$ using bounded actuator layers.

**Table 2**
Effect of electrical voltage on the tip deflection of 2*th*-layered cantilever bimorph beam.

| Tip Displacement [mm] | *V* [Volts] | | | | | | | | | |
|---|---|---|---|---|---|---|---|---|---|---|
| | *V* = 50 | *V* = 100 | *V* = 150 | *V* = 200 | *V* = 250 | *V* = 300 | *V* = 350 | *V* = 400 | *V* = 450 | *V* = 500 |
| [11] | 0.49 | 0.98 | 1.46 | 1.95 | 2.4 | 2.9 | 3.75 | 3.95 | 4.22 | 4.91 |
| [33] | 0.48 | 0.99 | 1.47 | 1.96 | 2.45 | 2.95 | 3.67 | 4.20 | 4.45 | 4.95 |
| Present study | 0.485 | 0.970 | 1.456 | 1.941 | 2.426 | 2.912 | 3.97 | 3.882 | 4.368 | 4.853 |

**Table 3**
Effect of electrical voltage on shape control of smart laminated cantilever piezo composite beam under uniform pressure $P_o$ using bounded actuator layers.

| Tip Displacement [mm] | $P_0 = 0$ [kPa] *V* [Volts] | | | | $P_0 = 2$ [kPa] *V* [Volts] | | | |
|---|---|---|---|---|---|---|---|---|
| | *V* = 50 | *V* = 100 | *V* = 150 | *V* = 200 | *V* = 0 | *V* = 100 | *V* = 200 | *V* = 250 |
| [33] | 0.07 | 0.17 | 0.25 | 0.33 | 0.65 | 0.50 | 0.33 | 0.23 |
| Present study | 0.074 | 0.161 | 0.243 | 0.324 | 0.647 | 0.486 | 0.324 | 0.243 |

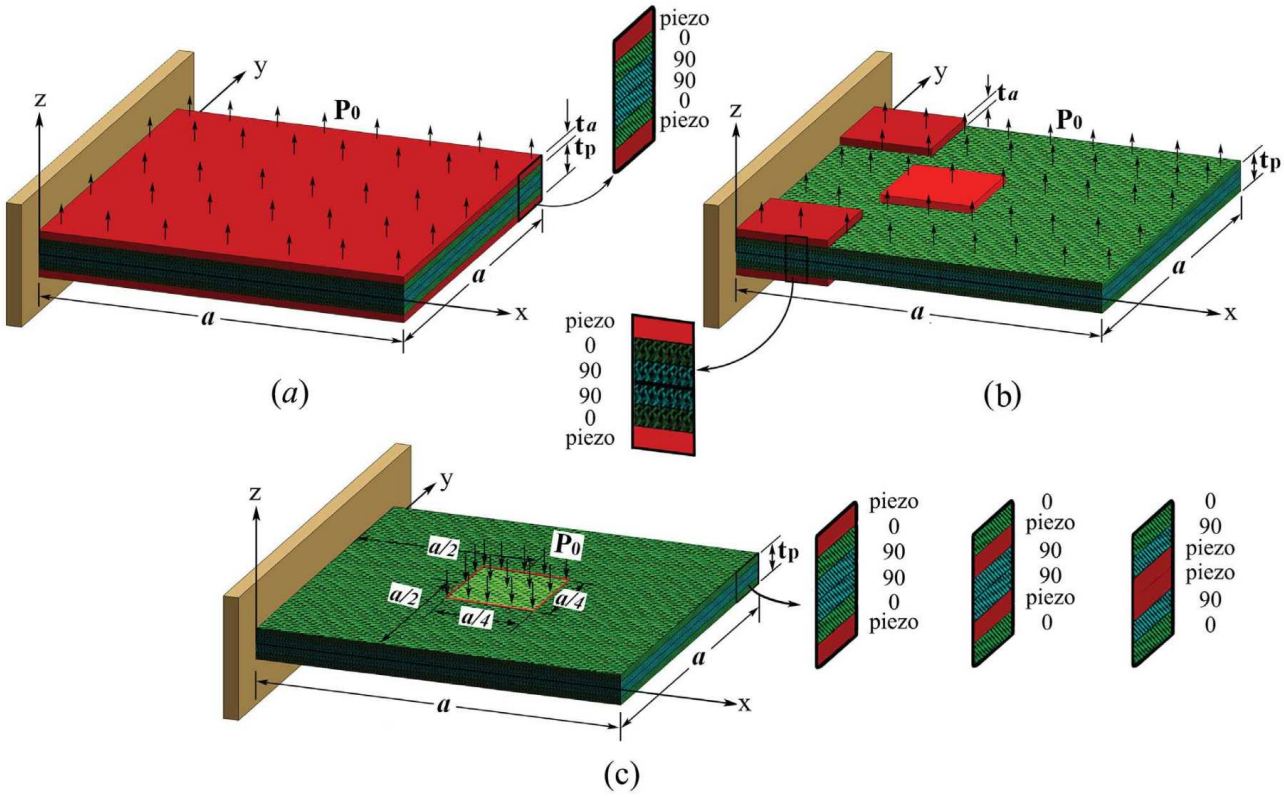


**Fig. 8.** Schematic of smart laminated cantilever piezo composite plate under electro-mechanical loads incorporated with (a) bounded actuator layers, (b) bounded actuator patches, (c) bounded/embedded/core actuator layers.

$$S_{mn}^{20} = \lambda_n(-1)^n\left[\frac{D_{11}\alpha_m^4}{16}+\frac{(D_{12}+2D_{66})\alpha_m^2\beta_n^2}{2}+D_{22}\beta_n^4\right]^{-1}\left(\frac{D_{12}\alpha_m^2}{4}+D_{22}\beta_n^2\right)$$
$$\times\left\{\sum_{L=1}^{Mn}C_{mn}^1\left(\frac{-2P_0}{\alpha_m\beta_n}\right)\left(\cos\left(\tfrac{\alpha_m}{2}x_{1M}\right)-\cos\left(\tfrac{\alpha_m}{2}x_{2M}\right)\right)_L\left(\sin(\beta_n y_{1M})-\sin(\beta_n y_{2M})\right)_L\right.$$
$$+\sum_{L=1}^{Pn}C_{mn}^2\left[\frac{[M_x^P]^{\Theta}\alpha_m^2+4[M_y^P]^{\Theta}\beta_n^2}{2\alpha_m\beta_n}\right]\left(\cos\left(\tfrac{\alpha_m}{2}x_{1P}\right)-\cos\left(\tfrac{\alpha_m}{2}x_{2P}\right)\right)_L$$
$$\times\left(\sin(\beta_n y_{1P})-\sin(\beta_n y_{2P})\right)_L+\sum_{L=1}^{Tn}C_{mn}^3\left[\frac{[M_x^T]^{\Theta}\alpha_m^2+4[M_y^T]^{\Theta}\beta_n^2}{2\alpha_m\beta_n}\right]$$
$$\left.\times\left(\cos\left(\tfrac{\alpha_m}{2}x_{1T}\right)-\cos\left(\tfrac{\alpha_m}{2}x_{2T}\right)\right)_L\left(\sin(\beta_n y_{1T})-\sin(\beta_n y_{2T})\right)_L\right\}$$

Computation of $S_{mn}^i$, $i=\{1,2,..,20\}$ leads to obtaining the unknown constants in Eqs. (26a–d) as four finite systems of linear simultaneous multivariable equations which are later substituted into Eq. (27) to calculate the double finite integral transformation of the mid-plane vertical displacement of function $w_o(x,y)$. Once the $w_{mn}$ is found, it can be substituted into Eq. (16) to calculate the exact mid-plane vertical displacement of function $w_o(x,y)$ in the smart laminated cantilever piezo composite hybrid plate subjected to thermo-electro-mechanical loads.

## 3. Results and discussions

In this section, various examples are intended to demonstrate and evaluate the accuracy of the proposed method for deformation analysis and shape control task of smart laminated cantilever piezo composite hybrid plates and beams under thermo-electro-mechanical loads using arbitrarily positioned multiple piezoelectric

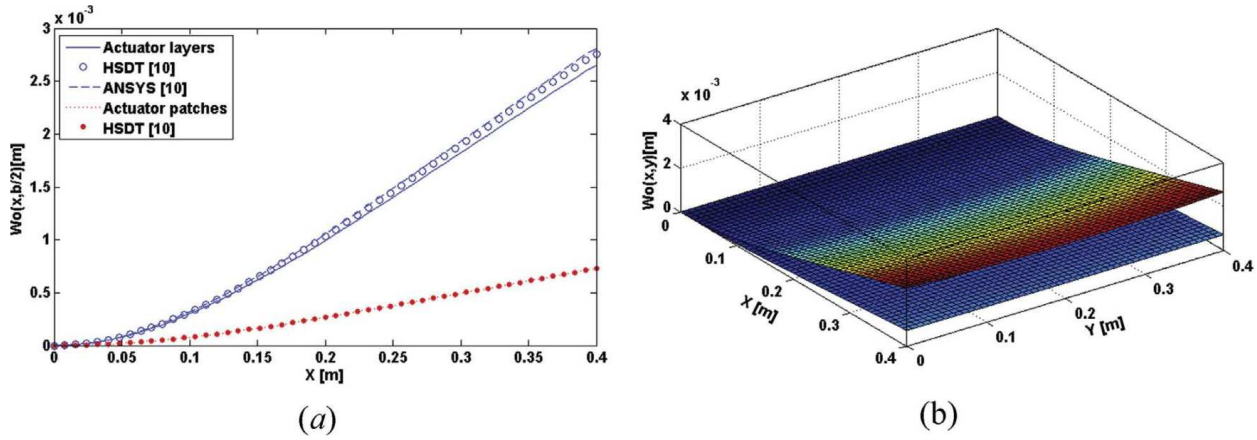


**Fig. 9.** Shape control of smart laminated cantilever piezo composite plate under uniform pressure $P_o$ using bounded actuator layers and patches. (a) $w_o(x,b/2)$, (b) $w_o(x,y)$.

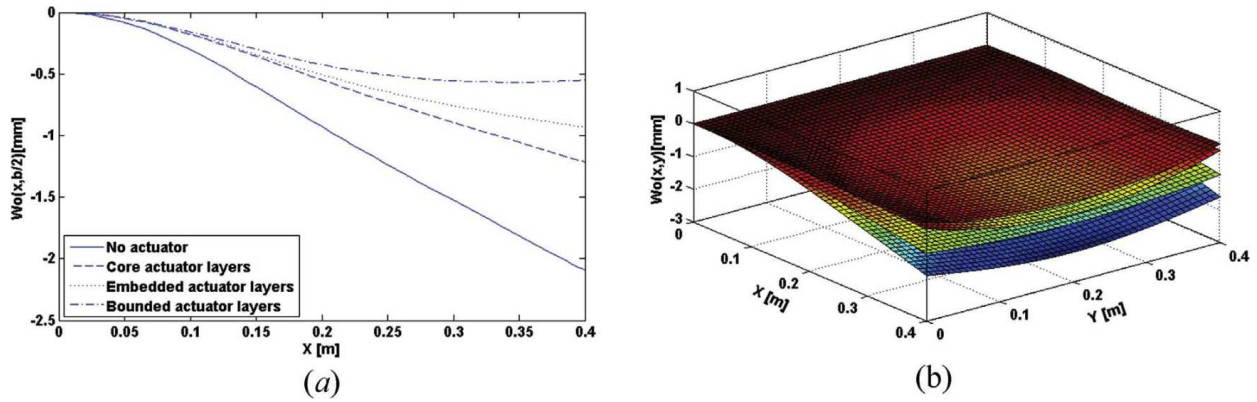


**Fig. 10.** Effect of bounded/embedded/core actuator layers on shape control of smart laminated cantilever piezo composite plate under uniform patch loading $P_o$. (a) $w_o(x,b/2)$, (b) $w_o(x,y)$.

actuators. The results were verified by some published benchmark results. In the first examples, the effect of electro-mechanical coupling was taken into account. The effect of residual thermal stresses as well as electro-mechanical coupling along with more complex load functions were considered, afterward. Generally, the effect of various parameters including: different complex loads, ply thickness, size and placement of bounded and embedded piezoelectric actuators, stacking sequence, and geometrical shape were emphasized. The effect of actuators and host structure weight is neglected in all examples. For greater actuation result, the activated piezoelectric actuators were symmetrically bounded and embedded with respect to the mid-plane under same amount of constant electrical voltage but different polarization direction. In general, for an upward displacements, the upper and lower actuators require a negative and positive voltage, respectively and vice versa [1]. Material properties of piezoelectric actuators and composite hybrid laminates used in the following examples are summarized in Table.1 [1,2,31,33–36]. The results are presented in 2D and 3D graphs, respectively.

### *3.1. Example 1: Placement effect of single bounded actuator on the shape control of smart laminated cantilever piezo composite beams*

As shown in Fig. 2a, a smart elastic cantilever beam ($a = 300$ [mm], $b = 40$ [mm]) with thickness $t_p = 10$ [mm] and made of unidirectional T300/976 GFRP is incorporated with bounded PZT G1195 N piezoelectric actuator patches with thickness $t_a = 0.2$ [mm] and under constant actuation voltage of $V = 200$ [Volts]. The material orientations are along $x$, $y$, and $z$ directions, respectively. A concentrated point load equal to $F = -4$ [$N$] was applied at the beam's free end at $y = b/2$. The effect of pure mechanical and thermo-mechanical coupling for the actuators separately placed at positions ①, ③, or ⑤, respectively is shown in Fig. 3a in 2D and Fig. 4a in 3D, respectively. It is seen that the effect of actuation on shape control task is significant. However, if one places actuators close to the fixed end, the shape control task will be more optimal and significant. It is also seen that unsolvable shape control task of reducing the beam's mid-line deflection at free end (location ⑤) which requires approximation solution through other approaches can accurately be performed using the proposed explicit solution. The results were verified with the ones presented in Ref [1] and good agreement was observed.

### *3.2. Example 2: Effect of multiple bounded actuators on shape control of smart laminated cantilever piezo composite beams*

A combination of multiple bounded actuator groups positioned at ① and ③ was considered in this example. The applied load, and actuator and composite beam characteristics are shown in Fig. 2a. The same material properties and dimensions, as used in Example 1, were adopted. The actuator patches were subjected to different electrical voltages $V = \{205, 120, 0\}$ [Volts] and the final shape results were plotted in Fig. 3b in 2D and Fig. 4b in 3D, respectively. It is obviously seen that the combination of actuator groups can

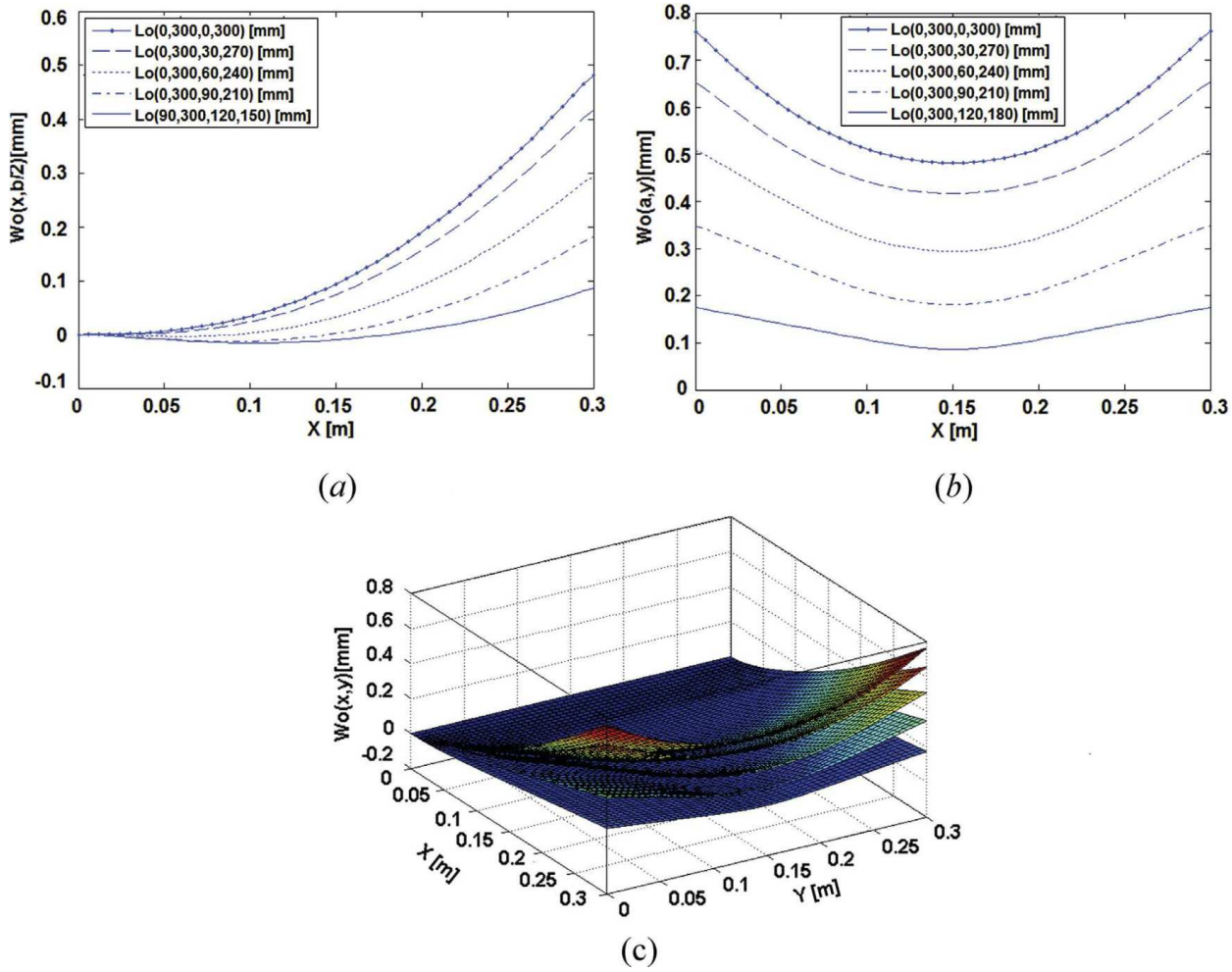


**Fig. 11.** Effect of in-plane transverse actuation on shape deformation of smart laminated cantilever piezo composite plate: (a) $w_o(x,b/2)$, (b) $w_o(a,y)$, (c) $w_o(x,y)$.

result in saving energy for shape control task. Compared with example 1, the multiple actuators proved to significantly reduce the mid-plane deflection. However, the best results were achieved when multiple actuators were subjected to the highest voltage. The results, illustrated were verified with the ones presented in Ref [1] and good agreement was achieved. According to Examples 1–2, it can be concluded that a higher electrical voltage and electrical filed intensity are required to suspend the effect of higher concentrated load applied at the free end. Thus, the use of multiple actuator patches would be more beneficial and optimal compared with a single actuator patch.

### *3.3. Example 3: Effect of multiple bounded/embedded actuators on shape control of smart laminated cantilever piezo composite beams*

The mid-plane deflection of a smart cantilever piezo composite beam as shown in Fig. 2a was suspended using multiple combined embedded and bounded actuator patches positioned at ① and ③. The same material properties and dimensions, as used in Example1, were considered in this example. In order to see the sole effect of embedded and bounded actuators on the host structure (laminated composite beam), the amount of electrical voltage was kept constant at $V = 43$ [Volts]. According to the 2D and 3D results presented in Figs. 3c and 4c, respectively, any increase in the number of embedded actuator patches results in the beam's deflection reducing significantly due to the two facts: (1) multiple actuator patches produce electrical bending moments independently, and (2) the multiple bounded/embedded actuator patches strengthen the beam's stiffness by increasing the layup thickness. The results were compared with the ones presented in Ref [1] and a good agreement was confirmed. However, as the number of embedded/bounded actuator layers increased, minor error was seen since the effect of transverse shear deformation on thick laminates become more significant.

### *3.4. Example 4: Effect of combined optimal electrical voltage and multiple bounded/embedded actuator patches on shape control of smart laminated cantilever piezo composite beams*

In this part, combined effect of optimal voltage and the number of embedded/bounded actuator patches on shape control of a smart cantilever piezo composite beam with characteristics as shown in Fig. 2a was investigated and the 2D and 3D results were plotted in Figs. 5a–d and Fig. 6a–d, respectively. The same material properties and dimensions, as used in Example1, were adopted. Embedded/bounded actuator patches were positioned at ① and ③. As seen in Example1, single bounded actuators require higher electrical voltage and electric field intensity for desired shape control performance compared with Examples 2–3. In addition, adding multiple bounded/embedded actuators to the host structure enhances the stiffness and boosts induced electrical bending moment as seen in Example 3. Higher electrical voltage leads to a strong electric field intensity and, therefore the higher risk of being destroyed in actuators. It is also cost effective and not

efficient, requiring more maintenance and inspections. Thus, in this example, the emphasis is placed on using optimal low control voltage for the desired shape control task. Through classical trial and error techniques, the optimal voltages were calculated. The results were then verified by Ref [1]. Again minor error was seen between the results for 4th-layered and 5th-layered embedded/bounded actuator patches since the effect of transverse shear deformation on thic$^k$ laminates become more significant. It was also obvious that when the number of embedded/bounded actuators was increased, the lower optimal electrical voltage was required for the desired shape control performance as seen in the results.

### 3.5. Example 5: Effect of electro-mechanical coupling on shape control of smart bimorph and laminated piezo composite beams

Bimorph beams (cantilever PZT benders) are potentially used for power and voltage generation by transforming ambient vibrations into electrical energy. This device can potentially replace the battery that supplies the power in a microwatt range necessary for operating sensors and data transmission. Thus, shape deformation analysis of these structures is important [37]. In this example, the effect of various pure electrical voltage on a 2*th*-layered KYNAR piezoelectric bimorph beam ($a$ = 80 [mm], $b$ = 10 [mm]) was investigated and the results were plotted in Fig. 7a. The schematic of the bimorph beam in this example is illustrated in Fig. 2b. Each KYNAR actuator layer has the thickness of $t_a$ = 0.2 [mm]. Subsequently, the tip deflection results were tabulated in Table.2 and then compared with the results in Refs [11] and [33]. The results were in excellent agreement. When an external voltage is applied through beam's thickness, the induced strain generates control moments capable of bending the beam and any increase in the electrical voltage resulted in a larger deflection as the maximum deflection was calculated to be at $V$ = 500 [Volts]. Shape control of a smart laminated cantilever piezo composite beam ($a$ = 0.254 [m], $b$ = 0.0254 [m]) was considered, afterward. The host structure was made of AS/3501 GFRP with stacking sequence of $[0/90]_s$ and sandwiched by a pair of thin actuator layers as shown in Fig. 2c. Actuators and host structure have the thickness of $t_a$ = 0.2 [mm], and $t_p$ = 5.08 [mm], respectively. The beam was first subjected to uniform pressure of $P_o$ = 2 [kPa] and various pure electrical loads. The results are shown in Fig. 7b. Furthermore, the tip deflection results were tabulated in Table 3 and then compared and verified with the results of Ref [33]. It was noticed that shape control task of reducing the mid-plane deflection of a uniformly pressurized smart cantilever laminate composite beam was excellently performed with the use of a pair of bounded actuator layers. For instance, by applying high electrical voltage of $V$ = 250 [Volts], the structure almost comes back to the undeformed shape.

### 3.6. Example 6: Effect of bounded actuator plies and patches on shape control of smart laminated cantilever piezo composite plates

Numerous FE studies have been carried out for the shape control analysis of smart plates. Plate's displacement fields can be calculated using Higher Order Shear Deformation theory (HSDT) [38] as an initial step to mathematically formulate the FE modeling. In this example, shape control task of a smart cantilever laminated piezo composite plate sandwiched by piezoelectric actuator layers and patches made of PZT G1195 N was implemented. The schematic of the cantilever plate with bounded actuator layers and patches under uniform pressure is shown in Fig. 8a–b, respectively. It was assumed that a square plate ($a$ = $b$ = 0.4 [m]) was under $P_o$ = 2.5 [kPa] and actuator layers/patches were under constant external voltage of $V$ = 40 [Volts]. The host structure is composed of $[0/90]_s$ configuration and made of T300/976 GFRP. When a pair of actuator layers was considered, $t_p = t_c$ = 1.25 [mm], while $t_a$ = 0.1 [mm] and $t_p$ = 2.5 [mm] when the actuator patches were considered. The 2D and 3D results are shown in Fig. 9a–b using the proposed explicit method and then verified with the results in the

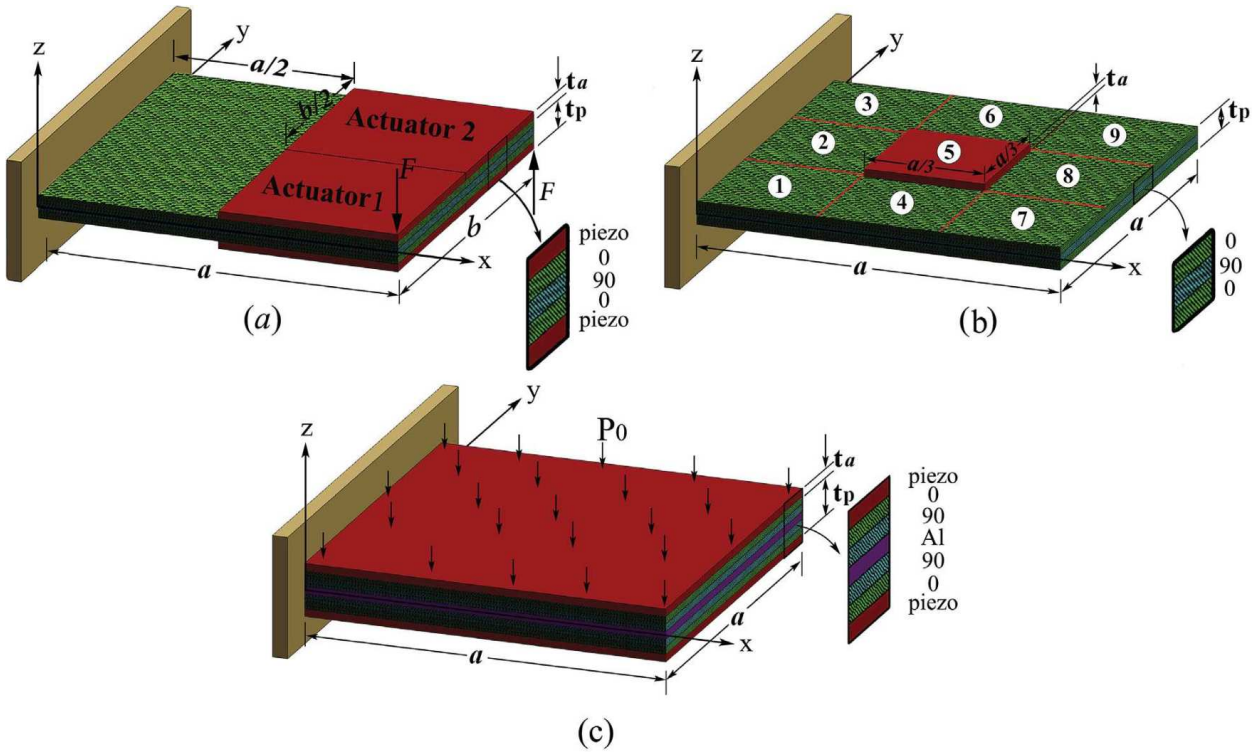


**Fig. 12.** Schematic of smart laminated cantilever piezo composite plate with (a) combined piezoelectric actuator patches, (b) separate actuator patches, (c) bounded actuator layers and core aluminum layer.

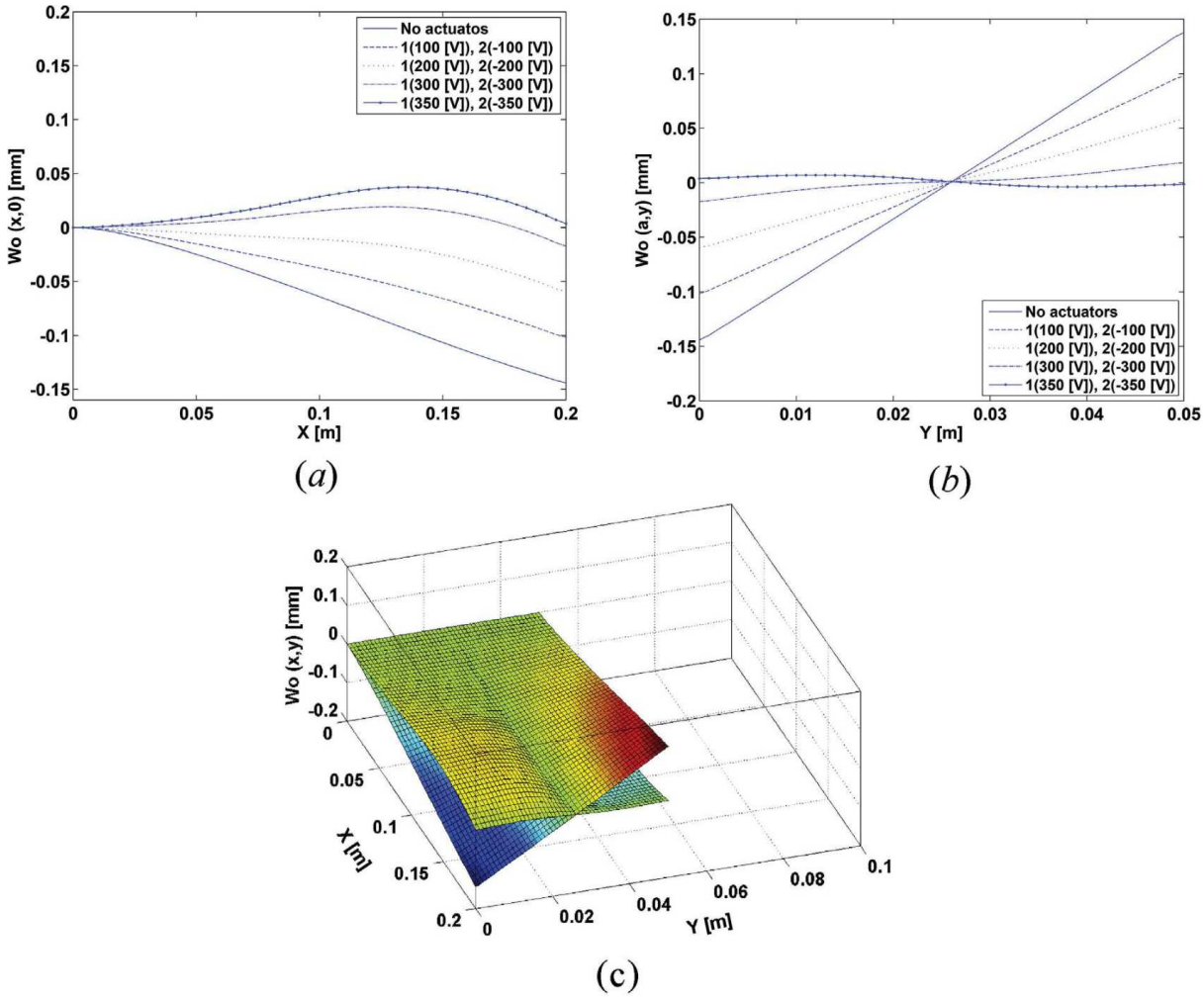


**Fig. 13.** Effect of optimal voltage to suppress twisting deformation of smart laminated cantilever piezo composite plate under twisting load: (a) $w_o(x,0)$, (b) $w_o(a,y)$, (c) $w_o(x,y)$.

literature based on FE formulation using HSDT theory and commercial FE package ANSYS [10]. Well agreement of the solutions was met. It was noticed that thicker actuators and composite plies resulted in the mid-plane deflection reducing significantly regardless of actuators size and placement.

### *3.7. Example 7: Effect of core/embedded/ bounded actuator layers on shape control of smart laminated cantilever piezo composite plates*

Some of the advantages of having actuators/sensors embedded into smart structures rather than bounded to the outer surface can be; (1) effect of shape ties on actuation in spots is difficult to access from outside, (2) protecting actuation system inside smart structures due to harsh environment affecting the actuation performance such as atmospheric agents. Thus, in this example, the effect of core/embedded actuator plies made of PZT G1195 N (see Fig. 8c) on the shape control of a smart laminated cantilever composite square plate ($a = b = 0.4$ [m]) made of T300/976 GFRP was investigated and compared with the bounded ones. The electrical voltage was kept constant at $V = 42$ [Volts]. Thickness of piezoelectric actuators and composite layers are $t_a = 0.2$ [mm] and $t_p = 2$ [mm], respectively. It was assumed that the plate was subjected to the uniform patch loading of $P_o = -1$ [kPa]. The 2D and 3D results for the stacking sequences of $[\text{Piezo}/0/90]_s$, $[0/\text{Piezo}/90]_s$, and $[0/90/\text{Piezo}]_s$ are shown in Fig. 10a–b, respectively. It was observed that the bounded actuator layers had the most effective shape control performance while the core actuators were the least to induce the structural shape. Thus, the core actuators would not be a good choice for shape control task of smart cantilever composite structures over embedded ones in harsh environments.

### *3.8. Example 8: Effect of piezoelectric size on transverse shape deformation of smart laminated cantilever piezo composite plates*

For width plates, the effect of transverse actuation on shape deformation performance as a result of piezoelectric dielectric constant $d_{32}$, can be significant. Transverse actuation is dependent on various factors such as piezoelectric placements and size, plate width, intensity of applied external electrical voltage, and piezoelectric actuator type. In this part, the effect of transverse actuation on a smart laminated cantilever square plate ($a = b = 0.3$ [m]) with bounded actuator patches was investigated. The plate was subjected to a constant voltage of $V = 50$ [Volts]. Various actuators made of PZT G1195 N with different size were selected for this purpose. The function $L_o(x_1,x_2,y_1,y_2)$ [mm] was defined to explain the size and placement of the bounded piezoelectric actuator patches. The effect of the bounded piezoelectric patches placement defined as $L_o(0,300,0,300)$, $L_o(0,300,30,270)$, $L_o(0,300,60,240)$, $L_o(0,300,90,210)$, and $L_o(90,300,120,150)$ on the shape deformation task of a smart laminated cantilever composite plate was

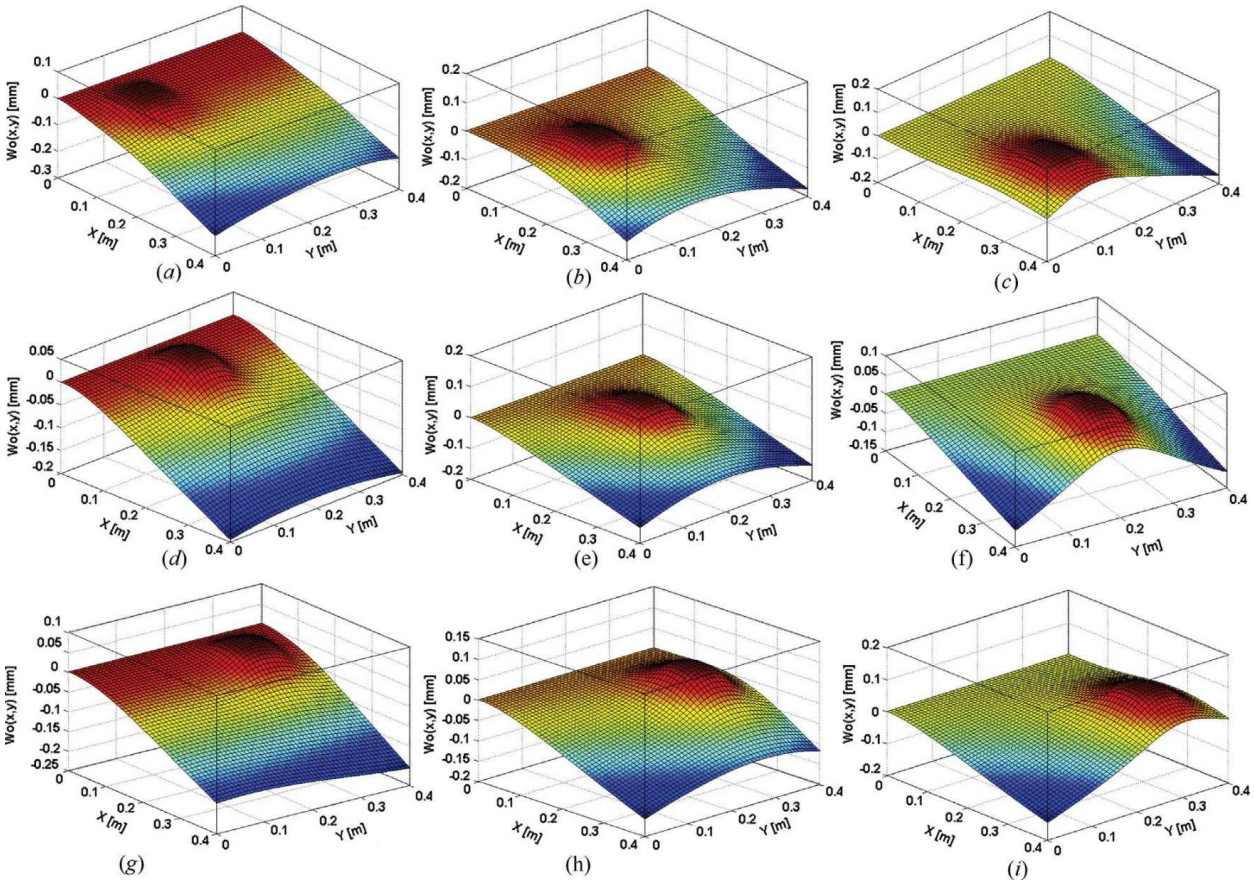


**Fig. 14.** Effect of actuator patches placement on shape deformation of smart laminated cantilever piezo composite plate (see Fig. 2h) centred at (a) ①, (b) ④, (c) ⑦, (d) ②, (e) ⑤, (f) ⑧, (g) ③, (h) ⑥, (i) ⑨.

investigated and their transverse actuation effect were compared. The host structure is composed of $[0/90]_s$ configuration and made of T300/976 GFRP. Thickness of the piezoelectric actuator patches and composite layers are $t_a = 0.2$ [mm] and $t_p = 2$ [mm], respectively. The 2D and 3D results are shown in Fig. 11a–c, respectively. According to the results, the wider actuator patches resulted in more deflection as the plate curvature increased while the narrow actuator patches with respect to $y$ axis resulted in less deflection and lower curvature.

### 3.9. Example 9: Effect of optimal electrical voltage on twisting suppression of smart laminated cantilever piezo composite plates

Some loading conditions can result in significant twisting moments in cantilever plates. In this example, through two pairs of bounded actuator patches made of PZT G1195 N and under constant optimal voltages, a shape control task was performed to supress the effect of twisting moment $M_{xy}$ caused by two concentrated loads ($F_1 = 1$ [$N$] and $F_2 = -1$ [$N$]) in the smart laminated cantilever piezo composite plate ($a = 0.2$ [m] and $b = 0.05$ [m]) (see Fig. 12a). The point loads resulted in twisting moment occurring in the plate. The host structure is composed of [0/90/0] configuration and made of T300/976 GFRP. Thickness of the piezoelectric actuator patches and composite layers are $t_a = 0.2$ [mm] and $t_p = 1.5$ [mm], respectively. Through classical trial and error techniques, the amounts of optimal voltage were calculated and the shape control task was then performed to fully supress the effect of twisting moment. The 2D results are shown in Fig. 13a–b, respectively. The initial and final shapes before and after applying the electrical voltage are illustrated in a 3D graph (see Fig. 13c). It was noticed that combination effect of piezoelectric actuators placement and applied electrical voltage on shape control task was significant. It was also noticed that shape control task could be perfectly implemented if each actuator received different constant electrical voltage.

### 3.10. Example 10: Effect of actuator patch placement on shape deformation of smart laminated cantilever piezo composite plates

In this example, the effect of thin pair of bounded actuator patches made of PZT G1195 N on shape deformation of a width and long smart cantilever piezo composite square plate ($a = b = 0.4$ [m]) was studied. The actuator patches placements are shown in Fig. 12b. The host structure is composed of [0/90/0] configuration and made of T300/976 GFRP. Thickness of the piezoelectric actuator patches and composite layers are $t_a = 0.2$ [mm] and $t_p = 1.5$ [mm], respectively. The constant electrical voltage of $V = 50$ [Volts] was applied to the actuators. The shape deformations considering various actuator placements are shown in Fig. 14a–i, respectively. The results clearly demonstrated that the amount of bending moments produced in the plate differs significantly and ultimately results in different shape deformation as the actuator placement varies. In addition, actuators positioned close to the plate's edges along the $y$ axis resulted in the unsymmetrical deformation.

**Table 4**
Effect of electrical voltage on shape control of smart laminated cantilever piezo composite beam induced by thermal loads using actuator patches centred at ① and ② (see Fig. 2a).

| $\Delta T$ [°C] | $V$ [Volts] | $\frac{w_0(\frac{a}{5},\frac{b}{2})}{H}$ | $\frac{w_0(\frac{2a}{5},\frac{b}{2})}{H}$ | $\frac{w_0(\frac{3a}{2},\frac{b}{2})}{H}$ | $\frac{w_0(\frac{4a}{5},\frac{b}{2})}{H}$ | $\frac{w_0(a,\frac{b}{2})}{H}$ |
|---|---|---|---|---|---|---|
| $\Delta T = 30$ | $V = 0$ | −0.0180 | −0.0713 | −0.1607 | −0.2869 | −0.4462 |
| | $V = 30$ | −0.0034 | −0.0129 | −0.0437 | −0.1107 | −0.2115 |
| | $V = 50$ | 0.0062 | 0.0260 | 0.0343 | 0.0068 | −0.0551 |
| | $V = 70$ | 0.0159 | 0.0649 | 0.1123 | 0.1243 | 0.1014 |
| | $V = 100$ | 0.0305 | 0.1232 | 0.2294 | 0.3005 | 0.3361 |
| $\Delta T = 70$ | $V = 0$ | −0.0419 | −0.1663 | −0.3750 | −0.6695 | −1.0412 |
| | $V = 30$ | −0.0274 | −0.1080 | −0.2580 | −0.4933 | −0.8065 |
| | $V = 50$ | −0.0177 | −0.0691 | −0.1800 | −0.3758 | −0.6501 |
| | $V = 70$ | −0.0080 | −0.0302 | −0.1020 | −0.2583 | −0.4936 |
| | $V = 100$ | 0.0065 | 0.0282 | 0.0151 | −0.0821 | −0.2589 |
| $\Delta T = 120$ | $V = 0$ | −0.0719 | −0.2851 | −0.6429 | −1.1477 | −1.7850 |
| | $V = 30$ | −0.0574 | −0.2267 | −0.5259 | −0.9715 | −1.5503 |
| | $V = 50$ | −0.0477 | −0.1878 | −0.4478 | −0.8540 | −1.3938 |
| | $V = 70$ | −0.0380 | −0.1489 | −0.3698 | −0.7365 | −1.2373 |
| | $V = 100$ | −0.0235 | −0.0906 | −0.2528 | −0.5603 | −1.0026 |
| $\Delta T = 175$ | $V = 0$ | −0.1584 | −0.6282 | −1.4166 | −2.5290 | −3.9333 |
| | $V = 30$ | −0.0903 | −0.3574 | −0.8205 | −1.4975 | −2.3684 |
| | $V = 50$ | −0.0806 | −0.3185 | −0.7425 | −1.3801 | −2.2119 |
| | $V = 70$ | −0.0709 | −0.2796 | −0.6645 | −1.2626 | −2.0555 |
| | $V = 100$ | −0.0564 | −0.2213 | −0.5475 | −1.0864 | −1.8207 |

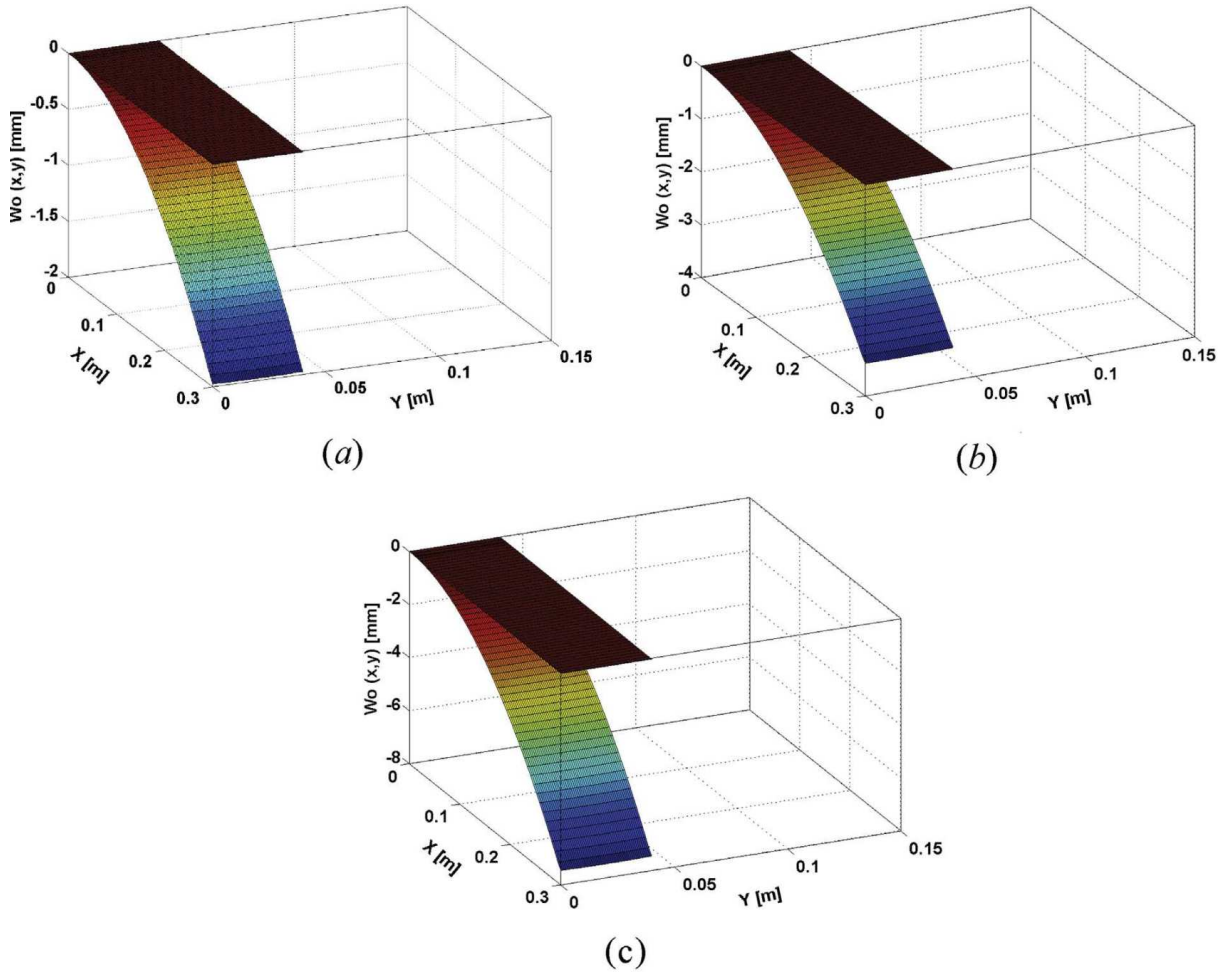


**Fig. 15.** Optimal electrical voltage for shape control of smart laminated piezo composite beam under non-uniform thermal loads using bounded actuator layers: (a) 86 [Volts] and 70[°C], (b) 148 [Volts] and 120[°C], (c) 215 [Volts] and 175[°C].

### 3.11. Example 11: Optimal shape control of smart laminated cantilever piezo composite beams under residual thermal stresses

Laminated composite structures are quite often subjected to harsh thermal environment in which residual thermal stresses are remained throughout laminates. Thermal stresses can result in early crack initiation and propagation in structures under arbitrary loads [39]. Thus, in particular cases, design against thermal loads can become a primary factor. Due to widely existence of non-uniform temperature fields, laminated structures are often affected by non-uniform thermal loads [40,41]. One of the aims of this research is to suspend shape deformation (snap-through) effect of residual thermal stresses occurring in smart laminated cantilever composite plates and beams using piezoelectric actuators. In this example, the schematic of the smart laminated cantilever piezo composite beam is same as Fig. 2a. The host structure consists of Prepreg CFRP [0/90/0] and is sandwiched by a pair of PZT G1195 N piezoelectric layers/patches. Before integrating the actuators into the host structure, the uniform transverse temperature gradient along $z$ direction was applied to the host structure whose bottom layer was presumably kept isolated to avoid the temperature passing through the thickness. Thus, it resulted in non-uniform temperature gradient through thickness. Subsequently, the actuators were incorporated into the composite laminate. In the first attempt, the beam was subjected to the thermal loads of $\Delta T = \{30, 70, 120, 175\}$ [°C], respectively. Two pairs of actuator patches were first positioned at ① and ② and then subjected to various constant electrical voltages. The effect of thermo-electrical loads on shape deformation is shown in Table.4. The results showed that the piezoelectric actuators can significantly induce smart laminated cantilever composite structures under residual thermal stresses. Therefore, by applying appropriate electrical voltage, shape control task of reducing thermal stresses snap-through effect can be perfectly implemented. In the second attempt, the actuator patches were replaced by a pair of bounded actuator layers. Through classical trial and error techniques, the optimal voltages $V = \{86, 148, 215\}$ [Volts] were calculated and applied to the beam subjected to $\Delta T = \{70, 120, 175\}$ [°C], respectively in order to fully suspend the non-uniform thermal loads snap-through effect. According to Fig. 15a–c, it is observed that as the thermal stresses increase, higher amount of optimal electrical voltage is required for optimal shape control performance and fully suppression of the snap-through effect.

### 3.12. Example 12: Effect of thermo-electro-mechanical loads on shape deformation of smart laminated cantilever piezo composite hybrid plates

In the final example, more complex loading system was presented. A smart laminated cantilever piezo composite hybrid plate made of bounded PZT G1195 N actuator layers, laminated Prepreg CFRP composite, and an aluminum core was subjected to the

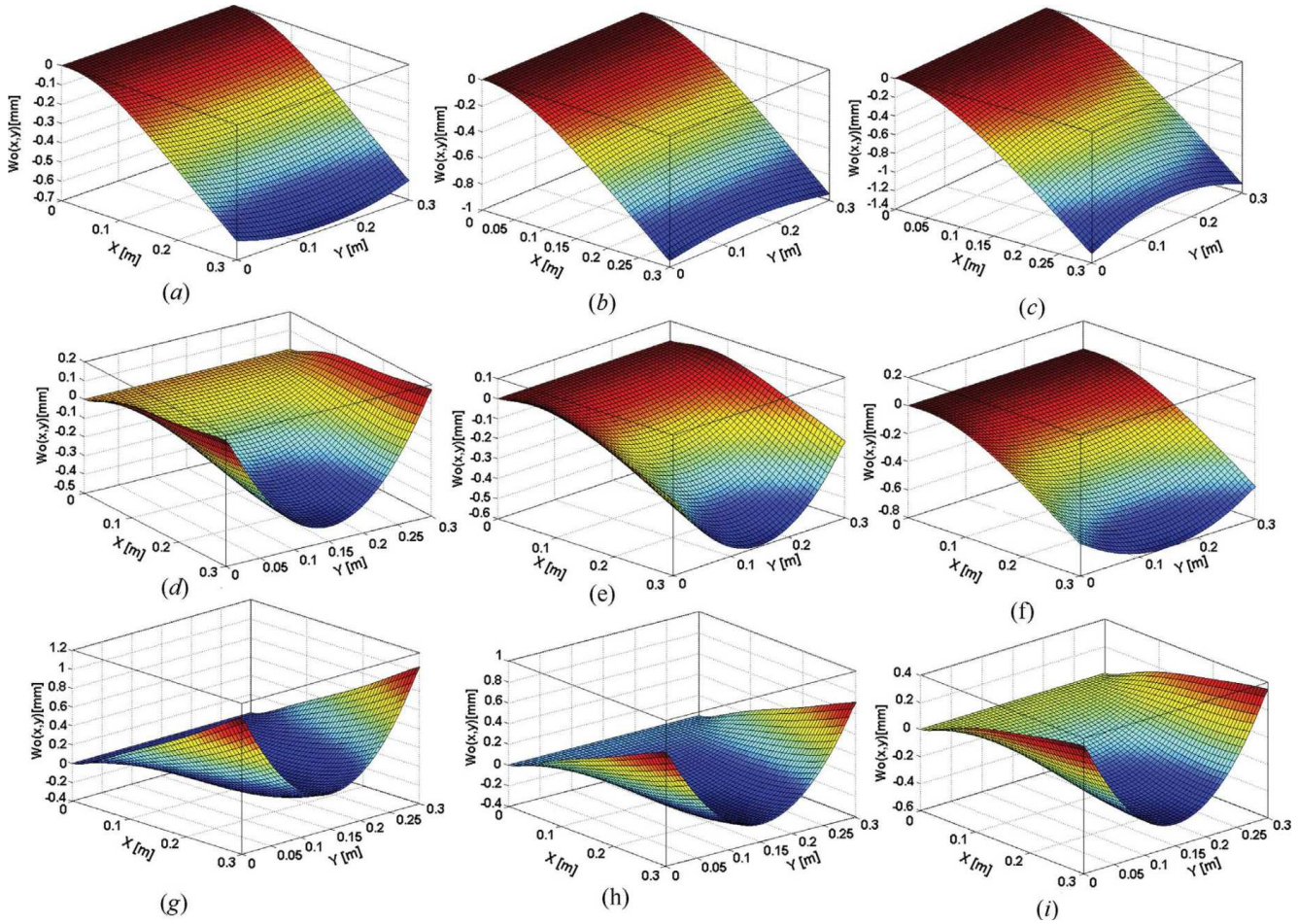


**Fig. 16.** Effect of thermo-electro-mechanical loads on shape deformation of smart laminated cantilever piezo composite hybrid plate under combined uniform pressure $P_o = -1$ [kPa] and non-uniform temperature function: (a–c) $T_{bot} = 30$ [°C] and $V = 0$, 100, 200 [Volts], respectively; (d–f) $T_{bot} = 70$ [°C] and $V = 0$, 100, 200 [Volts], respectively; (g–i) $T_{bot} = 120$ [°C] and $V = 0$, 100, 200 [Volts], respectively.

thermal load (see Fig. 12c). The temperature of the top surface $T_{top}$ was kept constant at the room temperature of 20[°C] while $T_{bot}$ = {30, 70, 120} [°C] were applied at the bottom surface. It is assumed that the thermal load varies non-uniformly through thickness, $\Delta T(z) = T_a H^{-1} z + T_b$, where: $T_a = T_{bot} - T_{top}$ and $T_b = 0.5(T_{bot} + T_{top})$. The uniform pressure $P_o = -1.0$ [kPa] was applied to the plate. In addition, the bounded actuator layers were activated by the various constant electrical voltages $V$ = {0, 100, 200} [Volts], respectively. The combination of thermo-electro-mechanical loading system changed the structural shape considerably as shown in Fig. 16a–i. The results illustrated the snap-through effect along the plate's edges using the activated bounded actuator layers is significant. Furthermore, the effect of uniform pressure on plate's curvature deformation was also noticeable. In a case, when the amount of thermal load is not significant as seen in Fig. 16a–c, the plate is subjected to the curvature sign transformation when the applied electrical voltage increase.

## 4. Conclusion

In this study, a new explicit exact analytical solution was proposed for the shape control analysis of smart laminated cantilever piezo composite hybrid plates and beams under thermo-electro-mechanical loads. Embedded/bounded piezoelectric layers/patches were used to achieve the desired shape control task. According to the results, following remarks can be concluded:

1. The shape control task in smart laminated cantilever piezo composite hybrid plates and beams can be well implemented using the proposed explicit exact analytical solution. Unlike previous studies, the new proposed method demonstrated its ability to cover more general problems concerning the shape control task of smart cantilever structures. The method is particularly well suited for long and wide plate cases where actuator patches were positioned far from fixed ends. Furthermore, unlike in previous studies, the explicit exact analytical solution proposed in this research does not require the characteristic and trial deflection function to be predetermined for shape control performance.
2. Higher electrical voltage leads to a greater actuation and more significant shape control performance. However, thicker actuators have less actuation power due to low electrical filed produced through actuators' thickness while improving the laminates' stiffness against flexural deformation. Thus, through selecting appropriate actuators in terms of size and elastic/electrical properties, the optimal shape control task can be achieved.
3. Effect of piezoelectric actuators' size and placement in shape control of smart structures is significant. Generally, actuator layers have higher actuation compared with actuator patches. Actuator patches placed close to the fixed end have more optimal shape control performance while their ability to overcome shape deformation reduces significantly as positioned far from fixed end. Furthermore, bounded actuator layers/patches proved to be a better choice for optimal shape control of smart structures compared with embedded and core actuators.

## Acknowledgements

Scott Gohery would like to thank for the Victoria University International Postgraduate Research scholarship (VUIPRS) offered by the College of Engineering and Science to undertake his Ph.D. study. This financial support is gratefully acknowledged.

## Appendix A

The simplified 2D thermo-electro-mechanical plate equations are derived from 3D equations of theory of elasticity and three charged equilibrium equations of piezoelectric medium as shown in Eq. (A1).

$$\begin{bmatrix}\sigma_{11}\\ \sigma_{22}\\ \sigma_{33}\\ \tau_{23}\\ \tau_{31}\\ \tau_{12}\end{bmatrix} = \begin{bmatrix} C_{1111} & C_{1122} & C_{1133} & 0 & 0 & 0\\ C_{1122} & C_{2222} & C_{2233} & 0 & 0 & 0\\ C_{1133} & C_{2233} & C_{3333} & 0 & 0 & 0\\ 0 & 0 & 0 & C_{2323} & 0 & 0\\ 0 & 0 & 0 & 0 & C_{3131} & 0\\ 0 & 0 & 0 & 0 & 0 & C_{1212}\end{bmatrix} \times \begin{bmatrix}\varepsilon_{11}-\alpha_{11}\Delta T\\ \varepsilon_{22}-\alpha_{22}\Delta T\\ \varepsilon_{33}\\ \gamma_{23}\\ \gamma_{31}\\ \gamma_{12}-\alpha_{12}\Delta T\end{bmatrix} - \begin{bmatrix} 0 & 0 & e_{311}\\ 0 & 0 & e_{322}\\ 0 & 0 & e_{333}\\ 0 & e_{223} & 0\\ e_{113} & 0 & 0\\ 0 & 0 & 0\end{bmatrix}\begin{bmatrix}E_1\\ E_2\\ E_3\end{bmatrix} \tag{A1}$$

$\sigma_{ij}, \varepsilon_{ij}, C_{ijkl}, \alpha_{ij}, \Delta T, e_{ijk}$, and $E_{ij}$ are the stresses, the strains, the elastic stiffness, thermal expansion coefficients, temperature difference from the reference point (room temperature), piezoelectric coefficients, and the components of the electric fields, respectively in the orthotropic material orientation. The plane stress assumption ($\sigma_{33} = \sigma_{23} = \sigma_{13} = 0$) is used to simplify Eqs. (A1) and (A2).

$$\begin{bmatrix}\sigma_{11}\\ \sigma_{22}\\ 0\\ 0\\ 0\\ \tau_{12}\end{bmatrix} = \begin{bmatrix} C_{1111} & C_{1122} & C_{1133} & 0 & 0 & 0\\ C_{1122} & C_{2222} & C_{2233} & 0 & 0 & 0\\ C_{1133} & C_{2233} & C_{3333} & 0 & 0 & 0\\ 0 & 0 & 0 & C_{2323} & 0 & 0\\ 0 & 0 & 0 & 0 & C_{3131} & 0\\ 0 & 0 & 0 & 0 & 0 & C_{1212}\end{bmatrix} \times \begin{bmatrix}\varepsilon_{11}-\alpha_{11}\Delta T\\ \varepsilon_{22}-\alpha_{22}\Delta T\\ \varepsilon_{33}\\ \gamma_{23}\\ \gamma_{31}\\ \gamma_{12}-\alpha_{12}\Delta T\end{bmatrix} - \begin{bmatrix} 0 & 0 & e_{311}\\ 0 & 0 & e_{322}\\ 0 & 0 & e_{333}\\ 0 & e_{223} & 0\\ e_{113} & 0 & 0\\ 0 & 0 & 0\end{bmatrix}\begin{bmatrix}E_1\\ E_2\\ E_3\end{bmatrix} \tag{A2}$$

The Kirchhoff assumption adapted for plate theory stipulates that $\gamma_{23} = \gamma_{31} = 0$. In addition, only a through-thickness electric field is considered ($E_1 = E_2 = 0$). Therefore, Eq. (A2) is reduced to Eq. (A3). Global stresses in the $k$th ply along $xyz$ direction can be calculated by transforming 2D stresses in the material direction through transformation matrix $[T]$ as stated in Eq. (A4).

$$\begin{bmatrix}\sigma_{11}\\ \sigma_{22}\\ \tau_{12}\end{bmatrix} = \begin{bmatrix} Q_{11} & Q_{22} & 0\\ Q_{12} & Q_{22} & 0\\ 0 & 0 & Q_{66}\end{bmatrix}\begin{bmatrix}\varepsilon_{11}-\alpha_{11}\Delta T\\ \varepsilon_{22}-\alpha_{22}\Delta T\\ \gamma_{12}-\alpha_{12}\Delta T\end{bmatrix} - \begin{bmatrix}e_{31}\\ e_{32}\\ 0\end{bmatrix}\begin{bmatrix}0\\ 0\\ E_3\end{bmatrix} \tag{A3}$$

$$[\sigma]_k^{Global} = [T]^{-1}[\sigma]_k^{Local} \tag{A4}$$

where,

$$[T] = \begin{bmatrix} c^2 & s^2 & 2cs\\ s^2 & c^2 & -2cs\\ -cs & cs & (c^2 - s^2)\end{bmatrix}$$

$c$ is $cos(\beta)$ and $s$ is $sin(\beta)$, $Q_{ij}$s and $e_{ij}$s are the reduced elastic stiffness and reduced piezoelectric coefficients, respectively, which are given in Eqs. (A5–10), respectively.

$$Q_{11} = C_{1111} - \frac{C_{1133}^2}{C_{3333}} = \frac{E_1}{1 - v_{12}v_{21}} \tag{A5}$$

$$Q_{22} = C_{2222} - \frac{C_{2233}^2}{C_{3333}} = \frac{E_2}{1 - v_{12}v_{21}} \tag{A6}$$

$$Q_{12} = C_{1122} - \frac{C_{1133}C_{2233}}{C_{3333}} = \frac{v_{12}E_2}{1 - v_{12}v_{21}} \tag{A7}$$

$$Q_{66} = C_{1212} = G_{12} \tag{A8}$$

$$e_{31} = e_{311} - \frac{C_{1133}}{C_{3333}}e_{333} = Q_{11}d_{31} - Q_{12}d_{32} \tag{A9}$$

$$e_{32} = e_{322} - \frac{C_{2233}}{C_{3333}}e_{333} = Q_{12}d_{31} - Q_{22}d_{32} \tag{A10}$$

## Appendix B

The first and second partial derivatives of the double Fourier series $w_o(x,y)$ in Eq. (16) for boundary value problems in a cantilever plate can be expanded by:

$$\frac{\partial w_0(x,y)}{\partial x} = \frac{4}{ab}\sum_{m=1,3,5,\ldots}^{\infty}\sum_{n=0,1,2,\ldots}^{\infty}\lambda_n\Gamma^* \cos\left(\frac{\alpha_m}{2}x\right)\cos(\beta_n y) = \frac{4}{ab}\sum_{m=1,3,5,\ldots}^{\infty}\sum_{n=0,1,2,\ldots}^{\infty}\lambda_n\left[\frac{\alpha_m}{2}w_{mn}\right]\cos\left(\frac{\alpha_m}{2}x\right)\cos(\beta_n y) \tag{B1}$$

$$\frac{\partial^2 w_0(x,y)}{\partial x^2} = \frac{4}{ab}\sum_{m=1,3,5,\ldots}^{\infty}\sum_{n=0,1,2,\ldots}^{\infty}\lambda_n\Gamma^{**}\sin\left(\frac{\alpha_m}{2}x\right)\cos(\beta_n y) = \frac{4}{ab}\sum_{m=1,3,5,\ldots}^{\infty}\sum_{n=0,1,2,\ldots}^{\infty}\lambda_n\left[(-1)^{\frac{m-1}{2}}\int_0^b\left(\frac{\partial w_0(x,y)}{\partial x}\middle|(x=a)\right)\times\cos(\beta_n y)dy - \frac{\alpha_m^2}{4}w_{mn}\right]\sin\left(\frac{\alpha_m}{2}x\right)\cos(\beta_n y) \tag{B2}$$

$$\frac{\partial w_0(x,y)}{\partial y} = \frac{4}{ab}\sum_{m=1,3,5,\ldots}^{\infty}\sum_{n=1,2,3,\ldots}^{\infty}\lambda_n\zeta^*\sin\left(\frac{\alpha_m}{2}x\right)\sin(\beta_n y) = \frac{4}{ab}\sum_{m=1,3,5,\ldots}^{\infty}\sum_{n=1,2,3,\ldots}^{\infty}\lambda_n[-\beta_n w_{mn}]\sin\left(\frac{\alpha_m}{2}x\right)\sin(\beta_n y) \tag{B3}$$

$$\frac{\partial^2 w_0(x,y)}{\partial y^2} = \frac{4}{ab}\sum_{m=1,3,5,\ldots}^{\infty}\sum_{n=0,1,2,\ldots}^{\infty}\lambda_n\zeta^{**}\sin\left(\frac{\alpha_m}{2}x\right)\cos(\beta_n y) = \frac{4}{ab}\sum_{m=1,3,5,\ldots}^{\infty}\sum_{n=0,1,2,\ldots}^{\infty}\lambda_n\left[(-1)^n\int_0^a\left(\frac{\partial w_0(x,y)}{\partial y}\middle|(y=b)\right)\times\sin\left(\frac{\alpha_m}{2}x\right)dx - \int_0^a\left(\frac{\partial w_0(x,y)}{\partial y}\middle|(y=0)\right)\sin\left(\frac{\alpha_m}{2}x\right)dx - \left(\frac{\alpha_m^2}{4}+\beta_n^2\right)w_{mn}\right]\sin\left(\frac{\alpha_m}{2}x\right)\cos(\beta_n y) \tag{B4}$$

## References


[1] Yu Y, Zhang XN, Xie SL. Optimal shape control of a beam using piezoelectric actuators with low control voltage. Smart Mater Struct 2009;18(9):1–15.
[2] Her SC, Lin CS. Deflection of cross-ply composite laminates induced by piezoelectric actuators. Sensors 2010;10(1):719–33.
[3] Kattimani SC, Ray MC. Smart damping of geometrically nonlinear vibrations of magneto-electro-elastic plates. Compos Struct 2014;114(1):51–63.
[4] Moghadam PY, Tahani M, Naserian-Nik AM. Analytical solution of piezolaminated rectangular plates with arbitrary clamped/simply-supported boundary conditions under thermo-electro-mechanical loadings. Appl Math Model 2013;37(5):3228–41.
[5] Sartorato M, De Medeiros R, Tita V. A finite element formulation for smart piezoelectric composite shells: mathematical formulation, computational analysis and experimental evaluation. Compos Strcut 2015;127:185–98.
[6] Milazzo A. Variable kinematics models and finite elements for nonlinear analysis of multilayered smart plates. Compos Strcut 2015;122:537–45.
[7] Panahandeh-shahraki D, Mirdamadi HR, Vaseghi O. Fully coupled electromechanical buckling analysis of active laminated composite plates considering stored voltage in actuators. Compos Struct 2014;118:94–105.
[8] Cook AC, Vel SS. Multiscale analysis of laminated plates with integrated piezoelectric fiber composite actuators. Compos Struct 2012;94(2):322–36.
[9] Zhang SQ, Schmidt R. Static and dynamic FE analysis of piezoelectric integrated thin-walled composite structures with large rotations. Compos Struct 2014;112:345–57.
[10] Tamijani AY, Abouhamze M, Mirzaeifar R, Ohadi AR, Eslami MR, Feedback control of piezo-laminate composite plate. In: 14th International congress on sounds and Vibration. Cairns Australia; 9–12 July, 2007.
[11] Koconis DB, Kollar LP, Springer GS. Shape control of composite plates and shells with embedded actuators.1. voltages specified. J Compos Mater 1994;28(5):415–58.
[12] Koconis DB, Kollar LP, Springer GS. Shape control of composite plates and shells with embedded actuators. II. desired shape specified. J Compos Mater 1994;28(3):459–82.
[13] Andakhshideh A, Tahani M. Free-edge stress analysis of general rectangular composite laminates under bending, torsion and thermal loads. Eur J Mech/A Solids 2013;42:229–40.
[14] Gohery S, Sharifi S, Vrcelj Z, Yahya MY. First-ply failure prediction of an unsymmetrical laminated ellipsoidal woven GFRP composite shell with incorporated surface-bounded sensors and internally pressurized. Compos Part B Eng 2015;77:502–18.
[15] Sader JE, White L. Theoretical analysis of the static deflection of plates for atomic force microscope applications. J Appl Phys 1993;74(1):1–9.
[16] Lachut MJ, Sader JE. Buckling of a cantilever plate uniformly loaded in its plane with applications to surface stress and thermal loads. J Appl Phys 2013;113(2):1–11.
[17] Shin DK, Lee JJ. Theoretical analysis of the deflection of a cantilever plate for wirebonding on overhang applications. IEEE Trans. Compon. Packag. Manuf. Technol. 2012;2(6):916–24.
[18] Milazzo A. Refined equivalent single layer formulations and finite elements for smart laminates free vibrations. Compos Part B Eng 2014;61:238–53.
[19] Zhang SQ, Li YX, Schmidt R. Modeling and simulation of macro-fiber composite layered smart structures. Compos Struct 2015;126:89–100.
[20] Plattenburg J, Dreyer JT, Singh R. Active and passive damping patches on a thin rectangular plate: a refined analytical model with experimental validation. J Sound Vib 2015;353:75–95.
[21] Lin JC, Nien MH. Adaptive modeling and shape control of laminated plates using piezoelectric actuators. J Mater Process Technol 2007;189(1–3):231–6.
[22] Bowen CR, Butler R, Jervis R, Kim HA, Salo AIT. Morphing and shape control using unsymmetrical composites. J Intell Mater Struct 2007;18(January).
[23] Giddings P, Bowen CR, Butler R, Kim HA. Characterisation of actuation properties of piezoelectric bi-stable carbon-fibre laminates. Compos Part A Appl Sci Manuf 2008;39(4):697–703.
[24] Thinh TI, Ngoc LK. Static behavior and vibration control of piezoelectric cantilever composite plates and comparison with experiments. Comput Mater Sci 2010;49(4 SUPPL.):S276–80.
[25] Khandelwal RP, Chakrabarti A, Bhargava P. Static and dynamic control of smart composite laminates. AIAA J 2014;52(9):1896–914.
[26] Huang GL, Sun CT. The dynamic behaviour of a piezoelectric actuator bonded to an anisotropic elastic medium. Int J Solids Struct 2006;43(5):1291–307.
[27] Li Y, Onoda J, Minesugi K. Simultaneous optimization of piezoelectric actuator placement and feedback for vibration suppression. Acta Astronaut 2002;50(6):335–41.
[28] Kim J, Varadan VV, Varadan VK, Bao XQ. Finite-element modeling of a smart cantilever plate and comparison with experiments. Smart Mater Struct 1996;5(2):165–70.
[29] Ren L. A theoretical study on shape control of arbitrary lay-up laminates using piezoelectric actuators. Compos Struct 2008;83(1):110–8.
[30] Reddy JN. On laminated composite plates with integrated sensors and actuators. Eng Struct 1999;21(7):568–93.
[31] Duc ND, Quan TQ, Luat VD. Nonlinear dynamic analysis and vibration of shear deformable piezoelectric FGM double curved shallow shells under damping-thermo-electro-mechanical loads. Compos Struct Jul. 2015;125:29–40.
[32] Foutsitzi GA, Gogos CG, Hadjigeorgiou EP, Stavroulakis GE. Actuator location and voltages optimization for shape control of smart beams using genetic algorithms. Actuators 2013;2(4):111–28.
[33] Liew KM, Lim HK, Tan MJ, He XQ. Analysis of laminated composite beams and plates with piezoelectric patches using the element-free Galerkin method. Comput Mech 2002;29(6):486–97.
[34] Honickman H, Johrendt J, Frise P. On the torsional stiffness of thick laminated plates. J Compos Mater 2014;48(21):2639–55.
[35] Shaik Dawood MSI, Iannucci L, Greenhalgh ES. Three-dimensional static shape control analysis of composite plates using distributed piezoelectric actuators. Smart Mater Struct 2008;17(2):1–10.
[36] Ren L. Theoretical study on shape control of thin cross-ply laminates using piezoelectric actuators. Compos Struct 2007;80(3):451–60.

[37] Ajitsaria J, Choe SY, Shen D, Kim DJ. Modeling and analysis of a bimorph piezoelectric cantilever beam for voltage generation. Smart Mater Struct 2007;16(2):447–53.
[38] Reddy JN. Theory and analysis of elastic plates and shells. Taylor and Francis Group; 2007.
[39] Gohery S, Sharifi S, Sharifishourabi G, Vrcelj Z, Abadi R. Effect of temperature on crack initiation in gas formed structures. J Mech Sci Technol 2013;27 (12):3745–54.
[40] Li J, Narita Y, Wang Z. The effects of non-uniform temperature distribution and locally distributed anisotropic properties on thermal buckling of laminated panels. Compos Struct 2015;119:610–9.
[41] Barut A, Madenci E. Thermomechanical stress analysis of laminates with a cutout via a complex potential-variational method. J Therm Stress 2004;27 (1):1–31.

Composite Structures 161 (2017) 477–504

Contents lists available at ScienceDirect

Composite Structures

journal homepage: www.elsevier.com/locate/compstruct

# A novel explicit solution for twisting control of smart laminated cantilever composite plates/beams using inclined piezoelectric actuators

Scott Gohery *, S. Sharifi, Zora Vrcelj

*College of Engineering and Science, Victoria University, Melbourne, VIC 8001, Australia*

ARTICLE INFO

*Article history:*
Received 6 August 2016
Revised 11 September 2016
Accepted 22 November 2016
Available online 23 November 2016

*Keywords:*
Twisting control
Electro-mechanical twisting coupling
Explicit solution
Finite element method (FEM)
Inclined piezoelectric actuators
Smart laminated cantilever composite plates/beams

ABSTRACT

In the present work, a novel explicit analytical solution is proposed for obtaining twisting deformation and optimal shape control of smart laminated cantilever composite plates/beams using inclined piezoelectric actuators. The linear piezoelectricity and plate theories are adapted for the analysis. A novel double integral multivariable Fourier transformation method and discretised higher order partial differential unit step function equations are employed. For the first time, an exact solution is developed to analyse electro-mechanical twisting moments in smart composite structures. Since there are no published benchmark results for verification, a series of simple, accurate and robust finite element (FE) analysis models and realistic electro-mechanical coupled FE procedures are developed for the effective prediction of the structural behaviour of the smart laminated piezo-composite structures under arbitrary loads. In addition to the novelty of the explicit solution, more comprehensive FE simulations of smart structures and step-by-step guidelines are discussed. The effect of various parameters including electro-mechanical twisting coupling, layup thickness, actuators size, placement, and inclination angle, electrical voltage, stacking sequence, and geometrical dimension are taken into account. The comparison of results shows an excellent agreement. Unlike the earlier studies, the proposed method does not require the characteristic and trial deflection function to be predetermined.



## 1. Introduction

Laminated and asymmetric composite structures are being used considerably in aerospace, automotive, civil, mechanical and structural engineering applications due to their high stiffness and strength to weight ratio, low density, and temperature resistance [1–3]. Laminated plates and beams are usually applied to achieve the desired stiffness and lightness for parts of load-bearing engineering structures [4,5]. For instance, laminated cantilever composite plates are adopted widely in various engineering applications such as airplane wings, corrugated plates, reinforced concrete slabs, decks of contemporary steel bridges, boom arms of industrial cranes, and flight control surfaces [6–8]. Piezoelectric materials have recently drawn much attention due to their low power consumption, high material linearity, and quick response when induced by external forces [9–11]. Piezoelectric materials can be integrated with laminated composite structures to provide smart-intelligent composite systems. Numerous smart engineering structures incorporated with smart devices such as piezoelectric sensors and actuators have proved to be superior to their conventional counterparts. Static analysis of advanced composite structures under axial, transverse, twisting, and torsional loads due to piezoelectric materials has potential application in mechanical systems, helicopter rotor blades, and blades for turbomachinery [12]. Some other applications of piezoelectric materials in adaptive engineering structures are acoustical noise reduction, damage identification, structural health monitoring, vibration suppression, deflection control in missile fines, and airfoil shape changes [13,14,15]. One of the great advantages of piezoelectric materials is their ability to respond to changing environment and control structural deformation, which has led to the new generation of aerospace structures like morphing airplanes [11]. Among piezoelectric materials, bounded piezo-ceramic actuators are commonly used for shape control of online monitoring systems. Piezoelectric actuators can also be embedded in laminated composite structures to induce structural stiffness system to the advantage [16–18].

Failure and deformation analysis of load-bearing structures made of isotropic/composite structures with/without piezoelectric materials have been studied broadly by several researchers using analytical methods, FEM and experimental work [19–21]. Milazzo

* Corresponding author. Tel.: +61423656484.
*E-mail addresses:* scott.gohery@unimelb.edu.au (S. Gohery), sharifi.te@gmail.com (S. Sharifi), Zora.Vrcelj@vu.edu.au (Z. Vrcelj).

http://dx.doi.org/10.1016/j.compstruct.2016.11.063
0263-8223/

[22] developed a FE model for the large deflection analysis of multi-layered smart plates. Sartorato et al. [23] worked on a FE formulation for smart composite shells. This smart shell FE formulation was used as a benchmark for his work on dynamic analysis of laminated curved isotropic and orthotropic structures integrated with piezoelectric layers. The presented FE model was then verified with experimental and numerical findings available in open literature. Milazzo [22] developed a family of two dimensional (2D) refined equivalent single layer models for vibration analysis of multilayered and functionally graded smart magneto-electro-elastic plates. The single layer FE model presented in his work was validated against available benchmark three dimensional (3D) solutions. Zhang et al. [24] developed a linear electro-mechanically coupled FE model for thin-walled smart composite laminates bounded with macro-fibre composite (MFC) actuators. Their proposed method was compared with numerical and experimental results. In a similar study, Zhang and Schmidt [25] formulated a FE model based on the large rotation shell theory for static and dynamic analysis of thin-walled smart piezoelectric composite laminates. Plattenburg et al. [26] studied analytically, numerically, and experimentally vibration excitation of a thin plate with free boundary conditions and with multiple bounded piezoelectric actuator patches. Numerical and experimental studies were undertaken by Lin and Nien [27] on static and dynamic shape deformations of laminated plates integrated with piezoelectric actuators and subjected to unknown loads. Their study demonstrated the effectiveness of piezoelectric actuators on the shape and deflection control of composite laminates. Other experimental and numerical studies concerning the deflection and shape control of smart laminated cantilever and simply-supported composite plates and beams, as well as unattached laminates, can be found in Refs. [27–30]. The FE simulation of composite structures with/without piezoelectric actuators have been studied by several researches using FE commercial software. Gohari et al. [31,32] studied the mechanical deformation of laminated composite domes under internal pressure using FE simulation and compared the results with the theoretical ones based on classical shell theory. There are also numerous studies regarding the FE simulation of laminated thin/thick composite cylindrical shells under arbitrarily static [33–35] and dynamic [36,37] loads. Several studies regarding the FE simulation of composite plates induced by piezoelectric actuators can be found in Refs. [38,39].

There are few works presenting the effect of flexural-torsion loads on composite structures with or without piezoelectric elements. Considering torsional-bending coupling mode of beams, a very limited published benchmark results are available. Sakawa and Luo [40], adapted a shear deformable theory for modelling of a mass-coupled beam considering the internal beam damping in which a motor shaft was used to create actuation torque. The effect of warping torsion on natural frequency of a composite beam, when considering the transverse shear deformation for various beam aspect ratios, was investigated in multiple studies [41–43]. In addition, the vibration analysis of a beam adopting Timoshenko's beam theory and excluding the effect of warping torque was studied by Banerjee and Williams [44].

There are a few researchers who studied the torsion-bending behaviour of smart structures analytically, numerically, and experimentally. Park et al. [45] developed new models for prediction of the torsion-bending and couple extension in a beam using piezoelectric patches with arbitrary orientation with respect to the beam axis. The model was based on a Newtonian shear lag formulation, neglecting the through-thickness strain variation in the actuator patches. However, the strain variation through-thickness of the beam was assumed to be linear. A new model to predict the effect of coupled extension and torsion-bending in a beam incorporated with piezoelectric actuators was then developed by Park and Chopra [46]. Their experimental results showed accuracy when the piezoelectric actuators had the inclination angles up to 45 degrees with respect to the beam axis. In another similar study by Chen and Chopra [47], the static bending and torsion response of a fraud-scale helicopter rotor blade was investigated. Takawa et al. [48] used the piezoelectric actuators with 90-degree inclination angle with respect to the beam principle axis to control the torsional vibration mode of the beam. Thirupathi et al. [49] investigated the effect of piezoelectric actuators on the blades for turbomachinery application using FEM. The quadrilateral shell FE model with eight nodes and curved edges was adapted for the numerical analysis of piezoelectric actuated blades. Subsequently, the results were verified using experimental findings and a good agreement between numerical and experimental results was observed. In their experimental work, the piezoelectric actuated blades were modelled as piezo-ceramic cantilevered bimorph beam.

It can be observed from available literature that most of the studies on smart piezo-composite laminates were based on experimental and/or numerical approach. In addition, there are no exact solutions for the twisting analysis of smart cantilever composite structures induced by electrical twisting moment. There are also very limited number of studies on the torsion and deflection of beams in which the effect of different parameters, such as electro-mechanical twisting coupling, layup thickness, piezoelectric actuators size, placement, and inclination angle, electrical potential intensity, stacking sequence, and geometrical dimension, were not taken into account. Furthermore, some theories adapted for the analysis of smart structures displacement fields result in significant computational time required due to a large number of degrees of freedom [50]. Smart cantilever composite plates and beams are important structural elements, but their exact analytical evaluation is one of the most difficult problems in the theory of elasticity. Multi-scale and approximation solutions, typically adapted for analytical evaluation of smart composite laminates, are complex and require characteristic and trial deflection functions to be predetermined.

In the present work, a new explicit solution is proposed for obtaining twisting-bending deformation and optimal shape control of smart laminated cantilever composite plates and beams using inclined piezoelectric actuators. The linear piezoelectricity and plates theories are adapted for the analysis. The results are then compared with the numerical results by using finite element method (FEM). A series of simple, accurate and robust FE analysis models and realistic electro-mechanical coupled FE procedures are developed for the accurate and reliable prediction of the structural behaviour of smart laminated cantilever piezo composite structures under arbitrary electro-mechanical loads. The ABAQUS FE package is adopted for this purpose. MATLAB was also employed to obtain structural twisting-bending deformations of smart cantilever piezo composite plates/beams for the explicit evaluation of the results. Calculation of required optimal voltages to suppress the twisting-bending deformation was based on classical trial and error techniques.

## 2. Mathematical modelling

Consider a cantilever laminated composite plate composed of $N$ orthotropic layers and with a total layup thickness of $H$. Each layer can be incorporated with arbitrarily positioned inclined piezoelectric actuators (see Fig. 1). Considering the material linearity for small displacements, the Kirchhoff hypothesis leads to the general form of displacement fields as shown in Eqs. (1a–c) [51]. For composite laminates and piezoelectric layers/patches, some initial assumptions for mathematical modelling are made as follows [51,52]:

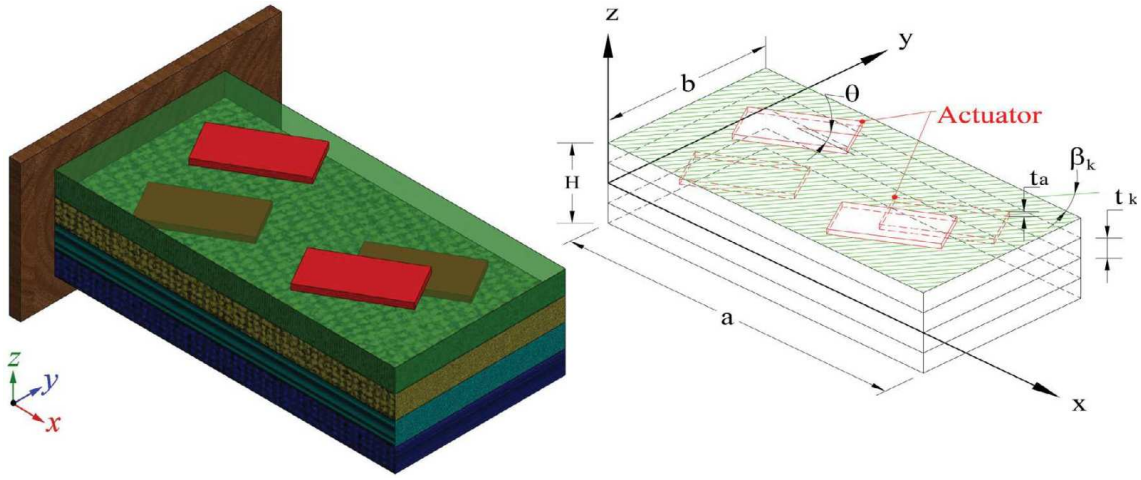


**Fig. 1.** Schematics of smart laminated cantilever piezo composite plate integrated with arbitrarily positioned inclined piezoelectric actuators.

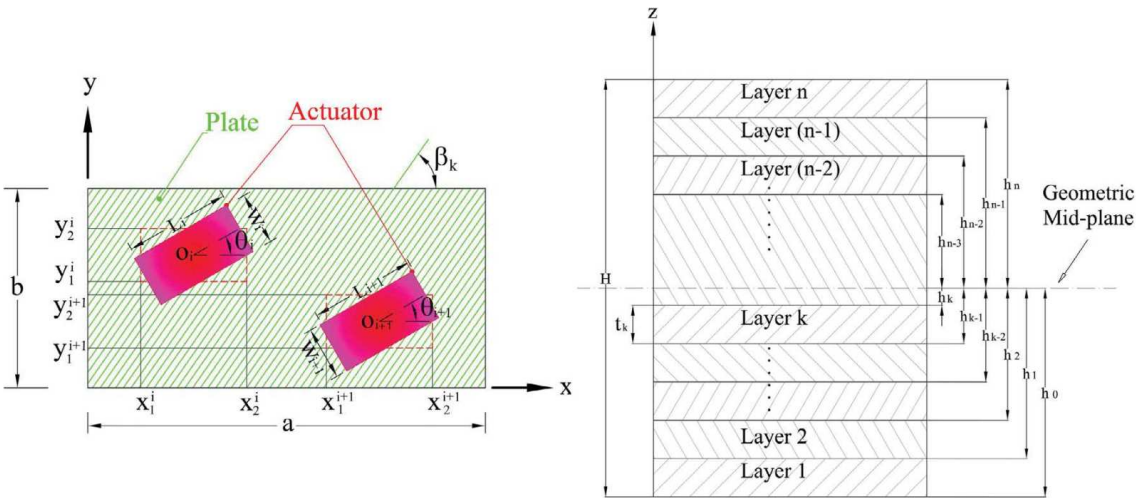


**Fig. 2.** Schematic of placement, geometry, and inclination angles of inclined piezoelectric actuators and smart composite laminate cross-section.

- Fibers distribution throughout the matrix is uniform;
- There is a perfect bonding between fibers and matrix, avoiding fibers dislocations and disarrangements through the matrix and no slip occurs between the lamina interfaces;
- The matrix is perfectly fabricated with no voids and impurity;
- The lamina is not initially pre-stressed, thus, there are no residual stresses in presence of matrix and fibers; and
- The matrix and fibers behave linearly within elastic domain.

For the smart part of the laminate, the linear piezoelectricity theory is adapted with assumptions made as follows [52]:

- The strain-electric filed varies linearly;
- The piezoelectric confidents are constant within the linear zone; thus, they cannot be electrically turned with a bias field;
- The electric field is assumed to be constant across each lamina; and
- The piezoelectric actuators are polarized through thickness; therefore, the electrical discharge through thickness $\Phi_3$ is considered in this study ($\Phi_1 = \Phi_2 = o$).

$$u(x,y,z) = u_0(x,y) - z\frac{\partial w_0}{\partial x} \tag{1a}$$

$$v(x,y,z) = v_0(x,y) - z\frac{\partial w_0}{\partial y} \tag{1b}$$

$$w(x,y,z) = w_0(x,y) \tag{1c}$$

$u_0$, $v_0$, and $w_0$ are the mid-plane displacements along $x$, $y$, and $z$ directions, respectively on the $xy$-plane [53]. $z$ is the vertical distance from the mid-plane to the $k$th layer which is located between $z = h_k$ and $z = h_{k+1}$ through laminate thickness, as shown in Fig. 2. After obtaining the mid-plane displacements, the displacements of any arbitrary point, $x$, $y$, and $z$ in 3D space can be determined. The linear strain-displacement relation is stated in Eqs. (2a–c) [54]. It is assumed that all strain components change linearly in the entire laminate independent from changes in material properties through layup thickness.

$$\begin{aligned}\begin{bmatrix}\varepsilon_{xx} & \varepsilon_{yy} & \gamma_{xy}\end{bmatrix}^T &= \begin{bmatrix}\frac{\partial u}{\partial x} & \frac{\partial v}{\partial y} & \frac{\partial u}{\partial y}+\frac{\partial v}{\partial x}\end{bmatrix}^T \\ &= \begin{bmatrix}\varepsilon^0_{xx} & \varepsilon^0_{yy} & \tau^0_{xy}\end{bmatrix}^T + z\begin{bmatrix}\varepsilon^f_{xx} & \varepsilon^f_{yy} & \tau^f_{xy}\end{bmatrix}^T\end{aligned} \tag{2a}$$

where,

$$\begin{bmatrix}\varepsilon^o_{xx} & \varepsilon^o_{yy} & \gamma^o_{xy}\end{bmatrix}^T = \begin{bmatrix}\frac{\partial u_o}{\partial x} & \frac{\partial v_o}{\partial y} & \frac{\partial u_o}{\partial y}+\frac{\partial v_o}{\partial x}\end{bmatrix}^T \tag{2b}$$

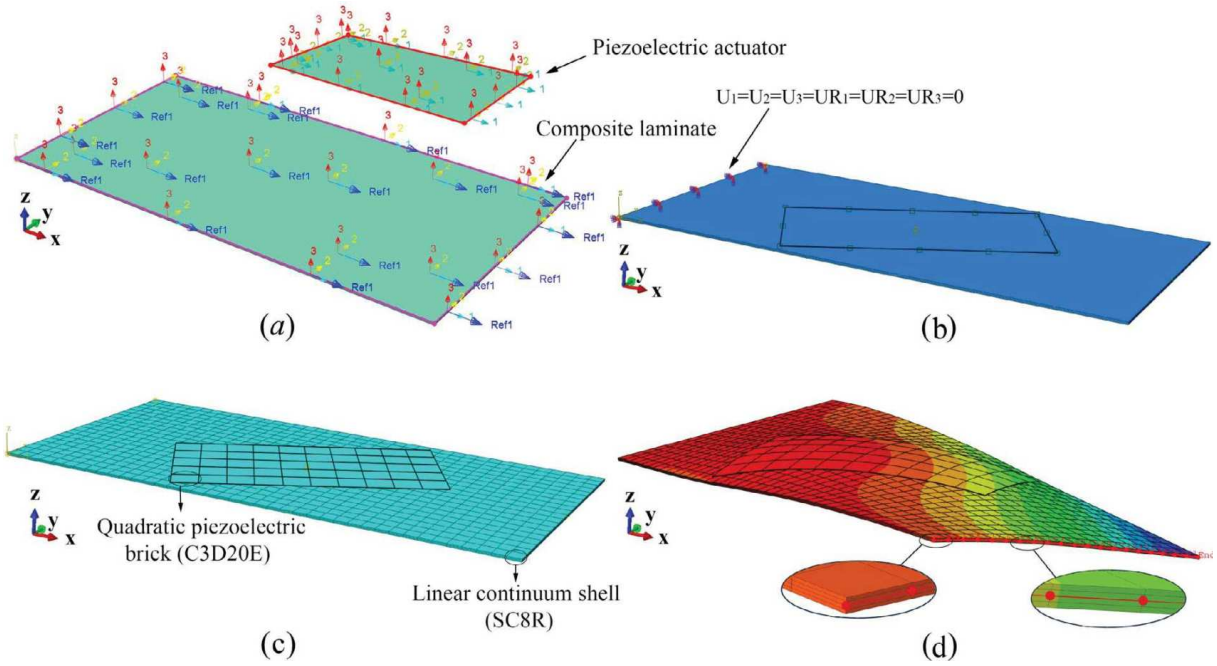


**Fig. 3.** The schematic of FE simulation of smart cantilever piezo composite plates and beams induced by electro-mechanical twisting loads using Commercial Finite Element software ABAQUS/CEA 6.13–1: (a) sketching and defining the dimensions and material properties to composite laminate and piezoelectric actuators, (b) applying the electro-mechanical boundary conditions, piezoelectric actuators groundings, inclination angles, and electrical surface charges, (c) Applying the FE meshing to the smart cantilever piezo composite and defining the element type of the host structure and the piezoelectric actuators, (d) defining a path along a specific direction in the smart cantilever piezo composite laminate mid-plane.

$$[\varepsilon_{xx}^{f} \quad \varepsilon_{yy}^{f} \quad \gamma_{xy}^{f}]^{T} = [-\frac{\partial^2 w_0}{\partial x^2} \quad -\frac{\partial^2 w_0}{\partial y^2} \quad -2\frac{\partial^2 w_0}{\partial x \partial y}]^{T} \tag{2c}$$

$\varepsilon_{xx}^{o}$, $\varepsilon_{yy}^{o}$, and $\gamma_{xy}^{o}$ are the laminate's mid-plane strains, $\varepsilon_{xx}^{f}$, $\varepsilon_{yy}^{f}$, and $\gamma_{xy}^{f}$ are the flexural (bending) strains and $w_o$ is the transverse deflection of a composite laminate mid-plane. The bending strains are typically caused by laminate's stacking sequence asymmetric or external electro-mechanical bending and twisting loads. Since the flexural shape control of the lateral displacements is considered in this study, the effect of laminate's mid-plane strains can be neglected and the effect of flexural strains are taken into account. Considering the plane stress assumption and neglecting the through-thickness stresses, the simplified 2D electro-mechanical plate equations are derived from the 3D equations of theory of elasticity and three charged equilibrium equations of piezoelectric medium, as stated in Eq. (3a) [55]. The electrical field potential relationships for an orthotropic static piezoelectric lamina is stated in Eq. (3b) [56].

$$\begin{bmatrix}\sigma_{11}\\ \sigma_{22}\\ 0\\ 0\\ 0\\ \tau_{12}\end{bmatrix}^{k} = \begin{bmatrix} C_{1111} & C_{1122} & C_{1133} & 0 & 0 & 0 \\ C_{1122} & C_{2222} & C_{2233} & 0 & 0 & 0 \\ C_{1133} & C_{2233} & C_{3333} & 0 & 0 & 0 \\ 0 & 0 & 0 & C_{2323} & 0 & 0 \\ 0 & 0 & 0 & 0 & C_{3131} & 0 \\ 0 & 0 & 0 & 0 & 0 & C_{1212} \end{bmatrix}^{k} \begin{bmatrix}\varepsilon_{11}\\ \varepsilon_{22}\\ \varepsilon_{33}\\ \gamma_{23}\\ \gamma_{31}\\ \gamma_{12}\end{bmatrix}^{k} - \begin{bmatrix} 0 & 0 & e_{311} \\ 0 & 0 & e_{322} \\ 0 & 0 & e_{333} \\ 0 & e_{223} & 0 \\ e_{113} & 0 & 0 \\ 0 & 0 & 0 \end{bmatrix}^{k} \begin{bmatrix}\Phi_1\\ \Phi_2\\ \Phi_3\end{bmatrix}^{k} \tag{3a}$$

$$\begin{bmatrix}\rho_1\\ \rho_2\\ \rho_3\end{bmatrix}^{k} = \begin{bmatrix} 0 & 0 & 0 & 0 & e_{113} & 0 \\ 0 & 0 & 0 & e_{223} & 0 & 0 \\ e_{311} & e_{322} & e_{333} & 0 & 0 & 0 \end{bmatrix}^{k} \begin{bmatrix}\varepsilon_{11}\\ \varepsilon_{22}\\ \varepsilon_{33}\\ \gamma_{23}\\ \gamma_{31}\\ \gamma_{12}\end{bmatrix}^{k} + \begin{bmatrix} \zeta_{11} & 0 & 0 \\ 0 & \zeta_{22} & 0 \\ 0 & 0 & \zeta_{33} \end{bmatrix}^{k} \begin{bmatrix}\Phi_1\\ \Phi_2\\ \Phi_3\end{bmatrix}^{k} \tag{3b}$$

$\sigma_{ij}$, $\varepsilon_{ij}$, $C_{ijkl}$, $e_{ijk}$, and $\Phi_i$ are the stresses, the strains, the elastic stiffness, the piezoelectric coefficients, and the components of the electric fields, respectively in the orthotropic material orientation. $p_i$ and $\zeta_{ij}$ are the electric displacement and the piezoelectric dielectric constants, respectively. The Kirchhoff assumption adapted for plate theory stipulates that $\gamma_{23} = \gamma_{31} = 0$. In addition, only a through-thickness electric field is considered. Therefore, Eqs. (3a–b) are reduced to Eq. (4a). Global stresses (Eq. (4b)) in the $k$th ply along $xyz$ direction can be calculated by transforming 2D stresses in the material direction through transformation matrix $[T]$ (Eq. (4c)) [57].

$$\begin{bmatrix}\sigma_{11}\\ \sigma_{22}\\ \tau_{12}\\ \rho_3\end{bmatrix}^{k} = \begin{bmatrix} Q_{11} & Q_{12} & 0 \\ Q_{12} & Q_{22} & 0 \\ 0 & 0 & Q_{66} \\ e_{31} & e_{32} & 0 \end{bmatrix}^{k} \begin{bmatrix}\varepsilon_{11}\\ \varepsilon_{22}\\ \gamma_{12}\end{bmatrix}^{k} - \begin{bmatrix}e_{31}\\ e_{32}\\ 0\\ \zeta_{33}\end{bmatrix}^{k} \Phi_3^{k} \tag{4a}$$

$$\begin{bmatrix}\sigma_{xx}\\ \sigma_{yy}\\ \sigma_{xy}\end{bmatrix}^{k} = [T]^{-1} \begin{bmatrix}\sigma_{11}\\ \sigma_{22}\\ \sigma_{12}\end{bmatrix}^{k} \tag{4b}$$

$$[T] = \begin{bmatrix} c^2 & s^2 & 2cs \\ s^2 & c^2 & -2cs \\ -cs & cs & (c^2 - s^2) \end{bmatrix} \tag{4c}$$

$c$ is cos($\beta$) and $s$ is sin($\beta$). $\beta$ is the winding angle between Fibers and $x$ axis. $Q_{ij}$ and $e_{ij}$ are the reduced elastic stiffness and the piezoelectric modules, respectively, as given in Eqs. (5e,f), respectively.

$$Q_{11} = C_{1111} - \frac{C_{1133}^2}{C_{3333}} = \frac{E_1}{1 - v_{12}v_{21}} \tag{5a}$$

$$Q_{22} = C_{2222} - \frac{C_{2233}^2}{C_{3333}} = \frac{E_2}{1 - v_{12}v_{21}} \tag{5b}$$

$$Q_{12} = C_{1122} - \frac{C_{1133}C_{2233}}{C_{3333}} = \frac{v_{12}E_2}{1 - v_{12}v_{21}} \tag{5c}$$

$$Q_{66} = C_{1212} = G_{12} \tag{5d}$$

**Table 1**
Material properties.

| Material properties | KYNAR [64] | PZT G1195N [61] | T300/976 GFRP [63] |
|---|---|---|---|
| $E_1$ [GPa] | 2 | 63 | 150 |
| $E_2$ [GPa] | 2 | 63 | 9 |
| $v_{12}$ | 0.29 | 0.3 | 0.3 |
| $G_{12}$ [GPa] | 0.77 | 24.2 | 7.1 |
| $G_{13}$ [GPa] | 0.77 | 24.2 | 2.5 |
| $d_{31}$[nm/V] | 0.023 | 0.254 | 0 |
| $d_{32}$[nm/V] | 0.0046 | 0.254 | 0 |
| $\rho_z$ [nF/m] | 0.1062 | 15 | 0 |

$$e_{31} = e_{311} - \frac{C_{1133}}{C_{3333}}e_{333} = Q_{11}d_{31} - Q_{12}d_{32} \tag{5e}$$

$$e_{32} = e_{322} - \frac{C_{2233}}{C_{3333}}e_{333} = Q_{12}d_{31} - Q_{22}d_{32} \tag{5f}$$

$E_1$, $E_2$, $v_{12}$, and $G_{12}$ are in-plane local elasticity modules of an orthotropic layer in the local material coordinate system. $d_{ij}$ is the piezoelectric dielectric constant. The in-plane stress-strain relationship for the $k$th smart orthotropic piezo-composite plate is shown in Eq. (6a) [38]. For the beam type laminates, the plane stress assumption is adapted and the width along $y$ direction is assumed to be stress free. Therefore, Eq. (6a) is reduced to Eq. (6b) and only the transformed piezoelectric coefficient along $x$ axis is considered [12].

$$\begin{bmatrix} \sigma_{xx} \\ \sigma_{yy} \\ \tau_{xy} \\ \rho_z \end{bmatrix}^k = \begin{bmatrix} \bar{Q}_{11} & \bar{Q}_{12} & \bar{Q}_{16} \\ \bar{Q}_{12} & \bar{Q}_{22} & \bar{Q}_{26} \\ \bar{Q}_{16} & \bar{Q}_{26} & \bar{Q}_{66} \\ \bar{e}_{31} & \bar{e}_{32} & \bar{e}_{36} \end{bmatrix}^k \begin{bmatrix} \varepsilon_{xx} \\ \varepsilon_{yy} \\ \gamma_{xy} \end{bmatrix}^k - \begin{bmatrix} \bar{e}_{31} \\ \bar{e}_{32} \\ \bar{e}_{36} \\ \zeta_{33} \end{bmatrix}^k \Phi_3^k \tag{6a}$$

$$\begin{bmatrix} \sigma_{xx} \\ \tau_{xy} \\ \rho_z \end{bmatrix}^k = \begin{bmatrix} \bar{Q}_{11} & \bar{Q}_{16} \\ \bar{Q}_{16} & \bar{Q}_{66} \\ \bar{e}_{31} & \bar{e}_{36} \end{bmatrix}^k \begin{bmatrix} \varepsilon_{xx} \\ \gamma_{xy} \end{bmatrix}^k - \begin{bmatrix} \bar{e}_{31} \\ \bar{e}_{36} \\ \zeta_{33} \end{bmatrix}^k \Phi_3^k \tag{6b}$$

$\overline{Q}_{ij}^k$ and $\bar{e}_{ij}^k$ are the transformed reduced stiffness matrix and transformed piezoelectric modules in the $k$th orthotropic layer, respectively. In Eqs. (6a,b), $\sigma_{ij}^k$ and $\varepsilon_{ij}^k$ are the in-plane stress, strain, and electrical field components of the $k$th orthotropic layer in $xyz$ coor-

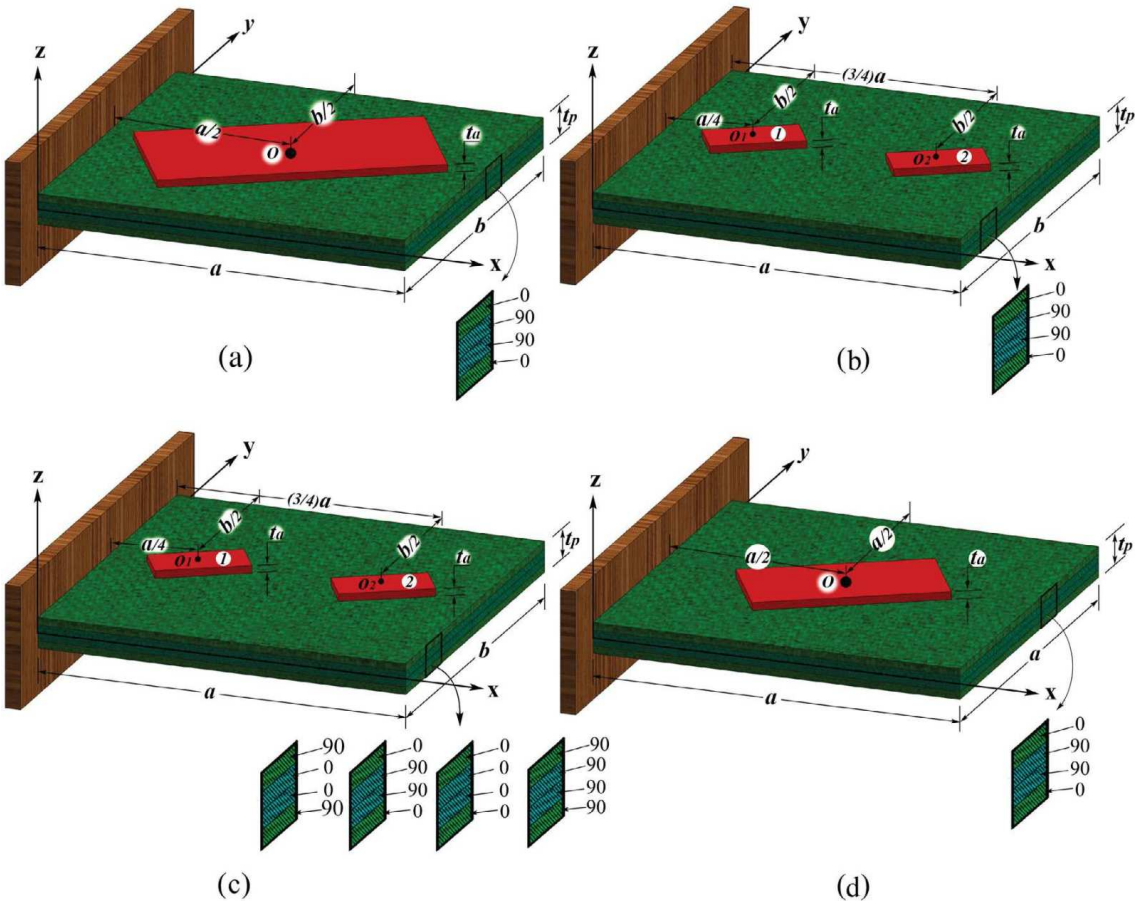


**Fig. 4.** Schematic of the smart laminated cantilever composite plates with (a) single bounded actuators pair, (b) double bounded actuators pairs, (c) double bounded actuators pairs and various stacking sequence configuration, (d) single bounded actuator pair and under various electrical voltage.

dinate system, respectively. The elements of transformed reduced stiffness matrix are described in Eqs. (7a–f), respectively [52].

$$\bar{Q}_{11} = Q_{11}c^4 + 2(Q_{12} + 2Q_{66})c^2s^2 + Q_{22}s \tag{7a}$$

$$\bar{Q}_{12} = (Q_{11} + Q_{22} - 4Q_{66})c^2s^2 + Q_{12}(c^4 + s^4) \tag{7b}$$

$$\bar{Q}_{22} = Q_{11}s^4 + 2(Q_{12} + 2Q_{66})c^2s^2 + Q_{22}c^4 \tag{7c}$$

$$\bar{Q}_{16} = -Q_{22}cs^3 + Q_{11}c^3s - (Q_{12} + 2Q_{66})(c^2 - s^2)cs \tag{7d}$$

$$\bar{Q}_{26} = -Q_{22}c^3s + Q_{11}cs^3 - (Q_{12} + 2Q_{66})(c^2 - s^2)cs \tag{7e}$$

$$\bar{Q}_{66} = (Q_{11} + Q_{22} - 2Q_{12})c^2s^2 + Q_{66}(c^2 - s^2)^2 \tag{7f}$$

The transformed piezoelectric modules are described in Eqs. (8a–c), respectively [52].

$$\begin{aligned}\bar{e}_{31} &= \overline{Q}_{11}\overline{d}_{31} + \overline{Q}_{12}\overline{d}_{32} \\ &= \overline{Q}_{11}(d_{31}\Gamma^2 + d_{32}\Gamma'^2) + \overline{Q}_{12}(d_{31}\Gamma'^2 + d_{32}\Gamma^2)\end{aligned} \tag{8a}$$

$$\begin{aligned}\bar{e}_{32} &= \overline{Q}_{12}\overline{d}_{31} + \overline{Q}_{22}\overline{d}_{32} \\ &= \overline{Q}_{12}(d_{31}\Gamma^2 + d_{32}\Gamma'^2) + \overline{Q}_{22}(d_{31}\Gamma'^2 + d_{32}\Gamma^2)\end{aligned} \tag{8b}$$

$$\bar{e}_{36} = \overline{Q}_{66}\overline{d}_{36} = 2\overline{Q}_{66}(d_{31} - d_{32})\Gamma\Gamma' \tag{8c}$$

$\bar{d}_{ij}{}^k$ are the transformed piezoelectric dielectric constants in the $k$th orthotropic layer. $\Gamma$ and $\Gamma'$ stand for $\cos(\theta)$ and $\sin(\theta)$, respectively. $\theta$ is the inclination angle between the piezoelectric actuators and $x$ axis, as shown in Figs.1, 2. The relationship between stress resultants and flexural-twisting moments for the mid-plane in a composite laminate is described in Eq. (9) [58]. First, Eq. (2a) is substituted into Eq. (6a). Subsequently, substituting Eq. (6a) into Eq. (9) leads to Eq. (10).

$$[M_{xx} \quad M_{yy} \quad M_{xy}]^T = \int_{-H/2}^{H/2} z(\sigma_{xx}, \sigma_{yy}, \tau_{xy})dz - \left[M_{xx}^P \quad M_{yy}^P \quad M_{xy}^P\right]^T \tag{9}$$

$$\begin{bmatrix} M_{xx} \\ M_{yy} \\ M_{xy} \end{bmatrix} = \begin{bmatrix} B_{11} & B_{12} & B_{16} \\ B_{12} & B_{22} & B_{26} \\ B_{16} & B_{26} & B_{66} \end{bmatrix} \begin{bmatrix} \frac{\partial u_o}{\partial x} \\ \frac{\partial v_o}{\partial y} \\ \frac{\partial u_o}{\partial y} + \frac{\partial v_o}{\partial x} \end{bmatrix} + \begin{bmatrix} D_{11} & D_{12} & D_{16} \\ D_{12} & D_{22} & D_{26} \\ D_{16} & D_{26} & D_{66} \end{bmatrix} \begin{bmatrix} -\frac{\partial^2 w_0}{\partial x^2} \\ -\frac{\partial^2 w_0}{\partial y^2} \\ -2\frac{\partial^2 w_0}{\partial x \partial y} \end{bmatrix} - \begin{bmatrix} M_{xx} \\ M_{yy} \\ M_{xy} \end{bmatrix}^P \tag{10}$$

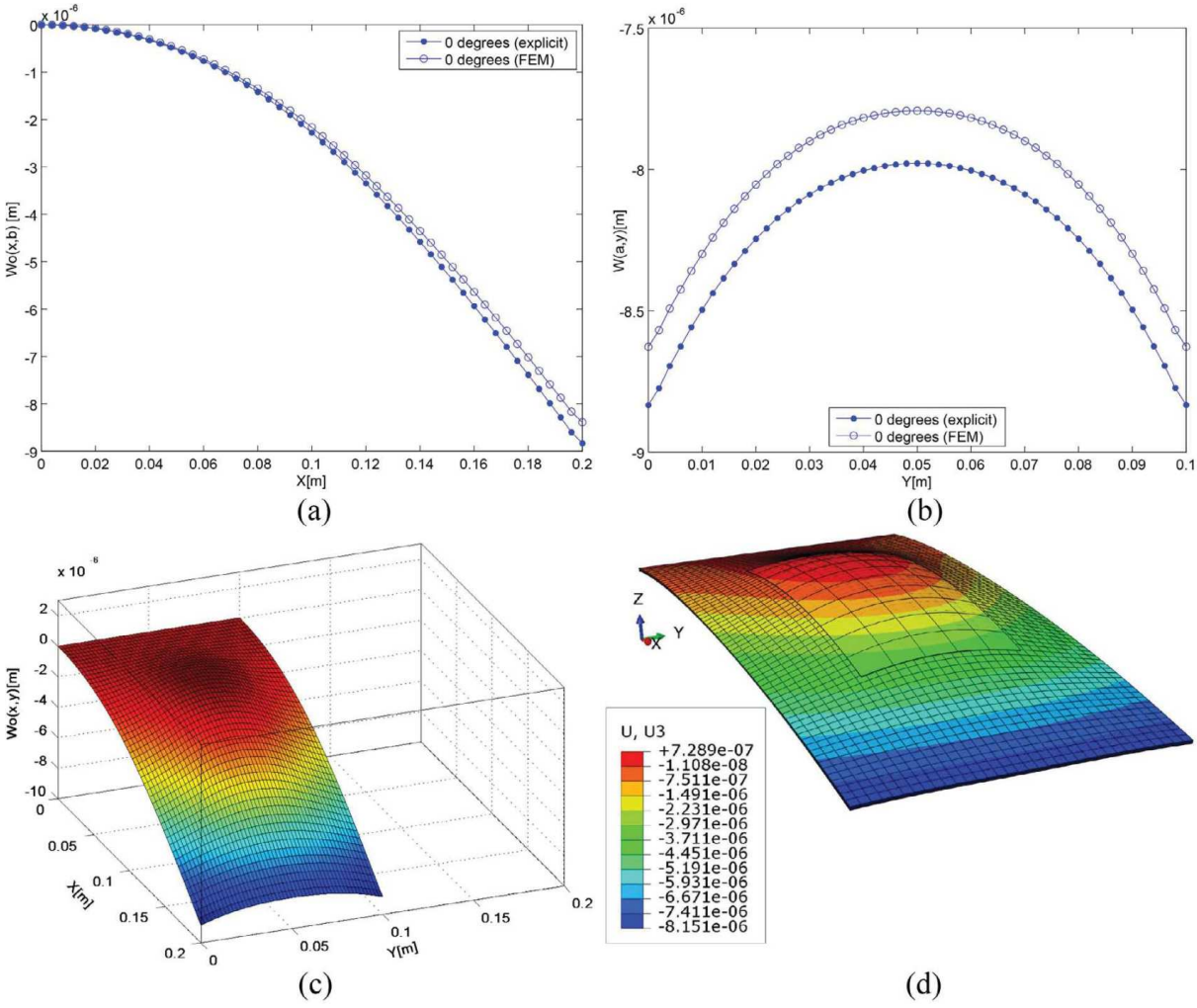


**Fig. 5.** Explicit and numerical analysis of shape deformation in the smart cantilever composite plate integrated with single piezoelectric actuators pair when $\theta = 0^o$: (a) $w_o(x, b)$, (b) $w_o(a,y)$, (c) $w_o(x,y)$: Explicit, (d) $w_o(x,y)$: Numerical.

$[M_{xx}]^P$, $[M_{yy}]^P$, and $[M_{xy}]^P$ are bending and twisting moments induced by electrical loads, respectively [59]. It is assumed that the electric positional fields vary linearly through laminate thickness. Therefore, the linear interpolation functions can be used to simplify the electrical gradients, as shown in Eq. (11) (Note: $\Phi_3 = \Phi_z$).

$$\Phi_3(x,y,z) = \Phi_a^k(x,y,z)\omega_1^k(z) + \Phi_b^k(x,y,z)\omega_2^k(z) \tag{11}$$

$\omega_i^k$, $i = \{1,2\}$ shown in Eq. (12) represents the linear interpolation function of the $k$th orthotropic layer in a smart piezo-composite laminate.

$$\omega_1^k = \frac{h_{k+1} - h}{t_k} = \frac{h_{k+1} - h}{P_n t_a + N t_p},\ \omega_2^k = \frac{h - h_k}{t_k} = \frac{h - h_k}{P_n t_a + N t_p},$$
$$h_k \leqslant h \leqslant h_{k+1} \tag{12}$$

$P_n$, $t_a$, and $t_p$ in Eq. (12) are the number of inclined piezoelectric actuators, and actuator thickness, and host structure (composite laminate) thickness, respectively (See Fig. 1). Governing partial differential equation relating the transverse bending and twisting moments to mid-plane displacements and electro-mechanical loads in a smart laminated piezo composite plate is stated in Eq. (13) [38]. In this study, thin symmetrical cross-ply laminates are considered. Thus, the effects of bending-stretching coupling matrix ($[B_{ij}] = 0$) and bending-twisting elements of flexural stiffness matrix ($D_{16} = D_{26} = 0$) in Eqs. (6a,b) are neglected. However, due to inclination angle between the inclined piezoelectric actuators and composite laminate with respect to $x$ axis, the effect of electrical twisting moment should not be neglected.

In the next step, the linear interpolation of the electrical functions stated in Eq. (11) is substituted into Eq. (10). Finally, by applying the initial conditions to Eq. (10), it can be simplified to Eq. (14). Substituting Eq. (14) into Eq. (13) leads to Eqs. (15a–d).

$$\frac{\partial^2 (M_{xx}^{total} - M_{xx}^P)}{\partial x^2} + 2\frac{\partial^2 (M_{xy}^{total} - M_{xy}^P)}{\partial x \partial y} + \frac{\partial^2 (M_{yy}^{total} - M_{yy}^P)}{\partial y^2} = P_m(x,y) \tag{13}$$

$$\begin{bmatrix} M_{xx} \\ M_{yy} \\ M_{xy} \end{bmatrix} = \begin{bmatrix} D_{11} & D_{12} & 0 \\ D_{12} & D_{22} & 0 \\ 0 & 0 & D_{66} \end{bmatrix} \begin{bmatrix} -\frac{\partial^2 w_0}{\partial x^2} \\ -\frac{\partial^2 w_0}{\partial y^2} \\ -2\frac{\partial^2 w_0}{\partial x \partial y} \end{bmatrix} - \begin{bmatrix} M_{xx}^P \\ M_{yy}^P \\ M_{xy}^P \end{bmatrix} \tag{14}$$

$$D_{11}\frac{\partial^4 w_0}{\partial x^4} + 2(D_{12} + 2D_{66})\frac{\partial^4 w_0}{\partial x^2 \partial y^2} + D_{22}\frac{\partial^4 w_0}{\partial y^4} = P_m(x,y) + \frac{\partial^2 M_{xx}^P}{\partial x^2} + \frac{\partial^2 M_{yy}^T}{\partial y^2} + 2\frac{\partial^2 M_{xy}^P}{\partial x \partial y} \tag{15a}$$

where,

$$P_e(x,y) = \frac{\partial^2 M_{xx}^P}{\partial x^2} + \frac{\partial^2 M_{yy}^T}{\partial y^2} + 2\frac{\partial^2 M_{xy}^P}{\partial x \partial y} \tag{15b}$$

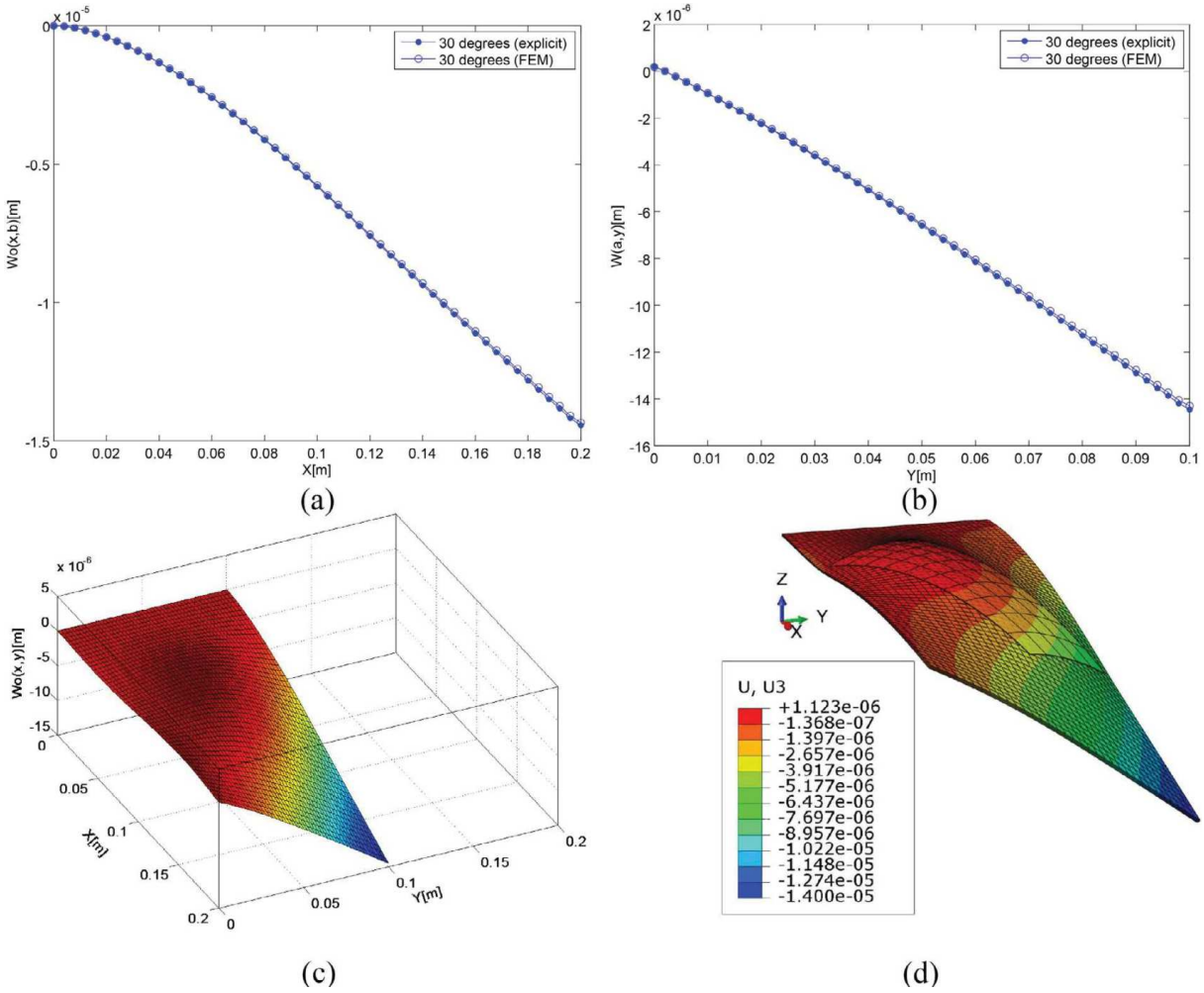


**Fig. 6.** Explicit and numerical analysis of shape deformation in the smart cantilever composite plate integrated with single piezoelectric actuators pair when $\theta = 30^\circ$: (a) $w_o(x, b)$, (b) $w_o(a,y)$, (c) $w_o(x,y)$: Explicit, (d) $w_o(x,y)$: Numerical.

$$[M_i^p] = \sum_{k=1}^{N} \int_{h_k}^{h_{k+1}} [\bar{Q}_{ij}]^k [\bar{d}_{3j}]^k \Phi_3^k z dz = \frac{1}{6} \sum_{k=1}^{N} \sum_{j=1,2,6} [\bar{Q}_{ij}]^k [\bar{d}_{3j}]^k \{\Phi_a^k (h_k + 3z_k) + \Phi_b^k (2h_k + 3z_k)\} h_k \quad (15c)$$

$$D_{ij} = \frac{1}{3} \sum_{K=1}^{N} \sum_{j=1,2,6} [\bar{Q}_{ij}]_k (h_K^3 - h_{K-1}^3) \quad (15d)$$

$i = j = \{1,2,6\}$, $D_{11}$ and $D_{22}$ are flexural stiffness about $x$ and $y$ axis, respectively, $D_{12}$ and $D_{66}$ stand for effective torsional rigidity. $P_m(x, y)$ and $P_e(x,y)$ are mechanical and electrical loads applied to the smart piezo composite laminate, respectively. $[M]^{total}$ is the combination of electrical and mechanical moments. The schematic of coordinate system and geometry of the smart laminated cantilever piezo composite plate with incorporated piezoelectric actuators and actuators size and placements is illustrated in Fig. 2. Activated inclined piezoelectric actuators are capable of inducing bending and twisting moments which can be expressed in terms of 2D unit step functions [38,60]. In this study, mechanical load and electrical moments are expressed in the form of multivariable unit step functions according to Eqs. (16a,b), respectively.

$$[M_{iP}] = \frac{1}{6} \sum_{L=1}^{Pn} \sum_{k=1}^{N} \sum_{j=1,2,6} [\bar{Q}_{ij}]^k [\bar{d}_{3j}]^k \{\Phi_a^k (h_k + 3z_k) + \Phi_b^k (2h_k + 3z_k)\} h_k \left[U_k^L (x - x_{1P}) - U_k^L (x - x_{2P})\right] \times \left[U_k^L (y - y_{1P}) - U_k^L (y - y_{2P})\right] \quad (16a)$$

$$P_m = \sum_{L=1}^{Mn} P_m(x,y) \left[U_k^L (x - x_{1M}) - U_k^L (x - x_{2M})\right] \left[U_k^L (y - y_{1M}) - U_k^L (y - y_{2M})\right] \quad (16b)$$

$i = j = \{1,2,6\}$and $U_k^L(x,y)$ presents the unit step function expressed for effective areas at which the electrical bending and twisting moments are applied at the $L$th location and in the $k$th ply. $M_n$ and $P_n$ are the number of effective areas at which the mechanical and electrical loads are applied, respectively (see Fig. 2). The general electro-mechanical load resultants applied to a plate element are expressed in Eqs. (17a–g).

$$M_{xx}^{total} = -\left[D_{11} \frac{\partial^2 w_0}{\partial x^2} + D_{12} \frac{\partial^2 w_0}{\partial y^2}\right] \quad (17a)$$

$$M_{yy}^{total} = -\left[D_{22} \frac{\partial^2 w_0}{\partial y^2} + D_{12} \frac{\partial^2 w_0}{\partial x^2}\right] \quad (17b)$$

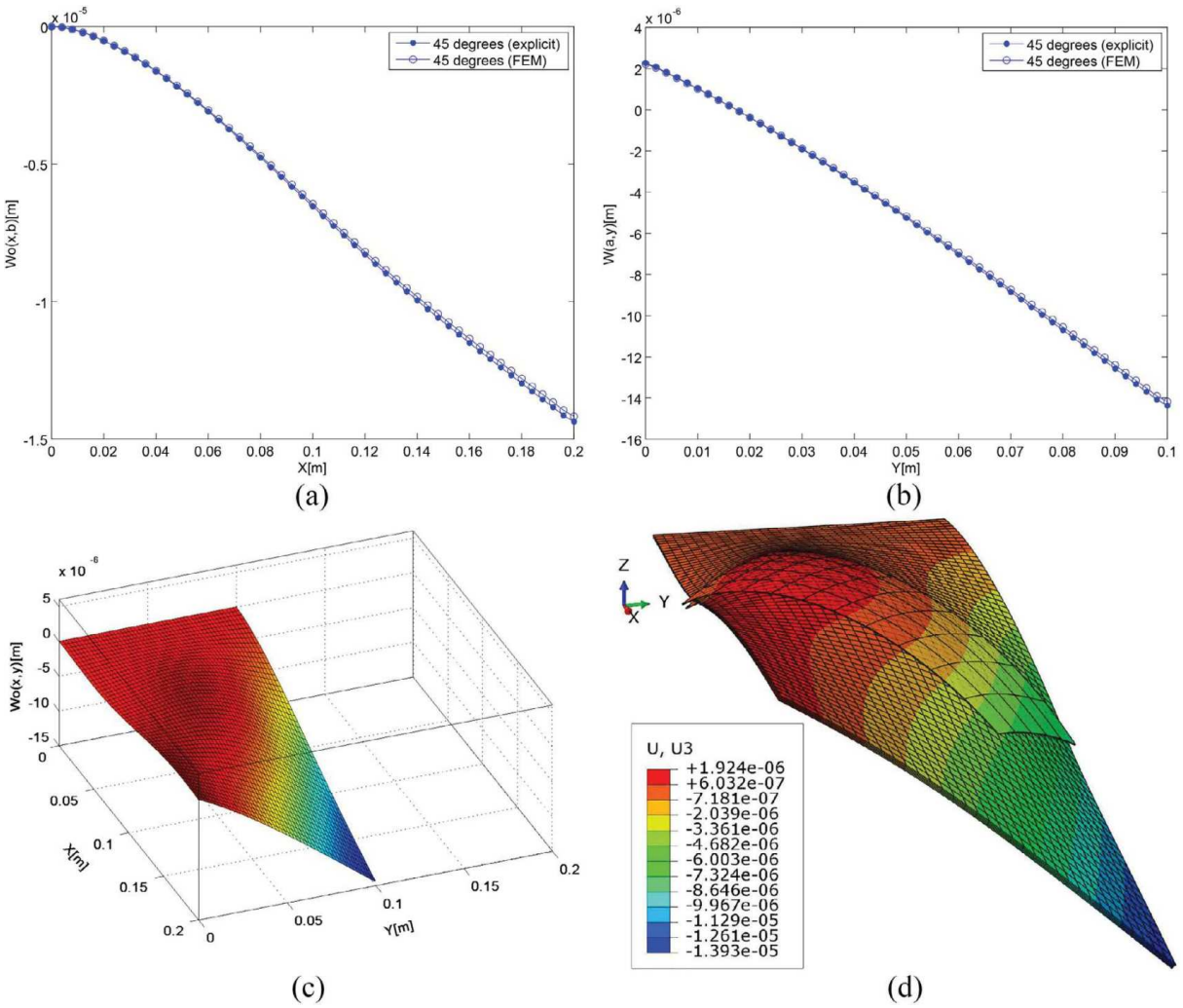


**Fig. 7.** Explicit and numerical analysis of shape deformation in the smart cantilever composite plate integrated with single piezoelectric actuators pair when $\theta = 45°$: (a) $w_o(x, b)$, (b) $w_o(a,y)$, (c) $w_o(x,y)$: Explicit, (d) $w_o(x,y)$: Numerical.

$$M_{xy}^{total} = -2D_{66}\frac{\partial^2 w_0}{\partial x \partial y} \tag{17c}$$

$$Q_{xx}^{total} = -\frac{\partial}{\partial x}\left[D_{11}\frac{\partial^2 w_0}{\partial x^2} + 2(D_{12}+D_{66})\frac{\partial^2 w_0}{\partial y^2}\right] \tag{17d}$$

$$Q_{yy}^{total} = -\frac{\partial}{\partial y}\left[D_{22}\frac{\partial^2 w_0}{\partial y^2} + 2(D_{12}+D_{66})\frac{\partial^2 w_0}{\partial x^2}\right] \tag{17e}$$

$$V_{xx}^{total} = -\frac{\partial}{\partial x}\left[D_{11}\frac{\partial^2 w_0}{\partial x^2} + 2(D_{12}+D_{66})\frac{\partial^2 w_0}{\partial y^2}\right] - 2D_{66}\frac{\partial}{\partial y}\left[\frac{\partial^2 w_0}{\partial x \partial y}\right] \tag{17f}$$

$$V_{yy}^{total} = -\frac{\partial}{\partial y}\left[D_{22}\frac{\partial^2 w_0}{\partial y^2} + 2(D_{12}+D_{66})\frac{\partial^2 w_0}{\partial x^2}\right] - 2D_{66}\frac{\partial}{\partial x}\left[\frac{\partial^2 w_0}{\partial x \partial y}\right] \tag{17g}$$

$M_{xx}$, $M_{yy}$, $M_{xy}$, $Q_{xx}$, $Q_{yy}$, $V_{xx}$, and $V_{yy}$ are bending moment resultants, torsional moment resultants, shear force resultants, and the total shear force resultants per unit length, respectively [58]. The boundary conditions for a cantilever plate are prescribed as stated in Eqs. (18a–j).

$$w_0(0,y) = 0 \tag{18a}$$

$$\frac{\partial w_o}{\partial x}(0,y) = 0 \tag{18b}$$

$$M_{xx}(a,y) = 0 \tag{18c}$$

$$M_{yy}(x,0) = 0 \tag{18d}$$

$$M_{yy}(x,b) = 0 \tag{18e}$$

$$V_{xx}(a,y) = 0 \tag{18f}$$

$$V_{yy}(x,0) = 0 \tag{18g}$$

$$V_{yy}(x,b) = 0 \tag{18h}$$

$$M_{xy}(a,0) = 0 \tag{18i}$$

$$M_{xy}(a,b) = 0 \tag{18j}$$

The double finite integral transformation of the mid-plane vertical displacement of function $w_o(x,y)$ is shown in Eq. (19).

$$w_{mn} = \int_0^a \int_0^a w_0(x,y)\sin\left(\frac{\alpha_m}{2}x\right)\cos(\beta_n y)dxdy \quad (m = 1,3,5,\ldots)\,(n = 0,1,2,\ldots) \tag{19}$$

Eq. (19) is then inversed to represent the exact mid-plane vertical displacement of function $w_o(x,y)$ as stated in Eq. (20).

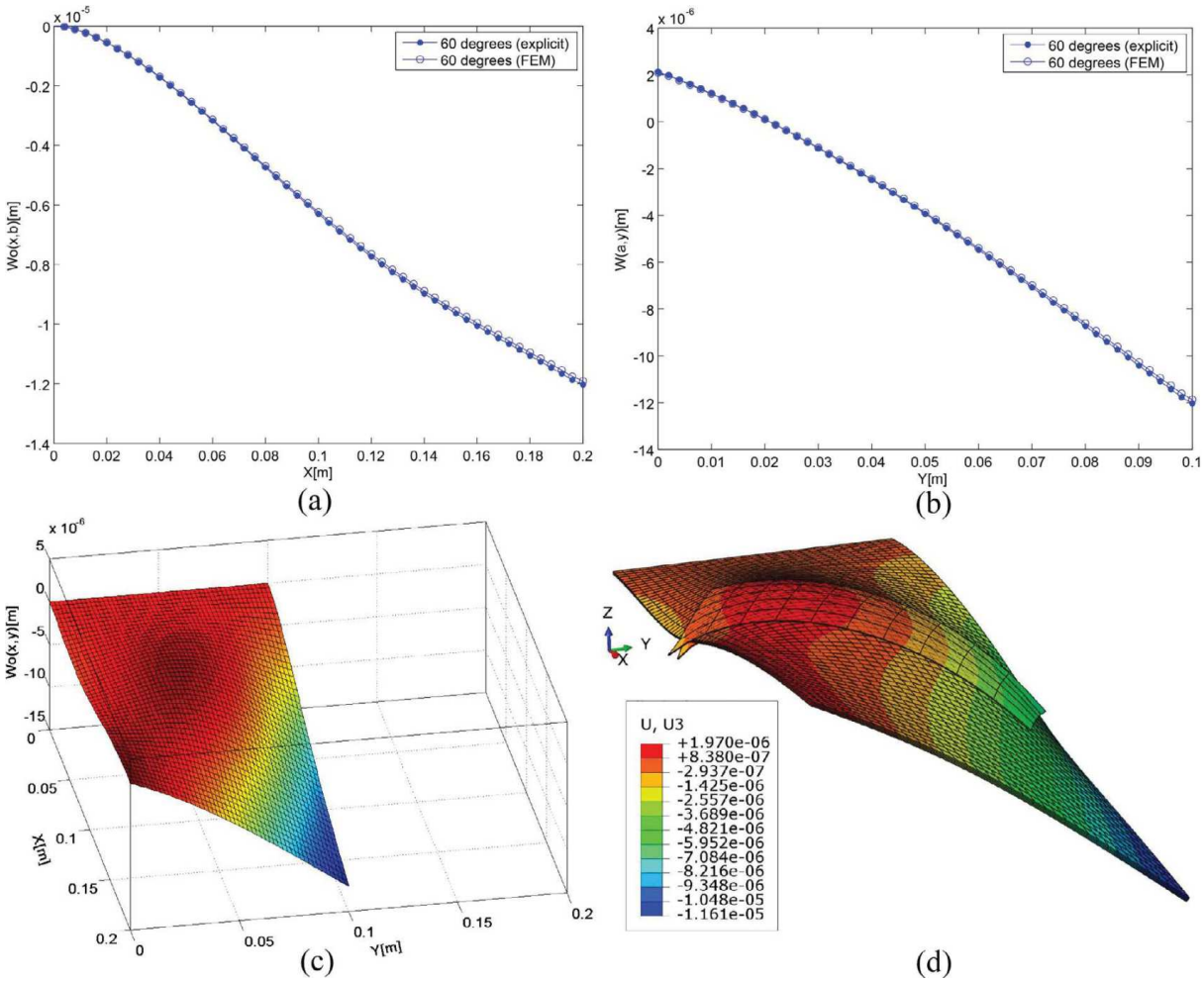


**Fig. 8.** Explicit and numerical analysis of shape deformation in the smart cantilever composite plate integrated with single piezoelectric actuators pair when $\theta = 60^\circ$: (a) $w_o(x, b)$, (b) $w_o(a,y)$, (c) $w_o(x,y)$: Explicit, (d) $w_o(x,y)$: Numerical.

$$w_0(x,y) = \frac{4}{ab}\sum_{m=1,3,5,\ldots}^{\infty}\sum_{n=0,1,2,\ldots}^{\infty} w_{mn}\lambda_n \sin\left(\frac{\alpha_m}{2}x\right)\cos(\beta_n y) \tag{20}$$

where,

$$\alpha_m = \frac{m\pi}{a},\ \beta_n = \frac{n\pi}{b} \text{ and } \lambda_n = \begin{cases} 0.5 \rightarrow (n=0) \\ 1 \rightarrow (n=1,2,3,\ldots) \end{cases}$$

In Eq. (20), $a$ and $b$ stand for the plate's length and width, respectively (see Fig. 1). The double integral transformation of higher-order partial derivatives of the multivariable function $w_o(x,y)$ over Eq. (15a) results in Eqs. (21a–f):

$$\begin{aligned}&\int_0^a\int_0^b\left[D_{11}\frac{\partial^4 w_0}{\partial x^4} + 2(D_{12}+2D_{66})\frac{\partial^4 w_0}{\partial x^2\partial y^2} + D_{22}\frac{\partial^4 w_0}{\partial y^4}\right] \\ &\quad\times\sin\left(\frac{\alpha_m}{2}x\right)\cos(\beta_n y)dxdy \\ &= \int_0^a\int_0^b\left[P_m(x,y) + \frac{\partial^2 M_{xx}^P}{\partial x^2} + 2\frac{\partial^2 M_{xy}^P}{\partial x\partial y} + \frac{\partial^2 M_{yy}^P}{\partial y^2}\right] \\ &\quad\times\sin\left(\frac{\alpha_m}{2}x\right)\cos(\beta_n y)dxdy\end{aligned} \tag{21a}$$

where,

$$I_1 = \int_0^a\int_0^b \frac{\partial^4 w_0}{\partial x^4}\sin\left(\frac{\alpha_m}{2}x\right)\cos(\beta_n y)dxdy \tag{21b}$$

$$I_2 = \int_0^a\int_0^b \frac{\partial^4 w_0}{\partial y^4}\sin\left(\frac{\alpha_m}{2}x\right)\cos(\beta_n y)dxdy \tag{21c}$$

$$I_3 = \int_0^a\int_0^b \frac{\partial^4 w_0}{\partial x^2\partial y^2}\sin\left(\frac{\alpha_m}{2}x\right)\cos(\beta_n y)dxdy \tag{21d}$$

$$I_4 = \int_0^a\int_0^b P_m(x,y)\sin\left(\frac{\alpha_m}{2}x\right)\cos(\beta_n y)dxdy \tag{21e}$$

$$I_5 = \int_0^a\int_0^b \left(\frac{\partial^2 M_{xx}^P}{\partial x^2} + 2\frac{\partial^2 M_{xy}^P}{\partial x\partial y} + \frac{\partial^2 M_{yy}^P}{\partial y^2}\right)\sin\left(\frac{\alpha_m}{2}x\right)\cos(\beta_n y)dxdy \tag{21f}$$

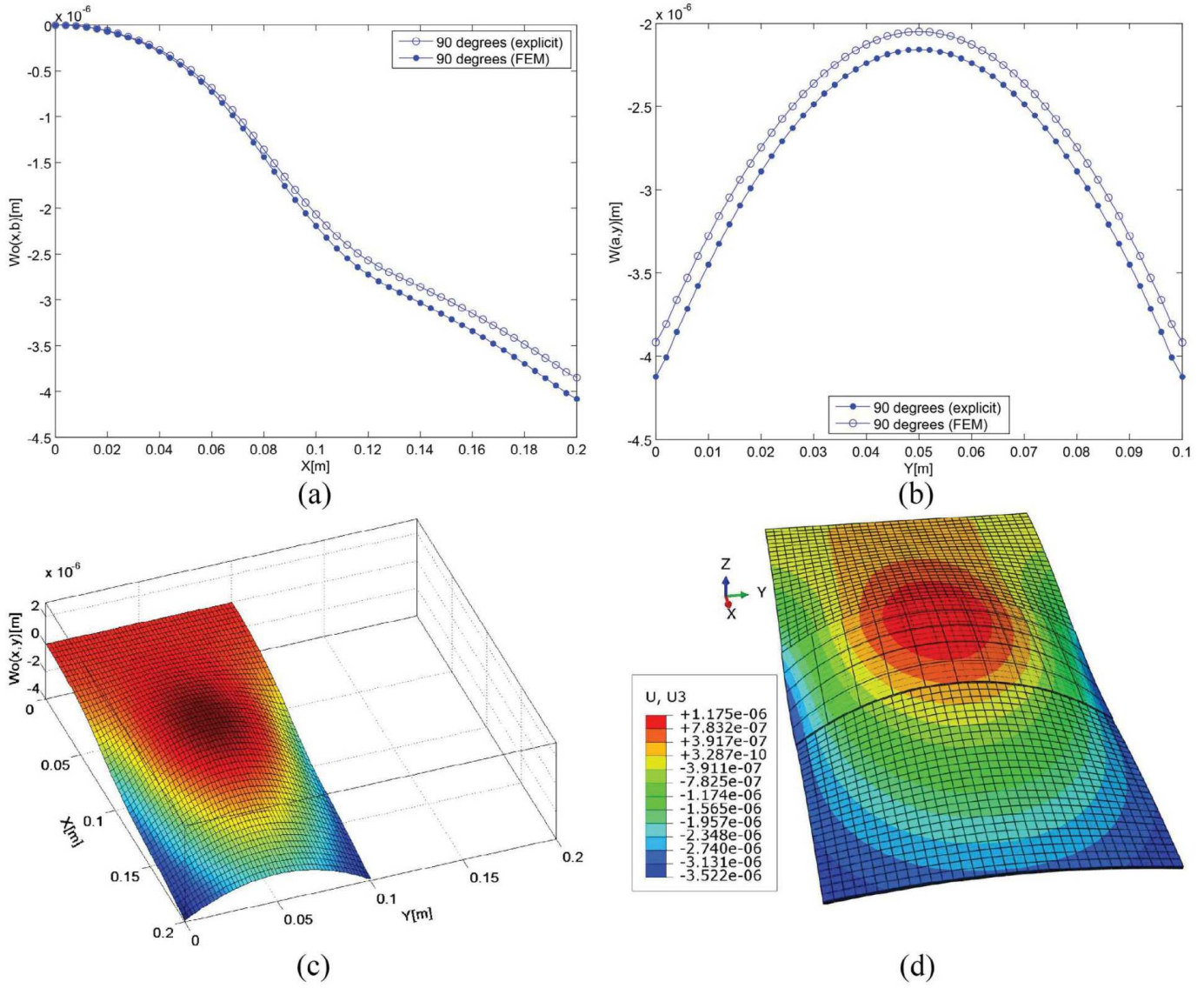


**Fig. 9.** Explicit and numerical analysis of shape deformation in the smart cantilever composite plate integrated with single piezoelectric actuators pair when $\theta = 90^\circ$: (a) $w_o(x, b)$, (b) $w_o(a,y)$, (c) $w_o(x,y)$: Explicit, (d) $w_o(x,y)$: Numerical.

Considering the integral by parts principle and applying the boundary conditions in Eqs. (18a,b,i,j) to $I_1$, $I_2$, and $I_3$, the double integral transformations of higher-order partial derivatives of the function $w_o(x,y)$ over Eqs. (21b–e) result in Eqs. (22a–e), respectively.

$$I_1 = \int_0^a \int_0^b \frac{\partial^4 w_0}{\partial x^4} \sin\left(\frac{\alpha_m}{2}x\right)\cos(\beta_n y)dxdy$$
$$= \int_0^b \left[(-1)^{\frac{m-1}{2}}\left(\frac{\partial^3 w_0}{\partial x^3}\middle| x=a\right) + \frac{\alpha_m}{2}\left(\frac{\partial^2 w_0}{\partial x^2}\middle| x=0\right)\right.$$
$$\left. -(-1)^{\frac{m-1}{2}}\frac{\alpha_m^2}{4}\left(\frac{\partial w_0}{\partial x}\middle| x=a\right) - \frac{\alpha_m^3}{8}(w_0|x=0)\right]\cos(\beta_n y)dy$$
$$+\frac{\alpha_m^4}{16}w_{mn} = \int_0^b \left[(-1)^{\frac{m-1}{2}}\left(\frac{\partial^3 w_0}{\partial x^3}\middle| x=a\right) + \frac{\alpha_m}{2}\left(\frac{\partial^2 w_0}{\partial x^2}\middle| x=0\right)\right.$$
$$\left. -(-1)^{\frac{m-1}{2}}\frac{\alpha_m^2}{4}\left(\frac{\partial w_0}{\partial x}\middle| x=a\right)\right]\cos(\beta_n y)dy + \frac{\alpha_m^4}{16}w_{mn} \quad (22a)$$

$$I_2 = \int_0^a \int_0^b \frac{\partial^4 w_0}{\partial y^4} \sin\left(\frac{\alpha_m}{2}x\right)\cos(\beta_n y)dxdy$$
$$= \int_0^a \left[(-1)^n\left(\frac{\partial^3 w_0}{\partial y^3}\middle| y=b\right) - \left(\frac{\partial^3 w_0}{\partial y^3}\middle| y=0\right)\right.$$
$$\left. -(-1)^n\beta_n^2\left(\frac{\partial w_0}{\partial y}\middle| y=b\right) + \beta_n^2\left(\frac{\partial w_0}{\partial y}\middle| y=0\right)\right]$$
$$\times \sin\left(\frac{\alpha_m}{2}x\right)dx + \beta_n^4 w_{mn} \quad (22b)$$

$$I_3 = \int_0^a \int_0^b \frac{\partial^4 w_0}{\partial x^2\partial y^2} \sin\left(\frac{\alpha_m}{2}x\right)\cos(\beta_n y)dxdy$$
$$= (-1)^n(-1)^{\frac{m-1}{2}}\left(\frac{\partial^2 w_0}{\partial x\partial y}\middle| \begin{matrix} x=a \\ y=b\end{matrix}\right) - (-1)^{\frac{m-1}{2}}\left(\frac{\partial^2 w_0}{\partial x\partial y}\middle| \begin{matrix} x=a \\ y=0\end{matrix}\right)$$
$$+(-1)^n\frac{\alpha_m}{2}\left(\frac{\partial w_0}{\partial y}\middle| \begin{matrix} x=0 \\ y=b\end{matrix}\right) - \frac{\alpha_m}{2}\left(\frac{\partial w_0}{\partial y}\middle| \begin{matrix} x=0 \\ y=0\end{matrix}\right)$$
$$+\frac{\alpha_m^2\beta_n^2}{4}w_{mn} - \frac{\alpha_m^2}{4}\int_0^a \left[(-1)^n\left(\frac{\partial w_0}{\partial y}\middle| y=b\right) - \left(\frac{\partial w_0}{\partial y}\middle| y=0\right)\right]$$
$$\times \sin\left(\frac{\alpha_m}{2}x\right)dx - \beta_n^2\int_0^b \left[(-1)^{\frac{m-1}{2}}\left(\frac{\partial w_0}{\partial x}\middle| x=a\right) + \frac{\alpha_m}{2}(w_0|x=0)\right]$$
$$\times \cos(\beta_n y)dy = -\frac{\alpha_m^2}{4}\int_0^a \left[(-1)^n\left(\frac{\partial w_0}{\partial y}\middle| y=b\right) - \left(\frac{\partial w_0}{\partial y}\middle| y=0\right)\right]$$
$$\times \sin\left(\frac{\alpha_m}{2}x\right)dx - (-1)^{\frac{m-1}{2}}\beta_n^2\int_0^b \left[\left(\frac{\partial w_0}{\partial x}\middle| x=a\right)\right]$$
$$\times \cos(\beta_n y)dy + \frac{\alpha_m^2\beta_n^2}{4}w_{mn} \quad (22c)$$

Let $P_m(x,y) = P_o$ be defined as uniform distributed pressure or patch loading magnitude, hence:

$$I_4 = \int_0^a \int_0^b \sum_{L=1}^{Mn} P_o[U_k^L(x-x_{1M}) - U_k^L(x-x_{2M})][U_k^L(y-y_{1M}) - U_k^L(y$$
$$- y_{2M})]\sin\left(\frac{\alpha_m}{2}x\right)\cos(\beta_n y)dxdy$$

If $n = \{0\}$, $m = \{1,3,5\ldots\}$, then,

$$I_4 = \sum_{L=1}^{Mn}\left(\frac{-2P_o}{\alpha_m}\right)(y_{1M} - y_{2M})_L\left(\cos\left(\frac{\alpha_m}{2}x_{1M}\right) - \cos\left(\frac{\alpha_m}{2}x_{2M}\right)\right)_L \quad (22d)$$

and if $n = \{1,2,3,\ldots\}$, $m = \{1,3,5,\ldots\}$, then,

$$I_4 = \sum_{L=1}^{Mn}\left(\frac{-2P_o}{\alpha_m\beta_n}\right)\left(\cos(\frac{\alpha_m}{2}x_{1M}) - \cos\left(\frac{\alpha_m}{2}x_{2M}\right)\right)_L$$
$$\times (\sin(\beta_n y_{1M}) - \sin(\beta_n y_{2M}))_L \quad (22e)$$

The second derivatives of partial differential 2D unit step function equations of electrical bending and twisting moments (Eq. (21f)) acting on a smart laminated cantilever piezo composite plate with respect to $x$ and $y$ are expanded in Eqs. (23a–f), respectively.

$$\frac{\partial^2 M_{xx}^P}{\partial x^2} = \frac{1}{6}\sum_{L=1}^{Tn}\sum_{k=1}^{N}\sum_{j=1,2,6}[\overline{Q}_{1j}]^k[\overline{d}_{3j}]^k h_k\{\Phi_a^k(h_k+3z_k) + \Phi_b^k(2h_k+3z_k)\}$$
$$\times\frac{\partial^2}{\partial x^2}\left([U_k^L(x-x_{1P}) - U_k^L(x-x_{2P})][U_k^L(y-y_{1P}) - U_k^L(y-y_{2P})]\right)$$
$$= \frac{1}{6}\sum_{L=1}^{Tn}\sum_{k=1}^{N}\sum_{j=1,2,6}[\overline{Q}_{1j}]^k[\overline{d}_{3j}]^k h_k\{\Phi_a^k(h_k+3z_k) + \Phi_b^k(2h_k+3z_k)\}$$
$$\times[U_k^L(y-y_{1P}) - U_k^L(y-y_{2P})][\delta_k'^L(x-x_{1P}) - \delta_k'^L(x-x_{2P})] \quad (23a)$$

$$\frac{\partial^2 M_{yy}^P}{\partial y^2} = \frac{1}{6}\sum_{L=1}^{Tn}\sum_{k=1}^{N}\sum_{j=1,2,6}[\overline{Q}_{2j}]^k[\overline{d}_{3j}]^k h_k\{\Phi_a^k(h_k+3z_k) + \Phi_b^k(2h_k+3z_k)\}$$
$$\times\frac{\partial^2}{\partial y^2}\left([U_k^L(x-x_{1P}) - U_k^L(x-x_{2P})][U_k^L(y-y_{1P}) - U_k^L(y-y_{2P})]\right)$$
$$= \frac{1}{6}\sum_{L=1}^{Tn}\sum_{k=1}^{N}\sum_{j=1,2,6}[\overline{Q}_{2j}]^k[\overline{d}_{3j}]^k h_k\{\Phi_a^k(h_k+3z_k) + \Phi_b^k(2h_k+3z_k)\}$$
$$\times[U_k^L(x-x_{1P}) - U_k^L(x-x_{2P})][\delta_k'^L(y-y_{1P}) - \delta_k'^L(y-y_{2P})] \quad (23b)$$

$$\frac{\partial^2 M_{xy}^P}{\partial x\partial y} = \frac{1}{6}\sum_{L=1}^{Tn}\sum_{k=1}^{N}\sum_{j=1,2,6}[\overline{Q}_{6j}]^k[\overline{d}_{3j}]^k h_k\{\Phi_a^k(h_k+3z_k) + \Phi_b^k(2h_k+3z_k)\}$$
$$\times\frac{\partial}{\partial x}[U_k^L(x-x_{1P}) - U_k^L(x-x_{2P})]\frac{\partial}{\partial y}[U_k^L(y-y_{1P}) - U_k^L(y-y_{2P})]$$
$$= \frac{1}{6}\sum_{L=1}^{Tn}\sum_{k=1}^{N}\sum_{j=1,2,6}[\overline{Q}_{6j}]^k[\overline{d}_{3j}]^k h_k\{\Phi_a^k(h_k+3z_k) + \Phi_b^k(2h_k+3z_k)\}$$
$$\times[\delta_k'^L(x-x_{1P}) - \delta_k'^L(x-x_{2P})][\delta_k'^L(y-y_{1P}) - \delta_k'^L(y-y_{2P})] \quad (23c)$$

$$I_5^A = \int_0^a \int_0^b \left(\frac{\partial^2 M_{xx}^P}{\partial x^2}\right)\sin\left(\frac{\alpha_m}{2}x\right)\cos(\beta_n y)dxdy$$
$$= \frac{1}{6}\int_0^a \int_0^b \sum_{L=1}^{Tn}\sum_{k=1}^{N}\sum_{j=1,2,6}[\overline{Q}_{1j}]^k[\overline{d}_{3j}]^k h_k\left\{\Phi_a^k(h_k+3z_k)\right.$$
$$\left. + \Phi_b^k(2h_k+3z_k)\right\}[U_k^L(y-y_{1P}) - U_k^L(y-y_{2P})][\delta_k'^L(x-x_{1P})$$
$$- \delta_k'^L(x-x_{2P})]\sin\left(\frac{\alpha_m}{2}x\right)\cos\left(\beta_n y\right)dxdy$$
$$= \frac{1}{6}\sum_{L=1}^{Tn}\sum_{k=1}^{N}\sum_{j=1,2,6}\frac{\alpha_m}{2\beta_n}[\overline{Q}_{1j}]^k[\overline{d}_{3j}]^k h_k\{\Phi_a^k(h_k+3z_k)$$
$$+ \Phi_b^k(2h_k+3z_k)\}\left(\cos\left(\frac{\alpha_m}{2}x_{1P}\right) - \cos\left(\frac{\alpha_m}{2}x_{2P}\right)\right)_L$$
$$\times(\sin(\beta_n y_{1P}) - \sin(\beta_n y_{2P}))_L \quad (23d)$$

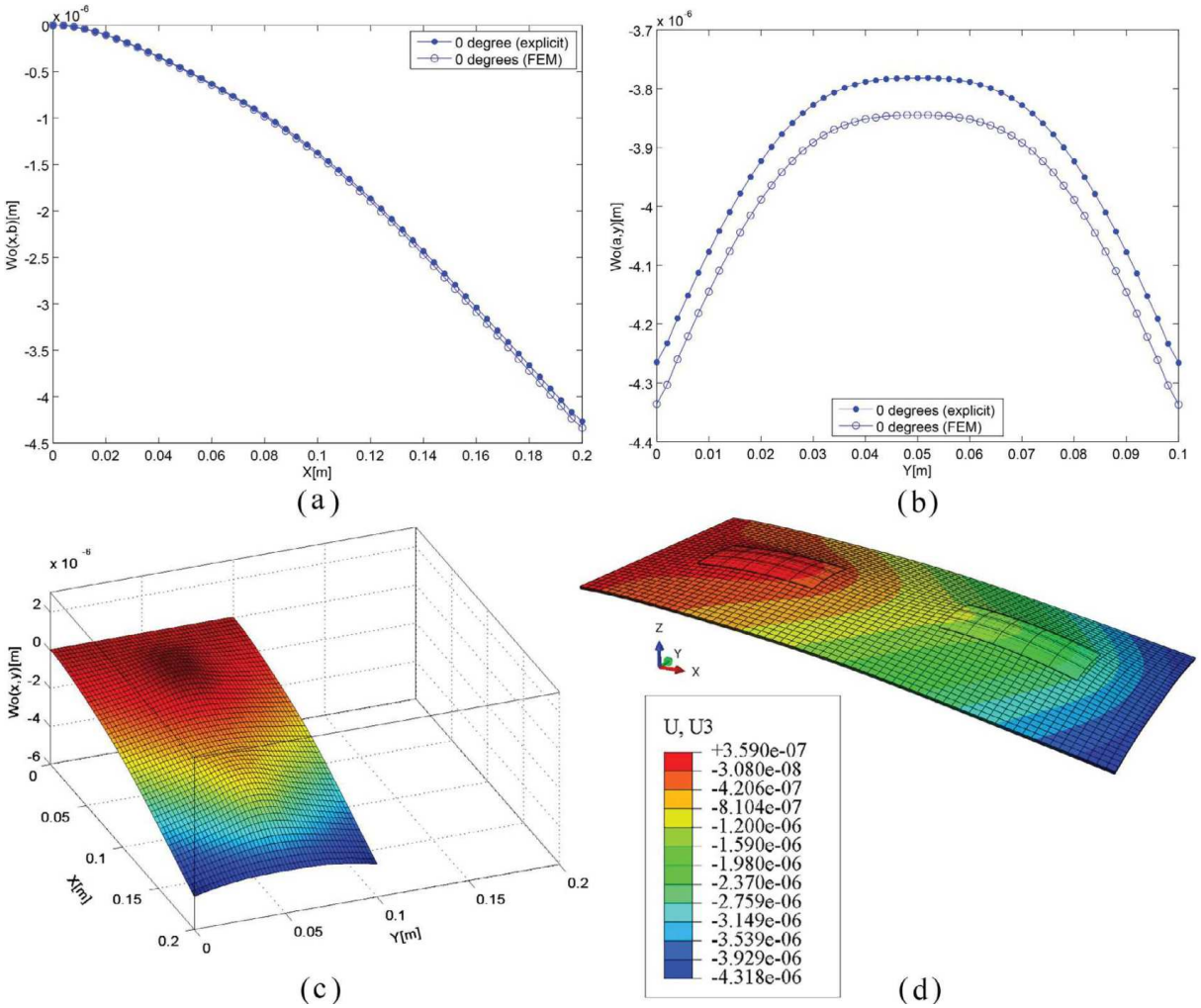


**Fig. 10.** Explicit and numerical analysis of shape deformation in the smart cantilever composite plate integrated with double piezoelectric actuators pairs when $\theta = 0^{\circ}$: (a) $w_o(x,b)$, (b) $w_o(a,y)$, (c) $w_o(x,y)$: Explicit, (d) $w_o(x,y)$: Numerical.

$$I_5^B = \int_0^a \int_0^b \left(\frac{\partial^2 M_{yy}^P}{\partial y^2}\right) \sin\left(\frac{\alpha_m}{2}x\right) \cos(\beta_n y)dxdy$$
$$= \frac{1}{6}\int_0^a \int_0^b \sum_{L=1}^{Tn}\sum_{k=1}^{N}\sum_{j=1,2,6} [\overline{Q}_{2j}]^k [\overline{d}_{3j}]^k h_k \Big\{\Phi_a^k(h_k+3z_k) + \Phi_b^k(2h_k+3z_k)\}[U_k^L(x-x_{1P}) - U_k^L(x-x_{2P})] \times [\delta_k'^L(y-y_{1P}) - \delta_k'^L(y-y_{2P})] \sin\left(\frac{\alpha_m}{2}x\right)\cos(\beta_n y)dxdy$$
$$= \frac{1}{6}\sum_{L=1}^{Tn}\sum_{k=1}^{N}\sum_{j=1,2,6} \frac{2\beta_n}{\alpha_m}[\overline{Q}_{2j}]^k [\overline{d}_{3j}]^k h_k \{\Phi_a^k(h_k+3z_k) + \Phi_b^k(2h_k+3z_k)\}\left(\cos\left(\frac{\alpha_m}{2}x_{1P}\right) - \cos\left(\frac{\alpha_m}{2}x_{2P}\right)\right)_L \times (\sin(\beta_n y_{1P}) - \sin(\beta_n y_{2P}))_L \quad (23e)$$

$$I_5^C = \int_0^a \int_0^b \left(2\frac{\partial^2 M_{xy}^P}{\partial x \partial y}\right) \sin\left(\frac{\alpha_m}{2}x\right)\cos(\beta_n y)dxdy$$
$$= \frac{1}{3}\int_0^a \int_0^b \sum_{L=1}^{Tn}\sum_{k=1}^{N}\sum_{j=1,2,6} [\overline{Q}_{6j}]^k [\overline{d}_{3j}]^k h_k \Big\{\Phi_a^k(h_k+3z_k) + \Phi_b^k(2h_k+3z_k)\}[\delta_k^L(x-x_{1P}) - \delta_k^L(x-x_{2P})] \times [\delta_k^L(y-y_{1P}) - \delta_k^L(y-y_{2P})] \sin\left(\frac{\alpha_m}{2}x\right)\cos(\beta_n y)dxdy$$
$$= \frac{1}{3}\sum_{L=1}^{Tn}\sum_{k=1}^{N}\sum_{j=1,2,6} [\overline{Q}_{6j}]^k [\overline{d}_{3j}]^k h_k \{\Phi_a^k(h_k+3z_k) + \Phi_b^k(2h_k+3z_k)\} \times \left(\sin\left(\frac{\alpha_m}{2}x_{1P}\right) - \sin\left(\frac{\alpha_m}{2}x_{2P}\right)\right)_L (\cos(\beta_n y_{1P}) - \cos(\beta_n y_{2P}))_L \quad (23f)$$

Hence, the effect of twisting-bending moments acting on a smart laminated cantilever piezo composite plate is stated in Eqs. (24a–f). According to Eq. (24f), it is assumed that the electrical intensity field varies linearly through piezoelectric actuators thickness.

If $n = \{0\}$, $m = \{1,3,5\ldots\}$, then,

$$I_5 = \sum_{L=1}^{Tn}\left[\frac{\alpha_m [M_x^P]^{\Theta}}{2}\right]\left(\cos\left(\frac{\alpha_m}{2}x_{1P}\right) - \cos\left(\frac{\alpha_m}{2}x_{2P}\right)\right)_L (y_{1P} - y_{2P})_L \quad (24a)$$

and if $n = \{1,2,3,\ldots\}$, $m = \{1,3,5,\ldots\}$, then,

$$I_5 = \sum_{L=1}^{Tn}\left[\left\{\frac{[M_x^P]^{\Theta}\alpha_m^2 + 4[M_y^P]^{\Theta}\beta_n^2}{2\alpha_m\beta_n}\left(\cos\left(\frac{\alpha_m}{2}x_{1P} - \cos\left(\frac{\alpha_m}{2}x_{2P}\right)\right)\right)_L (\sin(\beta_n y_{1P}) - \sin(\beta_n y_{2P}))_L\right\} + \left\{[M_{xy}^P]^{\Theta}\left(\sin\left(\frac{\alpha_m}{2}x_{1P}\right) - \sin\left(\frac{\alpha_m}{2}x_{2P}\right)\right)_L \times (\cos(\beta_n y_{1P}) - \cos(\beta_n y_{2P}))_L\right\}\right] \quad (24b)$$

where,

$$[M_x^P]^{\Theta} = \frac{1}{6}\sum_{k=1}^{N}\sum_{j=1,2,6} [\overline{Q}_{1j}]^k [\overline{d}_{3j}]^k \{\Phi_a^k(h_k+3z_k) + \Phi_b^k(2h_k+3z_k)\}h_k \quad (24c)$$

$$[M_y^p]^{\Theta} = \frac{1}{6}\sum_{k=1}^{N}\sum_{j=1,2,6}[\overline{Q}_{2j}]^k[\overline{d}_{3j}]^k\{\Phi_a^k(h_k+3z_k)+\Phi_b^k(2h_k+3z_k)\}h_k \tag{24d}$$

$$[M_{xy}^p]^{\Theta} = \frac{1}{3}\sum_{k=1}^{N}\sum_{j=1,2,6}[\overline{Q}_{6j}]^k[\overline{d}_{3j}]^k\{\Phi_a^k(h_k+3z_k)+\Phi_b^k(2h_k+3z_k)\}h_k \tag{24e}$$

$$\Phi_a^k = \Phi_b^k = \frac{V_a^k}{t_a^k} \tag{24f}$$

The values $x_{1M}$, $x_{2M}$, $x_{1P}$, $x_{2P}$, $y_{1M}$, $y_{2M}$, $y_{1P}$, and $y_{2P}$ are the placements of effective mechanical and electrical loads along $x$ and $y$ axis, respectively. $V_a^k$ stands for the applied electrical voltage through the $k$th layer's thickness and $t_a^k$ presents the thickness of the piezoelectric actuators in the $k$th layer. For the shell/plate type piezoelectric materials, only the transverse electric field component is dominant when the electrical voltage $V_a$ is applied to the actuators through thickness [61,62]. In the next step, parameters $I_1, I_2, \ldots, I_5$ are substituted into Eq. (21a), resulting in Eq. (25). Simplifying and rearranging both sides of Eq. (25) leads to Eqs. (26a–d). $x_{1P}$, $x_{2P}$, $y_{1P}$, and $y_{2P}$ can be obtained using Eqs. (24g–j), respectively.

$$x_{1p} = O_x - \frac{1}{2}\sqrt{L_a^2+W_a^2}\cos\left(\arctan\left(\frac{W_a}{L_a}\right)\right) \tag{24g}$$

$$x_{2p} = O_x + L_a - \frac{1}{2}\sqrt{L_a^2+W_a^2}\cos\left(\arctan\left(\frac{W_a}{L_a}\right)\right) \tag{24h}$$

$$y_{1p} = O_y + \frac{1}{2}\sqrt{L_a^2+W_a^2}\sin\left(\arctan\left(\frac{W_a}{L_a}\right)\right) \tag{24i}$$

$$y_{2p} = O_y + W_a + \frac{1}{2}\sqrt{L_a^2+W_a^2}\sin\left(\arctan\left(\frac{W_a}{L_a}\right)\right) \tag{24j}$$

$O_x$ and $O_y$ are the $x$ and $y$ coordinates of the inclined piezoelectric actuators, respectively (see Fig. 2).

$$\begin{aligned}
&D_{11}\int_0^b\left[(-1)^{\frac{m-1}{2}}\left(\frac{\partial^3 w_0}{\partial x^3}\middle|x=a\right)+\frac{\alpha_m}{2}\left(\frac{\partial^2 w_0}{\partial x^2}\middle|x=0\right)\right.\\
&\left.-(-1)^{\frac{m-1}{2}}\frac{\alpha_m^2}{4}\left(\frac{\partial w_0}{\partial x}\middle|x=a\right)\right]\cos(\beta_n y)dy\\
&+D_{11}\frac{\alpha_m^4}{16}w_{mn}D_{22}\int_0^a\left[(-1)^n\left(\frac{\partial^3 w_0}{\partial y^3}\middle|y=b\right)-\left(\frac{\partial^3 w_0}{\partial y^3}\middle|y=0\right)\right.\\
&\left.-(-1)^n\beta_n^2\left(\frac{\partial w_0}{\partial y}\middle|y=b\right)+\beta_n^2\left(\frac{\partial w_0}{\partial y}\middle|y=0\right)\right]\\
&\times\sin\left(\frac{\alpha_m}{2}x\right)dx+D_{22}\beta_n^4 w_{mn}+(D_{12}+2D_{66})\frac{\alpha_m^2\beta_n^2}{2}w_{mn}\\
&-(D_{12}+2D_{66})\frac{\alpha_m^2}{2}\int_0^a\left[(-1)^n\left(\frac{\partial w_0}{\partial y}\middle|y=b\right)-\left(\frac{\partial w_0}{\partial y}\middle|y=0\right)\right]\\
&\times\sin\left(\frac{\alpha_m}{2}x\right)dx-2(D_{12}+2D_{66})(-1)^{\frac{m-1}{2}}\beta_n^2\int_0^b\left[\left(\frac{\partial w_0}{\partial x}\middle|x=a\right)\right]\\
&\times\cos(\beta_n y)dy=\sum_{L=1}^{Mn}C_{mn}^1\left(\frac{-2P_0}{\alpha_m\beta_n}\right)\left(\cos\left(\frac{\alpha_m}{2}x_{1M}\right)-\cos\left(\frac{\alpha_m}{2}x_{2M}\right)\right)_L\\
&\times(\sin(\beta_n y_{1M})-\sin(\beta_n y_{2M}))_L+\sum_{L=1}^{Pn}C_{mn}^2\left[\frac{[M_x^p]^{\Theta}\alpha_m^2+4[M_y^p]^{\Theta}\beta_n^2}{2\alpha_m\beta_n}\right]\\
&\times\left(\cos\left(\frac{\alpha_m}{2}x_{1P}\right)-\cos\left(\frac{\alpha_m}{2}x_{2P}\right)\right)_L(\sin(\beta_n y_{1P})-\sin(\beta_n y_{2P}))_L\\
&+\sum_{L=1}^{Pn}C_{mn}^3[M_{xy}^p]^{\Theta}\left(\sin\left(\frac{\alpha_m}{2}x_{1P}\right)-\sin\left(\frac{\alpha_m}{2}x_{2P}\right)\right)_L\\
&\times(\cos(\beta_n y_{1P})-\cos(\beta_n y_{2P}))_L
\end{aligned} \tag{25}$$

$$\begin{aligned}
&D_{11}(-1)^{\frac{m-1}{2}}\int_0^b\left(\frac{\partial^3 w_0}{\partial x^3}\middle|x=a\right)\cos(\beta_n y)dy\\
&+D_{22}(-1)^n\int_0^a\left(\frac{\partial^3 w_0}{\partial y^3}\middle|y=b\right)\sin\left(\frac{\alpha_m}{2}x\right)dx\\
&-(-1)^n\left(D_{22}\beta_n^2+\frac{(D_{12}+2D_{66})\alpha_m^2}{2}\right)\int_0^a\left(\frac{\partial w_0}{\partial y}\middle|y=b\right)\sin\left(\frac{\alpha_m}{2}x\right)dx\\
&-D_{22}\int_0^a\left(\frac{\partial^3 w_0}{\partial y^3}\middle|y=0\right)\sin\left(\frac{\alpha_m}{2}x\right)dx\\
&+\left(D_{22}\beta_n^2+\frac{(D_{12}+2D_{66})\alpha_m^2}{2}\right)\int_0^a\left(\frac{\partial w_0}{\partial y}\middle|y=0\right)\sin\left(\frac{\alpha_m}{2}x\right)dx\\
&-(-1)^{\frac{m-1}{2}}\left(\frac{D_{11}\alpha_m^2}{4}+2(D_{12}+2D_{66})\beta_n^2\right)\int_0^b\left(\frac{\partial w_0}{\partial x}\middle|x=a\right)\\
&\times\cos(\beta_n y)dy+\left(\frac{D_{11}\alpha_m}{2}\right)\int_0^b\left(\frac{\partial^2 w_0}{\partial x^2}\middle|x=0\right)\cos(\beta_n y)dy\\
&+\left(\frac{D_{11}\alpha_m^4}{16}+\frac{(D_{12}+2D_{66})\alpha_m^2\beta_n^2}{2}+D_{22}\beta_n^4\right)w_{mn}\\
&=\sum_{L=1}^{Mn}C_{mn}^1\left(\frac{-2P_0}{\alpha_m\beta_n}\right)\left(\cos\left(\frac{\alpha_m}{2}x_{1M}\right)-\cos\left(\frac{\alpha_m}{2}x_{2M}\right)\right)_L\\
&\times(\sin(\beta_n y_{1M})-\sin(\beta_n y_{2M}))_L+\sum_{L=1}^{Pn}C_{mn}^2\left[\frac{[M_x^p]^{\Theta}\alpha_m^2+4[M_y^p]^{\Theta}\beta_n^2}{2\alpha_m\beta_n}\right]\\
&\times\left(\cos\left(\frac{\alpha_m}{2}x_{1P}\right)-\cos\left(\frac{\alpha_m}{2}x_{2P}\right)\right)_L(\sin(\beta_n y_{1P})-\sin(\beta_n y_{2P}))_L\\
&+\sum_{L=1}^{Pn}C_{mn}^3[M_{xy}^p]^{\Theta}\left(\sin\left(\frac{\alpha_m}{2}x_{1P}\right)-\sin\left(\frac{\alpha_m}{2}x_{2P}\right)\right)_L\\
&\times(\cos(\beta_n y_{1P})-\cos(\beta_n y_{2P}))_L
\end{aligned} \tag{26a}$$

where,

$$C_{mn}^1=\begin{cases}n=0,m=1,3,5,\ldots & \to 1\\ n=1,2,3,\ldots,m=1,3,5,\ldots & \to \beta_n\left[\frac{y_{1M}-y_{2M}}{\sin(\beta_n y_{1M})-\sin(\beta_n y_{2M})}\right]_L\end{cases} \tag{26b}$$

$$C_{mn}^2=\begin{cases}n=0,m=1,3,5,\ldots & \to \frac{[M_x^{P_1}]^{\Theta}\alpha_m^2\beta_n}{[M_x^{P_1}]^{\Theta}\alpha_m^2+4[M_y^{P_1}]^{\Theta}\beta_n^2}\left[\frac{y_{1P}-y_{2P}}{\sin(\beta_n y_{1P})-\sin(\beta_n y_{2P})}\right]_L\\ n=1,2,3,\ldots,m=1,3,5,\ldots & \to 1\end{cases} \tag{26c}$$

$$C_{mn}^3=\begin{cases}n=0,m=1,3,5,\ldots & \to 0\\ n=1,2,3,\ldots,m=1,3,5,\ldots & \to 1\end{cases} \tag{26d}$$

$C_{mn}^1$, $C_{mn}^2$, and $C_{mn}^3$ can be defined as effective mechanical and electrical bending and electrical twisting coefficients in the smart laminated cantilever piezo composite plate, respectively. The boundary conditions in Eqs. (18f–h) are expanded as shown in Eqs. (27a–c) and then substituted into Eq. (26a). Rearranging Eq. (26a) results in Eq. (28). For simplicity purposes, unknown variables $\Delta_m$, $\Omega_m$, $\Pi_n$, and $\Psi_n$ are defined as shown in Eqs. (29a–d), respectively.

$$\begin{aligned}
&D_{11}\int_0^b\left(\frac{\partial^3 w_0}{\partial x^3}\middle|x=a\right)\cos(\beta_n y)dy\\
&=(3D_{12}+2D_{66})\beta_n^2\int_0^b\left(\frac{\partial w_0}{\partial x}\middle|x=a\right)\cos(\beta_n y)dy
\end{aligned} \tag{27a}$$

$$D_{22}\int_0^a\left(\frac{\partial^3 w_0}{\partial y^3}\middle| y=0\right)\sin\left(\frac{\alpha_m}{2}x\right)dx = \frac{1}{4}(3D_{12}+2D_{66})\alpha_m^2\int_0^a\left(\frac{\partial w_0}{\partial y}\middle| y=0\right)\sin\left(\frac{\alpha_m}{2}x\right)dx \tag{27b}$$

$$D_{22}\int_0^a\left(\frac{\partial^3 w_0}{\partial y^3}\middle| y=b\right)\sin\left(\frac{\alpha_m}{2}x\right)dx = \frac{1}{4}(3D_{12}+2D_{66})\alpha_m^2\int_0^a\left(\frac{\partial w_0}{\partial y}\middle| y=b\right)\sin\left(\frac{\alpha_m}{2}x\right)dx \tag{27c}$$

$$\begin{aligned}
&-(-1)^n\left[D_{22}\beta_n^2+D_{12}\frac{\alpha_m^2}{4}\right]\int_0^a\left(\frac{\partial w_0}{\partial y}\middle| y=b\right)\sin\left(\frac{\alpha_m}{2}x\right)dx\\
&+\left[D_{22}\beta_n^2+D_{12}\frac{\alpha_m^2}{4}\right]\int_0^a\left(\frac{\partial w_0}{\partial y}\middle| y=0\right)\sin\left(\frac{\alpha_m}{2}x\right)dx-(-1)^{\frac{m-1}{2}}\\
&\times\left[D_{12}\beta_n^2+D_{11}\frac{\alpha_m^2}{4}\right]\int_0^b\left(\frac{\partial w_0}{\partial x}\middle| x=a\right)\cos(\beta_n y)dy+D_{11}\frac{\alpha_m}{2}\\
&\times\int_0^b\left(\frac{\partial^2 w_0}{\partial x^2}\middle| x=0\right)\cos(\beta_n y)dy\\
&+\left[\frac{D_{11}\alpha_m^4}{16}+\frac{(D_{12}+2D_{66})\alpha_m^2\beta_n^2}{2}+D_{22}\beta_n^4\right]w_{mn}\\
&=\sum_{L=1}^{Mn}C_{mn}^1\left(\frac{-2P_0}{\alpha_m\beta_n}\right)\left(\cos\left(\frac{\alpha_m}{2}x_{1M}\right)-\cos\left(\frac{\alpha_m}{2}x_{2M}\right)\right)_L\\
&\times(\sin(\beta_n y_{1M})-\sin(\beta_n y_{2M}))_L\\
&+\sum_{L=1}^{Pn}C_{mn}^2\left[\frac{[M_x^{P_1}]^{\Theta}\alpha_m^2+4[M_y^{P_1}]^{\Theta}\beta_n^2}{2\alpha_m\beta_n}\right]\left(\cos\left(\frac{\alpha_m}{2}x_{1P}\right)-\cos\left(\frac{\alpha_m}{2}x_{2P}\right)\right)_L\\
&\times(\sin(\beta_n y_{1P})-\sin(\beta_n y_{2P}))_L+\sum_{L=1}^{Pn}C_{mn}^3[M_{xy}^{P}]^{\Theta}\\
&\times\left(\sin\left(\frac{\alpha_m}{2}x_{1P}\right)-\sin\left(\frac{\alpha_m}{2}x_{2P}\right)\right)_L(\cos(\beta_n y_{1P})-\cos(\beta_n y_{2P}))_L
\end{aligned}\tag{28}$$

$$\Delta_m=\int_0^a\left(\frac{\partial w_0}{\partial y}\middle| y=b\right)\sin\left(\frac{\alpha_m}{2}x\right)dx \tag{29a}$$

$$\Omega_m=\int_0^a\left(\frac{\partial w_0}{\partial y}\middle| y=0\right)\sin\left(\frac{\alpha_m}{2}x\right)dx \tag{29b}$$

$$\Pi_n=\int_0^b\left(\frac{\partial w_0}{\partial x}\middle| x=a\right)\cos(\beta_n y)dy \tag{29c}$$

$$\Psi_n=\int_0^b\left(\frac{\partial^2 w_0}{\partial x^2}\middle| x=0\right)\cos(\beta_n y)dy \tag{29d}$$

Substituting Eqs. (29a–d) into Eq. (28) and then rearranging Eq. (28) yields Eq. (30), which satisfies the boundary conditions in Eq. (18). Eq. (30) represents the double finite integral transformation of the mid-plane vertical displacement of function $w_o(x,y)$ in the smart laminated cantilever piezo composite plate incorporated with arbitrarily positioned inclined piezoelectric actuators and under electro-mechanical loads, which can be expressed in terms of function $w_{mn}$. In the next attempt, the remaining boundary conditions in Eqs. (18c–e) are substituted in the first and second partial derivatives of the double Fourier series $w_o(x,y)$ in Eqs. (31a–d) [60]. Simplifying and rearranging Eqs. (31a–d) results in Eqs. (32a–d).

$$\begin{aligned}
w_{mn}=&\left[\frac{D_{11}\alpha_m^4}{16}+\frac{(D_{12}+2D_{66})\alpha_m^2\beta_n^2}{2}+D_{22}\beta_n^4\right]^{-1}\\
&\times\left\{\sum_{L=1}^{Mn}C_{mn}^1\left(\frac{-2P_0}{\alpha_m\beta_n}\right)\left(\cos\left(\frac{\alpha_m}{2}x_{1M}\right)-\cos\left(\frac{\alpha_m}{2}x_{2M}\right)\right)_L\right.\\
&\times(\sin(\beta_n y_{1M})-\sin(\beta_n y_{2M}))_L\\
&+\sum_{L=1}^{Pn}C_{mn}^2\left[\frac{[M_x^{P_1}]^{\Theta}\alpha_m^2+4[M_y^{P_1}]^{\Theta}\beta_n^2}{2\alpha_m\beta_n}\right]\\
&\times\left(\cos\left(\frac{\alpha_m}{2}x_{1P}\right)-\cos\left(\frac{\alpha_m}{2}x_{2P}\right)\right)_L(\sin(\beta_n y_{1P})-\sin(\beta_n y_{2P}))_L\\
&+\sum_{L=1}^{Pn}C_{mn}^3[M_{xy}^{P}]^{\Theta}\left(\sin\left(\frac{\alpha_m}{2}x_{1P}\right)-\sin\left(\frac{\alpha_m}{2}x_{2P}\right)\right)_L\\
&\times(\cos(\beta_n y_{1P})-\cos(\beta_n y_{2P}))_L+(-1)^n\left[D_{22}\beta_n^2+D_{12}\frac{\alpha_m^2}{4}\right]\Delta_m\\
&-\left[D_{22}\beta_n^2+D_{12}\frac{\alpha_m^2}{4}\right]\Omega_m+(-1)^{\frac{m-1}{2}}\left[D_{12}\beta_n^2+D_{11}\frac{\alpha_m^2}{4}\right]\Pi_n\\
&\left.-\left[\frac{D_{11}\alpha_m}{2}\right]\Psi_n\right\}
\end{aligned}\tag{30}$$

$$\begin{aligned}
\frac{\partial w_0(x,y)}{\partial x}&=\frac{4}{ab}\sum_{m=1,3,5,\ldots}^{\infty}\sum_{n=0,1,2,\ldots}^{\infty}\lambda_n\lambda^{*}\cos\left(\frac{\alpha_m}{2}x\right)\cos(\beta_n y)\\
&=\frac{4}{ab}\sum_{m=1,3,5,\ldots}^{\infty}\sum_{n=0,1,2,\ldots}^{\infty}\lambda_n\left[\frac{\alpha_m}{2}w_{mn}\right]\cos\left(\frac{\alpha_m}{2}x\right)\cos(\beta_n y)
\end{aligned}\tag{31a}$$

$$\begin{aligned}
\frac{\partial^2 w_0(x,y)}{\partial x^2}&=\frac{4}{ab}\sum_{m=1,3,5,\ldots}^{\infty}\sum_{n=0,1,2,\ldots}^{\infty}\lambda_n\lambda^{**}\sin\left(\frac{\alpha_m}{2}x\right)\cos(\beta_n y)\\
&=\frac{4}{ab}\sum_{m=1,3,5,\ldots}^{\infty}\sum_{n=0,1,2,\ldots}^{\infty}\\
&\quad\times\lambda_n\left[(-1)^{\frac{m-1}{2}}\int_0^b\left(\frac{\partial w_0(x,y)}{\partial x}\middle|(x=a)\right)\cos(\beta_n y)dy-\frac{\alpha_m^2}{4}w_{mn}\right]\\
&\quad\times\sin\left(\frac{\alpha_m}{2}x\right)\cos(\beta_n y)
\end{aligned}\tag{31b}$$

$$\begin{aligned}
\frac{\partial w_0(x,y)}{\partial y}&=\frac{4}{ab}\sum_{m=1,3,5,\ldots}^{\infty}\sum_{n=1,2,3,\ldots}^{\infty}\lambda_n\lambda^{*}\sin\left(\frac{\alpha_m}{2}x\right)\sin(\beta_n y)\\
&=\frac{4}{ab}\sum_{m=1,3,5,\ldots}^{\infty}\sum_{n=1,2,3,\ldots}^{\infty}\lambda_n[-\beta_n w_{mn}]\sin\left(\frac{\alpha_m}{2}x\right)\sin(\beta_n y)
\end{aligned}\tag{31c}$$

$$\begin{aligned}
\frac{\partial^2 w_0(x,y)}{\partial y^2}&=\frac{4}{ab}\sum_{m=1,3,5,\ldots}^{\infty}\sum_{n=0,1,2,\ldots}^{\infty}\lambda_n\lambda^{**}\sin\left(\frac{\alpha_m}{2}x\right)\cos(\beta_n y)\\
&=\frac{4}{ab}\sum_{m=1,3,5,\ldots}^{\infty}\sum_{n=0,1,2,\ldots}^{\infty}\\
&\quad\times\lambda_n\left[(-1)^n\int_0^a\left(\frac{\partial w_0(x,y)}{\partial y}\middle|(y=b)\right)\sin\left(\frac{\alpha_m}{2}x\right)dx\right.\\
&\quad\left.-\int_0^a\left(\frac{\partial w_0(x,y)}{\partial y}\middle|(y=0)\right)\sin\left(\frac{\alpha_m}{2}x\right)dx-\left(\frac{\alpha_m^2}{4}+\beta_n^2\right)w_{mn}\right]\\
&\quad\times\sin\left(\frac{\alpha_m}{2}x\right)\cos(\beta_n y)
\end{aligned}\tag{31d}$$

$$\sum_{m=1,3,5,\ldots}^{\infty}\sum_{n=0,1,2,\ldots}^{\infty}\alpha_m w_{mn}\cos(\beta_n y)=0 \tag{32a}$$

$$\sum_{m=1,3,5,\ldots}^{\infty}\sum_{n=0,1,2,\ldots}^{\infty}(-1)^{\frac{m-1}{2}}\left[D_{12}(-1)^{n}\Delta_m - D_{12}\Omega_m + D_{11}(-1)^{\frac{m-1}{2}}\Pi_n - \left[D_{12}\beta_n^2 + \frac{D_{11}\alpha_m^2}{4}\right]w_{mn}\right]\cos(\beta_n y) = 0 \tag{32b}$$

$$\sum_{m=1,3,5,\ldots}^{\infty}\sum_{n=0,1,2,\ldots}^{\infty}\lambda_n\left[D_{22}(-1)^{n}\Delta_m - D_{22}\Omega_m + D_{12}(-1)^{\frac{m-1}{2}}\Pi_n - \left[D_{22}\beta_n^2 + \frac{D_{12}\alpha_m^2}{4}\right]w_{mn}\right]\sin\left(\frac{\alpha_m}{2}x\right) = 0 \tag{32c}$$

$$\sum_{m=1,3,5,\ldots}^{\infty}\sum_{n=0,1,2,\ldots}^{\infty}\lambda_n\left[D_{22}\Delta_m - D_{22}(-1)^{n}\Omega_m + D_{12}(-1)^{n}(-1)^{\frac{m-1}{2}}\Pi_n - (-1)^{n}\left[D_{22}\beta_n^2 + \frac{D_{12}\alpha_m^2}{4}\right]w_{mn}\right]\sin\left(\frac{\alpha_m}{2}x\right) = 0 \tag{32d}$$

The double finite integral transformation $CI_n$ and $SI_m$ are performed over Eqs. (32a,b) and (32c–d), respectively. The $CI_n$ and $SI_m$ are stated in Eqs. (33a,b), respectively. Performing integration over the specified domains results in Eqs. (34a–d), respectively.

$$CI_n = \int_0^b \cos(\beta_n y)dy \tag{33a}$$

$$SI_m = \int_0^a \sin\left(\frac{\alpha_m}{2}x\right)dx \tag{33b}$$

$$\sum_{m=1,3,5,\ldots}^{\infty}\sum_{n=0,1,2,\ldots}^{\infty}\alpha_m w_{mn} = 0 \tag{34a}$$

$$\sum_{m=1,3,5,\ldots}^{\infty}\sum_{n=0,1,2,\ldots}^{\infty}(-1)^{\frac{m-1}{2}}\left[D_{12}(-1)^{n}\Delta_m - D_{12}\Omega_m + D_{11}(-1)^{\frac{m-1}{2}}\Pi_n - \left[D_{12}\beta_n^2 + \frac{D_{11}\alpha_m^2}{4}\right]w_{mn}\right] = 0 \tag{34b}$$

$$\sum_{m=1,3,5,\ldots}^{\infty}\sum_{n=0,1,2,\ldots}^{\infty}\lambda_n\left[D_{22}(-1)^{n}\Delta_m - D_{22}\Omega_m - D_{12}(-1)^{\frac{m-1}{2}}\Pi_n - \left[D_{22}\beta_n^2 + \frac{D_{12}\alpha_m^2}{4}\right]w_{mn}\right] = 0 \tag{34c}$$

$$\sum_{m=1,3,5,\ldots}^{\infty}\sum_{n=0,1,2,\ldots}^{\infty}\lambda_n\left[D_{22}\Delta_m - D_{22}(-1)^{n}\Omega_m + D_{12}(-1)^{n}(-1)^{\frac{m-1}{2}}\Pi_n - (-1)^{n}\times\left[D_{22}\beta_n^2 + \frac{D_{12}\alpha_m^2}{4}\right]w_{mn}\right] = 0 \tag{34d}$$

Finally, Eq. (30) is substituted into Eqs. (34a–d) to obtain the four finite systems of linear simultaneous multivariable equations, as stated in Eqs. (35a–d), respectively. The sufficient finite terms of $m$ and $n$ in each set of multivariable equations are considered in order to accurately compute the constant values of unknown variables $\Delta_m$, $\Omega_m$, $\Pi_n$, and $\Psi_n$.

$$\sum_{m=1,3,5,\ldots}^{\infty}\sum_{n=0,1,2,\ldots}^{\infty}S_{mn}^{1}\Delta_m + \sum_{m=1,3,5,\ldots}^{\infty}\sum_{n=0,1,2,\ldots}^{\infty}S_{mn}^{2}\Omega_m + \sum_{m=1,3,5,\ldots}^{\infty}\sum_{n=0,1,2,\ldots}^{\infty}S_{mn}^{3}\Pi_n + \sum_{m=1,3,5,\ldots}^{\infty}\sum_{n=0,1,2,\ldots}^{\infty}S_{mn}^{4}\Psi_n = \sum_{m=1,3,5,\ldots}^{\infty}\sum_{n=0,1,2,\ldots}^{\infty}S_{mn}^{5} \tag{35a}$$

$$\sum_{m=1,3,5,\ldots}^{\infty}\sum_{n=0,1,2,\ldots}^{\infty}S_{mn}^{6}\Delta_m + \sum_{m=1,3,5,\ldots}^{\infty}\sum_{n=0,1,2,\ldots}^{\infty}S_{mn}^{7}\Omega_m + \sum_{m=1,3,5,\ldots}^{\infty}\sum_{n=0,1,2,\ldots}^{\infty}S_{mn}^{8}\Pi_n + \sum_{m=1,3,5,\ldots}^{\infty}\sum_{n=0,1,2,\ldots}^{\infty}S_{mn}^{9}\Psi_n = \sum_{m=1,3,5,\ldots}^{\infty}\sum_{n=0,1,2,\ldots}^{\infty}S_{mn}^{10} \tag{35b}$$

$$\sum_{m=1,3,5,\ldots}^{\infty}\sum_{n=0,1,2,\ldots}^{\infty}S_{mn}^{11}\Delta_m + \sum_{m=1,3,5,\ldots}^{\infty}\sum_{n=0,1,2,\ldots}^{\infty}S_{mn}^{12}\Omega_m + \sum_{m=1,3,5,\ldots}^{\infty}\sum_{n=0,1,2,\ldots}^{\infty}S_{mn}^{13}\Pi_n + \sum_{m=1,3,5,\ldots}^{\infty}\sum_{n=0,1,2,\ldots}^{\infty}S_{mn}^{14}\Psi_n = \sum_{m=1,3,5,\ldots}^{\infty}\sum_{n=0,1,2,\ldots}^{\infty}S_{mn}^{15} \tag{35c}$$

$$\sum_{m=1,3,5,\ldots}^{\infty}\sum_{n=0,1,2,\ldots}^{\infty}S_{mn}^{16}\Delta_m + \sum_{m=1,3,5,\ldots}^{\infty}\sum_{n=0,1,2,\ldots}^{\infty}S_{mn}^{17}\Omega_m + \sum_{m=1,3,5,\ldots}^{\infty}\sum_{n=0,1,2,\ldots}^{\infty}S_{mn}^{18}\Pi_n + \sum_{m=1,3,5,\ldots}^{\infty}\sum_{n=0,1,2,\ldots}^{\infty}S_{mn}^{19}\Psi_n = \sum_{m=1,3,5,\ldots}^{\infty}\sum_{n=0,1,2,\ldots}^{\infty}S_{mn}^{20} \tag{35d}$$

Computation of $S_{mn}^{i}$, $i = \{1,2,\ldots,20\}$ as shown in Appendix A leads to obtaining the unknown constants in Eqs. (35a–d) as four finite systems of linear simultaneous multivariable equations, which are later substituted into Eq. (30) to calculate the double finite integral transformation of the mid-plane vertical displacement of function $w_o(x,y)$. Once the $w_{mn}$ is found, it is substituted into Eq. (20) to calculate the exact mid-plane twisting-bending displacements of the function $w_o(x,y)$ in the smart laminated cantilever piezo composite plates induced by electro-mechanical loads.

## 3. Numerical simulation: finite element method (FEM)

The electro-mechanical coupled FE simulation of smart cantilever piezo composite plates and beams induced by electro-mechanical twisting-bending loads is implemented using FE software package ABAQUS/CEA 6.13-1. The smart piezo composite structure consists of the host structure (fibre-reinforced composite laminate) and the piezoelectric actuator patches. First, each part is sketched, the dimensions and material properties are assigned, and material coordinate systems are defined to composite laminate and piezoelectric actuators separately (see Fig. 3a). Since the piezoelectric actuators are polarized through thickness, only the piezoelectric coefficients $d_{31}$ and $d_{32}$ for plate/piezo and $d_{31}$ for beam/piezo systems are considered, respectively. The host structure consists of multiple cross-ply fibre-reinforced composite plies in which each ply is defined through partitioning. The host structure and the piezoelectric actuators are considered passive and active parts, respectively, which will be later assembled together in the assembly module, and subsequently the boundary conditions, piezoelectric actuators groundings, and electro-mechanical loads are applied (see Fig. 3b). For a cantilever plate/beam, the displacements and angel of rotations are equal to zero at the fixed end as seen in Fig. 3b. In ABAQYS software, $U_1$, $U_2$, and $U_3$ are defined as the displacements and $UR_1$, $UR_2$, and $UR_3$ as the rotational angels along $x$,$y$, and $z$ directions, respectively. The inclination angle between the piezoelectric actuator patches and host structure is created during the assembly. To intensify the effect of electrical twisting-bending moments and greater actuation result, the

piezoelectric actuators were symmetrically bounded with respect to the mid-plane under the same amount of constant electrical voltage but different polarization direction. In general, for an upward displacement, the upper and lower actuator patches require a negative and positive voltage, respectively and vice versa [63]. After assembling and defining the boundary conditions and loads, the Structured Hex Element Shape was set as the finite element mesh control in the smart piezo composite structure. An 8-node quadrilateral in-plane general-purpose continuum shell, reduced integration with hourglass control, finite membrane strains (SC8R) was defined as the element type in the host structure while a 20-node quadratic piezoelectric brick, reduced integration (C3D20RE) was used to define the piezoelectric actuator patches element type (see Fig. 3c). Finally, after submitting the model through the job module for the full analysis, in order to obtain the displacements in the arbitrarily selected element nodes, a path is defined along a specific direction in the smart piezo composite laminate's mid-plane (see Fig. 3d). The displacement values ($U_3$) in each path is compared with the proposed explicit results for verification.

In order to prevent the low accuracy in computational results of twisting-bending type problems known as Locking phenomenon, the solid element in FEM linear approximations should be prevented whereas it shows the twisting-bending behaviour much stiffer in comparison with exact analytical solution. Locking is higher if the solid element looks like shell (thickness is smaller than two other sizes). However, it can be resolved by selecting an appropriate FE with quadratic shape functions such as continuum shell element (SC8R). Since the Locking phenomena may still be found for FE quadratic shape functions, taking many elements for the thickness, therefore, leads to higher accuracy of the results, despite increasing the computational time as a disadvantage. Considering the element type in the piezoelectric actuator patches, a 20-node quadratic piezoelectric brick, reduced integration (C3D20RE) has more accuracy over an 8-node linear piezoelectric brick (C3D8E).

## 4. Results and discussions

In this section, various examples are intended to demonstrate and evaluate the accuracy of the proposed method for twisting-bending deformation analysis and shape control task of smart laminated cantilever piezo composite plates and beams induced electro-mechanically. The results are verified with the ones

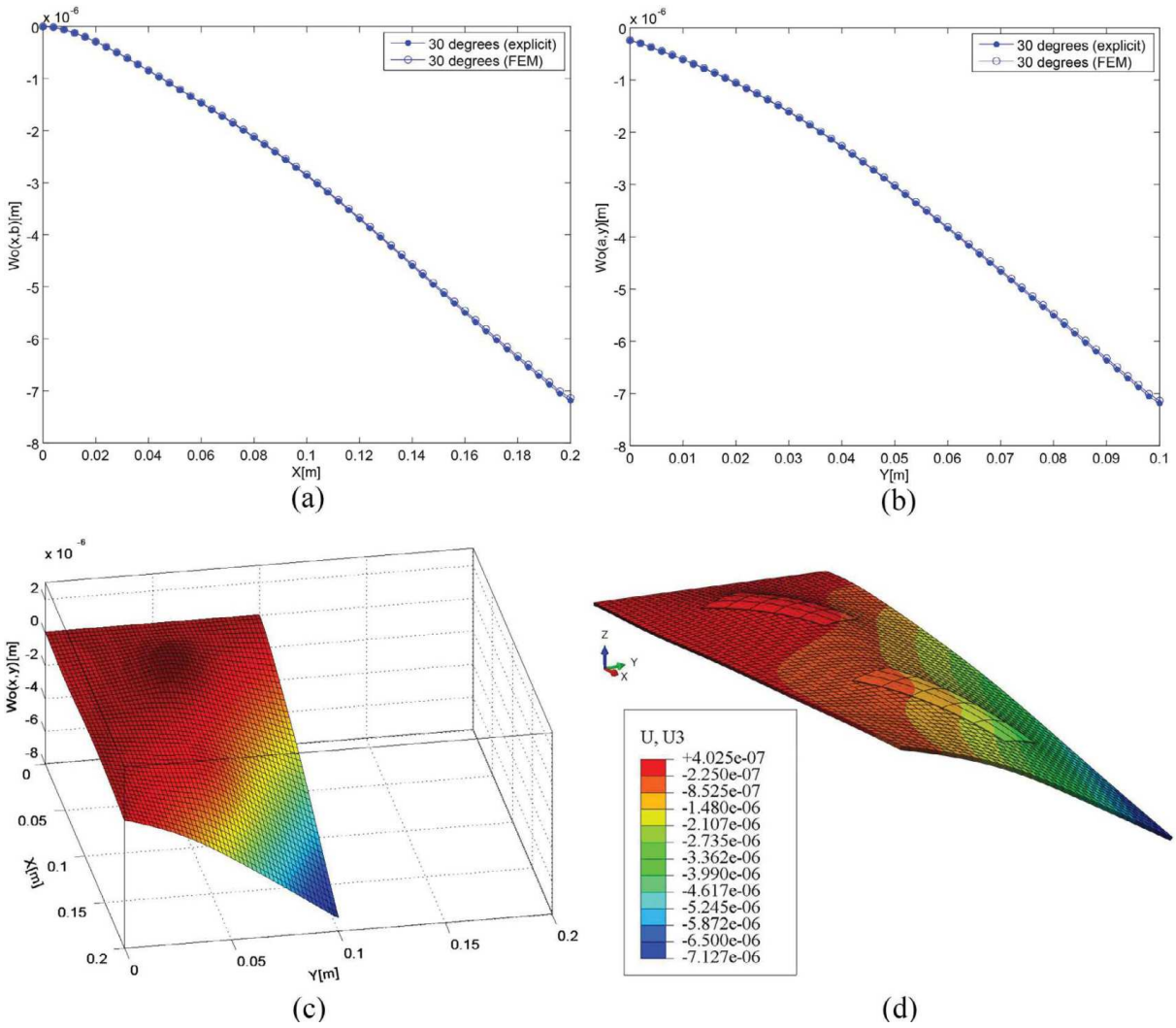


**Fig. 11.** Explicit and numerical analysis of shape deformation in the smart cantilever composite plate integrated with double piezoelectric actuators pairs when $\theta = 30^{\circ}$: (a) $w_o(x,b)$, (b) $w_o(a,y)$, (c) $w_o(x,y)$: Explicit, (d) $w_o(x,y)$: Numerical.

obtained from numerical simulation. In the first example, the effect of electrical twisting-bending coupling is taken into account. In the last example, a serious of bounded piezoelectric patches with various inclination angles are intended to control the twisting-bending deformation of the smart laminated cantilever fibre-reinforced composite beam induced by asymmetrical concentrated load at the free end corner. Generally, the effect of various parameters including electro-mechanical twisting coupling, layup thickness, piezoelectric actuators size, placement, and inclination angle, electrical potential intensity, stacking sequence, and geometrical dimension are considered using the proposed exact solution and FEM. Material properties of piezoelectric actuators and fibre-reinforced composite laminates used in the following examples are summarised in Table 1 [61,63,64].

### 4.1. Example 1: effect of single inclined actuators pair on twisting deformation of the smart laminated cantilever piezo composite plates

As shown in Fig. 4a, a smart elastic cantilever composite plate ($a = 0.2\ [m]$, $b = 0.04\ [m]$) with thickness $t_p = 1\ [mm]$ and made of unidirectional T300/976 GFRP is incorporated with KYNAR piezoelectric actuator patches ($t_a = 0.2\ [mm]$, $L_a = 0.1\ [m]$, $w_a = 0.05\ [m]$). The host structure is a fourth-layered cross-ply laminate with stacking sequence of $[0/90]_s$. Each composite ply is assumed to have the same thickness. A single inclined piezoelectric actuators pair, as shown in Fig. 4a, are bounded to the plate and then polarized with opposite directions (upper patch: 300 [V] and lower patch: −300 [V]). The inclination angle created in the piezoelectric actuators with respect to $x$ axis causes the plate to twist due to existence of electrical twisting moment $[M_{xy}^P]$. The mechanical twisting-bending deformation created in the smart cantilever composite plate as a result of electro-mechanical coupling is analysed against various inclination angles {0°,30°,45°, 60°,90°} through new proposed explicit solution and FEM (see Figs. 5–9). Good agreement between the results is observed. It can be noticed from the results obtained from both approaches that when the inclination angle is equal to 0 (see Fig. 5) and 90 (see Fig. 9) degrees, no twisting deformation occurs in the plate while the effect of longitudinal and transverse piezoelectric coefficients is switched when inclination angle is 90 degrees ($d_{31} \rightarrow d_{32}$ and $d_{32} \rightarrow d_{31}$). Moreover, according to Figs. 6–8, as the inclination angle increases, the electrical twisting moment effectiveness reduces. Thus, 30 degrees results in the most twisting deformation while 60 degrees the lowest.

### 4.2. Example 2: effect of double inclined actuators pairs on twisting deformation of the smart laminated cantilever piezo composite plates

A combination of the multiple bounded inclined actuators groups ($t_a = 0.2\ [mm]$, $L_a = 0.05\ [m]$, $w_a = 0.025\ [m]$) positioned at

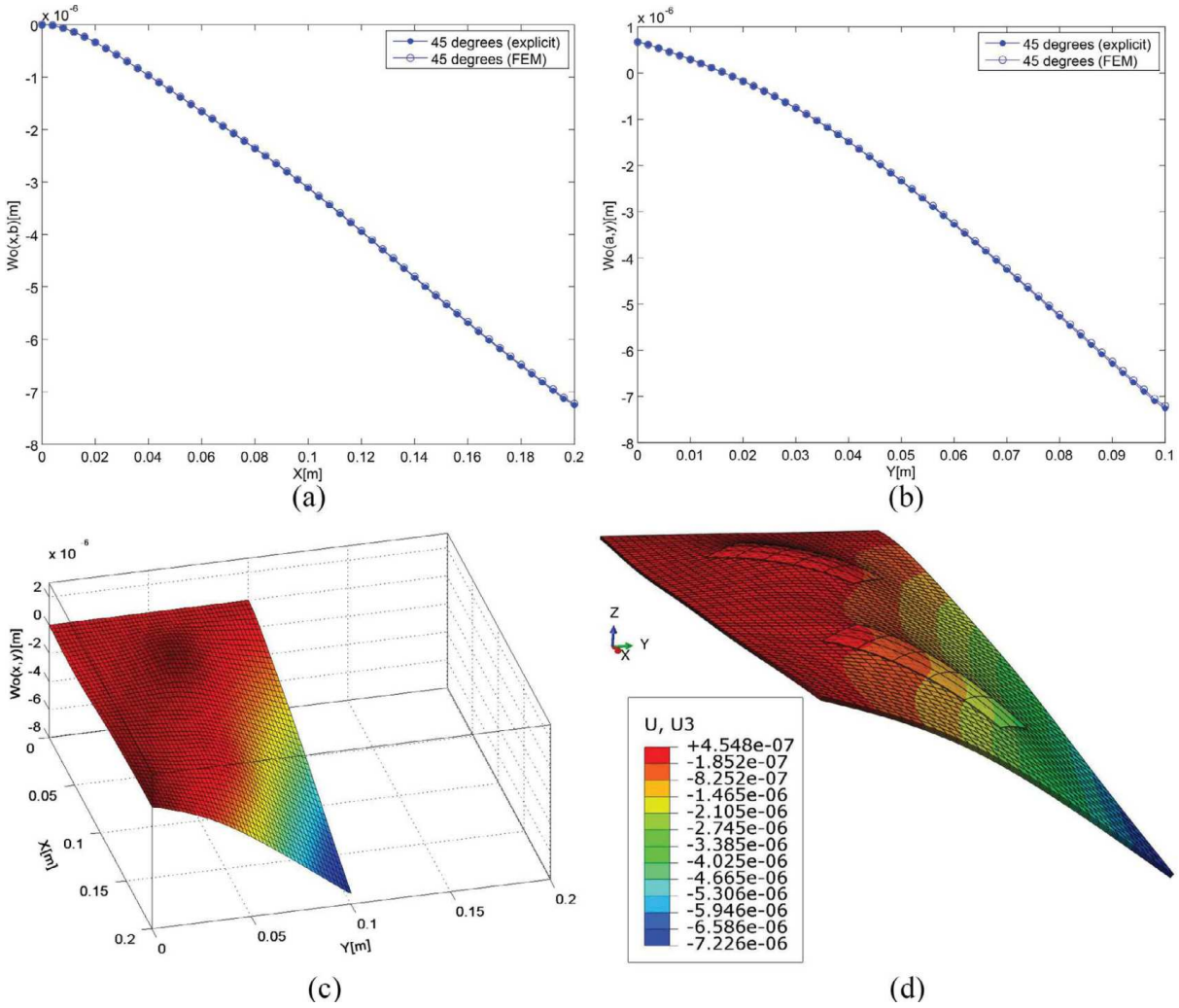


**Fig. 12.** Explicit and numerical analysis of shape deformation in the smart cantilever composite plate integrated with double piezoelectric actuators pairs when $\theta = 45°$: (a) $w_o(x,b)$, (b) $w_o(a,y)$, (c) $w_o(x,y)$: Explicit, (d) $w_o(x,y)$: Numerical.

① and ② in the smart elastic cantilever composite plate ($t_p = 1$ [$mm$], $a = 0.2$ [$m$], $b = 0.04$ [$m$]) is considered in this example (see Fig. 4b). The amount of applied electrical voltage, piezoelectric actuators polarization direction, actuator and composite plate material properties, and plate stacking sequence are the same as the ones used in Example 1. It can be easily seen that the combination of actuator groups can result in significantly higher twisting deformation in the composite plate. Thus, for twisting-bending shape control purposes, more energy can be saved to achieve the same results by applying lower electrical voltage than is it achieved when using single actuators pair. Again, the mechanical twisting-bending deformation created in the smart cantilever composite plate with multiple bounded actuators pairs is analysed against various inclination angles{0°,30°,45°,60°,90°} through new proposed explicit solution and FEM (see Figs. 10–14). Good agreement between the results is observed. The effect of inclination angle variation on shape deformation in composite plates under either multiple or single actuators pairs seems to be constant. However, since a higher electrical voltage and electrical filed intensity are required for shape deformation task, therefor, the use of multiple actuator patches would be more beneficial and optimal compared with a single actuator patch.

### *4.3. Example 3: effect of stacking sequence selection on shape deformation of smart laminated cantilever piezo composite plates*

In this example, the effect of various stacking sequence on shape deformation of smart cantilever piezo composite laminate is investigated. The relationship between the stacking sequence and the composite laminates stiffness can result in shape deformation varying considerably. Thus, it is important to choose the suitable layup to control the structural shape deformation of composite laminates to our advantage. A combination of the double bounded inclined actuators groups positioned at ① and ② is considered in this example (see Fig. 4c). The piezoelectric actuators polarization direction, actuator and composite plate properties, thickness and dimensions are the same as the ones used in Example 2. In order to observe the sole effect of stacking sequence on electro-mechanical twisting-bending coupling, same amount of electrical voltage is applied to each sample regardless of the stacking sequence configuration. However, 400 [$V$] and 300 [$V$] are applied to the bounded actuators pairs positioned at ① and ②, respectively. Upper and lower actuator patches are subjected to positive and negative voltage, respectively. The Samples stacking sequence configurations are selected as [Piezo/0/0]$_s$,

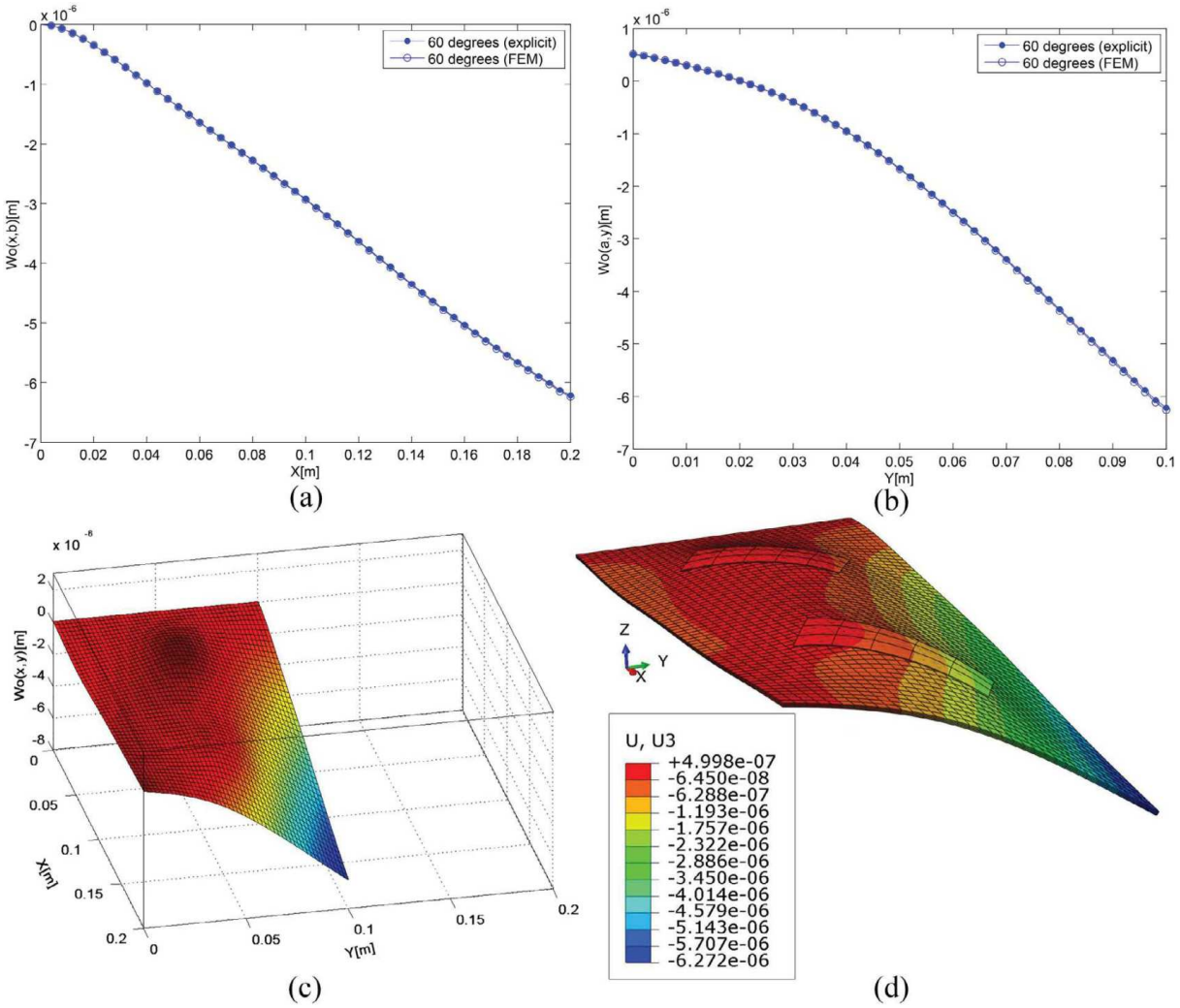


**Fig. 13.** Explicit and numerical analysis of shape deformation in the smart cantilever composite plate integrated with double piezoelectric actuators pairs when $\theta = 60°$: (a) $w_o(x,b)$, (b) $w_o(a,y)$, (c) $w_o(x,y)$: Explicit, (d) $w_o(x,y)$: Numerical.

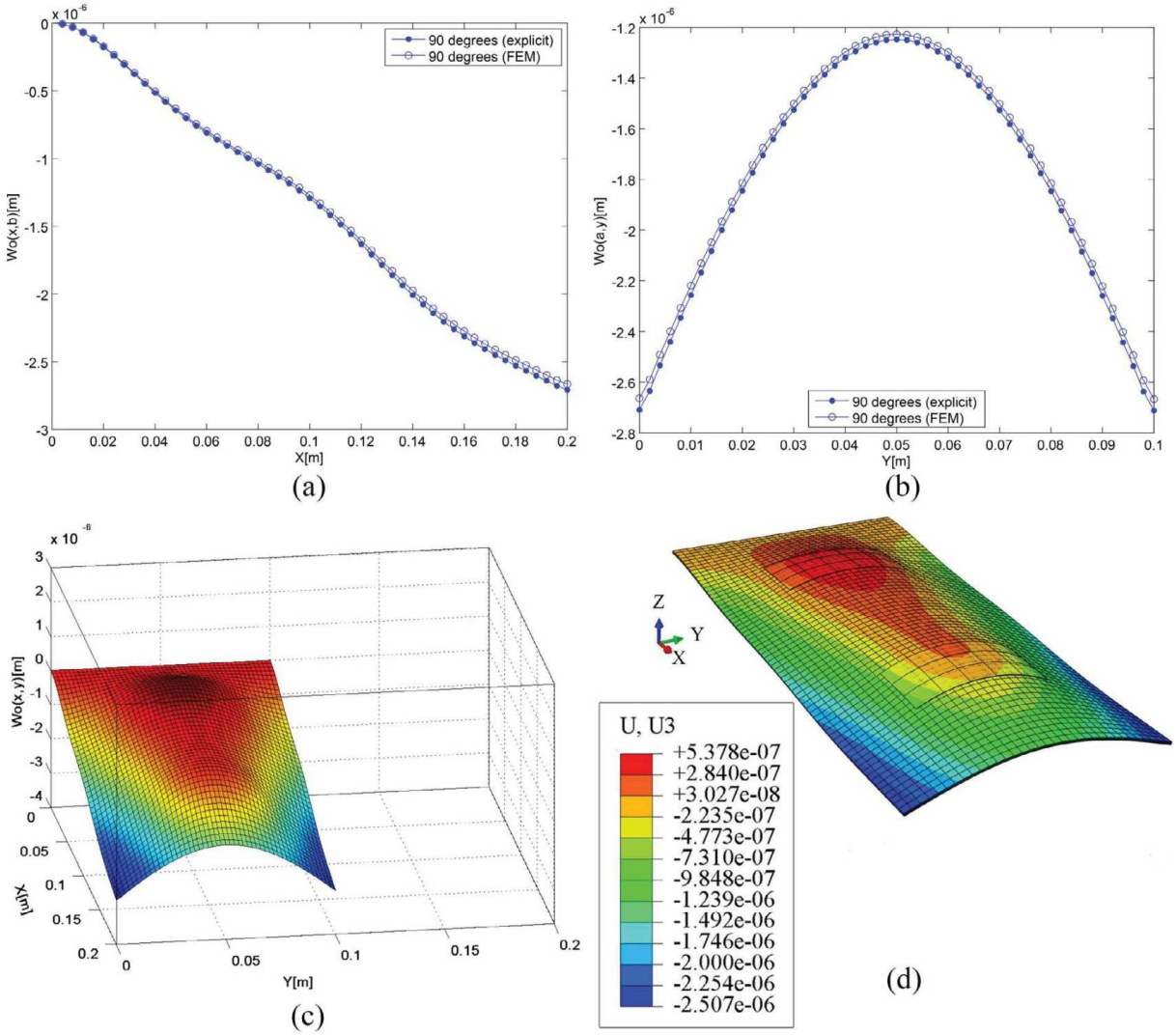


**Fig. 14.** Explicit and numerical analysis of shape deformation in the smart cantilever composite plate integrated with double piezoelectric actuators pairs when $\theta = 90^{\circ}$: (a) $w_o(x,b)$, (b) $w_o(a,y)$, (c) $w_o(x,y)$: Explicit, (d) $w_o(x,y)$: Numerical.

$[\text{Piezo}/90/90]_s$, $[\text{Piezo}/0/90]_s$, $[\text{Piezo}/90/0]_s$. The inclination angle is also kept constant for all actuators in each sample at 45 degrees. The results are then obtained using the proposed explicit solution and the numerical simulation. Fig. 15a–b represents the vertical displacements of mid-plane points along $w_o(x,b)$ and $w_o(a,y)$ along $x$ and $y$ directions, respectively, in a smart laminated cantilever piezo composite plate with various stacking sequence configurations. According to the results, the configuration $[\text{Piezo}/0/90]_s$ and $[\text{Piezo}/90/90]_s$ has the highest and lowest twisting-bending stiffness when subjected to electrical voltage, respectively. However, no major difference in results between the configurations $[\text{Piezo}/0/90]_s$ and $[\text{Piezo}/0/0]_s$ are observed. The results from both approaches show a good agreement. Subsequently, the $w_o(x,y)$ for each configuration are obtained. The 3D shape deformations obtained using the explicit solution (see Fig. 16) and the numerical simulation (see Fig. 17) show the same twisting-bending deformation trend.

### *4.4. Example 4: effect of electrical voltage intensity on shape deformation of smart laminated cantilever piezo composite plates*

In this example, the effect of electrical voltage intensity on a laminated cantilever piezo composite square plate ($a = b = 0.2$ $[m]$) is investigated numerically and analytically. The piezoelectric actuators and composite plate properties, thickness and stacking sequence are same as the ones used in Example 1, while opposite polarization direction is selected to polarize bounded piezoelectric actuator patches ($L_a = 0.1$ $[m]$, $w_a = 0.02$ $[m]$; upper and lower actuator patches are subjected to negative and positive voltage, respectively). To observe the sole effect of electrical voltage on twisting-bending deformation of the cantilevered composite plates, a series of electrical voltages, {100,250,350,500} $[V]$, are applied to the bounded piezoelectric patches and the results are presented in Figs. 18–20, respectively. According to results, any increase in the amount of electrical voltage results in higher twisting-bending deformation in the composite plates. The results from both approaches shows a good agreement. In addition, it is noticed that the twisting curvature increases as the electrical voltage is raised.

### *4.5. Example 5: effect of single inclined actuators pair on twisting deformation of the smart laminated cantilever piezo composite beams*

As shown in Fig. 21a, a smart fourth-layered cross-ply cantilever composite beam ($t_p = 1$ $[mm]$, $a = 0.2$ $[m]$, $b = 0.03$ $[m]$), made of unidirectional T300/976 GFRP, and with the stacking sequence of $[0/90]_s$, is incorporated with the bounded PZTG1195 piezoelectric

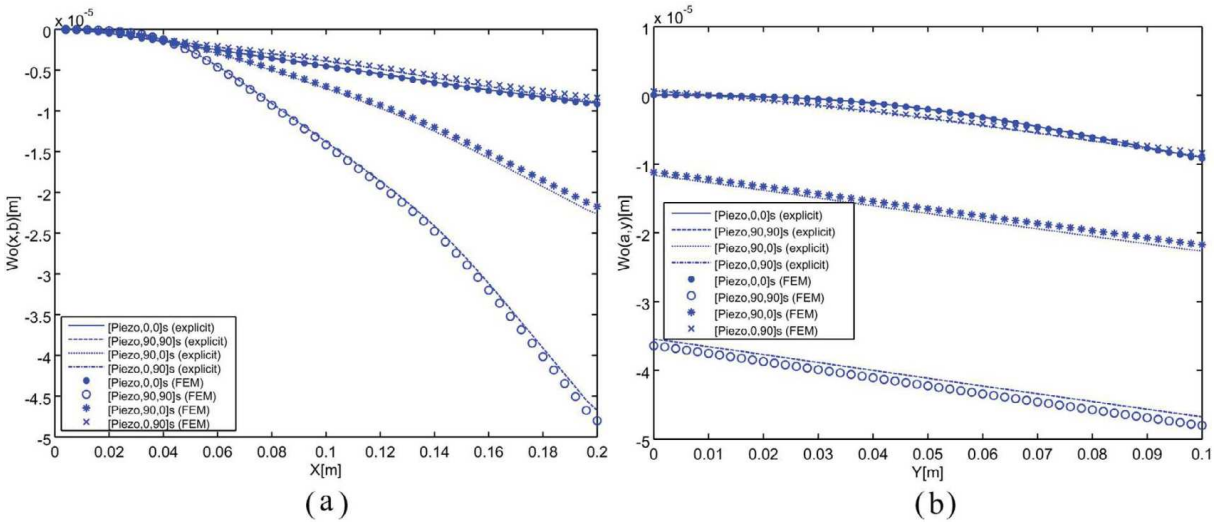


**Fig. 15.** Explicit and numerical analysis of stacking sequence configuration effect on shape deformation in the smart cantilever composite plate integrated with double piezoelectric actuators pairs: (a) $w_o(x,b)$, (b) $w_o(a,y)$.

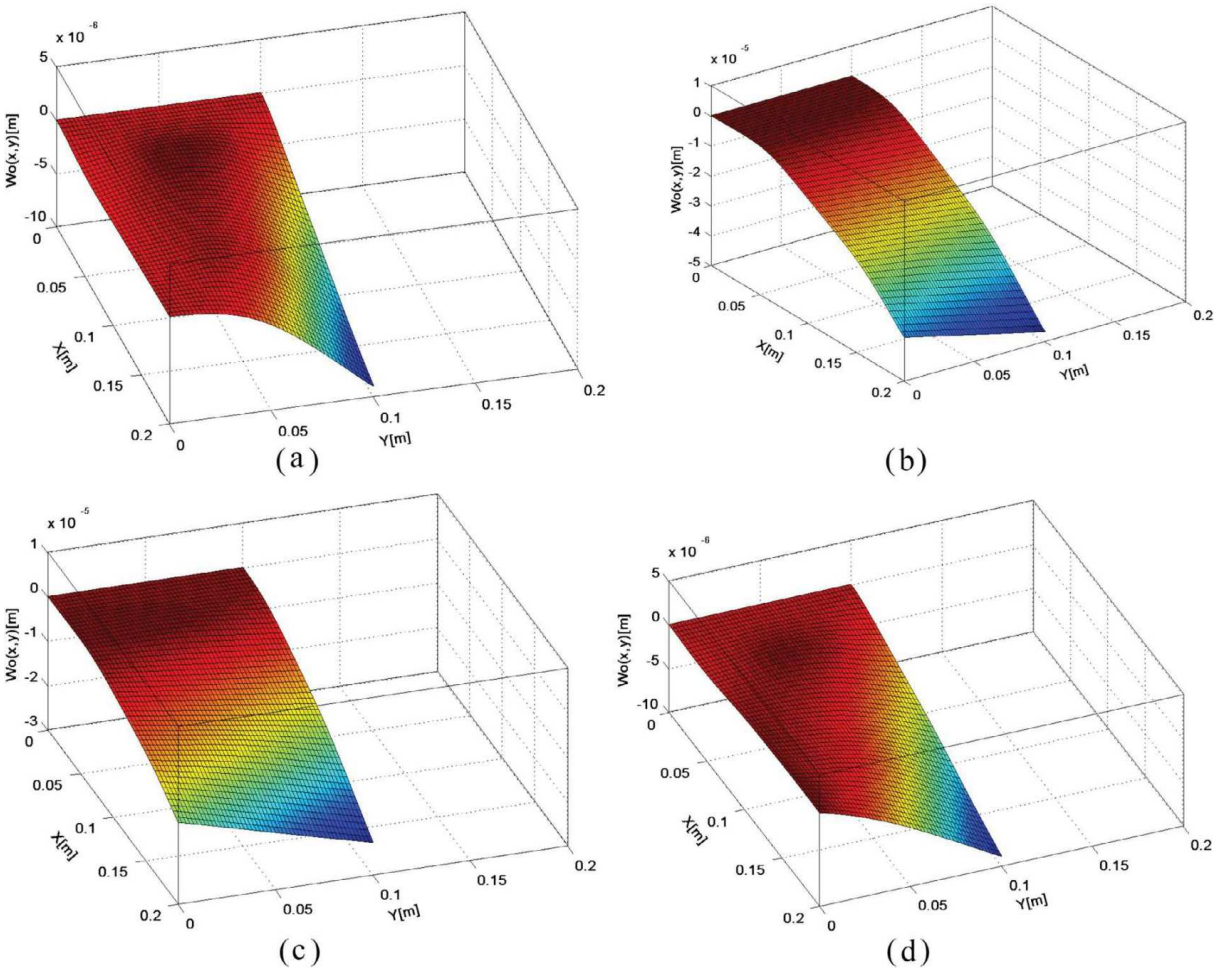


**Fig. 16.** Explicit analysis of stacking sequence configuration effect on shape deformation in the smart cantilever composite plate integrated with double piezoelectric actuators pairs: (a) $[Piezo,0,0]_s$, (b) $[Piezo,90,90]_s$, (c) $[Piezo,90,0]_s$, (d) $[Piezo,0,90]_s$.

actuator patches ($t_a = 1$ $[mm]$, $L_a = 0.05$ $[m]$, $w_a = 0.03$ $[m]$). The Inclined piezoelectric actuators pair are polarized with opposite directions (upper patch: $-300$ $[V]$ and lower patch: 300 $[V]$). The mechanical twisting-bending deformation created in the smart cantilever composite beam as a result of electro-mechanical coupling is analysed against various inclination angles {0°,30°,45°,60°,90°}

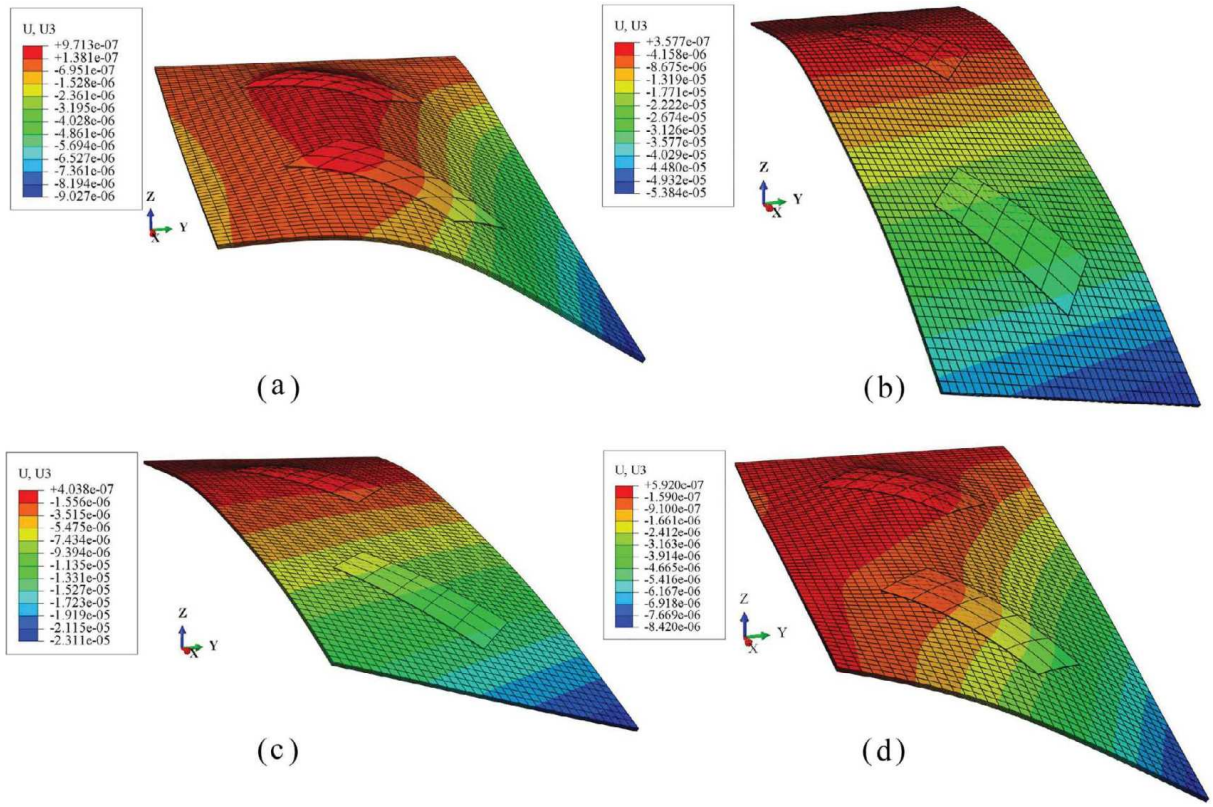


**Fig. 17.** Numerical analysis of stacking sequence configuration effect on shape deformation in the smart cantilever composite plate integrated with double piezoelectric actuators pairs: (a) $[Piezo,0,0]_s$, (b) $[Piezo,90,90]_s$, (c) $[Piezo,90,0]_s$, (d) $[Piezo,0,90]_s$.

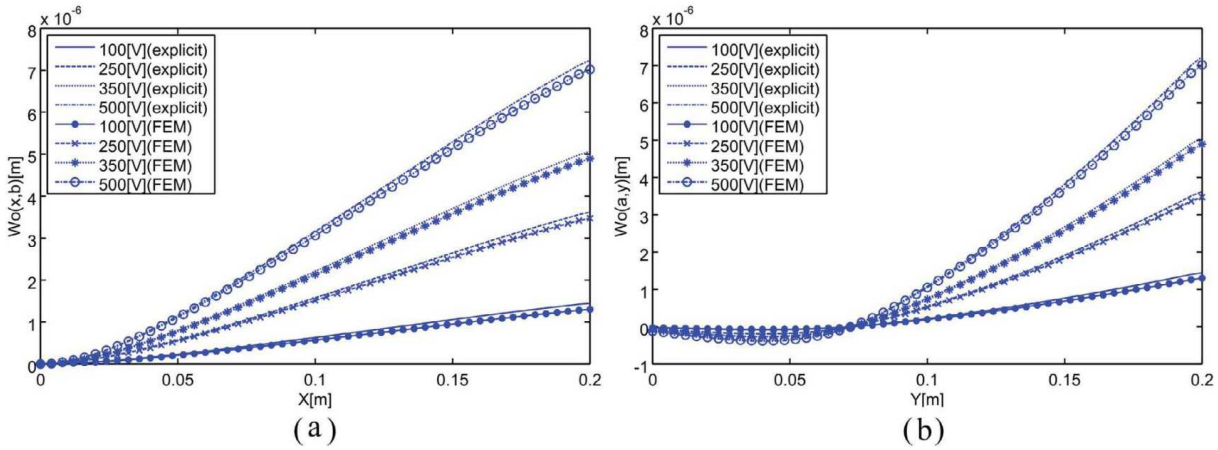


**Fig. 18.** Explicit and numerical analysis of electrical voltage effect on shape deformation in the smart cantilever composite plate integrated with single piezoelectric actuators pair: (a) $w_o(x,b)$, (b) $w_o(a,y)$.

through new proposed explicit solution and FEM (see Figs. 22–24). Good agreement between the results is observed. As discussed before, for beam type laminates, it is assumed that the width along $y$ direction is stress free while considering the plane stress assumption. Thus, only the longitudinal piezoelectric coefficient $d_{31}$ is taken into consideration. According to the results obtained from both approaches, any changes in inclination angle can results in the twisting-bending deformation varying considerably. In addition, as predicated by the explicit solution, no twisting deformation occurs for inclination angles 0 and 90 degrees.

### *4.6. Example 6: twisting-bending control of the smart laminated cantilever piezo composite beams under asymmetrical point load*

In the final example, the effectiveness of the piezoelectric actuators for the shape control of laminated composite structures under combination of twisting and bending deformations is investigated. As seen in Fig. 21b, a combination of the multiple bounded PZTG1195 actuators groups ($t_a = 0.2$ $[mm]$, $L_a = w_a = 0.05$ $[m]$), positioned at ① and ②, is considered. The host structure is a laminated cantilever composite beam ($t_p = 1$ $[mm]$, $a = 0.2$ $[m]$, $b = 0.05$ $[m]$)

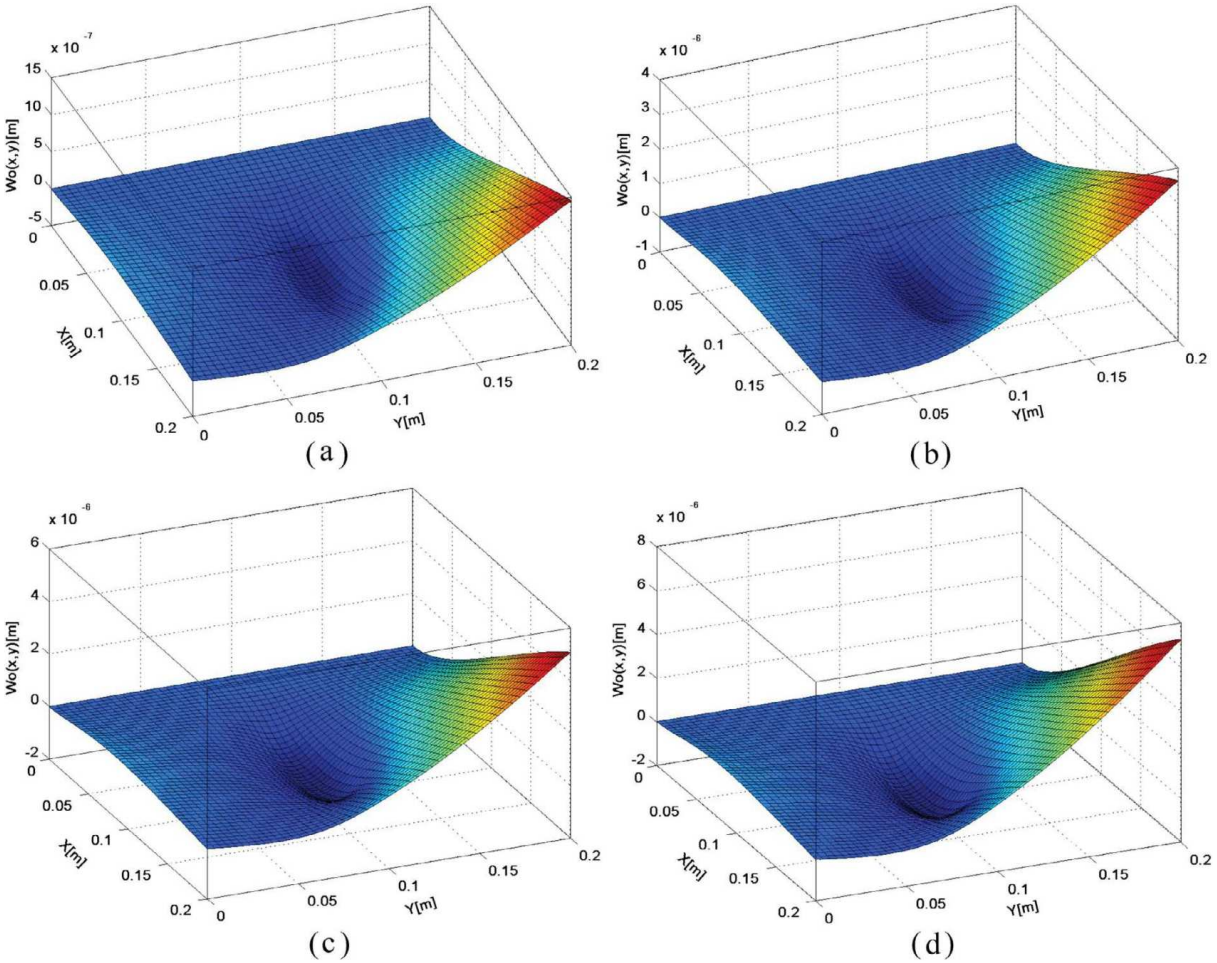


**Fig. 19.** Explicit analysis of electrical voltage effect on shape deformation in the smart cantilever composite plate integrated with single piezoelectric actuators pair: (a) 100 [*V*], (b) 250 [*V*], (c) 350 [*V*], (d) 500 [*V*].

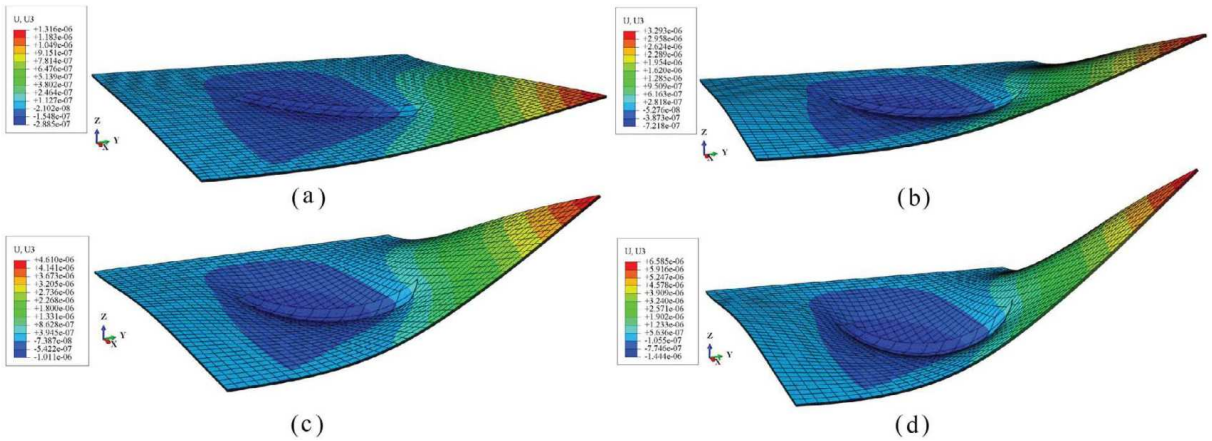


**Fig. 20.** Numerical analysis of electrical voltage effect on shape deformation in the smart cantilever composite plate integrated with single piezoelectric actuators pair: (a) 100 [*V*], (b) 250 [*V*], (c) 350 [*V*], (d) 500 [*V*].

made of unidirectional T300/976 GFRP. The composite beam is subjected to a point load $F = -1$ [N] as seen in Fig. 21b. Since the concentrated load is unsymmetrically applied to the composite beam, it results in in-plane twitting deformation while deflecting downward. In order to fully suspend the twisting-bending effect, actuators ① are positioned without any indication angle and actuators ②, in contrast, with a negative inclination angle of -30 degrees with respect to the *x* axis. The actuator patches ① and ② are used in a two-level attempt to suspend the twisting and bending deformations, respectively. Upper and lower actuator patches positioned at

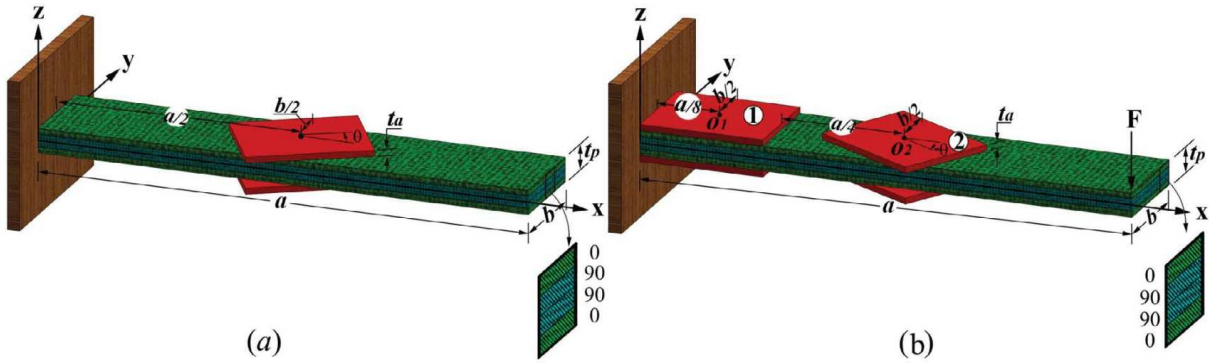


**Fig. 21.** (a) The smart laminated cantilever composite beam integrated with inclined single piezoelectric actuator pair, (b) shape control task of the smart composite laminate subjected to asymmetrical concentrated load using double piezoelectric actuators pairs.

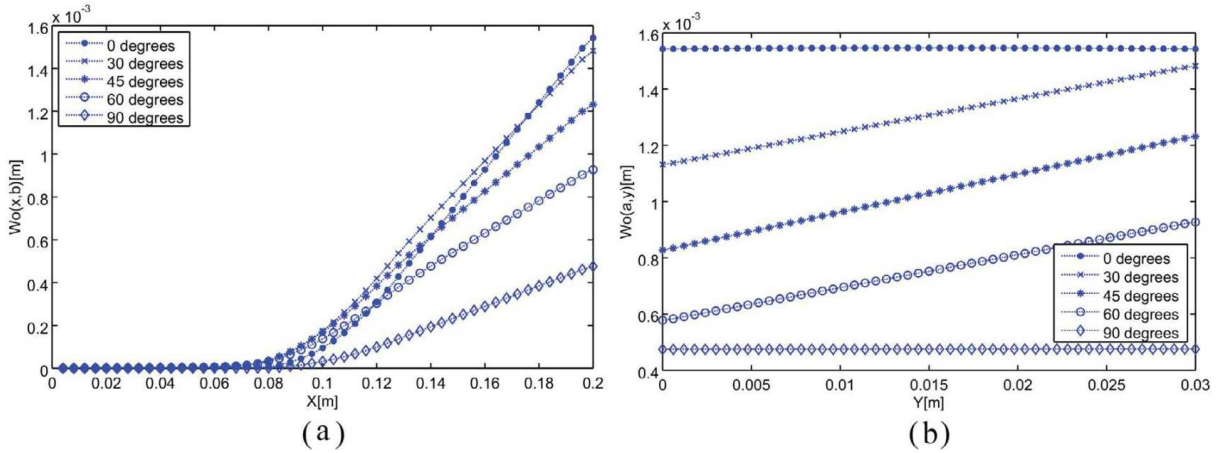


**Fig. 22.** Explicit and numerical analysis of various inclination angle effect on shape deformation in the smart cantilever composite plate integrated with single piezoelectric actuators pair: (a) $w_o(x,b)$, (b) $w_o(a,y)$.

① and ② receive same amount of electrical voltage but negative and positive values, respectively. First, for controlling the twisting deformation, actuator patches ② are subjected to an initial electrical voltage of 100 [*V*]. As seen in Fig. 25, the twisting deformation is slightly suspended and the beam starts restoring its original shape. Finally, by increasing the amount of electrical voltage applied to actuator patches ② up to the optimal level, the twisting deformation is fully suspended at 170 [*V*]. During these steps, no electrical voltage is applied to the actuator patches ①. Subsequently, in order to suspend the beam deflection, the actuator patches ① are initially subjected to the electrical voltage of 100 [*V*] and it is increased until the optimal voltage of 200 [*V*]. During the final steps, the electrical voltage applied to the actuator patches ② is kept constant at 170 [*V*]. It is observed that the beam deflection is significantly reduced as the electrical voltage increases. Therefore, by applying the optimal voltages of 200 [*V*] and 170 [*V*] to the actuator patches ① and ②, respectively, the twisting-bending deformations could be fully supressed according to the results illustrated in Fig. 25.

## 5. Conclusion

In this study, a new explicit analytical solution is presented for obtaining twisting-bending deformation and optimal shape control of smart laminated cantilever composite plates and beams using inclined piezoelectric actuators. For the first time, a mathematical relationship between the electrical and mechanical twisting moments are developed. The reliability of the proposed method is compared with the FE simulation results. The relationship between electro-mechanical twisting-bending deformation and various electro-mechanical parameters are taken into account. Generally, based on the results in the current research, the following remarks are concluded:

1. A good agreement observed between the proposed exact analytical solution and numerical simulation demonstrates the reliability of the model proposed in this paper.
2. Inclined piezoelectric actuators are capable of inducing twisting deformation in laminated composite structures through applying electrical voltage to piezoelectric actuators. The intensity of twisting shape deformation varies by changing the inclination angle. Therefore, through optimal inclination angle and applied electrical voltage, the shape control task of laminated composite structures under asymmetrical loads can be reliably implemented.
3. Piezoelectric actuator size and placement have direct effect on twisting-bending shape deformation of laminated composite structures. Typically, considering the constant electrical voltage, inclination angle, and composite laminate stiffness, larger ones have more power to induce twisting-bending deformation. In addition, the ones placed closed to the composite plates/beams fixed end show a better shape deformation while this effectiveness decreases as they are placed closer to the free end.

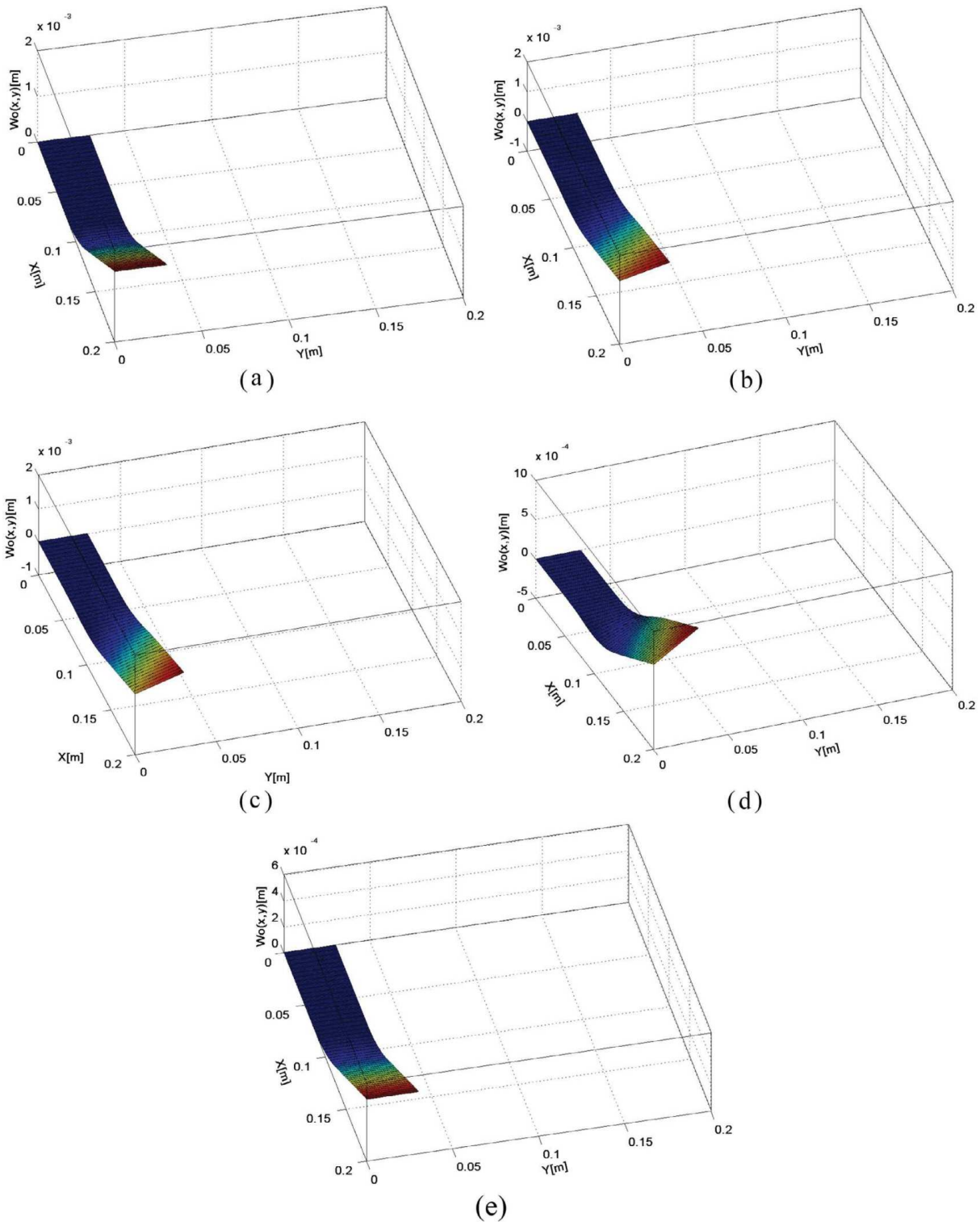


**Fig. 23.** Explicit analysis of various inclination angle effect on shape deformation in the smart cantilever composite plate integrated with single piezoelectric actuators pair: (a) $\theta = 0^{\circ}$, (b) $\theta = 30^{\circ}$, (c) $\theta = 45^{\circ}$, (d) $\theta = 60^{\circ}$, (e) $\theta = 90^{\circ}$.

4. Six samples with various inclination angles ({0°,30°,45°,60°,90°}) were selected in this study. According to the numerical and analytical results, for the inclination angles $\theta \neq 0^{o}, 90^{o}$, the twisting deformation reduces when the inclination angle increases. As predicted by the both approaches, when $\theta = 0^{o}, 90^{o}$, no twisting deformation occurs since the transformed piezoelectric twisting coefficient is equal to zero. Moreover, when the inclination angle is equal to 90°, the effect of longitudinal and transverse piezoelectric coefficients is switched ($d_{31} \rightarrow d_{32}$ and $d_{32} \rightarrow d_{31}$).

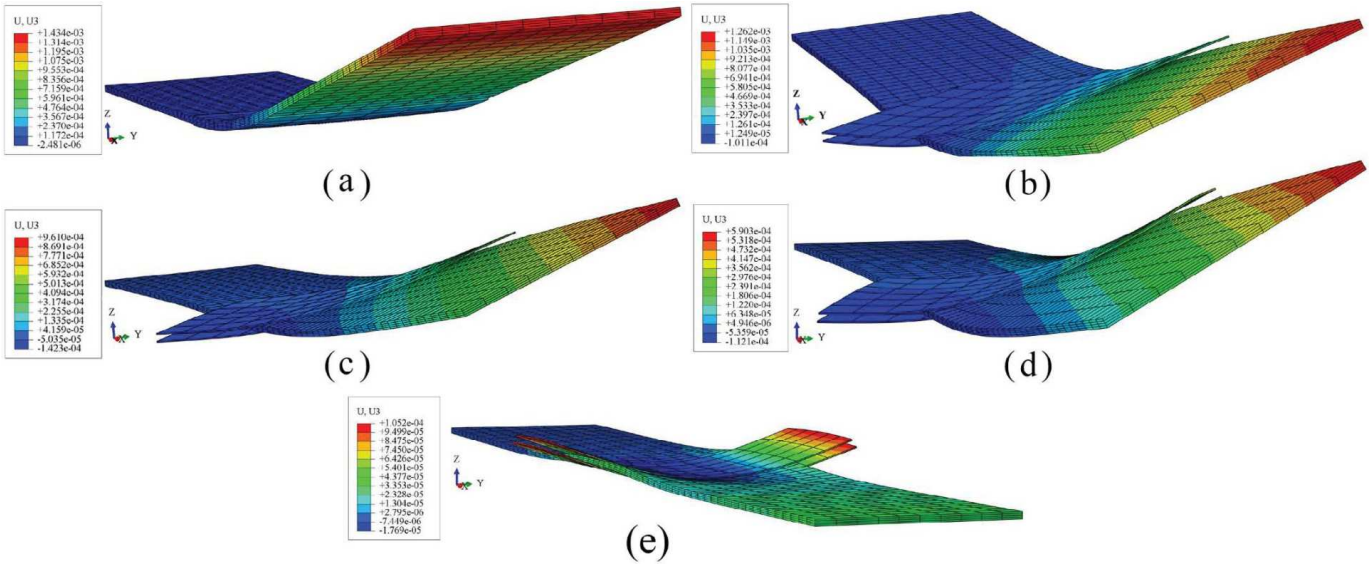


**Fig. 24.** Numerical analysis of various inclination angle effect on shape deformation in the smart cantilever composite plate integrated with single piezoelectric actuators pair: (a) $\theta = 0^{\circ}$, (b) $\theta = 30^{\circ}$, (c) $\theta = 45^{\circ}$, (d) $\theta = 60^{\circ}$, (e) $\theta = 90^{\circ}$.

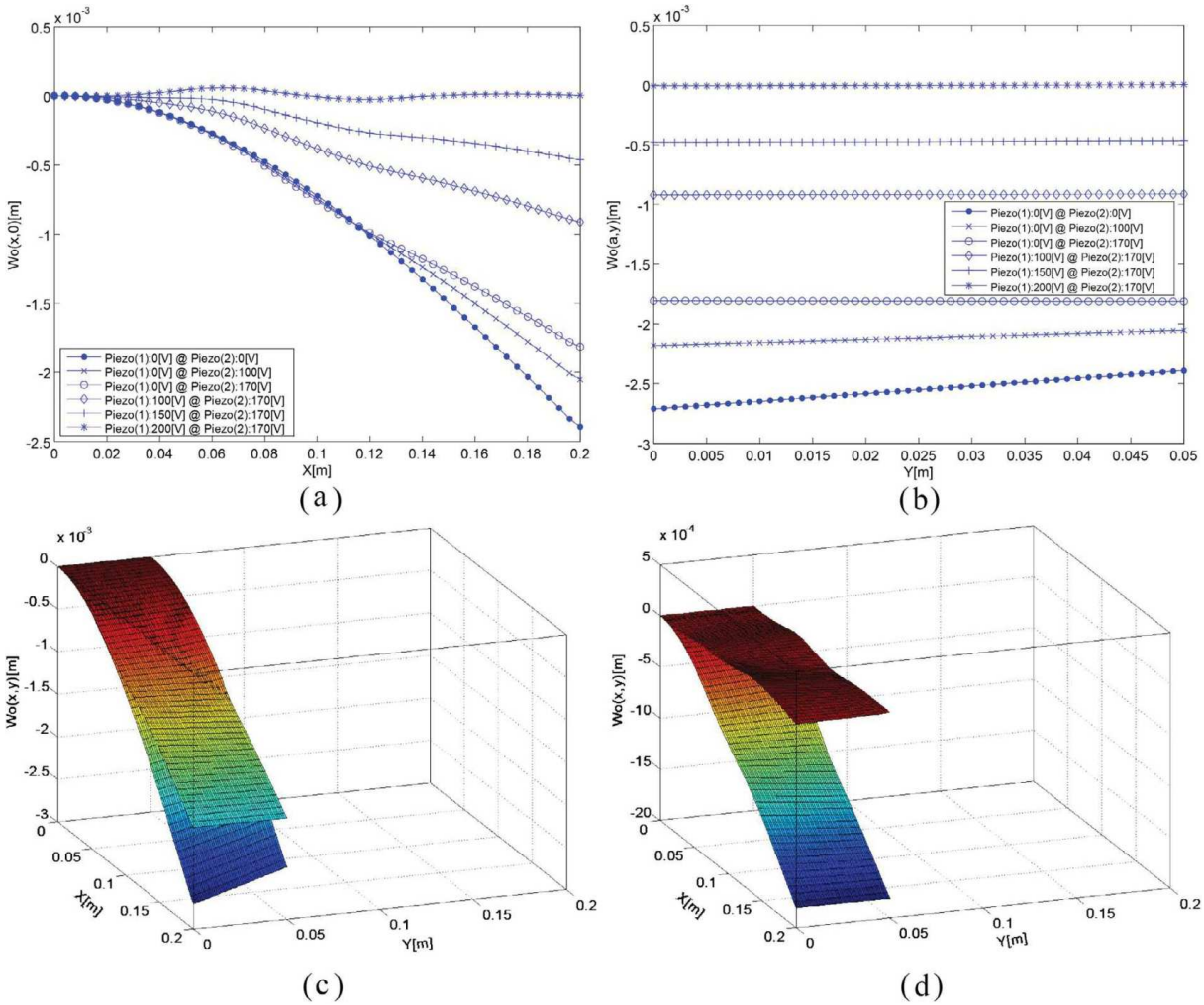


**Fig. 25.** Explicit analysis of shape control task of the smart composite laminate subjected to asymmetrical concentrated load using double piezoelectric actuators pairs: (a) $w_o(x,0)$, (b) $w_o(a,y)$, (c) $w_o(x,y)$: Pure twisting suspension using piezoelectric actuator patches ② ($\theta = -30^{\circ}$), (d) $w_o(x,y)$: Pure bending suspension using piezoelectric actuator patches ① ($\theta = 0^{\circ}$).

5. By increasing the applied electrical voltage and/or the number of inclined piezoelectric actuator patches, the maximum twisting deformation in a composite laminate can be achieved. Meanwhile, higher electrical voltage for shape deformation control purposes is difficult to control and may result in the piezoelectric actuators being destroyed [60]. Thus, the finding in the current research could be significant for shape control of laminated composite structures. For example, by selecting the optimal number of inclined piezoelectric actuator patches and/or adjusting the applied electrical voltage, optimal results can be achieved.
6. Composite laminates stiffness can significantly affect the electromechanical twisting-bending coupling. The stiffness matrix can be induced by selecting various stacking sequence configurations. Among those with symmetrical cross-ply configuration, $[\text{Piezo}/0/90]_s$ and $[\text{Piezo}/90/90]_s$ have the highest and lowest twisting-bending stiffness when subjected to electrical voltage, respectively. However, no major differences in results between the configurations $[\text{Piezo}/0/90]_s$ and $[\text{Piezo}/0/0]_s$ are observed.
7. The shape control task in smart laminated cantilever composite plates and beams can be reliably implemented using the proposed explicit analytical solution. The proposed method is well suited for laminated composite structures subjected to more complex and asymmetrical loading systems whereas the characteristic and trial deflection functions are not required to be predetermined for shape control performance. According to the results, through a two-step task, twisting-bending deformation in laminated composite structures can be suspended. For instance, piezoelectric actuators with no inclination angles could be exploited to control pure bending deformation while inclined ones can be used to suspend the pure twisting deformation.

## Acknowledgements

Scott Gohery would like to thank the College of Engineering and Science at Victoria University, Melbourne for offering the Victoria University International Postgraduate Research scholarship (VUIPRS) to undertake his Ph.D. study. This financial support is gratefully acknowledged.

## Appendix A

The coefficients $S^i_{mn}$, $i = \{1,2,\ldots,20\}$, in the four finite systems of the linear simultaneous multivariable Eqs. (35a–d), can be computed as follows:

$$S^1_{mn} = (-1)^n \left( \frac{\alpha_m \left( \frac{(D_{12})\alpha_m^2}{4} + D_{22}\beta_n^2 \right)}{\frac{D_{11}\alpha_m^4}{16} + \frac{(D_{12}+2D_{66})\alpha_m^2\beta_n^2}{2} + D_{22}\beta_n^4} \right)$$

$$S^2_{mn} = -\left( \frac{\alpha_m \left( \frac{(D_{12})\alpha_m^2}{4} + D_{22}\beta_n^2 \right)}{\frac{D_{11}\alpha_m^4}{16} + \frac{(D_{12}+2D_{66})\alpha_m^2\beta_n^2}{2} + D_{22}\beta_n^4} \right)$$

$$S^3_{mn} = (-1)^{\frac{m-1}{2}} \left( \frac{\alpha_m \left( \frac{D_{11}\alpha_m^2}{4} + D_{12}\beta_n^2 \right)}{\frac{D_{11}\alpha_m^4}{16} + \frac{(D_{12}+2D_{66})\alpha_m^2\beta_n^2}{2} + D_{22}\beta_n^4} \right)$$

$$S^4_{mn} = -\frac{D_{11}}{2} \left( \frac{\alpha_m^2}{\frac{D_{11}\alpha_m^4}{16} + \frac{(D_{12}+2D_{66})\alpha_m^2\beta_n^2}{2} + D_{22}\beta_n^4} \right)$$

$$\begin{aligned} S^5_{mn} = {} & \left( \frac{-\alpha_m}{\frac{D_{11}\alpha_m^4}{16} + \frac{(D_{12}+2D_{66})\alpha_m^2\beta_n^2}{2} + D_{22}\beta_n^4} \right) \\ & \times \left\{ \sum_{L=1}^{Mn} C^1_{mn} \left( \frac{-2P_0}{\alpha_m\beta_n} \right) \left( \cos\left(\frac{\alpha_m}{2}x_{1M}\right) - \cos\left(\frac{\alpha_m}{2}x_{2M}\right) \right)_L (\sin(\beta_n y_{1M}) \right. \\ & \left. - \sin(\beta_n y_{2M}))_L + \sum_{L=1}^{Pn} C^2_{mn} \left[ \frac{[M^P_x]^{\Theta}\alpha_m^2 + 4[M^P_y]^{\Theta}\beta_n^2}{2\alpha_m\beta_n} \right] \left( \cos\left(\frac{\alpha_m}{2}x_{1P}\right) \right. \right. \\ & \left. \left. - \cos\left(\frac{\alpha_m}{2}x_{2P}\right) \right)_L (\sin(\beta_n y_{1P}) - \sin(\beta_n y_{2P}))_L \\ & + \sum_{L=1}^{Pn} C^3_{mn} [M^P_{xy}]^{\Theta} \left( \sin\left(\frac{\alpha_m}{2}x_{1P}\right) - \sin\left(\frac{\alpha_m}{2}x_{2P}\right) \right)_L \\ & \times (\cos(\beta_n y_{1P}) - \cos(\beta_n y_{2P}))_L \end{aligned}$$

$$S^6_{mn} = (-1)^n (-1)^{\frac{m-1}{2}} \left[ D_{12} - \frac{\left( D_{22}\beta_n^2 + \frac{D_{12}\alpha_m^2}{4} \right)\left( \frac{D_{11}\alpha_m^2}{4} + D_{12}\beta_n^2 \right)}{\frac{D_{11}\alpha_m^4}{16} + \frac{(D_{12}+2D_{66})\alpha_m^2\beta_n^2}{2} + D_{22}\beta_n^4} \right]$$

$$S^7_{mn} = -(-1)^{\frac{m-1}{2}} \left[ D_{12} - \frac{\left( D_{22}\beta_n^2 + \frac{D_{12}\alpha_m^2}{4} \right)\left( \frac{D_{11}\alpha_m^2}{4} + D_{12}\beta_n^2 \right)}{\frac{D_{11}\alpha_m^4}{16} + \frac{(D_{12}+2D_{66})\alpha_m^2\beta_n^2}{2} + D_{22}\beta_n^4} \right]$$

$$S^8_{mn} = (-1)^{m-1} \left( D_{11} - \frac{\left( \frac{D_{11}\alpha_m^2}{4} + D_{12}\beta_n^2 \right)^2}{\frac{D_{11}\alpha_m^4}{16} + \frac{(D_{12}+2D_{66})\alpha_m^2\beta_n^2}{2} + D_{22}\beta_n^4} \right)$$

$$S^9_{mn} = \frac{D_{11}}{2}(-1)^{\frac{m-1}{2}} \left( \frac{\alpha_m \left( \frac{D_{11}\alpha_m^2}{4} + D_{12}\beta_n^2 \right)}{\frac{D_{11}\alpha_m^4}{16} + \frac{(D_{12}+2D_{66})\alpha_m^2\beta_n^2}{2} + D_{22}\beta_n^4} \right)$$

$$\begin{aligned} S^{10}_{mn} = {} & (-1)^{\frac{m-1}{2}} \left[ \frac{D_{11}\alpha_m^4}{16} + \frac{(D_{12}+2D_{66})\alpha_m^2\beta_n^2}{2} + D_{22}\beta_n^4 \right]^{-1} \\ & \times \left( \frac{D_{11}\alpha_m^2}{4} + D_{12}\beta_n^2 \right) \\ & \times \left\{ \sum_{L=1}^{Mn} C^1_{mn} \left( \frac{-2P_0}{\alpha_m\beta_n} \right) \left( \cos\left(\frac{\alpha_m}{2}x_{1M}\right) - \cos\left(\frac{\alpha_m}{2}x_{2M}\right) \right)_L (\sin(\beta_n y_{1M}) \right. \\ & \left. - \sin(\beta_n y_{2M}))_L + \sum_{L=1}^{Pn} C^2_{mn} \left[ \frac{[M^P_x]^{\Theta}\alpha_m^2 + 4[M^P_y]^{\Theta}\beta_n^2}{2\alpha_m\beta_n} \right] \right. \\ & \times \left( \cos\left(\frac{\alpha_m}{2}x_{1P}\right) - \cos\left(\frac{\alpha_m}{2}x_{2P}\right) \right)_L (\sin(\beta_n y_{1P}) - \sin(\beta_n y_{2P}))_L \\ & + \sum_{L=1}^{Pn} C^3_{mn} [M^P_{xy}]^{\Theta} \left( \sin\left(\frac{\alpha_m}{2}x_{1P}\right) - \sin\left(\frac{\alpha_m}{2}x_{2P}\right) \right)_L \\ & \left. \times (\cos(\beta_n y_{1P}) - \cos(\beta_n y_{2P})) \right\} \end{aligned}$$

$$S^{11}_{mn} = \lambda_n (-1)^n \left[ D_{22} - \frac{\left( \frac{D_{12}\alpha_m^2}{4} + D_{22}\beta_n^2 \right)^2}{\frac{D_{11}\alpha_m^4}{16} + \frac{(D_{12}+2D_{66})\alpha_m^2\beta_n^2}{2} + D_{22}\beta_n^4} \right]$$

$$S^{12}_{mn} = -\lambda_n \left[ D_{22} - \frac{\left( \frac{D_{12}\alpha_m^2}{4} + D_{22}\beta_n^2 \right)^2}{\frac{D_{11}\alpha_m^4}{16} + \frac{(D_{12}+2D_{66})\alpha_m^2\beta_n^2}{2} + D_{22}\beta_n^4} \right]$$

$$S^{13}_{mn} = \lambda_n (-1)^{\frac{m-1}{2}} \left[ D_{12} - \frac{\left( \frac{D_{12}\alpha_m^2}{4} + D_{22}\beta_n^2 \right)\left( \frac{D_{11}\alpha_m^2}{4} + D_{12}\beta_n^2 \right)}{\frac{D_{11}\alpha_m^4}{16} + \frac{(D_{12}+2D_{66})\alpha_m^2\beta_n^2}{2} + D_{22}\beta_n^4} \right]$$

$$S_{mn}^{14} = \frac{D_{11}}{2}\lambda_n\left[\frac{\alpha_m\left(\frac{D_{12}\alpha_m^2}{4}+D_{22}\beta_n^2\right)}{\frac{D_{11}\alpha_m^4}{16}+\frac{(D_{12}+2D_{66})\alpha_m^2\beta_n^2}{2}+D_{22}\beta_n^4}\right]$$

$$\begin{aligned}S_{mn}^{15} = {} & \lambda_n\left[\frac{D_{11}\alpha_m^4}{16}+\frac{(D_{12}+2D_{66})\alpha_m^2\beta_n^2}{2}+D_{22}\beta_n^4\right]^{-1}\\ & \times\left(\frac{D_{12}\alpha_m^2}{4}+D_{22}\beta_n^2\right)\\ & \times\left\{\sum_{L=1}^{Mn}C_{mn}^1\left(\frac{-2P_0}{\alpha_m\beta_n}\right)\left(\cos\left(\frac{\alpha_m}{2}x_{1M}\right)-\cos\left(\frac{\alpha_m}{2}x_{2M}\right)\right)_L(\sin(\beta_n y_{1M})\right.\\ & -\sin(\beta_n y_{2M}))_L+\sum_{L=1}^{Pn}C_{mn}^2\left[\frac{[M_x^{P_1}]^{\Theta}\alpha_m^2+4[M_y^{P_1}]^{\Theta}\beta_n^2}{2\alpha_m\beta_n}\right]\\ & \times\left(\cos(\tfrac{\alpha_m}{2}x_{1P})-\cos\left(\frac{\alpha_m}{2}x_{2P}\right)\right)_L(\sin(\beta_n y_{1P})-\sin(\beta_n y_{2P}))_L\\ & \left.+\sum_{L=1}^{Pn}C_{mn}^3[M_{xy}^P]^{\Theta}\left(\sin\left(\frac{\alpha_m}{2}x_{1P}\right)-\sin\left(\frac{\alpha_m}{2}x_{2P}\right)\right)_L(\cos(\beta_n y_{1P})-\cos(\beta_n y_{2P}))_L\right\}\end{aligned}$$

$$S_{mn}^{16} = \lambda_n\left[D_{22}-\frac{\left(\frac{D_{12}\alpha_m^2}{4}+D_{22}\beta_n^2\right)^2}{\frac{D_{11}\alpha_m^4}{16}+\frac{(D_{12}+2D_{66})\alpha_m^2\beta_n^2}{2}+D_{22}\beta_n^4}\right]$$

$$S_{mn}^{17} = -\lambda_n(-1)^n\left[D_{22}-\frac{\left(\frac{D_{12}\alpha_m^2}{4}+D_{22}\beta_n^2\right)^2}{\frac{D_{11}\alpha_m^4}{16}+\frac{(D_{12}+2D_{66})\alpha_m^2\beta_n^2}{2}+D_{22}\beta_n^4}\right]$$

$$S_{mn}^{18} = \lambda_n(-1)^n(-1)^{\frac{m-1}{2}}\left[D_{12}-\frac{\left(\frac{D_{12}\alpha_m^2}{4}+D_{22}\beta_n^2\right)\left(\frac{D_{11}\alpha_m^2}{4}+D_{12}\beta_n^2\right)}{\frac{D_{11}\alpha_m^4}{16}+\frac{(D_{12}+2D_{66})\alpha_m^2\beta_n^2}{2}+D_{22}\beta_n^4}\right]$$

$$S_{mn}^{19} = \lambda_n\frac{D_{11}}{2}(-1)^n\left[\frac{\alpha_m\left(\frac{D_{12}\alpha_m^2}{4}+D_{22}\beta_n^2\right)}{\frac{D_{11}\alpha_m^4}{16}+\frac{(D_{12}+2D_{66})\alpha_m^2\beta_n^2}{2}+D_{22}\beta_n^4}\right]$$

$$\begin{aligned}S_{mn}^{20} = {} & \lambda_n(-1)^n\left[\frac{D_{11}\alpha_m^4}{16}+\frac{(D_{12}+2D_{66})\alpha_m^2\beta_n^2}{2}+D_{22}\beta_n^4\right]^{-1}\\ & \times\left(\frac{D_{12}\alpha_m^2}{4}+D_{22}\beta_n^2\right)\\ & \times\left\{\sum_{L=1}^{Mn}C_{mn}^1\left(\frac{-2P_0}{\alpha_m\beta_n}\right)\left(\cos\left(\frac{\alpha_m}{2}x_{1M}\right)-\cos\left(\frac{\alpha_m}{2}x_{2M}\right)\right)_L\right.\\ & \times(\sin(\beta_n y_{1M})-\sin(\beta_n y_{2M}))_L+\sum_{L=1}^{Pn}C_{mn}^2\left[\frac{[M_x^{P_1}]^{\Theta}\alpha_m^2+4[M_y^{P_1}]^{\Theta}\beta_n^2}{2\alpha_m\beta_n}\right]\\ & \times\left(\cos\left(\frac{\alpha_m}{2}x_{1P}\right)-\cos\left(\frac{\alpha_m}{2}x_{2P}\right)\right)_L(\sin(\beta_n y_{1P})-\sin(\beta_n y_{2P}))_L\\ & +\sum_{L=1}^{Pn}C_{mn}^3[M_{xy}^P]^{\Theta}\left(\sin\left(\frac{\alpha_m}{2}x_{1P}\right)-\sin\left(\frac{\alpha_m}{2}x_{2P}\right)\right)_L\\ & \left.\times(\cos(\beta_n y_{1P})-\cos(\beta_n y_{2P}))_L\right\}\end{aligned}$$

## References


[1] Gohery S, Sharifi S, Vrcelj Z, Yahya MY. First-ply failure prediction of an unsymmetrical laminated ellipsoidal woven GFRP composite shell with incorporated surface-bounded sensors and internally pressurized. Compos Part B Eng 2015;77:502–18.

[2] Sharifi S, Gohery S, Sharifiteshnizi M, Vrcelj Z. Numerical and experimental study on mechanical strength of internally pressurized laminated woven composite shells incorporated with surface-bounded sensors. Compos Part B Eng 2016;94:224–37.

[3] Sharifishourabi G, Ayob A, Gohery S, Yahya MYB, Sharifi S, Vrcelj Z. Flexural behavior of functionally graded slender beams with complex cross-section. J Mech Mater Struct 2015;10(1):1–16.

[4] Coda HB. Continuous inter-laminar stresses for regular and inverse geometrically non linear dynamic and static analyses of laminated plates and shells. Compos Struct 2015;132:406–22.

[5] Liu Q. Analytical sensitivity analysis of eigenvalues and lightweight design of composite laminated beams. Compos Struct 2015;134:918–26.

[6] Sader JE, White L. Theoretical analysis of the static deflection of plates for atomic force microscope applications. J Appl Phys 1993;74(1):1–9.

[7] Lachut MJ, Sader JE. Buckling of a cantilever plate uniformly loaded in its plane with applications to surface stress and thermal loads. J Appl Phys 2013;113(2):1–11.

[8] Shin DK, Lee JJ. Theoretical analysis of the deflection of a cantilever plate for wirebonding on overhang applications. IEEE Trans Compon Packag Manuf Technol 2012;2(6):916–24.

[9] Kattimani SC, Ray MC. Smart damping of geometrically nonlinear vibrations of magneto-electro-elastic plates. Compos Struct 2014;114(1):51–63.

[10] Sawarkar S, Pendhari S, Desai Y. Semi-analytical solutions for static analysis of piezoelectric laminates. Compos Struct 2016;153:242–52.

[11] Murugan S, Friswell MI. Morphing wing flexible skins with curvilinear fiber composites. Compos Struct 2013;99:69–75.

[12] Adnan Elshafei M, Farid A, Omer AA. Modeling of torsion actuation of beams using inclined piezoelectric actuators. Arch Appl Mech 2014;85(2):171–89.

[13] Akbar M, Curiel-Sosa JL. Piezoelectric energy harvester composite under dynamic bending with implementation to aircraft wingbox structure. Compos Struct 2016;153:193–203.

[14] Kerboua M, Megnounif A, Benguediab M, Benrahou KH, Kaoulala F. Vibration control beam using piezoelectric-based smart materials. Compos Struct 2015;123:430–42.

[15] Brito-Santana H, de Medeiros R, Rodriguez-Ramos R, Tita V. Different interface models for calculating the effective properties in piezoelectric composite materials with imperfect fiber-matrix adhesion. Compos Struct 2016;151:70–80.

[16] Koconis DB, Kollar LP, Springer GS. Shape control of composite plates and shells with embedded actuators.1. voltages specified. J Compos Mater 1994;28(5):415–58.

[17] Koconis DB, Kollar LP, Springer GS. Shape control of composite plates and shells with embedded actuators. II. Desired shape specified. J Compos Mater 1994;28(3):459–82.

[18] Andakhshideh A, Tahani M. Free-edge stress analysis of general rectangular composite laminates under bending, torsion and thermal loads. Eur J Mech/A Solids 2013;42:229–40.

[19] Gohery S, Sharifi S, Sharifishourabi G, Vrcelj Z, Abadi R. Effect of temperature on crack initiation in gas formed structures. J Mech Sci Technol 2013;27(12):3745–54.

[20] Lin CC, Hsu CY, Huang HN. Finite element analysis on deflection control of plates with piezoelectric actuators. Compos Struct 1996;35(4):423–33.

[21] Cook AC, Vel SS. Multiscale analysis of laminated plates with integrated piezoelectric fiber composite actuators. Compos Struct 2012;94(2):322–36.

[22] Milazzo A. Refined equivalent single layer formulations and finite elements for smart laminates free vibrations. Compos Part B Eng 2014;61:238–53.

[23] Sartorato M, de Medeiros R, Tita V. A finite element formulation for smart piezoelectric composite shells: mathematical formulation, computational analysis and experimental evaluation. Compos Struct 2015;127:185–98.

[24] Zhang SQ, Li YX, Schmidt R. Modeling and simulation of macro-fiber composite layered smart structures. Compos Struct 2015;126:89–100.

[25] Zhang SQ, Schmidt R. Static and dynamic FE analysis of piezoelectric integrated thin-walled composite structures with large rotations. Compos Struct 2014;112:345–57.

[26] Plattenburg J, Dreyer JT, Singh R. Active and passive damping patches on a thin rectangular plate: a refined analytical model with experimental validation. J. Sound Vib. 2015;353:75–95.

[27] Bowen CR, Butler R, Jervis R, Kim HA, Salo AIT. Morphing and shape control using unsymmetrical composites. J Intell Mater Struct 2007;18(January).

[28] Giddings P, Bowen CR, Butler R, Kim HA. Characterisation of actuation properties of piezoelectric bi-stable carbon-fibre laminates. Compos Part A Appl Sci Manuf 2008;39(4):697–703.

[29] Thinh TI, Ngoc LK. Static behavior and vibration control of piezoelectric cantilever composite plates and comparison with experiments. Comput Mater Sci 2010;49(4 SUPPL.):S276–80.

[30] Khandelwal RP, Chakrabarti A, Bhargava P. Static and dynamic control of smart composite laminates. AIAA J 2014;52(9):1896–914.

[31] Gohery S, Golshan A, Ayob A. Theoretical analysis and finite element simulation of behavior of laminated hemispherical GRP dome subjected to internal pressure. Int Conf Comput Softw Model 2011;14:122–9.

[32] Gohery S, Golshan A, Nia AB, Hashemzadeh M. Prediction of failure in thin-walled hemispherical GRP dome subjected to static internal pressure based on a failure factor. Adv Mater Res 2012;488–489:358–66.

[33] Gohery S, Golshan A, Mostakhdemin M, Mozafari F, Momenzadeh A. Failure strength of thin-walled cylindrical GFRP composite shell against static internal and external pressure for various volumetric fiber fraction. Int J Appl Phys Math 2012;2(2):111–6.

[34] Gohery S, Golshan A, Firouzabadi F, Hosseininezhad N. Effect of Volumetric fiber fraction on failure strength of thin-walled GFRP composite cylindrical shell externally pressurized. Adv Mater Res 2012;488–489:530–6.

[35] Gohery S, Golshan A, Hashemzadeh M, Hosseininezhad N. First-ply strength of thick circular cylindrical GRP composite shell subjected to static external

pressure via finite element simulation and analytical approaches. Adv Mater Res 2012;463–464:477–83.
[36] Firouzabadi F, Ayob A, Arjmandi MR, Gohery S, Deirram N. Modeling of the impact on cylindrical composite shell as continuous patch loading. Int J Mech Mech Eng 2012;12(3):8–13.
[37] Sharifi S, Almula TADMS, Gohery S, Sharifishourabi G, Saed Y, Bin Yahya MY. Impact response of laminated composite cylindrical shell: finite element simulation approach. Appl Mech Mater 2013;393:387–92.
[38] Her SC, Lin CS. Deflection of cross-ply composite laminates induced by piezoelectric actuators. Sensors 2010;10(1):719–33.
[39] Her S-C, Lin C-S. Vibration analysis of composite laminate plate excited by piezoelectric actuators. Sensors 2013;13(3):2997–3013.
[40] Sakava Y, Member S, Luo ZH. Modeling and control of coupled bending and torsional vibrations of flexible beams. IEEE Trans Autom Control 1989;34 (9):970–7.
[41] Bureau HD, Limited HA. Structural dynamic analysis of composite beams. J Sound Vib 1990;143:503–19.
[42] Boresi AP, Schmidt RJ, Sidebottom OM. Advanced mechanics of materials. New York: Wiley; 1978. p. 242–9.
[43] Sankar BV. A beam theory for laminated composites and application to torsion problems. J Appl Mech 1993;60(1):246–9.
[44] Banerjee JR, Williams FW. Coupled bending-torsional dynamic stiffness matrix of an axially loaded timoshenko beam element. Int J Solids Struct 1994;31 (6):749–62.
[45] Park C, Walz C, Chopra I. Bending and torsion models of beams with induced strain actuators. In: SPIE Conf. Albuquerque, NM.
[46] Park C, Chopra I. Modeling piezoceramic actuation of beam in torsion. Proc. 35th AIAA/ASME/ASCE/AHS Struct. Struct. Dyn. Mater. Conf. Adapt. Struct. Forum. p. 438–50.
[47] Chen PC, Chopra I. Induced strain actuation of composite beams and rotor blades with embedded piezoceramic elements. Smart Mater Struct 1996;5:35–48.
[48] Takawa T, Fu kuda T, Takada T. Flexural–torsion coupling vibration control of fiber composite cantilevered beam by using piezo-ceramic actuators. Smart Mater Struct 1997;6:447–84.
[49] Thirupathi SR, Seshu P, Naganathan NG. A finite element static analysis of smart turbine blades. Smart Mater Struct 1997;6:607–15.
[50] Kim J, Varadan VV, Varadan VK, Bao XQ. Finite-element modeling of a smart cantilever plate and comparison with experiments. Smart Mater Struct 1996;5 (2):165–70.
[51] Ren L. A theoretical study on shape control of arbitrary lay-up laminates using piezoelectric actuators. Compos Struct 2008;83(1):110–8.
[52] Reddy JN. On laminated composite plates with integrated sensors and actuators. Eng Struct 1999;21(7):568–93.
[53] Kharghani N, Guedes Soares C. Behaviour of composite laminates with embedded delaminations. Compos Struct 2016;150:226–39.
[54] Shao D, Hu F, Wang Q, Pang F, Hu S. Transient response analysis of cross-ply composite laminated rectangular plates with general boundary restraints by the method of reverberation ray matrix. Compos Struct 2016;152:168–82.
[55] Yue YM, Xu KY, Chen T. A micro scale Timoshenko beam model for piezoelectricity with flexoelectricity and surface effects. Compos Struct 2016;136:278–86.
[56] Wu Z, Han C, Niu Z. A 3D exact analysis of the boundary layer effect of asymmetric piezoelectric laminates with electromechanical coupling. Int J Solids Struct 2015;72:118–29.
[57] Zhu J, Wang J, Zu L. Influence of out-of-plane ply waviness on elastic properties of composite laminates under uniaxial loading. Compos Struct 2015;132:440–50.
[58] Moghadam PY, Tahani M, Naserian-Nik AM. Analytical solution of piezolaminated rectangular plates with arbitrary clamped/simply-supported boundary conditions under thermo-electro-mechanical loadings. Appl Math Model 2013;37(5):3228–41.
[59] Kress G, Winkler M. Corrugated laminate homogenization model. Compos Struct 2010;92(3):795–810.
[60] Gohery S, Sharifi S, Vrcelj Z. New explicit solution for static shape control of smart laminated cantilever piezo-composite-hybrid plates/beams under thermo-electro-mechanical loads using piezoelectric actuators. Compos Struct 2016;145:89–112.
[61] Duc ND, Quan TQ, Luat VD. Nonlinear dynamic analysis and vibration of shear deformable piezoelectric FGM double curved shallow shells under damping-thermo-electro-mechanical loads. Compos Struct Jul. 2015;125:29–40.
[62] Foutsitzi GA, Gogos CG, Hadjigeorgiou EP, Stavroulakis GE. Actuator location and voltages optimization for shape control of smart beams using genetic algorithms. Actuators 2013;2(4):111–28.
[63] Yu Y, Zhang XN, Xie SL. Optimal shape control of a beam using piezoelectric actuators with low control voltage. Smart Mater Struct 2009;18(9):1–15.
[64] Shaik Dawood MSI, Iannucci L, Greenhalgh ES. Three-dimensional static shape control analysis of composite plates using distributed piezoelectric actuators. Smart Mater Struct 2008;17(2):1–10.

## 3.5. CONCLUDING REMARKS

This chapter presented a novel explicit analytical solution for bending-twisting shape control analysis of laminated cantilever piezo composite hybrid plates using piezoelectric actuators. The shape control task for the host structures under complex thermo-electro-mechanical loads was well implemented and the satisfactory results were achieved. The results comparison with some published benchmark results and numerical simulation demonstrated the reliability of the proposed analytical solution. Based on the findings of this chapter, the following conclusions can be drawn:

- Piezoelectric actuators can significantly induce the elastic stiffness of laminated composite hybrid structures, which make them an ideal solution for shape control task.

- Both embedded and bounded piezoelectric actuators can be considered using the proposed analytical solution.

- The shape control task can be well implemented to control both the bending and twisting deformation caused by external thermo-electro-mechanical loads.

- Higher electrical voltage leads to a greater actuation and more significant bending-twisting shape control performance.

- Thicker actuators have less actuation power due to the low electrical field produced through actuators thickness, while improving laminates stiffness against flexural deformation.

- Piezoelectric actuators with no inclination angle can be used to control the bending deformation while inclined actuators can be used for twisting deformation control task.

- Increasing the number of piezoelectric actuators regardless of their placement, inclination angle, thickness, and type can significantly increase the actuation power, which leads to a better shape control implementation. Thus, more actuators can be adopted if external loads applied to a host structure intensify.

- Composite laminate stiffness can significantly affect the electro-mechanical twisting-bending deformation. The stiffness matrix can be induced by selecting various stacking sequence configurations.

- The use of the analytical solution as proposed in the current research could be significant for shape control of laminated composite hybrid structures. For instance, by selecting the optimal number of inclined piezoelectric actuator patches and/or adjusting the applied electrical voltage, optimal results can be achieved.

# Chapter 5

# SHAPE CONTROL OF LAMINATED COMPOSITE STRUCTURES USING PIEZOELECTRIC ACTUATORS: A NOVEL NUMERICAL SOLUTION

## 5.1. INTRODUCTION

In this chapter, a quadratic 2D FE formulation is developed based on FOSDT for assessing the structural deformation in laminated composite plates induced by MFC actuators. The proposed FE modelling is used to obtain the linear strain-displacement static deformation accurately. FOSDT is adapted from the Reissner-Mindlin plate theory. To check the suitability and compatibility of the proposed method in shape deformation analysis of laminated composite plates with various boundary conditions, cantilevered and simply-supported plates are considered. An eight-node quadratic shell element with five degrees of freedom is introduced for the FE formulation. Two types

of MFC actuators are exploited: 1) MFC-$d_{31}$ and 2) MFC-$d_{33}$ which differ in their actuation forces.

The proposed electro-mechanically coupled quadratic FE model is then compared with the results using ABAQUS. MATLAB is also used to find the solution of the quadratic FE equations. Based on what is available in the literature, the lack of comprehensive and in-depth research on MFC materials is noticeable. Thus, in this study, the effect of various parameters such as boundary conditions, laminate stacking sequence configuration, unsymmetrical layup, electrical voltage intensity, MFC type, and piezoelectric fibre orientation on shape deformation of laminated composite structures induced by MFC actuators is investigated.

This chapter includes the following papers:

1) S. Gohery, S. Sharifi, and Z. Vrcelj, "Quadratic finite element analysis of smart laminated composite plates induced by MFC," *Smart Mater Struct,* 2016 (Revised and resubmitted).

VICTORIA UNIVERSITY
MELBOURNE AUSTRALIA

**PART B:**

**DECLARATION OF CO-AUTHORSHIP AND CO-CONTRIBUTION: PAPERS INCORPORATED IN THESIS BY PUBLICATION**

This declaration is to be completed for each conjointly authored publication and placed at the beginning of the thesis chapter in which the publication appears.

**Declaration by** [candidate name]: Scott Gohery **Signature:** [redacted] **Date:** 5/01/2017

**Paper Title:**

Quadratic finite element analysis of smart laminated piezo composite plates induced by MFC actuators

In the case of the above publication, the following authors contributed to the work as follows:

| Name | Contribution % | Nature of Contribution |
|---|---|---|
| Scott Gohery | 75 | Initial concept, Literature review, Numerical investigation, Computer programming, Writing of the manuscript |
| Shokrollah Sharifi | 20 | Provided critical revision of the manuscript, Sketching Figs using AutoCad and SolidWorks softwares |
| Zora Vrcelj | 5 | Provided critical revision of the manuscript, Initial and final approval of the manuscript |
| | | |
| | | |
| | | |

Page - 1 - of 2

VICTORIA UNIVERSITY
MELBOURNE AUSTRALIA

**DECLARATION BY CO-AUTHORS**

The undersigned certify that:

1. They meet criteria for authorship in that they have participated in the conception, execution or interpretation of at least that part of the publication in their field of expertise;
2. They take public responsibility for their part of the publication, except for the responsible author who accepts overall responsibility for the publication;
3. There are no other authors of the publication according to these criteria;
4. Potential conflicts of interest have been disclosed to a) granting bodies, b) the editor or publisher of journals or other publications, and c) the head of the responsible academic unit; and
5. The original data is stored at the following location(s):

| Location(s): |
| --- |
| College of Engineering and Science, Victoria University, Melbourne, VIC 8001, Australia |

and will be held for at least five years from the date indicated below:

| | | Date |
| --- | --- | --- |
| Signature 1 | [redacted] | 20/12/2016 |
| Signature 2 | | 20/12/2016 |
| Signature 3 | | 20/12/2016 |
| Signature 4 | | |

Page - 2 - of 2

Revised Manuscript resubmitted for publication in

# Smart Materials and Structures

December 2016

## Quadratic Finite Element Analysis of Smart Laminated Composite Plates Induced by MFC Actuators

**Scott Gohery*, S. Sharifi, Zora Vrcelj**

College of Engineering and Science, Victoria University, Melbourne, VIC 8001, Australia

***Corresponding Author:**

Scott Gohery

College of Engineering and Science, Victoria University, Melbourne, VIC 8001 Australia

Phone.+61423656484

Emails: scott.gohery@live.vu.edu.au

# Quadratic finite element analysis of smart laminated piezo composite plates induced by MFC actuators

**Scott Gohery*, S. Sharifi, Zora Vrcelj**

*Tel: +61423656484

*College of Engineering and Science, Victoria University, Melbourne, VIC 8001, Australia*

**Email Addresses:**

scott.gohery@live.vu.edu.au (S. Gohery)

**Abstract.** Macro Fiber Composite (MFC) actuators developed by the NASA have been increasingly used in engineering structures due to their high actuation power, compatibility, and flexibility. In this study, a quadratic 2D Finite Element (FE) formulation using First Order Shear Deformation Theory (FOSDT) is developed to predict the linear strain-displacement static deformation in the laminated piezo composite plates induced by MFC actuators. FOSDT is adapted from the Reissner-Mindlin plate theory. Laminated piezo composite plates are either cantilevered or simply-supported. An eight-node quadratic shell element with five degrees of freedom is introduced for the FE formulation. Two types of MFC actuators are exploited: 1) MFC-$d_{31}$ and 2) MFC-$d_{33}$ which differ in their actuation forces. Subsequently, the electro-mechanically coupled quadratic FE model is compared with the ABAQUS results. Unlike earlier studies, the proposed quadratic FE formulation in this research is simple, accurate, and most importantly efficient which eliminates the need for high-cost FE simulation software. Furthermore, due to the lack of comprehensive and in-depth research on MFC materials, the effect of various parameters such as boundary conditions, laminate stacking sequence

configuration, unsymmetrical layup, electrical voltage intensity, MFC type, and piezoelectric fibre orientation on shape deformation of laminated composite structures induced by MFC actuators is considered.

**Keywords:** MFC actuators; Quadratic FE analysis; First order shear deformation theory; Smart laminate composite plates; Numerical simulation.

## 1. Introduction

Laminated and asymmetric composite structures are being used considerably in aerospace, automotive, civil, mechanical and structural engineering applications due to their high stiffness and strength to weight ratio, low density, and temperature resistance. Laminated plates and beams are typically adopted to achieve the desired stiffness and lightness for parts of load-bearing engineering structures [1,2]. Piezoelectric materials have recently drawn much attention due to their low power consumption, high material linearity, and quick response when induced by external forces. As a results, they are being used in the fields of mechanical and electrical engineering [3,4]. Piezoelectric materials can be integrated with laminated composite structures to provide smart-intelligent composite systems [5,6].

Numerous smart engineering structures integrated with smart devices such as piezoelectric sensors and actuators have proved to be superior to their conventional counterparts. Static analysis of advanced composite structures under axial, transverse, twisting, and torsional loads in addition to the torsional actuation due to piezoelectric materials has potential application in mechanical systems, helicopter rotor blades,

and/or blades for turbomachinery [7]. Some other applications of piezoelectric materials in smart and adaptive engineering structures are acoustical noise reduction, structural shape control, damage identification, structural health monitoring, vibration suppression, deflection control in missile fins, and air foil shape changes [8-11]. One of the great advantages of piezoelectric materials is their ability to respond to changing environment and control structural deformation, which has led to the new generation of aerospace structures like morphing airplanes [12]. There has been recently a dramatic achievement in development of the new generation of piezoelectric materials called piezoelectric fibre composites (PFC) which have orthotropic material properties due to unidirectionally aligned piezoelectric fibres with circular cross-section. The fibres are impregnated into a resin matrix system to boost PFC properties when sharing the mechanical load. PFCs was later upgraded to interdigitated electrode piezoelectric fibre composites (IDEPFCs) which is also referred to as active fibre composites (AFCs) in order to increase the strain output, directional actuation, flexibility, and durability [13-15].

However, some difficulties were faced during the manufacturing of AFCs such as misalignment of piezoelectric fibres and their limited contact with flat electrodes due to fibre cross sectional configuration. Therefore, the NASA developed MFC actuators whose piezoelectric fibres have rectangular cross sectional shape. All fibres are surrounded by polymer matrix. The other components of MFCs are protective and electrode layers bounded to piezoelectric fibres. MFC materials are composed of seven active layers, two electrodes, two kapton and two acrylic layers [16]. AFCs are also more responsive than with conventional electrodes.

Developed by the NASA-Langley Research Centre, MFC actuators and sensors present superior qualities among AFCs in performance, behaviour, and manufacturability [17]. Understanding MFC properties is important to utilize them efficiently. There are several studies regarding the MFCs modelling using numerical and analytical approaches. Park and Kim [11]modelled the MFC mechanical properties theoretically using classical laminated plate theory (CLPT) and uniform field model (UFM). In another similar study, the mechanical properties of shear actuated fibre composites (SAFCs) were analysed using unit-cell approach by Raja and Ikeda [18]. Since piezoelectric materials are sensitive to thermal environment, therefore their effectiveness under thermal was examined using equivalent layered and unit-cell approach [19].

MFC materials can be integrated with plate and shell structures due to their flexibilities. One of the great application of MFCs is to control the effect of snap-through due to the unsymmetrical layup in a composite laminate. During the manufacturing process, with no external loads, they can undergo multiple equilibrium shapes when cooled from the curing temperature to a lower operating temperature. Therefore, through applying appropriate voltage to MFC actuators, the undesired shapes can be controlled and modified [20]. The application of MFCs in shape, thermal and vibrational control of plates and shells can be found in Refs [21-23].

There are numerous studies concerning 3D FE simulations of composite plates, beams, shells, and domes with/without conventional piezoelectric actuators. Gohery et al [24-25] studied the mechanical deformation of laminated composite domes under internal pressure using finite element simulation and compared it with theoretical results based

on classical shell theory. There are also numerous studies regarding the FE simulation of laminated thin/thick composite cylindrical shells under arbitrarily static [26-28] and dynamic [29,30] loads. There are several studies regarding FE simulation of composite plates induced by conventional piezoelectric actuators [31-33]. Various researches regarding the numerical modelling of MFCs using commercial FE packages, in which the results were compared with experimental data, can be found in refs [22,34].

There are also few analytical and numerical models reported in the literature for analysis of smart composite structures induced by MFC actuators [35,36]. Zhang et al [37] developed a linear electro-mechanically coupled FE model for thin-walled smart composite laminates sandwiched by macro-fibre composite (MFC) actuators. Their proposed method was compared with numerical and experimental results.

It can be noticed that computational analysis of the linear strain-displacement static deformation of smart composite structures induced by MFC actuators on the effect of various boundary conditions, laminate stacking sequence, unsymmetrical layup, electrical voltage intensity, MFC type, and piezoelectric fibre orientation are limited. In the current research a simple quadratic 2D Finite Element (FE) formulation using First Order Shear Deformation Theory (FOSDT) is developed to predict the linear strain-displacement static deformation in the laminated piezo composite plates induced by MFC actuators.

An in-depth study on consideration of transverse shear deformation in laminated composite plate structures and its application in static and dynamic structural analysis

can be found in Ref. [38]. An eight-node quadratic shell element with five degrees of freedom is introduced for the FE formulation. Two types of MFC actuators are exploited: 1) MFC-$d_{31}$ and 2) MFC-$d_{33}$ which differ in their actuation forces. MATLAB is exploited for obtaining the 2D FE results. Subsequently, the 3D electro-mechanically coupled FE analysis using ABAQUS is exploited for numerical simulation of smart composite structures integrated with MFC actuators.

## 2. Composite laminates and MFC actuators modelling

Consider a laminated composite plate (host structure) composed of $N$ orthotropic layers and with a total layup thickness of $H$. Each layer thickness is kept constant. The host structure is sandwiched by a pair of bounded MFC actuators and is either cantilevered (see Fig.1a) or simply supported at two edges (see Fig.1b).

Considering the material linearity for small displacements, plane stress assumption and effect of transverse shear deformation, the general form of displacement fields can be derived based on FOSDT as stated in Eqs.1a-c [39,40]. For composite laminates and MFC patches, some initial assumptions for 2D FE formulation are made as follows [34,41]:

- There is a perfect bonding between fibres and matrix, avoiding fibres dislocations and disarrangements through the matrix and no slip occurs between the lamina interfaces;

- Fibres distribution throughout the matrix is uniform;

- There is a perfect bonding between fibres and matrix, avoiding fibres dislocations and disarrangements through the matrix and no slip occurs between the lamina interfaces;

- The matrix is perfectly fabricated with no voids and impurity;

- The lamina is not initially pre-stressed, thus, there are no residual stresses in presence of matrix and fibres; and

- The matrix and fibres behave linearly within elastic domain.

For the smart part of the laminates, the linear piezoelectricity theory is adapted with assumptions made as follows [41]:

- The strain-electric field varies linearly;

- The piezoelectric confidents are constant within the linear zone; thus, they cannot be electrically turned with a bias field;

- The electric field is assumed to be constant across each lamina in all directions.

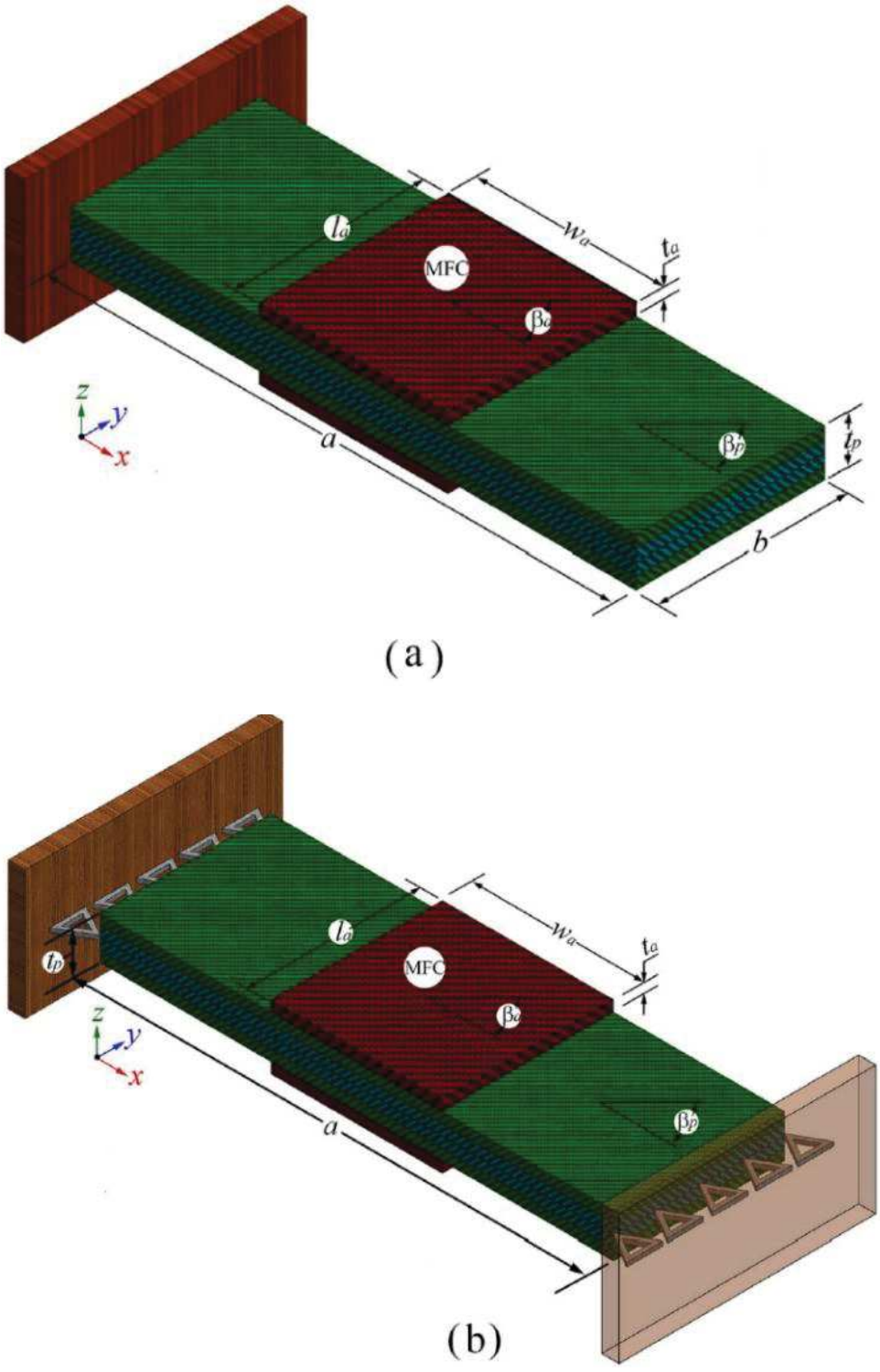


**Fig.1.** Schematic of the laminated composite plate sandwiched by a pair of MFC actuators: a) cantilevered, b) simply-supported.

$$u(x,y,z) = U_x(x,y) + z\varphi_x(x,y) = U_x(x,y) + z\left[\frac{\partial w}{\partial x} - \gamma_{xz}\right] \quad (1.a)$$

$$v(x,y,z) = U_y(x,y) + z\varphi_y(x,y) = U_y(x,y) + z\left[\frac{\partial w}{\partial y} - \gamma_{yz}\right] \quad (1.b)$$

$$w(x,y,z) = w_0(x,y) \quad (1.c)$$

$U_x$, $U_y$, and $w_0$ are the mid-plane displacements along $x$, $y$, and $z$ directions, respectively on the $xy$-plane [42]. $\varphi_x$ and $\varphi_y$ are rotation of transverse normal in the mid-plane along x and y directions, respectively. $z$ is the vertical distance from the mid-plane to the k$th$ layer which is located between $z = h_k$ and $z = h_{k+1}$ through laminate thickness [43]. After obtaining the mid-plane displacements, the displacements of any arbitrary point, *x, y,* and $z$ in 3D space can be determined. The linear strain-displacement relation is stated in Eqs.2a-d [44]. It is assumed that all strain components change linearly in the entire laminate independent from changes in material properties through layup thickness.

$$\begin{bmatrix}\varepsilon_{xx} & \varepsilon_{yy} & \gamma_{xy}\end{bmatrix}^T = \begin{bmatrix}\frac{\partial u}{\partial x} & \frac{\partial v}{\partial y} & \frac{\partial u}{\partial y} + \frac{\partial v}{\partial x}\end{bmatrix}^T = \begin{bmatrix}\varepsilon_{xx}^0 & \varepsilon_{yy}^0 & \tau_{xy}^0\end{bmatrix}^T + z\begin{bmatrix}\varepsilon_{xx}^f & \varepsilon_{yy}^f & \tau_{xy}^f\end{bmatrix}^T \quad (2a)$$

$$\begin{bmatrix}\varepsilon_{xx}^o & \varepsilon_{yy}^o & \gamma_{xy}^o\end{bmatrix}^T = \begin{bmatrix}\frac{\partial U_x}{\partial x} & \frac{\partial U_y}{\partial y} & \frac{\partial U_x}{\partial y} + \frac{\partial U_y}{\partial x}\end{bmatrix}^T \quad (2b)$$

$$\begin{bmatrix}\varepsilon_{xx}^f & \varepsilon_{yy}^f & \gamma_{xy}^f\end{bmatrix}^T = \begin{bmatrix}\frac{\partial \varphi_x}{\partial x} & \frac{\partial \varphi_y}{\partial y} & \frac{\partial \varphi_x}{\partial y} + \frac{\partial \varphi_y}{\partial x}\end{bmatrix}^T \quad (2c)$$

$$\begin{bmatrix}\gamma_{yz} & \gamma_{xz}\end{bmatrix}^T = \begin{bmatrix}\gamma_{yz}^o & \gamma_{xz}^o\end{bmatrix}^T = \begin{bmatrix}\varphi_y + \frac{\partial w_o}{\partial y} & \varphi_x + \frac{\partial w_o}{\partial x}\end{bmatrix}^T \quad (2d)$$

$\varepsilon_{xx}^{o}$, $\varepsilon_{yy}^{o}$, and $\gamma_{xy}^{o}$ are the laminate's mid-plane strains, $\varepsilon_{xx}^{f}, \varepsilon_{yy}^{f}$, and $\gamma_{xy}^{f}$ are the flexural (bending) strains and $w_o$ is the transverse deflection of a composite laminate's mid-plane. $\gamma_{yz}^{o}$ and $\gamma_{xz}^{o}$ are the transverse shear deformation in the *yz* and *xz* planes, respectively. Considering the plane stress assumption and neglecting the through-thickness stresses, the simplified 2D electro-mechanical plate equations are derived from the 3D equations of theory of elasticity and three charged equilibrium equations of piezoelectric medium, as stated in Eq.3a [45]. The electrical field potential relationships for an orthotropic static piezoelectric lamina is stated in Eq.3b [45].

$$\begin{bmatrix}\sigma_{11}\\ \sigma_{22}\\ 0\\ 0\\ 0\\ \tau_{12}\end{bmatrix}^{k} = \begin{bmatrix} C_{1111} & C_{1122} & C_{1133} & 0 & 0 & 0\\ C_{1122} & C_{2222} & C_{2233} & 0 & 0 & 0\\ C_{1133} & C_{2233} & C_{3333} & 0 & 0 & 0\\ 0 & 0 & 0 & C_{2323} & 0 & 0\\ 0 & 0 & 0 & 0 & C_{3131} & 0\\ 0 & 0 & 0 & 0 & 0 & C_{1212}\end{bmatrix}^{k} \begin{bmatrix}\varepsilon_{11}\\ \varepsilon_{22}\\ \varepsilon_{33}\\ \gamma_{23}\\ \gamma_{13}\\ \gamma_{12}\end{bmatrix}^{k} - \begin{bmatrix} 0 & 0 & e_{31}\\ 0 & 0 & e_{32}\\ 0 & 0 & e_{33}\\ 0 & e_{24} & 0\\ e_{15} & 0 & 0\\ 0 & 0 & 0\end{bmatrix}^{k} \begin{bmatrix}\Phi_1\\ \Phi_2\\ \Phi_3\end{bmatrix}^{k} \quad (3a)$$

$$\begin{bmatrix}\rho_1\\ \rho_2\\ \rho_3\end{bmatrix}^{k} = \begin{bmatrix} 0 & 0 & 0 & 0 & e_{15} & 0\\ 0 & 0 & 0 & e_{24} & 0 & 0\\ e_{31} & e_{32} & e_{33} & 0 & 0 & 0\end{bmatrix}^{k} \begin{bmatrix}\varepsilon_{11}\\ \varepsilon_{22}\\ \varepsilon_{33}\\ \gamma_{23}\\ \gamma_{13}\\ \gamma_{12}\end{bmatrix}^{k} + \begin{bmatrix} \zeta_{11} & 0 & 0\\ 0 & \zeta_{22} & 0\\ 0 & 0 & \zeta_{33}\end{bmatrix}^{k} \begin{bmatrix}\Phi_1\\ \Phi_2\\ \Phi_3\end{bmatrix}^{k} \quad (3b)$$

$\sigma_{ij}, \varepsilon_{ij}, C_{ijkl}, e_{ij}$, and $\Phi_i$ are the stresses, the strains, the elastic stiffness elements of the matrix [*Q*], the piezoelectric coefficients, and the components of the electric fields, respectively in the orthotropic material orientation. $p_i$ and $\zeta_{ij}$ are the electric displacement and the piezoelectric dielectric constants, respectively. Global stress-strains and electrical displacements as shown in Eqs.4a-c in the *kth* ply can be

calculated by transforming 2D stress-strains and electrical displacements in the material direction through transformation matrix [$T$] in Eq.4d [46].

$$\begin{bmatrix}\sigma_{xx}\\ \sigma_{yy}\\ \sigma_{xy}\\ \sigma_{yz}\\ \sigma_{xz}\end{bmatrix}^k = [T]^{-1}\begin{bmatrix}\sigma_{11}\\ \sigma_{22}\\ \sigma_{12}\\ \sigma_{23}\\ \sigma_{13}\end{bmatrix}^k = [\sigma], \quad \begin{bmatrix}\varepsilon_{xx}\\ \varepsilon_{yy}\\ \gamma_{xy}\\ \gamma_{yz}\\ \gamma_{xz}\end{bmatrix}^k == [T]^{-1}\begin{bmatrix}\varepsilon_{11}\\ \varepsilon_{22}\\ \gamma_{12}\\ \gamma_{23}\\ \gamma_{13}\end{bmatrix}^k = [\varepsilon], \tag{4a}$$

$$\begin{bmatrix}\zeta_{xx} & 0 & 0\\ 0 & \zeta_{yy} & 0\\ 0 & 0 & \zeta_{zz}\end{bmatrix}^k = \begin{bmatrix}\zeta_{11} & 0 & 0\\ 0 & \zeta_{22} & 0\\ 0 & 0 & \zeta_{33}\end{bmatrix}^k = [\zeta] \tag{4b}$$

$$\begin{bmatrix}\rho_{xx}\\ \rho_{yy}\\ \rho_{xy}\end{bmatrix}^k = \begin{bmatrix}0 & 0 & 0 & 0 & e_{15}\\ 0 & 0 & 0 & e_{24} & 0\\ e_{31} & e_{32} & 0 & 0 & 0\end{bmatrix}^k [T]\begin{bmatrix}\varepsilon_{xx}\\ \varepsilon_{yy}\\ \gamma_{xy}\\ \gamma_{yz}\\ \gamma_{xz}\end{bmatrix}^k + \begin{bmatrix}\zeta_{xx} & 0 & 0\\ 0 & \zeta_{yy} & 0\\ 0 & 0 & \zeta_{zz}\end{bmatrix}^k \begin{bmatrix}\Phi_1\\ \Phi_2\\ \Phi_3\end{bmatrix}^k = [\rho] \tag{4c}$$

$$[T] = \begin{bmatrix} C^2 & S^2 & SC & 0 & 0\\ S^2 & C^2 & -SC & 0 & 0\\ -2SC & 2SC & C^2-S^2 & 0 & 0\\ 0 & 0 & 0 & C & -S\\ 0 & 0 & 0 & S & C\end{bmatrix} \tag{4d}$$

$c$ is $cos(\beta)$ and $s$ is $sin(\beta).\beta$ as seen in Figs.1a-b is the winding angle between either fibers and $x$ axis in a fiber-reinforced composite ply ($\beta_p$) or piezoelectric fibres and $x$ axis in a MFC actuator ($\beta_a$). $Q_{ij}$ and $e_{ij}$ are the reduced elastic stiffness and the piezoelectric modules, respectively, as given in Eqs.5e-h, respectively.

$$Q_{11} = C_{1111} - \frac{C_{1133}^2}{C_{3333}} = \frac{E_1}{1-\nu_{12}\nu_{21}} \tag{5a}$$

$$Q_{22} = C_{2222} - \frac{C_{2233}^2}{C_{3333}} = \frac{E_2}{1-\nu_{12}\nu_{21}} \tag{5b}$$

$$Q_{12} = C_{1122} - \frac{C_{1133}C_{2233}}{C_{3333}} = \frac{\nu_{12}E_2}{1-\nu_{12}\nu_{21}} \tag{5c}$$

$$Q_{66} = C_{1212} = G_{12} \tag{5d}$$

$$e_{31} = Q_{11}d_{31} - Q_{12}d_{32} \tag{5e}$$

$$e_{32} = Q_{12}d_{31} - Q_{22}d_{32} \tag{5f}$$

$$e_{11} = Q_{11}d_{11} - Q_{12}d_{12} \tag{5g}$$

$$e_{12} = Q_{12}d_{11} - Q_{22}d_{12} \tag{5h}$$

$E_1$, $E_2$, $\nu_{12}$, and $G_{12}$ are in-plane local elasticity modules of an orthotropic layer in the local material coordinate system. $d_{ij}$ is the piezoelectric dielectric constant.

### 2.1 Electrical properties of MFC actuators ($d_{31}$-effect)

The polarization direction in MFC-$d_{31}$ type is through the thickness ($Z$ direction) and perpendicular to the piezoelectric fibres which are parallel to the mid-plane. Thus, the piezoelectric matrix in global direction can be rearranged to Eq.6a. The electrical field in MFC-$d_{31}$ is obtained using Eq.6b (see Fig.2b).

$$[e] = \begin{bmatrix} 0 & 0 & 0 & 0 & e_{15} \\ 0 & 0 & 0 & e_{24} & 0 \\ e_{31} & e_{32} & 0 & 0 & 0 \end{bmatrix} [T] \tag{6a}$$

$$\Phi_3 = -\frac{V_3}{t_a} \tag{6b}$$

where, $V_3$ and $t_a$ are the electrical voltage applied through thickness and a MFC-$d_{31}$ thickness, respectively.

### 2.2 Electrical properties of MFC actuators ($d_{33}$-effect)

The polarization direction in MFC-$d_{33}$ type is parallel to the piezoelectric fibres. In this type of MFC actuator, both the polarization direction and the piezoelectric fibres are parallel to the mid-plane. Thus, the piezoelectric matrix in global direction can be simplified to Eq.7a. the electrical filed through thickness for MFC-$d_{33}$ is obtained using Eq.7b (see Fig.2a).

$$[e]=\begin{bmatrix} e_{11} & e_{12} & 0 & 0 & 0 \\ 0 & 0 & e_{26} & 0 & 0 \\ 0 & 0 & 0 & 0 & e_{35} \end{bmatrix}[T] \tag{7a}$$

$$\Phi_1 = -\frac{V_1}{\Delta x} \tag{7b}$$

where, $V_1$ and $\Delta x$ are the electrical voltage applied along piezoelectric fibres and the distance between piezoelectric electrodes in a MFC-$d_{33}$, respectively.

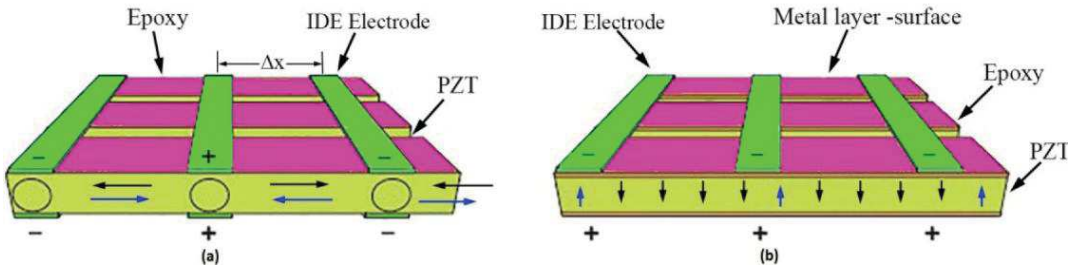


**Fig.2.** Schematic of a MFC actuator and its components: a) $d_{33}$ effect, b) $d_{31}$ effect.

## 2.3 Quadratic FE formulations considering first order shear deformation theory

In this study, a pair of MFC actuator patches are bounded to the laminated composite plate (host structure). Various boundary conditions (Cantilevered and simply-supported) are prescribed to the smart piezo composite plates. Each MFC actuator has embedded piezoelectric fibres with different orientation angle with respect to $x$ axis ($\beta$ $=\{0^o,30^o,45^o,60^o,90^o\}$). The applied electrical voltage ($V_a$) induces the host structure and creates electro-mechanical strains. The effect of MFC-$d_{31}$ and MFC-$d_{33}$ for each case need to be examined. Considering $N$ number of MFC actuators, the electric displacements, the electrical potentials, piezoelectric coefficients, and piezoelectric dielectric constants, the 2D FE matrixes can be derived as stated in Eq.8, respectively.

$$[\rho]=\begin{bmatrix}\rho_s^1\\ \rho_s^2\\ \vdots\\ \rho_s^N\end{bmatrix},[\Phi]=\begin{bmatrix}\Phi_s^1\\ \Phi_s^2\\ \vdots\\ \Phi_s^N\end{bmatrix},[\rho]=\begin{bmatrix}\rho_s^1\\ \rho_s^2\\ \vdots\\ \rho_s^N\end{bmatrix},[e]=\begin{bmatrix}e_{s1}^1 & e_{s2}^1 & 0 & 0 & 0\\ e_{s1}^2 & e_{s2}^1 & 0 & 0 & 0\\ \vdots & \vdots & \vdots & \vdots & \vdots\\ e_{s1}^N & e_{s2}^N & 0 & 0 & 0\end{bmatrix}$$

$$[\zeta]=\begin{bmatrix}\zeta_{s1}^1 & \zeta_{s2}^1 & 0 & 0 & 0\\ \zeta_{s1}^2 & \zeta_{s2}^1 & 0 & 0 & 0\\ \vdots & \vdots & \vdots & \vdots & \vdots\\ \zeta_{s1}^N & \zeta_{s2}^N & 0 & 0 & 0\end{bmatrix} \tag{8}$$

In Eq.8, the term $s$=3 for MFC-$d_{31}$ and $S$=1 for MFC-$d_{33}$. $N$ stands for the number of MFC actuators. In the current research, $N$=2 for bounded MFC patches. Using Eq.6b and Eq.7b, the electric field matrix for multiple MFC-$d_{31}$ and MFC-$d_{33}$ can be derived as stated in Eqs.9a-b. respectively.

$$[\Phi]=\begin{bmatrix}\Phi_s^1\\ \Phi_s^2\\ \vdots\\ \Phi_s^N\end{bmatrix}=\begin{bmatrix}\frac{-1}{t_a^N} & 0 & \cdots & 0\\ 0 & \frac{-1}{t_a^N} & \cdots & 0\\ \vdots & \vdots & \ddots & \vdots\\ 0 & 0 & \cdots & \frac{-1}{t_a^N}\end{bmatrix}\begin{bmatrix}V_3^1\\ V_3^2\\ \vdots\\ V_3^N\end{bmatrix}=[B_{3j}][V_m] \tag{9a}$$

$$[\Phi]=\begin{bmatrix}\Phi_s^1\\ \Phi_s^2\\ \vdots\\ \Phi_s^N\end{bmatrix}=\begin{bmatrix}\frac{-1}{\Delta x_a^N} & 0 & \cdots & 0\\ 0 & \frac{-1}{\Delta x_a^N} & \cdots & 0\\ \vdots & \vdots & \ddots & \vdots\\ 0 & 0 & \cdots & \frac{-1}{\Delta x_a^N}\end{bmatrix}\begin{bmatrix}V_1^1\\ V_1^2\\ \vdots\\ V_1^N\end{bmatrix}=[B_{3j}][V_m] \tag{9b}$$

In Eqs.9a-b, $m$=3 and $j$=1 for MFC-$d_{31}$ and $m$=1 and $j$=3 for MFC-$d_{33}$. $N$=2 for a pair of piezoelectric actuator patches bounded to the host structure. It must be noted that the piezoelectric fiber angle orientation doesn't affect a MFC actuator electrical potential matrix but rather modifies the piezoelectric coefficient matrix.

In the next step, a 2D FE formulation is developed using FOSDT which is in the Reissner-Mindlin plate theory. Consideration of transverse shear strains in composite laminates is important, since the deformed configuration of composite structures are necessarily not normal to the mid-plane, laying out the fact that additional transverse shear strains effect must be considered for more accurate perdition of strain-displacement values. To formulate the 2D FE equations, an eight-node quadratic shell element with five degrees of freedom is introduced in the current research. The five generalized displacements in the shell space can be defined as the derivative operation matrix $Z$ and the generalized displacement vector $U$ as stated in Eq.10.

$$\begin{bmatrix} u \\ v \\ w \end{bmatrix} = \begin{bmatrix} 1 & 0 & 0 & z & 0 \\ 0 & 1 & 0 & 0 & z \\ 0 & 0 & 1 & 0 & 0 \end{bmatrix} \begin{bmatrix} U_x \\ U_y \\ w_0 \\ \varphi_x \\ \varphi_y \end{bmatrix} = [Z_u][U] \tag{10}$$

Considering the small linear strain-displacement deformation and using Eqs.2a-d, the strain components can be rearranged in form of a matrix in Eq.11 which represents the product of the derivative operation matrix $D$ and the generalized displacement vector $U$.

$$\begin{bmatrix} \varepsilon_{xx} \\ \varepsilon_{yy} \\ \gamma_{xy} \\ \gamma_{yz} \\ \gamma_{xz} \end{bmatrix} = \begin{bmatrix} \frac{\partial}{\partial x} & 0 & 0 & z\frac{\partial}{\partial x} & 0 \\ 0 & \frac{\partial}{\partial y} & 0 & 0 & z\frac{\partial}{\partial y} \\ \frac{\partial}{\partial y} & \frac{\partial}{\partial x} & 0 & z\frac{\partial}{\partial y} & z\frac{\partial}{\partial x} \\ 0 & 0 & \frac{\partial}{\partial y} & 0 & 1 \\ 0 & 0 & \frac{\partial}{\partial x} & 1 & 0 \end{bmatrix} \begin{bmatrix} U_x \\ U_y \\ w_0 \\ \varphi_x \\ \varphi_y \end{bmatrix} = [D][U] \tag{11}$$

To approximate the displacements and rotations of transverse normal for any point at the mid-plane, nodal displacements with use of shape functions need to be introduced. For 2D eight-node quadratic shell element modelled in the present work, shape functions $N_i$ are defined in the local material orientations known as Jacobian coordinates in Eq.12. The schematic of the difference between linear and quadratic FE and their representation in the Jacobian coordinate system can be found in Figs.3a-c, respectively.

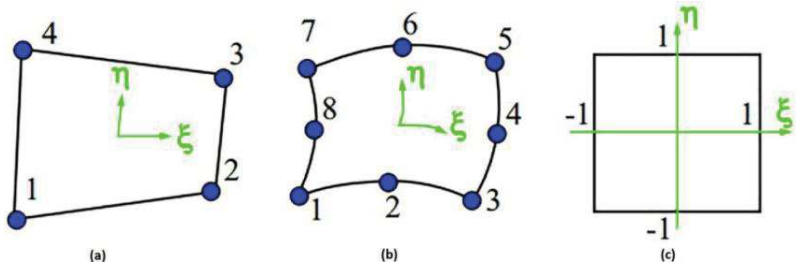


**Fig.3.** a) Linear element, b) Quadratic element, c) Jacobian coordinates system.

$$U_x = \sum N_i U_i^x \ , \ U_y = \sum N_i U_i^y \ , \ \varphi_x = \sum N_i \varphi_i^x \ , \ \varphi_y = \sum N_i \varphi_i^y \ , \ x = \sum N_i x_i \ ,$$

$$y = \sum N_i y_i \tag{12}$$

where, $N_i$ for $i$=1:8 are used for coordinates and displacements interpolations shape functions. The 2D eight-node isoparametric quadratic shell elements are given by Eq.13a-c.

$$N_i = \tfrac{1}{4}(1+\xi\xi_i)(1+\eta\eta_i) - \tfrac{1}{4}(1-\xi^2)(1+\eta\eta_i) - \tfrac{1}{4}(1-\eta^2)(1+\xi\xi_i) \ , i = 1,3,5,7 \tag{13a}$$

$$N_i = \tfrac{1}{2}(1-\xi^2)(1+\eta\eta_i) \ , i = 2,6 \tag{13b}$$

$$N_i = \tfrac{1}{2}(1-\eta^2)(1+\xi\xi_i) \ , i = 4,8 \tag{13c}$$

Differentiation of displacements operator expressed through the shape function in Eq.12 leads to the displacement differentiation matrix [$B$] in Eq.14.

$[B_u] = [D][N] =$

$$\begin{bmatrix}
\frac{\partial N_1}{\partial x} & 0 & 0 & z\frac{\partial N_1}{\partial x} & 0 & \frac{\partial N_2}{\partial x} & 0 & 0 & z\frac{\partial N_2}{\partial x} & 0 & \cdots & \frac{\partial N_8}{\partial x} & 0 & 0 & z\frac{\partial N_8}{\partial x} & 0 \\
0 & \frac{\partial N_1}{\partial y} & 0 & 0 & z\frac{\partial N_1}{\partial y} & 0 & \frac{\partial N_2}{\partial y} & 0 & 0 & z\frac{\partial N_2}{\partial y} & \cdots & 0 & \frac{\partial N_8}{\partial y} & 0 & 0 & z\frac{\partial N_8}{\partial y} \\
\frac{\partial N_1}{\partial y} & \frac{\partial N_1}{\partial x} & 0 & z\frac{\partial N_1}{\partial y} & z\frac{\partial N_1}{\partial x} & \frac{\partial N_2}{\partial y} & \frac{\partial N_2}{\partial x} & 0 & z\frac{\partial N_2}{\partial y} & z\frac{\partial N_2}{\partial x} & \cdots & \frac{\partial N_8}{\partial y} & \frac{\partial N_8}{\partial x} & 0 & z\frac{\partial N_8}{\partial y} & z\frac{\partial N_8}{\partial x} \\
0 & 0 & \frac{\partial N_1}{\partial y} & 0 & 1 & 0 & 0 & \frac{\partial N_2}{\partial y} & 0 & 1 & \cdots & 0 & 0 & \frac{\partial N_8}{\partial y} & 0 & 1 \\
0 & 0 & \frac{\partial N_1}{\partial x} & 1 & 0 & 0 & 0 & \frac{\partial N_2}{\partial x} & 1 & 0 & \cdots & 0 & 0 & \frac{\partial N_8}{\partial y} & 1 & 0
\end{bmatrix} \tag{14}$$

Computation of Jacobian matrix [$J$] entries at any quadrilateral location requires differentiation from the shape functions in Eq.12 with respect to the quadrilateral coordinates. Thus, the matrix [$J$] can be formed as stated in Eq.15.

$$[J]=\begin{bmatrix} J_{11} & J_{12} \\ J_{21} & J_{22} \end{bmatrix}=\frac{\partial(x,y)}{\partial(\xi,\eta)}=\begin{bmatrix} \frac{\partial x}{\partial \xi} & \frac{\partial y}{\partial \xi} \\ \frac{\partial x}{\partial \eta} & \frac{\partial y}{\partial \eta} \end{bmatrix}=\begin{bmatrix} \frac{\partial N_1^e}{\partial \xi} & \frac{\partial N_2^e}{\partial \xi} & \cdots & \frac{\partial N_8^e}{\partial \xi} \\ \frac{\partial N_1^e}{\partial \eta} & \frac{\partial N_2^e}{\partial \eta} & \cdots & \frac{\partial N_8^e}{\partial \eta} \end{bmatrix}\begin{bmatrix} x_1 & y_1 \\ x_2 & y_2 \\ \vdots & \vdots \\ x_8 & y_8 \end{bmatrix} \tag{15}$$

The shape function derivatives in global coordinates as the elements of the displacement differential matrix $[B_u]$ is obtained by inversing the Jacobian matrix $[J]$ multiplied to the shape function derivatives in Jacobian coordinates. The results are shown in Eq.16.

$$\begin{bmatrix} \frac{\partial N_i^e}{\partial x} \\ \frac{\partial N_i^e}{\partial y} \end{bmatrix}=[J]^{-1}\begin{bmatrix} \frac{\partial N_i^e}{\partial \xi} \\ \frac{\partial N_i^e}{\partial \eta} \end{bmatrix} \tag{16}$$

Finally, the strain-displacement matrix $[B]$ required for computation of the element stiffness matrix and 2D FE nodal displacement vector $[U]$ leads to computation of strains, considering the transverse shear deformation. Therefore, considering the small displacements and material linearity, the strain-displacement nodal parameter matrix can be obtained using Eq.17.

$$[\varepsilon]=[B_u][U]=$$

$$\begin{bmatrix} \frac{\partial N_1}{\partial x} & 0 & 0 & z\frac{\partial N_1}{\partial x} & 0 & \frac{\partial N_2}{\partial x} & 0 & 0 & z\frac{\partial N_2}{\partial x} & 0 & \cdots & \frac{\partial N_8}{\partial x} & 0 & 0 & z\frac{\partial N_8}{\partial x} & 0 \\ 0 & \frac{\partial N_1}{\partial y} & 0 & 0 & z\frac{\partial N_1}{\partial y} & 0 & \frac{\partial N_2}{\partial y} & 0 & 0 & z\frac{\partial N_2}{\partial y} & \cdots & 0 & \frac{\partial N_8}{\partial y} & 0 & 0 & z\frac{\partial N_8}{\partial y} \\ \frac{\partial N_1}{\partial y} & \frac{\partial N_1}{\partial x} & 0 & z\frac{\partial N_1}{\partial y} & z\frac{\partial N_1}{\partial x} & \frac{\partial N_2}{\partial y} & \frac{\partial N_2}{\partial x} & 0 & z\frac{\partial N_2}{\partial y} & z\frac{\partial N_2}{\partial x} & \cdots & \frac{\partial N_8}{\partial y} & \frac{\partial N_8}{\partial x} & 0 & z\frac{\partial N_8}{\partial y} & z\frac{\partial N_8}{\partial x} \\ 0 & 0 & \frac{\partial N_1}{\partial y} & 0 & 1 & 0 & 0 & \frac{\partial N_2}{\partial y} & 0 & 1 & \cdots & 0 & 0 & \frac{\partial N_8}{\partial y} & 0 & 1 \\ 0 & 0 & \frac{\partial N_1}{\partial x} & 1 & 0 & 0 & 0 & \frac{\partial N_2}{\partial x} & 1 & 0 & \cdots & 0 & 0 & \frac{\partial N_8}{\partial y} & 1 & 0 \end{bmatrix}\begin{bmatrix} U_1^x \\ U_1^y \\ w_{01} \\ \varphi_1^x \\ \varphi_1^y \\ U_2^x \\ U_2^y \\ w_{02} \\ \varphi_2^x \\ \varphi_2^y \\ \vdots \\ U_8^x \\ U_8^y \\ w_{08} \\ \varphi_8^x \\ \varphi_8^y \end{bmatrix} \tag{17}$$

To drive an assembly algorithm to formulate the FE equations, the total potential energy and principle of virtual works are topically adapted. In the current research, the principle of virtual work is employed to obtain a linear electro-mechanically coupled static FE equations. This FE modelling can be extended for sensor equations. However, since the aim of this research is to investigate the inverse effect of piezoelectric materials on shape deformation of laminated composite structures, the sensor equations are neglected. The principle of virtual work in Eqs.18a-b stipulates that the total internal work done on a mechanical system should be equal to the total external work.

$$\delta W_{\text{int}} = \delta W_{ext} \tag{18a}$$

$$\int_V \left(\delta[\varepsilon^e]^T[\sigma^e] - \delta[\Phi^e]^T[\rho^e]\right)dV = \int_V \left(\delta[U^e]^T f_b\right)dV + \int_\Omega \left(\delta[U^e]^T f_s\right)d\Omega - \int_\Omega \left(\delta[V_m^e]^T \psi_s\right) d\Omega + \delta[U^e]^T f_c - \delta[V_m^e]^T \psi_c \tag{18b}$$

In Eqs.18a-b, the subscripts $e$ and $\delta$ stand for the element on which the total internal/external work is done and the variation operator, respectively. In addition, $f_b$, $f_s$, and $f_c$ represent the body, surface, and concentrated charge vector, $\psi_s$, and $\psi_c$ are the surface and concentrated charge vectors in an element, respectively. Substituting Eqs.6a,7a,9a-b,10,14 into Eq18.b and considering linear strain-displacement deformation due to small displacements, the static equilibrium equations representing the electro-mechanically coupled FE model can be obtained (see Eq.19). Computation of the system matrix in Eq.19 leads to obtaining the generalized displacements vector $[U]$. Therefore, through use of the derivative operation matrix $[Z_u]$, the general form of displacement fields can be computed.

$$[U^e]\int_V [B_u^e]^T [T]^T [C][T][B_u^e]dV - V_m \int_V [B_u^e]^T [e]^T [B_{3j}^e]dV = \int_V [N^e]^T [Z_u^e]^T f_b dV + \int_\Omega [N^e]^T [Z_u^e]^T f_s dV + [N^e]^T [Z_u^e]^T f_c \quad (19)$$

## 2.4 Numerical simulation

The linear electro-mechanical coupled FE simulation of smart composite plates induced by a pair of MFC-$d_{31}$ and FMC-$d_{33}$ actuator patches is implemented using ABAQUS. The smart structure consists of the host structure (Laminate fibre-reinforced composite plate) and MFC patches bounded to the host structure.

Assigning the material properties to MFC patches and host structure in the local material ordinations (see Fig.4a), prescribing the boundary conditions and applying electrical loads to bounded MFC patches after assembly (see Fig.4b), and meshing MFC patches and composite laminate (see Fig.4c) are done step by step during the FE simulation. In ABAQUS software, $U_1$, $U_2$, and $U_3$ represent the displacements and $UR_1$, $UR_2$, and $UR_3$ as the rotational angles along $x$, $y$, and $z$ directions, respectively. Since MFC actuator type varies during the analysis, the piezoelectric coefficients $d_{31}$ and $d_{32}$ for MFC-$d_{31}$ type and $d_{11}$ and $d_{12}$ for MFC-$d_{33}$ type are considered. The piezoelectric and host structure local material orientations are defined, thereafter. The structured hex element shape is set as the FE mesh control in the smart piezo composite plate. An 8-node quadrilateral in-plane general-purpose continuum shell, reduced integration with hourglass control, finite membrane strains (SC8R) is defined as the element type in the host structure while a 20-node quadratic piezoelectric brick, reduced integration (C3D20RE) is used to define MFC patches element type (see Fig.4c).

To prevent the low accuracy in computational results of twisting-bending type problems known as Locking phenomenon, the solid element in FEM linear approximations should be prevented whereas it shows the twisting-bending behaviour much stiffer in comparison with explicit analytical solution. Locking is higher if the solid element looks like shell (thickness is smaller than two other sizes).

However, it can be resolved by selecting an appropriate FE with quadratic shape functions such as continuum shell element (SC8R). Since the Locking phenomena may still be found for FE quadratic shape functions, taking many elements for the thickness, therefore, leads to higher accuracy of the results, despite increasing the computational time as a disadvantage. Considering the element type in MFC patches, a 20-node quadratic piezoelectric brick, reduced integration (C3D20RE) has more accuracy over an 8-node linear piezoelectric brick (C3D8E) [47].

## 3. Results and discussions

In this section, various examples are intended to analyse the linear strain-displacement deformation of smart piezo CFRP composite plates induced by bounded MFC actuator patches (see Fig.1) using the electro-mechanically coupled quadratic FE formulation. The results are then compared with the ABAQUS results for various boundary conditions.

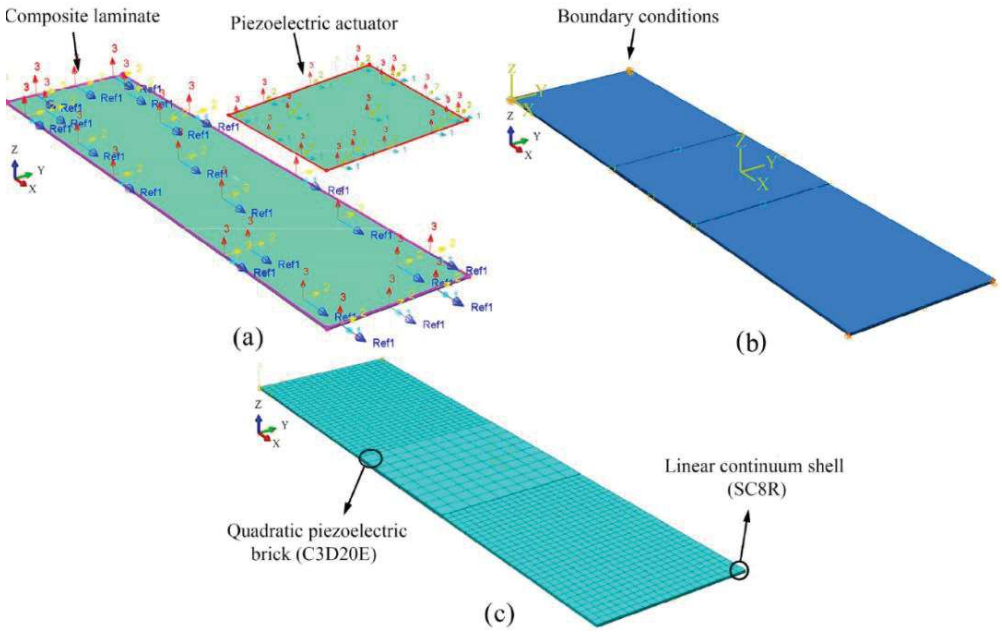


**Fig.4.** Schematic of FE simulation of smart laminated composite plates MFC actuators induced by a pair of bounded MFC actuators using ABAQUS: a) sketching, defining the dimensions, and material properties to composite laminate and MFC actuators, b) applying the electro-mechanical boundary conditions, piezoelectric actuators groundings, and electrical surface charges, c) Applying the FE meshing and defining the element type of host structure and MFC actuators.

In the current FE study, the effect of various parameters including MFC actuator type, applied electrical voltage, laminates stacking sequence, twisting-bending coupling due to unsymmetrical stacking sequence configuration, and prescribed boundary conditions are considered. Material properties of MFC actuator patches and CFRP composite laminate in the following examples are summarized in Table.1[16][43]. The plate dimension ($t_p$=1[mm], $a$=0.24[$m$], $b$=0.06[$m$]) and MFC patches dimension ($t_a$=0.2[$mm$] for MFC-$d_{31}$, $t_a$=0.4[$mm$] and $\Delta x$=0.04[$mm$] for MFC-$d_{33}$, $L_a$=$w_a$=0.06[$m$] for both MFC-$d_{31}$ and MFC-$d_{33}$), MFCs placement and composite laminate properties, and

composite laminate's number of layers (fourth-layered fibre-reinforced composite plate) are kept constant. Two types of boundary conditions are prescribed to the plate for all samples.

**Table.1.** Material properties.

| **Material properties** | **MFC-$d_{31}$** [16] | **MFC-$d_{33}$** [16] | **T300/976 CFRP** [43] |
|---|---|---|---|
| $E_1$ $[GPa]$ | 30.336 | 29.4 | 150 |
| $E_2$ $[GPa]$ | 15.857 | 15.2 | 9 |
| $E_3$ $[GPa]$ | 15.857 | 15.2 | 9 |
| $v_{12}$ | 0.31 | 0.312 | 0.3 |
| $v_{13}$ | 0.31 | 0.31 | 0.3 |
| $v_{23}$ | 0.438 | 0.31 | 0.3 |
| $G_{12}$ $[GPa]$ | 5.515 | 5.79 | 7.1 |
| $G_{13}$ $[GPa]$ | 5.515 | 6.06 | 7.1 |
| $G_{23}$ $[GPa]$ | 5.515 | 6.06 | 2.5 |
| $d_{31}\left[{}^{pm}/_{V}\right]$ | -170 | - | 0 |
| $d_{32}\left[{}^{pm}/_{V}\right]$ | -100 | - | 0 |
| $d_{11}\left[{}^{pm}/_{V}\right]$ | - | 467 | 0 |
| $d_{12}\left[{}^{pm}/_{V}\right]$ | - | -210 | 0 |

*Example.1: Effect of MFC actuators fibre angle*

First, the cross-ply laminated cantilevered and simply-supported plates with stacking sequence $[0/90]_s$ are considered. To examine the sole effect of MFC actuator fibre angle, same amount of electrical voltage is applied to all actuators. The MFC actuator

fibre angles are $\beta=\{0^o,30^o,45^o,60^o,90^o\}$. In the first attempt, the electrical voltage is applied to MFC-$d_{31}$ (upper patch: +240 [$V$] and lower patch: -120 [$V$]).

The results at $w(x,0)$ are plotted in Fig.5a and Fig.6a for the cantilevered and simply-supported boundary conditions, respectively. In the next attempt, MFC-$d_{31}$ actuators are replaced with MFC-$d_{33}$ actuators and different electrical voltage is then applied to them (upper patch: -500 [$V$] and lower patch: +1500 [$V$]). The results at $w(x,0)$ are plotted in Fig.5b and Fig.6b for the cantilevered and simply-supported boundary conditions, respectively. It is obvious that any change in piezoelectric fibre angle results in different shape deformation regardless of boundary condition.

However, the higher deformation rate is observed in MFC-$d_{33}$ actuator due to having the higher maximum voltage limit. Subsequently, numerical simulation was implemented. The vertical displacements in the cantilever and simply supported plates induced by MFC-$d_{31}$ actuators with various piezoelectric fibre angles are illustrated in Figs.7-8, respectively, while Figs.9-10 represent the vertical displacements of the plates with the same boundary conditions but induced by MFC-$d_{33}$ actuators. Comparison of results between the 2D linear electro-mechanically coupled static FE analysis and numerical simulation shows the same trend in mid-plane vertical displacements. As predicted by both 2D FE formulation and ABAQUS results, any fibre angle other than $0^o$ and $90^o$ results in twisting deformation while $0^o$ and $90^o$ result in pure cylindrical bending.

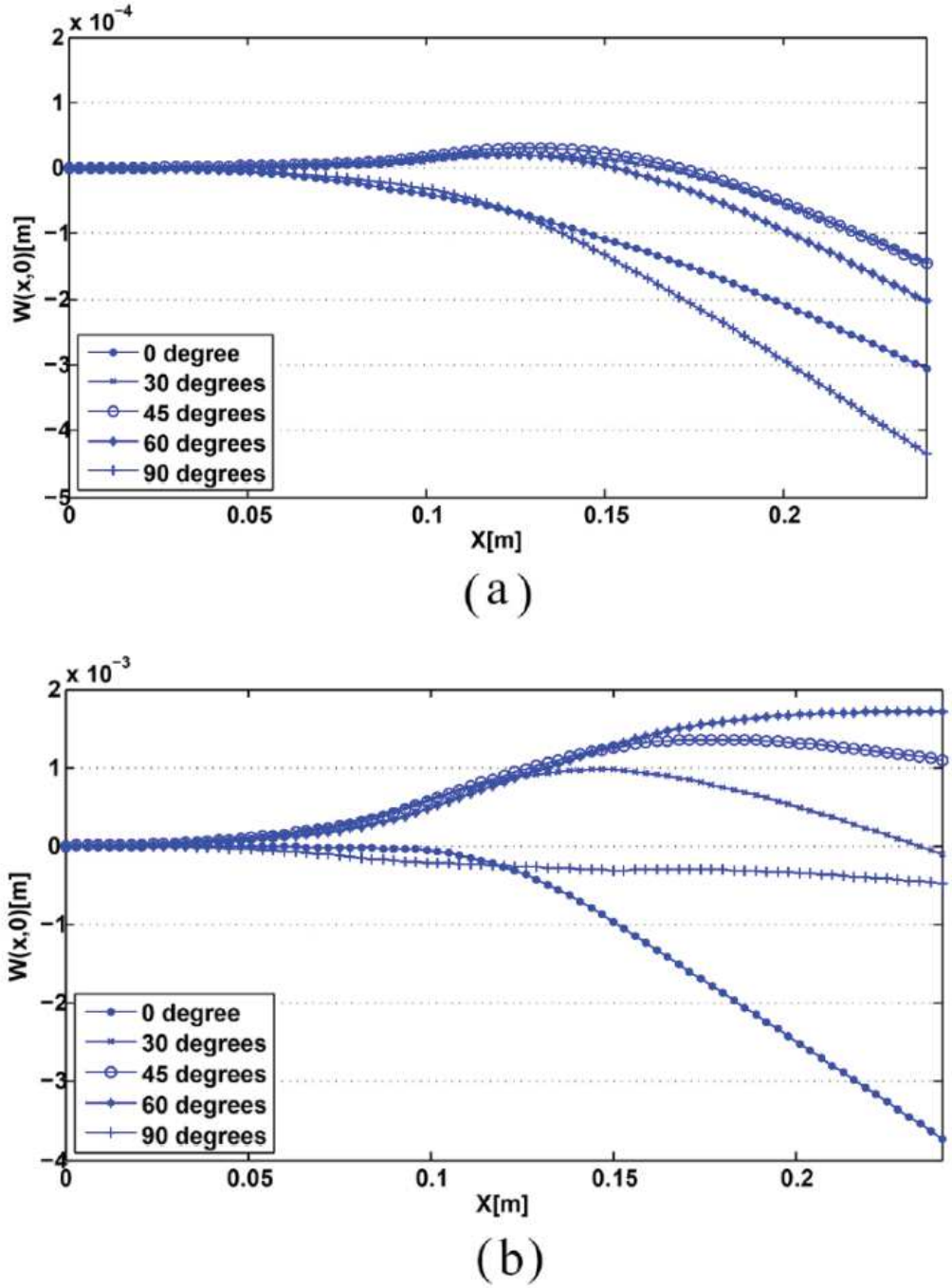


**Fig.5.** Quadratic 2D FE results of $w(x,0)$ in the laminated cantilevered composite plates induced by a pair of bounded MFCs with various piezoelectric fibre angles: a) MFC-$d_{31}$, b) MFC-$d_{33}$.

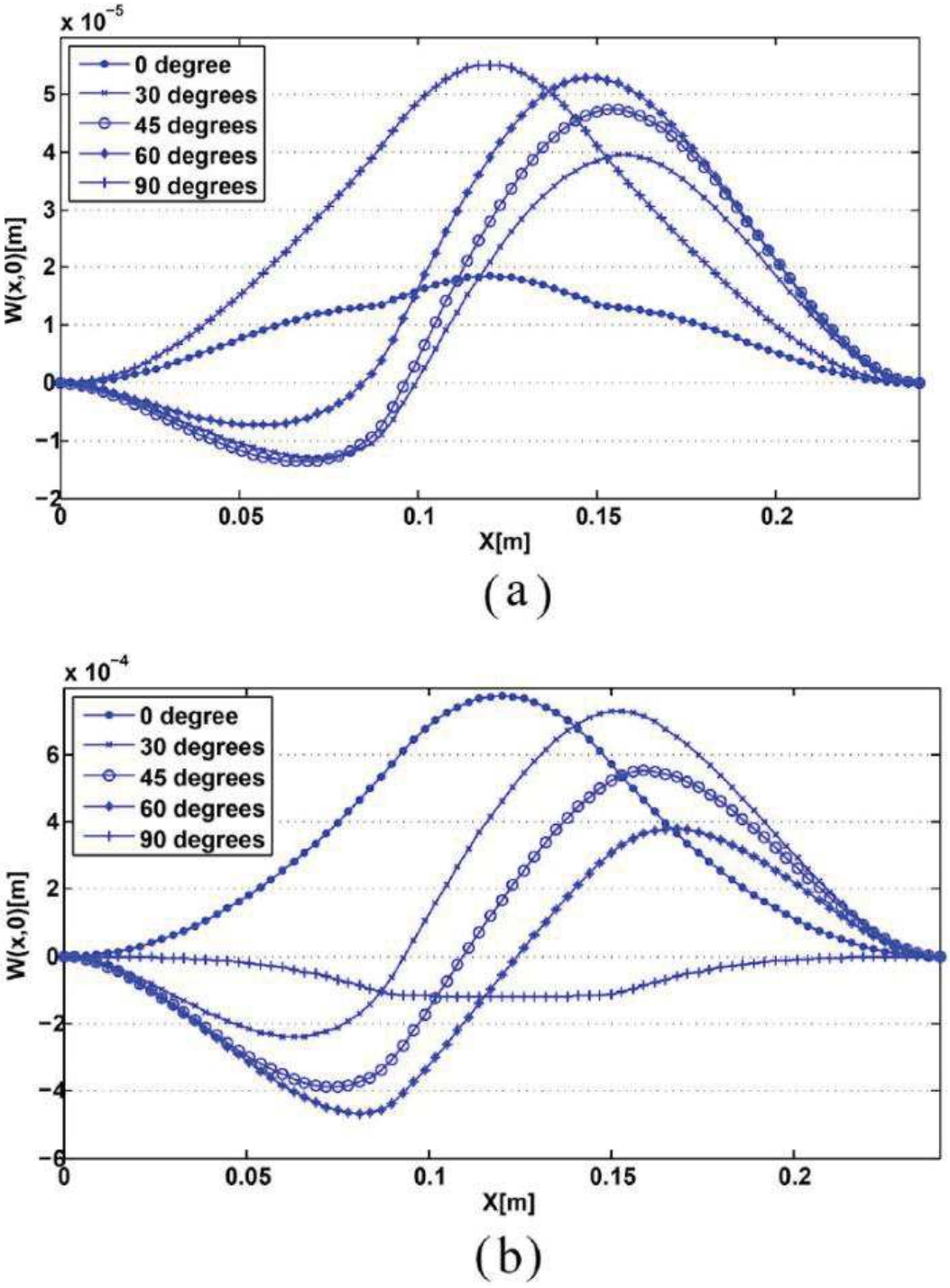


**Fig.6.** Quadratic 2D FE results of $w(x,0)$ in the laminated simply-supported composite plates induced by a pair of bounded MFC patches with various piezoelectric fibre angles: a) MFC-$d_{31}$, b) MFC-$d_{33}$.

*Example.2: Effect of host structure stacking sequence*

In this example, the effect of various symmetrical and unsymmetrical stacking sequence configurations on shape deformation of smart laminated composite plates induced by MFC actuators is investigated. The relationship between stacking sequence and composite laminate stiffness can result in shape deformation changing considerably. Thus, it is important to choose suitable layup to control the structural shape deformation of composite laminates to our advantage.

The samples with symmetrical stacking sequence are: $[\text{Piezo}/0/30]_s$, $[\text{Piezo}/0/45]_s$, $[\text{Piezo}/0/90]_s$, and unsymmetrical: [Piezo/0/30/-30/0/Piezo], [Piezo/0/45/-45/0/Piezo], [Piezo/0/90/0/90/Piezo]. Each layer thickness and applied electrical voltage are kept constant. Same boundary condition is prescribed to the host structure as in Example.1. All MFC actuators fibre angle orientation is kept constant at $0^o$. In the first attempt, the electrical voltage is applied to MFC-$d_{31}$ actuators (upper patch: -120 [$V$] and lower patch: +240 [$V$]). The results of 2D FE analysis at $w(x,0)$ are plotted in Fig.11a and Fig.12a for the cantilevered and simply-supported boundary conditions, respectively.

In the next attempt, MFC-$d_{31}$ actuators are replaced with MFC-$d_{33}$ actuators and different electrical voltage is then applied to them (upper patch: +1500 [$V$] and lower patch: -500 [$V$]). All MFC actuators fibre angle orientation is kept constant at $0^o$. The results at $w(x,0)$ are plotted in Fig.11b and Fig.12b for the cantilevered and simply-supported boundary conditions, respectively. Based on the results, the unsymmetrical stacking sequence configuration [Piezo/0/90/0/90/Piezo] seems to have the highest

vertical displacements for both MFC-$d_{31}$ and MFC-$d_{33}$ types while the vertical displacement for the rest of stacking sequence configurations is quite close regardless of boundary conditions.

Subsequently, based on numerical simulation results, the vertical displacements of the cantilever and simply supported plates induced by MFC-$d_{31}$ actuators are obtained (see Figs.13-14). After replacing the MFC-$d_{31}$ with MFC-$d_{33}$ actuators and running the same simulation procedures for the similar boundary conditions (see Figs.15-16), the same displacement trend but with higher intensity is observed.

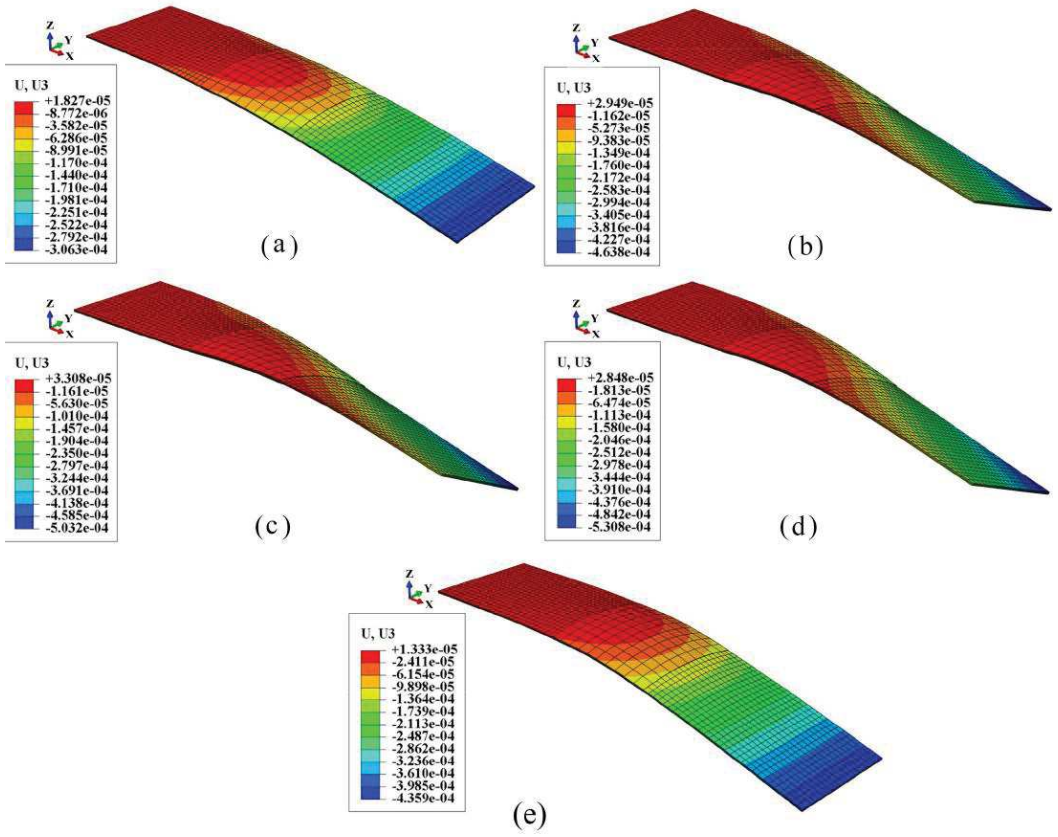


**Fig.7.** Numerical simulation results of $w(x,y)$ in the laminated cantilevered composite plates induced by a pair of bounded MFC-$d_{31}$ patches with various piezoelectric fibre angles.

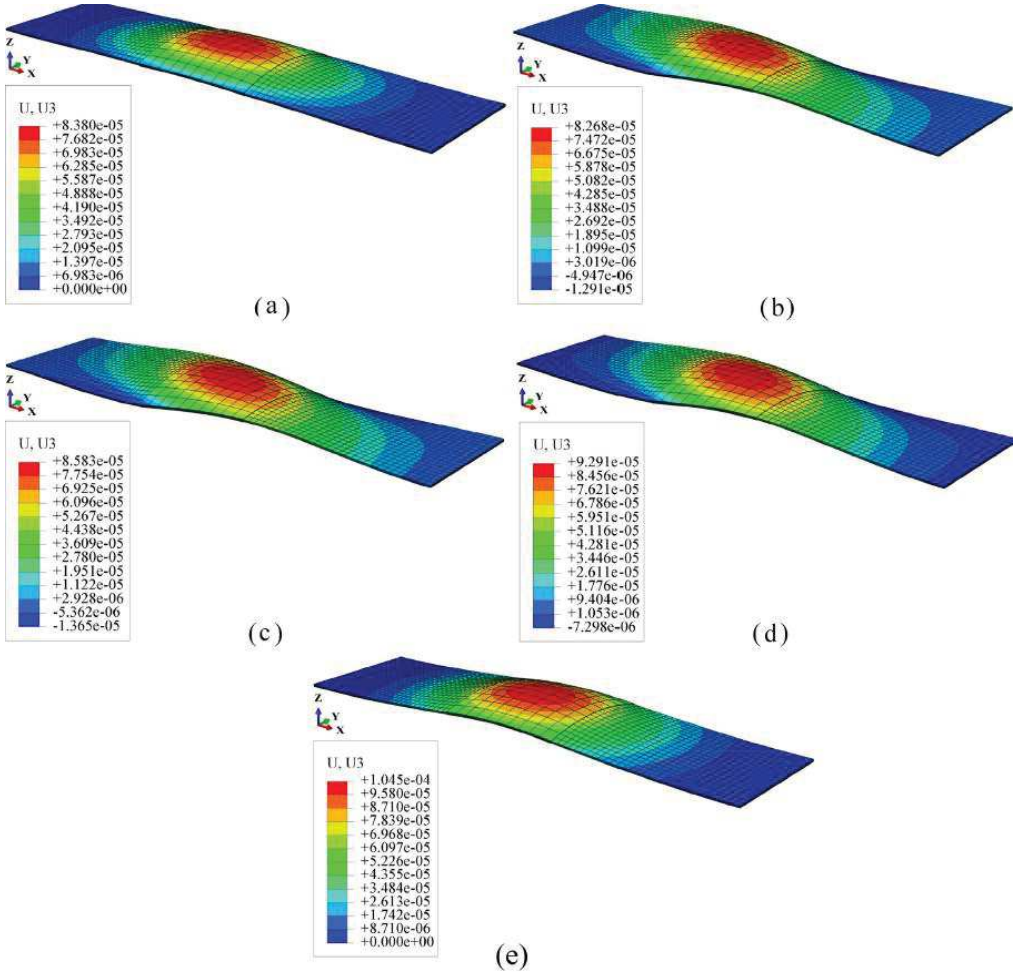


**Fig.8.** Numerical simulation results of $w(x,y)$ in the laminated simply-supported composites plate induced by a pair of bounded MFC-$d_{13}$ patches with various piezoelectric fibre angles.

*Example.3: Effect of MFC actuators applied electrical voltage*

Composite laminates shape can be significantly manipulated by changing the electrical voltage intensity. Therefore, in this example, the effect of applied electrical voltage on the shape deformation of the laminated composite plates is investigated. For that purpose, a series of arbitrarily selected electrical voltage ranging from lowest to maximum voltage limit are applied to the MFC actuators.

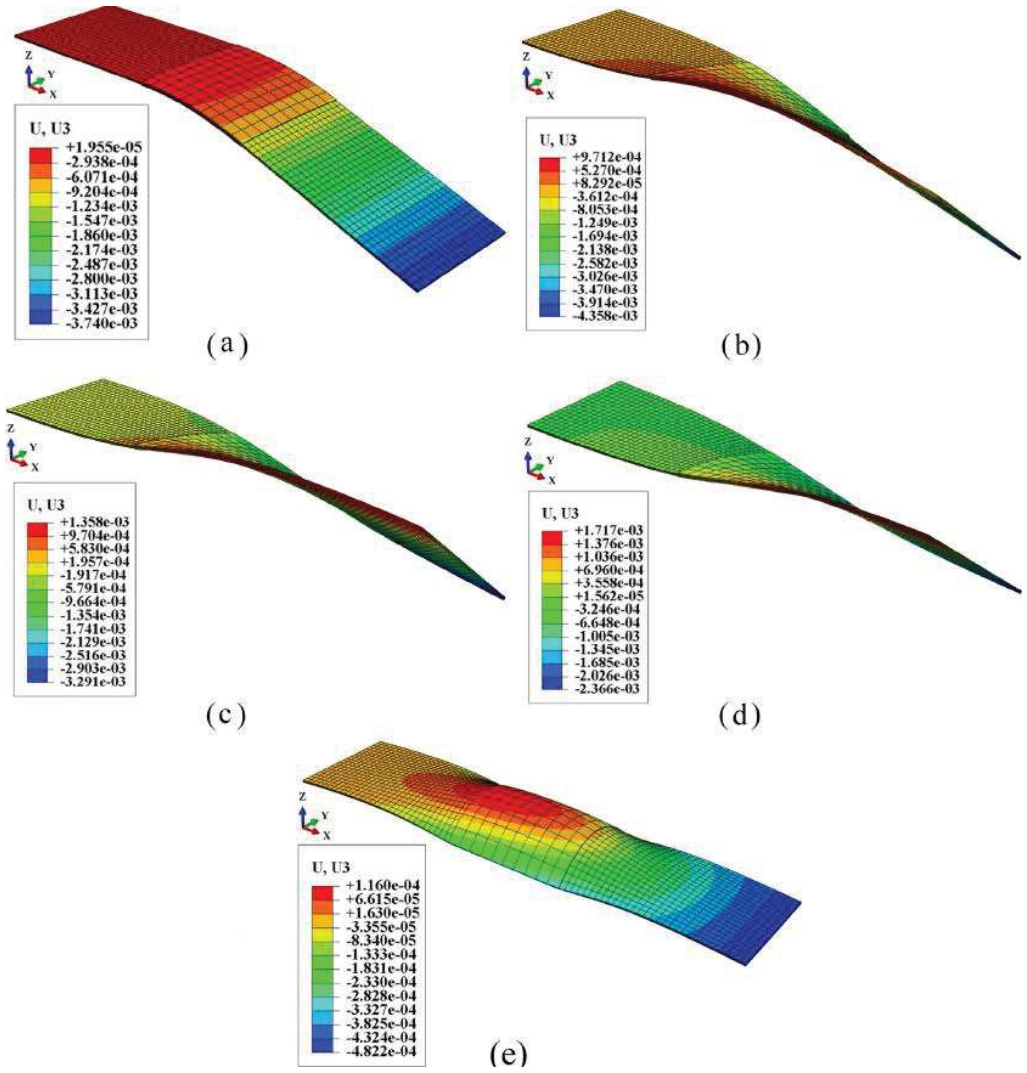


**Fig.9.** Numerical simulation results of $w(x,y)$ in the laminated cantilevered composite plates induced by a pair of bounded MFC-$d_{33}$ patches with various piezoelectric fibre angles.

According to the 2D FE formulation results for both cantilevered and simply supported composite plates induced by MFC-$d_{31}$ (see Fig.17a and Fig.18a) and MFC-$d_{33}$ (see Fig.17b and Fig.18b), any increase in voltage results in higher vertical displacement. The vertical displacements obtained by ABAQUS in the cantilever and simply supported composite plates induced by MFC-$d_{31}$ actuators are illustrated in Figs.19-20, respectively, while Figs.21-22 represent the vertical displacements of the composite

plates with the same boundary conditions but induced by MFC-$d_{33}$ actuators. The comparison of results showed the smart composite plates undergoing the same shape deformation by changing the electrical voltage.

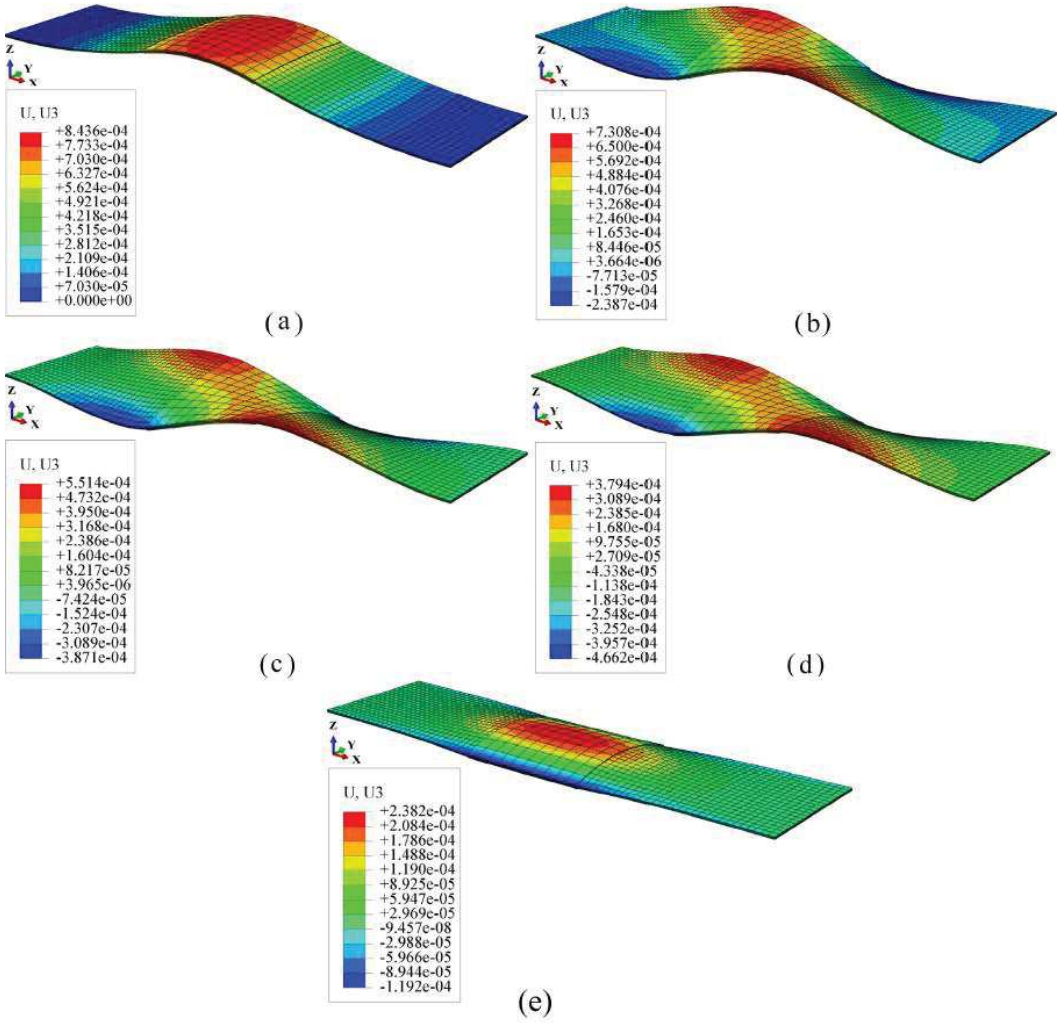


**Fig.10.** Numerical simulation results of $w(x,y)$ in the laminated simply-supported composite plate induced by a pair of bounded MFC-$d_{33}$ patches with various piezoelectric fibre angles.

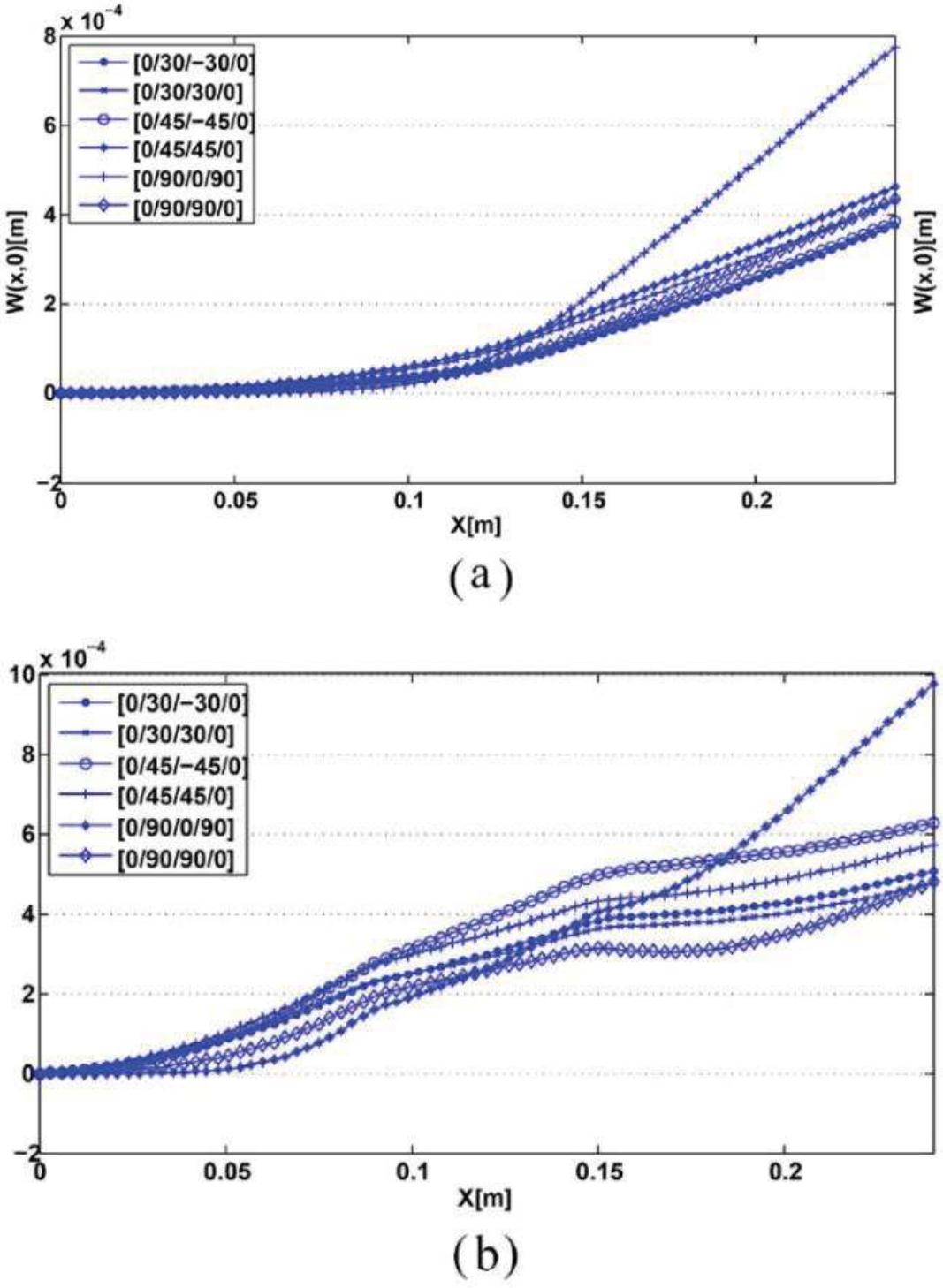


**Fig.11.** Quadratic 2D FE results of $w(x,0)$ in the laminated cantilevered composite plate induced by a pair of bounded MFC patches with various stacking sequences: a) MFC-$d_{31}$, b) MFC-$d_{33}$.

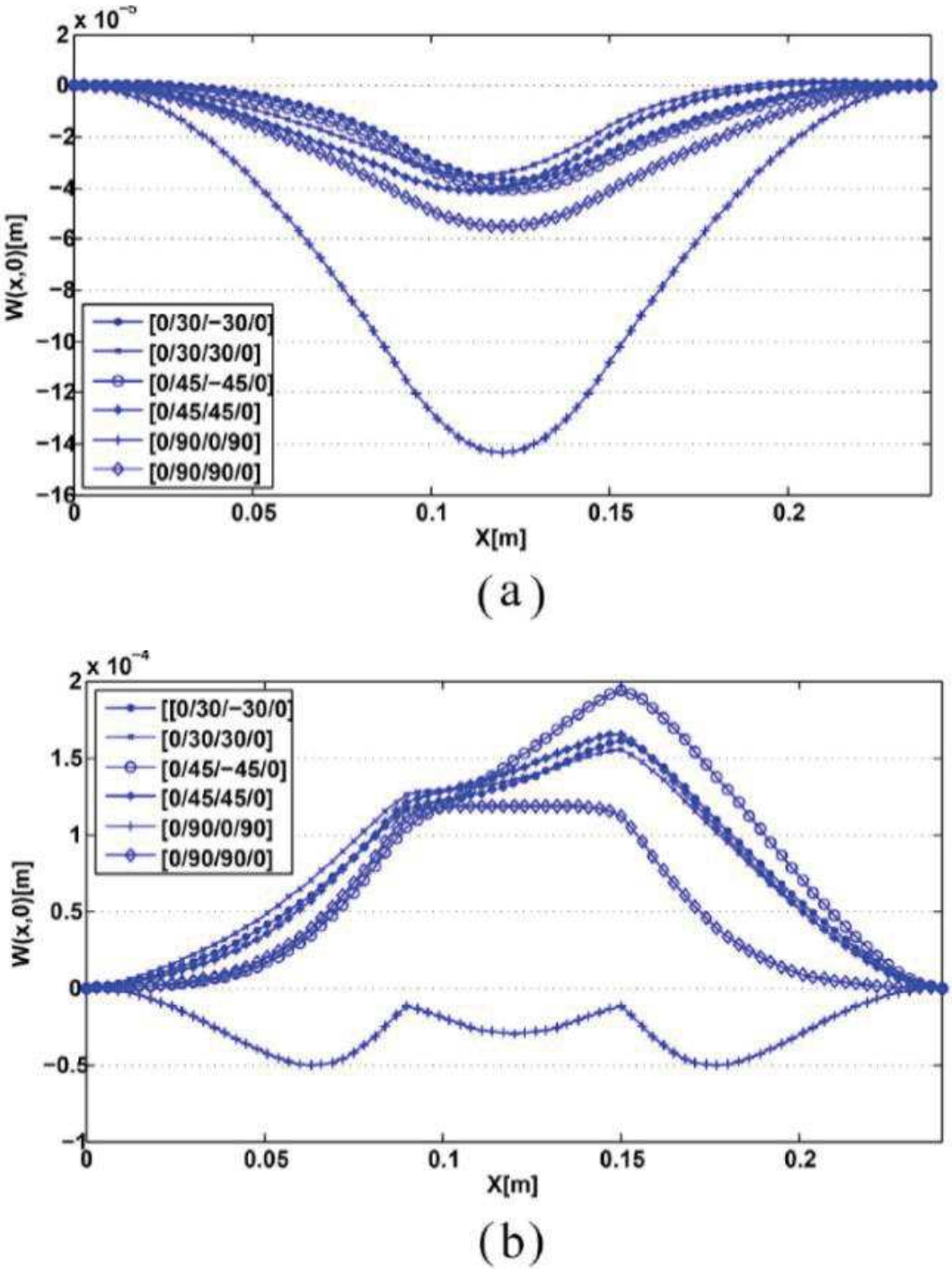


**Fig.12.** Quadratic 2D FE results of $w(x,0)$ in the laminated simply-supported composite plate induced by a pair of bounded MFC patches with various stacking sequences: a) MFC-$d_{31}$, b) MFC-$d_{33}$.

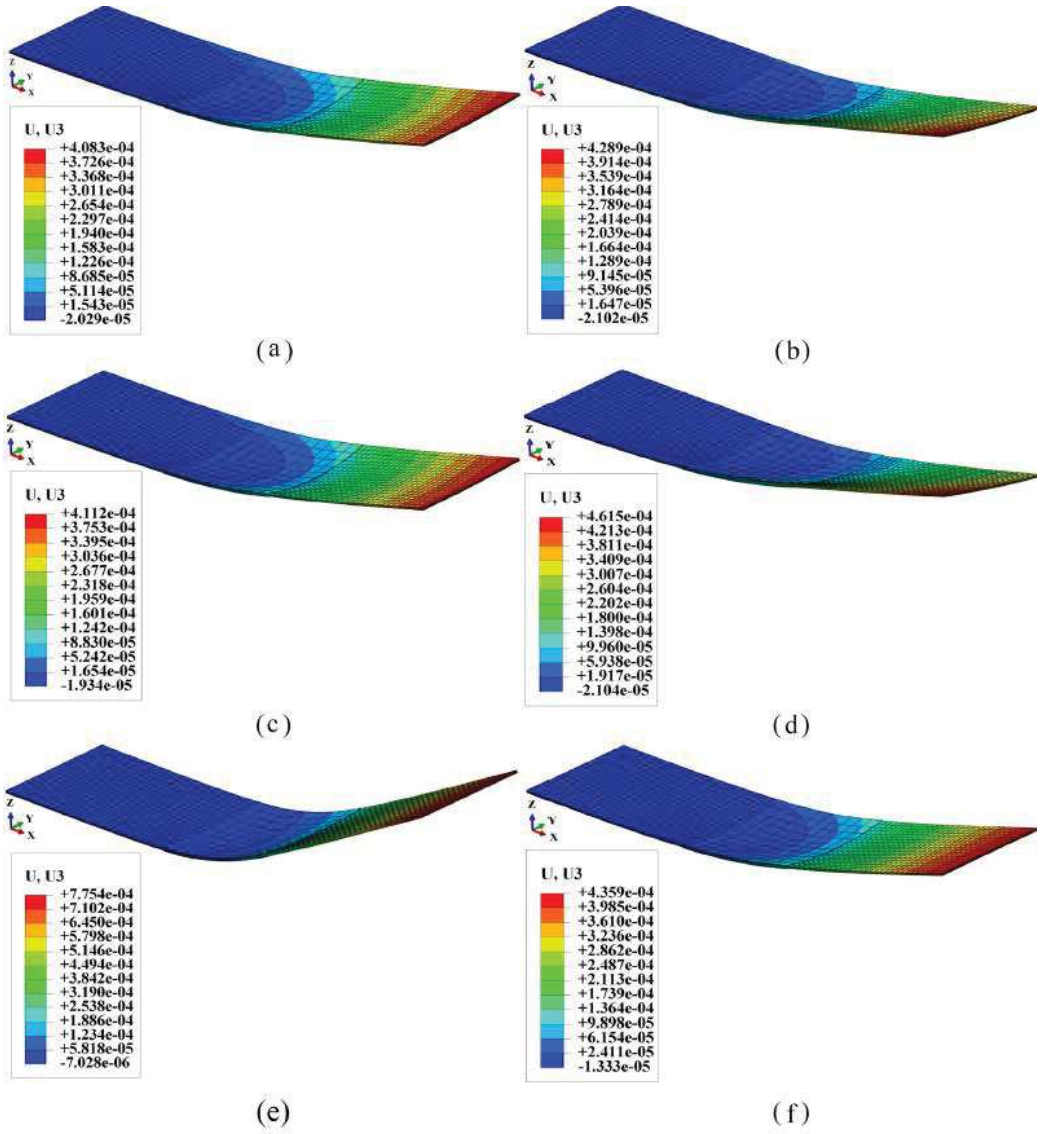


**Fig.13.** Numerical simulation results of $w(x,y)$ in the laminated cantilevered composite plate induced by a pair of bounded MFC-$d_{31}$ patches with various stacking sequences.

*Example.4: Shape deformation comparison between MFC-$d_{31}$ and MFC-$d_{33}$*

In the final example, the mid-plane displacements $U_x$, $U_y$, and $w$ due to the constant electrical voltage applied to MFC-$d_{31}$ and MFC-$d_{33}$ patches bounded to the cantilevered and simply-supported composite plates are investigated and then compared using the

developed quadratic 2D FE formulation. The same amount of electrical voltage is applied to MFC-$d_{31}$ and MFC-$d_{33}$ (upper patch: +200 [$V$] and lower patch: -100 [$V$]). The results for the cantilevered and simply-supported composite plates are illustrated in Figs.23a-c and Figs.24a-c, respectively.

According to the results, regardless of the prescribed boundary conditions, a significant fluctuation occurs in the displacements within the area at which the MFC actuators are bounded to. However, the displacements sign and intensity vary depending on which MFC type is exploited. The reason behind that are the major difference in MFC actuators material crystallization and their dielectric coefficient matrixes.

## 4. Conclusions and remarks

In this research, a quadratic 2D FE formulation using FOSDT is developed to predict the linear strain-displacement deformation in the laminated piezo composite plates induced by MFC actuators. Two types of MFC actuators are exploited: 1) MFC-$d_{31}$ and 2) MFC-$d_{33}$. FOSDT was adapted from the Reissner-Mindlin plate theory. Subsequently, the 3D electro-mechanical coupled FE simulation of smart piezo composite plates induced by MFC-$d_{31}$ and MFC-$d_{33}$ is implemented using ABAQUS.

Furthermore, the effect of various boundary conditions prescribed to the laminated composite plate, laminate stacking sequence, unsymmetrical layup, electrical voltage intensity, MFC type, and piezoelectric fibre angle orientation on the linear strain-

displacement deformation is then discussed thoroughly. Based on the results in the current research, the following remarks are concluded:

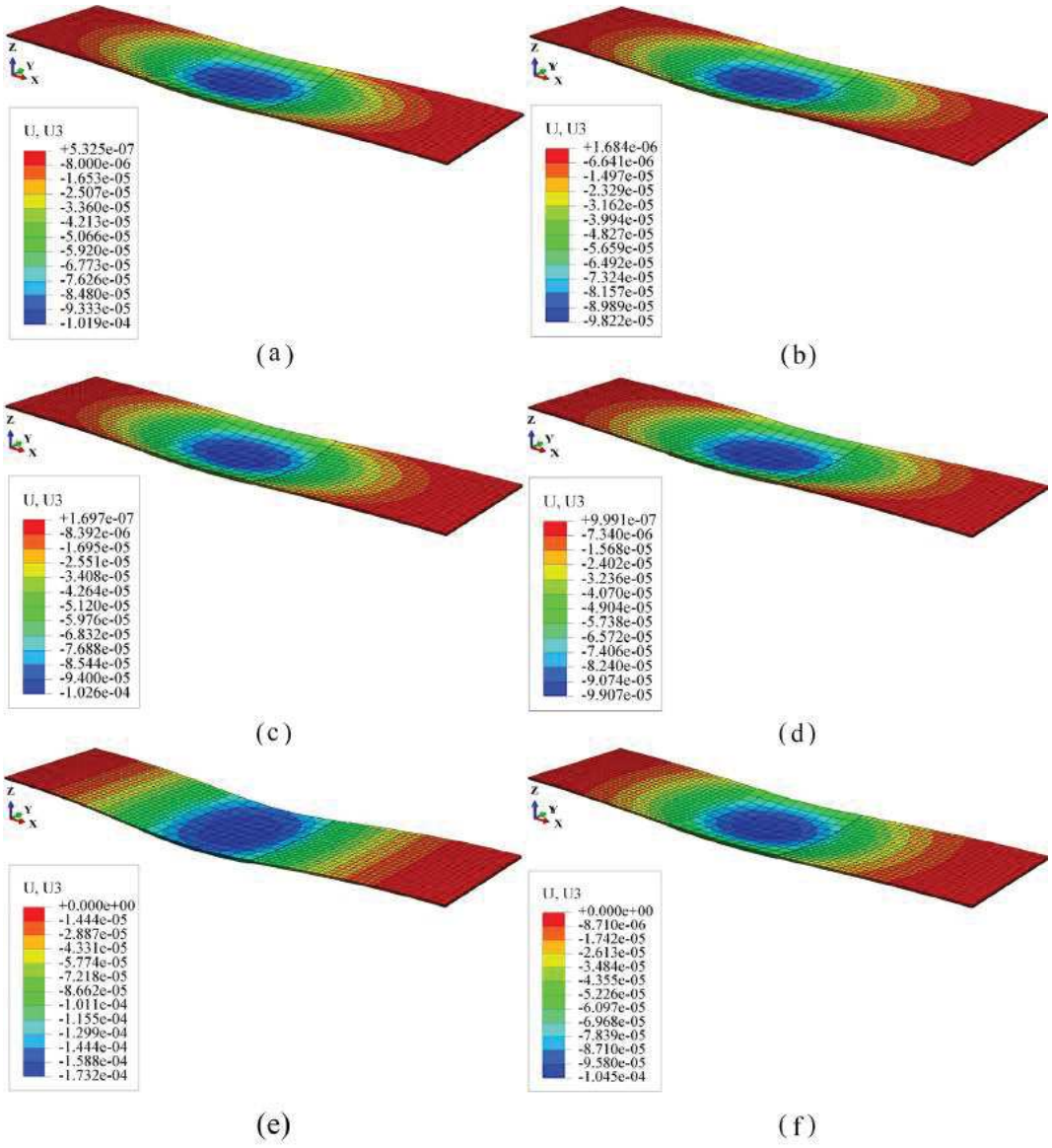


**Fig.14.** Numerical simulation results of $w(x,y)$ in the laminated simply-supported composite plate induced by a pair of bounded MFC-$d_{13}$ patches with various stacking sequences.

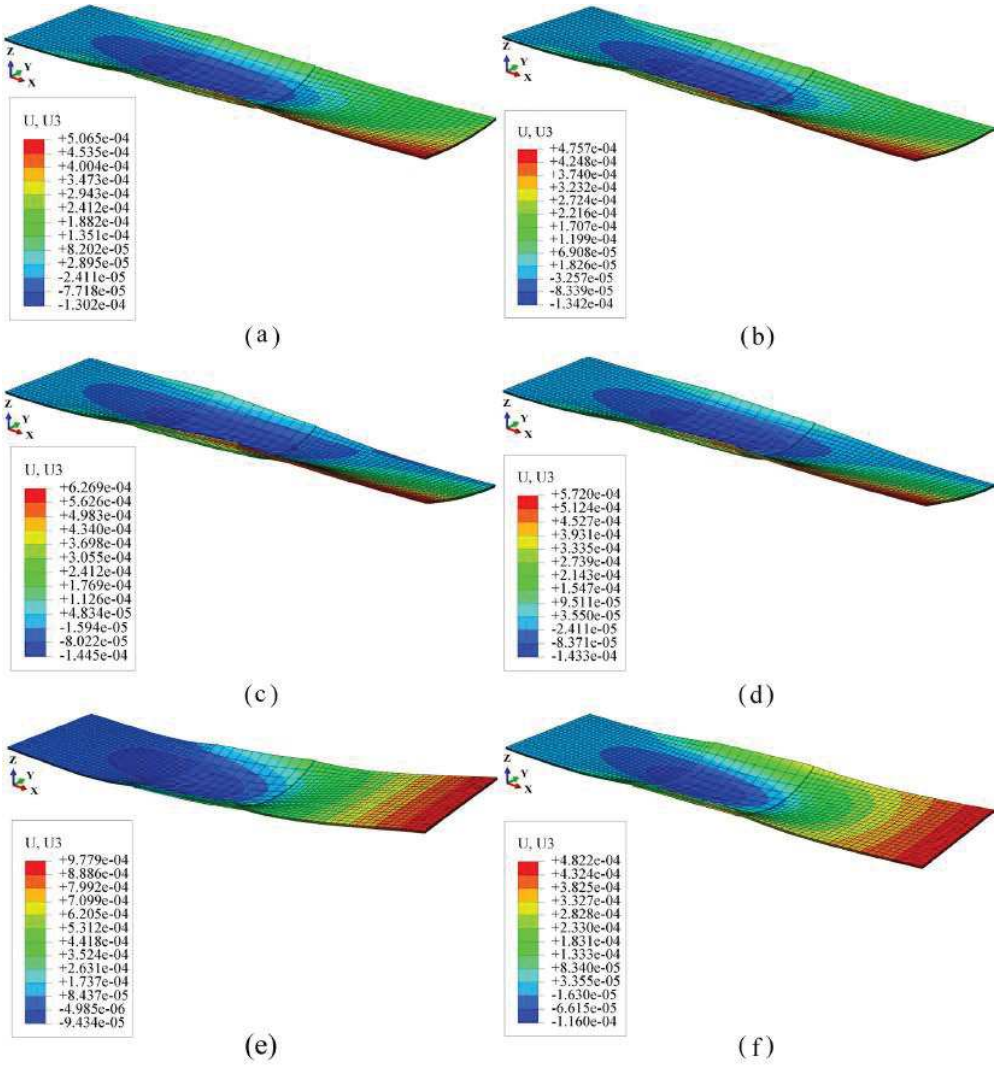


**Fig.15.** Numerical simulation results of $w(x,y)$ in the laminated cantilevered composite plate induced by a pair of bounded MFC-$d_{33}$ patches with various stacking sequences.

- The comparison of the results between the developed 2D FE formulation and ABAQUS results in some specific regions shows good agreement in terms of displacement values and deformation trend which demonstrates the reliability and cost-effectiveness of the model proposed in this paper for smart laminated piezo composite plates under various boundary conditions.

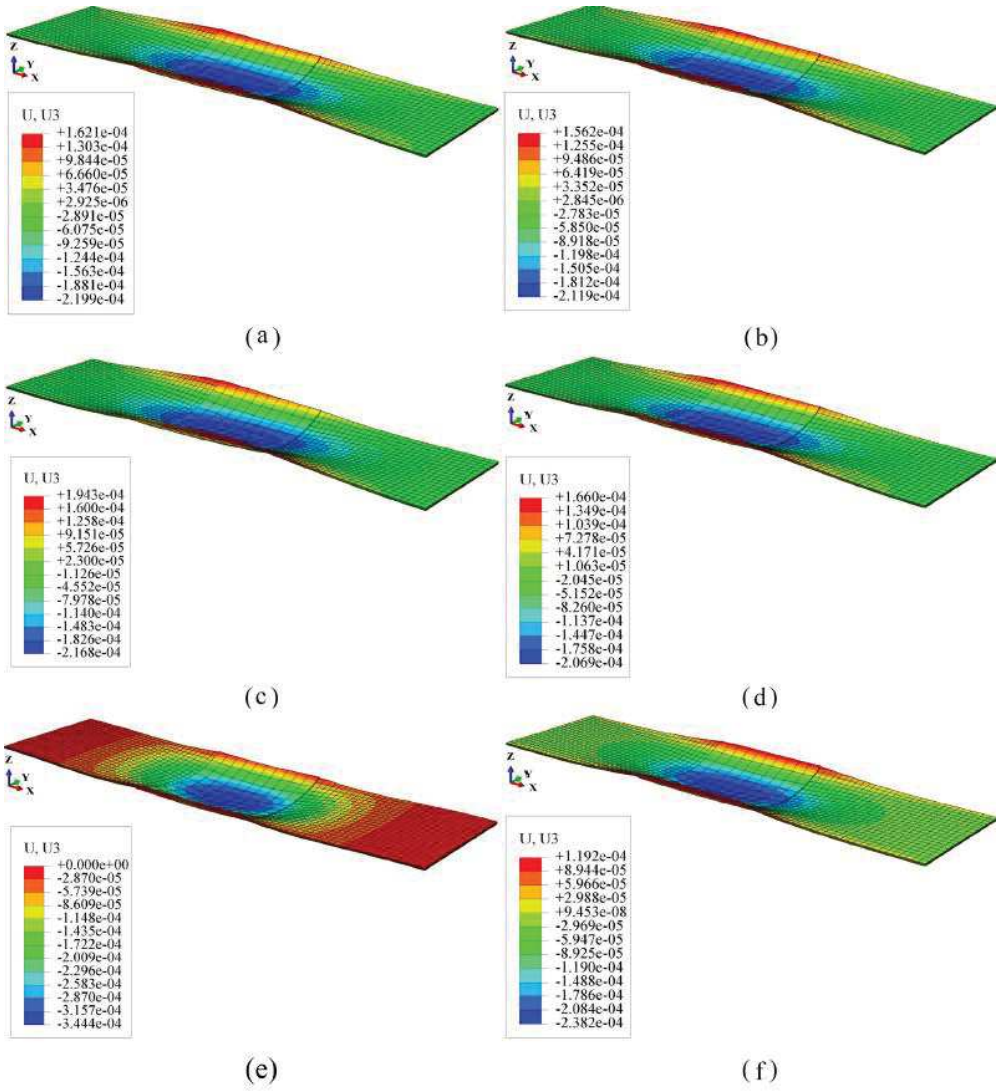


**Fig.16.** Numerical simulation results of $w(x,y)$ in the laminated simply-supported composite plate induced by a pair of bounded MFC-$d_{33}$ patches with various stacking sequences.

- MFC actuators can induce mechanical deformation in laminated composite structures through applying electrical voltage to them. The intensity of the shape deformation varies considerably by changing the piezoelectric fibres angle, stacking sequence configuration in the host structure, layup asymmetry, applied electrical voltage intensity, and MFC actuator type.

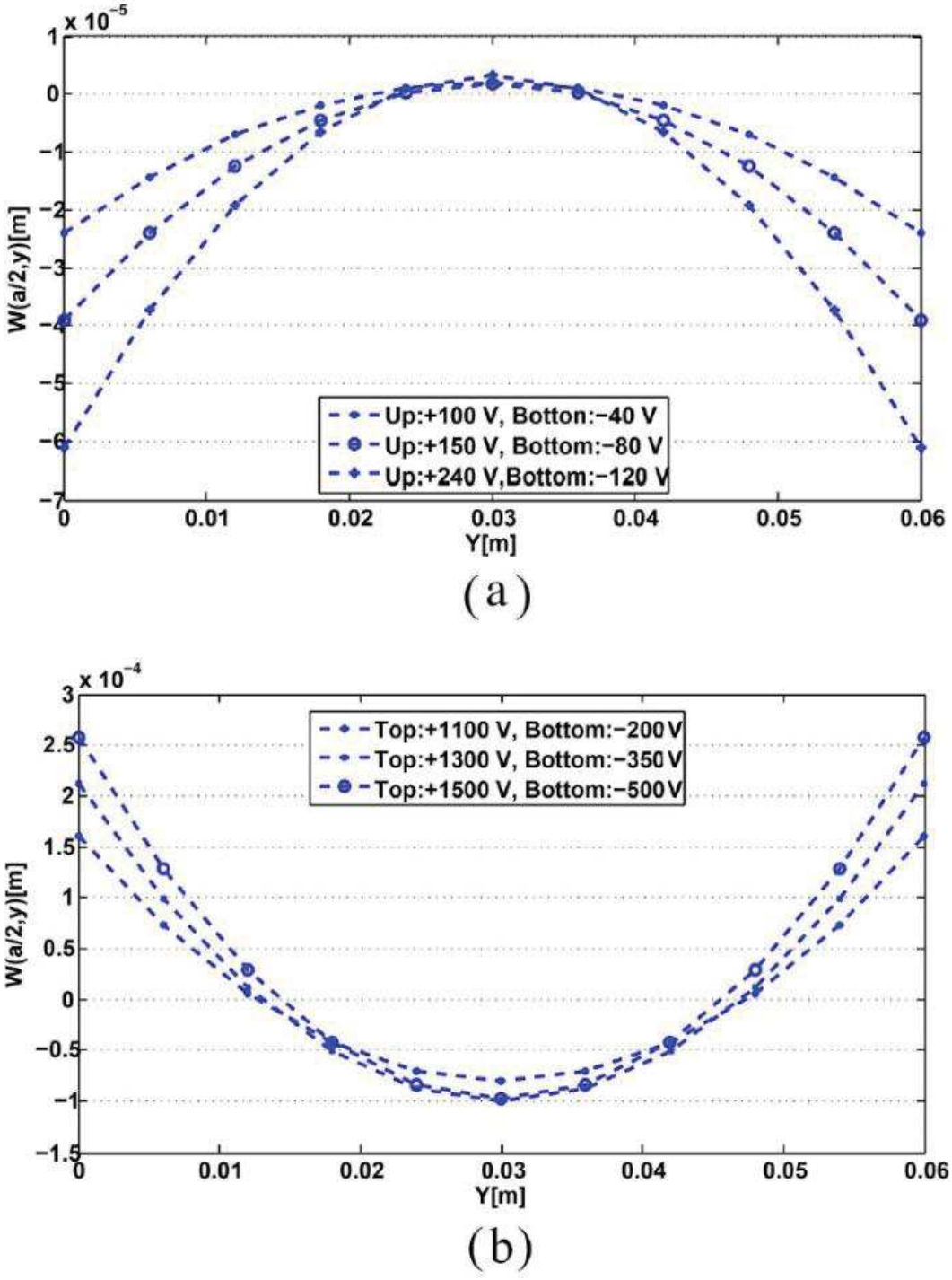


**Fig.17.** Quadratic 2D FE results of $w(x,0)$ in the laminated cantilevered composite plate induced by a pair of bounded MFC patches for various electrical voltage: a) MFC-$d_{31}$, b) MFC-$d_{33}$.

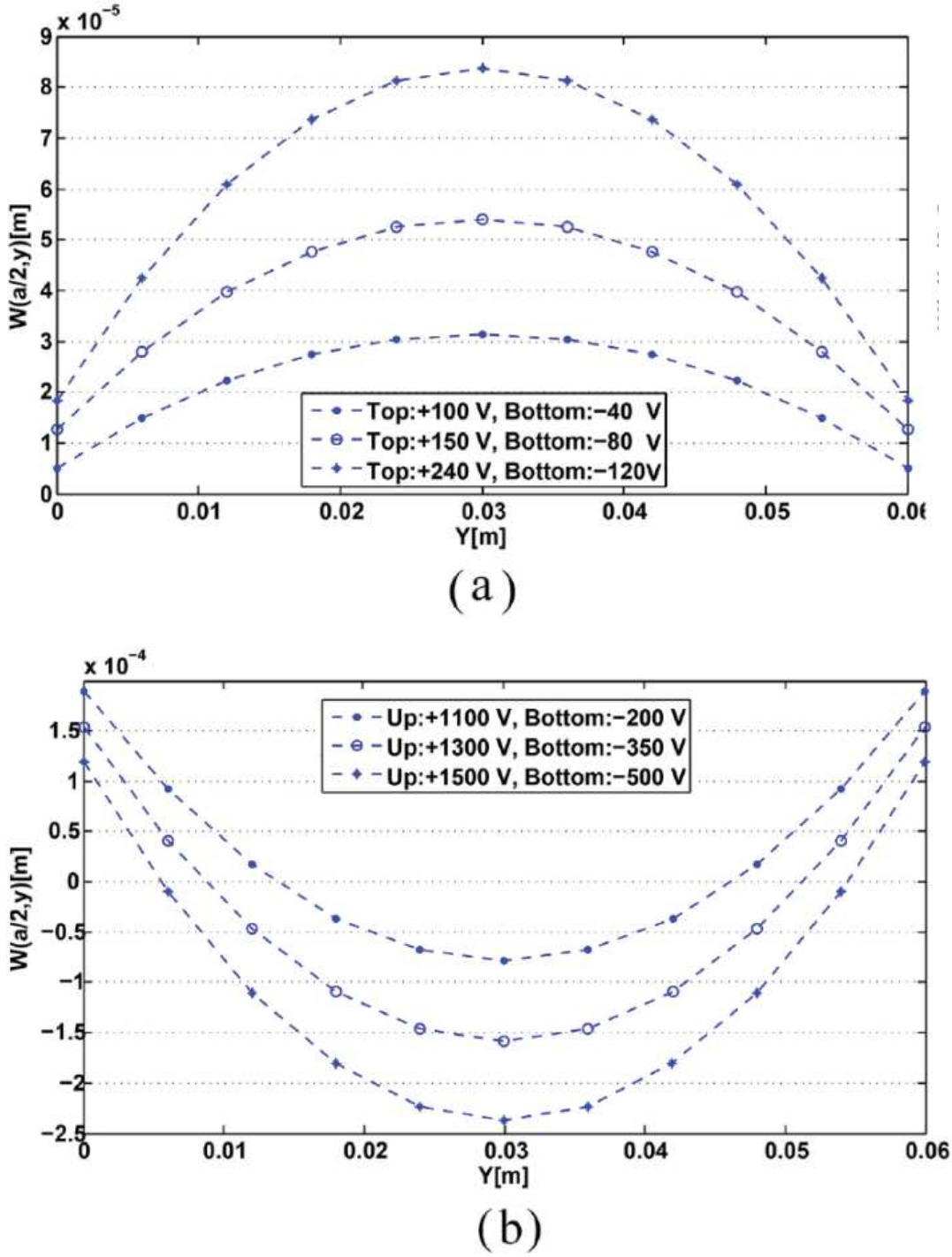


**Fig.18.** Quadratic 2D FE results of $w(x,0)$ in the laminated simply-supported composite plate induced by a pair of bounded MFC patches for various electrical voltage: a) MFC-$d_{31}$, b) MFC-$d_{33}$.

- Strain-displacement deformation induced by MFCs is affected by MFC actuator type due to changes in the elements of piezoelectric dielectric coefficient matrix ($d_{ij}$). Topically, MFC-$d_{33}$ produces higher actuation power than MFC-$d_{31}$ due to having much larger dielectric constants.

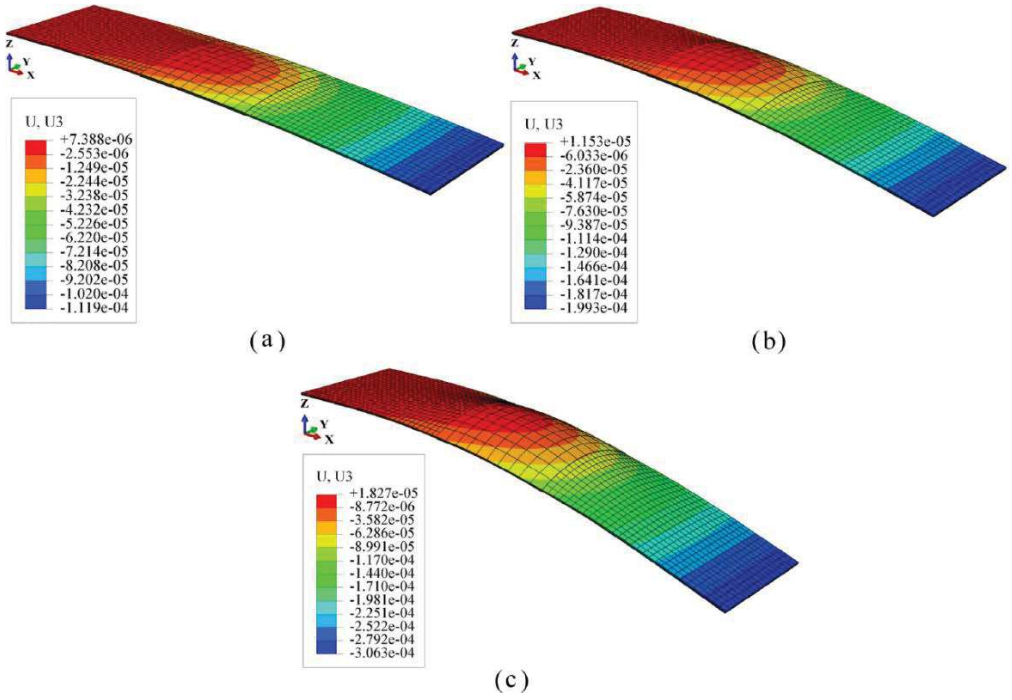


**Fig.19.** Numerical simulation results of $w(x,y)$ in the laminated cantilevered composite plate induced by a pair of bounded MFC-$d_{31}$ patches for various electrical voltage.

**Acknowledgements:**

The first author would like to thank the College of Engineering and Science at Victoria University, Melbourne for offering the Victoria University International Postgraduate Research scholarship (VUIPRS) to undertake his Ph.D. study. This financial support is gratefully acknowledged.

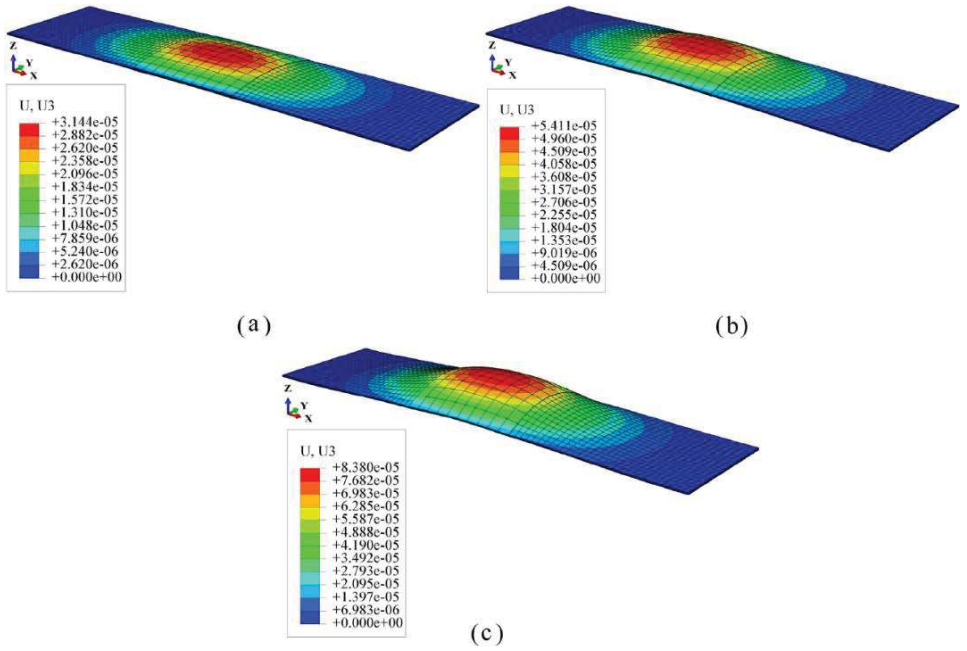


**Fig.20.** Numerical simulation results of $w(x,y)$ in the laminated simply-supported composite plate induced by a pair of bounded MFC-$d_{13}$ patches for various electrical voltage.

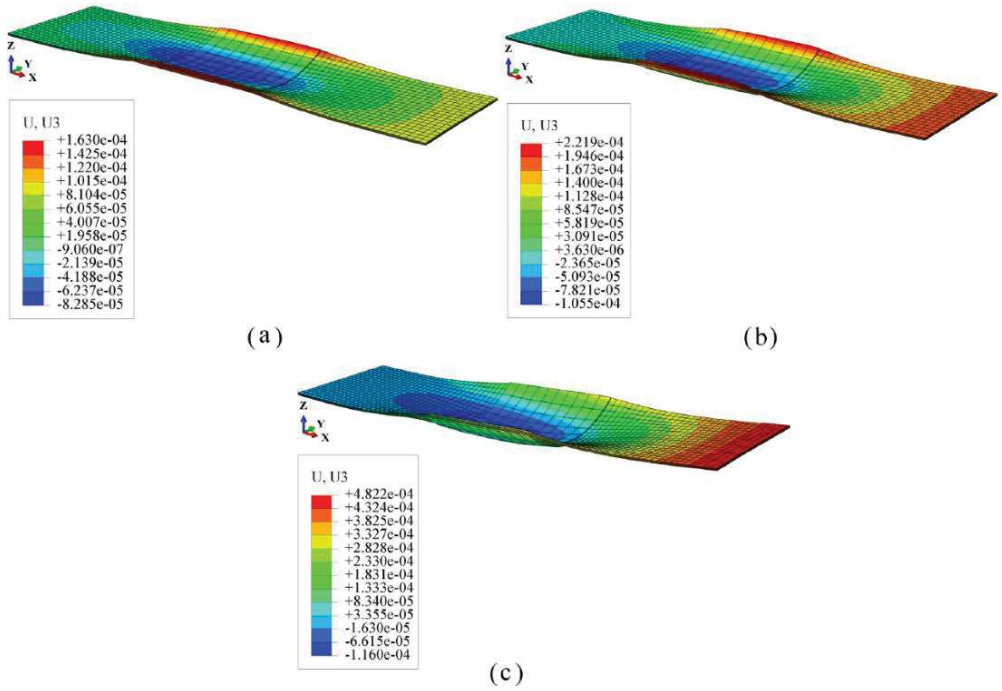


**Fig.21.** Numerical simulation results of w(x,y) in the laminated cantilevered composite plate induced by a pair of bounded MFC-$d_{33}$ patches for various electrical voltage.

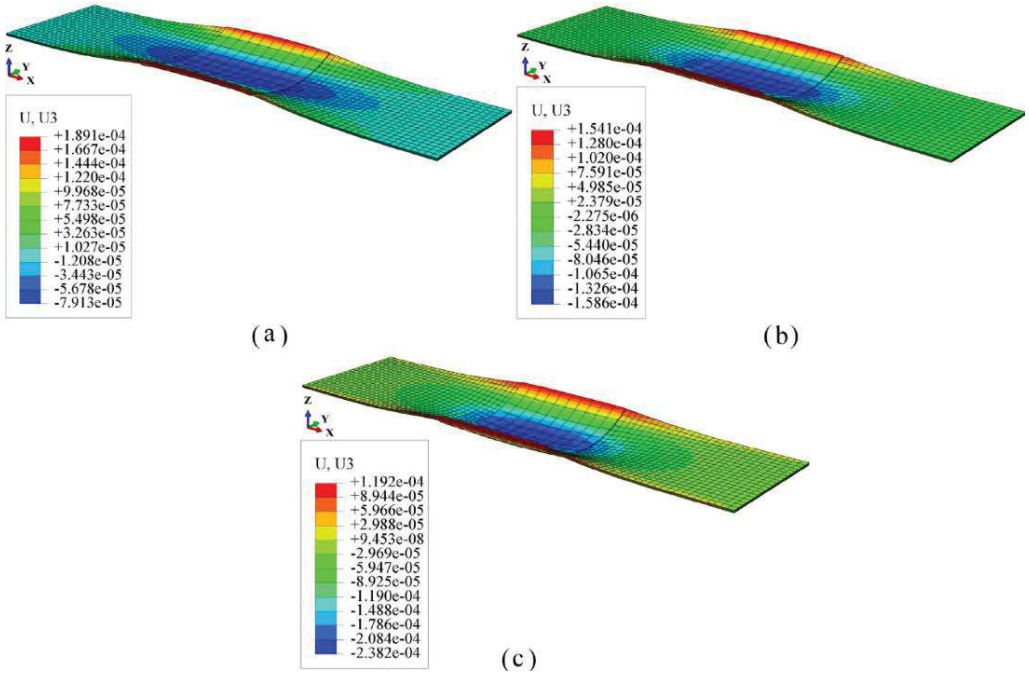


**Fig.22.** Numerical simulation results of $w(x,y)$ in the laminated simply-supported composite plate induced by a pair of bounded MFC-$d_{33}$ patches for various electrical voltage.

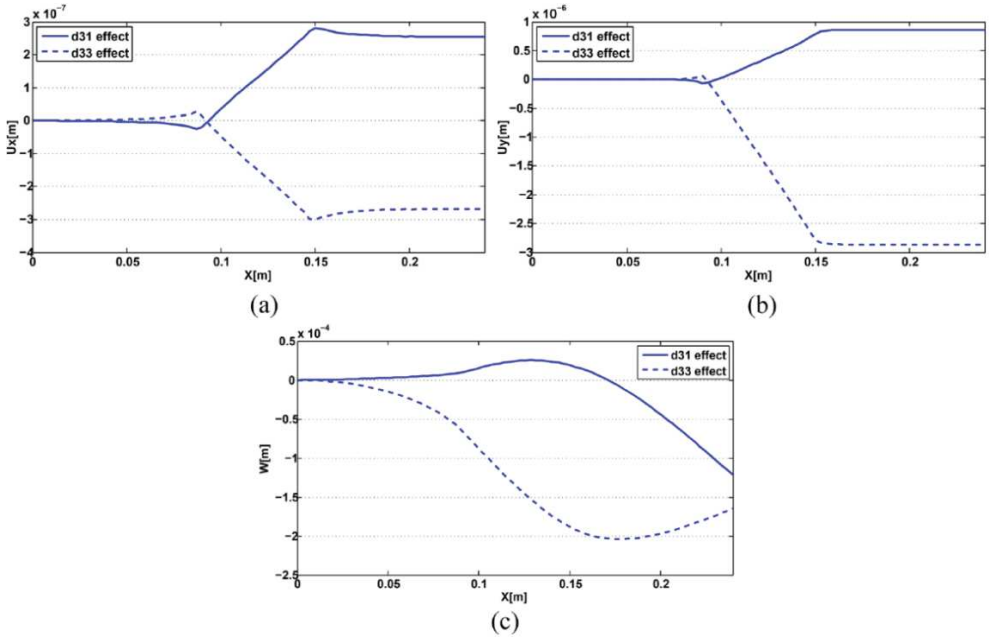


**Fig.23.** Quadratic 2D FE results of $w(x,0)$ in the laminated cantilevered composite plate induced by a pair of bounded MFC-$d_{13}$ and MFC-$d_{33}$ patches: a) $U_x$, b) $U_y$, and c) $w$.

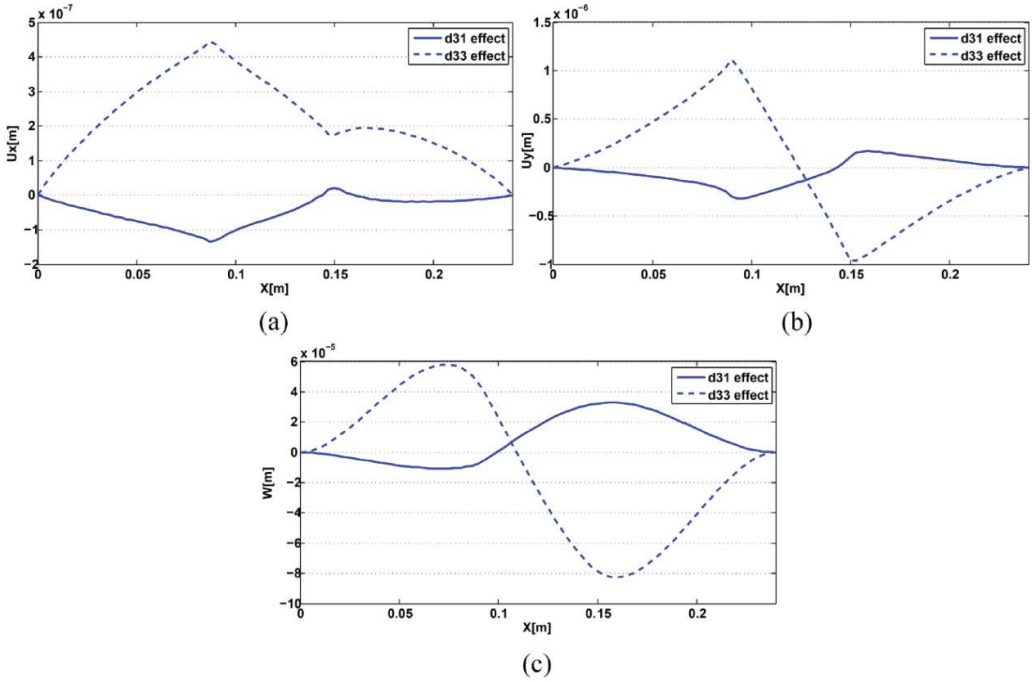


**Fig.24.** Quadratic 2D FE results of $w(x,0)$ in the laminated simply-supported composite plate induced by a pair of bounded MFC-$d_{13}$ and MFC-$d_{33}$ patches: a) $U_x$, b) $U_y$, and c) $w$.

**References:**

[1] G. Sharifishourabi, A. Ayob, S. Gohery, M. Y. B. Yahya, S. Sharifi, and Z. Vrcelj, "Flexural behavior of functionally graded slender beams with complex cross-section," *J. Mech. Mater. Struct.*, vol. 10, pp. 1–16, 2015.

[2] A. Rajaneesh, W. Satrio, G. B. Chai, and I. Sridhar, "Long-term life prediction of woven CFRP laminates under three point flexural fatigue," *Compos. Part B Eng.*, vol. 91, pp. 539–547, 2016.

[3] J. Ajitsaria, S. Y. Choe, D. Shen, and D. J. Kim, "Modeling and analysis of a

bimorph piezoelectric cantilever beam for voltage generation," *Smart Mater. Struct.*, vol. 16, pp. 447–453, 2007.

[4] J. Kim, V. V. Varadan, V. K. Varadan, and X. Q. Bao, "Finite-element modeling of a smart cantilever plate and comparison with experiments," *Smart Mater. Struct.*, vol. 5, pp. 165–170, 1996.

[5] Z. Shi and T. Zhang, "Static analyses for 2-2 multi-layered piezoelectric curved composites," *Int. J. Eng. Sci.*, vol. 45, pp. 509–524, 2007.

[6] M. S. I. Shaik Dawood, L. Iannucci, and E. S. Greenhalgh, "Three-dimensional static shape control analysis of composite plates using distributed piezoelectric actuators," *Smart Mater. Struct.*, vol. 17, pp. 1–10, 2008.

[7] M. Adnan Elshafei, A. Farid, and A. A. Omer, "Modeling of torsion actuation of beams using inclined piezoelectric actuators," *Arch. Appl. Mech.*, vol. 85, pp. 171–189, 2014.

[8] M. Akbar and J. L. Curiel-Sosa, "Piezoelectric energy harvester composite under dynamic bending with implementation to aircraft wingbox structure," *Compos. Struct.*, vol. 153, pp. 193–203, 2016.

[9] Y. Yu, X. N. Zhang, and S. L. Xie, "Optimal shape control of a beam using piezoelectric actuators with low control voltage," *Smart Mater. Struct.*, vol. 18,

pp. 1–15, 2009.

[10] M. L. Dano, M. Jean-St-Laurent, and A. Fecteau, “Morphing of bistable composite laminates using distributed piezoelectric actuators,” *Smart Mater. Res.*, vol. 2012, pp. 1–8, 2012.

[11] J.-S. Park and J.-H. Kim, “Analytical development of single crystal macro fiber composite actuators for active twist rotor blades,” *Smart Mater. Struct.*, vol. 14, p. 745, 2005.

[12] S. Murugan and M. I. Friswell, “Morphing wing flexible skins with curvilinear fiber composites,” *Compos. Struct.*, vol. 99, pp. 69–75, 2013.

[13] A. A. Bent and N. W. Hagood, “Piezoelectric fiber composites with interdigitated electrodes,” *J. Intell. Mater. Syst. Struct.*, vol. 8, pp. 903–919, 1997.

[14] J. S. Park and J. H. Kim, “Coefficients of thermal expansion for single crystal piezoelectric fiber composites,” *Compos. Part B Eng.*, vol. 38, pp. 795–799, 2007.

[15] J. S. Park and J. H. Kim, “Design and aeroelastic analysis of active twist rotor blades incorporating single crystal macro fiber composite actuators,” *Compos. Part B Eng.*, vol. 39, pp. 1011–1025, 2008.

[16] A. Pandey and A. Arockiarajan, “Actuation performance of macro-fiber

composite ( MFC ): modeling and experimental studies," *Sensors Actuators A Phys.*, vol. 248, pp. 114–129, 2016.

[17] F. Biscani, H. Nasser, S. Belouettar, and E. Carrera, "Equivalent electro-elastic properties of Macro Fiber Composite (MFC) transducers using asymptotic expansion approach," *Compos. Part B Eng.*, vol. 42, pp. 444–455, 2011.

[18] S. Raja and T. Ikeda, "Concept and electro-elastic modeling of shear actuated fiber composite using micro-mechanics approach," *J. Intell. Mater. Syst. Struct.*, vol. 19, pp. 1173–1183, 2007.

[19] S. Sreenivasa Prasath and A. Arockiarajan, "Experimental and theoretical investigation on the thermo-electro-elastic properties of macro-fiber composites (MFC)," *Compos. Struct.*, vol. 122, pp. 8–22, 2015.

[20] M. R. Schultz, M. W. Hyer, R. Brett Williams, W. Keats Wilkie, and D. J. Inman, "Snap-through of unsymmetric laminates using piezocomposite actuators," *Compos. Sci. Technol.*, vol. 66, pp. 2442–2448, 2006.

[21] P. F. Giddings, H. A. Kim, A. I. T. Salo, and C. R. Bowen, "Modelling of piezoelectrically actuated bistable composites," *Mater. Lett.*, vol. 65, pp. 1261–1263, 2011.

[22] M.-L. Dano, M. Gakwaya, and B. Julliere, "Compensation of thermally induced

distortion in composite structures using macro-fiber composites," *J. Intell. Mater. Syst. Struct.*, vol. 19, pp. 225–233, 2007.

[23] J. W. Sohn, S. B. Choi, and H. S. Kim, "Vibration control of smart hull structure with optimally placed piezoelectric composite actuators," *Int. J. Mech. Sci.*, vol. 53, pp. 647–659, 2011.

[24] S. Gohery, A. Golshan, and A. Ayob, "Theoretical analysis and finite element simulation of behavior of laminated hemispherical GRP dome subjected to internal pressure," *Int. Conf. Comput. Softw. Model.*, vol. 14, pp. 122–129, 2011.

[25] S. Gohery, A. Golshan, A. B. Nia, and M. Hashemzadeh, "Prediction of failure in thin-walled hemispherical GRP dome subjected to static internal pressure based on a failure factor," *Adv. Mater. Res.*, vol. 488–489, pp. 358–366, 2012.

[26] S. Gohery, a. Golshan, M. Mostakhdemin, F. Mozafari, and a. Momenzadeh, "Failure strength of thin-walled cylindrical GFRP composite shell against static internal and external pressure for various volumetric fiber fraction," *Int. J. Appl. Phys. Math.*, vol. 2, pp. 111–116, 2012.

[27] S. Gohery, A. Golshan, F. Firouzabadi, and N. Hosseininezhad, "Effect of volumetric fiber fraction on failure strength of thin-walled GFRP composite cylindrical shell externally pressurized," *Adv. Mater. Res.*, vol. 488–489, pp. 530–536, 2012.

[28] S. Gohery, A. Golshan, M. Hashemzadeh, and N. Hosseininezhad, "First-ply strength of thick circular cylindrical GRP composite shell subjected to static external pressure via finite element simulation and analytical approaches," *Adv. Mater. Res.*, vol. 463–464, pp. 477–483, 2012.

[29] F. Firouzabadi, A. Ayob, M. R. Arjmandi, S. Gohery, and N. Deirram, "Modeling of the impact on cylindrical composite shell as continuous patch loading," *Int. J. Mech. Mech. Eng.*, vol. 12, pp. 8–13, 2012.

[30] S. Sharifi, T. A. D. M. S. Almula, S. Gohery, G. Sharifishourabi, Y. Saed, and M. Y. Bin Yahya, "Impact response of laminated composite cylindrical shell: finite element simulation approach," *Appl. Mech. Mater.*, vol. 393, pp. 387–392, 2013.

[31] M. Elhadrouz, T. Ben Zineb, and E. Patoor, "Finite element analysis of a multilayer piezoelectric actuator taking into account the ferroelectric and ferroelastic behaviors," *Int. J. Eng. Sci.*, vol. 44, pp. 996–1006, 2006.

[32] S. C. Her and C. S. Lin, "Deflection of cross-ply composite laminates induced by piezoelectric actuators," *Sensors*, vol. 10, pp. 719–733, 2010.

[33] S.-C. Her and C.-S. Lin, "Vibration analysis of composite laminate plate excited by piezoelectric actuators.," *Sensors*, vol. 13, pp. 2997–3013, 2013.

[34] L. Ren, "A theoretical study on shape control of arbitrary lay-up laminates using

piezoelectric actuators," *Compos. Struct.*, vol. 83, pp. 110–118, 2008.

[35] S. Q. Zhang, Y. X. Li, and R. Schmidt, "Modeling and simulation of macro-fiber composite layered smart structures," *Compos. Struct.*, vol. 126, pp. 89–100, 2015.

[36] S. Q. Zhang, Z. X. Wang, X. S. Qin, G. Z. Zhao, and R. Schmidt, "Geometrically nonlinear analysis of composite laminated structures with multiple macro-fiber composite (MFC) actuators," *Compos. Struct.*, vol. 150, pp. 62–72, 2016.

[37] S. Q. Zhang, Y. X. Li, and R. Schmidt, "Modeling and simulation of macro-fiber composite layered smart structures," *Compos. Struct.*, vol. 126, pp. 89–100, 2015.

[38] A. S. Sayyad and Y. M. Ghugal, "On the free vibration analysis of laminated composite and sandwich plates : A review of recent literature with some numerical results," *Compos. Struct.*, vol. 129, pp. 177–201, 2015.

[39] M. Endo, "Study on an alternative deformation concept for the Timoshenko beam and Mindlin plate models," *Int. J. Eng. Sci.*, vol. 87, pp. 32–46, 2015.

[40] N. Radić and D. Jeremić, "Thermal buckling of double-layered graphene sheets embedded in an elastic medium with various boundary conditions using a nonlocal new first-order shear deformation theory," *Compos. Part B Eng.*, vol.

97, pp. 201–215, 2016.

[41] J. N. Reddy, “On laminated composite plates with integrated sensors and actuators,” *Eng. Struct.*, vol. 21, pp. 568–593, 1999.

[42] N. Kharghani and C. Guedes Soares, “Behaviour of composite laminates with embedded delaminations,” *Compos. Struct.* , vol. 150, pp. 226–239, 2016.

[43] S. Gohery, S. Sharifi, and Z. Vrcelj, “New explicit solution for static shape control of smart laminated cantilever piezo-composite-hybrid plates/beams under thermo-electro-mechanical loads using piezoelectric actuators,” *Compos. Struct.*, vol. 145, pp. 89–112, 2016.

[44] D. Shao, F. Hu, Q. Wang, F. Pang, and S. Hu, “Transient response analysis of cross-ply composite laminated rectangular plates with general boundary restraints by the method of reverberation ray matrix,” *Compos. Struct.*, vol. 152, pp. 168–182, 2016.

[45] Y. S. Li and E. Pan, “Static bending and free vibration of a functionally graded piezoelectric microplate based on the modified couple-stress theory,” *Int. J. Eng. Sci.*, vol. 97, pp. 40–59, 2015.

[46] J. Zhu, J. Wang, and L. Zu, “Influence of out-of-plane ply waviness on elastic properties of composite laminates under uniaxial loading,” *Compos. Struct.*, vol.

132, pp. 440–450, 2015.

[47] S. Gohery, S. Sharifi, and Z. Vrcelj, "A novel explicit solution for twisting control of smart laminated cantilever composite plates/beams using inclined piezoelectric actuators," *Compos. Struct.*, vol. 161, pp. 477–504, 2016.

## 5.4. CONCLUDING REMARKS

In this chapter, a novel numerical method was proposed to obtain the static linear strain-displacements in laminated composite structures induced by MFC actuators. The numerical analysis was based on quadratic FE modelling in which an eight-node quadratic shell element with five degrees of freedom was introduced. To increase the accuracy of the results, particularly for slightly thicker laminates, the effect of transverse shear deformation was taken into consideration. Therefore, the FOSDT adapted from the Reissner-Mindlin plate theory was applied to the quadratic 2D FE formulation. Two types of MFC actuators are investigated: 1) MFC-$d_{31}$ and 2) MFC-$d_{33}$, which differ in their actuation forces.

Subsequently, to verify the results, a series of simple, accurate, and robust 3D FE model analyses were employed using ABAQUS. Variety of mechanical and electrical factors affecting the electro-mechanically couple FE modelling was accounted for and design recommendations were then proposed. According to the finding in this chapter, the following conclusions are presented:

- Comparison of the quadratic 2D FE formulation proposed in this study with the ABAQUS results demonstrated the reliability and accuracy of the proposed quadratic FE modelling. Therefore, the use of commercial FE software packages, which are expensive and require extensive training, could be eliminated.

- MFC actuators can induce mechanical deformation in laminated composite structures through applying electrical voltage to them. The intensity of the shape deformation varies considerably by changing the piezoelectric fibres angle, stacking sequence configuration in the host structure, layup asymmetry, applied electrical voltage intensity, and MFC actuator type.

- Strain-displacement deformation induced by MFC actuators is significantly affected by MFC actuator type due to changes in the elements of piezoelectric dielectric coefficient matrix ($d_{ij}$). Topically, MFC-$d_{33}$ produces higher actuation power than MFC-$d_{31}$ due to having much larger dielectric constants.

# Chapter 6

# CONCLUSIONS

## 6.1 SUMMARY

In the presented research study, mechanical failure and shape control of smart laminated composite hybrid structures integrated with piezoelectric sensors and actuators were investigated comprehensively by developing novel analytical and numerical methods. Piezoelectric sensors were used to assess the critical mechanical deformation and possible failure in host structures (direct piezoelectric effect) while piezoelectric actuators were used to induce/control host structures shape (indirect piezoelectric effect). The piezoelectric sensors used in this study were made of PZT, which can act as strain gauge sensors for obtaining mechanical strains occurring in host structures. The piezoelectric actuators were made of variety of materials such as PVD, KENYAR, PZT G1195, MFC-$d_{31}$, and MFC-$d_{33}$.

To analyse the effectiveness of PZT sensors, mechanical shape deformation and possible failure of the internally pressurized laminated woven GFRP composite shells integrated with the surface-bounded PZT strain gauge sensors was investigated. Various types of shells such as hemispherical, ellipsoidal, and torispherical were investigated. The exact analytical solution and 3D non-linear FE simulation were utilised to obtain the critical mechanical and failure strain/displacements. In the analytical study, the linear interpolation technique was adopted to interpolate the critical points conveniently. The shell boundary was fixed at its end. Tsai-Wu failure criterion was used as the composite failure design factor. The analytical and numerical results, including critical internal pressure and strains in the global directions, were validated with the experimental results for some arbitrarily selected points on the shells surface along meridian axis. Manufacturing of laminated ellipsoidal composite shells for the experimental programme undertaken in this study was performed by using the Vacuum Infusion Process (VIP), a method commonly adopted for the fabrication of laminated composite shells. The surface-bounded sensors were installed on the shells' surface to measure the strain values after the internal pressure is applied. Subsequently, the effect of various parameters including thickness, aspect ratio, and stacking sequence on shape deformation and failure of the laminated woven GFRP composite shells were investigated and the critical mechanical factors to avoid failure were determined.

Subsequently, two novel explicit analytical methods were proposed for obtaining static bending, twisting deformation, and optimal shape control of laminated cantilever piezo composite hybrid plates and beams using the non-angled and inclined piezoelectric actuators. The linear piezoelectricity and plates theories were adapted during the

analysis. A double integral multivariable Fourier transformation method combined with discretised higher order partial differential unit step function equations were employed. The effect of various parameters including arbitrary loads such as non-uniform thermal stresses, electrical and mechanical loads, layup thickness, piezoelectric actuators size and placement, stacking sequence, and geometrical dimension were considered. The results were then compared with some published benchmark results and a series of simple, accurate and robust 3D nonlinear analysis models using ABAQUS.

A quadratic 2D FE formulation using FOSDT was also developed to predict the linear strain-displacement static deformation in the laminated piezo composite plates induced by MFC actuators. FOSDT was adapted from the Reissner-Mindlin plate theory. The laminated piezo composite plates were either cantilevered or simply-supported. An eight-node quadratic shell element with five degrees of freedom was introduced for the FE formulation. Two types of MFC actuators were exploited: 1) MFC-d31 and 2) MFC-d33 which differ in their actuation forces. The electro-mechanically coupled quadratic FE model was compared with the numerical simulation results derived by using ABAQUS. Furthermore, due to the lack of comprehensive and in-depth research on MFC materials, the effect of various parameters such as boundary conditions, laminate stacking sequence configuration, unsymmetrical layup, electrical voltage intensity, MFC type, and piezoelectric fibre orientation on shape deformation of laminated composite structures induced by MFC actuators was investigated.

## 6.2 NOVEL CONTRIBUTIONS

This thesis has made significant contributions to the area of smart composite materials and structures integrated with piezoelectric sensors and actuators. Research achievements are summarized as follows:

1. Developed an analytical solution to assess critical mechanical deformation and possible failure in smart laminated composite structures using PZT sensors.

2. Developed an experimental setup to assess the effectiveness of PZT sensors for structural monitoring and failure prediction of laminated composite structures.

3. Compared the analytical and experimental results together concerning possible mechanical failure assessment and proposed the design recommendations.

4. Developed an exact analytical solution for bending-twisting shape control of smart laminated composite hybrid structures induced by piezoelectric actuators.

5. Considered the effect of thermal stresses on the shape control performance of piezoelectric actuators by using an exact analytical solution.

6. Compared the exact analytical and ABAQUS results together regarding the structural shape control of smart laminated composite hybrid structures and proposed the design recommendations.

7. Developed a simple and accurate quadratic 2D FE solution for bending-twisting shape control of smart laminated composite structures induced by MFC actuators.

8. Developed a series of 3D nonlinear FE model analysis using ABAQUS and proposed the step-by-step guidelines for the numerical simulation of smart composite hybrid structures induced by piezoelectric actuators.

9. Compared the quadratic 2D FE formulation and ABAQUS results together concerning shape control of smart laminated composite structures and proposed the design recommendations.

## 6.3 FURTHER RESEARCH

The analytical and numerical models developed as part of this research project were shown to accurately predict the critical mechanical deformation and shape control of smart composite hybrid laminates using piezoelectric sensors and actuators under static conditions. The recommendations for further research are summarized as follows:

1. Piezoelectric sensors and actuators proved to have low power to be used in shape control tasks, as limited electrical voltage can be applied to them. Even when applying electrical voltage close to their maximum, there is a risk of piezoelectric actuators being destroyed. Thus, other smart materials such as shape memory alloys (SMAs) can serve as a suitable replacement to

piezoelectric materials. This class of materials is more suitable for shape control tasks when the magnitude of applied loads to host structures intensifies.

2. The developed analytical and numerical models in this study can be extended to cover smart materials and structures under more complex loading conditions such as dynamic, cycling, and impact loads.

3. The analytical and numerical models, as proposed in this study, are limited to bending-twisting problems. However, these can be easily extended to cover more complex analyses like pre/post buckling and free/force vibration, and problems regarding healing cracks using smart materials with shape recovery characteristics.

## REFERENCES

[1] R. M. Jones, “Mechanics of composite materials,” *Taylor Fr. Group, USA*, 1998.

[2] P. K. Mallick, “Fiber-reinforced composites materials: Manufacturing, and design,” Third edition, *Taylor Fr. Group, USA*, 2007.

[3] R. J. Vinson, “Plate and panel structures of isotropic, composite and piezoelectric materials, including sandwich construction,” *Springer, Netherlands*, 2005.

[4] S. Sharifi, S. Gohery, M. Sharifiteshnizi, and Z. Vrcelj, “Numerical and experimental study on mechanical strength of internally pressurized laminated woven composite shells incorporated with surface-bounded sensors,” *Compos. Part B Eng.*, vol. 94, pp. 224–237, 2016.

[5] F. Tanasa and M. Zanoaga, “Fiber-reinforced polymer composites as structural materials for aeronautics,” *Int. Conf. Sci. Pap. AFASES*, 2013.

[6] J. F. Tressler, S. Alkoy, and R. E. Newnham, “Piezoelectric sensors and sensor materials,” *J. Electroceramics*, vol. 2, pp. 257–272, 1998.

[7] J. Tichy, J. Erhart, E. Kittinger, J. Fousek, and J. Privatska, "Fundamentals of piezoelectric sensorics." *Springer, Netherlands*, 2010.

[8] S. Gohery, S. Sharifi, and Z. Vrcelj, “New explicit solution for static shape control of smart laminated cantilever piezo-composite-hybrid plates/beams under thermo-electro-mechanical loads using piezoelectric actuators,” *Compos. Struct.*, vol. 145, pp. 89–112, 2016.

[9] X. Lin, K. Zhou, X. Zhang, and D. Zhang, “Development, modeling and application of piezoelectric fiber composites,” *Trans. Nonferrous Met. Soc. China*, vol. 23, pp. 98–107, 2013.

[10] K. B. Katnam, L. F. M. Da Silva, and T. M. Young, “Bonded repair of composite aircraft structures: A review of scientific challenges and opportunities,” *Progress in Aerospace Sciences*, vol. 61. pp. 26–42, 2013.

[11] J. Cheng, B. Wang, and S. Y. Du, “A theoretical analysis of piezoelectric/composite anisotropic laminate with larger-amplitude deflection effect, Part I: Fundamental equations,” *Int. J. Solids Struct.*, vol. 42, pp. 6166–6180, 2005.

[12] J. N. Reddy, “On laminated composite plates with integrated sensors and actuators,” *Eng. Struct.*, vol. 21, pp. 568–593, 1999.

[13] D. B. Koconis, L. P. Kollar, and G. S. Springer, “Shape control of composite plates and shells with embedded actuators .1. voltages specified,” *J. Compos. Mater.*, vol. 28, pp. 415–458, 1994.

[14] A. Milazzo, “Refined equivalent single layer formulations and finite elements for smart laminates free vibrations,” *Compos. Part B Eng.*, vol. 61, pp. 238–253, 2014.

[15] N. Mallik and M. C. Ray, “Exact solutions for the analysis of piezoelectric fiber reinforced composites as distributed actuators for smart composite plates,” *Int. J. Mech. Mater. Des.*, vol. 1, pp. 347–364, 2004.

[16] A. C. Cook and S. S. Vel, “Multiscale analysis of laminated plates with integrated piezoelectric fiber composite actuators,” *Compos. Struct.*, vol. 94, pp. 322–336, 2012.

[17] R. B. Williams, D. J. Inman, and W. K. Wilkie, “Temperature-dependent thermoelastic properties for macro fiber composite actuators,” *J. Therm. Stress.*, vol. 27, pp. 903–915, 2004.

[18] “ABAQUS User’s Manual, ABAQUS Version 6.13, 2013” .

[19] S. Gohery, S. Sharifi, Z. Vrcelj, and M. Y. Yahya, “First-ply failure prediction of an unsymmetrical laminated ellipsoidal woven GFRP composite shell with incorporated surface-bounded sensors and internally pressurized,” *Compos. Part B Eng.*, vol. 77, pp. 502–518, 2015.

[20] A. Pandey and A. Arockiarajan, “Actuation performance of macro-fiber

composite (MFC): Modeling and experimental studies," *Sensors Actuators A Phys.*, vol. 248, pp. 114–129, 2016.

[21] Y. Zhang, N. Anderson, S. Bland, S. Nutt, G. Jursich, and S. Joshi, "All-printed strain sensors: Building blocks of the aircraft structural health monitoring system," *Sensors Actuators A Phys.*, vol. 253, pp. 165–172, 2017.

[22] Q. Nguyen, L. Tong, and Y. Gu, "Evolutionary piezoelectric actuators design optimisation for static shape control of smart plates," *Comput. Methods Appl. Mech. Eng.*, vol. 197, pp. 47–60, 2007.

[23] M. Kerboua, A. Megnounif, M. Benguediab, K. H. Benrahou, and F. Kaoulala, "Vibration control beam using piezoelectric-based smart materials," *Compos. Struct.*, vol. 123, pp. 430–442, 2015.

[24] S. Gohery, S. Sharifi, G. Sharifishourabi, Z. Vrcelj, and R. Abadi, "Effect of temperature on crack initiation in gas formed structures," *J. Mech. Sci. Technol.*, vol. 27, pp. 3745–3754, 2013.

[25] M. Martinez, R. Kernaghan, and A. Artemev, "Finite element analysis of broken fiber effects on hollow active fiber composites," *J. Intell. Mater. Syst. Struct.*, vol. 21, pp. 107–113, 2010.

[26] J. F. Nye, "Physical Properties of Crystals." *Oxford university press*, 1985.

[27] H. S. Kim, J. W. Sohn, and S.-B. Choi, “Vibration control of a cylindrical shell structure using macro fiber composite actuators,” *Mech. Based Des. Struct. Mach.*, vol. 39, pp. 491–506, Oct. 2011.

[28] S. Raja, T. Ikeda, and D. Dwarakanathan, “Deflection and vibration control of laminated plates using extension and shear actuated fiber composites,” *Smart Mater. Res.*, vol. 2011, pp. 1–15, 2011.

[29] J. W. Sohn, S.-B. Choi, and H. S. Kim, “Vibration control of smart hull structure with optimally placed piezoelectric composite actuators,” *Int. J. Mech. Sci.*, vol. 53, pp. 647–659, 2011.

[30] Y. Chen, W. Viresh, and D. Zimcik, “Development and verification of real-time controllers for the F/A-18 vertical fin buffet load alleviation,” *Proc. SPIE, Smart Struct. Mater. 2006 Smart Struct. Integr. Syst.*, vol. 6173, p. 1−12, 2006.

[31] P. A. Tarazaga, D. J. Inman, and W. K. Wilkie, “Control of a space rigidizable inflatable boom using macro-fiber composite actuators,” *J. Vib. Control*, vol. 13, pp. 935–950, 2007.

[32] H. A. Sodano, D. J. Inman, and G. Park, “Comparison of piezoelectric energy harvesting devices for recharging batteries,” *J. Intell. Mater. Syst. Struct.*, vol. 16, pp. 799–807, 2005.

[33] H. A. Sodano, J. Lloyd, and D. J. Inman, “An experimental comparison between several active composite actuators for power generation,” *Smart Mater. Struct.*, vol. 15, pp. 1211–1216, 2006.

[34] Y. Yang, L. Tang, and H. Li, “Vibration energy harvesting using macro-fiber composites,” *Smart Mater. Struct.*, vol. 18, pp. 1–8, 2009.

[35] K. Tungpimolrut, N. Hatti, J. Phontip, K. Komoljindakul, K. Pechrach, and P. Manooonpong, “Design of energy harvester circuit for a MFC piezoelectric based on electrical circuit modeling,” *Appl. Ferroelectr. (ISAF/PFM),International Symp. 2011 Int. Symp. Piezoresponse Force Microsc. Nanoscale Phenom. Polar Mater.*, pp. 1–4, 2011.

[36] S. Park, D. J. Inman, and C. B. Yun, “An outlier analysis of MFC-based impedance sensing data for wireless structural health monitoring of railroad tracks,” *Eng. Struct.*, vol. 30, pp. 2792–2799, 2008.

[37] A. K. Jha and J. N. Kudva, “Morphing aircraft concepts, classifications, and challenges,” *Proc. SPIE, Smart Struct. Mater. 2004 Ind. Commer. Appl. Smart Struct. Technol.*, vol. 5388, p. 213−224, 2004.

[38] J. W. Sohn, S. B. Choi, and H. S. Kim, “Vibration control of smart hull structure with optimally placed piezoelectric composite actuators,” *Int. J. Mech. Sci.*, vol. 53, pp. 647–659, 2011.

[39] A. A. Bent and N. W. Hagood, “Piezoelectric fiber composites with interdigitated electrodes,” *J. Intell. Mater. Syst. Struct.*, vol. 8, pp. 903–919, 1997.

[40] J. S. Park and J. H. Kim, “Coefficients of thermal expansion for single crystal piezoelectric fiber composites,” *Compos. Part B Eng.*, vol. 38, pp. 795–799, 2007.

[41] J. S. Park and J. H. Kim, “Design and aeroelastic analysis of active twist rotor blades incorporating single crystal macro fiber composite actuators,” *Compos. Part B Eng.*, vol. 39, pp. 1011–1025, 2008.

[42] D. Upadrashta and Y. Yang, “Experimental investigation of performance reliability of macro fiber composite for piezoelectric energy harvesting applications,” *Sensors Actuators A. Phys.*, vol. 244, pp. 223–232, 2016.

[43] A. A. Bent and N. W. Hagood, “Piezoelectric fiber composites with interdigitated electrodes,” *J. Intell. Mater. Syst. Struct.*, vol. 8, pp. 903–919, 1997.

[44] V. K. Wickramasinghe and N. W. Hagood, “Material characterization of active fiber composites for integral twist-actuated rotor blade application,” *Smart Mater. Struct.*, vol. 13, pp. 1155–1165, 2004.

[45] F. Biscani, H. Nasser, S. Belouettar, and E. Carrera, “Equivalent electro-elastic properties of macro fiber composite (MFC) transducers using asymptotic

expansion approach," *Compos. Part B Eng.*, vol. 42, pp. 444–455, 2011.

[46] W. K. Wilkie *et al.*, "Low-cost piezocomposite actuator for structural control applications," *Proc. SPIE, Smart Struct. Mater. 2000 Ind. Commer. Appl. Smart Struct. Technol.*, vol. 3991, pp. 323−324, 2000.

[47] R. B. Williams, B. W. Grimsley, D. J. Inman, and W. K. Wilkie, "Manufacturing and mechanics-based characterization of macro fiber composite actuators," *Proc. Adapt. Struct. Mater. Syst.*, pp. 79–89, 2002.

[48] C. Rainieri, G. Fabbrocino, and E. Cosenza, "Structural health monitoring systems as a Tool for seismic protection," *14th World Conf. Earthq. Eng. Beijing, China*, 2008.

[49] T. Kleckers, "Electrical Strain Gauges , Piezoelectric sensors or fiber bragg Sensors for Force Measurement : Prospects and Potentials," *AMA Conf. 2013, Sens. 2013, OPTO 2013, IRS 2013*, pp. 23–27, 2013.

[50] H. Gullapalli *et al.*, "Flexible piezoelectric zno-paper nanocomposite strain sensor," *Small*, vol. 6, pp. 1641–1646, 2010.

[51] H. P. Konka, M. A. Wahab, and K. Lian, "Piezoelectric fiber composite transducers for health monitoring in composite structures," *Sensors Actuators, A Phys.*, vol. 194, pp. 84–94, 2013.

[52] P. Selva, O. Cherrier, V. Budinger, F. Lachaud, and J. Morlier, “Smart monitoring of aeronautical composites plates based on electromechanical impedance measurements and artificial neural networks,” *Eng. Struct.*, vol. 56, pp. 794–804, 2013.

[53] L. Yin, X. M. Wang, and Y. P. Shen, “Damage-monitoring in composite laminates by piezoelectric films,” *Comput. Struct.*, vol. 59, pp. 623–630, 1996.

[54] S. H. Diaz Valdes and C. Soutis, “Delamination detection in composite laminates from variations of their model characteristics,” *J. Sound Vib.*, vol. 228, pp. 1–9, 1999.

[55] S. Song, Y. Hou, M. Guo, L. Wang, X. Tong, and J. Wu, “An investigation on the aggregate-shape embedded piezoelectric sensor for civil infrastructure health monitoring,” *Constr. Build. Mater.*, vol. 131, pp. 57–65, 2017.

[56] D. Ai, H. Zhu, and H. Luo, “Sensitivity of embedded active PZT sensor for concrete structural impact damage detection,” *Constr. Build. Mater.*, vol. 111, pp. 348–357, 2016.

[57] M. Martinez and A. Artemev, “Finite element analysis of broken fiber effects on the performance of active fiber composites,” *Compos. Struct.*, vol. 88, pp. 491–496, 2009.

[58] M. Martinez, R. Kernaghan, and A. Artemev, “Finite element analysis of broken fiber effects on hollow active fiber composites,” *J. Intell. Mater. Syst. Struct.*, vol. 21, pp. 107–113, 2010.

[59] J. Sirohi and I. Chopra, “Fundamental understanding of piezoelectric strain sensors,” *J. Intell. Mater. Syst. Struct.*, vol. 11, pp. 246–257, 2000.

[60] I.-G. Kim, “Impact damage detection in composite laminates using PVDF and PZT sensor signals,” *J. Intell. Mater. Syst. Struct.*, vol. 16, pp. 1007–1013, 2005.

[61] J. Schoeftner, G. Buchberger, A. Brandl, and H. Irschik, “Theoretical prediction and experimental verification of shape control of beams with piezoelectric patches and resistive circuits,” *Compos. Struct.*, vol. 133, pp. 746–755, 2015.

[62] Z. Wu, C. Han, and Z. Niu, “A 3D exact analysis of the boundary layer effect of asymmetric piezoelectric laminates with electromechanical coupling,” *Int. J. Solids Struct.*, vol. 72, pp. 118–129, 2015.

[63] Z. Hasan, “Shape and failure control of composite laminates using piezoelectric actuators,” *Proc. COMSOL Conf. 2010 Bost.*, pp. 1–8, 2010.

[64] C. K. Lee, “Theory of laminated piezoelectric plates for the design of distributed sensors/actuators. Part I: Governing equations and reciprocal relationships,” *J. Acoust. Soc. Am.*, vol. 87, pp. 1144–1158, 1990.

[65] D. B. Koconis, L. P. Kollar, and G. S. Springer, “Shape control of composite plates and shells with embedded actuators. II. desired shape specified,” *J. Compos. Mater.*, vol. 28, pp. 459–482, 1994.

[66] T. Kant and S. M. Shiyekar, “Cylindrical bending of piezoelectric laminates with a higher order shear and normal deformation theory,” *Comput. Struct.*, vol. 86, pp. 1594–1603, 2008.

[67] S. C. Her and C. S. Lin, “Deflection of cross-ply composite laminates induced by piezoelectric actuators,” *Sensors*, vol. 10, pp. 719–733, 2010.

[68] S. S. Vel and R. C. Batra, “Cylindrical bending of laminated plates with distributed and segmented piezoelectric actuators/sensors,” *AIAA J.*, vol. 38, pp. 857–867, 2000.

[69] W. D. Yang, W. Zhang, X. Wang, and G. Lu, “Nonlinear delamination buckling and expansion of functionally graded laminated piezoelectric composite shells,” *Int. J. Solids Struct.*, vol. 51, pp. 894–903, 2014.

[70] L. Wang, R. X. Bai, and H. Chen, “Analytical modeling of the interface crack between a piezoelectric actuator and an elastic substrate considering shear effects,” *Int. J. Mech. Sci.*, vol. 66, pp. 141–148, 2013.

[71] H. S. Tzou, J. P. Zhong, and J. J. Hollkamp, “Spatially distributed orthogonal

piezoelectric shell actuators: Theory and applications," *J. Sound Vib.*, vol. 177, pp. 363–378, 1994.

[72] S. K. Agrawal and D. Tong, "Modeling and shape control of piezoelectric actuator embedded elastic plates," *J. Intell. Mater. Syst. Struct.*, vol. 5, pp. 514–521, 1994.

[73] J.-H. Han and I. Lee, "Analysis of composite plates with piezoelectric actuators for vibration control using layerwise displacement theory," *Compos. Part B Eng.*, vol. 29, pp. 621–632, 1998.

[74] D. Varelis and D. A. Saravanos, "Coupled buckling and postbuckling analysis of active laminated piezoelectric composite plates," *Int. J. Solids Struct.*, vol. 41, pp. 1519–1538, 2004.

[75] C. R. Bowen, L. J. Nelson, R. Stevens, M. G. Cain, and M. Stewart, "Optimisation of interdigitated electrodes for piezoelectric actuators and active fibre composites," *J. Electroceramics*, vol. 16, pp. 263–269, 2006.

[76] J. George A. Rossetti, A. Pizzochero, and A. A. Bent, "Recent advances in active fiber composites technology," *ISAF 2000. Proc. 2000 12th IEEE Int. Symp. Appl. Ferroelectr. (IEEE Cat. No.00CH37076)*, vol. 2, pp. 753–756, 2001.

[77] D. J. Warkentin, "Modeling and electrode optimization for torsional IDE

piezoceramics," *Proc. SPIE 3985, Smart Struct. Mater. 2000 Smart Struct. Integr. Syst.*, vol. 3985, pp. 840–845, 2000.

[78] C. E. S. Cesnik and S. Shin, "On the modeling of integrally actuated helicopter blades," *Int. J. Solids Struct.*, vol. 38, pp. 1765–1789, 2001.

[79] R. B. Williams, D. J. Inman, M. R. Schultz, M. W. Hyer, and W. K. Wilkie, "Nonlinear tensile and shear behavior of macro fiber composite actuators," *J. Compos. Mater.*, vol. 38, pp. 855–869, 2004.

[80] Y. Chen, W. Viresh, and D. Zimcik, "Development and verification of real-time controllers for F / A-18 vertical fin buffet load alleviation," *Proc. SPIE, Smart Struct. Mater. 2006 Smart Struct. Integr. Syst.*, vol. 6173, pp. 1–12, 2006.

[81] A. K. Jha and J. N. Kudva, "Morphing aircraft concepts, classifications, and challenges," *SPIE, Smart Struct. Mater. 2004 Ind. Commer. Appl. Smart Struct. Technol.*, vol. 5388, pp. 213–224, 2004.

[82] D. Kim and J. Han, "Smart flapping wing using macro-fiber composite actuators," *Proc. SPIE, Smart Struct. Mater. 2006 Smart Struct. Integr. Syst.*, vol. 6173, 2006.

[83] R. Paradies and P. Ciresa, "Active wing design with integrated flight control using piezoelectric macro fiber composites," *Smart Mater. Struct.*, vol. 18, pp. 1–

9, 2009.

[84] F. Dai, H. Li, and S. Du, “Cured shape and snap-through of bistable twisting hybrid [0/90/metal]T laminates,” *Compos. Sci. Technol.*, vol. 86, pp. 76–81, 2013.

[85] S. C. Woo and N. S. Goo, “Effect of electric cyclic loading on fatigue cracking of a bending piezoelectric hybrid composite actuator,” *Compos. Sci. Technol.*, vol. 69, pp. 1764–1771, 2009.

[86] S.-C. Her and C.-S. Lin, “Vibration analysis of composite laminate plate excited by piezoelectric actuators.,” *Sensors*, vol. 13, pp. 2997–3013, 2013.